# Search for Dark Matter Produced in Association with Hadronically Decaying Bosons at $\sqrt{s} = 13\,\text{TeV}$ with the ATLAS Detector at the LHC

Paul Philipp Gadow

CERN-THESIS-2020-186
18 November 2020

Dissertation

Technische Universität München
Fakultät für Physik



Max-Planck-Institut für Physik
(Werner-Heisenberg-Institut)

# Search for Dark Matter Produced in Association with Hadronically Decaying Bosons at $\sqrt{s}$ = 13 TeV with the ATLAS Detector at the LHC

Paul Philipp Gadow

Vollständiger Abdruck der von der Fakultät für Physik der Technischen Universität München zur Erlangung des akademischen Grades eines

Doktors der Naturwissenschaften (Dr. rer. nat.)

genehmigten Dissertation.

*Vorsitzender:* apl. Prof. Dr. Norbert Kaiser

*Prüfer der Dissertation:* 1. Priv.-Doz. Dr. Oliver Kortner

2. Prof. Dr. Peter Fierlinger

Die Dissertation wurde am 12.10.2020 bei der Technischen Universität München eingereicht und durch die Fakultät für Physik am 26.10.2020 angenommen.

**Paul Philipp Gadow**
*Search for Dark Matter Produced in Association with Hadronically Decaying Bosons at $\sqrt{s} = 13$ TeV with the ATLAS Detector at the LHC*
Head of the thesis committee: apl. Prof. Dr. Norbert Kaiser
Reviewers: Priv.-Doz. Dr. Oliver Kortner and Prof. Dr. Peter Fierlinger
Supervisors: Dr. Sandra Kortner and Dr. Patrick Rieck

**Technische Universität München**
Physik-Department
James-Franck-Straße 1
85748 Garching bei München

**Max-Planck-Institut für Physik**
(Werner-Heisenberg-Institut)
Föhringer Ring 6
80805 München

# Abstract

Dark matter is a form of invisible matter which is predicted to constitute a vast portion of the universe. Although its existence is corroborated by numerous astrophysical observations on different cosmological scales, its direct observation is still pending, and its particle nature is an open question. This thesis describes searches for the production of dark matter particles using proton-proton collision data recorded by the ATLAS detector at the Large Hadron Collider at $\sqrt{s} = 13\,\text{TeV}$ centre-of-mass energy, investigating signatures of missing transverse momentum and hadronically decaying bosons. No significant deviations from the Standard Model prediction are observed, thereby providing constraints on the parameter space of models describing mediator-based dark matter production.

The $E_{\text{T}}^{\text{miss}} + V(q\bar{q})$ search targets processes with substantial missing transverse momentum $E_{\text{T}}^{\text{miss}}$ and hadronically decaying weak vector bosons $V$. It is based on a data sample corresponding to an integrated luminosity of $36.1\,\text{fb}^{-1}$. The results of the $E_{\text{T}}^{\text{miss}} + V(q\bar{q})$ search are interpreted in terms of a spin-1 $Z'$ mediator simplified model, excluding $Z'$ mediator masses of up to $830\,\text{GeV}$ for dark matter masses up to $280\,\text{GeV}$ at $95\,\%$ confidence level for mediator couplings to quarks of $0.25$ and dark matter particles of $1$. The results are also interpreted in terms of a simplified model with an extended Higgs sector and a pseudo-scalar mediator.

The $E_{\text{T}}^{\text{miss}} + \text{h}(\text{b}\bar{\text{b}})$ search investigates a similar experimental signature, targeting Higgs bosons $h$ decaying to $b$-quarks. It is based on a data sample corresponding to an integrated luminosity of $79.8\,\text{fb}^{-1}$ and exploits a jet algorithm with a variable radius parameter for the reconstruction of Higgs boson candidates in boosted event topologies. The results are interpreted in terms of a $Z'$-2HDM simplified model. For a specific choice of the model parameters, masses of the $Z'$ boson are excluded up to $2.85\,\text{TeV}$ at $95\,\%$ confidence level.

The $E_{\text{T}}^{\text{miss}} + s(\text{b}\bar{\text{b}})$ and $E_{\text{T}}^{\text{miss}} + s(VV)$ searches investigate the yet uncharted signature of missing transverse momentum and the production of a hypothetical dark Higgs $s$ decaying to $b$-quarks or pairs of weak vector bosons in their hadronic decay mode. While the $E_{\text{T}}^{\text{miss}} + s(\text{b}\bar{\text{b}})$ signature is investigated by a reinterpretation of the $E_{\text{T}}^{\text{miss}} + \text{h}(\text{b}\bar{\text{b}})$ search using the RECAST framework, the $E_{\text{T}}^{\text{miss}} + s(VV)$ search is based on the full Run-2 dataset corresponding to an integrated luminosity of $139\,\text{fb}^{-1}$. The reconstruction of the dark Higgs boson candidates is based on a novel jet reconstruction algorithm, which combines the calorimeter and inner detector tracking information. The results are interpreted in terms of a simplified model with spin-1 $Z'$ boson and spin-0 dark Higgs boson mediators, excluding dark Higgs boson masses of up to $230\,\text{GeV}$ and $Z'$ boson masses of up to $1.8\,\text{TeV}$ at $95\,\%$ confidence level for a specific choice of the other model parameters.

The implications of these results are discussed in the context of a summary of ATLAS dark matter searches.

# Contents


**1 Introduction** **1**

**I Foundations** **7**

**2 The Standard Model of Particle Physics** **9**
2.1 Introduction . . . 9
2.2 The Standard Model gauge group . . . 10
2.3 Particle content of the Standard Model . . . 10
2.4 The Standard Model in the Lagrangian formalism . . . 12
2.4.1 Gauge boson kinetic term . . . 13
2.4.2 Fermion kinetic and interaction term . . . 14
2.4.3 The Higgs mechanism in the Standard Model . . . 14
2.4.4 Yukawa interactions between fermions and the Higgs field . . . 17
2.5 Phenomenology of the Standard Model . . . 17
2.6 Limitations of the Standard Model . . . 18

**3 Dark matter** **21**
3.1 Introduction . . . 21
3.2 Cosmology in a nutshell . . . 22
3.3 Dark matter relic density . . . 26
3.4 Evidence for dark matter . . . 28
3.4.1 Galactic scale . . . 28
3.4.2 Galaxy cluster scale . . . 30
3.4.3 Cosmological scale . . . 32
3.5 Candidates for dark matter particles . . . 36
3.6 Search for WIMP dark matter . . . 38
3.6.1 Direct detection experiments . . . 39
3.6.2 Indirect detection experiments . . . 41
3.6.3 Searches for dark matter at particle colliders . . . 42
3.7 Theoretical frameworks for dark matter production at particle colliders 44
3.7.1 Simplified model for dark matter production with a spin-1 $Z'$ mediator . . . 46
3.7.2 Simplified model with an extended Higgs sector and a pseudo-scalar mediator . . . 47
3.7.3 $Z'$-2HDM simplified model . . . 49
3.7.4 Two mediator dark matter model . . . 50

**4 Proton-proton collision phenomenology** **53**
4.1 Basic concepts . . . 53
4.2 Parton density functions . . . 55
4.3 Calculation of cross-sections . . . 56
4.4 Event simulation . . . 59
4.5 Hadronic jets . . . 59

**5 Experimental apparatus** **63**
5.1 Introduction . . . 63
5.2 The Large Hadron Collider . . . 65
5.3 The ATLAS detector . . . 68
5.3.1 The ATLAS coordinate system . . . 69
5.3.2 Magnet system . . . 70
5.3.3 Inner Detector . . . 71
5.3.4 Calorimetry . . . 73
5.3.5 Muon Spectrometer . . . 77
5.3.6 Trigger . . . 78
5.3.7 Grid computing . . . 80

**6 Experimental methods** **81**
6.1 Event reconstruction . . . 81
6.1.1 Introduction . . . 81
6.1.2 Reconstruction of basic objects . . . 82
6.1.3 Electrons . . . 85
6.1.4 Muons . . . 88
6.1.5 Jets . . . 93
6.1.6 Tau leptons . . . 105
6.1.7 Missing transverse momentum . . . 105
6.2 Statistical methods . . . 109
6.3 RECAST . . . 112

**II Studies of the ATLAS muon trigger** **113**

**7 Improvements to the ATLAS muon trigger** **115**
7.1 Introduction . . . 115
7.2 Rate reduction of the L1MU4 trigger . . . 115
7.2.1 The ATLAS L1 muon trigger in Run-2 . . . 115
7.2.2 The L1MU4 coincidence logic tuning . . . 117
7.2.3 Data and method . . . 118
7.2.4 Results . . . 120

**III Searches for dark matter** **125**

**8 Searches for dark matter in association with heavy bosons** **127**
8.1 General search strategy . . . 127
8.2 Data and simulated events . . . 129

8.2.1 Collision data . . . 129
8.2.2 Simulated event samples . . . 131
8.2.3 Triggers . . . 133
8.3 Object definitions in searches for dark matter produced in association with heavy bosons . . . 136

**9 Search for dark matter produced in association with a hadronically decaying weak vector boson 139**
9.1 Introduction . . . 139
9.2 Signal and background processes . . . 139
9.2.1 Simplified model for dark matter production with a spin-1 $Z'$ mediator . . . 140
9.2.2 Simplified model with an extended Higgs sector and a pseudo-scalar mediator . . . 143
9.2.3 Background processes . . . 144
9.2.4 Simulated Monte Carlo samples . . . 144
9.3 Analysis strategy . . . 145
9.4 Object and event selection . . . 148
9.4.1 Object selection . . . 148
9.4.2 Baseline event selection . . . 149
9.4.3 Multijet-suppression event selection requirements . . . 150
9.4.4 Signal region event selection . . . 150
9.4.5 Validation region event selection . . . 157
9.5 Background estimation . . . 157
9.5.1 1 muon control region . . . 158
9.5.2 2 lepton control region . . . 158
9.5.3 Multijet background estimate . . . 159
9.6 Systematic uncertainties . . . 162
9.6.1 Experimental systematic uncertainties . . . 162
9.6.2 Theoretical systematic uncertainties . . . 163
9.7 Statistical model . . . 166
9.8 Results . . . 167
9.8.1 Observed results . . . 167
9.8.2 Impact of systematic uncertainties . . . 171
9.8.3 Constraints on the spin-1 $Z'$ mediator simplified model . . . 175
9.8.4 Constraints on the $a$-2HDM simplified model . . . 175
9.9 Conclusion of the $E_{\mathrm{T}}^{\mathrm{miss}} + V(q\bar{q})$ search . . . 177

**10 Search for dark matter in association with a Higgs boson decaying to $b$-quarks 181**
10.1 Introduction . . . 181
10.2 Signal and background processes . . . 182
10.2.1 $Z'$-2HDM simplified model . . . 182
10.2.2 Background processes . . . 183
10.2.3 Simulated Monte Carlo samples . . . 184
10.3 Analysis strategy . . . 185
10.4 Object and event selection . . . 186

10.4.1 Object selection . . . 187
10.4.2 Baseline selection . . . 190
10.4.3 Signal region selection . . . 191
10.5 Background estimation . . . 194
10.5.1 1 muon control region . . . 195
10.5.2 2 lepton control region . . . 196
10.5.3 Multijet background estimate . . . 197
10.6 Systematic uncertainties . . . 203
10.6.1 Experimental systematic uncertainties . . . 203
10.6.2 Theoretical systematic uncertainties . . . 204
10.7 Statistical model . . . 205
10.8 Results . . . 206
10.8.1 Observed results . . . 206
10.8.2 Impact of systematic uncertainties . . . 210
10.8.3 Constraints on the Z′-2HDM simplified model . . . 212
10.9 Conclusion of the $E_{\mathrm{T}}^{\mathrm{miss}} + \mathrm{h}(\mathrm{b\bar{b}})$ search . . . 215

**11 Search for dark matter in association with a dark Higgs boson decaying to $b$-quarks 217**
11.1 Introduction . . . 217
11.2 Signal processes . . . 218
11.2.1 2MDM simplified model . . . 218
11.2.2 Simulated Monte Carlo samples for signal processes . . . 219
11.3 Systematic uncertainties on the signal process . . . 219
11.4 Technical implementation . . . 220
11.5 Results . . . 222
11.6 Conclusion of the $E_{\mathrm{T}}^{\mathrm{miss}} + s(\mathrm{b\bar{b}})$ search . . . 223

**12 Search for dark matter in association with a dark Higgs boson decaying to a pair of weak vector bosons 227**
12.1 Introduction . . . 227
12.2 Signal and background processes . . . 227
12.2.1 Background processes . . . 228
12.2.2 Simulated Monte Carlo samples . . . 228
12.3 Analysis strategy . . . 229
12.4 Object and event selection . . . 232
12.4.1 Object selection . . . 232
12.4.2 Baseline selection . . . 235
12.4.3 Signal region selection . . . 236
12.5 Background estimation . . . 241
12.5.1 1 muon control region . . . 243
12.5.2 2 lepton control region . . . 243
12.5.3 Multijet background estimate . . . 243
12.6 Systematic uncertainties . . . 245
12.6.1 Experimental systematic uncertainties . . . 245
12.6.2 Theoretical systematic uncertainties . . . 246
12.7 Statistical model . . . 247

12.8 Results . . . . . 248
12.8.1 Observed results . . . . . 248
12.8.2 Impact of systematic uncertainties . . . . . 252
12.8.3 Constraints on the 2MDM simplified model . . . . . 256
12.9 Conclusion of the $E_{\mathrm{T}}^{\mathrm{miss}} + s(VV)$ search . . . . . 256

**13 Status of dark matter searches with ATLAS** **259**
13.1 Introduction . . . . . 259
13.2 Simplified models with spin-1 $\mathrm{Z}'$ mediators . . . . . 259
13.3 Simplified models with extended Higgs sector . . . . . 263
13.4 Simplified models with two mediators . . . . . 267

**14 Conclusion** **269**

# 1 Introduction

In the last century, particle physics has achieved a description of Nature at microscopic scales vastly exceeding the "small distances as hitherto escape Observation" whose exploration Isaac Newton foreshadowed [294]. The best theory in terms of accurately and fundamentally describing the observed phenomena to date is the Standard Model (SM) of electroweak and strong interactions. The SM is confirmed by a series of breakthrough discoveries [296], including the observation of the W and Z bosons in the year 1983 [31, 120, 32, 116] and the discovery of the Higgs boson in the year 2012 [67, 163], which completed the inventory of the Standard Model's particle content.

At the same time, astrophysical observations at macroscopic scales indicate the presence of gravitationally interacting but otherwise invisible non-baryonic matter in the universe [297]. Despite the tremendous success of the SM, it does not provide a particle candidate for the so-called dark matter. Elucidating on its potential particle nature, its origin and its interactions is among the most important problems in fundamental physics. Dark matter particles may be produced in high-energy proton-proton collisions at the Large Hadron Collider (LHC). If produced, dark matter remains elusive to the detectors and may only be detected via its recoil against other particles. The very same particles, whose discovery corroborated the SM are now used as probes for dark matter production.

This dissertation discusses four searches for dark matter at the LHC with the ATLAS detector.

First, a search for dark matter in association with a hadronically decaying weak vector boson is discussed. The hadronic decay products of the vector boson give rise to collimated sprays of particles, which are referred to as jets. Depending on the Lorentz boost of the weak vector boson candidate, it is reconstructed either using two well-separated jets or a single large-radius jet with jet substructure information.

Second, a search for dark matter production in association with a Higgs boson decaying to $b$-quarks is discussed. The Higgs boson candidate is reconstructed from the striking signature of two $b$-jets in the detector, which are identified using multivariate techniques, known as $b$-tagging. In events with boosted Higgs boson candidates, these are reconstructed using large-radius jets, while the $b$-tagging information is supplemented by sub-jets constructed from inner detector tracks. High $b$-tagging efficiency in event topologies with highly boosted Higgs boson candidates is achieved by reconstructing the sub-jets with a variable radius size which adapts to the momentum of the Higgs boson candidate.

Third, a reinterpretation of the previously discussed search in terms of a hypothetical dark Higgs boson decaying to a pair of $b$-quarks is discussed. The existence of a dark

Higgs boson is motivated by spontaneous symmetry breaking in the dark sector. The dark Higgs boson can be sought for in its decays into visible particles due to mixing with the SM Higgs boson. The reinterpretation is enabled by the RECAST framework and represents the proof-of-concept of faithful and automated reinterpretation of ATLAS dark matter searches.

Finally, a search for dark matter production in association with a dark Higgs boson decaying to a pair of weak vector bosons in the hadronic decay channel is discussed. The challenging event topology of up to four jets from diboson decay requires the use of a novel jet reconstruction technique. Track-assisted-reclustered (TAR) jets with large radius parameter are formed by reclustering small-radius jets. The jet substructure information is computed from inner detector tracks which are matched to the small-radius jets. Two event topologies are considered, in which the TAR jet either contains the full dark Higgs decay or is complemented by adding additional small-radius jets.

No significant deviations from the SM background predictions are observed in the searches. They are interpreted in terms of simplified models of dark matter production with varying degrees of complexity to set limits on the parameter space of these models.

In addition to the searches for dark matter, a study about the optimisation of the first-level ATLAS muon trigger is presented. Modifications of the trigger coincidence logic enable a reduction of the trigger rate in the forward region of the detector while maintaining a high trigger efficiency.

**Personal contributions**

High-energy physics experiments are conducted in extensive, international collaborations. The searches for dark matter presented in this dissertation have been performed using data recorded by the ATLAS experiment, which has been designed, constructed, and maintained by an international collaboration of more than 3000 persons. Most tasks, such as detector maintenance and operation, development and calibration of event reconstruction algorithms, and distributed analysis of the recorded data is carried out centrally in dedicated working groups. Therefore, this work builds on the contribution of many past and present members of the ATLAS collaboration, whose contributions are referenced throughout the text. Figures with

the label **ATLAS** have been shown in ATLAS peer-reviewed publications, while those with the label **ATLAS Preliminary** have been featured in ATLAS conference notes or public notes. Figures without those labels have been taken from non-ATLAS publications and are referenced accordingly. All figures and tables without such a reference in the caption have been produced by the author of this dissertation.

The results presented in this dissertation have been published as peer-reviewed journal publications and as ATLAS conference notes or ATLAS public notes, which have undergone a multi-stage internal peer-review process by the ATLAS collaboration. The contributions of the author in these endeavours are listed below.

- $E_{\mathrm{T}}^{\mathrm{miss}} + V(q\bar{q})$ search in Ref. [88] and in Ref. [40]
  *The author made large contributions to the analysis software development and produced the inputs on which the statistical analysis is based. He developed and applied the multijet background estimation technique, which was also used in Ref. [92]. The author was responsible for the derivation of the exclusion limits on models of dark matter production and carried out all studies on validating the statistical model. He further served as a liaison for incorporating the results in a publication summarising the broad ATLAS dark matter and dark energy research programme. Finally, the author was co-editor of the internal documentation.*

- $E_{\mathrm{T}}^{\mathrm{miss}} + \mathrm{h}(\mathrm{b\bar{b}})$ search in Ref. [91]
  *The author maintained the analysis software and made large contributions to it. He commissioned a novel object-based $E_T^{miss}$ significance observable and studied its optimal use in the analysis, including an estimate of its effect in reducing the multijet background. The author produced the inputs on which the statistical analysis is based. He was responsible for the derivation of the exclusion limits on models of dark matter production and carried out all studies on validating the statistical model. Furthermore, he investigated the relative improvement in the limits due to the novel variable-radius track jet algorithm.*

- $E_{\mathrm{T}}^{\mathrm{miss}} + s(\mathrm{b\bar{b}})$ reinterpretation in Ref. [76]
  *The author implemented the $E_T^{miss} + h(b\bar{b})$ search in the RECAST framework and devised the simulated signal samples. He co-coordinated the effort and co-edited Ref. [76] with Lukas Heinrich.*

- $E_{\mathrm{T}}^{\mathrm{miss}} + s(VV)$ (hadronic) search in Ref. [89]
  *The author developed the analysis software using the* XAMPP *framework and maintained it. He implemented the TAR jet algorithm and the associated systematic uncertainty estimation and validated its performance. The author devised the simulated signal samples and was responsible for managing the datasets of collision data and simulated events. He made large contributions towards designing the event selection. The author produced the inputs on which the statistical analysis is based and implemented the statistical model. He was responsible for the derivation of the exclusion limits on models of dark matter production and carried out all studies on validating the statistical model. Furthermore, he studied the effect of theory systematic uncertainties on signal and background processes. Finally, the author was co-editor of the internal documentation.*

### System of units

Throughout this dissertation, natural units are used. In contrast to the *Système international d'unités* (SI), the units of the most common observables are expressed by natural constants. Formally this is realised by setting the speed of light $c$, Planck's constant $\hbar$, and the electric field constant $\varepsilon_0$ to unity

$$c = \hbar = \varepsilon_0 = 1. \tag{1.1}$$

The unit of energy is not specified and is chosen to be the electron volt ($[E] = \mathrm{eV}$), which is the amount of kinetic energy a point charge of $1\,\mathrm{C}$ gains from acceleration in an electric field with potential difference of $1\,\mathrm{V}$. Consequently, all units are expressed in powers of $\mathrm{eV}$. As gravity usually is neglected in the description of sub-atomic phenomena, Newton's constant is still expressed in SI units.

# Part I

Foundations

# 2 The Standard Model of Particle Physics

> *Tyger, tyger, burning bright*
> *In the forests of the night,*
> *What immortal hand or eye*
> *Could frame thy fearful symmetry?*
>
> **— William Blake**
> Poems of William Blake, edited by W. B. Yeats.
> London: G. Routledge & Sons, 1905

## 2.1 Introduction

The Standard Model of electroweak and strong interactions (SM) is the relativistic quantum field theory, which describes the elementary constituents of matter and their interactions. It is the empirically adequate theory of Nature, as its validity is supported by a large number of measurements, including the observation of the weak gauge bosons [31, 120, 32, 116], the discovery of the top quark [184, 182], and the discovery of the Higgs boson [67, 163].

The constituents of matter are the particles with half-integer spin, which are called fermions. All known interactions between the particles in the SM are dictated by the underlying internal symmetries of the theory. The gauge principle naturally introduces the spin-1 gauge bosons as mediators of forces by insisting on the invariance of the theory under local phase transformations. Interactions between particles are described by the exchange of gauge bosons. The masses of the fermions and massive gauge bosons are generated in a gauge-invariant way by Yukawa-interactions and electroweak spontaneous symmetry breaking. The spin-0 Higgs boson is a direct consequence of the latter mechanism.

This chapter gives a brief introduction to the salient concepts of the SM, following the presentation in Refs. [251, 240] closely. A more complete and pedagogic treatment is given in Refs. [279, 300, 316].

## 2.2 The Standard Model gauge group

The SM is a Yang-Mills theory [348, 252] based on the gauge group

$$\mathrm{SU}(3)_C \times \mathrm{SU}(2)_L \times \mathrm{U}(1)_Y. \tag{2.1}$$

- The $\mathrm{SU}(3)_C$ component is the colour symmetry group associated with the **strong interaction**, which is described by quantum chromodynamics (QCD) [238, 237, 302, 224]. All particles carrying colour charge participate in the strong interaction. The gauge bosons of strong interactions are the eight massless gluons $G^a_\mu, a = 1, \ldots, 8$, which themselves also carry colour charge. The coupling constant of the strong interaction is $g_s$, or equivalently $\alpha_s = g_s^2/4\pi$.

- The $\mathrm{SU}(2)_L \times \mathrm{U}(1)_Y$ component is the symmetry group associated with **electroweak interactions** [229, 346, 312]. All particles carrying weak isospin $(I, I_3)$ and weak hypercharge $Y$ participate in electroweak interactions. The gauge bosons $W^i_\mu$, $i = 1, 2, 3$, and $B_\mu$, and the gauge coupling constants $g$ and $g'$ correspond to the factors $\mathrm{SU}(2)_L \times \mathrm{U}(1)_Y$, respectively. The electroweak symmetry has to be broken by the Brout-Englert-Guralnik-Hagen-Higgs-Kibble mechanism [218, 246, 247, 239, 248, 262] to describe the massive $\mathrm{W}^\pm$, Z gauge bosons of the weak interaction and unveil the electromagnetic $\mathrm{U}(1)_Q$ gauge symmetry. The quantum numbers classifying the fermions with respect to the $\mathrm{SU}(2)_L \times \mathrm{U}(1)_Y$ group and their electric charge $Q$ are related by the Gell-Mann-Nishijima relation $Q = I_3 + Y/2$ [293, 228].

  Only the left-handed chirality eigenstates of the fermions

  $$\psi(x)_L = \frac{1}{2}(1 - \gamma_5)\psi(x) \tag{2.2}$$

  carry weak isospin $I_3 = \pm 1/2$ and can participate in flavour-changing interactions via couplings to the charged $\mathrm{W}^\pm$ bosons.

  The right-handed chirality eigenstates of the fermions

  $$\psi(x)_R = \frac{1}{2}(1 + \gamma_5)\psi(x) \tag{2.3}$$

  carry weak isospin $I_3 = 0$ and do not couple to the weak gauge bosons, leading to maximum parity violation in the weak interaction.

## 2.3 Particle content of the Standard Model

The fermions are categorised in quarks and leptons. Figure 2.1 shows a schematic overview of the quarks and leptons arranged in three different generations. The three generations appear to have identical gauge interactions and only differ by their flavour quantum number and their mass. To every fermion, there is a corresponding

anti-fermion with the same mass and spin but inverted charge quantum numbers (not shown in Figure 2.1).

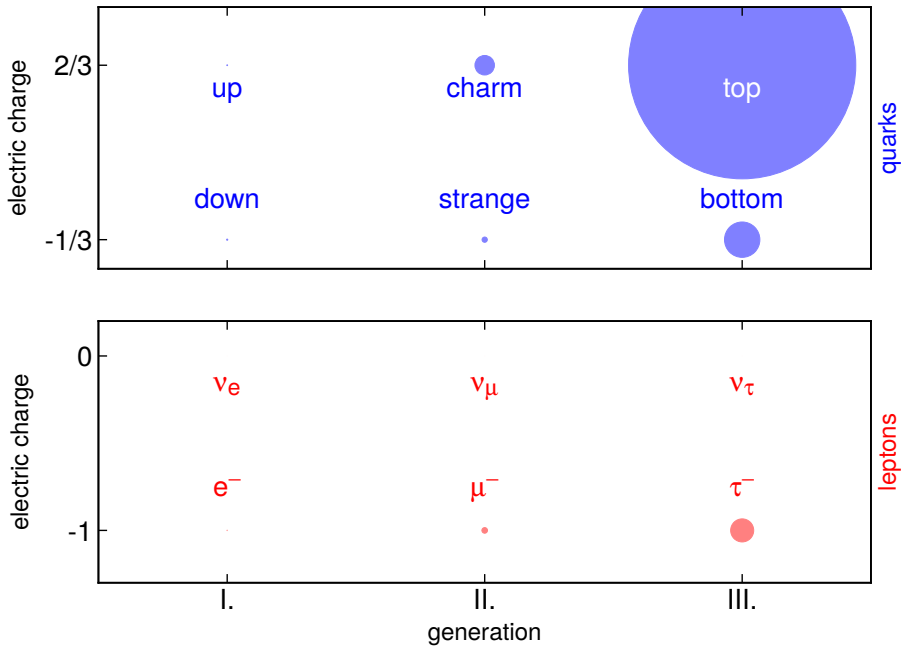



**Fig. 2.1.:** Schematic overview of quarks and leptons, grouped by affiliation to generation and electric charge. The size of the circles is proportional to the fermion mass.

There are six quark flavours, which can be grouped by their electric charge in the up-type quarks $\mathrm{u}_i$ ($i = 1, 2, 3$) with electric charge $2/3$ and down-type quarks $\mathrm{d}_i$ ($i = 1, 2, 3$) with electric charge $-1/3$. The up-type quarks are the up (u), charm (c), and top (t) quarks. The down-type quarks are the down (d), strange (s), and bottom (b) quarks. Quarks are the only fermions with colour charge $q^\alpha, \alpha = r, g, b$, and are represented as colour charge triplets under $\mathrm{SU}(3)_C$

$$q = \begin{pmatrix} q^r \\ q^g \\ q^b \end{pmatrix} . \tag{2.4}$$

The left-handed quarks carry weak isospin $I_3 = \pm 1/2$ and transform as doublets of up- and down-type quarks under $\mathrm{SU}(2)_L$

$$\begin{pmatrix} \mathrm{u} \\ \mathrm{d}' \end{pmatrix}_L , \begin{pmatrix} \mathrm{c} \\ \mathrm{s}' \end{pmatrix}_L , \begin{pmatrix} \mathrm{t} \\ \mathrm{b}' \end{pmatrix}_L , \tag{2.5}$$

whereas the right-handed quarks carry weak isospin $I_3 = 0$ and transform as singlets

$$\mathrm{u}_R, \mathrm{d}_R, \mathrm{c}_R, \mathrm{s}_R, \mathrm{t}_R, \mathrm{b}_R. \tag{2.6}$$

Here, $\mathrm{d}'_i = \mathrm{d}', \mathrm{s}', \mathrm{b}'$ are the weak eigenstates, which are obtained from of the mass eigenstates $\mathrm{d}_i = \mathrm{d}, \mathrm{s}, \mathrm{b}$ by a rotation $\mathrm{d}'_i = \sum_j V_{ij} d_j$ with the Cabibbo-Kobayashi-Maskawa mixing matrix [151, 264, 335]

$$\begin{aligned} V &= \begin{pmatrix} |V_{ud}| & |V_{us}| & |V_{ub}| \\ |V_{cd}| & |V_{cs}| & |V_{cb}| \\ |V_{td}| & |V_{ts}| & |V_{tb}| \end{pmatrix} \\ &= \begin{pmatrix} 0.974\,17 \pm 0.000\,21 & 0.2248 \pm 0.0006 & 0.000\,409 \pm 0.000\,039 \\ 0.220 \pm 0.005 & 0.995 \pm 0.016 & 0.004\,05 \pm 0.0015 \\ 0.0082 \pm 0.0006 & 0.04 \pm 0.0027 & 1.0009 \pm 0.031 \end{pmatrix}. \end{aligned} \tag{2.7}$$

Quarks participate in strong, electromagnetic, and weak interactions.

There are six lepton flavours, which also can be grouped by their electric charge in the charged leptons and neutral leptons. The charged leptons are the electron ($\mathrm{e}^-$), the muon ($\mu^-$), and the tau lepton ($\tau^-$). They carry the electromagnetic charge $q_{\ell^\pm_i} = -1$. The neutral leptons are the associated neutrinos $\nu_\mathrm{e}$, $\nu_\mu$, $\nu_\tau$. The left-handed leptons carry weak isospin $I_3 = \pm 1/2$ and transform as doublets under $\mathrm{SU}(2)_L$

$$\begin{pmatrix} \nu_\mathrm{e} \\ \mathrm{e}^- \end{pmatrix}_L, \begin{pmatrix} \nu_\mu \\ \mu^- \end{pmatrix}_L, \begin{pmatrix} \nu_\tau \\ \tau^- \end{pmatrix}_L, \tag{2.8}$$

whereas the charged right-handed leptons carry weak isospin $I_3 = 0$ and transform as singlets

$$\mathrm{e}^-{}_R, \mu^-{}_R, \tau^-{}_R. \tag{2.9}$$

To date, neither right-handed neutrinos nor left-handed anti-neutrinos have been observed. The charged leptons participate in electromagnetic and weak interactions, while the neutrinos only participate in weak interactions.

## 2.4 The Standard Model in the Lagrangian formalism

The SM is elegantly and concisely formulated in the Lagrangian formalism of quantum field theory. The particles are described by quantum fields, which are operators on the Hilbert space of particle states. The fermions are described by spin-1/2 spinor fields $\psi(x)$. The gauge bosons are described by spin-1 vector fields $A_\mu$. The Higgs boson, the only spin-0 particle in the SM, is described by a scalar field $\phi(x)$.

Remarkably, all dynamics of elementary particles are determined by the action

$$S[\varphi] = \int \mathrm{d}x\, \mathcal{L}\left(\varphi(x), \partial_\mu \varphi(x)\right), \tag{2.10}$$

where $\varphi$ is a generic field variable and $\mathcal{L}\left(\varphi(x)\right)$ is the Lorentz-invariant Lagrangian (density). The equations of motions for elementary particles are obtained by the means of Hamilton's principle

$$\delta S = S[\varphi + \delta\varphi] - S[\varphi] = 0. \tag{2.11}$$

The Lagrangian of the SM consists of the four parts[1]

$$\mathcal{L} = \mathcal{L}_{\text{Gauge}} + \mathcal{L}_{\text{Fermion}} + \mathcal{L}_{\text{Higgs}} + \mathcal{L}_{\text{Yukawa}}, \tag{2.12}$$

which are described in the following paragraphs.

### 2.4.1 Gauge boson kinetic term

The gauge-invariant gauge boson kinetic term

$$\mathcal{L}_{\text{Gauge}} = -\frac{1}{4} G^a_{\mu\nu} G_a^{\mu\nu} - \frac{1}{4} W^i_{\mu\nu} W_i^{\mu\nu} - \frac{1}{4} B_{\mu\nu} B^{\mu\nu} \tag{2.13}$$

is required to promote the gauge bosons, which emerge from the gauge principle, to dynamical fields. It consists of the field strength tensors of the strong interaction

$$G^a_{\mu\nu} = \partial_\mu G^a_\nu - \partial_\nu G^a_\mu - g_s f_{abc} G^b_\mu G^c_\nu, \tag{2.14}$$

where $f_{abc}$ denotes the structure constants of the $\mathrm{SU}(3)_C$ group, and the field strength tensors for the electroweak gauge bosons

$$W^i_{\mu\nu} = \partial_\mu W^i_\nu - \partial_\nu W^i_\mu + g W^a_\mu, \tag{2.15}$$

where the totally antisymmetric tensor $\varepsilon_{ijk}$ denotes the structure constants of the $\mathrm{SU}(2)_L$ group. The terms associated with the structure constants are responsible for the non-trivial gauge transformations and introduce the three- and four-point direct interactions among the weak gauge bosons and among the gluons. No explicit mass terms are present in $\mathcal{L}_{\text{Gauge}}$, as their presence would violate gauge invariance. They are introduced via electroweak spontaneous symmetry breaking.

[1] In principle, $\mathcal{L}$, could be extended by a term associated with the strong interaction, violating charge and parity (CP) symmetry. As there is no evidence for CP violation in strong interactions, this term is neglected. Also, additional gauge-fixing terms, e.g. $\delta\mathcal{L} = -(\partial_\mu A^\mu)^2/2\zeta$ with the parameter $\zeta$ for a gauge field $A_\mu$, are neglected in the following discussion.

### 2.4.2 Fermion kinetic and interaction term

The fermion kinetic term introducing interactions with the gauge bosons

$$\mathcal{L}_{\text{Fermion}} = \sum_j \overline{\psi}_L^j i\gamma^\mu D_\mu^L \psi_L^j + \sum_{j,\sigma} \overline{\psi}_{R\sigma}^j i\gamma^\mu D_\mu^R \psi_{R\sigma}^j \tag{2.16}$$

describes the left-handed fermion fields $\psi_L^{j,T} = (\psi_{L+}^j \psi_{L-}^j)$ and the right-handed fermion fields $\psi_R^{j\sigma}$. They carry the generation index $j$ and the component index $\sigma = \pm$, which denotes up-type fermions $(+)$ and down-type fermions $(-)$. Their interactions with the gauge bosons via the minimal substitution rule is introduced by the covariant derivative

$$D_\mu^{L,R} = \partial_\mu - ig_s T_a G_\mu^a - igI_j^{L,R} W_\mu^j + ig' \frac{Y}{2} B_\mu. \tag{2.17}$$

$T_a$, $I_a^L$, and $\frac{Y}{2}$ are the generators of the groups $\text{SU}(3)_C$, $\text{SU}(2)_L$, and $\text{U}(1)_Y$, respectively. They are defined by $[T_a, T_b] = if_{abc}T_c$ and $[I_a^L, I_b^L] = i\varepsilon_{abc}I_c^L$. In the triplet representation, $T_a = \frac{1}{2}\lambda_a$ can be written with the Gell-Mann matrices $\lambda_a, a = 1, \ldots, 8$. Similarly, $I_j^L = \frac{1}{2}\sigma_j$ can be written in the doublet representation with the Pauli matrices $\sigma_j, j = 1, 2, 3$. For the sake of consistent notation, the associated term for right-handed particles is $I_j^R = 0$. No mass terms for Fermions are included in $\mathcal{L}_{\text{Fermion}}$, as they would mix left- and right-handed fields and would explicitly break gauge invariance. The fermion mass terms are introduced via gauge-invariant Yukawa interactions between the fermions and the Higgs field.

### 2.4.3 The Higgs mechanism in the Standard Model

The Higgs field term

$$\mathcal{L}_{\text{Higgs}} = (D_\mu \phi)^\dagger (D^\mu \phi) - V(\phi) \tag{2.18}$$

introduces a complex scalar Higgs doublet $\phi = \begin{pmatrix} \phi^+ \\ \phi^0 \end{pmatrix}$ with hypercharge $Y = 1$ and the covariant derivative

$$D_\mu = \partial_\mu + ig\frac{1}{2}\sigma_j W_\mu^j + ig' \frac{Y}{2} B_\mu. \tag{2.19}$$

The Higgs potential

$$V(\phi) = \mu^2 \phi^\dagger \phi + \frac{\lambda}{4}(\phi^\dagger \phi)^2. \tag{2.20}$$

has two free parameters $\mu^2$ and $\lambda > 0$. For $\mu^2 > 0$, $\mathcal{L}_{\text{Higgs}}$ describes a scalar field with mass $\mu$ which can self-interact via a four-point interaction vertex with coupling $\lambda$ and whose ground state corresponds to $\phi = 0$. More interesting is the case

$\mu^2 < 0$, which is shown in Figure 2.2 for a specific choice of these parameters, as it allows introducing mass terms for the gauge bosons via spontaneous symmetry breaking while respecting the $\mathrm{SU}(2)_L \times \mathrm{U}(1)_Y$ gauge-invariance. The potential $V(\phi)$

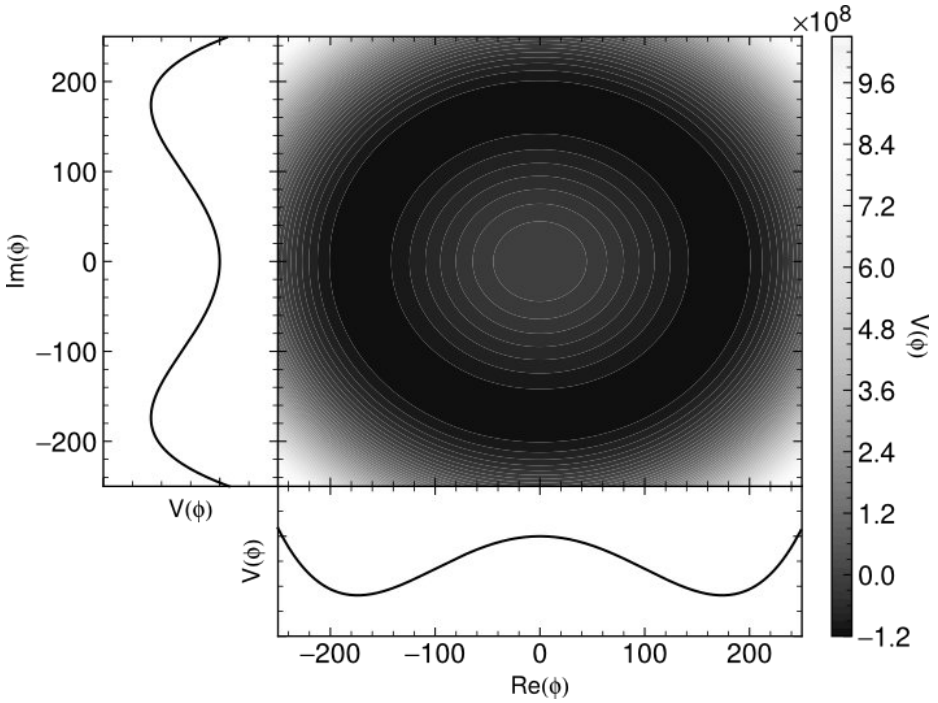



**Fig. 2.2.:** The Higgs potential $V(\phi)$ with parameters $\mu^2 = -(125\,\mathrm{GeV})^2/2$ and $\lambda = 0.13$ is shown in dependency of the real and imaginary part of $\phi$. For this choice of parameters $\mu^2 < 0$ and $\lambda > 0$ the potential assumes its minimum at the circle with radius $v/\sqrt{2} = 246\,\mathrm{GeV}/\sqrt{2}$, which is defined by the vacuum expectation value $v$.

is minimised by all field configurations on the circle in the $\mathrm{Re}(\phi)$-$\mathrm{Im}(\phi)$-plane defined by $|\phi|^2 = 2\mu^2/\lambda$. Choosing the specific real and electrically neutral ground state configuration

$$\phi_0 = \langle 0|\phi|0\rangle = \frac{1}{\sqrt{2}}\begin{pmatrix}0\\ v\end{pmatrix}, \tag{2.21}$$

spontaneously breaks the $\mathrm{SU}(2)_L \times \mathrm{U}(1)_Y$ symmetry of the Lagrangian. Here, $v = 2\mu/\sqrt{\lambda}$ denotes the vacuum expectation value. Although the specific choice of the ground state breaks the symmetry, the Lagrangian and the physical system are still invariant under symmetry operations[2].

[2]This statement can be illustrated by considering a scalar field $\phi$ and a potential $V = V(|\phi|)$. The potential possesses a U(1) symmetry and the associated Lagrangian density $\mathcal{L} = \left|\partial_\mu \phi\right|^2 - V(|\phi|)$ is symmetric under transformations $\phi \mapsto \phi' = e^{i\alpha}\phi$. If the minimum $\phi_0 = v$ of the potential $V$ does not occur at $v = 0$, the symmetry of the ground state is broken $\phi_0' = e^{i\alpha}v \neq \phi_0$.

The $U(1)_Q$ symmetry of the vacuum, corresponding to the conservation of electric charge, remains unbroken, as the operator associated with electric charge $Q = I_3 + \frac{Y}{2}$ leaves the ground state invariant.

Perturbative calculations should involve expansions around the ground state. The Higgs doublet can be expanded around the ground state $\phi_0$ in the real field $h(x)$ and the three real fields $\theta^i(x)$

$$\phi(x) = \frac{1}{\sqrt{2}} \begin{pmatrix} 0 \\ v + h(x) \end{pmatrix} e^{i I_j^L \theta^j(x)}. \tag{2.22}$$

In the unitary gauge, $\theta^j(x) = 0$, the massless Goldstone modes $\theta^j(x)$ are absorbed by the weak gauge bosons, giving them a longitudinal polarisation. The Higgs field term after spontaneous symmetry breaking now reads

$$\begin{aligned} \mathcal{L}_{\text{Higgs}} =& \frac{1}{2}\partial^\mu h \partial_\mu h - \mu^2 h^2 \\ &+ \frac{g^2}{8} v^2 \left( W_\mu^+ W^{\mu +} + W_\mu^- W^{\mu -} \right) + \frac{g^2}{4\cos^2\theta_W} v^2 Z_\mu Z^\mu \\ &+ (2vh + h^2) \left( \frac{g^2}{4} W_\mu^+ W^{\mu -} + \frac{g^2}{8\cos^2\theta_W} Z_\mu Z^\mu \right) \\ &+ \lambda v h^3 + \frac{\lambda}{4} h^4. \end{aligned} \tag{2.23}$$

It explicitly describes (with the number corresponding to the line in Equation (2.23))

1. the massive real scalar Higgs boson with explicit kinetic and mass term,
2. the mass terms $m_{\mathrm{W}^\pm} = g^2 v^2/4$ and $m_{\mathrm{Z}} = g^2/8\cos^2\theta_W$ for the massive weak vector gauge bosons $\mathrm{W}^\pm$ and Z, respectively,
3. interactions between the Higgs boson and the weak vector gauge bosons, and
4. triple and quartic couplings of the Higgs boson.

After electroweak symmetry breaking the associated four gauge fields are

$$W_\mu^\pm = \frac{1}{\sqrt{2}} \left( W_\mu^1 \pm W_\mu^2 \right), \tag{2.24}$$

$$Z_\mu = W_\mu \cos\theta_W - B_\mu \sin\theta_W \tag{2.25}$$

$$A_\mu = B_\mu \cos\theta_W + W_\mu^3 \sin\theta_W \tag{2.26}$$

where $Z_\mu$ and $W_\mu^\pm$ are the neutral and charged massive gauge bosons mediating the weak interaction. $A_\mu$ is the photon mediating the electromagnetic interaction. The Weinberg angle $\theta_W$ is defined by the couplings $g$ and $g'$ of $\mathrm{SU}(2)_L \times \mathrm{U}(1)_Y$

$$\sin\theta_W = \frac{g'}{\sqrt{g^2 + g'^2}} \quad \cos\theta_W = \frac{g}{\sqrt{g^2 + g'^2}}. \tag{2.27}$$

The electric charge is related to the couplings $g$ and $g'$ and to the Weinberg mixing angle by

$$e = g \sin\theta_W = g' \cos\theta_W. \tag{2.28}$$

The electromagnetic coupling constant is customarily expressed by the fine structure constant $\alpha_{\text{EM}} = e^2/4\pi$.

### 2.4.4 Yukawa interactions between fermions and the Higgs field

The Yukawa term in unitary gauge (neglecting flavour mixing in the quark sector)

$$\mathcal{L}_{\text{Yukawa}} = -\sum_f m_f \overline{\psi}_f \psi_f - \sum_f \frac{m_f}{v} \overline{\psi}_f \psi_f h \tag{2.29}$$

contains the mass terms $m_f = y_f v/\sqrt{2}$, which relate the individual Yukawa coupling constants $y_f$ to the mass of the charged fermions $f = \mathrm{u}, \mathrm{d}, \ldots, \tau$. The interactions between the massive fermions and the Higgs boson occur with coupling constants proportional to the fermion masses.

## 2.5 Phenomenology of the Standard Model

The non-Abelian structure of the $\mathrm{SU}(3)_C$ and $\mathrm{SU}(2)_L$ symmetry groups results in distinctive properties of strong and weak interactions. The non-trivial transformations of the strong and weak gauge bosons under their respective symmetry groups allow them to interact directly in three- or four-point interactions.

In particular, the direct coupling of gluons has dramatic implications for the strong interaction, which become apparent in considering the effects of charge screening. As an example, consider an electric probe charge near a charged source. The coupling constant of the electromagnetic interaction increases at small distances to a charged source due to the screening of $\mathrm{e}^+\mathrm{e}^-$ pairs of the vacuum. This behaviour is known as "running coupling". The coupling constant of the strong interaction shows precisely the opposite behaviour, as the vacuum is not only a polarisable medium due to $q\bar{q}$ pairs but also due to gluon pairs. The gluons spread out the effective colour charge of the quark and counteract the effect from quark pairs. The resulting behaviour of quarks interacting at small length scale (high energy) as nearly free particles is known as *asymptotic freedom* and is essential for turning quantum chromodynamics into a quantitative calculational scheme predicting the interactions at particle colliders.

The second defining feature of the strong interaction is the *colour confinement hypothesis*, stating that only colour-singlet states are observed. As a consequence, no free quarks have been observed to date but only bound states of two or more quarks.

These bound states are collectively called *hadrons*, with the *baryons* states $B$ and the *mesons* states $M$, which are defined by

$$B = \frac{1}{\sqrt{6}} \varepsilon^{\alpha\beta\gamma} \left| q_\alpha q_\beta q_\gamma \right\rangle \tag{2.30}$$

$$M = \frac{1}{\sqrt{3}} \delta^{\alpha\beta} \left| q_\alpha \overline{q}_\beta \right\rangle . \tag{2.31}$$

Recently, exotics bound states of four [186, 188] or five quarks [187] have been observed, which are in agreement with the colour confinement hypothesis. Another consequence of the confinement hypothesis, which strikingly manifests in high-energy hadron collision events, is the formation of jets [330]. Jets are collimated sprays of particles emerging from coloured states in a similar manner as a decelerating electric charge emits photons via Bremsstrahlung. When a quark anti-quark pair is separated, their colour interaction increases due to the "running coupling" and squeezes the colour field lines into tube-like regions until the increasing potential energy suffices for the creation of another quark anti-quark pair. The repeated formation of clusters of quarks and gluons forming hadrons is called *hadronisation*.

The free parameters SM are empirically determined with great precision. The discovery of the Higgs boson in 2012 [67, 163] concluded the experimental inventory of all SM particles and corroborated the local gauge theory with spontaneous symmetry breaking as the empirically adequate description of fundamental interactions.

The impressive success of the SM in accurately describing the observations across 15 orders of magnitude is demonstrated in cross-section measurements of SM processes by the ATLAS experiment at the Large Hadron Collider, which is shown in Figure 2.3.

## 2.6 Limitations of the Standard Model

Despite the SM's success in providing the most complete and solid theoretical framework to date, several observed phenomena cannot be explained by the SM. They suggest the existence of a more fundamental theory, of which the SM is the low-energy limit. This section presents a non-exhaustive account of both fundamental and aesthetic shortcomings of the SM and open questions in fundamental physics.

- The SM only describes three out of the four known fundamental interactions. Gravity is most successfully described by Einstein's theory of General Relativity, which is mathematically incompatible with the formulation of the SM as a renormalisable quantum field theory [204, 205, 206, 220]. At present, this is merely a theoretical problem, as current experiments are either sensitive to quantum effects, where the minuteness of particle masses justifies neglecting gravity, or to the gravitational pull of extended objects, which do not show quantum behaviour. Eventually, a complete and consistent quantum theory of gravity is required for a truly fundamental description of Nature.

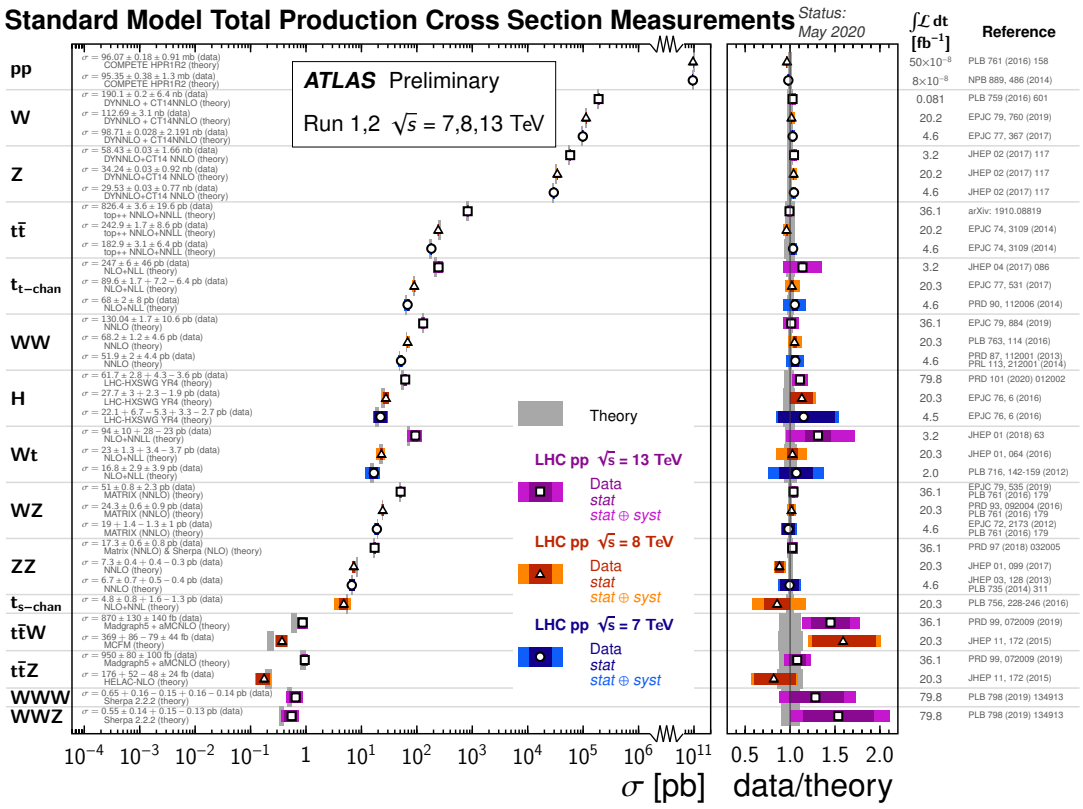



Fig. 2.3.: Summary of several Standard Model total production cross-section measurements, corrected for branching fractions, compared to the corresponding theoretical expectations and ratio with respect to best theory prediction. Figure reproduced from Ref. [102].

- In its original formulation, the SM does not account for neutrino masses. The experimental observation of neutrino flavour oscillations indicates that neutrinos have non-vanishing mass [232]. The mixing of the neutrino-mass eigenstates to give the weak neutrino eigenstates is described — similarly to the CKM matrix — by the Pontecorvo–Maki–Nakagawa–Sakata matrix [303, 280]. The direct measurement of the neutrino masses and the determination of the neutrino mass hierarchy is a current object of research [185].
- The vast prevalence of matter over antimatter in the universe is puzzling, as it is natural to assume that in the early universe both matter and antimatter were created in equilibrium. The violation of CP symmetry could explain the matter-antimatter asymmetry [311]. However, the CP violation in the SM, appearing as a complex phase in the quark mixing matrix of the weak interaction, is by far not sufficient to explain the observed asymmetry.
- The energy scale of electroweak symmetry breaking is $\mathcal{O}(100\,\mathrm{GeV})$. If the SM were the fundamental theory of Nature, it would be expected to describe phenomena up to the Planck scale, defined by $m_{\text{Planck}} = 1/\sqrt{8\pi G} = \mathcal{O}(10^{18}\,\mathrm{GeV})$, where $G$ denotes Newton's constant. The scalar Higgs boson mass receives quadratically divergent radiative loop corrections $\Delta m_h$ from all particles interacting with the Higgs field. Including these corrections, the square of the Higgs boson mass is

$$m_h^2 = (m_h^{\text{bare}})^2 + \Delta m_h^2 = (m_h^{\text{bare}})^2 + \text{const.} \times \Lambda^2, \tag{2.32}$$

  where $\Lambda$ is the fundamental scale parameter of the theory. Given the measured Higgs boson mass $m_h = 125\,\mathrm{GeV}$, the theory requires a precise fine-tuning of $m_h^{\text{bare}}$ over more than $10^{36}$ orders of magnitude, which is not considered to be aesthetic [291].
- Astrophysical observations strongly indicate that the baryonic matter described by the SM is insufficient to account for phenomena on scales ranging from galactic rotation curves to cosmology. An additional matter component, the so-called dark matter is required to describe the observed phenomena accurately. Chapter 3 provides a detailed discussion of the research programme defined by dark matter.

# Dark matter

# 3

> *We live on a placid island of ignorance in the midst of black seas of infinity, and it was not meant that we should voyage far.*
>
> — **Howard Phillips Lovecraft**
> The Call of Cthulhu, in Weird Tales Volume XI Number 2. Indianapolis: Popular Fiction Publishing Co., 1928

## 3.1 Introduction

Astrophysics and cosmological observations supply compelling evidence that the particle content of the SM can only account for a small fraction of the matter-energy-density of the universe. Several extensions of the SM suggest the existence of invisible particles, which can account for the missing component as *dark matter*. General relativity, the currently established theory of gravity, is only able to describe and explain the observed phenomena if there is dark matter in the universe. Although it has been almost a hundred years after dark matter's initial discovery, its particle nature remains an open question.

The term dark matter denotes a non-luminous and non-absorbing matter component. It was first coined in the year 1922 by the Dutch astronomer Jacobus Kapteyn in a study estimating the density of matter near the Sun [259]. The earliest, perhaps even the most convincing evidence for the existence of dark matter came from the observation that astrophysical objects move faster than one would expect if they were subject only to the gravitational interaction of visible objects. These observations disagree with the predictions of the well-established theories of gravitation.

However, the falsification of a theory by empirical tests is necessarily ambiguous, as every interpretation depends on further assumptions [213]. For instance, the observed anomalies could also be explained by the presence of additional, yet undiscovered gravitational potentials. Then, do such anomalies falsify the theory of gravitation or do they point towards unseen — in other words "dark" — celestial objects?

Two historical examples show how observations which seemingly refute the established theories advance scientific understanding [134]. Both examples consider observed anomalies in the motion of the planets in the Solar System.

1. In the case of the anomalous motion of Uranus, the French mathematician Urbain Le Verrier chose not to abandon Newtonian gravity. Instead, he confronted the troublesome orbit by conjecturing another planet — Neptune. Its discovery would add another planet to the inventory of our Solar System and corroborate Newtonian gravity. Indeed, the German astronomer Johann Gottfried Galle discovered the planet Neptune in 1846 within the same evening that Le Verrier's letter reached him and proved his predictions to be true [9, 340].

2. In a similar manner, Le Verrier tried to address the anomalies in the motion of Mercury, which were observed the first time in 1859, by postulating the existence of the hypothetical planet Vulcan. Conversely, this "dark planet" was never discovered. Consequentially, the research programme defined by Newtonian gravity had to be abandoned. The advent of Einsteinian gravity solved the problem by accurately predicting the anomalous perihelion shift of Mercury without the need for postulating new objects [161].

The verdict on whether dark matter defines a progressive research programme [271] or whether it will be eventually abandoned in favour of a new theory of gravitation is ultimately decided by experimental searches for dark matter. To date, it remains an open problem in fundamental physics.

## 3.2 Cosmology in a nutshell

The present knowledge about composition, evolution and structure of the universe is described by the $\Lambda$-CDM model. The model is based on the presence of a non-vanishing cosmological constant $\Lambda$ and cold dark matter, which shows a small velocity dispersion in contrast to warm or hot dark matter. The dark matter paradigm is at the heart of the currently established cosmological model, which describes the evolution of the universe from an initial, highly compressed state to its present state. According to the $\Lambda$-CDM model, the ordinary baryonic matter, building blocks to humankind and its terrestrial environment, only constitutes roughly $5\,\%$ of the universe's matter-energy content. Another $25\,\%$ is comprised of dark matter. The remaining $70\,\%$ is referred to as dark energy. The model is able to give an account of the thermal history of the universe and explains the universe's observed properties. It correctly predicts the observed relic abundances of light elements and provides an interpretation of the cosmic microwave background radiation in terms of fundamental cosmological parameters. Simulations based on the $\Lambda$-CDM model can reproduce the observed large scale structure of the universe.

The $\Lambda$-CDM model is based on three fundamental building blocks:

1. Einstein's field equations of General relativity

$$R_{\mu\nu} - \frac{1}{2} R g_{\mu\nu} + \Lambda g_{\mu\nu} = \frac{T_{\mu\nu}}{M_{\mathrm{Pl}}^2}, \tag{3.1}$$

- where $R_{\mu\nu} = R^{\alpha}_{\mu\alpha\nu}$ is the Ricci tensor, the only independent trace of the curvature tensor $R^{\alpha}_{\mu\beta\nu}$,
- $R = R^{\mu}_{\mu}$ is the Ricci scalar,
- $\Lambda$ is the so-called cosmological constant, a measure for the accelerated expansion of the universe due to the vacuum energy,
- $M_{\mathrm{Pl}} = 1/\sqrt{8\pi G}$ is the reduced Planck mass defined by Newton's constant $G$, and
- $T_{\mu\nu}$ is the energy-momentum tensor.

2. the Friedmann-Lemaître-Robertson-Walker (FLRW) metric defined by the line element

$$\mathrm{d}s^2 = \mathrm{d}t^2 - a(t)^2 \left( \frac{\mathrm{d}r^2}{1 - \kappa r^2} + r^2 \, \mathrm{d}\theta^2 + r^2 \sin(\theta)^2 \, \mathrm{d}\phi^2 \right), \tag{3.2}$$

   - where $a(t)$ is the spatial scale factor describing the relative expansion of the universe
   - $\kappa$ is the curvature parameter describing the spatial curvature of the universe. $\kappa$ can take values of $0$, $1$, and $-1$, corresponding to a flat, a closed, or an open universe, respectively.

3. the equation of state relating pressure $p_j$ and energy density $\rho_j$ of a species $j$

$$p_j(t) = w_j \rho_j, \tag{3.3}$$

   where $w_j$ is a dimensionless constant, which is

$$w_j = \begin{cases} 0 & \text{for non-relativistic matter} \\ 1/3 & \text{for relativistic radiation} \\ -1 & \text{for vacuum energy.} \end{cases} \tag{3.4}$$

These building blocks themselves can be derived from fairly general principles, which are based on empirical observations. Einstein's field equations can be derived from almost first principles, assuming invariance under general coordinate transformations and equivalence to Newton's law in the limit of weak gravitational fields. The FLRW metric is based on the assumptions of the homogeneity and isotropy of space, which is in agreement with observations on large scales above $100\,\mathrm{Mpc}$. George Lemaître and Edwin Hubble discovered the expansion of the universe around the year 1930, which is described by the Hubble parameter

$$H(t) = \frac{\dot{r}(t)}{r(t)} = \frac{\dot{a}(t)}{a(t)}. \tag{3.5}$$

$H(t)$ can be expressed equivalently in terms of a co-moving distance $r$ or in terms of the scale factor $a$. The expansion of the universe causes a cosmological redshift $z$ of

the light emitted by distant galaxies, which is defined as the ratio of the observed wavelength $\lambda_o$ and the emitted wavelength $\lambda_e$ as

$$1 + z = \frac{\lambda_o}{\lambda_e}. \tag{3.6}$$

The redshift can be related to the scale parameter $a$ at time of emission $t_e$ and time of observation $t_o$ via $1 + z = a(t_o)/a(t_e)$, thereby giving an estimate of the expansion rate of the universe. The observed expansion at the present time is described by the Hubble constant $H_0 = 67.27 \pm 0.60\,\mathrm{km\,s^{-1}\,Mpc^{-1}}$ [301][1]. The expansion of the universe can be equivalently expressed in the temperature $T$, using the thermodynamic relation

$$a(T) \propto \frac{1}{T}. \tag{3.7}$$

The Einstein field equations can be solved with the FLRW metric, yielding the Friedmann equation

$$H^2 + \frac{k}{a^2} = \frac{\rho_{\mathrm{tot}}}{3M_{\mathrm{Pl}}} \tag{3.8}$$

and similar, second condition

$$H^2 + \frac{2\ddot{a}}{a} + \frac{k}{a^2} = -\frac{p}{M_{\mathrm{Pl}}} \tag{3.9}$$

where $\rho_{\mathrm{tot}}$ denotes the total average energy density of the universe and $p$ denotes the corresponding pressure, defined as the direction-independent contribution to the diagonal entries $T_{jj} = p_j$ of the energy-momentum tensor. The universe is flat with curvature parameter $\kappa = 0$, if the energy density equals the critical density $\rho_c = 3(HM_{\mathrm{Pl}})^2$. Customarily, the abundance of a species $j$ is quoted in units of the critical density

$$\Omega_j = \frac{\rho_j}{\rho_c}. \tag{3.10}$$

An important task of observational cosmology is to measure the resulting density parameters $\Omega_r$ for radiation, $\Omega_m$ for matter, and $\Omega_\Lambda$ for the vacuum energy. Adopting this convention, the total energy density in units of the critical density is

$$\Omega = \sum_i \Omega_i = \sum_i \frac{\rho_i}{\rho_c}. \tag{3.11}$$

and the Friedmann equation reads

$$\Omega - 1 = \frac{k}{H^2 a^2}. \tag{3.12}$$

[1] There are competing measurements of the Hubble constant with some discrepancy among them [256].

The dependence of the energy density $\rho_j$ on the scale parameter $a$ is

$$\rho_j(a) = \rho_{j,0}\, a^{-3}(1+w_j) \propto \begin{cases} a^{-3} & \text{for non-relativistic matter} \\ a^{-4} & \text{for relativistic radiation} \\ \text{const.} & \text{for vacuum energy.} \end{cases} \tag{3.13}$$

Finally, the spatial evolution of the universe's expansion can be stated in terms of the the density parameters

$$H^2 = \left( \frac{\Omega_r}{a^4} + \frac{\Omega_m}{a^3} + \Omega_\Lambda \right) H_0^2. \tag{3.14}$$

The evolution of energy densities for matter, radiation, and vacuum energy (cosmological constant) is shown in Figure 3.1. The universe was dominated by a single component through most of its history: first radiation, then matter, then vacuum energy [124].

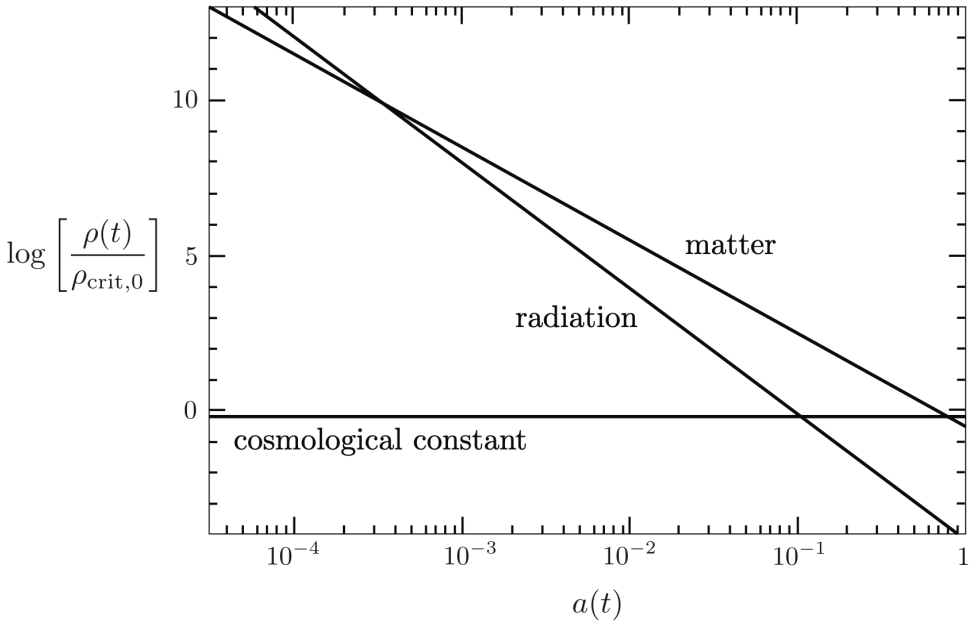



**Fig. 3.1.:** Evolution of the energy densities in the universe. Figure reproduced from Ref. [124].

## 3.3 Dark matter relic density

The early universe was sufficiently hot and dense for dark matter $\chi$ and other particle species $f$ to be in thermal equilibrium. Reactions $\chi\overline{\chi} \leftrightarrow f\overline{f}$ took place with the interaction rate

$$\Gamma = n\langle\sigma v\rangle, \tag{3.15}$$

where $n$ denotes the particle number density and $\langle\sigma v\rangle$ denotes the thermally averaged product of the interaction cross-section and the average velocity of the particles. The expansion of the universe decreases the particle number density, until at some point it drops to a point at which interactions hardly occur and dark matter decouples from other particles. The point, at which the interaction rate $\Gamma|_{T_{\text{dec}}}$ drops below the Hubble expansion $H|_{T_{\text{dec}}}$, is defined by the decoupling temperature $T_{\text{dec}}$. This process is referred to *freeze-out* because the dark matter particle number density approaches a constant value for $T < T_{\text{dec}}$. This constant value is the dark matter relic density.

The dark matter relic density can be derived by solving the Boltzmann equation

$$\frac{\mathrm{d}n}{\mathrm{d}t} = \langle\sigma_{\text{ann}}v\rangle(n_{\text{eq}}^2 - n^2) - 3Hn, \tag{3.16}$$

where $n_{\text{eq}}$ denotes the particle number density in equilibrium, $H$ denotes the Hubble constant and $\langle\sigma_{\text{ann}}v\rangle$ denotes the thermally averaged product of the annihilation cross-section and the velocity of the annihilating particles.

The Boltzmann equation is solved numerically under the condition of constant entropy. The dark matter relic density density in terms of the density parameter and the reduced Hubble constant $h = H_0/100\,\mathrm{km\,s^{-1}\,Mpc^{-1}} \approx 0.7$ can be approximated as

$$\Omega_X h^2 \approx \frac{3 \times 10^{-27}\,\mathrm{cm^3\,s^{-1}}}{\langle\sigma_{\text{ann}}v\rangle}. \tag{3.17}$$

The dark matter relic density is determined by the annihilation cross-section at the time of the freeze-out. Figure 3.2 shows the dark matter particle number density as a function of the dimensionless parameter $x = m_\chi/T$. The dotted line corresponds to the evolution of the number density for dark matter remaining in equilibrium without occurrence of any freeze-out. The number density decreases exponentially as a function of $x$ until the interaction rate becomes too small for dark matter particles to remain in thermal equilibrium, resulting in a constant number density $N_X^\infty$ determined by the point of freeze-out $x_F = m_\chi/T_{\text{dec}}$. The strength of the interaction defines the dark matter relic density: a large dark matter annihilation cross-section corresponds to a smaller relic density.

For typical weak interaction cross-sections of the order $\mathcal{O}(\sigma) = 1\,\mathrm{pb}$ and for a dark matter particle with its mass at the electroweak scale, the observed dark matter relic density $\Omega_\chi h^2 = 0.1188$ is obtained. This striking coincidence is known as the “WIMP

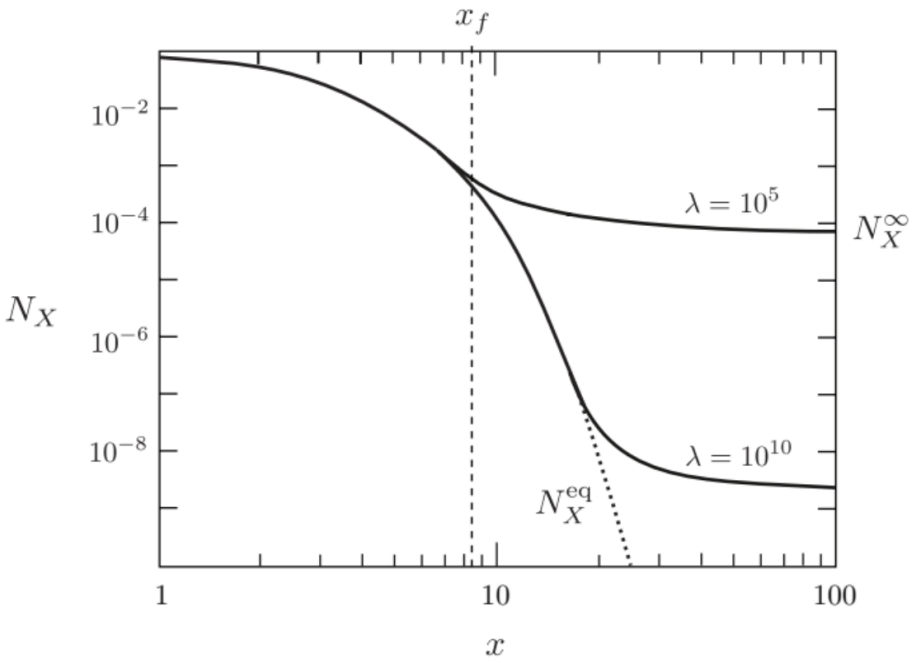



**Fig. 3.2.:** Abundance of dark matter particles $N_X$ in dependence of the dimensionless parameter $x = m_\chi/T$. The freeze-out occurs at the point, where the temperature $T$ drops below the dark matter particle mass $m_\chi$. The annihilation cross-section is expressed as $\lambda = \frac{2\pi^2}{45} g^\star \frac{m_\chi \langle \sigma_{\mathrm{ann}} v \rangle}{H(m_\chi)}$, where $g_{S\star}$ denotes the effective number of degrees of freedom in entropy. Figure reproduced from Ref. [124].

miracle", referring to the dark matter particle candidate being a weakly interacting massive particle (WIMP).

The simplified calculation discussed here neglects several aspects, which can lead to significant changes in the relic density. It has been shown that the presence of a scalar field in the early universe could modify the value of the relic density. If the dark matter particle mass is similar to other particles, which share a quantum number with the dark matter particle, or if there are several different dark matter particles, co-annihilations occur. In this case, the first term in Equation (3.16) needs to account for interactions among the different species, typically resulting in a much more efficient annihilation of dark matter. Radiative corrections in resonant Sommerfeld enhancement are another effect, which can cause dramatic changes in the relic density.

## 3.4 Evidence for dark matter

There is compelling evidence for the existence of dark matter on all astrophysical scales, including rotation curves of gas and stars in galaxies, large samples of galaxy clusters, strong and weak gravitational lensing, distant supernovae, studies of the cosmic microwave background, and large structure formation.

### 3.4.1 Galactic scale

The first evidence for the existence of dark matter on sub-galactic scales comes from observations of the Dutch astronomer Jan Oort in 1932. He studied the motion of the stars in our galactic neighbourhood and measured the velocity of stars near the galactic plane by studying their Doppler shifts. His observations found them moving faster than expected — even so fast that they should be able to escape the gravitational pull of the luminous mass in the Milky Way. Consequentially, he postulated that there must be more galactic mass present to keep the stars on their Keplerian orbits.

The strongest evidence for dark matter on galactic scales is based on the observation of the rotation curves of galaxies. These rotation curves are graphs of the circular velocities of the galaxy's constituents (stars and gas) as a function of their distance from the galactic centre. Figure 3.3 shows the rotation curve of the NGC 6503 galaxy. The most striking feature is that the rotation curve approaches a flat shape at large distances, even beyond the edge of the visible disk. The circular velocity of an object on a stable Keplerian orbit is expected to be

$$v(r) = \sqrt{\frac{GM(r)}{r}} = \sqrt{4\pi G \frac{\int \rho(r) r^2 \, \mathrm{d}r}{r}}, \tag{3.18}$$

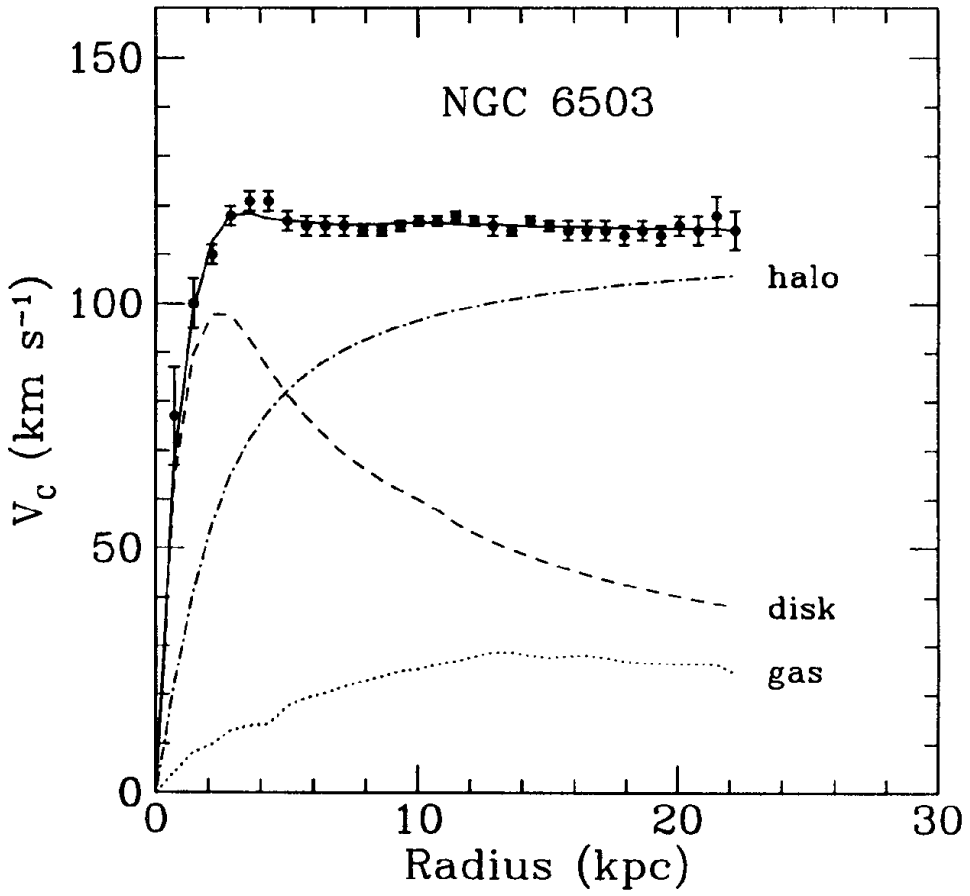



**Fig. 3.3.:** Galactic rotation curve for NGC 6503 (observed data taken from Ref. [147]). The decomposition of the rotation curve in contributions from disk and gas potentials shows that an additional contribution due to the dark matter halo is required to match the data. Figure reproduced from Ref. [223].

where $\rho(r)$ is the mass density profile. Beyond the edge of the visible disk, the rotation curve should be falling proportional to $1/\sqrt{r}$. The observation of an approximately constant distribution for large distances implies the existence of a dark matter halo with a mass density profile approaching $\rho = 1/r^2$ for large distances. The dark matter halo is expected to fall off faster at some point to keep the total mass of the galaxy finite.

Although there is consensus about the shape of dark matter haloes in the large-distance-limit, the predicted shape in the innermost region of the halo is subject of contention. Cosmological N-body simulations predict dark matter halos with density increasing steeply at small distances ("cusps"). The observed rotation curves of most dwarf galaxies, however, suggest flat, central dark matter density profiles ("cores"). This "cusp-core problem" is subject of ongoing investigation.

The velocity dispersion of dwarf spheroidal galaxies (dSphs), small satellite galaxies mostly within $300\,\mathrm{kpc}$ of the Milky Way, is another hint for the existence of dark matter [332]. Dwarf spheroidal galaxies are the nearest, smallest and least luminous galaxies observed to date. They are among the galaxies most strongly dominated by dark matter [344].

Further evidence on galactic scales comes from weak gravitational lensing of distant galaxies by foreground structures [122]. Light originating from a luminous source is deflected by a large amount of matter between the source and the observer. The resulting image distortion is known as gravitational lensing and enables the determination of the mass of the foreground structure. Weak gravitational lensing data can provide constraints on the extent and shapes of the galactic dark matter halos [250] and gives strong constraints on alternative theories of gravity.

### 3.4.2 Galaxy cluster scale

The investigation of the velocity dispersion of galaxies in the Coma cluster by Fritz Zwicky arguably pioneered the field of dark matter. Zwicky studied the Doppler-shift of several galaxies in a data set published by Edwin Hubble and Milton Humason and noticed at least eight galaxies with an apparent velocity exceeding $6000\,\mathrm{km\,s^{-1}}$. For these galaxies to be gravitationally bound, the galaxy cluster is required to have a sufficiently large gravitational potential. Using the virial theorem, he inferred the mass density of the Coma cluster. The estimate for the total mass of the cluster is

$$m_{\text{cluster}} = \sum_i m_{\text{galaxy},i} \approx \frac{2\langle v^2 \rangle}{G\langle 1/r \rangle}, \tag{3.19}$$

where $\langle v^2 \rangle$ is the average velocity of galaxies in the cluster and $\langle 1/r \rangle$ is the average inverse distance between galaxies. Another way to estimate the total mass of the cluster is to measure its luminosity. Comparing the two estimates, he found the estimate based on the cluster's gravitational potential to be 400 times larger than that derived from observations of luminous matter. Zwicky's use of the phrase "dunkle (kalte) Materie" is typically regarded as the first use of the term "dark matter"

and established the convention of including the photograph of Fritz Zwicky making a silly face in public talks on dark matter.

Zwicky also pioneered the idea that entire galaxy clusters could act as gravitational lenses [349]. Weak gravitational lensing provides accurate estimates of the total mass of galaxy clusters and thereby provides evidence for the existence of dark matter. In strong gravitational lensing [121], the light-bending effect is even strong enough to produce multiple images or arcs of the source. If the source, the observer and the matter in between (also called the "lens") are aligned, the source is observed in the form of an Einstein ring [215]. The ring's angular radius $\theta_E$ allows estimating the mass $M$ of the lens via

$$\theta_E = \sqrt{4GM \frac{d_{LS}}{d_L d_S}}, \tag{3.20}$$

where $G$ denotes Newton's constant, $d_L$ denotes the distance to the lens, $d_{LS}$ denotes the distance between source and lens and $d_S$ denotes the distance to the source.

Figure 3.4 shows an image of the Abell 2218 galaxy cluster, an exceptionally rich lensing cluster at redshift $z = 0.175$. The galaxies lying behind the cluster's core are magnified and distorted into long arcs, some of them are even multiply imaged. The mass estimated from gravitational lensing exceeds the X-ray based estimate by at least a factor of 2.5 [5].

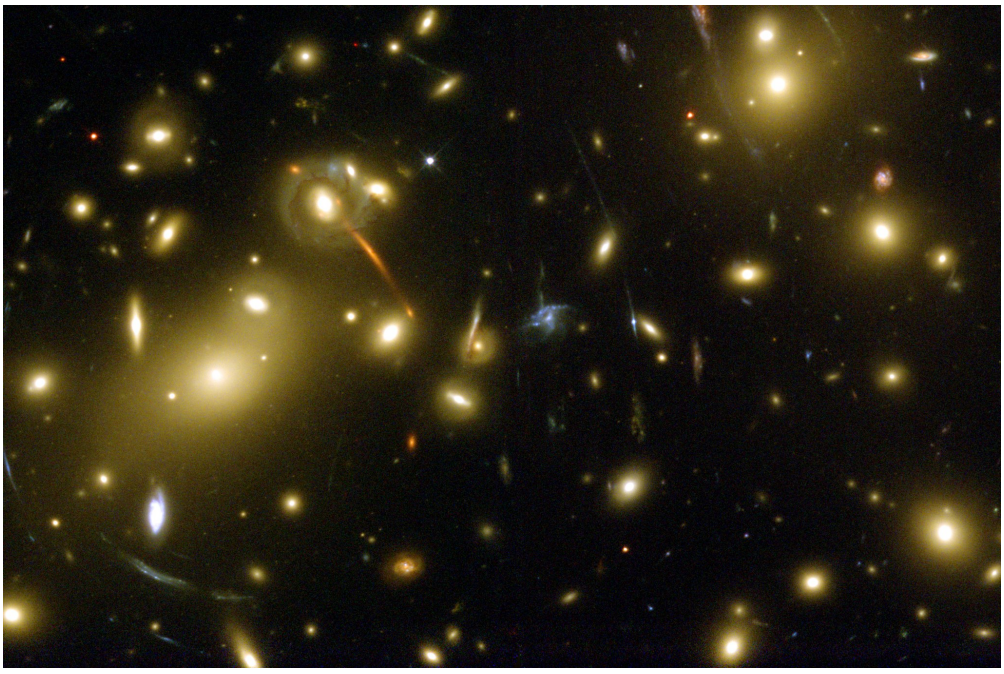


**Fig. 3.4.:** Image of the galaxy cluster Abell 2218 and its gravitational lenses, taken by the Hubble space telescope in 1999. Image by Andrew Fruchter (STScI) et al., WFPC2, HST, NASA / Public domain.

Arguably the most dramatic evidence for dark matter is provided by observations of the galaxy cluster 1E657-558 [342], also known as "bullet cluster". It consists of two sub-clusters of galaxies, which are thought to have previously collided. Figure 3.5 shows images of the bullet cluster from different sources, overlaid with the reconstructed cluster surface mass density $\kappa$ obtained from weak gravitational lensing. The visible matter of the bullet cluster consists of clouds of hot gas (visible in the optical image), which constitute the majority of the cluster's baryonic matter, and stellar objects (visible in the X-ray image).

The stars are cleanly separated into two distinct sub-clusters, as the probability of individual galaxies colliding is small. In contrast, the clouds of hot gas have interacted ferociously, as the collision of the sub-clusters slowed the gas and left it displaced from the stars. Most of the matter of the sub-clusters, however, is dark matter, which is indicated by the distribution of the reconstructed cluster surface mass density $\kappa$.

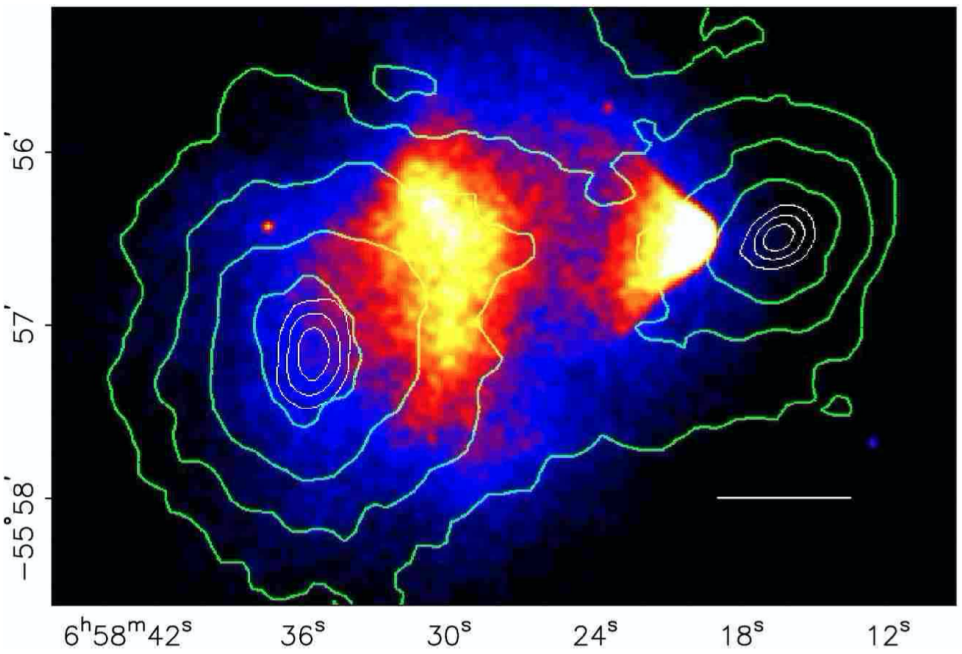
The dark matter in each of the two sub-clusters passed through, seemingly unaffected by the collision. These observations indicate that dark matter interacts weakly both with baryonic matter and with itself. The spatial offset of the centre of the total mass distribution from the centre of the baryonic mass distribution is highly significant ($8\sigma$) and gives strong constraints on alternative models of gravity.

### 3.4.3 Cosmological scale

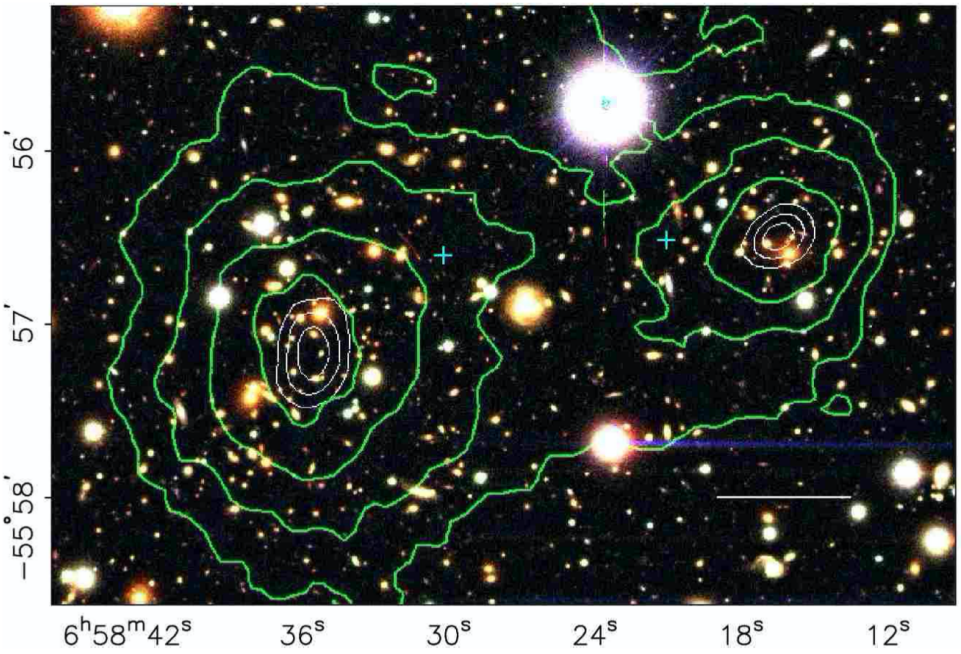
Although the evidence on the scales of galaxies and galaxy clusters for themselves is compelling, the observations do not allow for an estimate of the total amount of dark matter in the universe. This information can be extracted from the analysis of cosmic microwave background data.

The cosmic microwave background (CMB), which was discovered in 1965 by Arno Penzias and Robert Wilson [299], is electromagnetic radiation with a black body radiation spectrum at temperature $T_{\text{CMB}} = 2.725\,48 \pm 0.000\,57\,\text{K}$ [221]. It consists of primordial photons created in the early universe, which were in thermal equilibrium (c.f. the discussion for dark matter particles in Section 3.3). Photons and free electrons frequently interacted via scattering processes, as space was filled by a charged plasma. The interaction rate decreased when the electrons combined with protons to form electrically neutral hydrogen atoms. Consequentially, the photons decoupled and could propagate undisturbed. The CMB can be thought of as the sphere of the last scattering with the observer in the centre and allows probing the conditions in the early universe directly.

In the last three decades, the CMB has been mapped by experiments with increasing precision [324, 127, 326, 325, 308, 292, 301]. The almost uniform temperature of the CMB suggests a phase of rapid, inflationary expansion of the universe, which is driven by the cosmological constant $\Lambda$. After subtracting the dipole moment associated with the movement of the earth, the CMB exhibits temperature fluctuations with the characteristic scale $\delta T / T_{\text{CMB}} \approx 10^{-5}$. These tiny fluctuations are




(a) Colour image of 1E657-558 from the $6.5\,\mathrm{m}$ Magellan telescopes located at the Las Campanas observatory, Chile.




(b) X-ray image of 1E657-558 from NASA Chandra satellite observatory.

**Fig. 3.5.:** Images of 1E657-558 based on optical (top) and X-ray observations (bottom). The green contours of the reconstructed cluster surface mass density $\kappa$ obtained from weak gravitational lensing are overlaid in both images. The three white contours show the uncertainty in the position of the two primary galaxy concentration centres, corresponding to $1\sigma$, $2\sigma$, and $3\sigma$ confidence levels. Figures reproduced from Ref. [162].

used to determine the cosmological parameters. The temperature fluctuations are parametrised as an expansion in spherical harmonics $Y_{lm}(\theta, \varphi)$[2]

$$\frac{\delta T}{T_{\text{CMB}}}(\theta, \varphi) = \sum_{l=2}^{\infty} \sum_{m=-l}^{l} a_{lm} Y_{lm}(\theta, \varphi). \tag{3.21}$$

Assuming the values of the coefficients $a_{lm}$ are independent of the index $m$, it is possible to define the observed angular power spectrum

$$C_l^{TT} = \frac{1}{2l+1} \sum_{m=-l}^{l} |a_{lm}|^2 \tag{3.22}$$

for discrete values of the multi-pole moment $l \propto \pi/\phi$. The CMB map and the power spectrum measured by PLANCK [292] is shown in Figure 3.6.

The measured power spectrum consists of a set of peaks, which each define an angular scale with particularly large contributions to the temperature fluctuations. The cosmological parameters can be inferred from a fit of the positions, shapes and relative sizes of the peaks in the spectrum. The peaks originate from acoustic waves in the baryon-photon fluid before the photon decoupling. These acoustic waves can be understood as the competing effects of gravity and radiative pressure. The baryon-photon fluid gets pulled into gravitational wells around regions of considerable matter accumulation. As more baryonic matter accumulates, the increasing photon pressure acts against the gravitational potential of the wells.

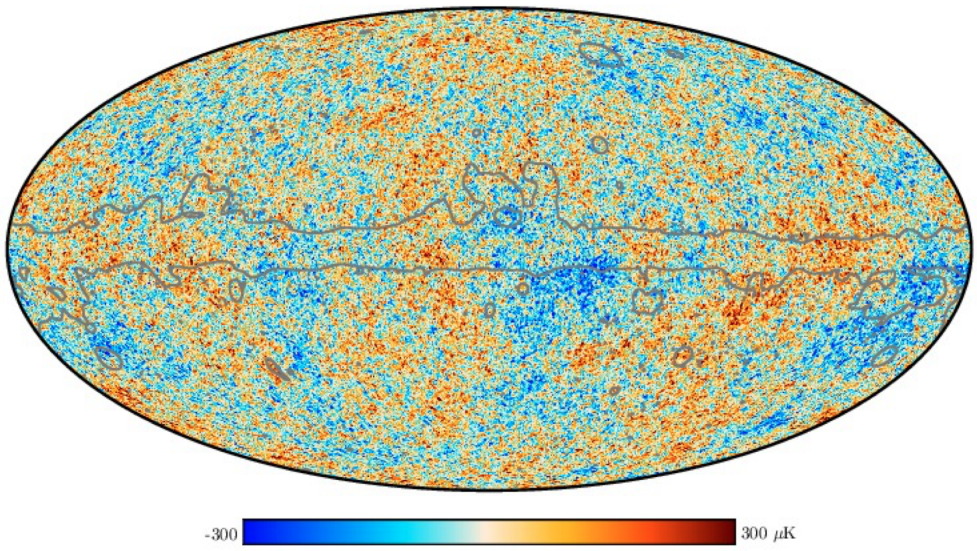
Even-numbered peaks are associated with the compression of the baryon-photon fluid due to gravity, whereas odd-numbered peaks are associated with the counteracting effect of radiative pressure. A higher baryon content in the baryon-photon fluid corresponds to smaller radiative pressure and larger compression peaks. Therefore, the relative amplitude between odd- and even-numbered peaks is a measure of the baryon density parameter $\Omega_b$. Dark matter only contributes to the gravitational wells and does not respond to radiative pressure. The size of the third peak indicates a sizeable dark matter component at the time of the last scattering. The first peak corresponds to waves, which have only compressed once. Its position is used to determine the spatial curvature parameter $\kappa$.

The estimates for the products of the cosmological density parameters and reduced Hubble constant $h$ [301] are

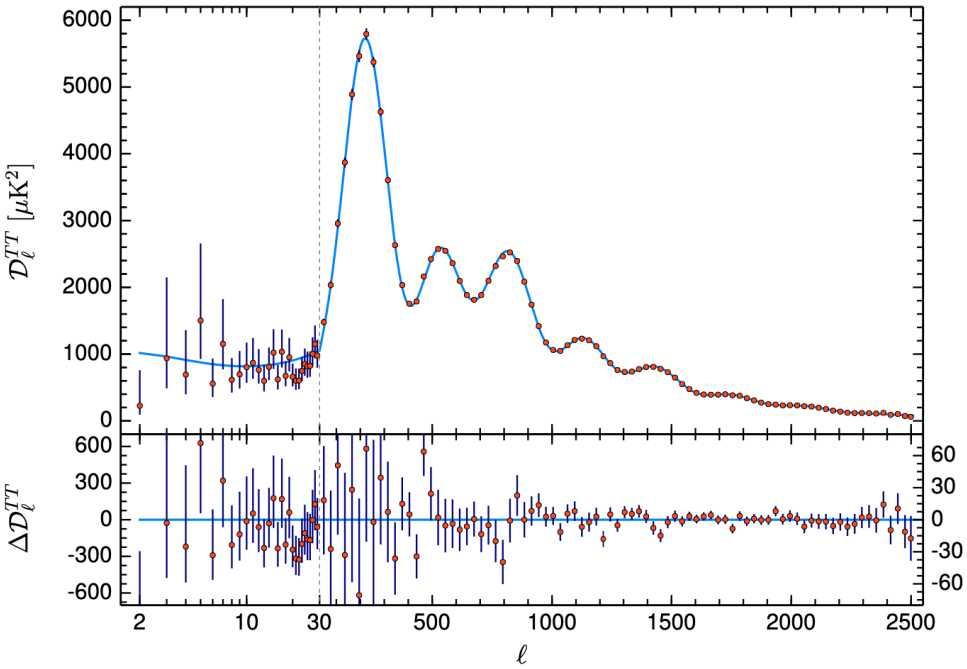
- baryon density parameter $\Omega_b h^2 = 0.022\,37 \pm 0.000\,15$
- dark matter (DM) density parameter $\Omega_{\text{DM}} h^2 = 0.1200 \pm 0.0012$.

The estimates are compatible with the predictions from Big Bang nucleosynthesis [318] and with those obtained from the Sloan Digital Sky Survey [337].

[2] The base mode $l = 0$ corresponds to the CMB temperature $T_{\text{CMB}}$. The first mode $l = 1$ corresponds to the dipole anisotropy. Therefore, the expansion in the fluctuations starts at $l = 2$.




**(a)** CMB sky map. The grey line delineates a region, which lies mostly around the Galactic plane, where residuals from foreground emission are expected to be substantial and which is therefore masked in the analysis.




**(b)** CMB temperature power spectrum. The upper panel shows the scaled power spectrum modes $D_l^{TT} = l(l+1)C_l^{TT}/(2\pi)$. The $\Lambda$-CDM model best fit to the data is overlaid in light blue in the upper panel. The residuals with respect to this model are shown in the lower panel. For better visualisation, the horizontal scale changes at $l = 30$ from a logarithmic scale to a linear scale.

**Fig. 3.6.:** Planck (2018) observations of the CMB. Figures reproduced from Refs. [292] (top) and [301] (bottom).

A global fit of the $\Lambda$-CDM model allows constraining the amount of dark energy by extracting the

- cosmological constant density parameter $\Omega_\Lambda = 0.6847 \pm 0.0073$.

The knowledge of these fundamental cosmological parameters allows for a breakdown of the present composition of the universe in $4.9\,\%$ baryonic matter, $26.8\,\%$ dark matter and $68.3\,\%$ dark energy.

The current structure of the universe is a result of the initial matter fluctuations in the early universe. The temperature fluctuations in the CMB indicate that the early universe was not entirely homogeneous and isotropic. These density fluctuations have grown into the galaxies and galaxy clusters observed today. However, this could not have been achieved by baryonic matter alone.

Structure formation could only have occurred after the universe cooled down sufficiently for the photons to decouple. Then, however, there would not have been sufficient time to form the amount of structure observed today. Dark matter, on the other hand, is thought to decouple from the photons much earlier. Its density perturbations can form the gravitational wells acting as a seed for the gravitational collapse of visible matter. The observed large scale structure of the universe is compatible with the cold dark matter hypothesis [136].

## 3.5 Candidates for dark matter particles

It would be an understatement to say that several compelling candidates for dark matter have been proposed. The parameter space of dark matter models is vast and covers at least $30$ orders of magnitude in the mass and $40$ orders of magnitude in the interaction cross-section with protons [254].

In analogy to the example of hidden planets in the Solar System in Section 3.1, one could naively assume dark matter to consist of yet unobserved baryonic matter. Massive Astrophysical Compact Halo Objects (MACHOs) [235], compact objects much less luminous but otherwise equivalent to ordinary stars, were among the first dark matter candidates. Possibilities for such objects include planets, brown dwarfs, neutron stars, Jupiter-like objects, and black holes. However, searches based on micro-lensing surveys and determinations of the cosmic baryon density from measurements of the primordial light element abundances and the CMB data strongly constrain the fraction of the dark matter constituted by MACHOs [133].

There are several compelling candidates for a non-baryonic dark matter particle. A suitable dark matter particle candidate must be able to be probed experimentally and needs to satisfy the following conditions [336]:

1. It has to be an electrically neutral, [284] stable [114] particle with sufficiently low interactions to match the appropriate relic density [327].
2. It must lead to sufficiently low velocity during decoupling to allow for the observed large scale structure formation in the universe.

3. It has to be compatible with the constraints
    - on its self-interactions [306, 343],
    - due to stellar evolution [317],
    - from Big Bang nucleosynthesis [261]
    - from direct searches for dark matter [275],
    - from indirect searches for dark matter [193],
    - from collider searches for dark matter [144], and
    - due to other astrophysical observations.

A possible non-baryonic dark matter candidate in the SM appears to be the neutrino, as it has the "undisputed virtue of being known to exist" [128]. Neutrinos are neutral, have non-vanishing mass and only interact weakly with SM particles. They are an example of hot dark matter since they are still relativistic at the time of their decoupling due to their small mass $m_\nu < 1\,\mathrm{eV}$ [17]. However, neutrinos alone are not able to account for the total dark matter mass in the universe. The relic density parameter for neutrinos with mass $\sum_i m_{\nu_i} = 0.264\,\mathrm{eV}$ is predicted to be [278]

$$\Omega_\nu h^2 \approx \sum_i \frac{m_{\nu_i}}{92.5\,\mathrm{eV}} \lesssim 0.00285. \tag{3.23}$$

The relic density parameter is too small for neutrinos to be the dominant component of dark matter. Furthermore, the observed amount of structure in galaxy clustering is inconsistent with the predictions for a neutrino-dominated universe [347].

These arguments prove that the SM does not contain a viable candidate for a dark matter particle. However, several extensions of the SM predict viable candidates:

**Sterile neutrinos** [207, 140] are right-handed ($\mathrm{SU}(2)_L$ singlet) neutrinos, which do not interact with SM particles except by small mixing $\theta$ with left-handed $\mathrm{SU}(2)_L$-active neutrinos. They can overcome the constraints which ruled out the SM neutrinos as dark matter. The mass of sterile neutrinos is expected to be in the $\mathrm{keV}$-range. Although sterile neutrinos are expected to decay predominantly to three left-handed neutrinos, their radioactive decay mode to one left-handed neutrino and a photon gives rise to a quasi-monochromatic photon line at half the sterile neutrino-mass and can be exploited for searches.

**Axions** are very light pseudo-scalar bosons, which have been originally proposed as a solution to preserve $CP$ symmetry in strong interactions [298]. Axion-like-particles (ALPs) define a more general class of very light, weakly coupled bosons, which are excellent candidates for particle dark matter in the ALP mass range $10^{-6}\,\mathrm{eV} < m_A < 10^{-2}\,\mathrm{eV}$ [233]. The main search strategy for axion searches is based on the axion-photon conversion in external magnetic fields.

The **WIMP** paradigm (weakly interacting massive particle, denoted as $\chi$) defines a class of particularly well-motivated candidates for dark matter particles. WIMPs are neutral, stable or very long-lived particles. The interactions of WIMPs with the SM

occur with similar strength as typical electroweak interactions. The WIMP mass is expected to range from $10\,\mathrm{GeV} < m_\chi < 100\,\mathrm{TeV}$ [266, 236]. Therefore, thermally produced WIMPs are non-relativistic by the time of decoupling and are a typical example of cold dark matter. Consequentially, the WIMP paradigm provides a simple mechanism to obtain the observed relic density, which is referred to as the "WIMP miracle" (c.f. Section 3.3). In regions of large WIMP density, they can annihilate and produce a flux of $\gamma$-rays, anti-particles and neutrinos. WIMP searches are discussed in detail in Section 3.6.

A notable example of a framework predicting WIMPs is the minimal supersymmetric extension of the SM (MSSM) [222]. In this model, the lightest supersymmetric particle (LSP), whose decay to SM particles is prohibited by a custodial symmetry, is a WIMP. Other theories predicting WIMPs include theories with extra-dimensions [160] with Kaluza-Klein states, Little Higgs models [135] with the lightest $T$-odd particle, or technicolor theory [258] with a massive fourth family neutrino, to name only a few.

The dark matter searches discussed in this dissertation focus on the WIMP paradigm.

## 3.6 Search for WIMP dark matter

There are several complementary approaches to search for dark matter:

- direct detection experiments measure the recoil of dark matter particles in the vicinity of the Earth on nuclei in the active detector material.
- indirect detection experiments search for an excess in the particle flux observed by earth-bound and satellite detectors due to pair annihilation of dark matter particles in regions of enhanced dark matter density.
- searches for dark matter at particle colliders investigate signatures of missing momentum in the detector plane transverse to the colliding beams due to dark matter pair production.

The experimental approaches for detecting the interactions of dark matter particles with SM particles are complementary. While direct and indirect detection experiments can establish the galactic origin of a signal, their sensitivity to the details of the interaction between dark matter and SM particles is limited. Collider searches, on the other hand, are unable to probe the lifetime of dark matter particles beyond the time scale required for traversing the detector but can probe their interactions in greater detail [144]. Figure 3.7 shows the relevant momentum ranges in the different kinds of searches with prototypical Feynman graphs.

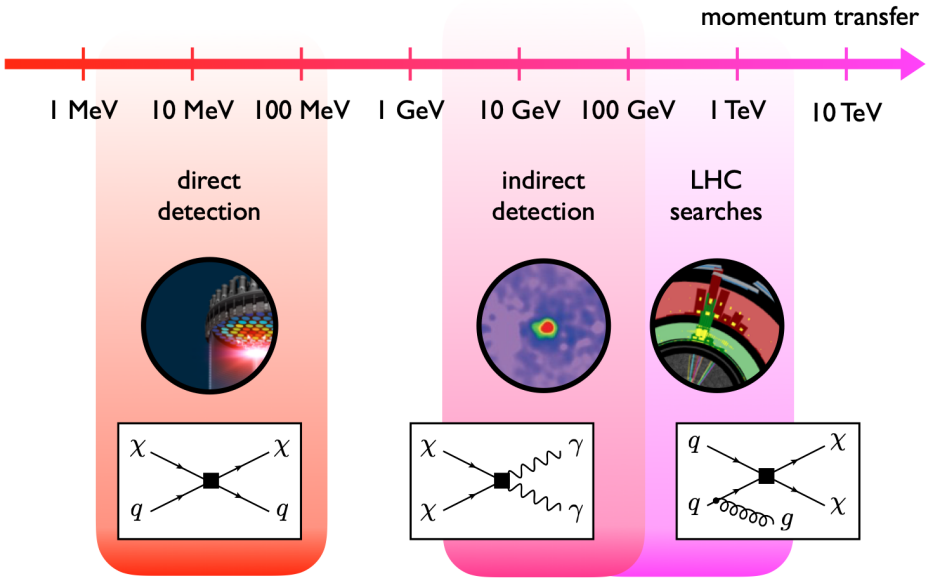



Fig. 3.7.: Range of momentum transfers probed by direct detection experiments, indirect detection experiments and collider searches with prototypical Feynman graphs illustrating the underlying processes. Figure reproduced from Ref. [6].

### 3.6.1 Direct detection experiments

Direct detection experiments (c.f. Refs. [275, 314] for a review) aim to detect the nuclear recoil in the scattering of galactic WIMPs off target nuclei. The interaction rate of WIMPs with nuclei in the detector [134]

$$R \approx \sum_i N_i n_\chi \langle \sigma_{i\chi} \rangle \tag{3.24}$$

depends on

- the number of target nuclei $N_i = m_{\text{detector}}/m_{A_i}$ in the active detector material for nucleons of species $i$ with atomic weight $A_i$,
- the local WIMP density $n_\chi = \rho_\chi / m_\chi$, where $\rho_\chi$ is the local WIMP energy density and $m_\chi$ is the WIMP mass, and
- the cross-section $\sigma_{i\chi}$ for interactions between WIMPs and nucleons of species $i$, averaged over the relative WIMP velocity with respect to the detector.

The values of the astrophysical parameters are set to typical assumptions [314] for the Solar System. The canonical value for the local WIMP energy density is $\rho_\chi = 0.3\,\text{GeV}\,\text{cm}^{-3}$. The WIMP velocity distribution $f(\mathbf{v})$ is defined by the mean WIMP velocity $v_c \approx 220\,\text{km}\,\text{s}^{-1}$ at the solar distance from the galactic centre and by the galactic escape velocity $v_{\text{esc}} \approx 544\,\text{km}\,\text{s}^{-1}$, which determines the truncation of $f(\mathbf{v})$. The remaining free parameters are the WIMP mass $m_\chi$ and the WIMP-nucleon interaction cross-section. The exclusion limits obtained from the non-observation

of WIMP signals are usually shown as contours in the plane defined by these two parameters.

The primary signal in direct detection experiments are nuclear recoils. For WIMPs with mass in the range $1\,\mathrm{GeV} < m_\chi < 1\,\mathrm{TeV}$, the typical elastic recoil energy of the atomic nucleus ranges from $1\,\mathrm{keV} < E_{\mathrm{recoil}} < 100\,\mathrm{keV}$. Electron recoil events can also be investigated, although their typical recoil energy is smaller.

The nuclear recoil energy can be converted into

- thermal motion (phonons),
- ionisation (electrons) of the detector material,
- scintillation light (photons) through the Coulomb field of the charged nucleus.

These modes define the different detection channels of direct detection experiments. Typically, two channels are combined to achieve more powerful discrimination against electron recoil backgrounds from radioactivity.

Direct detection experiments require a very low background environment because of the meagre interaction rates for WIMP-nucleon interactions. Therefore, direct detection experiments are hosted in deep underground laboratories to suppress background produced by cosmic rays. Also, they employ passive shielding and active vetoes to suppress external backgrounds and are made of high-purity detector components to minimise internal backgrounds. As the experiments increase their sensitivity to lower recoil energies, an irreducible background from the scattering of atmospheric and solar neutrinos becomes an issue. This background is referred to as the "neutrino floor" and poses new challenges to the future generation of experiments.

WIMP-nucleon scattering can be classified depending on the type of WIMP-nucleon coupling in

- spin-independent (SI) interactions, which are mediated by scalar or vector couplings, with coherent and elastic WIMP scattering off all nucleons in the nucleus, and
- spin-dependent (SD) interactions, which are mediated by axial-vector couplings, with a $J(J+1)$ dependence of the cross-section on the nuclear spin $J$.

SI interactions give a larger signal than SD interactions because of the coherent scattering and the ensuing $A^2$ dependence of the interaction cross-section on the atomic weight. SD interactions can be studied in WIMP-proton scattering of ${}^{19}_{9}\mathrm{Fl}$ and in WIMP-neutron scattering of ${}^{73}_{32}\mathrm{Ge}$, ${}^{129}_{54}\mathrm{Xe}$, and ${}^{131}_{54}\mathrm{Xe}$.

Direct detection experiments can be based on

- liquid noble gas detectors, such as Xenon (XENON1T [28], LUX [18], PandaX-II [334]) or Argon (DEAP-3600 [24], DarkSide-50 [11]), which are sensitive mostly to small cross-sections,

- cryogenic crystals, such as Calcium tungstate (CRESST-III [4]) or Germanium (SuperCDMS [13], CDMSlite [12]), which are sensitive mostly to small masses,
- crystal scintillators, such as Sodium iodide (DAMA/LIBRA [130]).

The DAMA/LIBRA [130] experiment has reported an annually modulated signal consistent with a WIMP interpretation. However, the results are in conflict with non-observations and resulting exclusion limits obtained from other experiments. Figure 3.8 shows an overview of the constraints placed on the SI WIMP-nucleon cross-section for WIMPs with mass $m_\chi$.

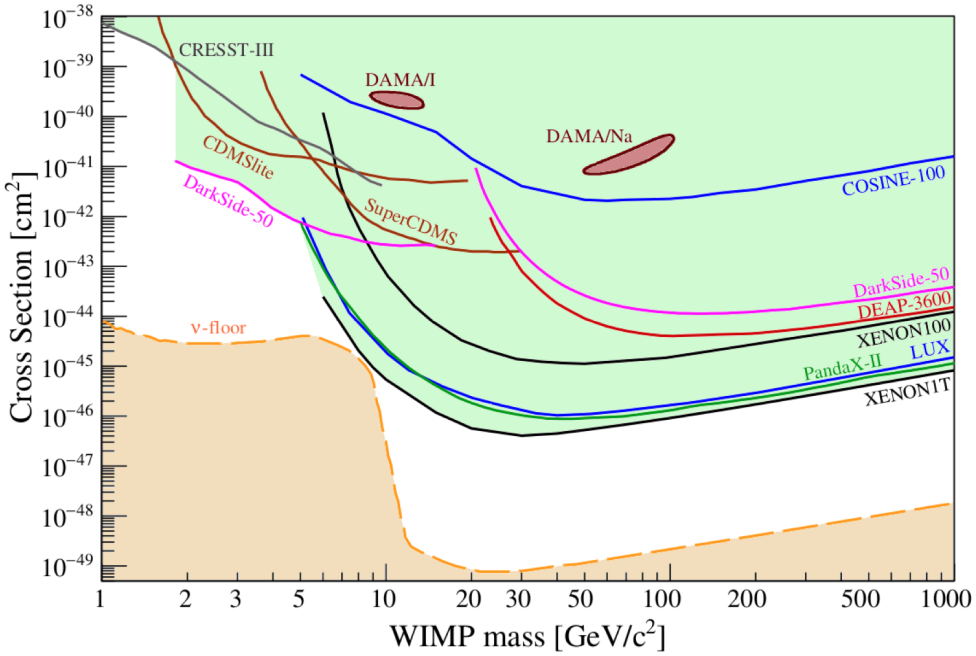



Fig. 3.8.: Constraints placed on the SI WIMP-nucleon cross-section for WIMPs with mass $m_\chi$ by direct detection experiments. Figure reproduced from Ref. [314].

## 3.6.2 Indirect detection experiments

Indirect detection experiments (c.f. Refs. [193, 244] for a review) search for excess in flux of gamma rays, neutrinos or cosmic rays due to dark matter pair annihilation. WIMPs can annihilate in regions of large density, such as galaxy cores, the Sun or the Earth.

The gamma-ray, neutrino or cosmic ray flux (denoted $x$) from an object under consideration [244]

$$\frac{\mathrm{d}\phi}{\mathrm{d}E_x} = \frac{1}{4\pi}\frac{\langle\sigma_{\chi\chi\to X}v\rangle}{2m_\chi^2}\frac{\mathrm{d}N_x}{\mathrm{d}E_x} \times \int \mathrm{d}\Omega \int_{\text{line of sight}} \mathrm{d}r\, \rho_\chi(r)^2 \tag{3.25}$$

depends on

- the thermally averaged product of the dark matter self-annihilation cross-section times the dark matter velocity $\langle \sigma_{\chi\chi \to X} v \rangle$
- the WIMP mass $m_\chi$
- the expected particle spectrum $\mathrm{d}N_x \, \mathrm{d}E_x$, and
- the so-called "J-factor", the integrated squared dark matter density along the line of sight to the object under consideration $\int_{\text{line of sight}} \rho_\chi(r)^2 \, \mathrm{d}r \, \mathrm{d}\Omega$.

Searches for gamma-ray emission have focused on nearby dwarf spheroidal galaxies with considerably low backgrounds, the inner region of the Milky Way with a considerable background at almost any wavelength, and nearby clusters of galaxies. A potential signal of dark matter annihilation manifests as a nearly mono-energetic line in the spectrum, with an energy close to the WIMP mass and a width proportional to the dark matter velocity [335].

A variety of different experiments aim for indirect detection of dark matter. The Fermi Large Area Telescope (LAT) [113] and the ground-based facilities HESS [16], VERITAS [29], HAWC [8], and MAGIC [20] probe the gamma-ray spectrum for WIMPs in the mass range $1\,\mathrm{GeV} < m_\chi < 10\,\mathrm{TeV}$. Fermi LAT observed an excess emission at energies of a few GeV in the gamma-ray flux from the galactic centre. Although several interpretations suggest compatibility with a potential signal [253, 260], this interpretation is subject of contestation [137]. Additional experiments looking for indirect detection are AMS [15], PAMELA [10], and IceCube [1].

Figure 3.9 shows an overview of constraints on WIMPs from indirect detection experiments.

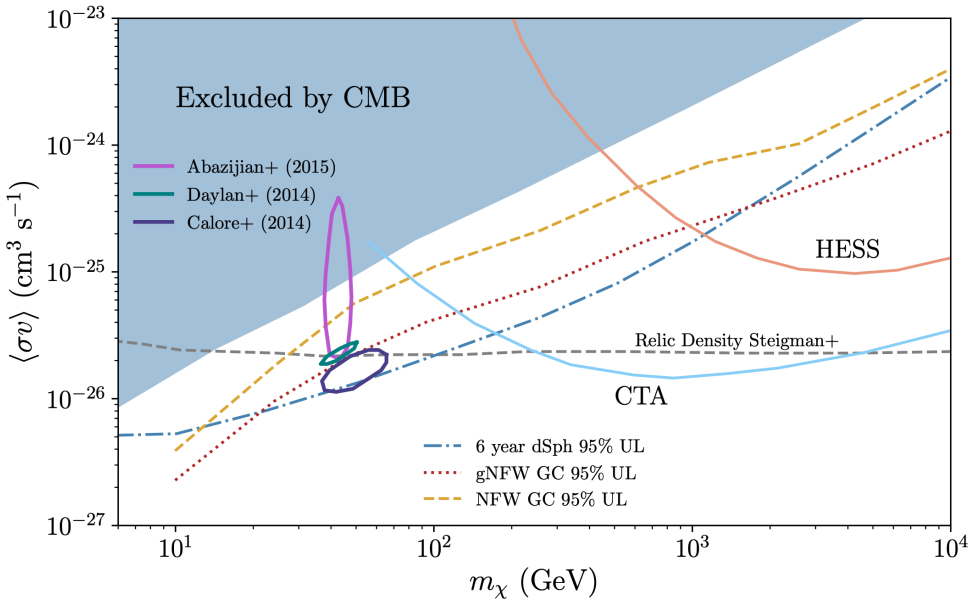



**Fig. 3.9.:** Constraints placed on the self-annihilation cross-section for WIMPs with mass $m_\chi$ by indirect detection experiments. Figure reproduced from Ref. [335].

### 3.6.3 Searches for dark matter at particle colliders

Hadron collider searches (c.f. Ref. [144] for a review) aim to detect signals of WIMPs produced when colliding proton beams in a controlled laboratory environment. Dark matter particles leave no trace in the detectors surrounding the collision point due to their feeble interactions with SM particles. The absence of a reconstructed particle trajectory allows inferring the presence of dark matter using momentum conservation in the plane perpendicular to the colliding beams. As the net transverse momentum before the collision is zero, it must also be so after the collision. An imbalance in the transverse plane is quantified by the missing transverse momentum $E_{\mathrm{T}}^{\mathrm{miss}}$, which is obtained as the negative vector sum of the transverse momenta of all detected particles. The characteristic signature for WIMP production at particle colliders is the observation of significant $E_{\mathrm{T}}^{\mathrm{miss}}$ in association with one or more additional SM particles. This signature is known as "$E_{\mathrm{T}}^{\mathrm{miss}} + X$" and underpins the searches presented in this dissertation. The interaction between SM and dark matter particles typically takes place via a spin-1 or spin-0 mediator. The ATLAS and CMS experiments carry out a range of $E_{\mathrm{T}}^{\mathrm{miss}} + X$ searches:

- $E_{\mathrm{T}}^{\mathrm{miss}}$ + jets,
- $E_{\mathrm{T}}^{\mathrm{miss}}$ + photon $\gamma$ or weak vector boson $\mathrm{W}^{\pm}$/ Z,
- $E_{\mathrm{T}}^{\mathrm{miss}}$ + heavy flavour quarks.
- $E_{\mathrm{T}}^{\mathrm{miss}}$ + SM Higgs boson h,

The $E_{\mathrm{T}}^{\mathrm{miss}}$ + jets search [82, 175] is one of the most inclusive types of searches by considering final states with one or more jets originating from initial state radiation. The accurate theoretical description of SM background processes, which is improved by data-driven methods, establishes the sensitivity to potential signals in the tails of the $E_{\mathrm{T}}^{\mathrm{miss}}$ distribution. Similarly, dark matter particles may be produced in association with a vector boson radiated off from a quark in the initial state. The $E_{\mathrm{T}}^{\mathrm{miss}}$ + photon searches [84, 176] benefit from a very clean signature of $E_{\mathrm{T}}^{\mathrm{miss}}$ and a high-energetic photon. The much lower backgrounds compared to the $E_{\mathrm{T}}^{\mathrm{miss}}$ + jets search make up for the smaller production cross-section than for QCD radiation. The $E_{\mathrm{T}}^{\mathrm{miss}}$ + weak vector boson searches can investigate different decay modes of the vector boson. While a leptonically decaying Z boson [80] also presents a very clean signature, the hadronic decay channel [172] is appealing due to the larger branching fraction. The searches targeting $E_{\mathrm{T}}^{\mathrm{miss}}$ + heavy flavour quarks [94, 171, 165, 168] can probe dark matter production via the exchange of spin-0 mediators. Finally, searches targeting the $E_{\mathrm{T}}^{\mathrm{miss}}$ + SM Higgs boson final state can investigate the various decay modes of the Higgs boson [167]. The decay to $b$-quarks [92, 91] if favoured by having the largest branching fraction. Searches also explore the cleaner $\mathrm{h} \to \tau^{\pm}\tau^{\mp}$ [169] and $\mathrm{h} \to \gamma\gamma$ [86] final states with smaller branching fractions. Searches probing the invisible decay of the Higgs boson in vector-boson-fusion topology or associated production with vector bosons [80] serve as another test of the WIMP hypothesis. To date, no collider search has made claims of discovery of dark matter.

A second approach in constraining dark matter models at colliders is searching for the visible decays of the mediators. Assuming the existence of such a mediator, at least the visible mediator decay to the same SM particles which produced the mediator – quarks or gluons — is guaranteed. Also, possible decays to leptons are considered. The signature of visible mediator decays is a narrow excess in the otherwise smoothly falling background spectrum of the invariant mass of two jets or leptons with the largest momentum. The ATLAS and CMS experiments carry out a range of dijet [99, 173] or dilepton searches [174]. While the high-mass dijet resonance searches constrain the mediator mass from $1.5\,\mathrm{TeV}$ to $3.5\,\mathrm{TeV}$, the searches for low-mass dijet resonances are limited by the process high rates. Searches in this regime are enabled by recording only a limited amount of information of the full event record [97] or by requiring the presence of a resonance produced in association with an additional high-energetic particle or jet [98].

The current status and perspectives for collider based dark matter searches are presented in Chapter 13.

## 3.7 Theoretical frameworks for dark matter production at particle colliders

The theoretical frameworks predicting the production of WIMPs are an indispensable part of collider searches. They guide the design and optimisation of the searches by elucidating the phenomenology of potential dark matter particle candidates in specific final states. In addition, they allow connecting the results of collider searches with direct and indirect detection experiments.

The range of models predicting dark matter production at the LHC varies in generality and plausibility. The two end-points of the spectrum are defined by the effective field theory (EFT) approach and complete theories, such as supersymmetry. Figure 3.10 shows an overview of theoretical frameworks describing dark matter production at particle colliders with varying degrees of completeness and complexity.

The effective field theory (EFT) approach introduces the WIMP as the only additional state which is accessible at the LHC and describes its interaction with SM particles through a four-point effective contact interaction. Similar to Fermi's theory of weak interactions, heavy intermediate states are mapped to effective operators, which are characterised by the energy scale of the interaction. Complete theoretical frameworks, on the other hand, are well-motivated and consistent theories with perturbative ultraviolet (UV) completions. They make specific predictions for invisible, heavy particles with mass at the electroweak scale. Typically, these complete theories are characterised by a large number of model parameters.

While the LHC experiments also have a broad array of searches in the context of complete theories, the dedicated LHC dark matter searches follow a theory-agnostic approach by specifying only the interaction between SM particles and WIMPs relevant to the signature of dark matter pair production.

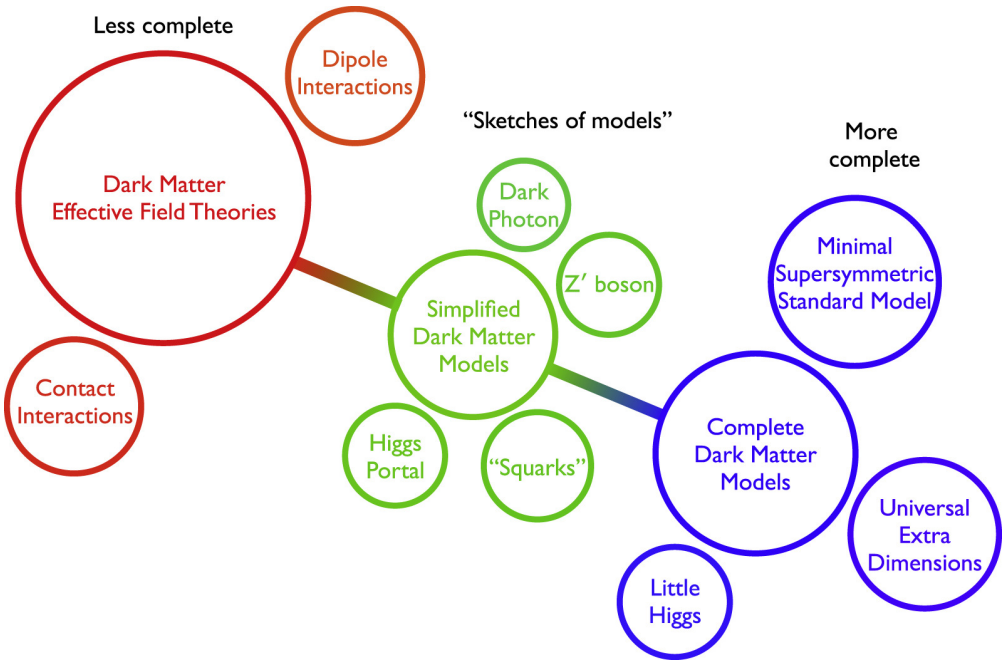



**Fig. 3.10.:** Overview of theoretical frameworks describing dark matter production at particle colliders. The models range from dark matter effective field theory, over various simplified models, to complete dark matter models. Figure reproduced from Ref. [3].

It has been shown that the EFT approach is overly simplistic to capture the phenomenology of more complete models fully. Their kinematic distributions differ significantly from the ones obtained in an EFT description. Moreover, the EFT approach breaks down at the TeV energy scale probed in LHC interactions, as the momentum transfer in the process is sufficient to resolve the underlying processes. As a consequence, the preferred theoretical framework of LHC dark matter searches are *simplified models*, which make explicit assumptions about at least two additional states: a WIMP and a particle mediating the interaction between WIMP and SM particles. Scenarios with an SM mediator are almost ruled out, therefore suggesting the mediator to be a yet-undiscovered particle. Although simplified models are characterised by only a small number of parameters and make no assumptions about extended particle sectors, they can be designed to be fully consistent at all energy scales.

The searches for dark matter presented in this dissertation are motivated by a range of simplified models with varying degree of complexity. The following paragraphs discuss a simplified model for dark matter production with a spin-1 $Z'$ mediator, two simplified models with an extended Higgs sector, and a simplified model with two mediators.

### 3.7.1 Simplified model for dark matter production with a spin-1 $\mathrm{Z}'$ mediator

The simplified model with a vector or axial-vector mediator ($V/A$ simplified model) [7] is a minimal extension of the SM describing the production of dark matter particles via $s$-channel exchange. The model postulates a Dirac fermion dark matter particle $\chi$ with mass $m_\chi$, which is charged under an additional $\mathrm{U}(1)$ gauge symmetry. Assuming that also some SM particles are charged under this group, dark matter pair production can occur via the exchange of a new $\mathrm{Z}'$ gauge boson of mass $m_{\mathrm{Z}'}$, which is referred to as the *mediator*. Both vector and axial-vector couplings between the spin-1 mediator are possible. The corresponding interaction Lagrangian densities are (neglecting mediator couplings to leptons with coupling strength $g_\ell$)

$$\mathcal{L}_{\text{vector}} = g_q \sum_{q=\mathrm{u,d,s,c,b,t}} \mathrm{Z}'_\mu \bar{q}\gamma^\mu q + g_\chi \mathrm{Z}'_\mu \bar{\chi}\gamma^\mu \chi \tag{3.26}$$

$$\mathcal{L}_{\text{axial-vector}} = g_q \sum_{q=\mathrm{u,d,s,c,b,t}} \mathrm{Z}'_\mu \bar{q}\gamma^\mu\gamma^5 q + g_\chi \mathrm{Z}'_\mu \bar{\chi}\gamma^\mu\gamma^5 \chi \tag{3.27}$$

The mediator couples universally to all quarks and leptons with the coupling strengths $g_q$ and $g_\ell$, respectively, and couples to dark matter particles $\chi$ with coupling strength $g_\chi$ [19]. The universal coupling to all quarks or leptons ensures that the general structure of flavour-changing neutral current processes is preserved in the extension of the SM via Minimal Flavour Violation [202]. Assuming that no additional visible or invisible decays contribute to the width of the mediator and ignoring possible decays to leptons, the minimal width is fixed by the couplings $g_q$ and $g_\chi$. The minimal widths for the vector and axial vector mediator are

$$\begin{aligned}\Gamma^V_{\text{min}} =& \Gamma^V_{\chi\chi} + \Gamma^V_{qq} \\ =& \frac{g_\chi^2 m_{\mathrm{Z}'}}{12\pi}\left(1+\frac{2m_\chi^2}{m_{\mathrm{Z}'}^2}\right)\beta_\chi \theta(m_{\mathrm{Z}'}-2m_\chi) \\ &+ \sum_{q=\mathrm{u,d,s,c,b,t}} \frac{3g_q^2 m_{\mathrm{Z}'}}{12\pi}\left(1+\frac{2m_q^2}{m_{\mathrm{Z}'}^2}\right)\beta_q \theta(m_{\mathrm{Z}'}-2m_q)\end{aligned} \tag{3.28}$$

$$\begin{aligned}\Gamma^A_{\text{min}} =& \Gamma^A_{\chi\chi} + \Gamma^A_{qq} \\ =& \frac{g_\chi^2 m_{\mathrm{Z}'}}{12\pi}\beta_\chi^3 \theta(m_{\mathrm{Z}'}-2m_\chi) \\ &+ \sum_{q=\mathrm{u,d,s,c,b,t}} \frac{3g_q^2 m_{\mathrm{Z}'}}{12\pi}\beta_q^3 \theta(m_{\mathrm{Z}'}-2m_\chi),\end{aligned} \tag{3.29}$$

where $\theta$ denotes the Heaviside step function and $\beta_f = \sqrt{1-4m_f^2/m_{\mathrm{Z}'}^2}$ is the velocity of the fermion $f$ with mass $m_f$ in the rest frame of the $\mathrm{Z}'$ mediator.

Under the minimal width assumption, the model is specified by the set of parameters shown in Table 3.1.

**Tab. 3.1.:** Parameters in the $V/A$ simplified model

| Parameter | Description |
|---|---|
| $m_{Z'}$ | Z′ mediator mass |
| $m_\chi$ | dark matter particle mass |
| $g_q$ | coupling strength of Z′ mediator to quarks |
| $g_\ell$ | coupling strength of Z′ mediator to leptons |
| $g_\chi$ | coupling strength of Z′ mediator to dark matter particles |

Both the vector mediator and the axial-vector mediator model are available in event generators up to next-to-leading order (NLO) accuracy in QCD.

### 3.7.2 Simplified model with an extended Higgs sector and a pseudo-scalar mediator

The $a$-2HDM [123] is a self-consistent simplified model with an extended Higgs sector, allowing the model to be embedded in a UV-complete and renormalisable framework. It is based on a Two-Higgs-doublet model (2HDM) [141] with five physical scalar states in the Higgs sector and an additional pseudo-scalar mediator.

The 2HDM potential for the two Higgs doublets $H_1, H_2$ is given by

$$\begin{aligned} V_H =& \mu_1 H_1^\dagger H_1 + \mu_2 H_2^\dagger H_2 + (\mu_3 H_1^\dagger H_2 + \text{h.c.}) \\ &+ \lambda_1 (H_1^\dagger H_1)^2 + \lambda_2 (H_2^\dagger H_2)^2 + \lambda_3 (H_1^\dagger H_1)(H_2^\dagger H_2) \\ &+ \lambda_4 (H_1^\dagger H_2)(H_2^\dagger H_1) + \left[\lambda_5 (H_1^\dagger H_2)^2 + \text{h.c.}\right], \end{aligned} \tag{3.30}$$

where h.c. denotes the Hermitian conjugate and $\mu_i, i = 1, 2, 3$ and $\lambda_i, i = 1, \ldots, 5$ are free parameters. The potential is CP-conserving and has a softly broken $\mathbb{Z}_2$ custodial symmetry to suppress flavour-changing neutral currents. The Higgs doublets have the vacuum expectation values $\langle H_i \rangle = (0, v_i/\sqrt{2})^T, i = 1, 2$ with $v = \sqrt{v_1^2 + v_2^2} = 246\,\text{GeV}$ and their ratio defines $\tan\beta = v_2/v_1$. The physical CP-even states h and H result from mixing of the neutral CP-even weak eigenstates with a corresponding mixing angle $\alpha$. The extended Higgs sector contains also two charged states $\text{H}^\pm$ of identical mass.

The interaction term for the pseudo-scalar mediator $P$

$$V_P = \frac{1}{2} m_P^2 P^2 + P(i b_P H_1^\dagger H_2 + \text{h.c.}) + P^2(\lambda_{P_1} H_1^\dagger H_1 + \lambda_{P_2} H_2^\dagger H_2), \tag{3.31}$$

with the pseudo-scalar mass parameter $m_P$ and the portal couplings $b_P, \lambda_{P_1}, \lambda_{P_2}$, mixes the mediator with the CP-odd state in the extended Higgs sector with mixing angle $\theta$. The resulting physical CP-odd states are $a$ and A.

The dark matter particle $\chi$ is a Dirac fermion with mass $m_\chi$. The pseudo-scalar mediator couples to the dark matter particle with the real Yukawa coupling $y_\chi$ via

$$\mathcal{L}_\chi = -iy_\chi P\overline{\chi}\gamma_5\chi. \tag{3.32}$$

The alignment limit $\sin(\beta-\alpha)=1$ is assumed, allowing the identification of the lightest CP-even scalar h with the SM Higgs boson. A type-II 2HDM coupling structure is assumed, letting up- and down-type quarks couple to separate doublets. The model is specified by the set of 14 parameters shown in Table 3.2.

**Tab. 3.2.:** Parameters in the $a$-2HDM simplified model

| Parameter | Description |
|---|---|
| $\alpha$ | mixing angle of neutral CP-even weak eigenstates |
| $\tan\beta$ | ratio of Higgs doublet vacuum expectation values |
| $\theta$ | mixing angle of neutral CP-odd weak eigenstates |
| $v$ | electroweak vacuum expectation value |
| $\lambda_3, \lambda_{P_1}, \lambda_{P_2}$ | quartic couplings of scalar bosons |
| $m_\mathrm{h}, m_\mathrm{H}$ | masses of neutral CP-even Higgs bosons |
| $m_a, m_\mathrm{A}$ | masses of neutral CP-odd Higgs bosons |
| $m_{\mathrm{H}^\pm}$ | charged Higgs bosons mass |
| $m_\chi$ | dark matter particle mass |
| $y_\chi$ | Yukawa coupling of dark matter particle |

The $a$-2HDM model is characterised by a rich phenomenology so that it can be probed by all $E_\mathrm{T}^\mathrm{miss}$ + X searches, which are discussed in Section 3.6.3. In particular, the $E_\mathrm{T}^\mathrm{miss}$ + Higgs boson and $E_\mathrm{T}^\mathrm{miss}$ + Z boson final states are expected to provide leading constraints in the theoretically best-motivated region of the parameter space.

### 3.7.3 Z′-2HDM simplified model

The Z′-2HDM [129] is another simplified model with an extended Higgs sector. It is based on a 2HDM (c.f. the discussion in Section 3.7.2) with an additional $\mathrm{U}(1)_{\mathrm{Z}'}$ symmetry, which gives rise to a Z′ boson. The Z′ boson can mix with the Z boson. It is implicitly assumed that there is a mechanism for generating the Z′ boson mass in a gauge-invariant way.

After symmetry breaking, the two Higgs doublets can be parametrised as

$$H_1 = \begin{pmatrix} -\mathrm{H}^{\pm} \sin\beta \\ v_1 - \mathrm{h}\sin\alpha + \mathrm{H}\cos\alpha - i\mathrm{A}\sin\beta \end{pmatrix} \tag{3.33}$$

$$H_2 = \begin{pmatrix} \mathrm{H}^{\pm} \cos\beta \\ v_2 + \mathrm{h}\cos\alpha + \mathrm{H}\sin\alpha + i\mathrm{A}\cos\beta \end{pmatrix}, \tag{3.34}$$

where similar conventions for denoting the Higgs doublets, the states in the extended Higgs sector and the mixing angles have been adopted as in Section 3.7.2. The alignment limit $\sin(\beta - \alpha) = 1$ is assumed, allowing the identification of the lightest CP-even scalar h with the SM Higgs boson. The model specifies a type-II 2HDM coupling structure, letting up- and down-type quarks couple to separate doublets. As only the right-handed up-type quarks $\mathrm{u}_{i,R}$ and the Higgs doublet $H_1$ are charged under $\mathrm{U}(1)_{\mathrm{Z}'}$, the Z′ boson only couples to the Higgs doublet which couples to the up-type quarks and to right-handed quarks. The CP-odd physical state A in the extended Higgs sector couples to dark matter particles.

The model is specified by the set of nine parameters shown in Table 3.3.

**Tab. 3.3.:** Parameters in the Z′-2HDM simplified model

| Parameter | Description |
|---|---|
| $\alpha$ | mixing angle of neutral CP-even weak eigenstates |
| $\tan\beta$ | ratio of Higgs doublet vacuum expectation values |
| $m_{\mathrm{h}}, m_{\mathrm{H}}$ | masses of neutral CP-even Higgs bosons |
| $m_{\mathrm{H}^{\pm}}$ | mass of charged Higgs bosons |
| $m_{\mathrm{A}}$ | neutral CP-odd Higgs boson mass |
| $m_{\mathrm{Z}'}$ | Z′ boson mass |
| $g_{\mathrm{Z}'}$ | coupling strength of the Z′ boson |
| $m_{\chi}$ | dark matter particle mass |

The model describes resonant production of a Z′ boson, which subsequently decays into the SM Higgs boson h and the CP-odd Higgs boson A. The latter enables dark matter pair production due to its large branching fraction to dark matter.

### 3.7.4 Two mediator dark matter model

The two mediator dark matter model [212, 211] (2MDM model) is a consistent simplified model with a Z′ boson and a dark Higgs boson as mediators. The model postulates a Majorana fermion as dark matter particle $\chi$, a complex Higgs field $S$ and an additional $\mathrm{U}(1)_{\mathrm{Z}'}$ gauge group. It satisfies the requirements of gauge invariance and perturbative unitarity by incorporating more features of complete theories: the masses of the fermionic dark matter particle and of the Z′ boson are generated by spontaneous symmetry breaking of the $\mathrm{U}(1)_{\mathrm{Z}'}$ group. The symmetry breaking gives

rise to the dark Higgs boson $s$. The dark matter particle $\chi$ with mass $m_\chi$ couples via axial coupling to the Z′ boson. The interaction Lagrangian density is

$$\mathcal{L}_\chi = -\frac{1}{2} g_\chi \mathrm{Z}'^\mu \overline{\chi} \gamma^5 \gamma_\mu \chi - g_\chi \frac{m_\chi}{m_{\mathrm{Z}'}} s \overline{\chi} \chi + 2 g_\chi \mathrm{Z}'^\mu \mathrm{Z}'_\mu (g_\chi s^2 + m_{\mathrm{Z}'} s). \tag{3.35}$$

with the four independent parameters

- dark matter particle mass $m_\chi$,
- Z′ boson mass $m_{\mathrm{Z}'}$,
- dark Higgs boson mass $m_s$,
- $g_\chi = g_{\mathrm{Z}'} q_\chi$ dark matter coupling, with the $\mathrm{U}(1)_{\mathrm{Z}'}$ gauge coupling $g_{\mathrm{Z}'}$ and charge of the dark matter particle $q_\chi = q_S/2$.

The dark sector is coupled to the SM by postulating vector couplings of the Z′ to quarks ($q$) by gauging baryon number. The corresponding interaction Lagrangian is

$$\mathcal{L}_q = -g_q \mathrm{Z}'^\mu \bar{q} \gamma_\mu q \tag{3.36}$$

with the coupling strength of the Z′ boson to quarks $g_q$. Axial-vector couplings and couplings to leptons are neglected for simplicity.

The model is specified by the set of five parameters shown in Table 3.4.

**Tab. 3.4.:** Parameters in the two mediator dark matter simplified model

| Parameter | Description |
|---|---|
| $m_\chi$ | dark matter particle mass |
| $m_{\mathrm{Z}'}$ | Z′ mediator mass |
| $m_s$ | the dark Higgs boson mass |
| $g_\chi$ | coupling strength of Z′ mediator to dark sector |
| $g_q$ | coupling strength of Z′ mediator to quarks |
| $\theta$ | mixing angle between the SM Higgs boson and the dark Higgs boson |

The model can be thought of as a combination of two simplified models: one with a spin-1 mediator (c.f. Section 3.7.1) and one with a spin-0 mediator. In this dissertation, the resonant production of a dark Higgs boson decaying to SM particles is investigated.

Non-zero mixing between the dark Higgs boson and the SM Higgs boson with mixing angle $\theta$ ensures that the dark Higgs boson is unstable and can instantly decay into SM states. Consequentially, the dark Higgs boson inherits the branching fractions of an SM-like Higgs boson with mass $m_s$, which are shown in Figure 3.11.

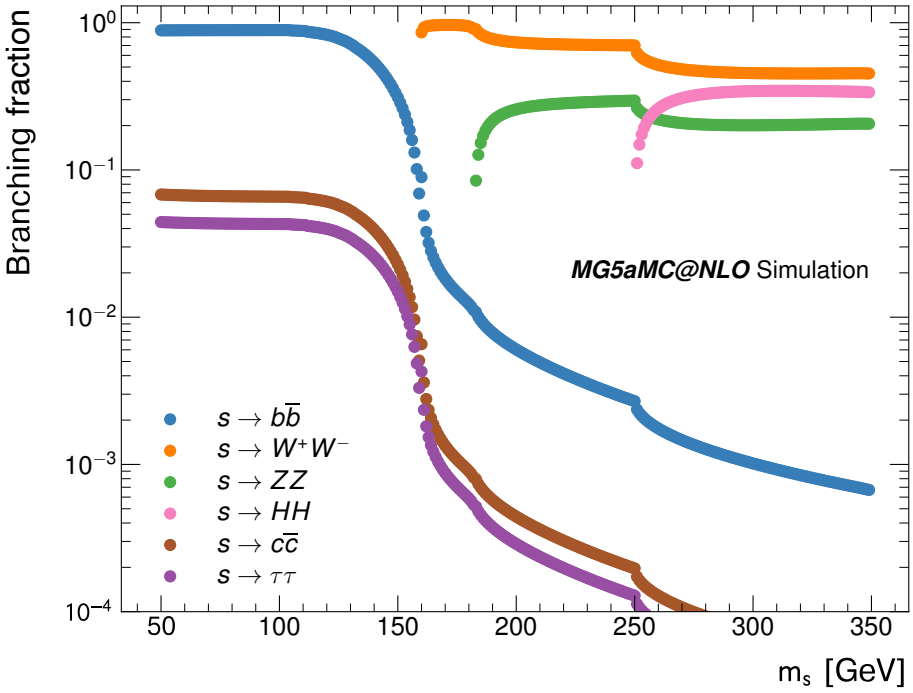



Fig. 3.11.: Branching fractions of dark Higgs boson decays to SM particles (produced on-shell) in dependence of $m_s$.

# 4 Proton-proton collision phenomenology

## 4.1 Basic concepts

Collisions of protons at high energy scales can be described by perturbative quantum field theory. Matrix elements of strong interaction processes can be calculated systematically at fixed orders in the strong coupling constant $\alpha_s$. However, the description of pp collision events involves additional complexity, as protons are strongly interacting and composite objects. In $e^-e^+$ collisions, the participants in the scattering process are the same elementary particles which are accelerated. In contrast, in a typical pp collision, it is the proton beams which are accelerated but two partons which take part in the hard scattering process. The debris of the initial protons gives rise to additional activity in the event. Furthermore, the interactions which convert the coloured parton states into hadrons occur at low momentum scale, where the strong coupling becomes large, and consequently, they cannot be described by perturbation theory.

The detailed description of a pp collision event can be decomposed into various processes. Figure 4.1 shows a proton-proton collision event with the production of a top quark pair and a Higgs boson in the hard scattering process. The various colours encode different processes, which are listed ordered by the respective momentum transfer $Q^2$, starting with the hardest process.

1. Hard interaction (red)
2. Initial state radiation (ISR) (blue)
3. Final state radiation (FSR) (red)
4. Hadronisation and hadron decays (green)
5. Underlying event (purple)

The hard scattering process involves the largest momentum scales, allowing for a description at fixed-order perturbation theory in QCD. The description of the hard scattering process includes the relevant features of the event, such as the production of heavy states or hard QCD jets. Typically, the description of the hard scattering process is achieved by automated evaluation of the relevant Feynman diagrams and numerical integration over the phase-space of the final state particles. Secondary emissions include ISR from the incident partons and FSR from the particles produced in the hard scattering process. The ISR originates from the breakdown of the coherent quantum states initiated by the parton taking part in the

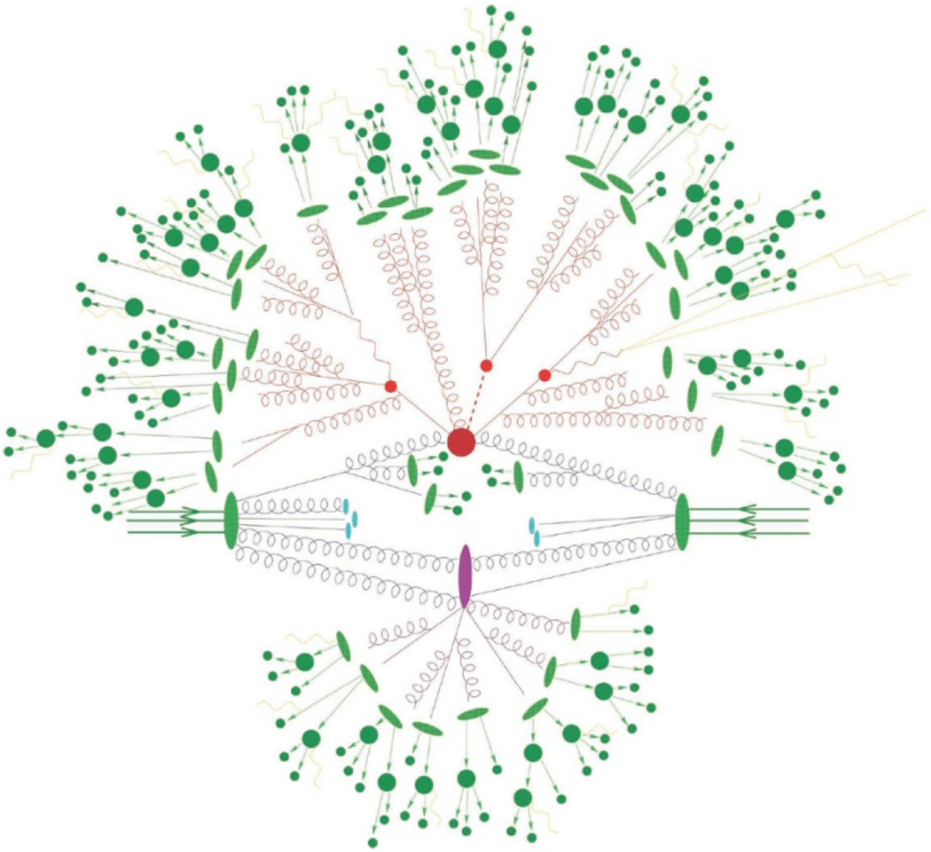


Fig. 4.1.: Sketch of a proton-proton collision event in which a top quark pair and a Higgs boson are produced in the hard scattering process. The incoming protons are shown as the central green ellipses with three incoming valence quark lines. The hard scattering process is depicted as the central red blob. The initial and final state radiation processes are shown in blue and red, respectively. The underlying event of other partons scattering and producing further activity is shown in purple. All emerging partons undergo hadronisation, resulting in cascading showers of hadrons, which are shown in green. Figure reproduced from Ref. [155].

hard interaction. The FSR is due to Bremsstrahlung of particles produced in the hard scattering process, which results in the emission of particles at lower scales. The emitted QCD radiation initiates a parton shower via parton fragmentation, c.f. the splitting processes $q \to qg$, $g \to gg$, and $g \to q\bar{q}$. As the result of the parton shower, a set of coloured partons at the scale of a few $\mathrm{GeV}$ emerges. At this momentum scale, confinement becomes relevant, and the coloured parton states break up into a primary generation of colour-neutral hadrons. This process is called hadronisation. The description of this process involves simulation in non-perturbative models. The most prominent models are the Lund string model [27] and the cluster model [345, 281, 282]. These initial hadrons decay further in cascades of hadrons, resulting in the formation of QCD jets. The underlying event refers to multi-parton interactions in the event, which are difficult to model. Typically, the momentum transfer in these additional parton interactions is soft compared to the hard interaction. The description of the underlying event employs models with tunable parameters.

## 4.2 Parton density functions

A key insight of the parton model is that the quarks and gluons inside a proton can be described in terms of parton density functions (PDFs) $f_{a/\mathrm{p}}(x, Q^2)$ that parametrise the probability of finding a parton $a$ with momentum fraction $x$ at a scale of $Q^2$ inside a proton. PDFs can be measured in different processes and at different scales. These can be related to each other by the Dokshitser-Gribov-Lipatov-Altarelli-Parisi (DGLAP) equations [209, 234, 22]

$$\frac{\partial}{\partial \log Q^2} \begin{pmatrix} f_{q/\mathrm{p}}(x, Q^2) \\ f_{g/\mathrm{p}}(x, Q^2) \end{pmatrix} = \frac{\alpha_s(Q^2)}{2\pi} \int_x^1 \frac{\mathrm{d}z}{z} \begin{pmatrix} \mathcal{P}_{qq}(\frac{x}{z})\mathcal{P}_{qg}(\frac{x}{z}) \\ \mathcal{P}_{gq}(\frac{x}{z})\mathcal{P}_{gg}(\frac{x}{z}) \end{pmatrix} \begin{pmatrix} f_{q/\mathrm{p}}(z, Q^2) \\ f_{g/\mathrm{p}}(z, Q^2) \end{pmatrix}. \quad (4.1)$$

The splitting functions $\mathcal{P}_{gg}(\frac{x}{z})$ can be expanded in perturbation theory and are listed, for instance, in Ref. [155].

The PDFs can be determined from fits to a wide range of experimental data. In typical PDF fits, about $3000$ data points are used [155], including deep inelastic scattering data from fixed-target experiments and the HERA electron-proton collider, and data from Drell-Yan and jet production processes at the Tevatron and the Large Hadron Collider. The CT14 [214], MMHT2014 [241], and NNPDF3.0 [119] PDF sets are the primary choices to describe proton-proton collisions at the Large Hadron Collider [149] and provide PDFs at leading order (LO), next-to-leading order (NLO) and next-to-next-to-leading order (NNLO ) precision in $\alpha_s$.

Figure 4.2 shows the PDFs from the CT14 PDF set for the scales $Q^2 = 2\,\mathrm{GeV}^2$ and $Q^2 = 100\,\mathrm{GeV}^2$. The proton valence quark PDFs (u and d) are the largest for high $x$-values, while the sea-quark and gluon PDFs dominate at low $x$-values. For higher scale $Q^2$, the gluon and sea-quark contributions are enhanced together with the valence quarks at low $x$-values, as more parton structure is resolved. Figure 4.3 shows a comparison of the CT14 PDF set to the MMHT2014 and NNPDF3.0 PDF sets with their respective uncertainty bands. The discrepancies between different

PDF sets originate from different input data, different choices for the parameters and PDF parametrisation.

## 4.3 Calculation of cross-sections

According to factorisation theorems [192], the total cross-section for any process pp $\to X$ can be written as a sum over the partonic cross-sections $\hat{\sigma}_{ab\to X}$ for all parton types $a$ and $b$

$$\sigma_{\mathrm{pp}\to X} = \sum_a \sum_b \int_0^1 \mathrm{d}x_1 \int_0^1 \mathrm{d}x_2 \, f_a(x_1, \mu_\mathrm{F}) f_b(x_2, \mu_\mathrm{F}) \hat{\sigma}_{ab\to X}(x_1 p_1, x_2 p_2, \mu_\mathrm{F}, \mu_\mathrm{R}). \tag{4.2}$$

The PDFs in proton-proton collisions evolve with the factorisation scale $\mu_\mathrm{F}$ according to the same non-perturbative interactions that give rise to scaling violations in deep inelastic scattering. The renormalisation scale $\mu_\mathrm{R}$ is another process-dependent quantity, which indicates the scale at which the coupling constants are evaluated. Typical choices for $\mu_\mathrm{F}$ and $\mu_\mathrm{R}$ are dictated by one hard scale $Q^2$ of the process like the mass of an $s$-channel resonance of mass $M$, such that $\mu_\mathrm{F} = \mu_\mathrm{R} = Q^2 = M^2$.

As the momentum of the partons is distributed according to the PDFs, the centre-of-mass frame of the process is unlikely to coincide with the laboratory frame of reference. In the parton model, one parton has momentum $p_{z_1} = x_1\sqrt{s}/2$ in the detector frame, while the other has the momentum $p_{z_2} = -x_2\sqrt{s}/2$, where $\sqrt{s}$ is the centre-of-mass energy of the proton-proton-system. In the partonic centre-of-mass frame, the energy of the parton is $\hat{s} = x_1 x_2 s$ and it has net momentum along the beam axis of $\hat{p}_z = (x_1 - x_2)$.

The partonic cross-section in the limit of massless partons

$$\hat{\sigma}_{ab\to X}(x_1 p_1, x_2 p_2, \mu_\mathrm{F}, \mu_\mathrm{R}) = \frac{1}{2\hat{s}} \int \mathrm{d}\Phi_n \, |\mathcal{M}_{ab\to X}|^2(\Phi_n, \mu_\mathrm{F}, \mu_\mathrm{R}) \tag{4.3}$$

can be evaluated in perturbation theory by calculation of the matrix element $\mathcal{M}_{ab\to X}$ and the $n$-parton phase space element

$$\mathrm{d}\Phi_n = \prod_{i=1}^{n} \left[ \frac{\mathrm{d}{p_i}^4}{(2\pi)^4} (2\pi)\delta(p_i^2 - m_i^2)\Theta(p_i^0) \right] (2\pi)^4 \delta^4(p_a + p_b - \sum_{i=1}^{n} p_i). \tag{4.4}$$

The cross-sections of typical processes at (anti-)proton-proton colliders for various centre-of-mass energies $\sqrt{s}$ are shown in Figure 4.4. The cross-sections have been calculated in perturbative QCD at NLO and NNLO using the MSTW2008 PDF set [283]. Processes of interest, such as weak gauge boson production or Higgs boson production, or hypothetical dark matter particle production occur with cross-sections which are magnitudes below the total inelastic cross-section in pp collisions at a centre-of-mass energy of $13\,\mathrm{TeV}$ of $78.1 \pm 2.9\,\mathrm{mb}$ [60]. Consequentially, a

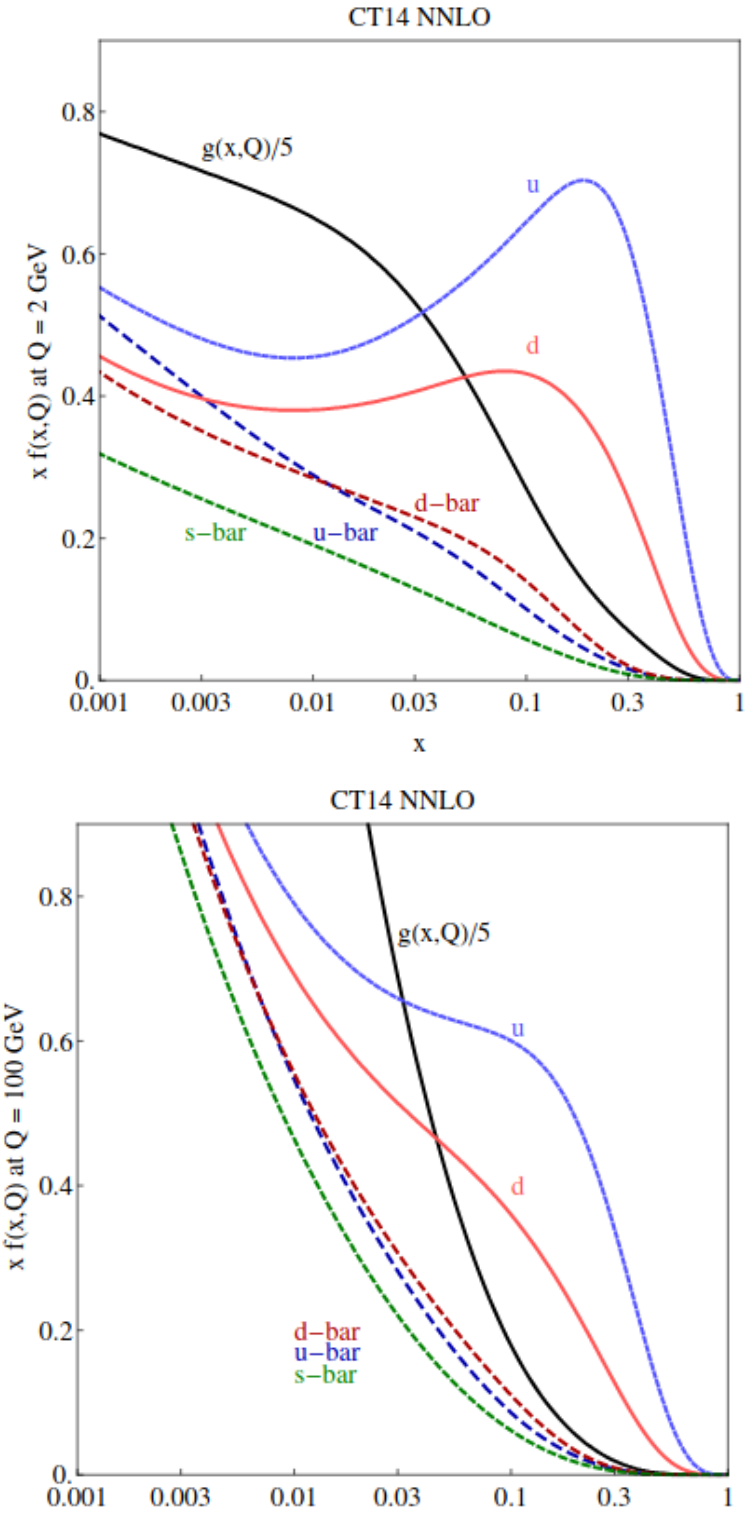



Fig. 4.2.: The CT14 parton distribution functions at the scales of 2 GeV (top) and 100 GeV (bottom) for u $\bar{u}$, d, $\bar{d}$, $\bar{s}$, and g. Figure reproduced from Ref. [214].

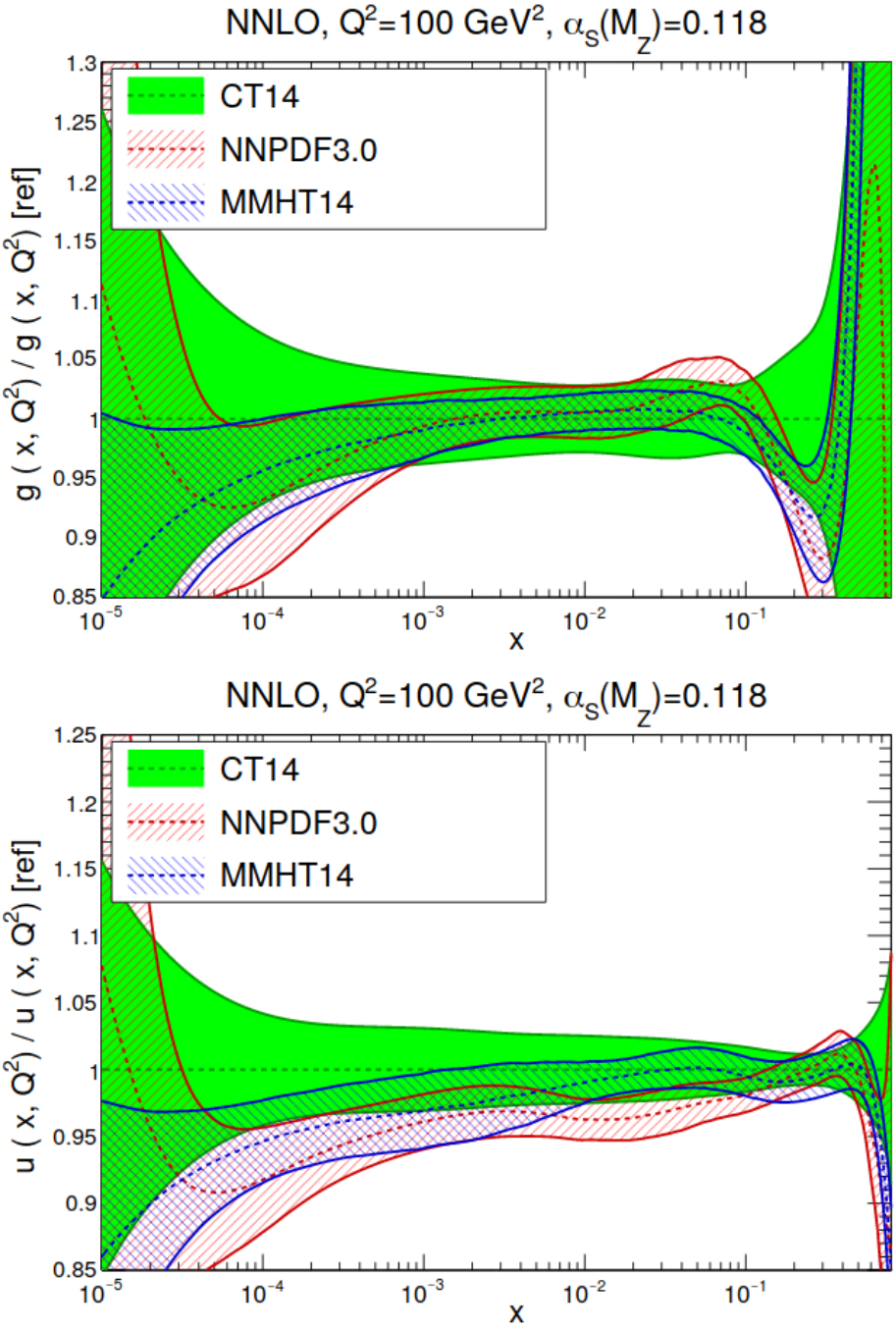



Fig. 4.3.: Comparison of the gluon (top) and up quark (bottom) PDFs from the CT14, MMHT14 and NNNPDF3.0 sets at next-to-next-to-leading order (NNLO ) at a scale of $Q^2 = 100\,\mathrm{GeV}^2$. The results are shown relative to the central value of CT14. Figure reproduced from Ref. [149].

resource-efficient description of selected collision events for investigating these processes starts with the hard process and builds up the event from there.

## 4.4 Event simulation

The processes of interest in pp collisions are simulated by Monte Carlo (MC) event generators [145, 319]. The matrix elements of the hard scattering process are computed in perturbative QCD at fixed orders in $\alpha_s$ in a highly automated way, together with the corresponding phase-space parametrisations. Event generators describing hard processes are MADGRAPH5_aMC@NLO [23] (providing LO and NLO accuracy in QCD) and POWHEG [21] (providing NLO accuracy in QCD). The PDFs are parametrised in the LHAPDF format [146]. The secondary emissions are described by parton showers. Potential overlap of the multiple softer emissions of the parton showers and the higher-order matrix elements is resolved by matching and merging prescriptions.

The three general-purpose event generators SHERPA [230], HERWIG [125], and PYTHIA [320] provide combined descriptions of hard processes interfaced with parton showers. In particular, the HERWIG and PYTHIA generators can be interfaced with MADGRAPH5_aMC@NLO or POWHEG to supplement the parton shower description.

Finally, the interactions of final state particles with the ATLAS detector are simulated with the GEANT4 [14] simulation tool-kit to provide the detector response [104]. The resulting set of simulated collision events is processed in the same manner as observed data with the reconstruction and event selection software.

## 4.5 Hadronic jets

The parton shower evolution is dominated by the emission of partons which are either soft or collinear with the outgoing partons. Consequentially, the emerging hadrons are distributed in localised collimated sprays, which are called jets. The intriguing feature of jets is the correspondence between the total momentum of the hadrons contained in a jet and that of the corresponding partons described by perturbative calculations. This correspondence allows inferring the properties of the hard scattering process from the detector signature produced by QCD jets.

Jets are no fundamental objects but are instead defined by a jet algorithm. A jet algorithm provides a prescription on how to construct jets from input objects. Thereby, the algorithms need to fulfil two tasks. First, they need to identify all potential jet constituents. Second, they need to define the jet's four-vector based on the information provided by the constituents. A jet algorithm is agnostic to the precise nature of the input objects as long they can be parametrised as four-vectors.

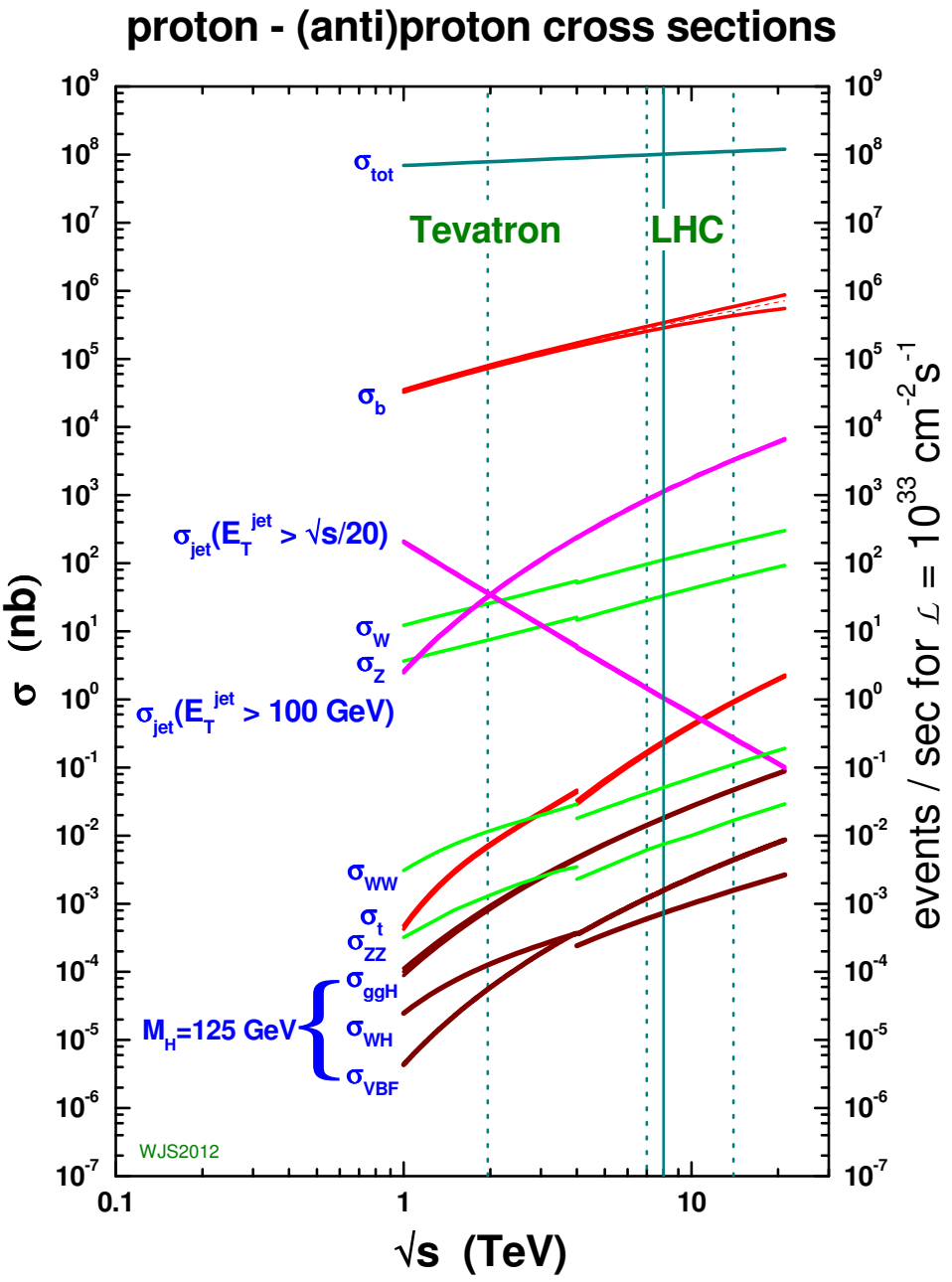



Fig. 4.4.: Cross-sections and event rates for various centre-of-mass energies $\sqrt{s}$ in antiproton-proton (Tevatron, $\sqrt{s} < 4\,\mathrm{GeV}$) and proton-proton (LHC, $\sqrt{s} > 4\,\mathrm{GeV}$) collisions. The cross-sections have been calculated in perturbative QCD at NLO and NNLO using the MSTW2008 PDF set [283]. Figure reproduced from Ref. [331].

Therefore, the input objects can be partons, hadrons or energy deposits in the detectors.

A jet algorithm must be well-defined in arbitrarily high orders of perturbation theory, which involve additional parton emissions, to allow the direct comparison of perturbative calculations with observations. A well-defined jet algorithm, therefore, needs to satisfy the requirements of collinear and infra-red safety: neither collinear splitting nor soft emissions should alter the result of the jet algorithm.

There are two categories of jet algorithms, which differ in their method of identifying the jet constituents. Cone-based algorithms, such as thee SISCone algorithm [313], are based on purely geometric considerations by defining a jet axis and associating all objects within a specific radius parameter. Sequential algorithms cluster and combine pairs of objects until all objects have been used.

The $k_{\mathrm{T}}$ algorithms are a family of sequential algorithms, which satisfy the requirements of collinear and infra-red safety and are successfully employed at the Large Hadron Collider experiments. They iteratively group objects $i$ and $j$ (referred to as pseudo-jets) into jets, using the two generalised distance measures in momentum space between two pseudo-jets ($d_{ij}$) and a pseudo-jet and the beam ($d_{iB}$)

$$d_{iB} = \left(p_{\mathrm{T}}\right)^{2p} \tag{4.5}$$

$$d_{ij} = \min\left\{\left(p_{\mathrm{T},i}\right)^{2p}, \left(p_{\mathrm{T},j}\right)^{2p}\right\} \times \frac{R_{ij}}{R_0}, \tag{4.6}$$

which are based on the transverse momenta of the pseudo-jets $p_{\mathrm{T},i}$ and on the distance between the two objects in the $\eta$-$\varphi$-plane $R_{ij} = \sqrt{\Delta\eta^2 + \Delta\varphi^2}$.

The algorithm evaluates all possible $d_{ij}$ and $d_{iB}$ and identifies the smallest distance. If the smallest distance is between a pseudo-jet and the beam, the pseudo-jet is promoted to a jet and is added to the list of output objects. Otherwise, the two pseudo-jets are discarded, and a new pseudo-jet $k$ whose kinematic properties are based on their vector sum is created. This step is repeated until all pseudo-jets have been promoted to jets.

The parameter $p$ defines the type of jet algorithm in the $k_{\mathrm{T}}$ family:

- $k_{\mathrm{T}}$ algorithm ($p = 1$) [158, 216]
- Cambridge/Aachen algorithm ($p = 0$) [208]
- Anti-$k_t$ algorithm ($p = -1$) [153]

The jet area can be determined by populating the $\eta$-$\varphi$-plane of an event with ghost particles, which have infinitely small momentum [154]. As the $k_{\mathrm{T}}$ algorithms are collinear and infra-red safe, the reconstructed jets are not changed by the addition of ghost particles. However, the association of the ghost particles with jets allows inferring the jet catchment area.

Figure 4.5 shows a comparison of the resulting jet areas for the three algorithms of the $k_{\mathrm{T}}$ family and the SISCone algorithm. The $k_{\mathrm{T}}$ and Cambridge/Aachen algorithms

produce jets with more irregular jet shapes, while the SISCone and anti-$k_t$ algorithms have more regular jet shapes.

The anti-$k_t$ algorithm, which is used as the standard jet algorithm in this dissertation, is collinear and infra-red safe and provides jets with a nearly conical shape at excellent reconstruction efficiency. Depending on the use-case, a different radius parameter is used for the jet reconstruction. The jet algorithms are implemented in the FastJet package [152].

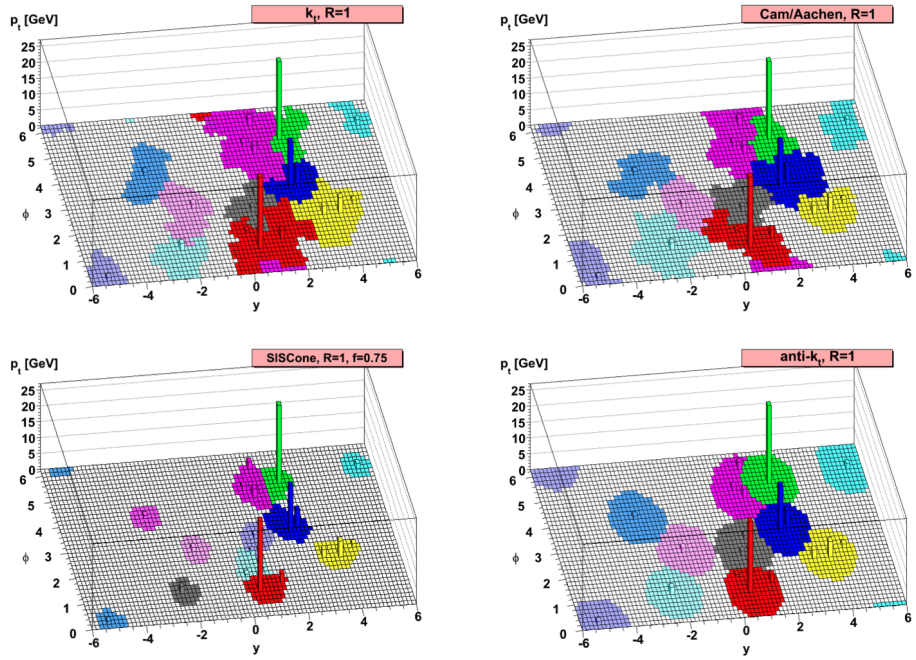



Fig. 4.5.: Clustering of a sample parton-level event with four different jet algorithms, illustrated by the active catchment area of the resulting hard jets. Figure reproduced from Ref. [153].

# 5 Experimental apparatus

## 5.1 Introduction

Scattering experiments have been the key to furthering our understanding of the elementary constituents of matter and their interactions. The seminal work of Geiger, Marsden, and Rutherford [227] on the scattering of $\alpha$-particles[1] from thin metal foils in 1908 unravelled the structure of the atom and led to the discovery of the atomic nucleus. Today, scattering experiments have evolved to using the very same atomic nuclei discovered over a century ago as probes for the uncharted frontiers of particle physics.

The natural observable of scattering experiments is the cross-section $\sigma$ [341]. In a classical interpretation, the number of scattered objects is related to the cross-sectional area of a scattering object, which allowed Rutherford to deduce the size of the atomic nucleus. However, the quantum nature of elementary particles ultimately only allows for a probabilistic description of nature by predicting the probability for a process to happen. In this interpretation, the cross-section has a more abstract meaning as a measure of the interaction strength. It is related to the underlying theory by the equation [316]

$$\sigma = \frac{1}{\Phi_i} \int |\langle f| \mathcal{M} |i\rangle|^2 \, \mathrm{d}\Pi_f \,. \tag{5.1}$$

Here, $\Phi_i$ is the flux of initial state particles $|i\rangle$ and $\mathrm{d}\Pi_f$ is the differential kinematically allowed phase space of the final states $|f\rangle$. The modulus square of the matrix element $\langle f| \mathcal{M} |i\rangle$ gives the probability $P(|i\rangle \to |f\rangle)$ for a transition from $|i\rangle$ to $|f\rangle$. The preparation of initial states $|i\rangle$ and measurement of final states $|f\rangle$ dictates the experimental setup of a scattering experiment with the aim of empirically testing the underlying theory and exploring the structure of matter.

The momentum of initial states $|i\rangle$ determines the scale on which nature can be investigated[2]. Rays of particles with considerable momentum and consequently smaller wavelength allow probing structures on more minor length scales. Although cosmic rays from astrophysical sources can achieve ultra-relativistic energies up to $10^{20}\,\mathrm{eV}$, their rate is vanishingly small [226], so that one can only hope for their detection by terrestrial experiments.

[1] The kinetic energy of the $\alpha$-particles used in Rutherford's experiment is $8\,\mathrm{MeV}$. Modern particle accelerators achieve millionfold beam energy of $6.5\,\mathrm{TeV}$.

[2] The de Broglie relation $\lambda = 1/p$ relates the momentum $p$ of a probe with the size of the structure that can be resolved.

The invention of modern particle accelerators marked a turning point. Particle accelerators not only allow for a reproducible preparation of initial states $|i\rangle$ in a controlled laboratory environment but also their production in abundant number. Remarkably, the kinetic energy of colliding particles also determines the mass scale of the particles created in the collision, possibly giving access to previously inaccessible heavy states. As their production cross-section often is small, only particle accelerators can produce these heavy states in sufficient quantities to allow for their observation. In summary, in a modern scattering experiment, particle accelerators prepare the initial states $|i\rangle$. The two defining quantities of equal importance for a collider experiment are the energy and the rate of collision events. The total beam energy in the centre-of-mass frame $\sqrt{s}$ is the first defining characteristic of particle accelerators. High centre-of-mass energy is required for probing the structure of matter at smallest scales and for producing yet unobserved heavy states. The luminosity is the second defining characteristic of a collider experiment. The number of scattering events measured in a collider experiment for a process with cross-section $\sigma$ during a time $\Delta T$ is

$$N = \sigma \cdot \int_{\Delta T} \mathrm{d}T \, L_{\text{inst}} = \sigma \cdot L. \tag{5.2}$$

It is determined by the instantaneous luminosity $L_{\text{inst}}$. The amount of collected data is quantified by the integrated luminosity $L$, typically stated in the unit $\mathrm{fb}^{-1}$[3].

Particle detectors measure properties of final states $|f\rangle$. To this end, they typically employ three specific types of detector subsystems situated in the increasing distance to the interaction point. First, tracking detectors immersed in magnetic fields provide precision position and momentum-measurements of charged particles. Second, calorimeters measure the energy deposited by electrons, photons, and hadrons. Finally, muon detectors measure the path and momentum of muons passing the calorimeter.

From this discussion, three experimental design requirements for dark matter searches become evident.

1. Processes resulting in the production of dark matter particles at a collider experiment are expected to occur with minute cross-sections at the order of $\mathcal{O}(\mathrm{fb})$. Also, dark matter production might involve heavy states which are only accessible with sufficient beam energy above their production threshold. Consequently, the exploration of terrestrial dark matter production in a laboratory requires a particle accelerator with both high beam energy and high beam intensity.

2. A pp machine is the optimal choice for probing dark matter in collider experiments. Although the models for the production of dark matter particles discussed in Section 3.7 specify the type and interactions of the new states they

[3] Cross-sections are stated in units of length-squared as multiples of a barn, with $1\,\mathrm{b} = 10^{-28}\,\mathrm{m}^2$. The whimsical name owes its creation to physicists of Purdue University. They associated the typical cross-sectional size of a U atomic nucleus with the dominant feature of Midwestern farmlands, which is referred to by the idiom “you can’t hit the side of a barn”.

predict, they make no exact predictions about their mass. Searches for dark matter are required to be sensitive to new physics across a large mass range. To this end, the use of composite objects, such as protons, as initial states allows probing a wide range of possible new heavy states at a fixed collision energy $s$. As only the partons and not the entire proton participate in the hard scattering process, the effective centre-of-mass energy of the interaction $s' = x_a \cdot x_b \cdot s$ depends on the momentum fractions $x_a$ and $x_b$ of the initial state partons. As a result, the energy available for the resonant production of new particles is not fixed as it is the case for electron-positron colliders, making hadron colliders powerful discovery machines.

3. Once produced, dark matter particles do not interact with detector material. They can only be observed via their recoil on other particles, which results in a missing component $E^{\text{miss}}$ in the observed energy-momentum balance of the collision. Therefore, an ideal detector for dark matter searches must not only reconstruct all types of physics objects with excellent precision but also provide hermetical $4\pi$ coverage in full solid angle.

These requirements are met by the Large Hadron Collider (LHC) and the ATLAS detector at the European Organisation for Nuclear Research CERN. Section 5.2 explores the LHC as the culminating part of the CERN accelerator complex and gives an overview of its operation parameters during the years 2015 to 2018. The discussion of the ATLAS detector and its subsystems is provided in Section 5.3.

## 5.2 The Large Hadron Collider

The Large Hadron Collider (LHC) [219] is, at the time of writing, the most powerful terrestrial particle accelerator. Its approximately circular geometry extends $26.7\,\text{km}$ in circumference. The LHC is located in the tunnel which formerly hosted the Large Electron-Positron (LEP) collider and lies $75\,\text{m}$ to $175\,\text{m}$ below the surface of the Franco-Swiss border at CERN near Geneva. The LHC is designed to accelerate and collide two counter-rotating beams of protons in an ultra-high vacuum with a maximum centre-of-mass energy of $\sqrt{s} = 14\,\text{TeV}$. During Run-1 operation during $2009$ to $2013$ at centre-of-mass energies of $\sqrt{s} = 7\,\text{TeV}$ and $7\,\text{TeV}$. This dissertation is based on data taken during Run-2 operation in 2015 to 2018, where the LHC was operated at the centre-of-mass energy of $\sqrt{s} = 13\,\text{TeV}$ and at peak luminosity of $2.1 \times 10^{34}\,\text{cm}^{-2}\,\text{s}^{-1}$. Although the LHC's design also allows for colliding heavy lead ions with an energy of up to $2.8\,\text{TeV}$ per nucleon, heavy ion physics is beyond the scope of this dissertation and only the proton physics programme is briefly discussed in the following. A more detailed account is given in Refs. [143, 142, 126].

The protons injected to the LHC undergo several stages of acceleration in a pre-accelerator-chain [126], shown in Figure 5.1.

They start their journey as hydrogen atoms, supplied from a simple gas bottle and ionised by stripping them of their electrons in a duoplasmatron machine [117]. The protons emerge as a beam with $300\,\text{mA}$ current and are first accelerated to

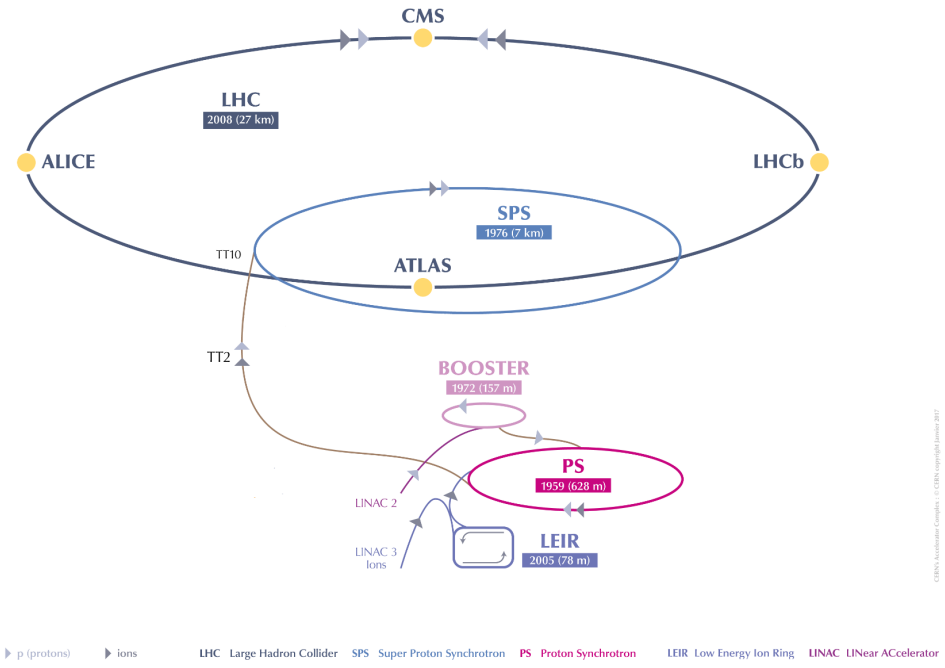



**Fig. 5.1.:** The CERN accelerator complex. The illustration shows the LHC ring and the associated pre-accelerator chain relevant for producing pp collisions. Figure adapted from Ref. [290].

$\sqrt{s} = 50\,\mathrm{MeV}$ by the LINAC2 linear accelerator. The Proton Synchroton Booster (PSB) and the Proton Synchrotron (PS) perform the next acceleration stages. Both are synchrotron accelerators. The PSB consists of four synchrotron rings with a radius of $25\,\mathrm{m}$, which are stacked on top of each other, and accelerates the protons to $\sqrt{s} = 1.4\,\mathrm{GeV}$. The PS extends over large parts of the CERN Meyrin site with a radius of $100\,\mathrm{m}$ and raises the beam energy to $25\,\mathrm{GeV}$. As each of the four PSB rings extends one-quarter of the PS circumference, the PSB beam can be extracted sequentially to the PS. As the beams are extracted and injected by kicker magnets, pulsed dipole magnets with swift time response, they arrive not continuously but in discrete bunches. The Super Proton Synchrotron, extending $7\,\mathrm{km}$ in circumference, ramps up the beam energy to $450\,\mathrm{GeV}$ before the proton beams are injected in the two storage rings of the LHC.

In the LHC, particles are accelerated by radio frequency (RF) cavities driven by high power klystrons. The RF system is operated at $400.79\,\mathrm{MHz}$ with each cavity providing a field gradient of $5.5\,\mathrm{MV\,m^{-1}}$ and $2\,\mathrm{MeV}$ acceleration voltage, resulting in a total increase of the beam energy by $485\,\mathrm{keV}$ per revolution.

The LHC beams are kept on their circular trajectories by $1232$ superconducting niobium-titanium dipole magnets operated at a temperature of $1.9\,\mathrm{K}$ with magnetic field strengths of $8.33\,\mathrm{T}$. The space constraints imposed by the tunnel require a twin-bore magnet design, hosting the two beam pipes and two sets of magnet coils

Tab. 5.1.: Essential LHC parameters with their description and values during Run-2 operation [219].

| Parameter | Description | Value |
|---|---|---|
| $E$ | beam energy | $6.5\,\mathrm{TeV}$ |
| $L_{\mathrm{inst}}$ | peak luminosity | $2 \times 10^{34}\,\mathrm{cm}^{-2}\,\mathrm{s}^{-1}$ |
| $N_b$ | particles per bunch | $1.15 \times 10^{11}$ |
| $n_b$ | bunches per beam | 2808 |
| $f_{\mathrm{rev}}$ | revolution frequency | $11.245\,\mathrm{kHz}$ |
| $\gamma$ | relativistic gamma factor | 7461 |
| $\varepsilon_n$ | normalised transverse beam emittance | $3.75\,\mu\mathrm{m}$ |
| $\beta^*$ | $\beta$ function at collision point | $0.5\,\mathrm{m}$ |
| $F$ | geometric luminosity reduction factor due to crossing angle at interaction point | 0.836 |

within the same mechanical structure and cryostat. The beams are focussed using quadrupole and higher-order multipole magnets.

The machine luminosity is determined by several beam parameters, which are listed in Table 5.1, and can be written as

$$L = \frac{N_b^2 n_b f_{\mathrm{rev}} \gamma_r F}{4\pi \varepsilon_n \beta^*}. \tag{5.3}$$

The luminosity is determined by in-situ measurements performed with dedicated detectors and van-der-Meer scans [285, 56].

The two beams intersect at four interaction points, each within a cavern hosting one of the four extensive LHC experiments ATLAS [178], LHCb [189], CMS [183], and ALICE [177]. In total, there are eight LHC experiments. The three smaller experiments, TOTEM [191], LHCf [190], MoEDAL [289], and FASER [30], complement the LHC physics programme by more specific measurements. TOTEM and LHCf use detectors positioned close to the CMS and ATLAS experiment, respectively, to investigate the physics of particles generated almost directly in line with the colliding proton beams. The prime goal of the MoEDAL experiment, which shares the cavern with LHCb, is the search for magnetic monopoles and exotic particles. The FASER experiment, which is located in a service tunnel downstream from the interaction point used by the ATLAS experiment, searches for light, weakly-coupled particles and investigates the interactions of high-energy neutrinos. The LHCb experiment is a specialised detector investigating flavour physics. The ALICE experiment investigates physics of strongly interacting matter at extreme energy densities by analysing heavy lead ion collisions. The two all-purpose detectors ATLAS and CMS, operated at peak luminosity, are located in opposed caverns. Their independent operation and different detector design are crucial for cross-checks and reciprocal corroboration in the event of a potential discovery.

Although high beam intensities enhance searches for rare processes by increasing the collected data over time, they also increase the number of simultaneous pp interactions in a single collision event. Such multiple pp interactions are known as pile-up and are typically uncorrelated with the hard-scattering process. Therefore, they contribute a largely diffuse background of primarily soft energy depositions in the detector. One distinguishes between in-time pile-up, which refers to multiple collision events within the same bunch crossing, and out-of-time-pileup, which refers to energy deposits from previous and following bunch crossings concerning the triggered event. The total expected amount of pile-up $\mu$ is related to the instantaneous luminosity by the equation

$$\mu = \frac{\mathcal{L}\sigma_{\text{inel}}}{N_b n_b f_{\text{rev}}}, \tag{5.4}$$

where $\sigma_{\text{inel}} = 78.1 \pm 2.9\,\text{mb}$ is the inelastic pp cross-section [60].

## 5.3 The ATLAS detector

The ATLAS detector is a multi-purpose detector for recording collisions at the LHC. Its design is influenced by both the extreme conditions at the LHC and by the requirements for precision measurements and potential discovery of new physics processes at the TeV scale. The high interaction rates and radiation doses delivered to LHC detectors require fast, radiation-hard electronics and detector elements with high granularity. The demands for performing high precision tests of quantum chromodynamics, exploring the mechanism of electroweak symmetry breaking, and searching for signatures of new physics phenomena dictate the design of the detector and its subsystems.

The ATLAS detector has a cylindrical geometry and extends $44\,\text{m}$ in length and $25\,\text{m}$ in diameter with a weight of $7000\,\text{t}$. A sketch of the ATLAS detector, highlighting its various subsystems, is provided in Figure 5.2.

The detector consists of a cylindrical barrel region and two wheel-shaped end-caps, each instrumented with detector subsystems to achieve full coverage in the full $4\pi$ solid angle. The detector geometry possesses an eightfold symmetry around the beam axis and a forward-backwards symmetry to the interaction point. The detector is comprised of three main subsystems, starting with the innermost component, the inner detector, calorimeters and muon spectrometer. They are introduced briefly in the following. A detailed description of the ATLAS detector is provided in Ref. [178].

### 5.3.1 The ATLAS coordinate system

The ATLAS coordinate system is used throughout this dissertation and defined by expressing space-time events in terms of a right-handed Cartesian coordinate system

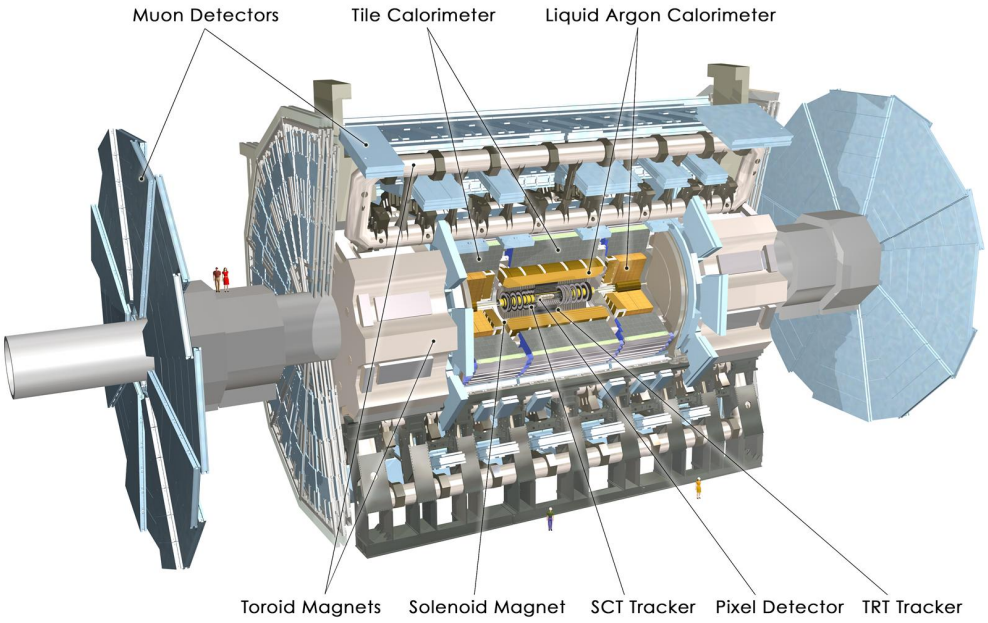



**Fig. 5.2.:** Schematic representation of the ATLAS detector and its various subsystems. Figure reproduced from Ref. [178].

with its origin located at the nominal interaction point. The $z$-axis is defined by the beam axis, the positive $x$-axis points from the interaction point to the centre of the LHC ring, and the positive $y$-axis points towards the earth's surface. The symmetry of the experiment favours a cylindrical coordinate system with the azimuthal angle $\varphi$ measured around the beam axis and the polar angle $\theta$ measured from the beam axis. In collider experiments, it is common practice to express the inclination of a particle with four-momentum $p = (E, \mathbf{p})$ to the beam with the pseudorapidity

$$\eta = -\ln \tan \frac{\theta}{2} = \frac{1}{2} \cdot \ln \frac{|\mathbf{p}| + p_z}{|\mathbf{p}| - p_z}. \tag{5.5}$$

The pseudorapidity is zero in transverse direction and increases rapidly for smaller inclinations with respect to the beam axis. In the relativistic limit, the pseudorapidity approaches to the rapidity

$$y = \frac{1}{2} \cdot \ln \frac{E + p_z}{E - p_z}. \tag{5.6}$$

The phase-space measure of a particle $\mathrm{d}\Pi_f$ is proportional to the rapidity, thus the particle flux per rapidity interval is approximately constant. Differences in rapidity (and by extension also the pseudorapidity) are invariants under Lorentz boosts along the beams axis. As a consequence, measurements of rapidity differences $\Delta y$ between particles are the same in different reference frames connected by a Lorentz

boost along the beam axis. An invariant distance measure can be defined in the pseudorapidity-azimuthal angle space as

$$\Delta R = \sqrt{\Delta\eta^2 + \Delta\varphi^2} = \sqrt{(\eta_1 - \eta_2)^2 + (\varphi_1 - \varphi_2)^2}. \tag{5.7}$$

The composite nature of the colliding protons only allows specifying the transverse momentum component of initial state partons taking part in the hard-scattering process. The aforementioned property of the rapidity therefore is crucially important for interpreting measurements of particles created in pp collisions. In a similar vein, it is useful to define transverse quantities of observables, such the transverse momentum

$$p_{\mathrm{T}} = |\mathbf{p}| \sin\theta = |\mathbf{p}| \cosh\eta \tag{5.8}$$

which is the projection of the momentum $p$ onto the $x$-$y$ plane. Similarly, the missing transverse momentum component in the $x$-$y$ plane $E_{\mathrm{T}}^{\mathrm{miss}}$ is of particular importance for dark matter searches. Other variables to describe the trajectory of a particle are the transverse impact parameter $d_0$ and the longitudinal impact parameter $z_0$. These are defined as the closest distance between the particle's trajectory and the reconstructed primary vertex in the transverse plane or longitudinal $z$-direction, respectively.

### 5.3.2 Magnet system

Momentum and charge measurement of charged particles requires the bending of their trajectories by being immersed in magnetic fields. To this end, ATLAS is equipped with a magnet system consisting of four large superconducting magnets. All magnets employ superconducting niobium-titanium technology and are cooled to about $4.5\,\mathrm{K}$ using liquid helium-3. The energy stored in the ATLAS magnets during operation amounts to $1.6\,\mathrm{GJ}$. The central solenoid magnet is aligned on the beam pipe and provides a $2\,\mathrm{T}$ axial magnetic field for charged particle measurements in the inner detector. It extends over $5.3\,\mathrm{m}$ length and has a diameter of $2.5\,\mathrm{m}$. As the magnet is situated between tracking and calorimetry system, a large material budget would impact the calorimeter resolution. The solenoid assembly contributes roughly $0.66$ radiation lengths at normal incidence, realised by an extremely light-weight structure and shared cooling elements of the solenoid and the calorimeter system. The barrel toroid and two end-cap toroids are defining for the ATLAS experiment as they not define the name of the experiment but also shape the total dimensions of the detector. The barrel toroid consists of eight air-core race-track shaped coils with an overall length of $25.3\,\mathrm{m}$ covering the region in between $9.4\,\mathrm{m}$ to $20.1\,\mathrm{m}$ from the interaction region. The end-cap toroids are octagonal wheels equipped with eight flat, square toroidal coil units and eight keystone wedges. Together, the toroids provide toroidal magnetic fields of approximately $0.5\,\mathrm{T}$ and $1.0\,\mathrm{T}$ for the muon detectors in the central and the end-cap regions, respectively. The highly non-uniform toroidal field requires a high-precision field mapping by approximately $1800$ Hall sensors distributed throughout the spectrometer volume.

### 5.3.3 Inner Detector

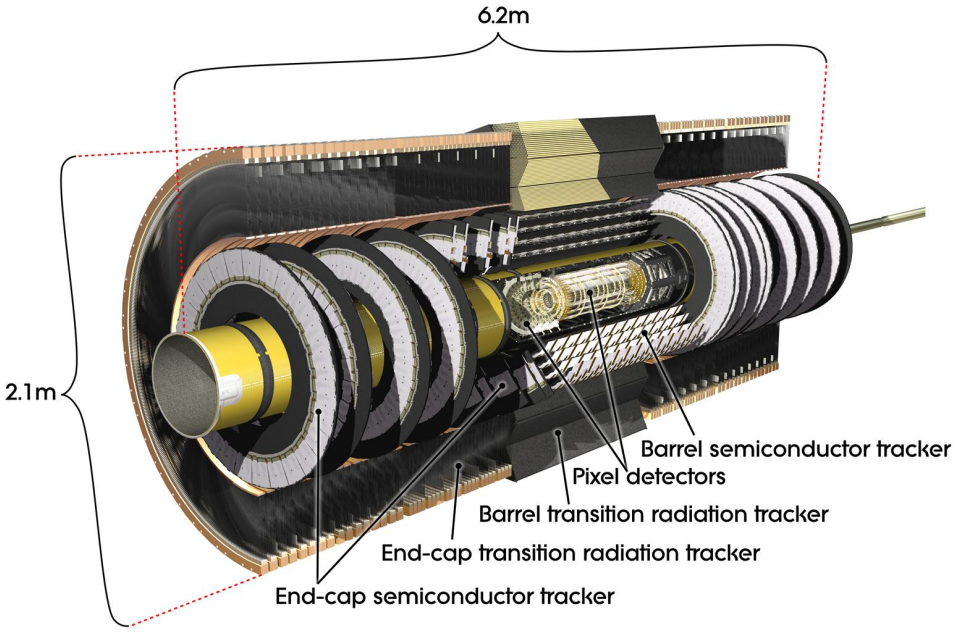
The inner detector provides precision measurements of charged particle trajectories. As it is immersed in the $2\,\mathrm{T}$ solenoid magnetic field, the track curvature can be used for determining the track's transverse momentum $p_\mathrm{T}$. The reconstructed particle tracks are used for pattern recognition to identify common points of origin, which are called vertices. The primary vertex is the vertex with the highest scalar $p_\mathrm{T}$ sum of associated tracks satisfying transverse and longitudinal impact parameter requirements. The primary vertex corresponds to the hardest interaction in the event, which typically is the interaction of interest. Other vertices in the same bunch crossing can be used to identify signatures associated with pile-up. Additionally, secondary vertices, which correspond to the displaced decays of short-lived particles, are used to identify the production of $b$-quarks or $\tau$ leptons. To this end, the inner detector is located close to the interaction region. It is comprised of discrete, high-resolution semiconductor pixel and strip detectors in the inner part of the tracking volume and straw tube tracking detectors in the outer part, with additional capability for particle identification by generating and detecting transition radiation. An essential design requirement is a light material budget to reduce energy losses in the ID. The momentum resolution of the inner tracker for trajectories of particles with transverse momentum $p_\mathrm{T}$is approximately

$$\frac{\sigma(p_\mathrm{T})}{p_\mathrm{T}} = \sqrt{\left(0.05\% \cdot \left(\frac{p_\mathrm{T}}{\mathrm{GeV}}\right)\right)^2 + (1\%)^2}. \tag{5.9}$$

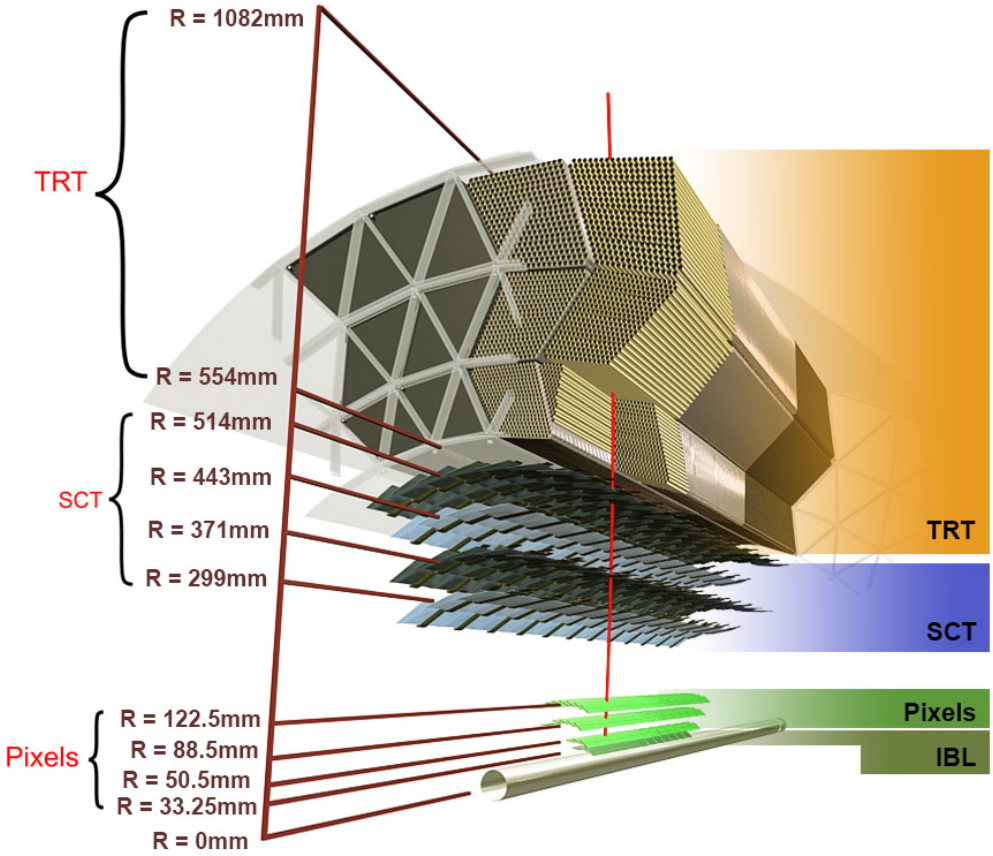
The layout of the inner detector is illustrated in Figure 5.3.

The silicon pixel detector (PXD) is located closest to the beam axis in $12\,\mathrm{cm}$ radial distance. Four layers of silicon pixel modules with $8.4 \times 10^7$ readout channels provide accurate three-dimensional information with the highest granularity. In the barrel region, the detector modules are arranged on four concentric cylinders around the beam axis positioned at radii of $33.25\,\mathrm{mm}$, $50.5\,\mathrm{mm}$, $88.5\,\mathrm{mm}$, and $122.5\,\mathrm{mm}$, while in the end-cap regions they are located on six disks perpendicular to the beam axis at distances $\pm 495\,\mathrm{mm}$, $\pm 580\,\mathrm{mm}$, and $\pm 650\,\mathrm{mm}$ from the collision point. The innermost barrel module, the insertable $b$-layer (IBL) [2, 156, 111], substantially contributes to the high precision impact parameter measurements, which are critical for vertex identification, by its proximity to the beamline and high spatial resolution. The PXD provides typically four measurement points for charged particles originating in the beam-interaction region with $10\,\mu\mathrm{m}$ spatial resolution in the transverse plane and $115\,\mu\mathrm{m}$ in the longitudinal $z$-direction.

The silicon microstrip tracker (SCT) forms the middle layer of the ID and extends up to $52\,\mathrm{cm}$ in the radial distance. As it is located further away from the beamline than the PXD, coarser granularity achieved by $6.3 \times 10^6$ readout channels is sufficient. It consists of four concentric layers of silicon strip detectors in the barrel region and 18 wheel-shaped disks containing the sensor modules in the end-cap regions. Each module hosts two single-sided silicon micros-trip sensor plates rotated about a stereo angle of $40\,\mathrm{mrad}$ to enable two-dimensional position measurements. The two precision semiconductor tracking detectors cover the region $|\eta| < 2.5$. They are




(a) Overview of the ID and its sub-detectors. Figure reproduced from Ref. [178].




(b) Detailed layout of the ID traversed by a charged track in the barrel region at $\eta = 0.3$. The track traverses the beam pipe, the four cylindrical PXD layers, the four SCT layers, and approximately 36 axial straws contained within the TRT modules. Figure reproduced from Ref. [304].

Fig. 5.3.: Illustrations of the ID layout and its spatial dimensions.

connected to a cooling system to reduce noise after irradiation. Their alignment is monitored by comparing positions of module hits with intersections of reconstructed tracks with the modules. Additionally, the SCT alignment is monitored by an interferometry system. The SCT provides typically eight hits per track at intermediate radii with $17\,\mu\mathrm{m}$ spatial resolution in the transverse plane and $580\,\mu\mathrm{m}$ in the longitudinal $z$-direction.

The transition radiation tube tracker (TRT) constitutes the outermost layer of the ID and operates with $3.4 \times 10^5$ readout channels. The TRT employs proportional drift tube arrays made of polyimide for track measurements. The choice of drift tubes as detector technology not only allows for the instrumentation of a large volume at comparably low cost but also avoids cooling issues and supports maintaining a low material budget for the ID. The tubes with diameter of $4\,\mathrm{mm}$ contain a $30\,\mu\mathrm{m}$ gold-plated tungsten wire in their centre and are filled with a ($70\,\%$ Xe / $27\,\%$ $CO_2$ / $3\,\%$ $O_2$) gas mixture[4]. The tubes are kept at the negative voltage of $1530\,\mathrm{V}$ with their wire kept at ground. The resulting electric field accelerates particles traversing the tubes, which then ionise the gas mixture. As a result, the ionisation products drift to the respective electrode of opposite polarity. Near the wire anode, the field strength is sufficiently high for the electron to create an avalanche of new ionisation processes, manifesting in a signal proportional to the number of primary charges. This measurement determines the primary electron drift time. Based on the knowledge of the drift velocity of electrons in the gas mixture, the radius of the closest approach between the particle trajectory and the wire can be computed. Combining measurements from several individual drift tubes allows determining the particle trajectory unambiguously. The TRT covers the region $|\eta| < 2.0$. It provides typically $35$ hits per track with $p_\mathrm{T} > 0.5\,\mathrm{GeV}$ with $130\,\mu\mathrm{m}$ spatial resolution in the plane orthogonal to the drift tubes.

### 5.3.4 Calorimetry

The ATLAS calorimeter can identify electrons, photons, and hadrons and provides measurements of their energy and position. The principle underpinning calorimetry is the destructive energy measurement of incoming particles by a chain of inelastic reactions leading to a shower of secondary particles, which in turn deposit their energy to active detector material. There, a fraction of the energy is converted into measurable quantities, which can be related to the total absorbed energy by a calibration procedure. Position measurements with coarse resolution can be achieved by segmenting the calorimeter into individual cells. Electromagnetically and hadronically interacting particles have different mechanisms for shower formation. The energy loss of electrons happens mostly via bremsstrahlung, whereas the dominant process for photons is pair production. The interplay of both processes results in the electromagnetic shower. The characteristic length scale for both processes is the radiation length $X_0$, defined as the distance over which an electron radiates

[4] As gas leaks occurred during operation of the TRT, some of the TRT modules instead contain an Ar-based gas mixture. The presence of this gas mixture is taken into account in the simulation, and the reduced efficiency of Ar is partially mitigated by dedicated reconstruction algorithms.

off $63\,\%$ of its energy. The interactions of hadrons are more complex and involve a cascade of inelastic hadronic interactions. The characteristic length scale for hadronic interactions with matter is the interaction length $\lambda$, which is defined as the mean distance travelled by a hadronic particle before undergoing an inelastic nuclear interaction. Two particular types of calorimeters are encountered in collider experiments. Electromagnetic calorimeters typically employ inorganic crystals or liquid noble gases with high nuclear charge $Z$ as the active material. Hadronic calorimeters typically layer the active material with very dense material, such as iron, to stop the hadronic showers, whose depth of penetration into the calorimeter exceeds that of electromagnetic showers.

Calorimetry complements the tracking detectors in two ways.

1. The energy resolution of calorimeters increases for larger energy $\sigma(E)/E \propto 1/\sqrt{E}$ due to the Poisson statistics of the shower, whereas the resolution of curvature-based momentum measurements deteriorates for larger momenta, following the relation $\sigma(p)/p \propto p$.

2. Calorimeters are sensitive to both charged and neutral particles. As the emergent parton shower due to hadronic final states, which are at the focus of this dissertation, is a mixture of both neutral and charged particles, calorimeters are essential for their accurate measurement.

An overview of the ATLAS calorimetry system is given in Figure 5.4.

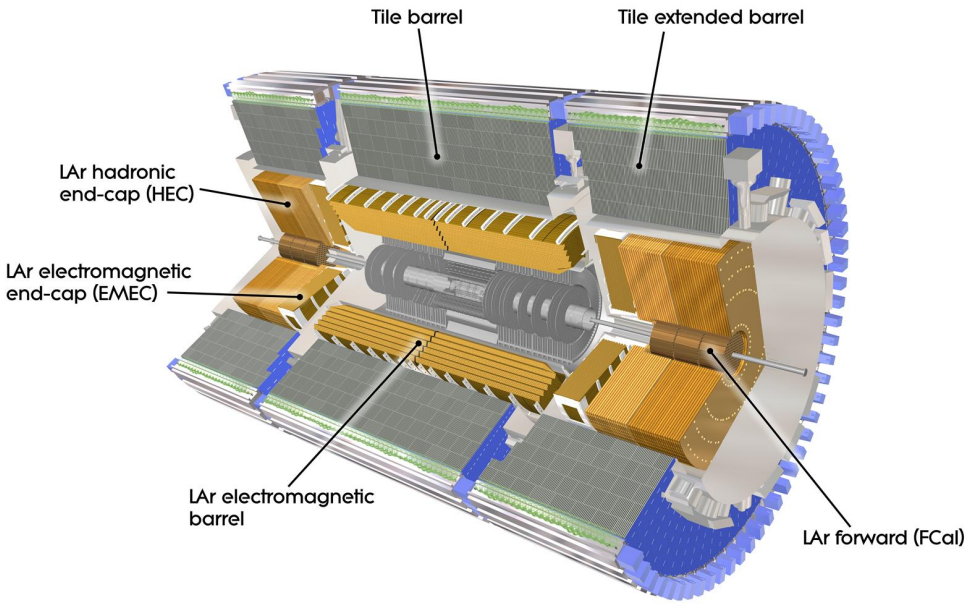



**Fig. 5.4.:** The ATLAS calorimeter system with its various components. Figure reproduced from Ref. [178].

The ATLAS calorimeter system surrounds both the ID and the solenoid. It has a length of $12.2\,\mathrm{m}$ and extends to an outer radius of $4.25\,\mathrm{m}$. Its geometry is fully symmetric in $\varphi$ and has full coverage around the beam axis and covers the pseudorapidity range $|\eta| < 4.9$. The enormous energy of particles created in LHC pp collisions necessitates shortening of the absorption length by the use of calorimeters with alternating layers of active detector material and passive, purely absorbing material. This sampling calorimeter design is used in all ATLAS calorimeters. The calorimeter system is comprised of electromagnetic calorimeters in the barrel and end-cap regions, enclosed by the hadronic calorimeters and complemented by dedicated calorimeters in the forward region close to the beam pipe. The ATLAS calorimeter system is hosted in three cryostats. The barrel cryostat contains the central solenoid and the electromagnetic barrel calorimeter. The end-cap cryostats each contain one electromagnetic end-cap calorimeter, one hadronic end-cap calorimeter, and one forward calorimeter. The design of the calorimetry system ensures full containment of electromagnetic and hadronic showers and reduction of punch-through into the muon spectrometer. The electromagnetic calorimeters have more than $22$ radiation lengths $X_0$ in the barrel region and more than $24$ radiation lengths in the end-cap regions. The hadronic calorimeters have an interaction length $\lambda$ of approximately $9.8$ in the barrel region and an interaction length of about $10$ in the end-cap region. The forward calorimeter has an interaction length $\lambda$ of approximately $10$.

The electromagnetic calorimeters cover the pseudorapidity range $|\eta| < 3.2$. The active detector medium is radiation hard Liquid Argon (LAr), which is chosen for its stability and linear response. The passive layers are made of lead. The absorber plates are shaped in an accordion geometry, thus providing full coverage in $\varphi$ without cracks. The barrel electromagnetic calorimeter covers the pseudorapidity range $0 < |\eta| < 1.475$. It consists of two identical components separated by a $4\,\mathrm{mm}$ gap at $\eta = 0$. The two end-cap electromagnetic calorimeters (EMEC) cover the pseudorapidity range $1.375 < |\eta| < 3.2$. They consist each of two coaxial wheels with a small non-overlapping region at $|\eta| = 2.5$. The transition region between the barrel and the end-cap ($1.37 < |\eta| < 1.52$) contains a relatively large amount of inactive material. In the precision physics region $|\eta| < 2.47$, where tracking information is available, the electromagnetic calorimeters are segmented in three layers with different granularity to allow for measurements of the electromagnetic shower profile. The first layer is finely segmented in strips to allow for excellent discrimination between photons from the hard interaction and photons from $\pi^0$ decays. Most of the electron and photon energy is collected in the second layer, while the third layer measures the energy deposits due to the shower's tails. The remaining acceptance is segmented in two layers with uniform granularity $\Delta\phi \times \Delta\eta = 0.1 \times 0.1$. The energy measurement in the region $|\eta| < 1.8$ is corrected for the energy loss of particles before entering the calorimeter by the use of two pre-sampling detectors, made of a thin LAr layer. The combined electromagnetic calorimeter energy resolution is

$$\frac{\sigma_E}{E} = \frac{10\,\%}{\sqrt{E}} \oplus 0.7\,\%, \tag{5.10}$$

where $\oplus$ indicates the quadratic sum.

The hadronic calorimeter encloses the electromagnetic calorimeters, as the depth of hadronic showers typically exceeds that of electromagnetic showers. Two different calorimeter technologies are employed to address the increasing irradiation in regions closer to the beam pipe. The pseudorapidity range $|\eta| < 1.7$ is instrumented with a tile calorimeter, subdivided in a barrel region enclosing the electromagnetic barrel calorimeter and two extended barrel regions, which surround the end-cap calorimeters. The barrel region covers $|\eta| < 1.0$ and the two extended barrel regions cover $0.8 < |\eta| < 1.7$. Scintillator tiles are used as the active detector medium, while steel is used as the absorber medium. The tile calorimeter extends $2.28\,\mathrm{m}$ to $4.25\,\mathrm{m}$ in the radial direction. Each barrel region is azimuthally divided into 64 modules, corresponding to $\Delta\varphi = 0.1$, and is segmented into three layers. The scintillating tiles are read out by wavelength shifting fibres, which are grouped into photomultiplier tubes. The tile calorimeter provides measurements with an energy resolution of $\frac{\sigma_E}{E} = \frac{50\%}{\sqrt{E}}$. The pseudorapidity range $1.5 < |\eta| < 3.2$[5] is instrumented with a LAr hadron end-cap calorimeter (HEC). It consists of two cylindrical wheels per end-cap, both extending $2.03\,\mathrm{m}$ in the radial direction and hosting each 32 identical wedge-shaped modules. Each wheel is longitudinally divided into two regions of depth and composed from copper plates interspersed with $8.5\,\mathrm{mm}$ LAr gaps. The combined hadronic calorimeter energy resolution for hadronic jets for tile and end-cap calorimeters is

$$\frac{\sigma_E}{E} = \frac{50\,\%}{\sqrt{E}} \oplus 3\,\%. \tag{5.11}$$

The forward region is instrumented with a LAr forward calorimeter (FCal). It covers the pseudorapidity range $3.1 < |\eta| < 4.9$, thereby ensuring an almost hermetic coverage of the calorimetry system around the interaction point, which is essential for dark matter searches. The FCal consists of three modules in each end-cap, with the first made of copper targeting electromagnetic showers and the remaining two made of tungsten targeting hadronic interactions. The forward region hadronic calorimeter has an energy resolution for hadronic jets of

$$\frac{\sigma_E}{E} = \frac{100\,\%}{\sqrt{E}} \oplus 10\,\%. \tag{5.12}$$

### 5.3.5 Muon Spectrometer

As muons are substantially heavier than electrons, they do not lose energy by bremsstrahlung and leave only a track footprint because of ionisation energy loss in the calorimeter. Consequently, the particles emerging from the calorimeters are considered to be muons and are detected by a dedicated detector system. The muon spectrometer provides measurements of charged particles exiting the calorimeters, covering the pseudorapidity range $|\eta| < 2.7$. It is also able to provide track information in coarser granularity but with timing resolution within a few tens

[5] The HEC is overlapping with both the tile calorimeter and the FCal to reduce drops in material density in the transition regions between the calorimeters.

of a nanosecond for the sake of triggering or bunch crossing identification in the pseudorapidity range $|\eta| < 2.4$. To this end, the muon spectrometer is equipped with sets of precision tracking detectors and trigger chambers. The magnetic field provided by the toroid magnets allows measuring the muon momentum based on the sagitta of the curved trajectory. The detector resolution is optimised for measurements in the plane in the principal bending direction, the so-called bending plane. The layout of the ATLAS muon spectrometer is shown in Figure 5.5.

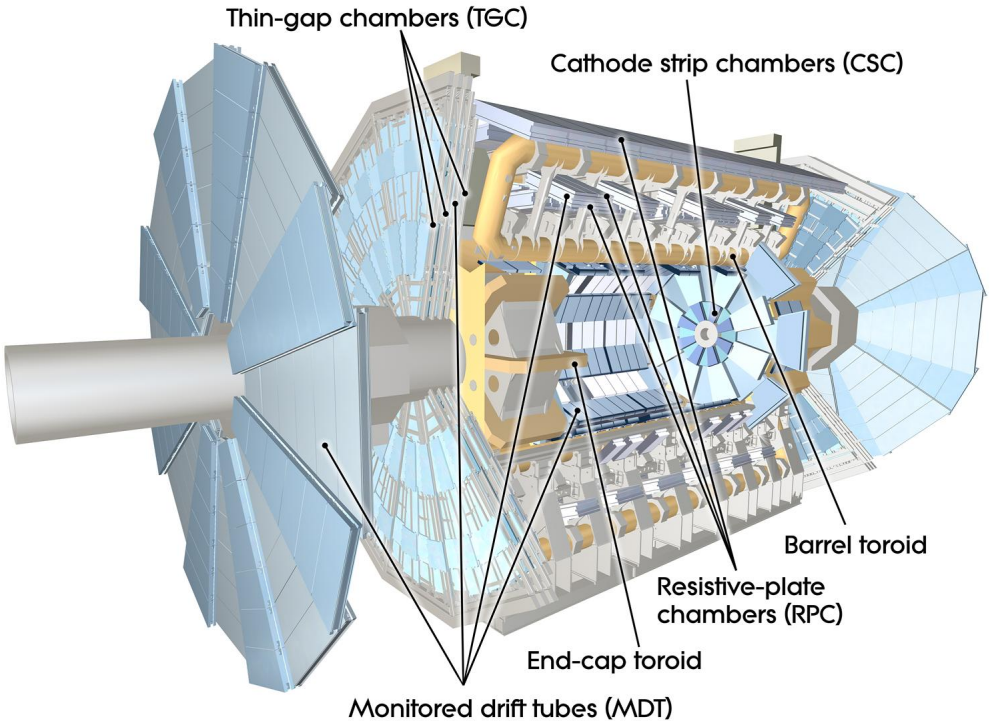



**Fig. 5.5.:** The ATLAS muon spectrometer with its various components. Figure reproduced from Ref. [178].

The $1150$ monitored drift tube (MDT) chambers, whose length and shape depends on their position in the detector, perform the precision measurements. In the barrel region, they are located between and on the toroid coils. The symmetry of the toroid magnet is reflected in the muon system's geometry, which is divided into octants. Each octant is subdivided in the azimuthal direction into a large and small sector. The overlap between the different sector types minimises gaps in acceptance and allows for relative alignment of adjacent sectors using tracks measured in both sectors. The chambers in the barrel region are arranged in three concentric cylindrical shells, located at $5\,\mathrm{m}$, $7.5\,\mathrm{m}$, and $10\,\mathrm{m}$ in the radial distance to the beam axis. In the end-cap region the MDT chambers form four large wheels perpendicular to the $z$-axis, which are located in front and behind the end-cap toroid magnet. They are located at distances of $|z| = 7.4\,\mathrm{m}$, $|z| = 10.8\,\mathrm{m}$, $|z| = 14\,\mathrm{m}$, and $|z| = 21.5\,\mathrm{m}$ to the interaction point. An MDT chamber consists of two multi-layers with three or four layers of drift tubes per multi-layer, operated at an absolute pressure of $3\,\mathrm{bar}$. The drift tubes are made of aluminium with a tungsten-rhenium anode wire in the centre.

The detection principle is similar to the TRT operation, described in Section 5.3.3. The resolution of a single drift tube on average is $35\,\mu\mathrm{m}$. MDT chambers provide position measurements in the bending plane with $35\,\mathrm{mm}$ resolution. The sagitta-based measurement achieves an excellent momentum resolution, based on both precise measurements of muon trajectories and precise knowledge of the chamber positions within $30\,\mu\mathrm{m}$. To this end, each chamber is equipped with a RASNIK optical alignment system, which monitors mechanical deformations of the chambers and movements of the chambers relative to each other.

In the pseudorapidity range $2 < |\eta| < 2.7$, the innermost wheel is instrumented with $32$ cathode strip chambers (CSC) instead of MDT chambers, in order to meet the demands on rate capability and time resolution. The CSC chambers are multi-wire proportional chambers with cathode plates segmented into strips in orthogonal directions, enabling measurements of two coordinates from the charge-induced signal distribution. They provide position measurements with $40\,\mu\mathrm{m}$ in the bending plane and $5\,\mathrm{mm}$ in the transverse plane.

The precision tracking detectors are complemented by a system of fast trigger chambers. In the barrel region, extending up to $|\eta| < 1.05$, $606$ resistive plate chambers (RPC) are employed for providing fast detection of muons with a timing of $1.5\,\mathrm{ns}$. The RPC chambers provide measurements with a resolution of $10\,\mathrm{mm}$ in both the bending plane and the azimuthal plane. The end-cap region, covering the pseudorapidity range from $1.05 < |\eta| < 2.4$, is instrumented with thin gap chambers (TGC) with timing of $4\,\mathrm{ns}$. They provide measurements with a resolution of $2\,\mathrm{mm}$ to $6\,\mathrm{mm}$ in the bending plane and $3\,\mathrm{mm}$ to $7\,\mathrm{mm}$ in the azimuthal plane.

### 5.3.6 Trigger

The event rate of pp interactions at the design luminosity $10^{34}\,\mathrm{cm}^{-1}\,\mathrm{s}^{-1}$ is $\mathcal{O}(1\,\mathrm{GHz})$. Using a popular analogy, sampling physics from the LHC is like drinking water from a fire hose [155]. As technical constraints limit the maximum possible event recording rate to $1\,\mathrm{kHz}$, a highly selective trigger system is required to filter events associated with processes of interest. The ATLAS Trigger and Data Acquisition (TDAQ) systems consist of a hardware-based Level-1 (L1) trigger, followed by a software-based high-level trigger (HLT). The schematics of the TDAQ system are shown in Figure 5.6.

The L1 trigger system reduces the data rate to approximately $100\,\mathrm{kHz}$. It uses a subset of the full detector information to decide between keeping or discarding events within a latency of $2.5\,\mu\mathrm{s}$. The L1 trigger decision is formed in the Central Trigger Processor (CTP), which receives information from the L1 calorimeter (L1 Calo) and the L1 muon (L1 Muon) triggers.

The L1 Calo trigger processes analogue signals from the electromagnetic and hadronic calorimeters, which are digitised and calibrated by a preprocessor system in approximately 7000 trigger towers with a granularity of $\Delta\eta \times \Delta\phi = 0.1 \times 0.1$.

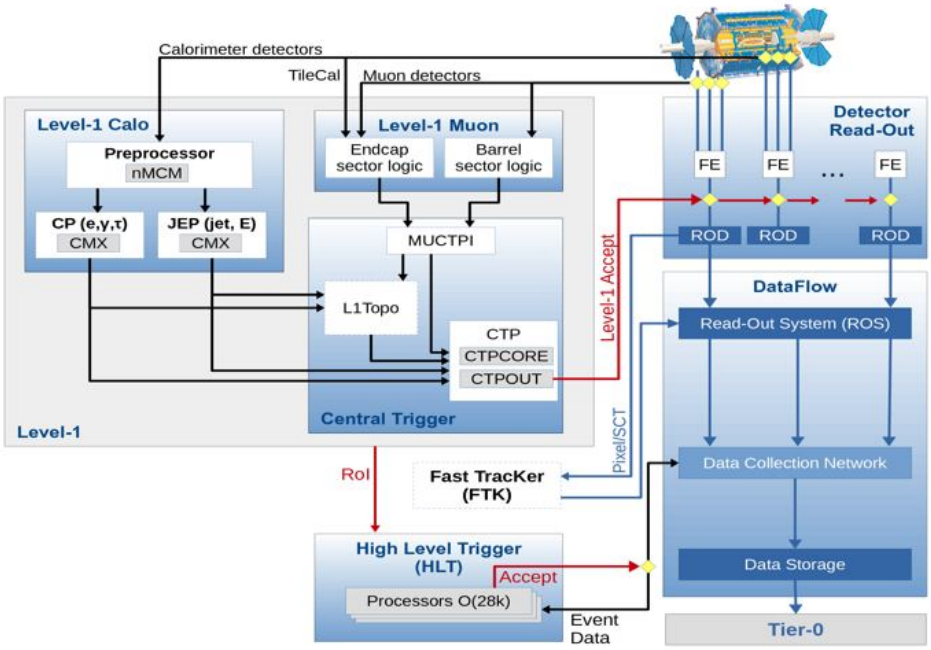



**Fig. 5.6.:** The ATLAS trigger logic in Run-2. Figure reproduced from Ref. [310].

Electron, photon and hadronically decaying $\tau$ lepton candidates with specified energy thresholds and isolation criteria[6] are identified by the Cluster Processor (CP). A Jet/Energy-sum Processor (JEP) is able to reconstruct jet candidates and compute scalar and missing energy sums from trigger elements with $\Delta\eta \times \Delta\phi = 0.2 \times 0.2$ granularity. The L1 Muon trigger processes signals from three stations.

The L1 Muon trigger processes signals from either three stations of RPC chambers in the barrel region or from three stations of TGC chambers in the end-cap. The principle underpinning the muon trigger is a coincidence of hits in the different trigger stations within the road of a muon candidate. The hit in the trigger chamber layer, which is referred to as the pivot plane, defines the infinite momentum track as the connecting line to the interaction point. As the muon candidate's $p_{\mathrm{T}}$ affects the curvature and consequently the width of the muon road, the deviation of a hit in other chamber layers from the infinite momentum track is used for a quick momentum estimate through a programmable coincidence logic. Three low-$p_{\mathrm{T}}$ thresholds ($4\,\mathrm{GeV}$, $6\,\mathrm{GeV}$, and $10\,\mathrm{GeV}$) are defined by coincidence windows using information from two trigger chamber layers. In addition, three high-$p_{\mathrm{T}}$ thresholds ($11\,\mathrm{GeV}$, $15\,\mathrm{GeV}$, and $20\,\mathrm{GeV}$) are defined by taking into account additional coincidence requirements with regard to the third layer. The trigger signals from the barrel and end-cap triggers are combined into a set of six threshold multiplicities for each bunch crossing in the muon to CTP interface and passed on to the CTP.

[6] Isolation implies that the energetic particle must have a minimum angular separation from any other significant energy deposit in the same event.

Events accepted by the L1 trigger are buffered in the Read-Out System (ROS), awaiting further confirmation from the HLT. The HLT decision is evaluated by a computing farm, which can run reconstruction algorithms with the same precision used in the offline reconstruction, with access to the event information in full granularity. It receives Region-of-Interest (RoI) information, consisting of essential features identified by the L1 trigger and the geographical coordinates of those regions within the detector where its selection process has identified those features. These form a starting point for the HLT algorithms. Their significantly better particle identification and momentum resolution sharpens the HLT decision and thus reduces the final data-taking rate to approximately 200 Hz.

### 5.3.7 Grid computing

Large-scale computing infrastructure is required to analyse a large amount of data recorded by the LHC experiments. The Worldwide LHC Computing Grid (WLCG) is designed to preserve, distribute and analyse LHC collision data. It is a distributed computing grid, consisting of more than 160 computing centres in more than 40 countries. Different tiers hierarchically structure the role of computing centres:

- The Tier-0 centre is located at the CERN data centre and is responsible for the first-pass reconstruction.
- The thirteen Tier-1 centres receive raw data and reconstruction output from Tier-0 and are responsible for the safe-keeping of a proportional share of data and simulations and large-scale reprocessing.
- The over 160 Tier-2 centres are typically hosted by universities and other scientific institutes. They provide storage and adequate computing power for specific analysis tasks.
- Tier-3 resources refer to computing clusters offered by research institutions to individual users. There is no formal engagement between WLCG and Tier 3 resources, but they often provide access to the respective WLCG sites.

# 6 Experimental methods

> *The idea of a method that contains firm, unchanging, and absolutely binding principles for conducting the business of science meets considerable difficulty when confronted with the results of historical research.*
>
> — **Paul Feyerabend**
> Against Method. London: New Left Books, 1975

The experimental methods for analysing the recorded data set of pp collision events are outlined in this Chapter. Section 6.1 describes the algorithms used for the reconstruction of compound physics objects. The statistical techniques used to obtain results from fits of the statistical model to data are described in Section 6.2. The RECAST framework, which enables faithful and efficient reinterpretation of searches, is introduced in Section 6.3.

## 6.1 Event reconstruction

### 6.1.1 Introduction

The various sub-systems of the ATLAS detector record detailed information about the pp collisions, which occur in the interaction region. The elementary detector signatures are the hits in the sensitive tracking detector planes and the energy deposits in the calorimeters. These measurements serve as inputs for sophisticated reconstruction algorithms, which define compound physical objects, such as electrons, photons, muons, tau leptons, jets, and missing transverse momentum. These compound physical objects are used to define the selection requirements in the searches for dark matter and to construct discriminating observables for the statistical analysis.

The object reconstruction is subject to inefficiencies in the particle identification and afflicted with systematic uncertainties due to various detector effects. The reconstructed kinematic properties of the compound physical objects can deviate from their true value for the same reasons. These discrepancies can be reduced to some extent by employing calibration methods. In the ATLAS collaboration, the standard recommendations for object identification, reconstruction, calibration, and evaluation of the associated systematic uncertainties are centrally provided by the Combined Performance (CP) groups.

### 6.1.2 Reconstruction of basic objects

All reconstructed physics objects are based on reconstructed tracks, vertices, and topological clusters.

**Tracks** are reconstructed by connecting the hits in different layers of the ID. Their momentum and charge can be inferred from their deflection in the solenoidal magnetic field. The tracks are parametrised, as shown in Figure 6.1, by a set of five parameters

- the transverse and longitudinal impact parameters $d_0$ and $z_0$,
- the azimuthal and polar angles $\varphi$ and $\theta$, and
- the ratio of charge and transverse momentum $q/p_{\mathrm{T}}$.

Tracks are reconstructed by a set of tracking algorithms [71, 74]. Two approaches — an "inside-out" algorithm, mostly sensitive to primary charged particles produced in the pp interaction, and an "outside-in" algorithm, mostly sensitive to secondary decay products — are employed to ensure high reconstruction efficiency. The "inside-out" algorithm considers seeds containing three hits in the silicon PXD and SCT detectors and extends the track seed to the TRT using a combinatorial Kalman filter [225] to add hits further away from the interaction point. The "outside-in" algorithm considers TRT track segments and extrapolates them to the vicinity of the interaction point by adding hits in the silicon detectors, which have not been associated with tracks yet. All ID tracks are required to satisfy $p_{\mathrm{T}} > 0.4\,\mathrm{GeV}$ and $|\eta| < 2.4$. The impact parameter resolution is shown in Figure 6.2. In addition to the tracks in the ID, the muon reconstruction employs tracks recorded by the MS. These are reconstructed by dedicated algorithms based on Hough transforms or iterative combination of hits [295].

**Vertices** are defined as points at which either a pp interaction or a decay takes place. The iterative reconstruction of vertices employs tracks and consists of two steps [139].

1. Vertex finding. The vertices in a collision event are reconstructed using tracks satisfying certain quality criteria, including $|d_0| < 4\,\mathrm{mm}$ and requirements on the impact parameter resolution $\sigma(d_0) < 5\,\mathrm{mm}$ and $\sigma(z_0) < 10\,\mathrm{mm}$. The seed position for the first vertex is defined by the transverse coordinates of the beam spot and the $z$-coordinates or tracks at their points of closest approach to the beam spot. All vertices require at least two associated tracks.

2. Vertex fitting. The tracks and the seed are used to estimate the best vertex position with a fit based on an iterative annealing procedure. In each iteration of the fit, the weights of less compatible tracks are decreased, to determine the best vertex position.

The primary vertex (PV) is the point at which a hard scattering process in the pp interaction occurred. It is reconstructed as the vertex with the largest sum of squared transverse momenta of all tracks associated with it. Figure 6.3 shows the

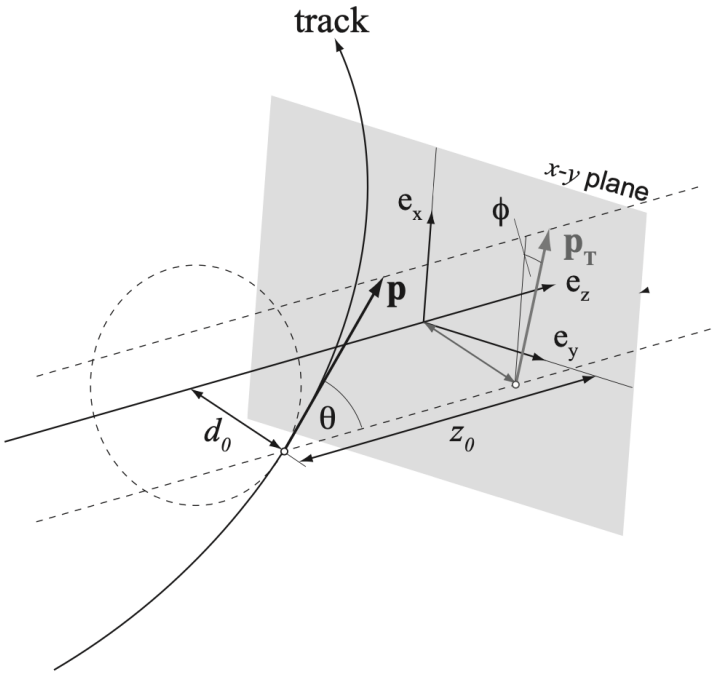



Fig. 6.1.: A track parametrised with respect to the nominal $z$-axis through the azimuthal angle $\varphi$, the polar angle $\theta$, the charged inverse momentum $q/p$, and the transverse and longitudinal impact parameters $d_0$ and $z_0$. Figure reproduced from Ref. [194].

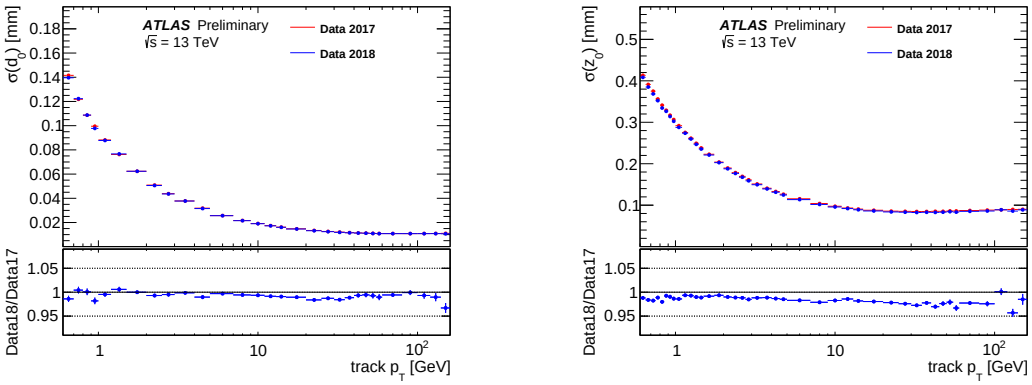



Fig. 6.2.: Resolution of the transverse impact parameter $d_0$ and the longitudinal impact parameter $z_0$ of tracks associated with jets with $p_{\mathrm{T}} > 20\,\mathrm{GeV}$, measured in pp collision data recorded in 2017 and 2018 with dijet triggers. Figure reproduced from Ref. [181].

vertex performance in two runs of 2018 pp data with different average number of interactions per bunch crossing.

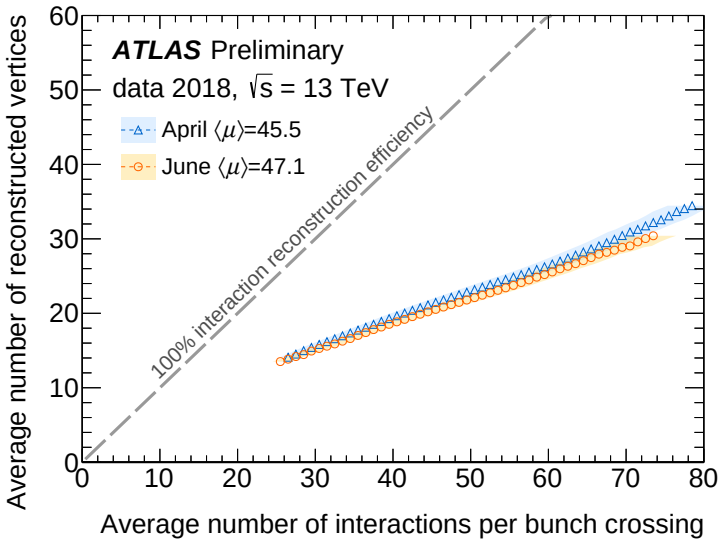



**Fig. 6.3.:** Vertex performance in 2018 pp data, indicated by the number of reconstructed vertices in dependence of the average number of interactions per bunch crossing. Figure reproduced from Ref. [181].

**Topological clusters** are groups of topologically connected energy deposits in neighbouring calorimeter cells due to incident particles. Their reconstruction [108] is seeded by energy deposits which are significantly greater than the expected noise due to the detector electronics and pile-up events. The reconstruction is based on the cell signal significance $\xi = E_{\text{cell}}/\sigma(E_{\text{cell}})$, which is defined as the ratio of the detector signal $E_{\text{cell}}$ and the expected noise $\sigma(E_{\text{cell}})$ on the electromagnetic scale. All calorimeter cells adjacent to the seed cells, which satisfy certain noise-suppression thresholds, are iteratively added to form "proto-clusters". These "proto-clusters" are subsequently split if they contain two or more local maximums of the detector signal with $E_{\text{cell}} > 500\,\text{MeV}$ to separate individual showers. The clusters are parametrised by the azimuthal and polar angles defined by the energy-weighted barycentre of the associated calorimeter cells and by the cluster energy. The cluster energy can be calibrated to different scales to adequately describe the physical objects initiating the shower in the calorimeters [43].

- Electromagnetic (EM) scale calibration. Topological clusters in their basic definition are reconstructed at the EM scale to describe particles depositing their energy in the calorimeter via electromagnetic showers.
- Local Calibration Weighting (LCW) calibration. This alternative calibration [53] takes into account the response of the calorimeter to hadrons produced in the interaction point. Clusters are classified either as electromagnetic or hadronic before the appropriate energy corrections derived from single pion MC simulations are applied. The LCW calibration can improve the energy resolution of reconstructed jets in comparison to jets based on EM-scale clusters.

### 6.1.3 Electrons

Electrons passing the ATLAS detector leave a track in the ID and initiate an electromagnetic shower in the high-granularity EM calorimeter. The electron candidates are reconstructed based on the combined information of the two sub-detectors. The performance of the electron reconstruction, identification, and isolation algorithms is evaluated in data and simulated MC samples using electrons from $Z \to e^- e^+$ and $J/\psi \to e^- e^+$ decays.

#### Electron reconstruction

Electron candidates are reconstructed by matching reconstructed tracks to clusters in the EM calorimeter. The coverage of the ID limits the electron reconstruction to $|\eta| < 2.47$. The path of an electron through the detector is shown in Figure 6.4.

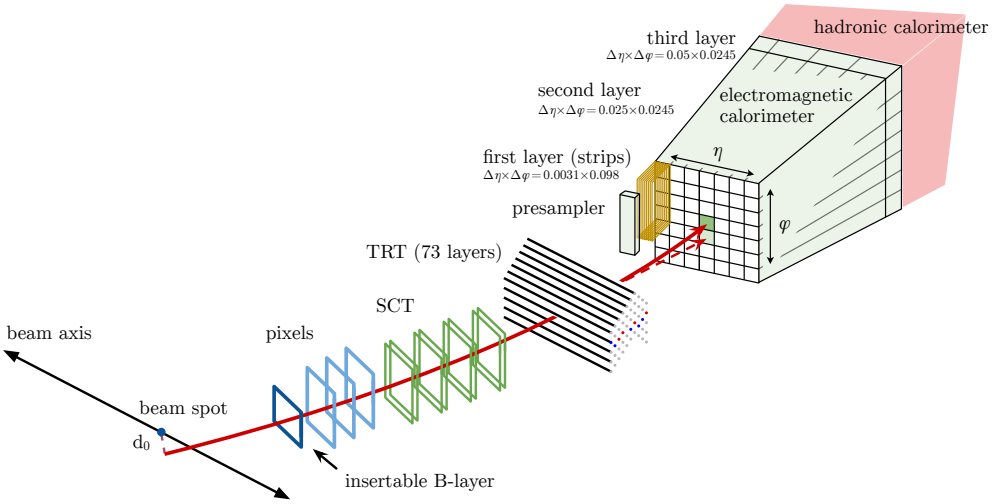



**Fig. 6.4.:** Schematic illustration of an electron's trajectory (red) through the detector, first traversing the tracking system comprised of PXD detectors, SCT detectors and lastly the TRT, and then enters the EM calorimeters. The dashed trajectory (red) illustrates the path of a photon radiated off the electron due to interactions with the detector material. Figure reproduced from Ref. [47].

The electron reconstruction [47] starts from fixed-size seed clusters, which are selected by a sliding-window algorithm. The inputs to the algorithms are towers of calorimeter cells in the first three calorimeter layers, which have a granularity of $\Delta\eta\times\Delta\varphi = 0.025\times0.025$. The algorithm considers seeds composed of $N_\eta\times N_\varphi = 3\times5$ towers of EM calorimeter cells, which are required to have a minimal energy deposit of $E_\mathrm{T} > 2.5\,\mathrm{GeV}$.

ID tracks are matched to the clusters using the distance measure $\Delta R$ between the position of the track extrapolated to the middle layer of the calorimeter and the cluster barycentre. The tracks are re-fitted with the Gaussian Sum Filter (GSF) [49]

algorithm to account for Bremsstrahlung effects. The resulting electron candidate consists of a cluster seed, which is successfully matched to at least one track.

In the 2017–2018 data taking campaign, new electron reconstruction algorithms are employed [46, 45]. These algorithms replace the electron reconstruction based on fixed-size windows with a dynamic approach based on variable-size topological clusters.

### Electron identification

The electron identification (ID) algorithm discriminates between electron candidates from signal processes, such as prompt production in the hard-scattering vertex or from the decay of heavy resonances, and background-like objects, such as hadronic jets or converted photons. A likelihood-based approach (LH) is employed, which considers the information provided by clusters and tracks, such as the resolution parameters of the associated tracks and the calorimeter shower shape. The LH based discriminant and the number of hits in the track are used to calculate the probability of an electron candidate being either an electron from signal processes or a background-like object.

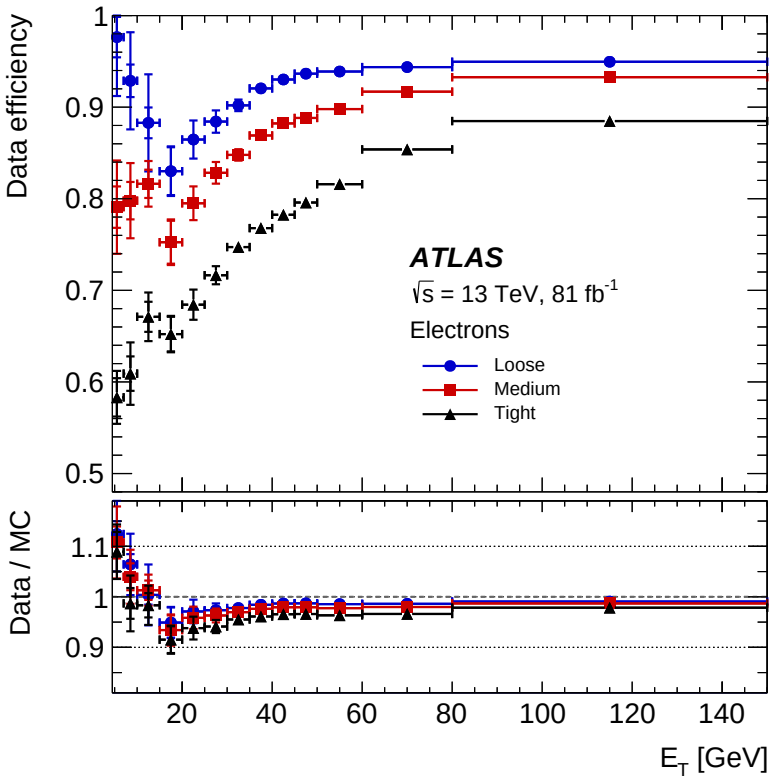
Three electron ID operating points (OPs) with increasing background rejection are defined. The LOOSE OP corresponds to an average electron identification efficiency of $93\,\%$. Similarly, the MEDIUM and TIGHT OPs correspond to efficiencies of $88\,\%$ and $80\,\%$, respectively. These points are inclusive, meaning that the TIGHT electrons are a subset of the MEDIUM electrons and the MEDIUM electrons are a subset of the LOOSE electrons. In addition, the LOOSEANDBLAYER OP is defined as a variation of the LOOSE OP with the additional requirement of at least one hit in the innermost layer of the PXD detector. Out of these definitions, LOOSE and LOOSEANDBLAYER electrons are considered in the searches for dark matter presented in this dissertation.

The electron identification efficiency in bins of $E_{\mathrm{T}}$ and $\eta$ is shown in Figure 6.5. The identification efficiency gradually increases from low to high $E_{\mathrm{T}}$. In the range $20\,\mathrm{GeV} < E_{\mathrm{T}} < 50\,\mathrm{GeV}$, the MEDIUM and TIGHT OPs have an improved rejection of background processes by $2.0$ and $3.5$, respectively, with respect to the LOOSE OP.

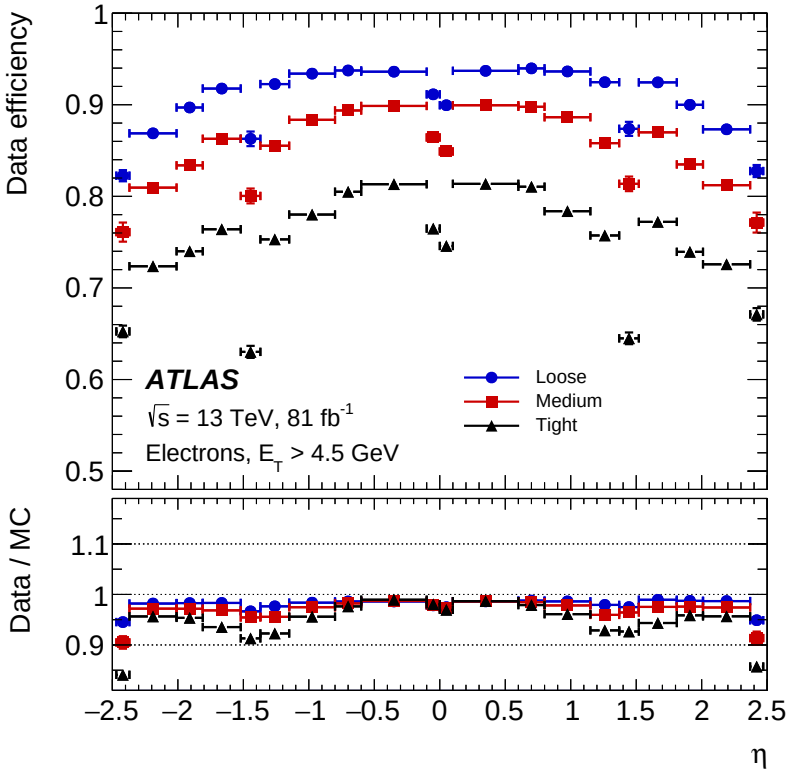
### Electron isolation

The electron isolation algorithm provides additional information to discriminate between electrons from signal processes and background-like objects. Typically, the latter are characterised by comparatively larger activity in an area of $\eta \times \varphi$ surrounding the electron candidate. The amount of activity in the vicinity of the electron is quantified by variables summing the transverse energy of clusters or transverse momenta of tracks in a cone of radius $\Delta R$ around the direction of the electron, excluding the electron itself.

Two types of variables are defined.




(a) Electron identification efficiency in bins of $E_{\mathrm{T}}$.




(b) Electron identification efficiency in bins of $\eta$.

**Fig. 6.5.:** Electron identification efficiencies for the different operating points LOOSE, MEDIUM, and TIGHT. Figures reproduced from Ref. [45].

- The track isolation variable $p_T^{\text{varcone},0.2}$ is defined as the sum of the transverse momenta of all tracks in a cone of variable size $R = \min\{0.2, 10\,\text{GeV}/E_\text{T}\}$ around the direction of the electron candidate with transverse energy $E_\text{T}$. The $p_T^{\text{varcone},0.3}$ variable is defined similarly.
- The calorimeter $E_T^{\text{cone},0.2}$ isolation variable is defined as the sum of the transverse energies of all calorimeter cells, which are calibrated to the electromagnetic cell, in a cone with fixed size $R = 0.2$ around the electron.

Various electron isolation OPs are defined. These can be based either on targeting a fixed value of the isolation efficiency dependent on $E_\text{T}$ and uniform in $\eta$ ("Gradient") or by imposing fixed requirements on the value of the isolation variable ("Fixed Cut").

The electron isolation efficiency for various OPs in bins of $p_\text{T}$ and $\eta$ is shown in Figure 6.6.

### 6.1.4 Muons

Muons traversing the ATLAS detector leave a track in the ID and the MS, as they pass the calorimeters with only minimal energy loss. The muon trajectory is reconstructed independently in the ID and the MS. Then, the two measurements are combined, potentially supplemented with calorimeter information, to form muon candidates.

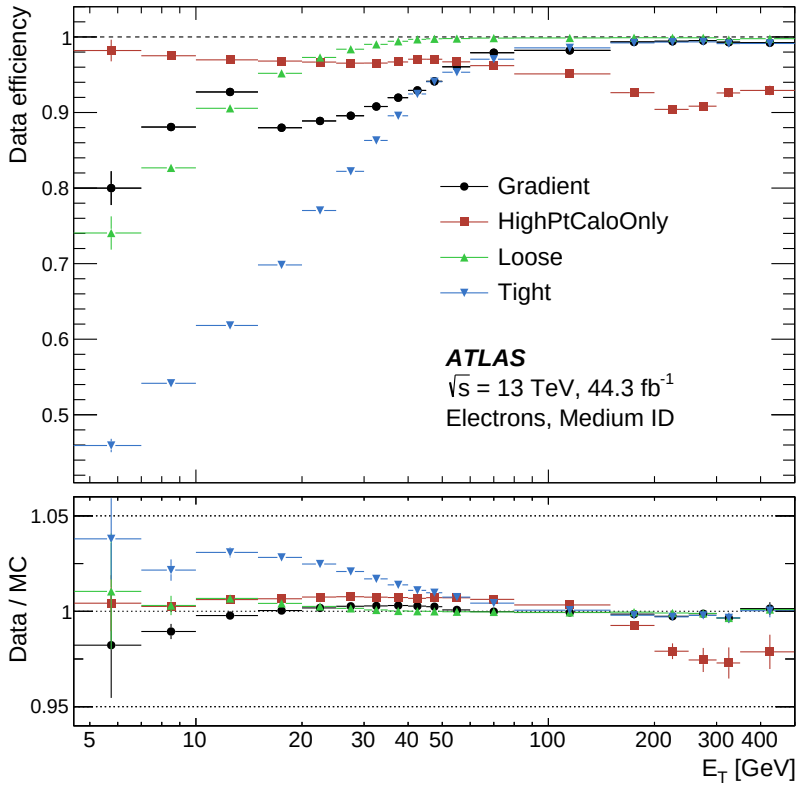
The performance of the muon reconstruction, identification, and isolation algorithms is evaluated in data and simulated MC samples using muons from $\text{Z} \to \mu^-\mu^+$ and $\text{J}/\psi \to \mu^-\mu^+$ decays.

#### Muon reconstruction

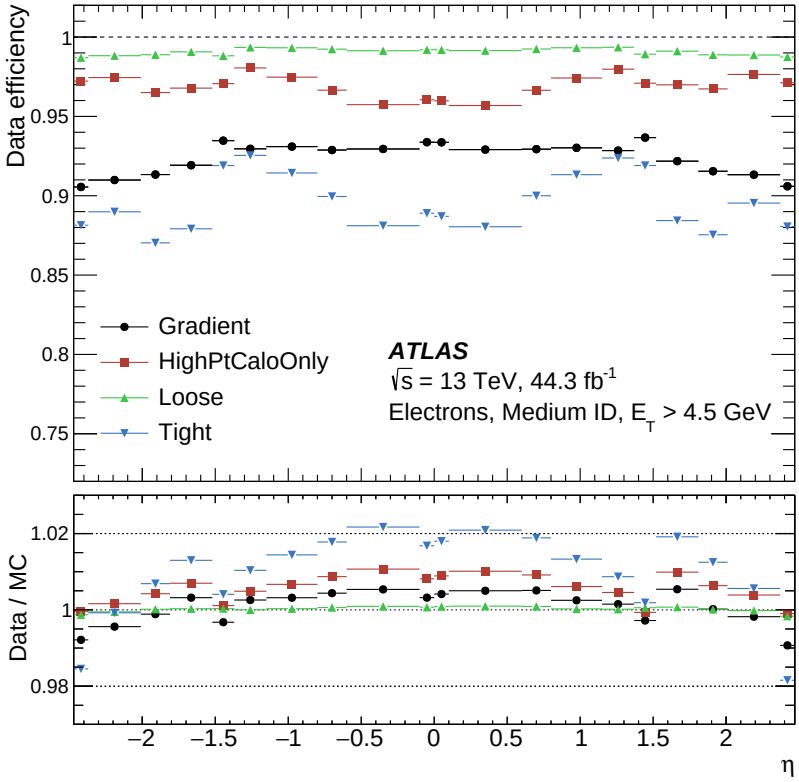
The muon reconstruction [64, 63] is performed separately in the ID and the MS. While the muon reconstruction in the ID is identical to that of other charged particles (c.f. Section 6.1.2), it based on a combinatorial search algorithm in the MS. The algorithm constructs the track candidates from at least two matching track segments, which are identified in the individual layers of the MS by pattern finding algorithms.

Six types of muons are reconstructed depending on the available sub-detector information and based on different reconstruction algorithms. The reconstructed muon types are combined (CB) muons, silicon-associated forward (SiF) muons, inside-out combined (IO) muons, segment-tagged (ST) muons, calorimeter-tagged (CT) muons and extrapolated (ME) muons.

- **Combined muons** are reconstructed with an "outside-in" approach by matching MS tracks to ID tracks and performing a global re-fit of the hits from both the ID and MS sub-detectors to construct the muon candidate. The global fit procedure allows for addition or removal of MS hits from the track to improve




(a) Electron isolation efficiency in bins of $E_{\mathrm{T}}$.




(b) Electron isolation efficiency in bins of $\eta$.

**Fig. 6.6.:** Electron isolation efficiencies for the fixed cut OPs "Loose", "Tight", and "HighPtCaloOnly", as well as for the "Gradient" OP. Figures reproduced from Ref. [45].

the fit quality. Typically, CB muon candidates have the highest muon purity among all muon definitions.

- **Inside-out combined muons** complement the reconstruction of CB muons by an "inside-out" approach, in which ID tracks are extrapolated outward and matched to MS tracks while taking into account the energy loss in the calorimeters.
- **Silicon-associated forward muons** are a subset of CB muons, which are reconstructed for $|\eta| > 2.5$ by combining MS tracks with short track segments reconstructed from hits in the pixel and SCT detectors.
- **Segment-tagged muons** are reconstructed from muons with either insufficient momentum to traverse the full MS or which fall in regions with reduced acceptance. They are based on ID tracks which are extrapolated to at least one local track segment in an MDT or CSC detector.
- **Calorimeter-tagged muons** are reconstructed from muons, whose trajectory only extends to the calorimeters. They are based on ID tracks which are matched to an energy deposit in the calorimeters compatible with a minimum-ionising particle. CT muons are designed to recover acceptance in the region $|\eta| < 0.1$, where the MS is only partially instrumented, but have the lowest purity among all muon types.
- **Extrapolated muons** are reconstructed using only the track reconstructed in the MS, which is required to satisfy a loose requirement of being compatible with originating from the interaction point. They are designed to extend the acceptance for the region $2.5 < |\eta| < 2.7$, which is not covered by the ID. The parameters of the muon track are defined at the interaction point, taking into account the estimated energy loss of the muon in the calorimeters.

The collections of muons used in physics analysis have the overlaps between the different muon types resolved. When two muons share the same ID track, priority is given to CB or IO muons (choosing the type with better fit quality), then to SiF, then to ST, and then to CT muons. When a muon of the previously mentioned types overlaps with an ME muon, the overlap is resolved by selecting the track with a better fit quality and a larger number of hits.

### Muon identification

The muon identification algorithms discriminate between prompt muons originating from signal processes and background-like objects. The identification of CB muons is based on three variables

- $q/p$ significance, which is defined as the ratio of $|(q/p)_{\text{ID}} - (q/p)_{\text{MS}}|$ and $\sqrt{\sigma(q/p)^2_{\text{ID}} + \sigma(q/p)^2_{\text{MS}}}$, where $(q/p)_{\text{ID (MS)}}$ is the ratio of the charge and momentum of the muons measured in the ID (MS) and $\sigma(q/p)_{\text{ID (MS)}}$ is the corresponding resolution,

- residual between the momentum measurements in the ID and MS divided by the transverse momenta of the combined track $\rho' = |p_{\text{T,ID}} - p_{\text{T,MS}}|/p_{\text{T}}^{\text{comb}}$,

- normalised $\chi^2$ of the combined track fit.

Five OPs are defined based on these variables, which address the specific needs of a wide range physics analyses, including LOOSE, MEDIUM, TIGHT, LOWPT, and HIGHPT OPs. Out of these definitions, LOOSE and MEDIUM muons are considered in the searches for dark matter presented in this dissertation.

- LOOSE muons are identified from all muon types. CB muons are required to have at least three hits in at least two MDT layers, except for muons in the sparsely instrumented region $|\eta| < 0.1$). ME muons are required to have hits in at least three MDT or CSC layers. ST and CT muons are considered in the region $|\eta| < 0.1$. Contamination due to hadrons misidentified as muons is suppressed by requiring a $q/p$ significance less than seven and imposing a loose selection on the compatibility between ID and MS momentum measurements.

- MEDIUM muons are identified only from CB or ME muons, which satisfy all requirements defined for the LOOSE OP.

The muon identification efficiency in bins of $p_{\text{T}}$ and two-dimensional binning in $\eta$-$\varphi$ are shown in Figure 6.7. The efficiency for the LOOSE and MEDIUM OPs exceeds $98\,\%$ for muons with $0.1 < |\eta| < 2.5$. The agreement between collision data and detector simulation is very good, with average differences at the level of $0.5\,\%$.

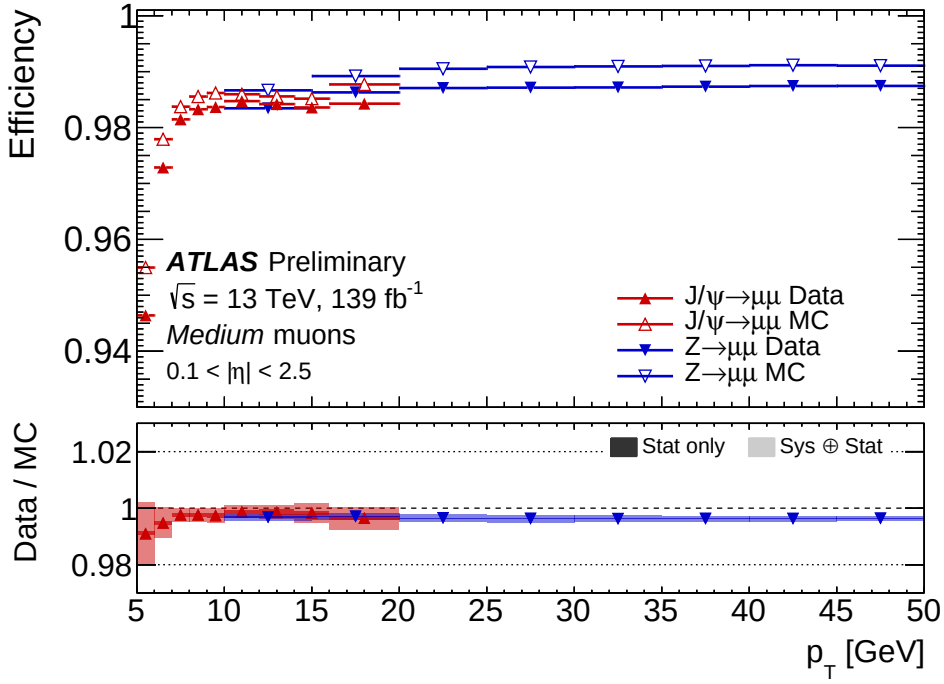
Additional requirements are imposed on the impact parameters of the muon track to associate the muon candidates with the PV and thereby reject muons originating from cosmic rays, pile-up interactions, or muons originating from secondary hadron decays. The shortest distance from the muon track to the primary vertex in a longitudinal projection is required to satisfy $|z_0| \sin\theta < 0.5\,\text{mm}$ and the transverse impact parameter significance is required to satisfy $|d_0|/\sigma(d_0) < 3$.

### Muon isolation

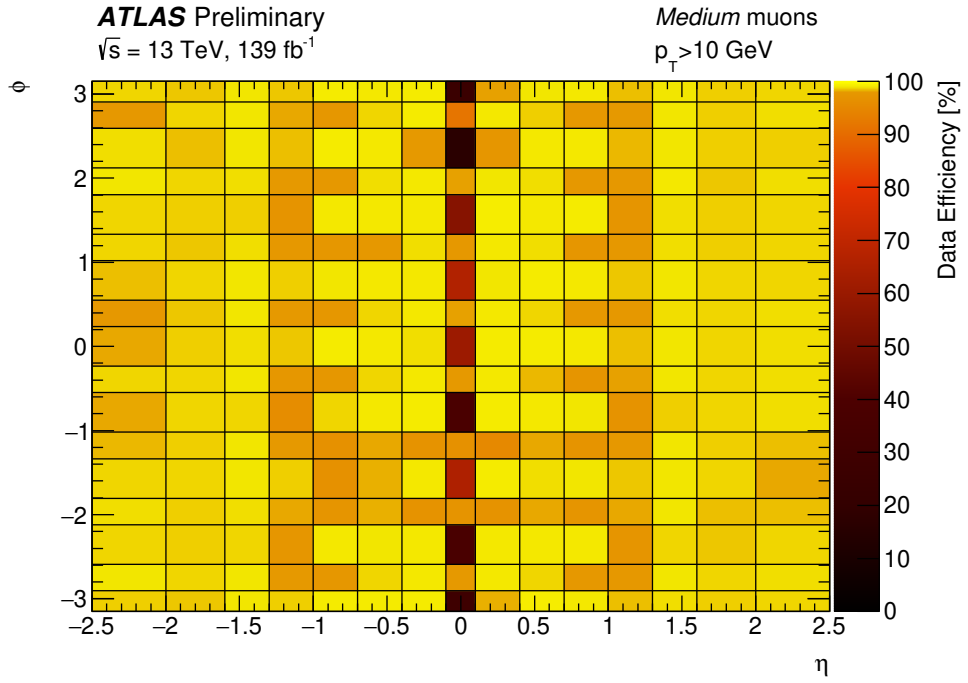
Similar to the case of electrons, specific isolation requirements allow for better discrimination between muons from signal processes and background-like objects. Track-based and calorimeter-based isolation variables are employed.

- The track isolation variable $p_T^{\text{varcone},0.2}$ is defined as the sum of the transverse momenta of all tracks in a cone of variable size $R = \min\{0.2, 10\,\text{GeV}/p_{\text{T}}\}$ around the direction of the muon with transverse momentum $p_{\text{T}}$. The $p_T^{\text{varcone},0.3}$ variable is defined similarly.

- The calorimeter $E_T^{\text{cone},0.2}$ isolation variable is defined as the sum of the transverse energies of all calorimeter clusters in a cone with fixed size $R = 0.2$ around the muon.




(a) Muon reconstruction and identification efficiencies in bins of $p_{\mathrm{T}}$ for muons with $0.1 < |\eta| < 2.5$. The bottom panel shows the ratio of the measured to predicted efficiencies, with statistical and systematic uncertainties (shaded boxes).

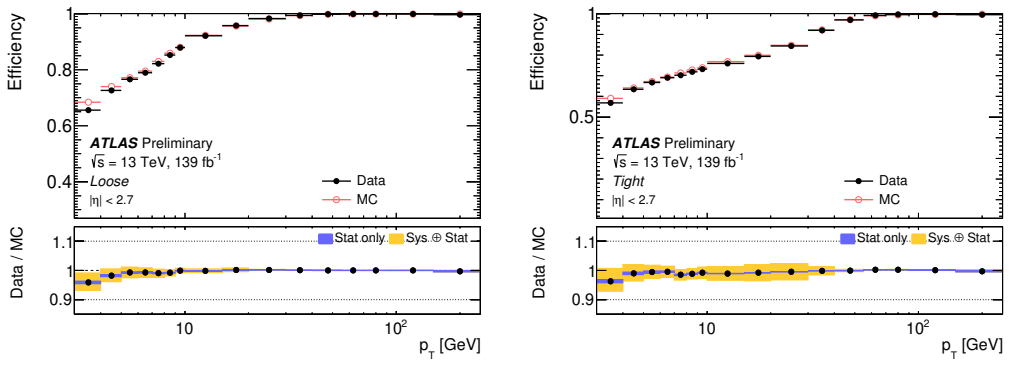



(b) reconstruction and identification efficiencies measured in collision data in bins of $\eta$-$\varphi$ for muons with $p_{\mathrm{T}} > 10\,\mathrm{GeV}$ as a function of $\eta$ and $\varphi$.

**Fig. 6.7.:** Muon reconstruction and identification efficiencies for MEDIUM muons with $p_{\mathrm{T}} > 10\,\mathrm{GeV}$. Figures reproduced from Ref. [63].

Several OPs can be defined using these variables, which either apply a fixed cut on the selected isolation variable or target a specific value of the isolation efficiency in dependence on the muon $p_{\mathrm{T}}$.

Figure 6.8 shows the muon isolation efficiency for the LOOSE and TIGHT fixed cut OPs in bins of $p_{\mathrm{T}}$.




(a) LOOSE OP (b) TIGHT OP

**Fig. 6.8.:** Muon isolation efficiency in bins of $p_{\mathrm{T}}$ for the LOOSE and TIGHT fixed cut OPs. Figures reproduced from Ref. [63].

### 6.1.5 Jets

Jets are collimated and localised sprays of particles, which can be reconstructed using jet algorithms (c.f. Section 4.5). The anti-$k_t$ algorithm is used to build jets from topological clusters in the calorimeters, tracks in the ID or stable particles defined by MC event generators. Various radius parameters are used to define in the jet reconstruction, ranging from $0.2$, $0.4$, to $1.0$, including definitions of $p_{\mathrm{T}}$-dependent radius parameters. Jets are essential for analyses targeting hadronic final states because they allow associating detector measurements with the parton shower initiated by a single final-state parton.

Jets on detector-level can be built from the energy deposits in the calorimeter, referred to as calorimeter jets or simply jets, or from ID tracks of charged particles, referred to as track jets. While calorimeter jets have a better energy resolution due to the calorimeters also measuring the energy deposits of neutral particles, the track jets have a better spatial resolution due to the intrinsically finer granularity of the ID. Jets built from stable particles (except muons, neutrinos, and particles from pile-up interactions) in the MC simulation of physics processes are referred to as truth jets. They are used as a reference for the jets reconstructed from detector information in performance studies or early optimisation studies of analyses.

In the following, the reconstruction and calibration of calorimeter jets with small radius parameter, calorimeter jets with large radius parameter, and track jets with fixed and variable radius parameters are described.

### Small-radius calorimeter jets

Small-radius calorimeter jets are reconstructed from the topological clusters in the calorimeters calibrated to the EM scale using the anti-$k_t$ algorithm with a radius parameter $R = 0.4$. The energy scale of the reconstructed small-radius jets is calibrated to the scale particles in MC simulations using a sequence of data- and simulation-based calibrations [55, 54].

The jets produced in the hard-scattering process are expected to originate from the primary vertex. Therefore, the jet direction is recalculated to account for the position of the primary vertex in each event. As a result, the spatial resolution of jets is improved, while keeping the jet energy unchanged.

The sequential calibration scheme, which involves five steps, is illustrated in Figure 6.9.

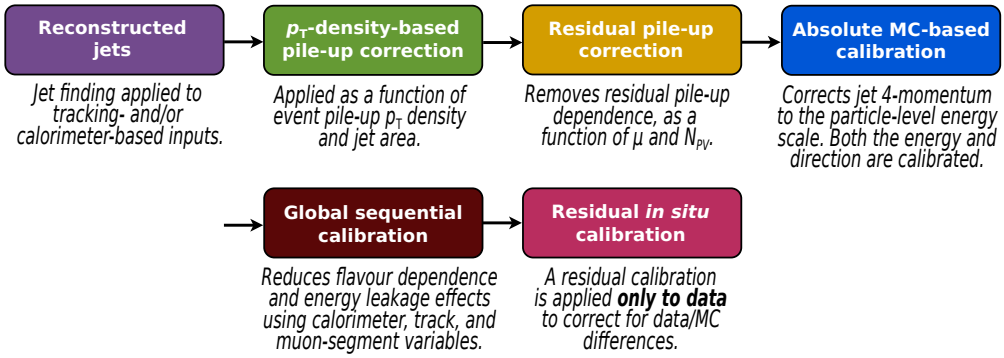



**Fig. 6.9.:** Stages of jet energy scale calibrations. Each one is applied to the four-momentum of the jet. Figure reproduced from Ref. [54]

The reconstructed jets first need to be corrected for pile-up by removing the excess energy due to additional pp interactions. The pile-up corrections consist of two steps. First, a correction based on the jet area and transverse momentum density of the event is applied. Second, a residual correction derived from MC simulations is applied to remove the remaining dependence on pile-up contributions. The pile-up corrected jets are calibrated to the particle-level using an MC-based calibration, which corrects their energy and direction. The jet $p_{\mathrm{T}}$ resolution is improved by applying a global sequential calibration. Finally, a residual in-situ calibration is applied to the jets, which corrects for remaining differences between data and simulation.

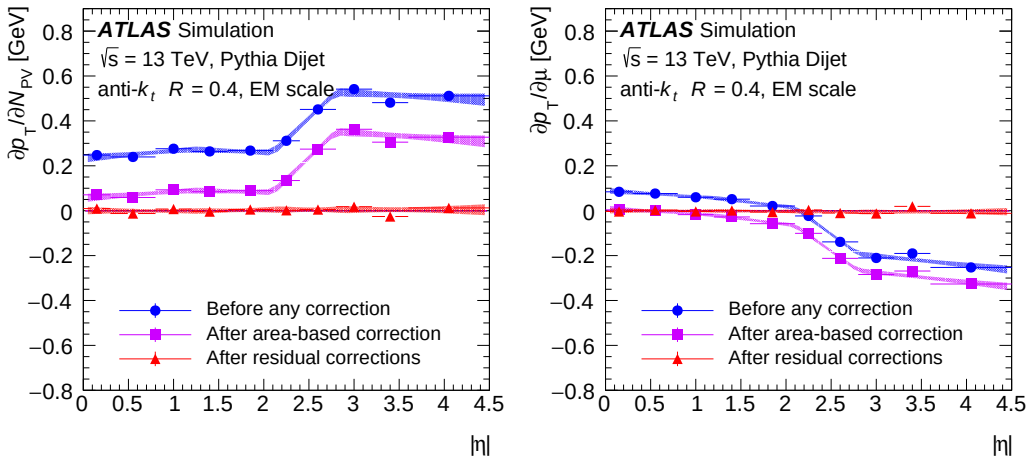
1. **$p_{\mathrm{T}}$-density based pile-up correction**. A $p_{\mathrm{T}}$-density-based subtraction of the event pile-up is performed based on the jet area $A$ (c.f. Section 4.5, which is a measure of the susceptibility of the jet to pile-up contributions. The median jet $p_{\mathrm{T}}$-density $\rho = \langle p_{\mathrm{T}}/A \rangle$ is used to estimate the median pile-up contribution in jets. It is calculated from jets in the central lower-occupancy regions $|\eta| < 2.0$

of the calorimeter, which are reconstructed from topological clusters using the $k_{\mathrm{T}}$ algorithm with $R = 0.4$ in the rapidity-$\varphi$ plane.

2. **Residual pile-up correction**. After the $p_{\mathrm{T}}$-density-based correction, some residual dependence on the pile-up activity remains. It is estimated in MC simulations by geometrically matching the reconstructed jets to truth jets within $\Delta R < 0.3$ and parametrising the difference between the reconstructed jet $p_{\mathrm{T}}^{\mathrm{reco}}$ and the corresponding truth jet $p_{\mathrm{T}}^{\mathrm{truth}}$ as a function of the number of reconstructed primary vertices $N_{\mathrm{PV}}$ and the mean number of interactions per bunch crossing $\mu$. The former number is a measure of the in-time pile-up, while the latter is a measure for out-of-time pile-up. The residual momentum dependence on $N_{\mathrm{PV}}$ and $\mu$ is parametrised as linear functions.

   The jet $p_{\mathrm{T}}$ after both pile-up corrections is $p_{\mathrm{T}}^{\mathrm{PU\ corr}} = p_{\mathrm{T}}^{\mathrm{reco}} - \rho \times A - \alpha \times (N_{\mathrm{PV}} - 1) - \beta \times \mu$, where $p_{\mathrm{T}}^{\mathrm{reco}}$ denotes the reconstructed jet $p_{\mathrm{T}}$ before pile-up corrections and $\alpha, \beta$ are coefficients defined in $p_{\mathrm{T}}$ and $\eta$ of the truth jet.

   The dependence of the jet $p_{\mathrm{T}}$ on $N_{\mathrm{PV}}$ and $\mu$ is shown in Figure 6.10.




**(a)** Dependence of jet $p_{\mathrm{T}}$ on $N_{\mathrm{PV}}$, averaged over $\mu$.

**(b)** Dependence of jet $p_{\mathrm{T}}$ on $\mu$, averaged over $N_{\mathrm{PV}}$.

**Fig. 6.10.:** Dependence of jet $p_{\mathrm{T}}$ on in-time pile-up (left) and out-of-time pile-up (right) as a function of $|\eta|$ for truth jet $p_{\mathrm{T}} = 25\,\mathrm{GeV}$. Figures reproduced from Ref. [55].

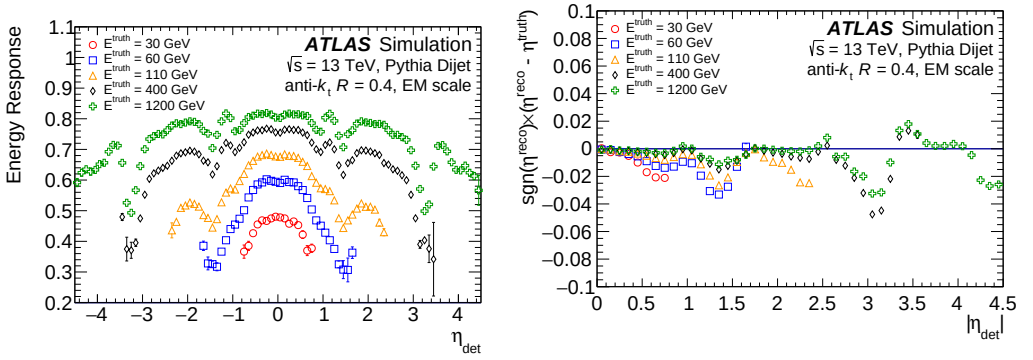
3. **Absolute MC-based calibration**. The absolute jet energy scale (JES) and $\eta$-calibrations correct the reconstructed and pile-up corrected jet four momenta to the energy scale of final-state particles by accounting for non-compensating calorimeter response, energy losses in the dead material, out-of-cone effects, and biases in the jet $\eta$-reconstruction. Both JES and $\eta$ calibration are parametrised in the reconstructed jet energy $E^{\mathrm{reco}}$ and the pseudorapidity in the detector coordinate frame $\eta_{\mathrm{det}}$.

   The JES calibration applies a correction, which is taken as the inverse of the average jet energy response $\mathcal{R}$. The jet energy response $\mathcal{R}$ is defined as the

mean of a Gaussian fit to the core of the $E^{\text{reco}}/E^{\text{truth}}$ distribution. The average jet energy response for jets with different $E^{\text{truth}}$ as a function of $\eta_{\text{det}}$ is shown in Figure 6.11a.

The $\eta$ calibration corrects for biases in the reconstructed jet $\eta$, which are defined as deviations from zero in the signed difference between the reconstructed pseudorapidity $\eta^{\text{reco}}$ and the truth pseudorapidity $\eta^{\text{truth}}$. Figure 6.11b shows the signed difference as a function of $\eta_{\text{det}}$.

These calibrations only change the jet $p_{\text{T}}$ and $\eta$, not the full four-momentum. Jets calibrated with the full JES and $\eta$ calibration, are considered to be at the EM+JES scale.




(a) Average jet energy response.

(b) Signed difference between reconstructed and truth $\eta$ as a function of $\eta_{\text{det}}$.

Fig. 6.11.: The average jet energy response (left) and the signed difference between the truth and the reconstructed jet pseudorapidity (right) as functions of $\eta_{\text{det}}$ for jets with truth energy of 30, 60, 110, 400, and 1200 GeV. Figures reproduced from Ref. [55].

4. **Global Sequential Calibration**. The residual dependencies of jets at the EM+JES scale on features of the jet due to fluctuations in the jet particle composition and the distribution of energy within the jet are taken into account by a Global Sequential Calibration (GSC). The GSC is a series of multiplicative corrections, which are based on five jet observables, such as jet topological energy distributions or number of tracks associated with the jets. For each jet observable, an independent correction of the jet four-momentum is derived as a function jet $p_{\text{T}}$, jet energy, and $|\eta_{\text{det}}|$.

5. **Residual in-situ calibration**. The final in-situ calibration step accounts for differences between the jet response in data and simulation by measuring the jet response in data and MC simulation separately and applying the ratio as an additional correction in data only. There are three in-situ calibrations, which are obtained from dedicated measurements involving well-calibrated reference objects. First, the jets in the forward region of the detector ($0.8 < |\eta_{\text{det}}| < 4.5$) receive an additional correction, which brings them to the same energy scale as the jets in the central region with $|\eta_{\text{det}}| < 0.8$. Second, the jet $p_{\text{T}}$ is calibrated in $\text{Z}(\ell\ell)$ + jets and $\gamma$ + jets events by balancing the hadronic recoil against a

well-calibrated Z boson or photon. Third, single high-$p_{\mathrm{T}}$ jets are calibrated in multijet events by balancing the momentum against a system of several well-calibrated low-$p_{\mathrm{T}}$ jets. The calibration factors of the three steps are combined to a final in-situ calibration map, as shown in Figure 6.12.

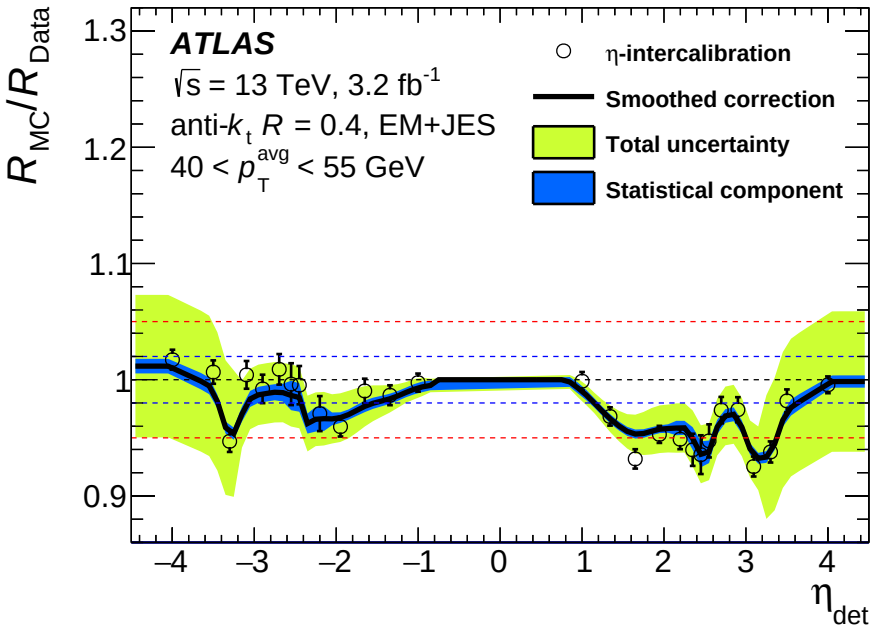



**Fig. 6.12.:** Binned ratio (open circles) of the jet response in simulated events to that in data as a function of $\eta_{\mathrm{det}}$ for jets at the EM+JES and GSC scale with $40\,\mathrm{GeV} < p_{\mathrm{T}}^{\mathrm{avg}} < 55\,\mathrm{GeV}$. The smoothed correction (black line) with corresponding statistical (dark blue) and total (light green) uncertainty bands is overlaid, together with horizontal dotted lines to guide the eye. Figure reproduced from Ref. [55].

The JES calibration is accompanied by systematic uncertainties, which are defined using more than $90$ components. As most of these uncertainties are of minor importance for most physics analyses, reduced sets of JES uncertainties are available, which combine groups of uncertainties and thereby reduce the complexity of statistical models.

In addition to the central value of the JES and the associated calibration uncertainties, the jet energy resolution (JER) needs to be determined [43]. It can be parametrised by

$$\frac{p_{\mathrm{T}}}{\sigma(p_{\mathrm{T}})} = \frac{\mathcal{N}}{p_{\mathrm{T}}} \oplus \frac{\mathcal{S}}{\sqrt{p_{\mathrm{T}}}} \oplus \mathcal{C}, \tag{6.1}$$

where $\mathcal{N}$ accounts for the effect of electronic and pile-up noise, $\mathcal{S}$ denotes the stochastic term arising from the sampling nature of the calorimeters, and $\mathcal{C}$ denotes the constant term. All terms are added in quadrature.

The JER is measured using the in-situ techniques described above, with the exception that the observable of interest is not the mean of the jet response $\mathcal{R}$ but its width $\sigma(\mathcal{R})$.

### Identification of $b$-jets

The identification of $b$-jets— jets originating from the fragmentation of $b$-quarks— is an essential experimental technique to identify processes of interest even in the presence of large background contributions [68, 35].

The characteristic signature of $b$-jets manifests as at least one displaced decay vertex with respect to the primary vertex because of the relatively long lifetime of B-mesons of roughly $1.5\,\mathrm{ps}$, which corresponds to a proper decay length of $450\,\mu\mathrm{m}$.

The identification of $b$-jets consists of two steps. First, various low-level algorithms process features of ID tracks and estimate their association with displaced vertices. Second, the output of these algorithms is processed by multivariate (MVA) classifiers to provide a powerful discriminant for identifying $b$-jets. This procedure is commonly referred to as $b$-tagging.

The low-level $b$-tagging algorithms include impact parameter based algorithms (IP2D and IP3D) [68], the secondary vertex finder algorithm (SV1) [100], and the topological multi-vertex algorithm (JetFitter) [107]. The algorithms are briefly introduced below.

- The **IP2D and IP3D algorithms** are based on exploiting the large impact parameters of the tracks originating from B-hadron decays. While the IP2D algorithm constructs a discriminating variable using only the signed transverse impact parameter significance of tracks, the IP3D algorithm considers both the transverse and longitudinal impact parameter significances $d_0/\sigma(d_0)$ and $\sin\theta z_0/\sigma(\sin\theta z_0)$. Based on these discriminating variables and reference distributions from MC simulation, likelihood ratio discriminants are calculated for $b$-jet, charm jet ($c$-jet) and light-flavour jet identification.

- The **SV1 algorithm** reconstructs the single displaced vertex inside the jet which corresponds to the B-hadron decay using selected tracks, which have to satisfy a set of quality requirements. Likelihood ratio discriminants are constructed from vertex variables, such as the vertex mass, and the number of two-track vertices.

- The **JetFitter algorithm** is designed to reconstruct the full B-hadron decay chain, exploiting the topological features of heavy-flavour decays inside the jet. The algorithm is based on a modified Kalman filter, which is used to find a common line on which the primary, bottom and charm vertices lie, approximating the b-hadron flight path as well as the vertex positions. Likelihood ratio discriminants are constructed from the displaced vertex variables.

The commonly used high-level $b$-tagging algorithm is the MV2 Boosted Decision Tree (BDT) [68], which combines the outputs of the low-level $b$-tagging algorithms with kinematic properties $p_{\mathrm{T}}$ and $\eta$ of the jets using MVA techniques. The MV2 algorithm is trained on a mixed sample of simulated $\mathrm{t\bar{t}}$ and $\mathrm{Z}'$ events, whose background composition is adjusted to $7\,\%$ $c$-jets and $93\,\%$ light-flavour jets.

The $b$-tagging performance is evaluated using a sample of $\mathrm{t\bar{t}}$ events. Several $b$-tagging single-cut OPs are defined, which are based on a fixed cut on the $b$-tagging algorithm discriminant distribution and correspond to a specific $b$-tagging efficiency. The searches for dark matter presented in this dissertation use OPs corresponding to $70\,\%$ and $77\,\%$ $b$-tagging efficiency. Figure 6.13 shows the distribution of the MV2 output discriminant, with the selections corresponding to $70\,\%$ and $77\,\%$ efficiency indicated.

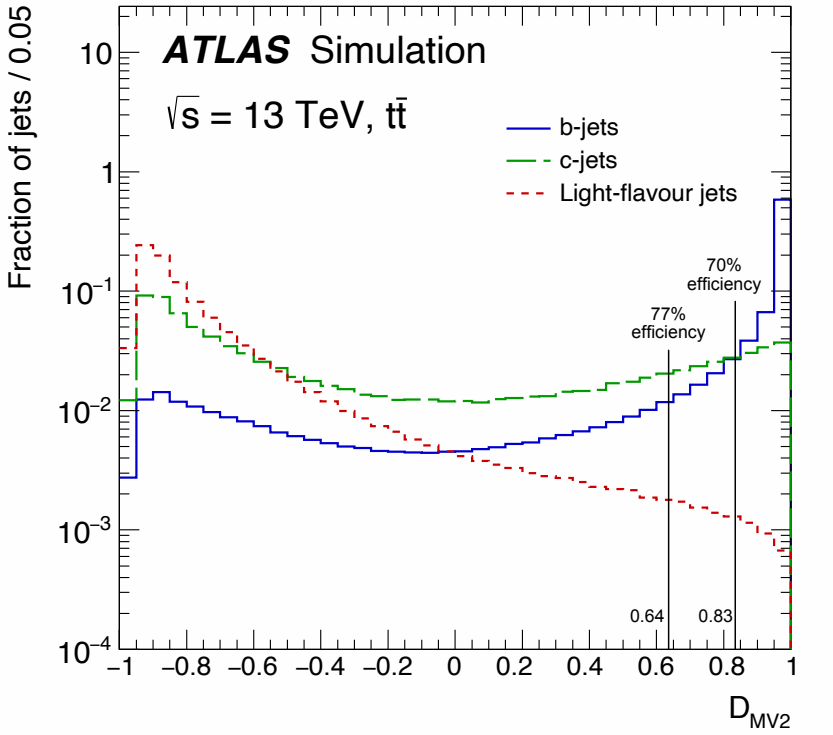


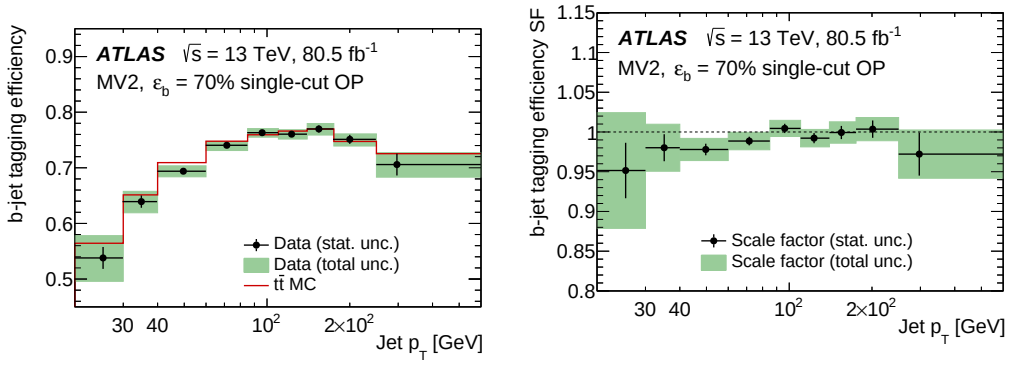

**Fig. 6.13.:** Distribution of the output discriminant of the MV2 $b$-tagging algorithm for $b$-jets (blue), $c$-jets (green) and light-flavour jets (red) in a sample of MC simulated $\mathrm{t\bar{t}}$ events. Figure adapted from Ref. [35].

The corresponding rejection factors for $c$-jets and light-flavour jets at the $77\,\%$ ($70\,\%$) fixed-cut efficiency selection are approximately $5$ and $110$ ($9$ and $300$), respectively.

The $b$-tagging efficiency, as well as the misidentification rates of $c$-jets and light-flavour jets, are compared between data and simulations. Corrections in the form of scale factors are applied to simulated events to account for discrepancies between

data and simulations due to imperfections in the modelling of physics processes or the detector response.

Figure 6.14 shows the measured $b$-tagging efficiency in dependence of the jet $p_{\mathrm{T}}$ and the scale factors, which are applied to simulated events. The scale factors have values close to unity and are approximately constant throughout the entire $p_{\mathrm{T}}$ range.




(a) $b$-tagging efficiency

(b) $b$-tagging efficiency simulation-to-data scale factors

**Fig. 6.14.:** The $b$-tagging efficiency (left) and $b$-tagging efficiency simulation-to-data scale factors (right) for the $70\,\%$ single-cut OP of the MV2 tagger as a function of jet $p_{\mathrm{T}}$. The efficiency measurement is shown in data (dots) and in simulated $\mathrm{t\bar{t}}$ events (red line), together with the total uncertainty (green band). Figures reproduced from Ref. [35].

### Large-radius calorimeter jets

The reconstruction of hadronically decaying heavy bosons using a pair of small-radius jets becomes infeasible for boosted objects. The strong collimation of their decay products as a consequence of the Lorentz boost makes it impossible to resolve the decay's partonic sub-structure. As a rule-of-thumb, the separation between the two decay products of a boosted heavy boson with mass $m$ and transverse momentum $p_{\mathrm{T}}$ can be estimated [150] as

$$R = \frac{1}{z(1-z)} \times \frac{m}{p_{\mathrm{T}}}, \tag{6.2}$$

where $z$, $1-z$ are the momentum fractions of the two decay products. As heavy bosons have a larger transverse momentum, their decay products become increasingly collimated, as illustrated in Figure 6.15. Therefore, the reconstruction of the boosted object is based on a single jet with large radius parameter, which can fully contain the boosted heavy boson decay.

The reconstruction and calibration procedure of large-radius jets consists of several stages, which are illustrated by Figure 6.16.

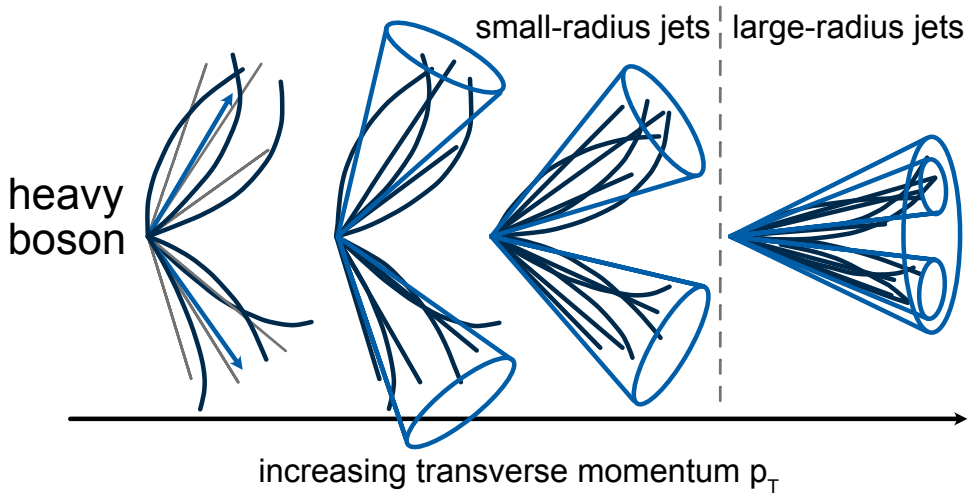



Fig. 6.15.: Illustration of boosted event topologies: the distance between the decay products of a boosted boson decreases with increasing transverse momentum of the boosted boson.

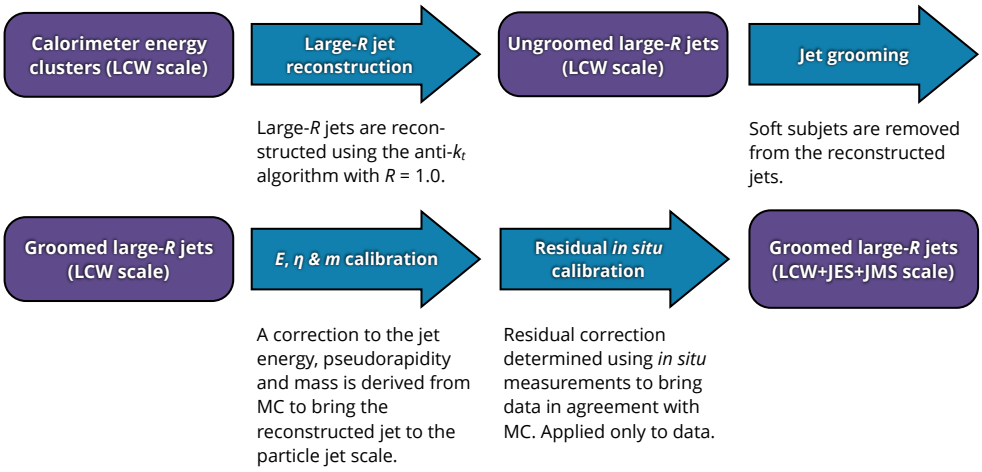



Fig. 6.16.: Overview of the large-radius jet reconstruction and calibration procedure. Illustration reproduced from Ref. [51].

Large-radius jets are reconstructed from topological clusters in the calorimeters, which are calibrated to the hadronic scale in the LCW scheme, using the anti-$k_t$ algorithm with a radius parameter $R = 1.0$.

The large radius parameter makes the reconstructed jets particularly susceptible to contamination from pile-up, initial-state radiation, and multiple parton interactions. The contributions of these processes are generally softer than those of the hard scattering process and can therefore be suppressed by jet grooming algorithms [265]. Among the large variety of algorithms which has been studied [203, 217, 273, 210], the commonly adapted jet trimming algorithm [268] is used to remove soft contaminations of the large-radius jets. All particles in a large-radius jet with radius $R$ are re-clustered into sub-jets with radius parameter $R_{\text{sub}} < R$ using the $k_{\text{T}}$-algorithm. The resulting sub-jets that satisfy the condition $p_{\text{T}}^{\text{sub-jet}} > f_{\text{cut}} p_{\text{T}}^{\text{large-radius jet}}$ are kept and merged to form the trimmed large-radius jet. The algorithm is illustrated in Figure 6.17.

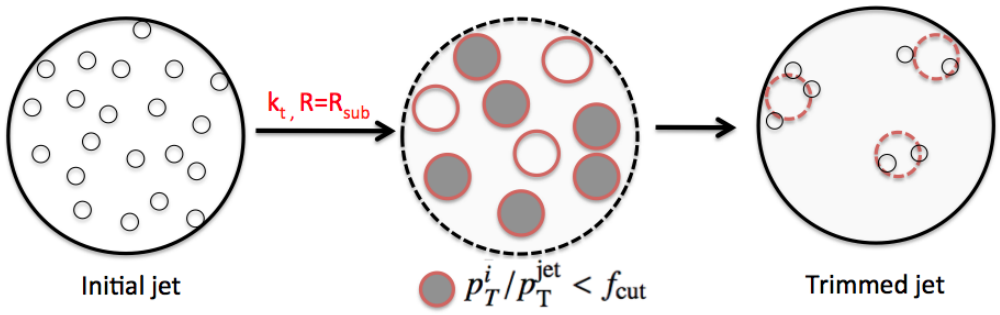



**Fig. 6.17.:** Illustration of the jet-trimming algorithm for large-radius jets. Figure reproduced from Ref. [70].

The trimmed large-radius jets are calibrated to the energy scale of final-state particles using corrections derived in MC simulations. These simulations correct the $p_{\text{T}}$, $\eta$, and the jet mass. Finally, the jets undergo a residual in-situ calibration using jet response measurements in pp collision data. Similar to the small-radius jets, the correction is derived from a statistical combination of data-to-simulation ratios of these response measurements and is applied only to data.

The large-radius jet mass resolution is improved by using both calorimeter and tracking information in the reconstruction. The calorimeter-based (CA) jet mass is computed from the energies $E_i^{\text{topo}}$ and momenta $\mathbf{p}_i^{\text{topo}}$ of topological clusters in the calorimeter as

$$m^{\text{CA}} = \sqrt{\left(\sum_i E_i^{\text{topo}}\right)^2 - \left(\sum_i \mathbf{p}_i^{\text{topo}}\right)^2}. \tag{6.3}$$

The track-assisted (TA) mass is computed in a similar way from a mass measurement based on ID tracks $m^{\text{track}}$ but additionally weighted with the ratio of the transverse

momenta measured by the calorimeters ($p_{\mathrm{T}}^{\mathrm{calo}}$) and the ID ($p_{\mathrm{T}}^{\mathrm{track}}$) to account for neutral hadrons. It is defined as

$$m^{\mathrm{TA}} = m^{\mathrm{track}} \times \frac{p_{\mathrm{T}}^{\mathrm{calo}}}{p_{\mathrm{T}}^{\mathrm{track}}}. \tag{6.4}$$

The combined jet mass is defined as the weighted least-squares combination of the CA and TA mass definitions

$$m^{\mathrm{comb}} = \frac{\sigma_{\mathrm{CA}}^{-2}}{\sigma_{\mathrm{CA}}^{-2} + \sigma_{\mathrm{TA}}^{-2}} \times m^{\mathrm{CA}} + \frac{\sigma_{\mathrm{TA}}^{-2}}{\sigma_{\mathrm{CA}}^{-2} + \sigma_{\mathrm{TA}}^{-2}} \times m^{\mathrm{TA}}, \tag{6.5}$$

with the respective mass resolutions $\sigma_{\mathrm{CA}}$ and $\sigma_{\mathrm{TA}}$.

The combined jet mass definition improves the jet mass resolution and reduces the systematic uncertainties, as shown in Figure 6.18.

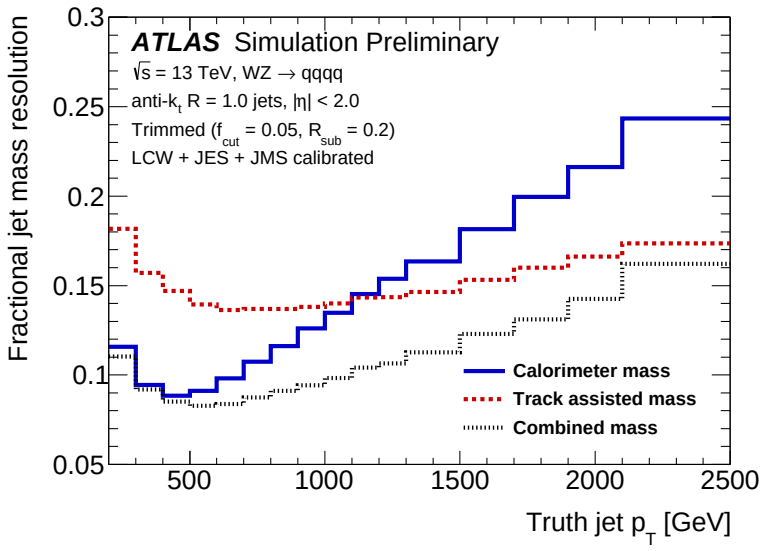



**Fig. 6.18.:** The fractional jet mass resolution, defined as half the ratio of the $68\,\%$ confidence interval inter-quantile range of the jet mass response distribution and the median jet response, estimated in dependence of the truth jet $p_{\mathrm{T}}$ using simulated hadronic decays of diboson processes. Figure reproduced from Ref. [179].

### Track jets

The track jets supplement the reconstruction of boosted heavy bosons based on large-radius jets by enabling the identification of the large-radius jet's flavour content.

Track jets with fixed radius parameter are reconstructed using the anti-$k_t$ algorithm with $R = 0.2$ on ID tracks originating from the PV with $p_{\mathrm{T}} > 0.5\,\mathrm{GeV}$ and $|\eta| < 2.5$. The tracks are required to have at least seven hits in total in the SCT and PXD detectors, no more than one hit shared by multiple tracks in the PXD detector, and

at most one missing hit in the PXD or two missing hits in the SCT detectors. An additional requirement on the longitudinal impact parameter $|z_0 \sin\theta| < 3\,\mathrm{mm}$ with respect to the PV reduces the pile-up contribution.

The smaller radius parameter and superior angular resolution of the tracking detector allow resolving the partonic substructure of the heavy boson decay even in dense environments. However, for substantially boosted event topologies, even the track jets can overlap if they are reconstructed with a fixed radius parameter. The problem of track jet merging is overcome by the use of a modified jet algorithm in which the radius parameter decreases with increasing jet transverse momentum as the jet is being formed. The scaling of the effective jet radius

$$R_{\text{eff}} = \frac{\rho}{p_{\text{T}}}, \tag{6.6}$$

with the transverse momentum of the pseudo-jet $p_{\text{T}}$ as it is being formed (c.f. Section 4.5) is determined by the parameter $\rho = 30\,\mathrm{GeV}$. The effective jet radius is bounded by $0.02 \leq R_{\text{eff}} \leq 0.4$. The resulting jets are referred to as variable-radius (VR) track jets [269, 110]. The reconstruction of VR track jets in comparison to that of FR track jets with radius parameter $R = 0.2$ is illustrated in Figure 6.19.

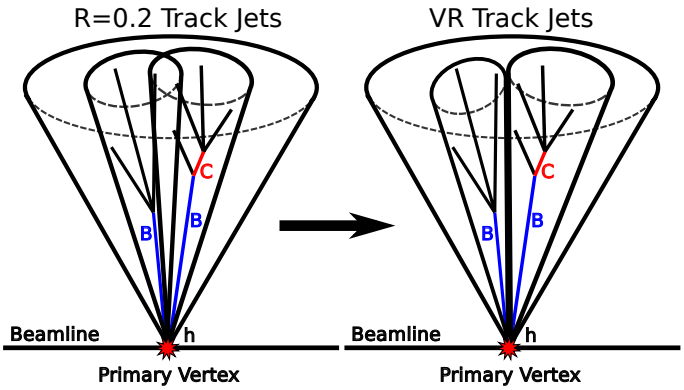



**Fig. 6.19.:** Illustration of the sub-jet reconstruction using either fixed radius (left) or variable radius (right) track jets. Figure reproduced from Ref. [110].

The track jets are uniquely associated with a large-radius jet using the ghost-association technique, in which ghost particles — copies of the track jet four-momentum with vanishing momentum — are added to the inputs of the large-radius jet algorithm. This procedure allows for the unique association of the track jets with a large-radius jet by identifying the ghost particles associated with the non-trimmed large-radius jet.

Track jets undergo no calibration procedure, as the kinematic properties of the heavy boson are reconstructed from large-radius jet information and the track jets are only used for the identification of the large-radius jet flavour. Similar to small-radius jets, the MV2 $b$-tagging algorithm is used to identify track jets originating from $b$-quarks. The $b$-tagging efficiency and the misidentification rates for $c$-jets and light-flavour jets are compared between data and MC to derive corrections for simulated events.

### 6.1.6 Tau leptons

As $\tau$ leptons have a proper decay length of $c\tau = 87\,\mu\text{m}$ [335] and subsequently decay within the LHC beam pipe, their leptonic decays are reconstructed as stable electrons or muons.

The hadronically decaying $\tau$ leptons are reconstructed as small-radius jets and identified using MVA techniques, conceptually similar to $b$-tagging. $\tau$ decays exhibit a characteristic signature of either 1 or 3 charged hadrons collimated along the jet axis accompanied by neutral hadrons. A combination of boosted decision trees targets the 1-prong and 3-prong $\tau$ decay modes and allows for the definition of working points with increasing purity and decreasing efficiency, including the LOOSE BDT OP which is used in the dark matter searches presented in this dissertation.

### 6.1.7 Missing transverse momentum

The missing transverse momentum $E_{\text{T}}^{\text{miss}}$ is a key observable when searching for undetected objects such as dark matter particles or neutrinos. The almost hermetic design of the ATLAS detector enables the reconstruction of these objects via the transverse momentum balance in a collision event. The composite nature of the protons undergoing the collision restricts the knowledge of the momentum before the collision to the transverse plane, where it is zero since the full momentum is aligned in the beam direction. Thus, any momentum imbalance in the transverse plane after the collision can be attributed to undetected objects.

The missing transverse momentum is defined as the negative sum of all physics object transverse momentum vectors and a component due to the track soft term (TST)

$$E_{\text{T}}^{\text{miss}} = -\left| \sum_{e,\mu,\gamma,\tau,\text{jets}} \mathbf{p}_{\text{T}} + \sum_{\text{soft term}} \mathbf{p}_{\text{T}} \right|. \tag{6.7}$$

A high reconstruction efficiency for objects entering the $E_{\text{T}}^{\text{miss}}$ computation is desirable, therefore loose object definitions are employed when calculating the missing transverse momentum. The TST is composed of all tracks not associated with physics objects and is particularly relevant for estimating the $E_{\text{T}}^{\text{miss}}$ scale and resolution.

As $E_{\text{T}}^{\text{miss}}$ is of paramount importance not only for dark matter searches, several OPs are defined for the competing needs of various analyses in terms of pile-up suppression and $E_{\text{T}}^{\text{miss}}$ resolution.

- LOOSE. The $E_{\text{T}}^{\text{miss}}$ calculation includes jets with $p_{\text{T}} > 20\,\text{GeV}$ and $|\eta| < 4.5$. Jets with $p_{\text{T}} < 60\,\text{GeV}$ and $|\eta| < 2.4$ are required to pass the Jet Vertex Tagger (JVT) selection with a JVT score of JVT $> 0.59$.
- TIGHT. The $E_{\text{T}}^{\text{miss}}$ calculation includes the jets described in the LOOSE OP definition. In addition, forward jets ($2.4 < |\eta| < 4.5$ must satisfy $p_{\text{T}} > 30\,\text{GeV}$.

The TIGHT OP offers better pile-up suppression at the cost of inferior $E_{\mathrm{T}}^{\mathrm{miss}}$ resolution for low pile-up events with respect to the LOOSE OP. Figure 6.20 shows the $E_{\mathrm{T}}^{\mathrm{miss}}$ resolution in dependence of the number of primary vertices $N_{\mathrm{PV}}$ in the event for the two OPs.

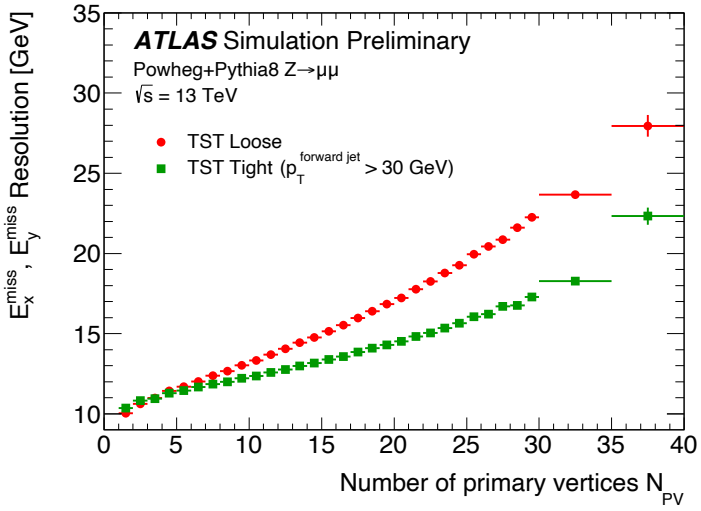



**Fig. 6.20.:** Distribution of the $E_{\mathrm{T}}^{\mathrm{miss}}$ resolution in dependence of the number of primary vertices $N_{\mathrm{PV}}$ in the event for $E_{\mathrm{T}}^{\mathrm{miss}}$ reconstructed with the LOOSE and TIGHT operating points in $\mathrm{Z} \to \mu\mu$ events. Figure adapted from Ref. [34].

A related variable $E_{\mathrm{T}}^{\mathrm{miss,\,track}}$ is defined as the negative vectorial sum of the transverse momenta of all tracks associated with the primary vertex. This variable is used to reduce beam-induced and non-collision backgrounds.

The **missing transverse momentum significance** is used to separate events in which the reconstructed missing transverse momentum $E_{\mathrm{T}}^{\mathrm{miss}}$ is genuinely coming from dark matter particles or neutrinos from events with fake $E_{\mathrm{T}}^{\mathrm{miss}}$ being observed due to contributions from particle-measurement or resolution effects. In addition to historical definitions of the $E_{\mathrm{T}}^{\mathrm{miss}}$ significance, where the scalar sum of objects entering the $E_{\mathrm{T}}^{\mathrm{miss}}$ calculation $\sum E_{\mathrm{T}}^{\mathrm{miss}}$ serves as an event-based approximation to the full $E_{\mathrm{T}}^{\mathrm{miss}}$ resolution, an object-based $E_{\mathrm{T}}^{\mathrm{miss}}$ significance definition is considered.

The object-based $E_{\mathrm{T}}^{\mathrm{miss}}$ significance $\mathcal{S}$ [65] takes into account the resolutions and full correlation among all objects entering the $E_{\mathrm{T}}^{\mathrm{miss}}$ reconstruction. In a coordinate system, which is rotated parallel (longitudinal L) and perpendicular (transverse T) to the direction of the missing transverse momentum vector, the object-based $E_{\mathrm{T}}^{\mathrm{miss}}$ significance definition can be written as

$$\mathcal{S}^2 = \begin{pmatrix} E_{\mathrm{T}}^{\mathrm{miss}} & 0 \end{pmatrix} \begin{pmatrix} \sigma_L^2 & \rho_{LT}\sigma_L\sigma_T \\ \rho_{LT}\sigma_L\sigma_T & \sigma_T^2 \end{pmatrix}^{-1} \begin{pmatrix} E_{\mathrm{T}}^{\mathrm{miss}} \\ 0 \end{pmatrix} \tag{6.8}$$

$$= \frac{\left(E_{\mathrm{T}}^{\mathrm{miss}}\right)^2}{\sigma_L^2\left(1-\rho_{LT}^2\right)}, \tag{6.9}$$

where $\sigma_L^2$ and $\sigma_T^2$ are the total variances in the longitudinal (L) and transverse (T) directions to the $\mathbf{E}_{\mathrm{T}}^{\mathrm{miss}}$ vector, respectively, and $\rho_{LT}$ is the correlation factor of the two measurements. These variances consider all fluctuations in the direction (L) or perpendicular (T) to the direction of the reconstructed $E_{\mathrm{T}}^{\mathrm{miss}}$ from the hard objects entering the $E_{\mathrm{T}}^{\mathrm{miss}}$ calculation.

A high value of $\mathcal{S}$ is an indication that the observed $E_{\mathrm{T}}^{\mathrm{miss}}$ in the event cannot be accounted for by resolution smearing alone, suggesting that the event may contain unseen objects such as neutrinos or dark matter particles.

Figure 6.21 illustrates the performance of the object-based $E_{\mathrm{T}}^{\mathrm{miss}}$ significance in comparison to an event-based definition of $E_{\mathrm{T}}^{\mathrm{miss}}$ significance and $E_{\mathrm{T}}^{\mathrm{miss}}$ itself. The object-based $E_{\mathrm{T}}^{\mathrm{miss}}$ significance definition is clearly superior, as it provides rejection of over $98\,\%$ of the background processes with fake $E_{\mathrm{T}}^{\mathrm{miss}}$ while retaining a signal efficiency over $80\,\%$. In comparison, $E_{\mathrm{T}}^{\mathrm{miss}}$ and the event-based $E_{\mathrm{T}}^{\mathrm{miss}}$ significance provide background rejection of $55\,\%$ and $75\,\%$, respectively [65].

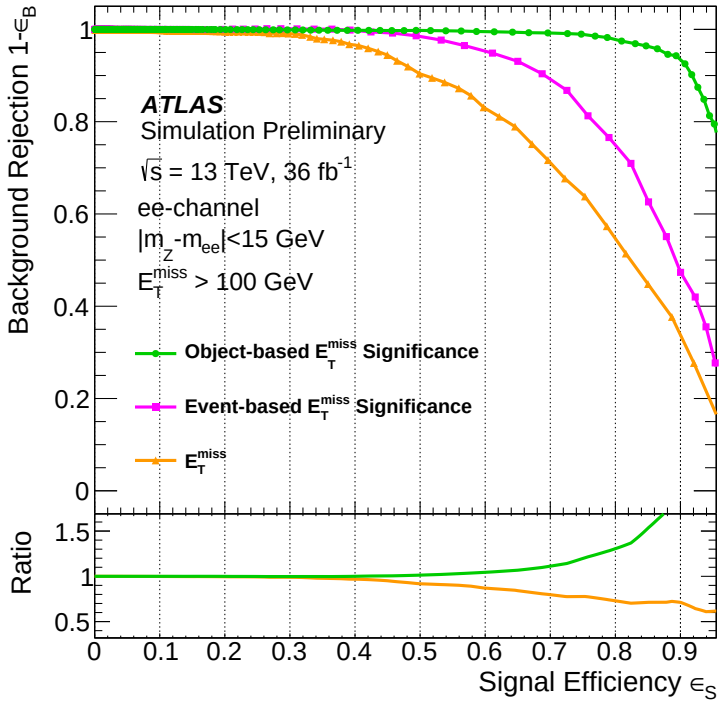



**Fig. 6.21.:** Performance of the $E_{\mathrm{T}}^{\mathrm{miss}}$ significance in terms of background rejection versus signal efficiency in simulated Z $\rightarrow$ ee and Z $\rightarrow$ ee$\nu\nu$ samples with a Z$to$ee selection. The performance is shown for $E_{\mathrm{T}}^{\mathrm{miss}}$ (orange), event-based $E_{\mathrm{T}}^{\mathrm{miss}}$ significance (pink), and object-based $E_{\mathrm{T}}^{\mathrm{miss}}$ significance (green) as discriminants in events with a $E_{\mathrm{T}}^{\mathrm{miss}} > 100\,\mathrm{GeV}$ pre-selection. The lower panel shows the ratio of other definitions to the event-based $E_{\mathrm{T}}^{\mathrm{miss}}$ significance. Figure reproduced from Ref. [65].

## 6.2 Statistical methods

Common statistical methods used in all searches for dark matter presented in this dissertation are introduced in this section.

The simplest definition of a fit is based on a statistical model only considering the total number of selected events. Typically, the statistical model is based on simulated samples of the signal ($S$) and background ($B$) processes, which provide the predicted event yields for the respective processes. A maximum-likelihood fit of the model to data determines the best-fit values of the parameter of interest (POI) and the nuisance parameters (NP) $\theta$. The POI is typically taken to be the signal strength $\mu$, which is defined as the ratio of the signal cross section to a reference signal cross section predicted by theory. The NPs denote further parameters in the model which are subject to uncertainties, e.g. the individual background normalisation parameters. The total predicted event yield is

$$N^{\text{exp}}(\mu, \theta) = \mu S(\theta) + B(\theta). \tag{6.10}$$

The sensitivity to signal processes can be enhanced by considering not only the total event yield but distributions of discriminating variables. These variables are chosen to provide strong separation between signal and background processes. The statistical model for such a fit based on binned distributions of the discriminating variables is described by the likelihood function

$$\mathcal{L}(N^{\text{obs}}|\mu, \theta) = \text{Pois}(N^{\text{obs}}|N^{\text{exp}}(\mu, \theta)) \times \left[\prod_{i \in \text{bins}} \frac{\mu S_i(\theta) + B_i(\theta)}{N^{\text{exp}}(\mu, \theta)}\right] \times \prod_{\theta_i \in \theta} f(0|\theta_i), \tag{6.11}$$

where $N^{\text{obs}}$ denotes the total observed event yield and $S_i$, $B_i$ denote the number of predicted signal and background events in bin $i$, respectively. The systematic uncertainties are implemented as the NPs $\theta_i$ with the associated probability density functions $f(0|\theta_i)$. These are parametrised as standard Gaussian prior distributions with the expectation value $\theta_i$, or in the case of normalisation uncertainties as Log-normal distributions to ensure a positive value of the likelihood function.

A common technique to reduce the uncertainties on the background modelling is the use of control region data. Auxiliary measurements in dedicated selections which are enriched in the respective background processes provide constraints on the normalisation of the simulated backgrounds.

The searches presented in this dissertation use a profile likelihood fit which is based on Equation (6.11) and is implemented using the HISTFACTORY [199] software. The results are obtained by maximising the likelihood function $\mathcal{L}(N^{\text{obs}}|\mu, \theta)$ under

consideration of the likelihood ratio test statistic $q_\mu$. The latter is the most powerful test statistic one can construct [255] and is defined by

$$q_\mu = -2\ln\left(\frac{\mathcal{L}(\mu,\hat{\hat{\theta}})}{\mathcal{L}(\hat{\mu},\hat{\theta})}\right), \tag{6.12}$$

where $\mathcal{L}(\mu,\hat{\hat{\theta}})$ is maximised over all NPs for a given value of $\mu$ and $\mathcal{L}(\hat{\mu},\hat{\theta})$ denotes the global maximum of the full parameter space $\mu,\theta$. Here, $\hat{\hat{\theta}}$ is referred to as the conditional maximum-likelihood estimator of $\theta$, whereas $\hat{\mu}$ and $\hat{\theta}$ are referred to as the unconditional maximum-likelihood estimators of $\mu$ and $\theta$, respectively.

The test statistic $q_\mu$ can be used to test a given signal strength $\mu$ hypothesis. Searches for new physics processes, which manifest as a significant excess over the SM background, consider the "background-only" hypothesis with $\mu = 0$ as the null hypothesis. The test for discovery is performed by rejecting the null hypothesis using the test statistic

$$q_0 = \begin{cases} -2\ln\left(\frac{\mathcal{L}(0,\hat{\hat{\theta}})}{\mathcal{L}(\hat{\mu},\hat{\theta})}\right) & \text{for } \hat{\mu} > 0 \\ 0 & \text{for } \hat{\mu} \leq 0. \end{cases} \tag{6.13}$$

Large values of $q_0$ correspond to more observed events than could be explained by "background-only" hypothesis, suggesting the presence of a signal.

Typically, tests for discovery are stated in terms of the significance

$$Z_\mu = 1 - \Phi^{-1}(1 - p_\mu), \tag{6.14}$$

which is defined by the inverse of the cumulative distribution of the standard Gaussian $\Phi^{-1}$.

If no excess is found in these searches, constraints on the parameter space of specific models for the new physics processes can be set using a different hypothesis test. The test for exclusion is performed by rejecting the "signal + background" hypothesis, using the test statistic

$$q_\mu = \begin{cases} -2\ln\left(\frac{\mathcal{L}(\mu,\hat{\hat{\theta}})}{\mathcal{L}(0,\hat{\theta})}\right) & \text{for } \hat{\mu} \leq 0 \\ -2\ln\left(\frac{\mathcal{L}(\mu,\hat{\hat{\theta}})}{\mathcal{L}(\hat{\mu},\hat{\theta})}\right) & \text{for } 0 < \hat{\mu} \leq \mu \\ 0 & \text{for } \hat{\mu} > \mu. \end{cases} \tag{6.15}$$

Here, the additional condition for $\hat{\mu}$ avoids considering an excess in data incompatible with the "signal + background" hypothesis. Large values of $q_\mu$ indicate smaller compatibility of the "signal + background" hypothesis and the observed data. The fact that the test-statistic is defined to be non-zero only for $\hat{\mu} \leq \mu$ implies that only upper limits on $\mu$ are considered.

The result of the hypothesis test is described by the $p$-value

$$p_\mu = \int_{q_\mu^{\text{obs}}} f(q_\mu|\mu)\,\mathrm{d}q_\mu\,, \tag{6.16}$$

which quantifies the level of disagreement between the observed data and the statistical model defined by the probability density function $f(q_{\mu|\mu})$ of $q_\mu$ for a signal strength $\mu$.

Corresponding $p$-values for the "background-only" ($b$) and the "signal + background" ($s+b$) hypotheses for a given $q_\mu^{\text{obs}}$ are defined by

$$p_b = \int_{-\infty}^{q_\mu^{\text{obs}}} f(q_\mu|b)\,\mathrm{d}q_\mu \tag{6.17}$$

$$p_{s+b} = \int_{q_\mu^{\text{obs}}}^{\infty} f(q_\mu|s+b)\,\mathrm{d}q_\mu\,. \tag{6.18}$$

These definitions, however, might lead to accidental exclusion of signals for searches which are insensitive to those signals. This might occur if, for instance, there is a downward fluctuation in data relative to the expectation of the background-only hypothesis. The accidental rejection of signal hypotheses can be avoided by using the $\text{CL}_s$ method [307], in which the $p_{s+b}$ value is weighted by a penalty factor that increases with decreasing sensitivity. The $\text{CL}_s$ value is defined by

$$\text{CL}_s = \frac{p_{s+b}}{1-p_b}. \tag{6.19}$$

Adopting the $\text{CL}_s$ definition, a point in the parameter space of a model is excluded with confidence level $1-\alpha$ if one finds $\text{CL}_s < \alpha$. Evidently, the $\text{CL}_s$ is more conservative, as the $\text{CL}_s$-based exclusion criterion is more stringent than the usual requirement $p_\mu < \alpha$. However, it should be pointed out that $\text{CL}_s$ limits have no well-defined coverage and should be interpreted such that the probability of having falsely excluded a signal is less than $\alpha$.

The observed value of the test statistic $q_\mu^{\text{obs}}$ will differ in independent experiments, as it is subject to statistical fluctuations. When computing the expectation value of $q_\mu$, the underlying probability distribution of the test statistic can in general not be evaluated analytically. It can, however, be approximated. The approximation can be based on evaluating a large number of simulated toy experiments. Although, in principle, these replicas enable the determination of the expectation value of $q_\mu$ with arbitrarily high precision, it comes at the price of high computational cost.

The Asimov method [196, 195] is an alternative approach which is based on an artificially constructed, representative dataset. The use of the Asimov dataset is formally justified in the limit of large numbers, in which $\hat{\mu}$ follows a Gaussian distribution. It can be used to validate the statistical model and to estimate various properties, such as the expected $p$-values, exclusion limits, or the impact of different sources of uncertainty. The expected median discovery significance is estimated with Asimov data generated under the assumption of the nominal signal model ($\mu = 1$).

Conversely, the expected exclusion limits are estimated with Asimov data generated under the assumption of the background-only hypothesis ($\mu = 0$).

## 6.3 RECAST

The searches for new physics phenomena beyond the SM represent a significant investment in time and both human and computational resources. Moreover, as there are plenty of models predicting new phenomena, it becomes increasingly difficult to experimentally test all of them with dedicated searches considering only specific models in their interpretation. Given the steadily growing number of potentially interesting models and seeing the dawn of the high-luminosity era, a powerful reinterpretation framework is urgently needed. Existing searches for new phenomena often are sensitive to a larger class of new physics theory models. Therefore, it is the sustainable approach to reinterpret existing searches instead of designing a new one.

The RECAST framework [200] is designed to reuse estimates of backgrounds, systematic uncertainties, and observed data from preserved searches to test alternative signal hypotheses. A faithful reinterpretation entails processing the MC generated samples associated with the alternative signals using the full analysis workflow, including the algorithmic implementation of object reconstruction, event selection, and statistical evaluation. RECAST provides the computational infrastructure of preserving the analysis software and automating the corresponding workflow to organise systematic reinterpretation of analyses efficiently.

The analysis software is preserved in a manner that is portable and compatible with an extensive range of computing infrastructures. This is achieved by building Docker container images [131, 287], which can be thought of as a snapshot of a file-system containing the analysis software with all its dependencies. The preservation of the workflow is achieved through the use of the YADAGE [198] workflow description language. The workflow is modelled as a directed acyclic graph, consisting of several interdependent processing steps (referred to as jobs), which culminate in the statistical inference. Within YADAGE, the workflow structure and the job templates are captured as YAML documents. The parametrised job templates specify the commands which configure and execute the analysis software, while the workflow orchestrates the individual steps.

Capturing both the software and the workflow allows for re-executing the analysis software chain without expert knowledge, which otherwise might get lost if the original authors leave the collaboration. A growing number of ATLAS searches is archived using RECAST, thereby providing faithful reinterpretations even for searches with involved analysis techniques [78], which cannot be captured by simplified third-party implementations.

# Part II

Studies of the ATLAS muon trigger

# 7 Improvements to the ATLAS muon trigger

## 7.1 Introduction

Searches for new physics phenomena motivated by the presence of dark matter in the universe rely on the accurate description of electroweak background processes. The wealth of data collected at the LHC with the ATLAS experiment improves the understanding of these background processes. A large range of LHC physics measurements depends crucially on the reliable identification and efficient reconstruction of leptons with momenta at the electroweak scale.

The ATLAS muon trigger constitutes the first stage of the muon detection and reconstruction. It selects events containing muons with their momentum above specified thresholds out of the extremely high background. Improvements to the trigger systems directly impact all physics measurements, as the trigger decision irreversibly determines which data is recorded. The trigger performance is quantified by the muon efficiency and the trigger rate. The muon efficiency is the fraction of events accepted by the trigger, which contain muons above a certain transverse momentum threshold. The trigger rate is the total rate of recorded events. Good muon trigger performance is characterised by high muon efficiency and a low fraction of fake or low-$p_{\mathrm{T}}$ muons in the trigger rate.

This section presents a study about the potential reduction of the trigger rate of the muon trigger with the lowest $p_{\mathrm{T}}$ threshold of $4\,\mathrm{GeV}$ (L1MU4) by careful tuning of the trigger logic.

## 7.2 Rate reduction of the L1MU4 trigger

### 7.2.1 The ATLAS L1 muon trigger in Run-2

The first stage of the ATLAS muon trigger (L1 muon trigger) performs an initial selection of collision events containing muons with transverse momentum above certain thresholds. The trigger decision is based on a subset of detectors with reduced granularity but excellent timing resolution, which allows associating the events with individual bunch-crossings. The L1 muon trigger searches for patterns of hits consistent with muons originating from the interaction region and provides six independently programmable $p_{\mathrm{T}}$ thresholds. The trigger decision is based on

the coincidence of two (three) trigger stations for the low-$p_{\mathrm{T}}$ (high-$p_{\mathrm{T}}$) trigger thresholds.

Figure 7.1 shows a longitudinal view of the muon trigger system. The muon trigger consists of two systems, covering the barrel region in the pseudo-rapidity range $|\eta| < 1.05$ and the end-cap region in the pseudo-rapidity range $1.05 < |\eta| < 2.4$.

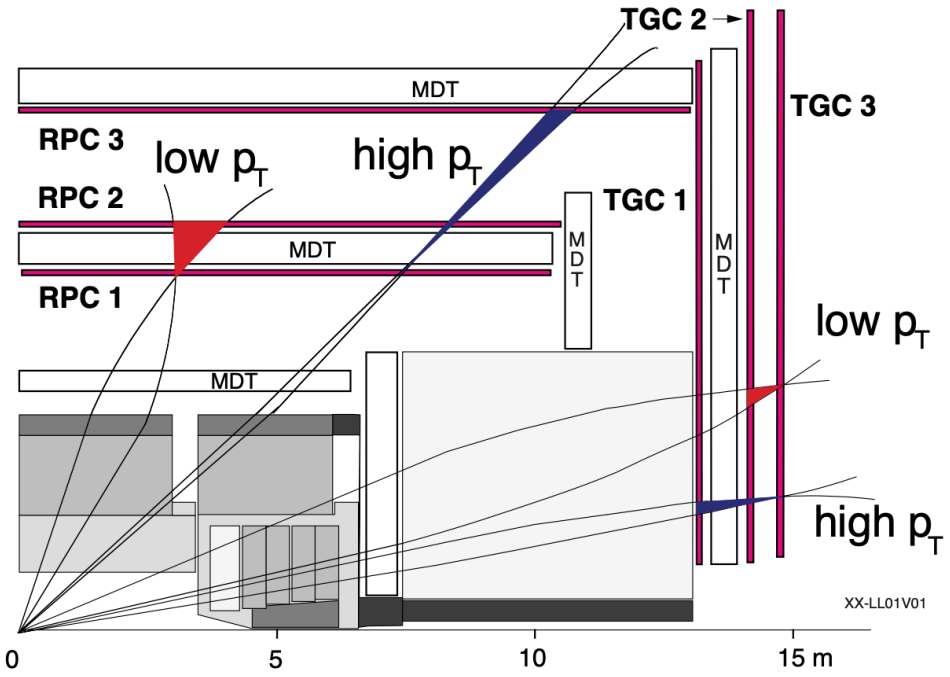



Fig. 7.1.: Longitudinal view of the barrel and end-cap muon trigger system. Representative tracks of muon trigger candidates for the low-$p_{\mathrm{T}}$ and high-$p_{\mathrm{T}}$ triggers illustrate the coincidence logic of trigger stations used for the trigger decision. Adapted from Ref. [112]

.

The barrel region is instrumented with three stations of Resistive Plate Chamber (RPC) detectors. RPCs are wireless strip detectors, consisting of two gas gaps designed for operation in saturated avalanche mode with planes of read-out strips in the transverse and longitudinal direction. They have an excellent timing $\times$ position-resolution of $1\,\mathrm{ns} \times 1\,\mathrm{cm}$ and a rate capability of $10\,\mathrm{kHz\,cm^{-2}}$. Two stations are located above (RPC2) and below (RPC1) the middle MDT layer. Coincidences between hits in the two layers define the muon track candidates. While the low-$p_{\mathrm{T}}$ trigger thresholds are based on the track candidates defined by the two innermost RPC layers, the high-$p_{\mathrm{T}}$ thresholds require additional coincidence with a third (RPC3) station, which is located below the outermost layer of MDT chambers. The RPC chambers provide information for the $\eta$ and $\phi$ coordinates of a muon track candidate.

The end-cap region is instrumented with Thin Gap Chamber (TGC) detectors. TGCs are multi-wire detectors consisting of a plane of closely spaced wires maintained

at a positive high voltage enclosed by two resistive grounded cathode strip planes. The TGC chambers have excellent rate capability of more than $30\,\mathrm{kHz\,cm^{-2}}$ and a better granularity than the RPC chambers, making them capable of operation in the end-cap region. The TGCs are arranged in three planes in each end-cap at $|z| = 14\,\mathrm{m}$. The innermost plane consists of three layers of TGCs (triplet unit), while the two outer planes consist of two layers of TGCs (doublet unit). The outermost plane is designed without gaps in acceptance or overlaps and constitutes the so-called pivot plane. Coincidences between hits in the pivot plane and the adjacent doublet plane, which is located in $0.5\,\mathrm{m}$ distance, define the low-$p_\mathrm{T}$ trigger candidates. The trigger decision can be sharpened by requiring an additional coincidence with the triplet plane, which is located in $1.6\,\mathrm{m}$ distance from the pivot plane. In particular, the high-$p_\mathrm{T}$ triggers make use of this requirement. The TGC wire channels provide information for the $r$-coordinate, while the TGC strip channels provide information for the $\phi$-coordinate of a muon track candidate.

A positive trigger decision associated with a certain $p_\mathrm{T}$ threshold requires the spatial coincidence to be consistent with the associated deviation from an infinite momentum track, thereby defining coincidence windows for the individual $p_\mathrm{T}$ thresholds. The coincidence windows are defined for the two projections in $\eta$ and $\phi$ (barrel) or $r$ and $\phi$ (end-cap), respectively.

### 7.2.2 The L1MU4 coincidence logic tuning

The L1MU4 muon trigger is designed to select muon candidates with $p_\mathrm{T} > 4\,\mathrm{GeV}$. The decision whether the $p_\mathrm{T}$ of the track is above the desired momentum threshold or not is based on coincidence windows, which are implemented as look-up-tables (LUTs). The amount of deviation of the muon track candidate from an infinite momentum track in $r$ and $\phi$ is referred to as $\Delta r$ and $\Delta\phi$, respectively, and is used as input for the LUTs. For a given input of $\Delta r$ and $\Delta\phi$ the LUT determines a positive (pass) or negative (fail) trigger decision. A custom set of LUTs is defined for each region-of-interest (ROI) in each module of trigger chambers.

In Run-1, the L1MU4 employed a two-station full-open coincidence. In Run-2, a more sophisticated implementation is used, which uses requires three-station coincidence for the strip ($\phi$) coordinate and either two-station or three-station coincidence for the wire ($r$) coordinate. The LUT for the three-station wire ($r$) / three-station strip ($\phi$) coincidence is referred to as HH CW, whereas the two-station wire ($r$) / three-station strip ($\phi$) coincidence is referred to as LH CW.

The L1MU4 trigger rate can be reduced by tuning the LUTs, resulting in tighter coincidence windows for hits in the trigger chambers. This study investigates modifications affecting the forward trigger chambers, covering the pseudorapidity range $2 < |\eta| < 2.4$, by tuning the LH CW LUTs. A uniform modification of all LUTs corresponding to the 64 ROIs for the forward TGC modules 2a/b, 5a/b, and 8a/b is applied. Figure 7.2 shows the LUT implementation of the coincidence windows for a representative module of the detector end-cap before and after its optimisation. Prior to the optimisation, all hits within two-station coincidence window of $-15 \leq$

$\Delta r \leq 15$ and the three-station coincidence window of $-7 \leq \Delta\phi \leq 7$ resulted in a positive trigger decision. After the optimisation, only hits within coincidence window of $-7 \leq \Delta r \leq 7$ and $-5 \leq \Delta\phi \leq 5$ resulted in a positive trigger decision.

### 7.2.3 Data and method

The effect of modifying the coincidence windows on the muon trigger efficiency is evaluated with a tag-and-probe method [242, 72] based on the J/$\psi$ resonance into a pair of oppositely charged muons. The two muons are referred to as *tag* and *probe* muon. The *tag* muon is the reconstructed muon, which fired the trigger for recording the event. The *probe* muon is the other muon in the event. The *probe* muons are used for an unbiased study whether a muon track candidate would fire the trigger for a given coincidence window definition. The muon trigger efficiency is estimated by

$$\varepsilon_{\mu-\text{trigger}} = \frac{N_{\text{match}}}{N_{\text{probe}}}, \tag{7.1}$$

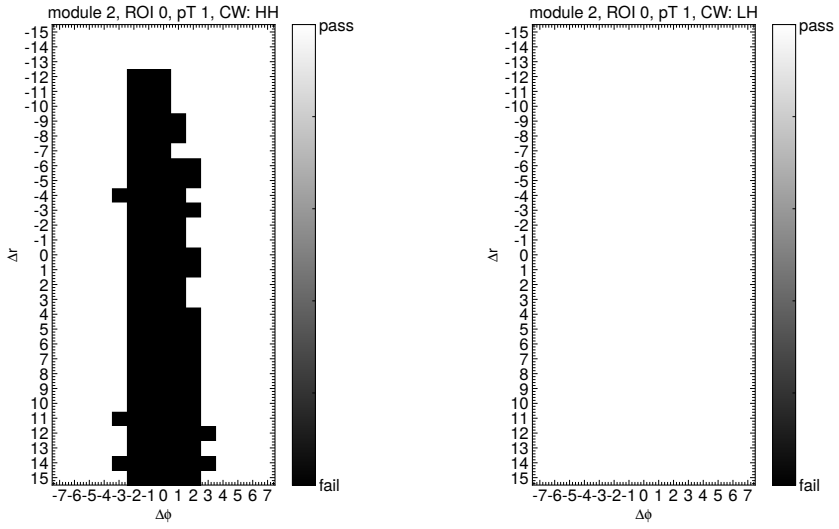
where $N_{\text{match}}$ is the number of muon track candidates matched with a reconstructed muon within the $p_{\text{T}}$-dependent cone size of $\Delta R$ in the $\eta$–$\phi$ plane listed in Table 7.1, and $N_{\text{probe}}$ is the total number of probe muons.

**Tab. 7.1.:** Cone size $\Delta R$ used for matching the muon track candidate with a reconstructed muon in the $\eta$–$\phi$, depending on the transverse momentum $p_{\text{T}}$ and pseudorapidity $\eta$ of the reconstructed muon.

| Minimum $p_{\text{T}}$ of reconstructed muon | $\Delta R$ (barrel) | $\Delta R$ (end-cap) |
|---|---|---|
| 4 GeV | 0.3 | 0.3 |
| 6 GeV | 0.2 | 0.2 |
| 10 GeV | 0.14 | 0.14 |
| 15 GeV | 0.11 | 0.09 |
| 20 GeV | 0.10 | 0.07 |

The tag-and-probe muon pairs are selected in data by the requirements listed in Table 7.2. The muons are required to have opposite charge, and their invariant mass has to be consistent with the J/$\psi$ resonance.

The reconstructed muons are subject to quality requirements listed in Table 7.3. Their pseudorapidity $\eta$ is required to be within the trigger chamber acceptance of $|\eta| < 2.4$. Muons are required to be reconstructed with either *Medium* or *High-*$p_T$ working point, as defined in Ref. [64]. Specific requirements on the number of hits in the inner detector of the reconstructed ensure a robust momentum measurement. Additional requirements are placed on the *tag* muon, which has to satisfy $p_{\text{T}} > 4\,\text{GeV}$




(a) HH CW before optimisation

(b) LH CW before optimisation

(c) HH CW after optimisation

(d) LH CW after optimisation

**Fig. 7.2.:** Modification of coincidence windows in the $\Delta r$–$\Delta\eta$ plane. The 0-th region-of-interest (ROI) LUTs for the HH CW and LH CW are shown for module 2a before (top row) and after (bottom row) the optimisation of the LH CW.

Tab. 7.2.: Event selection requirements

| Event selection | Requirement |
|---|---|
| Trigger | pass HLT_NOALG_L1MU4 |
| Muon multiplicity | $N_\mu \geq 2$ |
| Muon pair invariant mass | $2.7\,\text{GeV} < m_{\mu\mu} < 3.5\,\text{GeV}$ |
| Muon pair opposite charge | $q_{\text{tag}} \times q_{\text{probe}} < 0$ |

and has to be matched with the muon track candidate of a single muon trigger within $\Delta R < 0.05$ in the $\eta$–$\phi$ plane.

Tab. 7.3.: Selection requirements on tag and probe muons

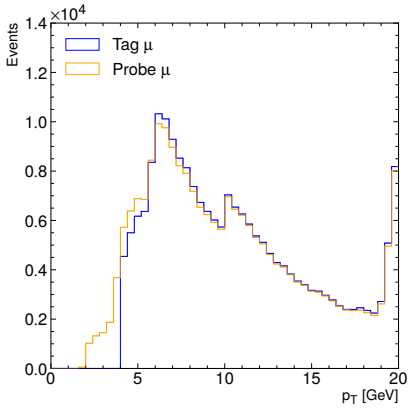
| Reconstructed muons | Quality requirement |
|---|---|
| | $\lvert\eta\rvert < 2.4$<br>Medium or High-$p_{\text{T}}$ working point<br>1 or more hits in PXD detector<br>4 or more hits in SCT detector<br>1 or more hits in Pixel detector<br>2 or less holes in PXD + SCT detectors |
| Tag muon | Additional quality requirement |
| | $p_{\text{T}} > 4\,\text{GeV}$<br>matched with single-lepton trigger by requiring<br>$\Delta R(\mu, \text{muon trigger track candidate}) < 0.05$ |

The data for the efficiency study was taken in 2016 and amounts to over $159\,264\,525$ recorded collision events. The kinematic distributions of the selected *tag* and *probe* muon pairs and their invariant mass is shown in Figure 7.3. The threshold structure in the muon $p_{\text{T}}$ distribution is due to limited bandwidth of the low-$p_{\text{T}}$ muon triggers. The structure of the $\eta$ distribution is due to gaps in the detector acceptance at the central maintenance shaft and the transition region between barrel and end-cap. The reduced acceptance for $\phi = -1.1$ and $\phi = -2.0$ originates from the inferior instrumentation in the feet region of the ATLAS detector.

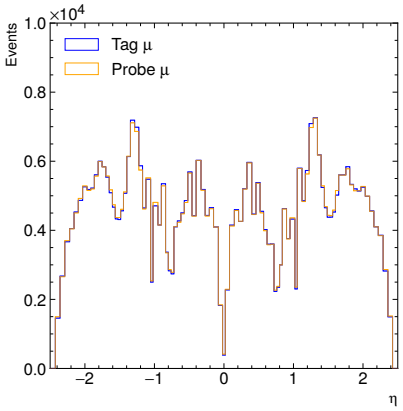
### 7.2.4 Results

Modifications to the coincidence windows of the end-cap trigger stations result in a $4.5\,\%$ reduction of the trigger rate while maintaining a muon efficiency of $99.8\,\%$.

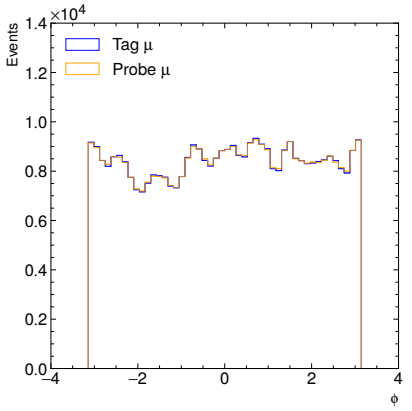
Figure 7.4 shows the L1MU4 trigger efficiency before and after the optimisation of the forward module coincidence windows. The coincidence window optimisation has an almost negligible effect on the L1MU4 trigger efficiency. Only for the muons in the forward region $2.0 < |\eta| < 2.4$ with $p_{\text{T}} < 5\,\text{GeV}$, a drop in trigger efficiency in the sub-percent-range is observed. The overall impact of the modification on the



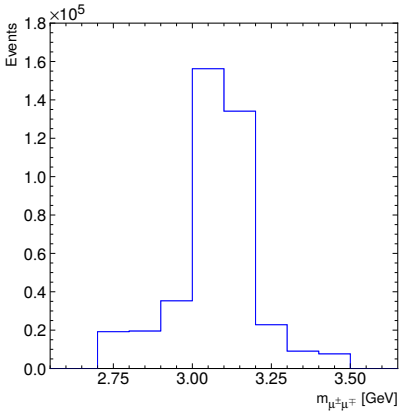

(a) Muon transverse momentum $p_{\mathrm{T}}$




(b) Muon pseudorapidity $\eta$



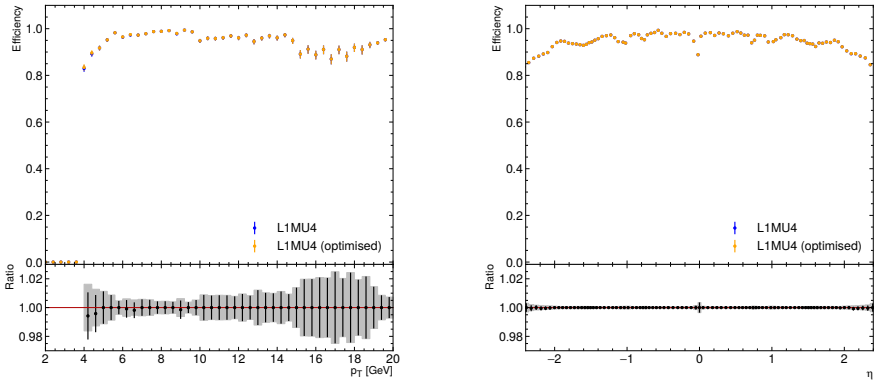

(c) Muon azimuthal coordinate $\phi$




(d) Invariant mass of muon pair

**Fig. 7.3.:** Kinematic distributions of *tag* and *probe* muons and invariant mass of the di-muon system after the full event selection.

L1MU4 trigger efficiency is sufficiently small not to impact the performance of the L1MU4 trigger.




**(a)** Trigger efficiency vs. muon track candidate $p_T$ for $2.0 < |\eta| < 2.4$

**(b)** Trigger efficiency vs. muon track candidate $\eta$

**Fig. 7.4.:** L1MU4 trigger efficiency before and after the optimisation of the forward module coincidence windows estimated with the tag-and-probe method based on the J/$\psi$ resonance.

The reduction in the muon trigger rate is shown in Figure 7.5 in dependency of the pseudorapidity $\eta$ of the muon track candidate. The modification of the LUTs for the forward modules ($2.0 < |\eta| < 2.4$) resulted in a decrease of the trigger rate without affecting the rate of triggers matched to reconstructed muons. In the forward region $2.0 < |\eta| < 2.4$, the L1MU4 trigger rate is reduced by $20\,\%$ while maintaining a muon efficiency of $99.0\,\%$.

The reduction of the trigger rate and the effect on the trigger efficiency for triggers with multiple muons is shown in Table 7.4. For events with two (three) or more muon track candidates leading to a positive trigger decision, the optimised coincidence windows result in a reduction of the L1MU4 trigger rate by $6\,\%$ ($9\,\%$), while keeping $99.2\,\%$ ($100\,\%$) of the muon trigger efficiency.

**Tab. 7.4.:** Effect of the coincidence window optimisation in the forward TGC modules on the L1MU4 trigger rate and trigger efficiency $\varepsilon$ for muon triggers with different muon multiplicities.

| | L1MU4 rate reduction | $\varepsilon_{\text{L1MU4, mod.}}/\varepsilon_{\text{L1MU4}}$ |
|---|---|---|
| 1 or more muon track candidate | $5\,\%$ | $99.8\,\%$ |
| 2 or more muon track candidates | $6\,\%$ | $99.2\,\%$ |
| 3 or more muon track candidates | $9\,\%$ | $100\,\%$ |

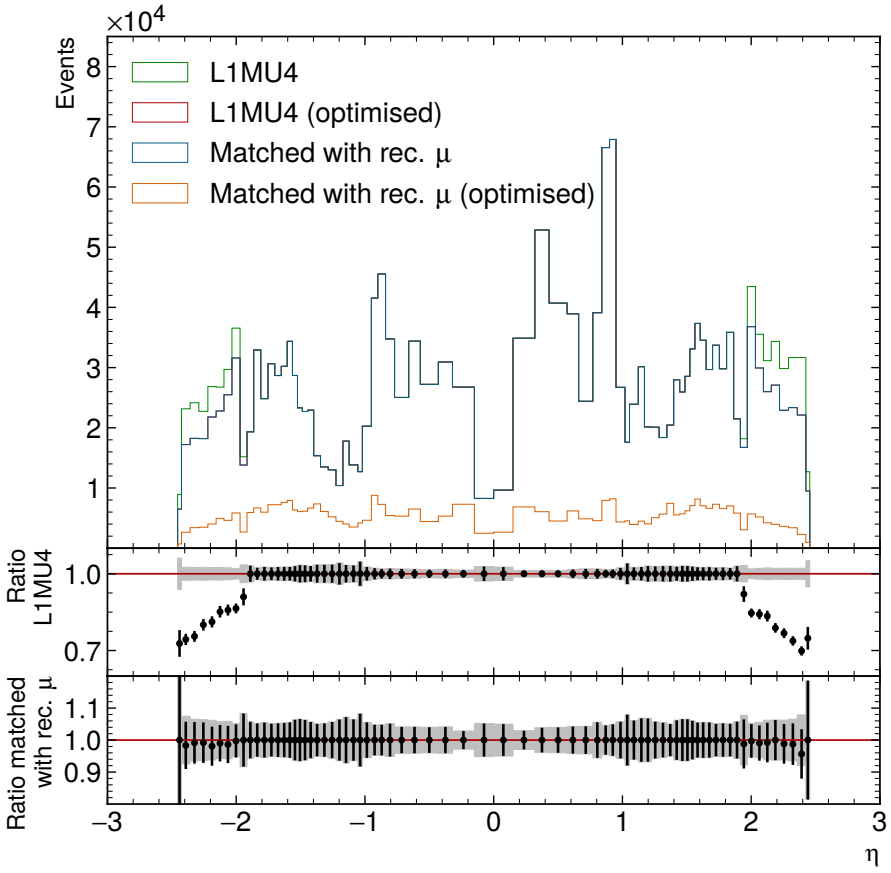



Fig. 7.5.: L1MU4 trigger rate in dependency of the muon track candidate pseudorapidity $\eta$ before and after the optimisation of the coincidence windows of the forward TGC modules. In addition, the rate of positive trigger decisions which could be matched with a reconstructed muon satisfying $p_{\mathrm{T}} > 4\,\mathrm{GeV}$ is shown before and after the coincidence window modification. The two insets show the ratio of the L1MU4 trigger rate after and before the coincidence window modification and the ratio of positive trigger decisions matched with reconstructed muons after and before the coincidence window modification, respectively.

# Part III

Searches for dark matter

# 8 Searches for dark matter in association with heavy bosons

The searches for dark matter in association with heavy bosons presented in this dissertation share a general search strategy, datasets of collision as well as background simulation events, and object definitions. These common features are described in this chapter.

## 8.1 General search strategy

Searches for dark matter at the LHC investigate the pp collision data for a signal which is additive on top of background. The signal process is characterised by the signature of large missing transverse momentum $E_{\mathrm{T}}^{\mathrm{miss}}$ due to the production of dark matter particles and jets due to the hadronic decay of the heavy boson, which is illustrated in Figure 8.1.

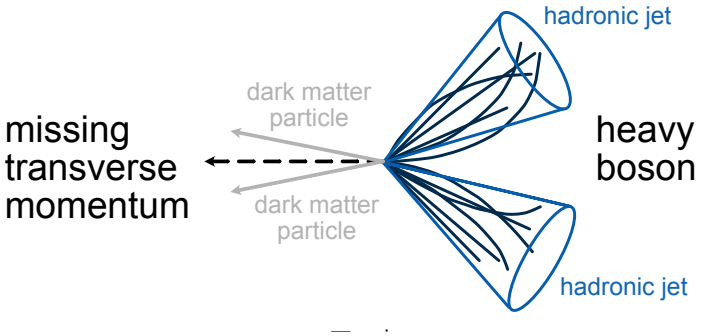
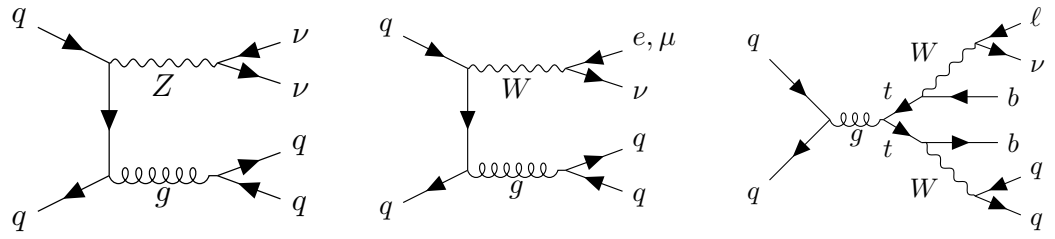



**Fig. 8.1.:** Illustration of the signature indicating dark matter particle production in association with heavy bosons in the transverse plane of the detector. The recoil of the undetected dark matter particles on the heavy boson results in missing transverse momentum. The hadronic decay of the heavy boson results in the formation of hadronic jets.

The background processes can produce the same signature and therefore need to be accounted for in a statistical model. A common irreducible background process is the production of Z bosons in association with jets, referred to as Z + jets, in which $E_{\mathrm{T}}^{\mathrm{miss}}$ arises from the $\mathrm{Z} \to \nu\nu$ decay and non-resonantly produced jets coincidentally resemble a heavy boson candidate.

Another background process is the production of W bosons in association with jets, referred to as W+jets, which have intrinsic $E_{\mathrm{T}}^{\mathrm{miss}}$ due to the $\mathrm{W} \to \ell\nu$ decay and can pass the signal region selection because of inefficiencies in the lepton reconstruction. Together, the Z + jets and W+ jets background processes are referred to as $V$ + jets.

Similarly, top quark pair production, referred to as $\mathrm{t\bar{t}}$, can pass the signal region selection if the leptons in the semi-leptonic top quark decays are missed by the reconstruction. The $\mathrm{t\bar{t}}$ background is particularly relevant for searches targeting final states with $b$-jets. These background processes are illustrated by the exemplary Feynman graphs in Figure 8.2.




(a) Z + jets (b) W + jets (c) $\mathrm{t\bar{t}}$ production

**Fig. 8.2.:** Example Feynman graphs for the dominant background processes in searches for dark matter with heavy bosons.

Other background processes include WW, WZ, and ZZ diboson production and production of single top quarks.

Finally, processes of pure strong interactions (referred to as multijet events) with poorly measured jet momenta give rise to fake $E_{\mathrm{T}}^{\mathrm{miss}}$ and therefore can contribute as background. Although poor measurements of the jet momenta such that the fake $E_{\mathrm{T}}^{\mathrm{miss}}$ is sufficient to pass the selection requirements occur infrequently, the overwhelming amount of multijet events at the LHC makes it necessary to adequately estimate this background.

The reconstructed pp collision events need to be categorised as either signal events or background events. To this end, the characteristic properties of the signal process are exploited to define discriminating variables, which can be used to separate signal and background events.

Event selection requirements based on the kinematic properties of reconstructed compound physics objects and on the event topology define a region enriched in signal processes, which is called the signal region (SR) and is characterised by a good sensitivity to the signal process.

The background contribution in the SR is estimated with samples of simulated events. As the simulation is subject to uncertainties, it is supplemented by data in dedicated control regions (CRs), which cover a similar phase-space as the SR but are enriched in the respective background processes. The SR and the CRs are defined by event selections which require different lepton multiplicities and therefore are disjoint. The sharing of the background contributions among events with different

lepton multiplicities depends on the W and Z boson branching ratios and the lepton reconstruction efficiencies, which are both well understood. Therefore, the control region data enable reliable constraints of the background contributions in the SR, avoiding the sole reliance on theory predictions.

Figure 8.3 illustrates the definition of SR and CRs in the searches for dark matter with heavy bosons. The 1 lepton CR allows constraining the W + jets and $t\bar{t}$ processes in the SR, while the 2 lepton CR allows constraining the Z + jets background in the SR using $Z \to \ell\ell$ events.

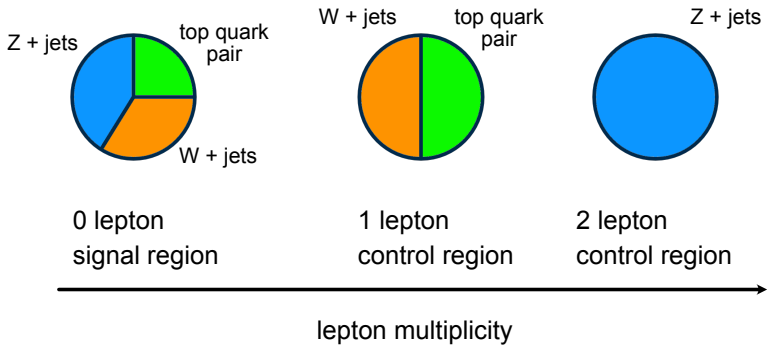



**Fig. 8.3.:** Illustration of the signal and control region definitions based on the lepton multiplicity. The control regions are enriched in specific background processes which populate the signal region and thereby allow for the estimation of these background contributions in the SR using data.

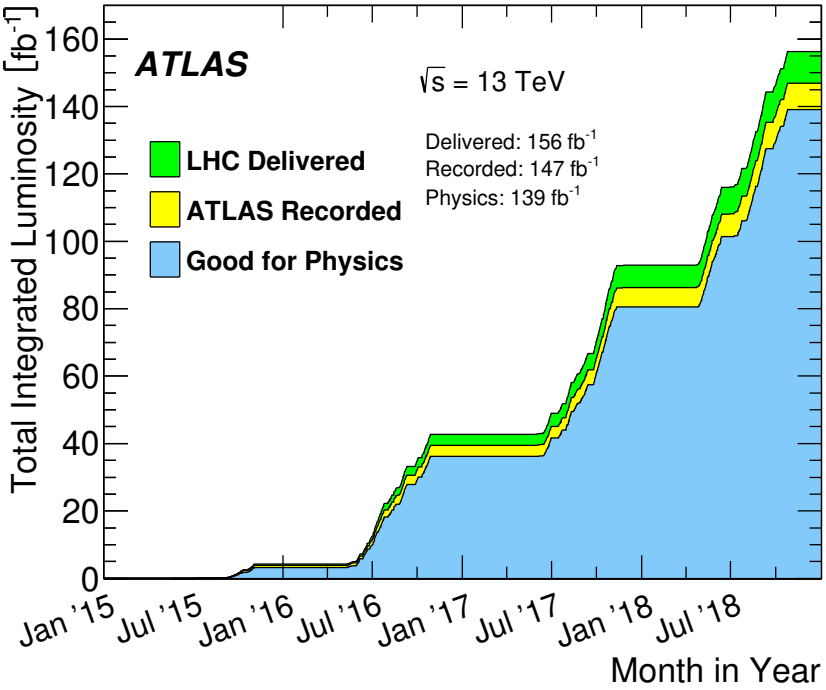
## 8.2 Data and simulated events

The pp collision data and the simulated physics processes are described in Section 8.2.1 and Section 8.2.2, respectively. The triggers used to select collision events are summarised in Section 8.2.3.

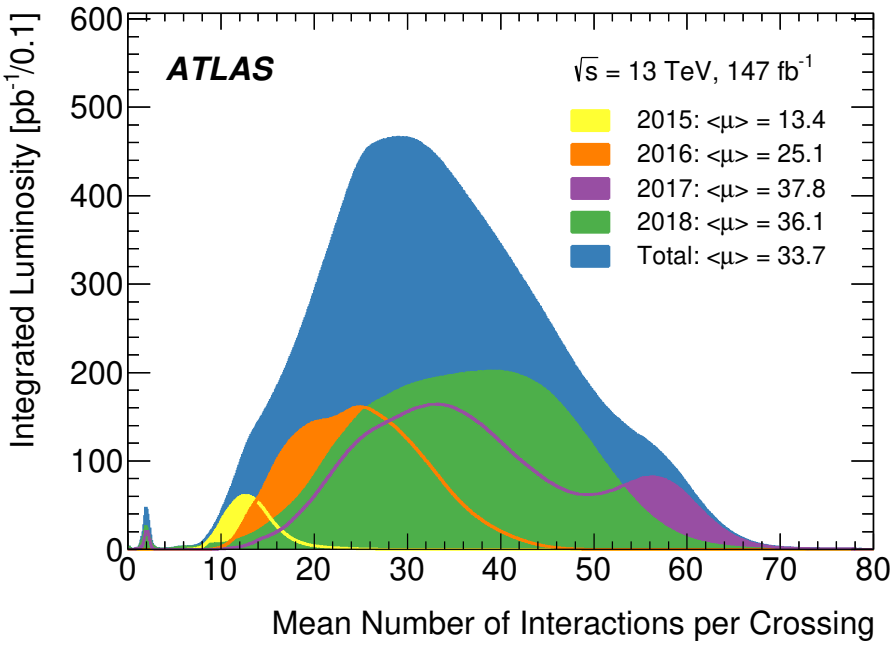
### 8.2.1 Collision data

The searches for dark matter in association with heavy bosons are based on the LHC pp collision data recorded by the ATLAS detector in the years 2015–2018. Only collision events recorded during stable beam conditions with all detector subsystems fully operational are used for the physics analysis.

Figure 8.4 demonstrates the ATLAS data-taking performance during the Run-2 data-taking campaign, showing the total integrated luminosity and the mean number of interactions per bunch crossing.




(a) Total integrated luminosity delivered by the LHC and recorded by the ATLAS detector during the Run-2 pp data-taking campaign. The fraction of the dataset satisfying the data quality requirements for physics analysis is indicated as "Good for physics".




(b) Luminosity-weighted distribution of the mean number of interactions per bunch crossing for 2015, 2016, 2017, and 2018 pp collision data.

Fig. 8.4.: ATLAS data-taking performance during the Run-2 pp data-taking campaign. Figures reproduced from Ref. [36].

In 2015, data with an integrated luminosity of $3.2\,\text{fb}^{-1}$ was recorded with a data-taking efficiency of $93\,\%$, while in 2016 data corresponding to $32.9\,\text{fb}^{-1}$ was recorded with a data-taking efficiency of $92\,\%$, resulting in a total integrated luminosity of $36.1\,\text{fb}^{-1}$. The average number of interactions per bunch crossing $\langle\mu\rangle$ was $13.7$ during 2015 data-taking and $24.9$ during 2016 data-taking.

The dataset recorded in 2017 with a data-taking efficiency of $94\,\%$ corresponds to an integrated luminosity of $43.8\,\text{fb}^{-1}$. The average number of interactions per bunch crossing $\langle\mu\rangle$ was $37.8$ during 2017 data-taking. The 2015–2017 dataset corresponds to an integrated luminosity of $79.8\,\text{fb}^{-1}$

In 2018, data with an integrated luminosity of $59.2\,\text{fb}^{-1}$ was recorded with a data-taking efficiency of $93\,\%$. The average number of interactions per bunch crossing $\langle\mu\rangle$ was $37.8$ during 2018 data-taking. The full Run-2 dataset recorded during the years 2015–2018 corresponds to an integrated luminosity of $59.2\,\text{fb}^{-1}$.

### 8.2.2 Simulated event samples

The signal and background contributions are estimated with Monte Carlo (MC) simulated event samples. The simulated events are produced by MC event generators. The interactions of the generated particles with the detector are modelled with the GEANT 4 [14] based ATLAS detector simulation [104]. The simulated collision events are reconstructed with the same trigger and reconstruction algorithms that are employed in collision data.

The simulated signal and background samples include the effect of in-time and out-of-time pile-up. This is achieved by overlaying inelastic pp collision events simulated using PYTHIA 8, the A3 tune [105], and the NNPDF23LO PDF set [118]. Simulated events are corrected using per-event weights to match the distribution of the number of interactions per bunch crossing as observed in data.

The $V$ + jets backgrounds are simulated with the SHERPA 2.2.1 event generator [138], with matrix elements computed at NLO accuracy in QCD for up to two final-state partons and LO accuracy in QCD for up to four final-state partons using Comix [231] and OpenLoops [157] with the NNPDF30NNLO PDF set [119]. The matrix elements are merged with the Sherpa parton shower [315] using the ME+PS@NLO prescription [249]. The simulated events are normalised to an inclusive cross section with NNLO precision in QCD [286]. Details of the generator configurations can be found in Ref. [38].

Two sets of simulated samples for the top quark pair production and single top quark production backgrounds are available. The top quark mass was set to $172.5\,\text{GeV}$ in the event simulation. In the first set, the simulation of top quark pair production involves matrix elements computed at NLO accuracy in QCD with POWHEG-BOX 2 [21] and the CT10 PDF set [270]. The simulation of single top quark backgrounds in the $s$-channel and $t$-channels as well as the W$t$ associated production are computed with POWHEG-BOX 1 [21] using the fixed four-flavour PDF set CT10F4 [270]. In all top-quark decays, the spin correlations were preserved using MadSpin [33]. The parton

shower and hadronisation is simulated using PYTHIA 6.428 [321], the CTEQ6L1 PDF set [305] and the corresponding Perugia 2012 set [322] of tuned parameters. The properties of b and c quark decays are described with EVTGEN 1.2.0 [272]. In the second set, the simulation of both top quark pair production and single top quark production processes involves matrix elements computed accurately to NLO QCD with POWHEG-BOX 2 [21] using the NNPDF30NLO PDF set [119], interfaced to the PYTHIA 8.230 parton shower and hadronisation model [320] using the A14 set of tuned parameters [37]. The simulated events are normalised to a NNLO QCD prediction for top quark pair production, including next-to-next-to-leading logarithmic corrections (NLL) for soft gluon radiation [201], and to NLO QCD predictions for single top quark processes [329, 328, 323, 263]. Details on the configurations of both sets can be found in Ref. [50].

Two sets of simulated samples for diboson processes are available, in which the diboson backgrounds are simulated with SHERPA. In the first set, the diboson production backgrounds with one weak gauge boson decaying leptonically and the other one decaying hadronically, are simulated with the SHERPA 2.1.1 event generator [138]. The matrix elements of the ZZ process were calculated in NLO QCD accuracy for final states with at most one jet and in LO QCD accuracy for final states with two or three jets, whereas those for WZ and WW processes were generated in LO QCD for final states with up to three jets. In both cases, Comix [231] and OpenLoops [157] were used in conjunction with the CT10 PDF set [270] and a dedicated tune provided by the Sherpa authors. In the second set, all diboson background processes are simulated with the SHERPA 2.2.1 event generator [138]. The matrix elements of the process were calculated accurately to NLO QCD for final states with at most one jet and accurate to LO QCD for final states with two or three jets. The NNPDF30NLO PDF set [119] and a dedicated tune provided by the Sherpa authors were used. Details of the generator configurations can be found in Ref. [62].

Background processes from associated $Vh, h \to b\bar{b}$ production were generated with POWHEG-BOX 2 interfaced to PYTHIA 8 using the NNPDF30NLO PDFs [119] and the AZNLO tune [58]. Both the quark-induced WH and ZH production, as well as the gluon-induced ZH production are considered. The event samples are normalised to the best available theoretical predictions at NNLO accuracy in QCD and NLO accuracy in electroweak corrections [159].

Multijet background processes are typically estimated using data-driven methods, as their MC simulation is computationally costly. However, for the development and optimisation of these background estimation methods, a MC simulated sample is used. This sample is generated using the PYTHIA 8.230 event generator [138], incorporating LO matrix elements and a model describing parton shower and hadronisation, both computed using the NNPDF23LO PDF set [118]. The A14 set of tuned parameters [37] is used.

A summary of all simulated background samples is provided in Table 8.1.

**Tab. 8.1.:** List of the simulated background processes in searches for dark matter with heavy vector bosons with the event generators, PDF sets, parton shower models, set of tuned parameters ("tunes"), and the accuracy in QCD of the modelling and the cross-section.

| Process | Generator | Parton shower | PDF | Tune | Accuracy in QCD (modelling / inclusive cross-section) |
|---|---|---|---|---|---|
| ***V* + jets** | | | | | |
| W + jets | SHERPA 2.2.1 | SHERPA 2.2.1 | NNPDF30NNLO | SHERPA-tune | NLO/ NNLO |
| Z + jets | SHERPA 2.2.1 | SHERPA 2.2.1 | NNPDF30NNLO | SHERPA-tune | NLO/ NNLO |
| **Top quark** | | | | | |
| $t\bar{t}$ | POWHEG-BOX 2 | PYTHIA 6.428 | CT10 | Perugia 2012 | NLO/ NNLO + NLL |
| | POWHEG-BOX 2 | PYTHIA 8.230 | NNPDF30NLO | A14 | NLO/ NNLO + NLL |
| t ($s$-channel) | POWHEG-BOX 1 | PYTHIA 6.428 | CT10 | Perugia 2012 | NLO/ NLO |
| | POWHEG-BOX 2 | PYTHIA 8.230 | NNPDF30NLO | A14 | NLO/ NLO |
| t ($t$-channel) | POWHEG-BOX 1 | PYTHIA 6.428 | CT10 | Perugia 2012 | NLO/ NLO |
| | POWHEG-BOX 2 | PYTHIA 8.230 | NNPDF30NLO | A14 | NLO/ NLO |
| t (W$t$) | POWHEG-BOX 1 | PYTHIA 6.428 | CT10 | Perugia 2012 | NLO/ NLO |
| | POWHEG-BOX 2 | PYTHIA 8.230 | NNPDF30NLO | A14 | NLO/ NLO |
| **Diboson** | | | | | |
| WW | SHERPA 2.1.1 | SHERPA 2.1.1 | CT10 | SHERPA-tune | NLO/ NLO |
| | SHERPA 2.2.1 | SHERPA 2.2.1 | NNPDF30NLO | SHERPA-tune | NLO/ NLO |
| WZ | SHERPA 2.1.1 | SHERPA 2.1.1 | CT10 | SHERPA-tune | NLO/ NLO |
| | SHERPA 2.2.1 | SHERPA 2.2.1 | NNPDF30NLO | SHERPA-tune | NLO/ NLO |
| ZZ | SHERPA 2.1.1 | SHERPA 2.1.1 | CT10 | SHERPA-tune | NLO/ NLO |
| | SHERPA 2.2.1 | SHERPA 2.2.1 | NNPDF30NLO | SHERPA-tune | NLO/ NLO |
| $Vh, h \to b\bar{b}$ | POWHEG-BOX 2 | PYTHIA 8.212 | NNPDF30NLO | AZNLO | NLO/ NNLO |
| Multijet | PYTHIA 8.230 | PYTHIA 8.230 | NNPDF23LO | A14 | LO/ LO |

### 8.2.3 Triggers

The events are selected by a combination of trigger algorithms, which are based on the two-staged trigger system comprised by the L1 trigger and the HLT (c.f. Section 5.3.6). Two types of trigger algorithms are employed in the searches for dark matter with heavy bosons.

- $E_{\mathrm{T}}^{\mathrm{miss}}$ triggers are used to select events for the 0 lepton SR and for the 1 muon CR.
- Single lepton (e/ $\mu$) triggers are used to select events for the 2 lepton CR.

The use of $E_{\mathrm{T}}^{\mathrm{miss}}$ triggers for the 1 muon CR is enabled by restricting the corresponding lepton selection to muons, as the particular computation of $E_{\mathrm{T}}^{\mathrm{miss}}$ on trigger level takes into account only information provided by the calorimeters. Muons traversing the calorimeter only deposit a negligible amount of their energy, therefore they contribute to $E_{\mathrm{T}}^{\mathrm{miss}}$ on trigger level.

The instantaneous luminosity increases with data-taking periods, therefore the trigger thresholds have to be adapted accordingly. The triggers are defined by the L1 and HLT algorithms (c.f. Section 5.3.6) and corresponding thresholds, which are encoded in their names. For instance, the HLT_XE90_MHT_L1XE50 trigger requires the L1 $E_{\mathrm{T}}^{\mathrm{miss}}$ to exceed $50\,\mathrm{GeV}$ and the $E_{\mathrm{T}}^{\mathrm{miss}}$ reconstructed by the HLT algorithm to exceed $90\,\mathrm{GeV}$. Similarly, the HLT_MU50 trigger requires that an HLT algorithm detects a muon with $p_{\mathrm{T}} > 50\,\mathrm{GeV}$.

The $E_{\mathrm{T}}^{\mathrm{miss}}$ triggers are based different algorithms [75]. The $E_{\mathrm{T}}^{\mathrm{miss}}$ trigger used in 2015 data-taking is based on an the CELL algorithm, which calculates $E_{\mathrm{T}}^{\mathrm{miss}}$ on trigger level using towers of calorimeter cells. The MHT algorithm employed in 2016 data-taking calculates the $E_{\mathrm{T}}^{\mathrm{miss}}$ on trigger level as the negative $p_{\mathrm{T}}$ vector sum of all jets with $p_{\mathrm{T}} > 7\,\mathrm{GeV}$ before JES calibration, which were reconstructed using the anti-$k_t$ algorithm with radius parameter $R = 0.4$ from calorimeter topological clusters. The PUFIT algorithm employed in 2017–2018 data-taking calculates the $E_{\mathrm{T}}^{\mathrm{miss}}$ from $\eta$-$\varphi$ patches that correspond approximately the size of jets with radius parameter $R = 0.4$, which are created from calorimeter topological clusters and are corrected for pile-up contributions by a $\chi^2$-fit. The $E_{\mathrm{T}}^{\mathrm{miss}}$ trigger thresholds range from $70\,\mathrm{GeV}$ to $110\,\mathrm{GeV}$ during the 2015–2018 data-taking periods.

The single-lepton triggers impose requirements on electrons and muons identified by the L1 and HLT algorithms. The L1 requirement on the electron $E_{\mathrm{T}}$ or muon $p_{\mathrm{T}}$ imposes a looser threshold than that of the HLT algorithms. The better resolution of the HLT algorithms allows setting tighter cuts, ranging from $24\,\mathrm{GeV}$ to $300\,\mathrm{GeV}$ for electrons and $20\,\mathrm{GeV}$ to $50\,\mathrm{GeV}$ for muons. Additional requirements on the lepton identification (LHLOOSE, LHMEDIUM, LHTIGHT), on the isolation criteria (ILOOSE, IMEDIUM), and on the transverse impact parameter (NOD0) are defined, which improve the trigger selectivity. A combination of lepton triggers with low-$p_{\mathrm{T}}$ thresholds requiring additional isolation criteria and triggers with high-$p_{\mathrm{T}}$ thresholds but no further requirements is used to preserve the trigger efficiency for high-$p_{\mathrm{T}}$ leptons.

The trigger efficiency is defined as

$$\varepsilon = \frac{N(\text{trigger}|\mathcal{S}_i)}{N(\mathcal{S}_i)}, \tag{8.1}$$

where $N(\mathcal{S}_i)$ denotes the number of events satisfying the selection $\mathcal{S}_i$ and $N(\text{trigger}|\mathcal{S}_i)$ denotes the number of events that also satisfies the trigger requirement.

The $E_{\text{T}}^{\text{miss}}$ trigger efficiency for different years of the Run-2 data-taking is shown in Figure 8.5.

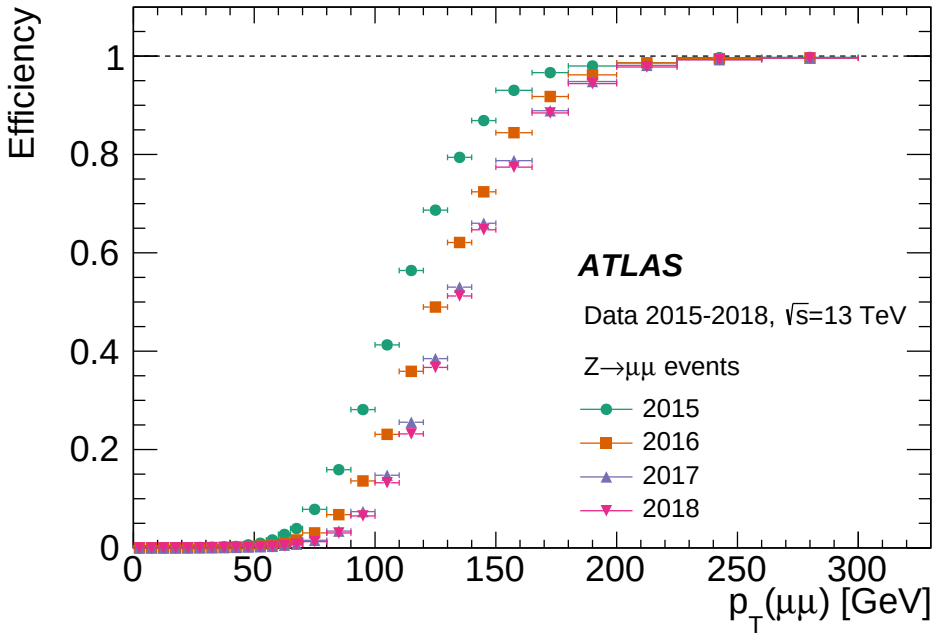



**Fig. 8.5.:** Combined L1 and HLT efficiency of the $E_{\text{T}}^{\text{miss}}$ triggers with lowest threshold used in each year of data-taking. The $E_{\text{T}}^{\text{miss}}$ trigger efficiency is measured in data using $\text{Z} \to \mu\mu$ events and is shown as a function of the Z boson transverse momentum $p_{\text{T}}^{\mu\mu}$. Figure reproduced from Ref. [75].

The reduced efficiency for $E_{\text{T}}^{\text{miss}} < 200\,\text{GeV}$ is due to the limited detector resolution, which results in differences between $E_{\text{T}}^{\text{miss}}$ reconstructed on trigger level and the offline $E_{\text{T}}^{\text{miss}}$.

In the searches for dark matter with heavy bosons, the $E_{\text{T}}^{\text{miss}}$ trigger threshold dictates the lowest possible selection requirement on $E_{\text{T}}^{\text{miss}}$. As these searches investigate events with $E_{\text{T}}^{\text{miss}} > 150\,\text{GeV}$, the trigger (in)efficiency needs to be studied in data and MC to derive corrections for potential discrepancies between simulation and data.

The $E_{\text{T}}^{\text{miss}}$ trigger calibration is performed in events passing single-muon triggers, since the calculation of $E_{\text{T}}^{\text{miss}}$ on trigger level does not involve muons. The $E_{\text{T}}^{\text{miss}}$ trigger efficiency is measured as a function of $E_{\text{T}}^{\text{miss,no}\mu}$, which is calculated by

excluding muons from the $E_{\mathrm{T}}^{\mathrm{miss}}$ reconstruction. It is parametrised in the region $120\,\mathrm{GeV} < E_{\mathrm{T}}^{\mathrm{miss,no}\mu} < 300\,\mathrm{GeV}$ by the function

$$f(E_{\mathrm{T}}^{\mathrm{miss,no}\mu}) = \frac{1}{2}\left[1 + \mathrm{Erf}\left(\frac{E_{\mathrm{T}}^{\mathrm{miss,no}\mu} - a}{\sqrt{2}b}\right)\right], \tag{8.2}$$

where $\mathrm{Erf}(x)$ denotes the error function and $a, b \in \mathbb{R}$ are free parameters in the fit.

The $E_{\mathrm{T}}^{\mathrm{miss}}$ trigger efficiency corrections for simulated events are obtained as the ratio of the $E_{\mathrm{T}}^{\mathrm{miss}}$ trigger efficiency measured in data and in simulated samples of background processes. These corrections can depend on the multiplicity of $b$-jets in the event due to the different calorimeter responses for light-flavour and heavy-flavour jets. While the nominal $E_{\mathrm{T}}^{\mathrm{miss}}$ trigger efficiency corrections are derived from a selection inclusive in the $b$-jet multiplicity, the associated systematic uncertainties are evaluated by comparing the nominal scale-factors obtained from the inclusive selection with scale-factors obtained from a selection requiring the presence of at least one $b$-tagged jet. The total uncertainty on the $E_{\mathrm{T}}^{\mathrm{miss}}$ trigger calibration additionally takes into account the $1\sigma$ confidence interval of the fit based on Equation (8.2).

A similar calibration is performed for the single lepton triggers [73, 69]. The object definitions of leptons are designed to ensure that the lepton triggers are fully efficient.

## 8.3 Object definitions in searches for dark matter produced in association with heavy bosons

The physical objects used for the event selection and the reconstruction of the kinematic properties of collision events in the searches for dark matter with heavy bosons are introduced in the following. Various object definitions with different requirements on kinematic properties, identification and isolation criteria are employed to accommodate the competing needs concerning purity and reconstruction efficiency.

Three types of jets are considered in the physics object definitions and in the definition of selection criteria to enhance the sensitivity of the searches. The small-radius jets and large-radius jets are used for reconstructing the hadronic decays of heavy bosons, while the track jets supplement the large-radius jets with $b$-tagging information.

The **small-radius jets** are divided into two categories based on their pseudorapidity. The jets with $|\eta| < 2.5$ are referred to as central jets. Jets originating from pile-up are suppressed by requiring the central jets with $p_{\mathrm{T}} < 60\,\mathrm{GeV}$ and $|\eta| < 2.4$ to be associated with the primary vertex. Therefore, these jets are required to pass the Jet Vertex Tagger (JVT) requirements with a JVT score of JVT $> 0.59$. Residual differences in the JVT score evaluation between data and simulation are taken into account by applying scale-factors to the weight of MC simulated events. The central

jets originating from $b$-quarks are referred to as $b$-jets. They are identified using the MV2 $b$-tagging algorithm with fixed-cut efficiency operating points corresponding to 70 % and 77 % $b$-tagging efficiency. The small-radius jets with $2.5 < |\eta| < 4.5$ and $p_{\mathrm{T}} > 30\,\mathrm{GeV}$ are referred to as forward jets. They are used only in selection requirements to suppress background processes. In particular, the requirements to reject multijet background events with fake $E_{\mathrm{T}}^{\mathrm{miss}}$ use the information provided by these jets. The common definitions of small-radius jets are summarised in Table 8.2.

**Tab. 8.2.:** Common definitions of small-radius jets.

| | Central jets | $b$-jets | Forward jets |
|---|---|---|---|
| Jet algorithm | anti-$k_t$ | anti-$k_t$ | anti-$k_t$ |
| $R$-parameter | 0.4 | 0.4 | 0.4 |
| Input constituents | EMTopo | EMTopo | EMTopo |
| Pseudorapidity range | $\|\eta\| < 2.5$ | $\|\eta\| < 2.5$ | $2.5 < \|\eta\| < 4.5$ |
| Transverse momentum | $p_{\mathrm{T}} > 20\,\mathrm{GeV}$ | $p_{\mathrm{T}} > 20\,\mathrm{GeV}$ | $p_{\mathrm{T}} > 30\,\mathrm{GeV}$ |
| JVT | $> 0.59$ for $p_{\mathrm{T}} < 60\,\mathrm{GeV}$, $\|\eta\| < 2.4$ | | no |
| $b$-tagging | no | MV2 (70 % / 77 % efficiency) | no |

The **large-radius jets** are used to identify weak vector bosons with large Lorentz boost. The trimming algorithm (c.f. Section 6.1.5) is applied to remove energy deposits from pile-up with radius parameter $R_{\mathrm{sub}} = 0.2$ and momentum fraction $f_{\mathrm{cut}} = 0.05$. The requirements on the kinematic properties $p_{\mathrm{T}} > 100\,\mathrm{GeV}$ and $|\eta| < 2.0$ ensure the reconstruction of high-$p_{\mathrm{T}}$ jets in the central region of the detector with good overlap between the ID and the calorimeters.

The **track jets** are used to identify the flavour content of the large-radius jets. In the scope of this dissertation, both track jet definitions with a fixed radius parameter $R = 0.2$ (FR) and a variable radius parameter (VR) are considered. Both FR and VR track jets are required to satisfy $p_{\mathrm{T}} > 10\,\mathrm{GeV}$, $|\eta| < 2.5$, and are required to have at least two constituent tracks. The VR track jets must satisfy an additional requirement on the separation of individual VR track jets $\Delta R > 0.02$ to rejects events with concentric pairs of VR track jets, which are problematic for a stable $b$-tagging performance. The $b$-tagged track jets are identified using the MV2 $b$-tagging algorithm with fixed-cut efficiency of either 70 % or 77 % $b$-tagging efficiency. The $b$-tagging performance of track jets in simulations is corrected to that in data by a calibration based on a combinatorial likelihood approach in a sample of $\mathrm{t\bar{t}}$ events [61]. The common definitions of large-radius jets and track jets are summarised in Table 8.3.

Two types of **electron** definitions are considered. Baseline electron candidates are used to define vetoes on electrons in the event selection. They are reconstructed using the LOOSE ID OP in conjunction with the LOOSETRACKONLY isolation OP and have to satisfy the kinematic requirements $p_{\mathrm{T}} > 7\,\mathrm{GeV}$ and $|\eta| < 2.47$. Signal electron candidates are used to select pairs of electrons. They are required to satisfy stricter requirements on their transverse energy. In searches considering 2015–2016 data, $E_{\mathrm{T}} > 25\,\mathrm{GeV}$ is required, while the increased single electron trigger

Tab. 8.3.: Common definitions of jets used for boosted heavy boson reconstruction

| | Large-radius jets | VR track jets | FR track jets |
|---|---|---|---|
| Jet algorithm | anti-$k_t$ | anti-$k_t$ | anti-$k_t$ |
| $R$-parameter | 1.0 | $R_{\text{eff}}$ | 0.2 |
| Grooming algorithm | trimming | no | no |
| $R_{\text{sub}}$ | 0.2 | no | no |
| $f_{cut}$ | 0.05 | no | no |
| Input constituents | LCTopo | tracks | tracks |
| Pseudorapidity range | $\|\eta\| < 2.0$ | $\|\eta\| < 2.5$ | $\|\eta\| < 2.5$ |
| Transverse momentum | $p_{\text{T}} > 100\,\text{GeV}$ | $p_{\text{T}} > 10\,\text{GeV}$ | $p_{\text{T}} > 10\,\text{GeV}$ |
| $b$-tagging | no | MV2 (77 % efficiency) | MV2 (70 % / 77 % efficiency) |

thresholds in 2017–2018 necessitate signal electron candidates with $E_{\text{T}} > 27\,\text{GeV}$ in order to ensure the full efficiency of the employed single electron trigger. Both baseline and signal electron candidates have to satisfy requirements on the impact parameters $|d_0|/\sigma(d_0) < 5$ and $|z_0|\sin\theta < 0.5\,\text{mm}$. The definitions of baseline and signal electron candidates are summarised in Table 8.4.

Tab. 8.4.: Common definitions of electron candidates.

| | Baseline | Signal |
|---|---|---|
| Pseudorapidity range | $\|\eta\| < 2.47$ | $\|\eta\| < 2.47$ |
| Transverse energy | $E_{\text{T}} > 7\,\text{GeV}$ | $E_{\text{T}} > 25\,\text{GeV}/27\,\text{GeV}$ |
| Identification | Loose | Medium |
| Isolation | LooseTrackOnly | LooseTrackOnly |
| Track to vertex association | $\|d_0\|/\sigma(d_0) < 5$<br>$\|z_0\|\sin\theta < 0.5\,\text{mm}$ | $\|d_0\|/\sigma(d_0) < 5$<br>$\|z_0\|\sin\theta < 0.5\,\text{mm}$ |

Three types of **muon** definitions are considered. Baseline muon candidates are used to define the vetoes on muons in the event selection. They are reconstructed using the LOOSE ID OP in conjunction with the LOOSETRACKONLY isolation OP and have to satisfy the kinematic requirements $p_{\text{T}} > 7\,\text{GeV}$ and $|\eta| < 2.7$. Signal muon candidates are used to select pairs of muons. They are required to satisfy stricter kinematic requirements $p_{\text{T}} > 25\,\text{GeV}$ and $|\eta| < 2.5$. Tight signal muon candidates are used to select individual muons. They are reconstructed using the MEDIUM ID OP in conjunction with the TIGHTTRACKONLY isolation OP and otherwise satisfy the signal muon candidate kinematic requirements. Baseline, signal, and tight signal muon candidates have to satisfy requirements on the impact parameters $|d_0|/\sigma(d_0) < 3$ and $|z_0|\sin\theta < 0.5\,\text{mm}$. The definitions of baseline, signal, and tight signal muons are summarised in Table 8.5.

Hadronically decaying **tau leptons** are identified using small-radius jets. Baseline tau lepton candidates can be used to veto events containing tau leptons, as the signature targeted by the searches with heavy bosons does not include these. Baseline tau lepton candidates are required to satisfy $p_{\text{T}} > 20\,\text{GeV}$ and $|\eta| < 2.5$, excluding the region $1.37 < |\eta| < 1.52$ because of a gap in the instrumentation of the calorimeters. The topology of tau decays is exploited to avoid the misidentification of jets, electrons,

Tab. 8.5.: Common definitions of muon candidates.

| | Baseline | Signal | Tight signal |
|---|---|---|---|
| Pseudorapidity range | $\lvert\eta\rvert < 2.7$ | $\lvert\eta\rvert < 2.5$ | $\lvert\eta\rvert < 2.5$ |
| Transverse momentum | $p_{\mathrm{T}} > 7\,\mathrm{GeV}$ | $p_{\mathrm{T}} > 25\,\mathrm{GeV}$ | $p_{\mathrm{T}} > 25\,\mathrm{GeV}$ |
| Identification | Loose | Loose | Medium |
| Isolation | LooseTrackOnly | LooseTrackOnly | TightTrackOnly |
| Track to vertex association | $\lvert d_0\rvert/\sigma(d_0) < 3$<br>$\lvert z_0\rvert \sin\theta < 0.5\,\mathrm{mm}$ | $\lvert d_0\rvert/\sigma(d_0) < 3$<br>$\lvert z_0\rvert \sin\theta < 0.5\,\mathrm{mm}$ | $\lvert d_0\rvert/\sigma(d_0) < 3$<br>$\lvert z_0\rvert \sin\theta < 0.5\,\mathrm{mm}$ |

or muons as tau leptons, by using a set of Boosted Decision Trees (BDTs) to classify the tracks associated with the jet and requiring the presence of either one or three core tracks. The object definition for baseline tau lepton candidates is summarised in Table 8.6.

Tab. 8.6.: Common definition of tau lepton candidates.

| | Baseline |
|---|---|
| Pseudorapidity range | $\lvert\eta\rvert < 2.5$, excluding $1.37 < \lvert\eta\rvert < 1.52$ |
| Transverse momentum | $p_{\mathrm{T}} > 20\,\mathrm{GeV}$ |
| Track selection | 1 or 3 tracks |

# 9 Search for dark matter produced in association with a hadronically decaying weak vector boson

## 9.1 Introduction

This chapter describes the search for dark matter in association with a hadronically decaying weak vector boson $V$, referred to as $E_{\mathrm{T}}^{\mathrm{miss}} + V(q\bar{q})$. The signature of the signal process is missing transverse momentum originating from the dark matter particle pair production and the resonant production of jets from the $V \to qq$ decay.

Searches for dark matter in the $E_{\mathrm{T}}^{\mathrm{miss}} + V(q\bar{q})$ final state have been carried out by the ATLAS collaboration using $20.3\,\mathrm{fb}^{-1}$ pp collision data collected at a centre-of-mass energy $\sqrt{s} = 8\,\mathrm{TeV}$ [87] and using $3.2\,\mathrm{fb}^{-1}$ pp collision data collected at a centre-of-mass energy $\sqrt{s} = 13\,\mathrm{TeV}$ [90]. Similar searches have been carried out also by the CMS collaboration [166, 172].

This search is based on proton-proton collision data at a centre-of-mass energy of $13\,\mathrm{TeV}$ recorded in the years 2015 and 2016 with the ATLAS detector at the LHC, corresponding to the integrated luminosity of $36.1\,\mathrm{fb}$.

Improvements in the detector performance and event reconstruction, as well as the more extensive data sample, result in an enhanced sensitivity concerning previous results. The results of this search have been published in Ref. [88].

Section 9.2 introduces the signal and background processes in the $E_{\mathrm{T}}^{\mathrm{miss}} + V(q\bar{q})$ search. The analysis strategy is briefly outlined in Section 9.3. The object and event selection, including the definition of the signal and validation regions, is described in Section 9.4, whereas the background estimation strategy and the definitions of control regions are described in Section 9.5. The systematic uncertainties taken into account in the statistical model are described in Section 9.6, while the statistical model itself is provided in Section 9.7. Finally, the observed results are presented and discussed in Section 9.8. A conclusion is given in Section 9.9.

## 9.2 Signal and background processes

Two signal models are considered for the interpretation of the results. The analysis was optimised based on a simplified model with a vector Z′ mediator, which is described in Section 9.2.1. The obtained results are also interpreted in the context of the $a$-2HDM simplified model, which is described in Section 9.2.2. The background processes are described in Section 9.2.3. The simulated signal and background samples are summarised in Section 9.2.4.

### 9.2.1 Simplified model for dark matter production with a spin-1 Z′ mediator

In the $V/A$ mediator simplified model for dark matter production (c.f. Section 3.7.1, the dark matter particles are produced via s-channel exchange of a Z′ boson, which can have either vector or axial-vector couplings. The weak vector boson is produced in initial-state-radiation. The signal process is illustrated in Figure 9.1.

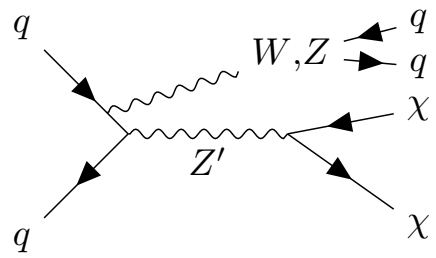



Fig. 9.1.: Dark matter particle ($\chi$) pair production in association with a W or Z boson in the simplified model with a vector or an axial-vector Z′ boson mediator.

The interaction Lagrangian is given in Equation (3.27). The model contains six free parameters, which are summarised in Table 9.1. The chosen values for the parameters $g_q$, $g_\ell$, and $g_\chi$ follow the recommendations of the LHC dark matter working group (LHC DM WG) [19]. The choice of $g_q$ and $g_\chi$ was initially motivated by constraints from dijet searches and from the $E_{\mathrm{T}}^{\mathrm{miss}}$ + jet search, which is the most sensitive final state among all $E_{\mathrm{T}}^{\mathrm{miss}} + X$ searches. The mediator coupling to leptons $g_\ell$ is set to zero to evade the stringent dilepton constraints [96]. The mediator decay width is assumed to be minimal, allowing only the decays of the Z′ boson to dark matter or quarks, and consequentially it is fully determined by the other parameters in the model. Variations in the coupling strengths only modify the production cross-section and do not affect the kinematic distribution of signal processes for heavy mediators with sufficiently narrow width [7]. Therefore, the results of the search are interpreted for a scan over the $m_\chi$-$m_{\mathrm{Z}'}$ plane for fixed choices of the coupling values.

For a fixed mediator mass $m_{\mathrm{Z}'}$, the dark matter mass defines three regimes:

1. **on-shell**: when $2m_\chi < m_{Z'}$, the mediator is on-shell. The kinematic distributions do not strongly depend on $m_\chi$, as the hardness of the ISR process is determined mostly by $m_{Z'}$. Consequentially, the results for signal model samples with same $m_{Z'}$ and different $m_\chi$ can be re-scaled, reducing the required set of generated samples to a fine scan in the $m_{Z'}$ axis (see below). The cross-section decreases as $m_\chi$ approaches the diagonal defined by $2m_\chi = m_{Z'}$.

2. **threshold**: when $m_\chi \approx m_{Z'}/2$, the production is resonantly enhanced, resulting in a much stronger dependence of the cross-section and kinematic distributions on the two masses. A scan with fine granularity is required in this regime.

3. **off-shell**: when $m_\chi$ is larger than $m_{Z'}$, the dark matter particles are produced by an off-shell mediator, associated with strong suppression of ISR. The $E_T^{miss} + X$ searches are not sensitive in this regime.

The grid of generated signal samples is based on recommendations by the LHC DM WG [7]. It is shown in Figure 9.2. Most of the 28 generated signal model samples belong to the on-shell regime, as it is the most sensitive region in parameter space.

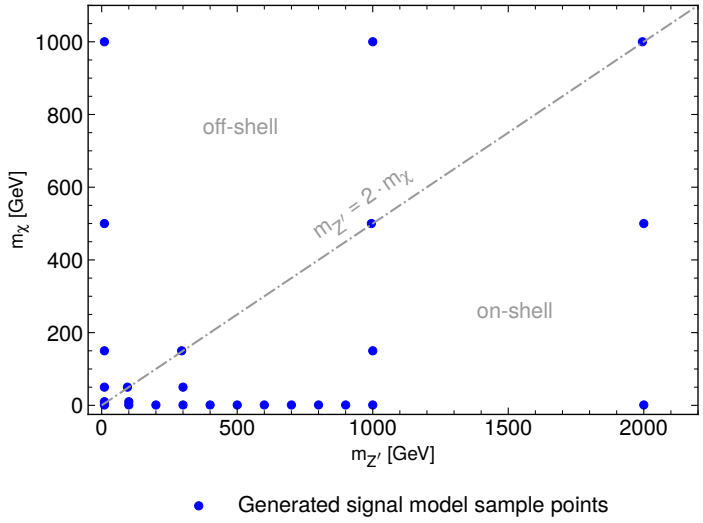



**Fig. 9.2.:** Grid of generated signal model samples in the Z′ vector mediator simplified model for different configurations of $m_{Z'}$ and $m_\chi$.

The coverage of the on-shell region in the $m_{Z'}$-$m_\chi$ parameter space is extended by an interpolation procedure. The expected number of signal events

$$S = L \times (\mathcal{A} \times \varepsilon) \times \sigma_{pp \to Z' \to \chi\overline{\chi}} \tag{9.1}$$

for a sample with $m_{Z'}$ and $m_\chi$ depends on the total integrated luminosity $L$, the product of detector acceptance and selection efficiency $\mathcal{A} \times \varepsilon$, and the cross section for the process $pp \to Z' \to \chi\overline{\chi}$.

Assuming that $\mathcal{A} \times \varepsilon$ is constant for signal processes with the same $m_{Z'}$ but different $m_\chi$, it is possible to estimate the number of signal events for other signal points using the simulated samples with $m_\chi = 1\,\text{GeV}$ as the baseline.

Assuming the narrow width approximation that the mediator is always produced at its pole as an asymptotic final state so that its decay is an independent process, the cross-section $\sigma_{pp\to Z'\to\chi\overline{\chi}}$ can be factorised as

$$\sigma_{pp\to Z'\to\chi\overline{\chi}}(m_{Z'}, m_\chi) = \sigma_{pp\to Z'}(m_{Z'}) \times \mathcal{B}_{Z'\to\chi\overline{\chi}}(m_\chi), \tag{9.2}$$

where the cross-section $\sigma_{pp\to Z'}$ only depends on $m_{Z'}$ and the branching fraction $\mathcal{B}_{Z'\to\chi\overline{\chi}}$ only depends on $m_\chi$.

Thus, the limits on the signal strength $\mu$ can be re-scaled using the branching fraction

$$\mathcal{B}_{Z'\to\chi\overline{\chi}} = \frac{\Gamma^V_{\chi\chi}}{\Gamma^V_{\chi\chi} + \Gamma^V_{qq}}, \tag{9.3}$$

which is defined by the two partial decay widths $\Gamma^V_{\chi\chi}$ and $\Gamma^V_{qq}$ (c.f. Section 3.7.1).

The interpolation procedure reduces the amount of required simulated signal points to those at the border of the on-shell region and those with $m_\chi = 1\,\text{GeV}$ for a given $m_{Z'}$, whereas the limit on $\mu$ for the signal points with $m_\chi$ in between is interpolated as

$$\mu(m_\chi) = \mu(m_\chi = 1\,\text{GeV}) \times \frac{\mathcal{B}_{Z'\to\chi\overline{\chi}}(m_\chi = 1\,\text{GeV})}{\mathcal{B}_{Z'\to\chi\overline{\chi}}(m_\chi)}. \tag{9.4}$$

The validity of the interpolation procedure was verified to be a reliable approximation for $2m_\chi < m_{Z'}$ by comparing the interpolation to predictions computed with MadGraph 5 [23] for selected mass points.

**Tab. 9.1.:** Parameters of the Z′ vector mediator simplified model in the $E_T^{miss} + V(q\bar{q})$ search.

| Parameter | Description | Chosen value |
|---|---|---|
| $m_{Z'}$ | Z′ mediator mass | free |
| $m_\chi$ | dark matter mass | free |
| $g_q$ | coupling of Z′ mediator to SM quarks | 0.25 |
| $g_\ell$ | coupling of Z′ mediator to SM leptons | 0 |
| $g_\chi$ | coupling of Z′ mediator to dark matter | 1 |
| $\Gamma$ | decay width Z′ mediator | minimal width |

### 9.2.2 Simplified model with an extended Higgs sector and a pseudo-scalar mediator

The $a$-2HDM (c.f. Section 3.7.2) describes dark matter production via an pseudo-scalar mediator in a 2HDM framework. Unlike the Z′ vector mediator simplified model, the $a$-2HDM predicts resonant production of Z bosons in the hard scattering process through a HZ$a$ vertex for a sufficiently heavy neutral Higgs boson H. The signal process is illustrated in Figure 9.3.

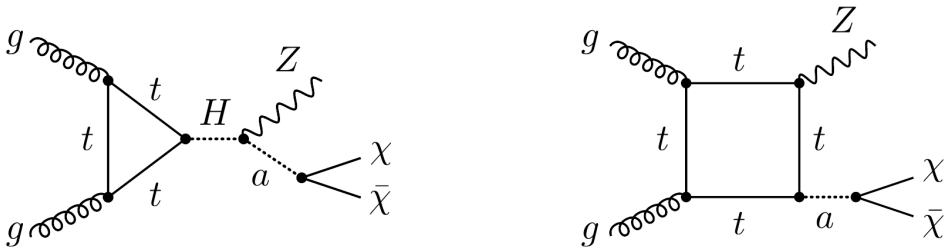



**Fig. 9.3.:** DM particle ($\chi$) pair production in association with a Z boson in the $a$-2HDM. In addition to the diagram shown on the right, another graph contributes, which includes the exchange of the pseudo-scalar $A$ instead of $a$.

The process $\mathrm{H} \to \mathrm{Z}a(\chi\overline{\chi})$ leads to the resonant production of a Z boson whose $p_\mathrm{T}$ distribution is characterised by a Jacobian peak with an endpoint at

$$p_\mathrm{T}^{\mathrm{Z,max.}} = \frac{\sqrt{(m_\mathrm{H}^2 - m_\mathrm{Z}^2 - m_a^2)^2 - 4m_\mathrm{Z}^2 m_a^2}}{2m_\mathrm{H}}. \tag{9.5}$$

The model parameters and their chosen values, following the recommendations of the LHC DM WG [6] are summarised in Table 9.2. The free parameters chosen to investigate the model are $m_a$, $m_\mathrm{A}$, $\tan\beta$, and $m_\chi$.

**Tab. 9.2.:** Parameters of the $a$-2HDM simplified model in the $E_\mathrm{T}^\mathrm{miss} + V(q\bar{q})$ search.

| Parameter | Description | Chosen value |
|---|---|---|
| $\tan\beta$ | ratio of Higgs doublet vacuum expectation values | 1.0 |
| $m_\mathrm{H} = m_\mathrm{A} = m_{\mathrm{H}^\pm}$ | masses of heavy Higgs bosons | free (600 GeV) |
| $m_\chi$ | dark matter particle mass | free (10 GeV) |
| $m_a$ | pseudo-scalar mediator mass | free |
| $m_\mathrm{h}$ | light CP-even Higgs boson mass | 125 GeV |
| $\sin\theta$ | mixing angle of neutral CP-odd weak eigenstates | free (0.35) |
| $\cos(\beta-\alpha)$ | alignment limit | 0 |
| $v/\sqrt{2}$ | electroweak vacuum expectation value | $246\,\mathrm{GeV}/\sqrt{2}$ |
| $\lambda_3 = \lambda_{P_1} = \lambda_{P_2}$ | quartic couplings of scalar bosons | 3 |
| $y_\chi$ | Yukawa coupling of dark matter particle | 1 |

Three scans in different sets of parameters are performed, following the recommendations of the LHC DM WG [6]:

1. scan in the two-dimensional $m_{\mathrm{H}}$-$m_a$ plane with $\tan\beta = 1.0$, $m_\chi = 10\,\mathrm{GeV}$, and $\sin\theta = 0.35$,
2. scan in $\sin\theta$ for two fixed choices of parameters
   a) $\tan\beta = 1.0$, $m_{\mathrm{H}} = 600\,\mathrm{GeV}$, $m_a = 200\,\mathrm{GeV}$, and $m_\chi = 10\,\mathrm{GeV}$,
   b) $\tan\beta = 1.0$, $m_{\mathrm{H}} = 1000\,\mathrm{GeV}$, $m_a = 350\,\mathrm{GeV}$, and $m_\chi = 10\,\mathrm{GeV}$.
3. scan in dark matter mass $m_\chi$ with $\tan\beta = 1.0$, $m_{\mathrm{H}} = 600\,\mathrm{GeV}$, $m_a = 250\,\mathrm{GeV}$, and $\sin\theta = 0.35$,

### 9.2.3 Background processes

The dominant background processes are Z + jets production ($46\,\%$ background contribution), W+ jets production ($38\,\%$ background contribution), and $\mathrm{t\bar{t}}$ production ($10\,\%$ background contribution).

Sub-dominant background processes include WW, WZ, and ZZ diboson production, single top quark production, and multijet events.

The dominant background processes are estimated using simulated samples, whose normalisation is constrained by control region data. The smaller background processes are estimated purely by simulation. The multijet background is estimated with a data-driven estimate.

### 9.2.4 Simulated Monte Carlo samples

The signal and background processes with the MC event generators, parton shower and hadronisation models and PDF sets used for their description are summarised in Table 9.3. Detailed descriptions of the background samples are provided in Section 8.2.2.

The signal process in the vector mediator simplified model is generated on a grid of 28 mass points defined by mediator mass $m_{\mathrm{Z}'}$ and dark matter particle mass $m_\chi$. The process is simulated at leading-order (LO) accuracy in QCD with the MadGraph5_aMC@NLO 2.2.2 event generator [23] interfaced to the Pythia 8.186 [320] parton shower and hadronisation model. The NNPDF23LO PDF set [118] is used with the A14 set of tuned parameters [37].

The signal process in the $a$-2HDM simplified model is simulated at next-to-leading-order (NLO) accuracy in QCD with the MadGraph5_aMC@NLO 2.4.3 event generator interfaced to the Pythia 8.212 parton shower and hadronisation model. The NNPDF30LO PDF set [119] is used with the A14 set of tuned parameters [37]. The generation of signal samples with $m_H < 800\,\mathrm{GeV}$ uses a fast detector simulation [106] with a parametrisation of the calorimeter response.

Tab. 9.3.: List of the signal and background processes with the MC event generators, sets of PDFs and tunes used for their description in the $E_{\mathrm{T}}^{\mathrm{miss}} + V(q\bar{q})$ search.

| Process | Generator | PDF / Parton shower tune |
|---|---|---|
| **Signal** | | |
| $V/A$ simplified model | MadGraph5_aMC@NLO 2.2.2 + Pythia 8.186 | NNPDF23LO / A14 |
| $a$-2HDM simplified model | MadGraph5_aMC@NLO 2.4.3 + Pythia 8.212 | NNPDF23LO / A14 |
| ***V*** **+ jets** | | |
| W + jets | Sherpa 2.2.1 | NNPDF30NNLO / Sherpa-tune |
| Z + jets | Sherpa 2.2.1 | NNPDF30NNLO / Sherpa-tune |
| **Top quark** | | |
| $\mathrm{t\bar{t}}$ | Powheg-Box 2 + Pythia 6.428 | CT10 / Perugia 2012 |
| t ($s$-channel) | Powheg-Box 1 + Pythia 6.428 | CT10 / Perugia 2012 |
| t ($t$-channel) | Powheg-Box 1 + Pythia 6.428 | CT10 / Perugia 2012 |
| t (W$t$) | Powheg-Box 1 + Pythia 6.428 | CT10 / Perugia 2012 |
| **Diboson** | | |
| WW | Sherpa 2.1.1 | CT10 / Sherpa-tune |
| WZ | Sherpa 2.1.1 | CT10 / Sherpa-tune |
| ZZ | Sherpa 2.1.1 | CT10 / Sherpa-tune |

## 9.3 Analysis strategy

The signature of dark matter particle production in association with a hadronically decaying weak vector boson arises from the recoil of the weak vector boson against the dark matter particle pair, resulting in substantial missing transverse momentum $E_{\mathrm{T}}^{\mathrm{miss}}$. The hadronic decay of the weak vector boson is reconstructed using either a pair of well-separated jets in events with moderate vector boson boost or as a jet with large radius-parameter in events with a highly boosted vector boson. Consequently, the signal region (SR) is defined by a merged and a resolved event selection, targeting the two event topologies. The two selections are disjoint by construction. Events satisfying both merged and resolved event selections are given preference for the merged selection. Figure 9.4 illustrates the two event topologies in the transverse plane of the detector.

The SR is defined by the invariant mass of the reconstructed weak vector boson candidate $m_V$. The merged SR is partitioned by jet substructure requirements in high-purity and low-purity selections. The multiplicity of $b$-tagged jets in the events further partitions the SR, as the tagging of heavy-flavour jets establishes sensitivity to $\mathrm{Z} \to \mathrm{b\bar{b}}$ decays in signal events and provides discrimination between the W + jets and $\mathrm{t\bar{t}}$ background processes.

The control regions (CRs) are defined by the lepton multiplicity in the event (c.f. Section 8.1), therefore they do not overlap with the SR. While the SR event selection employs a veto on electrons and muons, the CRs are defined by the presence of either one muon (1 muon CR) or two electrons or muons (2 lepton CR). The CRs are partitioned by $m_V$ in a mass window (MW) and a mass side-band (SB) selection.

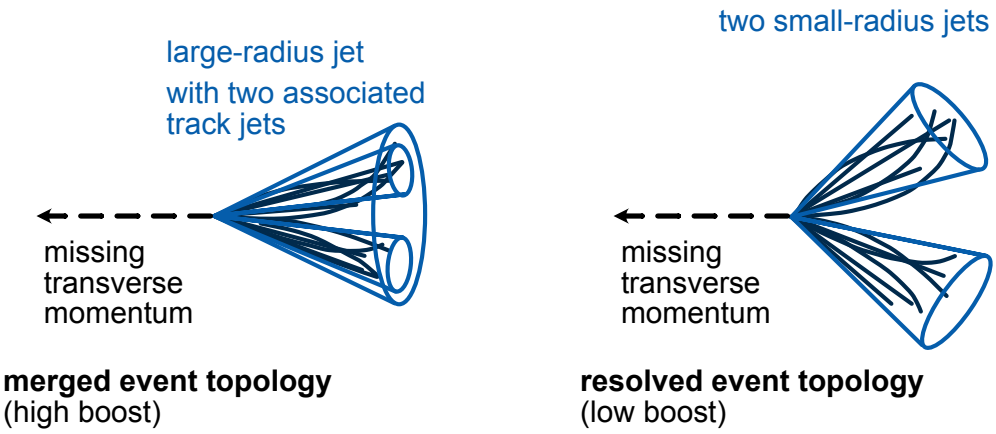



**Fig. 9.4.:** Illustrations of the merged and resolved event topologies in the $E_{\mathrm{T}}^{\mathrm{miss}} + V(q\bar{q})$ search.

The extrapolation of the CR information to the SR is verified by using a validation region (VR), which satisfies the requirements of the SR except for the mass window requirement on $m_V$. Therefore, the VR is also referred to as the mass side-band region.

The SR, CRs, and VR considered in the analysis are

- 0 lepton SR with no electrons and no muons, satisfying a W/ Z mass window requirement on the vector boson candidate, and partitioned in 8 categories with 0 / 1 / 2 $b$-tag $\times$ (high-purity and low purity merged) and resolved topologies,

- 0 lepton VR with no electrons and no muons, failing the W/ Z mass window requirement on the vector boson candidate, and partitioned in 8 categories with 0 / 1 / 2 $b$-tag $\times$ (high-purity and low purity merged) and resolved topologies,

- 1 muon CR with one muon and no electrons, partitioned in 12 categories with 0 / 1 / 2 $b$-tag $\times$ merged and resolved topologies $\times$ satisfying or failing the mass window requirement,

- 2 lepton CR with two same-flavour leptons, partitioned in 12 categories with 0 / 1 / 2 $b$-tag $\times$ merged and resolved topologies $\times$ satisfying or failing the mass window requirement.

A graphical overview of all regions and categories considered in the analysis with their relative background composition is given in Figure 9.5.

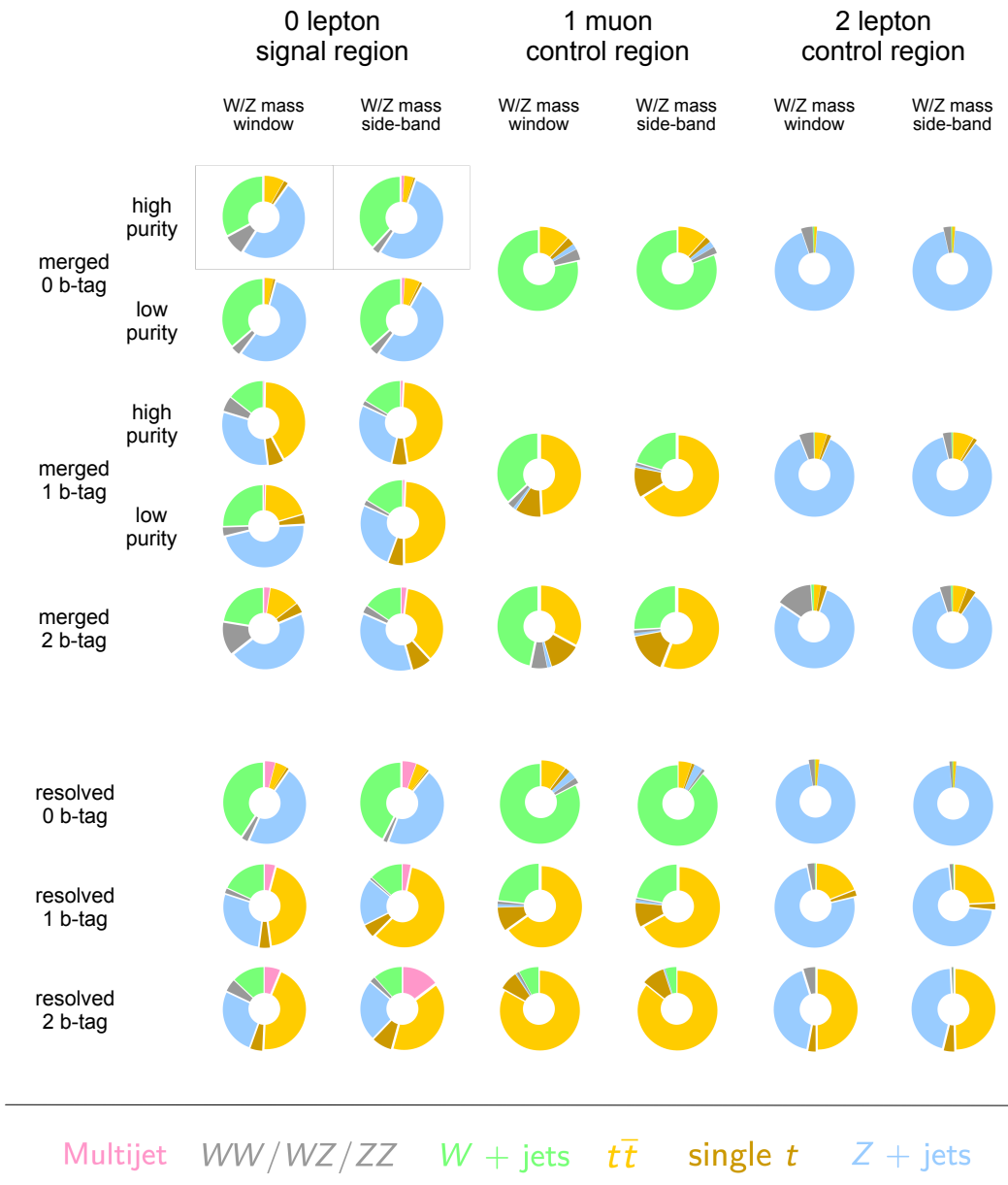



**Fig. 9.5.:** Overview of all regions and categories considered in the $E_{\mathrm{T}}^{\mathrm{miss}} + V(q\bar{q})$ search with their relative background composition. The 0 lepton signal region is defined for a selection enriched in signal processes targeting W/ Z mass window and a selection targeting the W/ Z mass side-bands, which are used as a validation region. The control regions are also split by W/ Z mass window and mass side-bands selections. Each region is partitioned in merged and resolved event topology categories, which are defined by the $b$-tag multiplicity. The 0 lepton merged signal region categories with zero or one $b$-tagged jets are further divided in high-purity and low-purity selections, which have different signal efficiencies.

## 9.4 Object and event selection

The selection requirements for events considered in the SR are outlined below. The specific choices for physics object definitions are summarised in Section 9.4.1. The SR, VR and CR definition is based on a common baseline selection, which is defined in Section 9.4.2, and common requirements to suppress the multijet background, which are provided in Section 9.4.3. The SR definition is outlined in Section 9.4.4.

### 9.4.1 Object selection

The physical compound objects used in the $E_{\mathrm{T}}^{\mathrm{miss}} + V(q\bar{q})$ search are based on the object definitions, which are introduced in Section 8.3.

Central jets and forward jets are used in defining the selection requirements on the event topology. The weak vector boson reconstruction is based on the two most energetic central jets in the resolved event topology and on the most energetic large-radius jet in the merged category. The MV2 discriminant with a fixed-cut working point corresponding to $70\,\%$ $b$-tagging efficiency is used to identify $b$-jets among the central jets and the fixed-radius (FR) track jets associated with large-radius jets via ghost-matching.

Baseline electron and muon candidates have high reconstruction efficiency and therefore are used for the definition of lepton vetoes. Signal electron and muon candidates, in turn, are characterised by high purity in the reconstruction and therefore are used to select electron or muon pairs for the 2 lepton CR. Tight signal muons are used to select the muon in the 1 muon CR.

The missing transverse momentum $E_{\mathrm{T}}^{\mathrm{miss}}$ is reconstructed using the LOOSE working point from the calibrated physics objects in the event and the track-based soft term (TST).

Closely related definitions are employed in the CRs to accommodate how background processes are contributing to the SR. In the CRs, the $E_{\mathrm{T}}^{\mathrm{miss,no}\ell}$ variable is used, which is reconstructed by excluding leptons from the $E_{\mathrm{T}}^{\mathrm{miss}}$ calculation. Thereby, the $E_{\mathrm{T}}^{\mathrm{miss,no}\ell}$ variable corresponds to the vector sum of $E_{\mathrm{T}}^{\mathrm{miss}}$ and the muon transverse momentum in the 1 muon CR or the vector sum of $E_{\mathrm{T}}^{\mathrm{miss}}$ and the transverse momentum of the dilepton system in the 2 lepton CR.

Additional definitions of the missing transverse momentum constructed just from tracks, which are referred to as track-based missing transverse momentum $E_{\mathrm{T}}^{\mathrm{miss,\ track}}$, are used in selection requirements to suppress multijet background processes. In analogy to $E_{\mathrm{T}}^{\mathrm{miss}}$, a $E_{\mathrm{T}}^{\mathrm{miss,\ track,\ no}\ell}$ variable is defined for use in the CRs.

The reconstruction algorithms for the various physics objects are mostly independent. Therefore, potential ambiguities in associating a single signature in the detector to multiple reconstructed objects must be resolved by an overlap removal procedure.

The overlap removal procedure applies three stages in the order listed as follows.

1. Electron-muon overlap removal. If an event contains a reconstructed electron and a reconstructed muon sharing the same track, the electron is removed from the event.

2. Electron-jet overlap removal. All jets within the distance[1] $\Delta R = \sqrt{\Delta y^2 + \Delta\varphi^2} < 0.2$ of electrons surviving the previous stage of the overlap removal procedure are removed from the event. Then, all reconstructed electrons of transverse energy $E_{\mathrm{T}}$ within the distance $\min\{0.4, 0.04 + 10\,\mathrm{GeV}/E_{\mathrm{T}}\}$ of jets are removed from the event to avoid double-counting of energy.

3. Muon-jet overlap removal. All jets within the distance $\Delta R < 0.2$ of any reconstructed muon are removed, if they either have fewer than three associated tracks or if the muon $p_{\mathrm{T}}$ is greater than $\max\{0.5 p_{\mathrm{T}}^{\mathrm{jet}}, 0.7 \sum_i p_{\mathrm{T}}^{\mathrm{track,\,i}}\}$, where $p_{\mathrm{T}}^{\mathrm{track}}$ denotes the transverse momentum of tracks associated with the jet. Then, all reconstructed muons of transverse momentum $p_{\mathrm{T}}$ within the distance $\min\{0.4, 0.04 + 10\,\mathrm{GeV}/p_{\mathrm{T}}\}$ of jets are removed from the event.

### 9.4.2 Baseline event selection

All selected events are required to satisfy the following baseline event selection requirements.

- **Data quality.** The selected events are required to satisfy basic data quality requirements encoded in so-called GOODRUNLISTS, which ensure that all subdetectors required in the event reconstruction were fully operational during data-taking. Events with corrupted data, for instance, due to noise bursts in the calorimeters, are vetoed.

- **Vertex reconstruction.** A successfully reconstructed PV with at least two associated tracks is required for the selected events.

- **Jet cleaning.** Events containing jets originating from sources other than the energy flow due to the hard scattering process, such as non-collision background processes, are vetoed. To this end, the events containing jets flagged as BADLOOSE jets [101] are vetoed. Events in data are required to satisfy the stricter TIGHT jet cleaning requirement to better suppress the non-collision background. It corresponds to the BADLOOSE definition with an additional requirement for jets with $|\eta| < 2.4$ on the ratio between the jet charged particle fraction and the jet energy fraction in the calorimeter layer with the maximum energy deposit.

- **Trigger.** Events in the SR, the VR and the 1 muon CR are required to pass the $E_{\mathrm{T}}^{\mathrm{miss}}$ trigger selection, while events in the 2 lepton CR are required to pass the single lepton trigger selection (c.f. Section 8.2.3).

[1] The distance measure employed for the overlap removal procedure is based on the rapidity distance $\Delta y$ instead of the pseudorapidity distance $\Delta\eta$.

### 9.4.3 Multijet-suppression event selection requirements

Multijet background events with an apparent momentum imbalance due to poorly measured jets can pass the baseline event selection requirements. Dedicated multijet-suppression selection requirements are designed to remove specifically events with fake $E_{\mathrm{T}}^{\mathrm{miss}}$ arising from as dijet or multijet processes. The selected events in the SR and the 1 muon CR are required to pass the following multijet-suppression requirements.

- $\min \Delta\varphi(\mathrm{jets}_{1,2,3}, E_{\mathrm{T}}^{\mathrm{miss}}) > 20°$ is a requirement on the minimum azimuthal distance between the three highest-$p_{\mathrm{T}}$ central jets and the $E_{\mathrm{T}}^{\mathrm{miss}}$ vector. If there are less than three central jets in the event, the distance is computed using a set of three jets consisting of the central jets in the event and the highest-$p_{\mathrm{T}}$ forward jets. This requirement exploits the characteristic topology of multijet events: if the energy of a jet is poorly measured, e.g. with too large energy, the resulting fake $E_{\mathrm{T}}^{\mathrm{miss}}$ is collinear with the jet.
- $\Delta\varphi(E_{\mathrm{T}}^{\mathrm{miss}}, V) > 120°$ is a requirement on the event topology of the reconstructed weak vector boson candidate $V$ and the $E_{\mathrm{T}}^{\mathrm{miss}}$ vector in signal events, in which the dark matter particles and the weak vector boson are back-to-back.
- $\Delta\varphi(E_{\mathrm{T}}^{\mathrm{miss}}, E_{\mathrm{T}}^{\mathrm{miss,\,track}}) < 90°$ is a requirement exploiting the correlation of $E_{\mathrm{T}}^{\mathrm{miss}}$ and $E_{\mathrm{T}}^{\mathrm{miss,\,track}}$ for events with true $E_{\mathrm{T}}^{\mathrm{miss}}$. In dijet events, $E_{\mathrm{T}}^{\mathrm{miss}}$ and $E_{\mathrm{T}}^{\mathrm{miss,\,track}}$ will both align with one of the two jets, resulting in $\Delta\varphi(E_{\mathrm{T}}^{\mathrm{miss}}, E_{\mathrm{T}}^{\mathrm{miss,\,track}})$ being distributed closely around zero due to a bias introduced by the combined application of the other multijet-suppression requirements.
- $E_{\mathrm{T}}^{\mathrm{miss,\,track}} > 30\,\mathrm{GeV}$ is required for events containing less than two $b$-jets. Fluctuations in the calorimeter jet energy measurements are uncorrelated with those of charged particle tracks in the ID. Therefore, it is unlikely for multijet events to result both in substantial fake $E_{\mathrm{T}}^{\mathrm{miss}}$ and fake $E_{\mathrm{T}}^{\mathrm{miss,\,track}}$. Hence, a threshold on $E_{\mathrm{T}}^{\mathrm{miss,\,track}}$ allows reducing the multijet background further.

Figure 9.6 shows distributions of the variables used in the definition of the three most important multijet-suppression requirements.

### 9.4.4 Signal region event selection

The events are either associated with the merged topology event selection or with the resolved topology event selection, depending on the Lorentz boost of the weak vector boson which is quantified by the amount of $E_{\mathrm{T}}^{\mathrm{miss}}$ in the event. The two selections are disjoint by construction, as events satisfying both merged and resolved selections are selected with priority to the merged selection.

The **merged event topology selection** is optimised for events containing a highly boosted weak vector boson, in which the weak vector boson decay products cannot be resolved by individual jets. Therefore, the weak vector boson candidate is reconstructed as a single large-radius jet. The jet mass and its characteristic jet

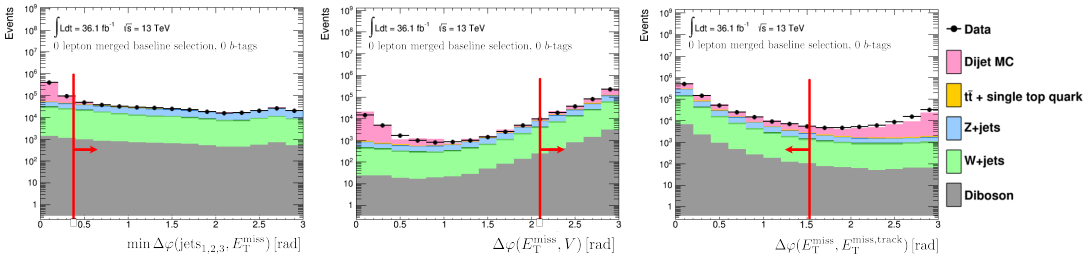
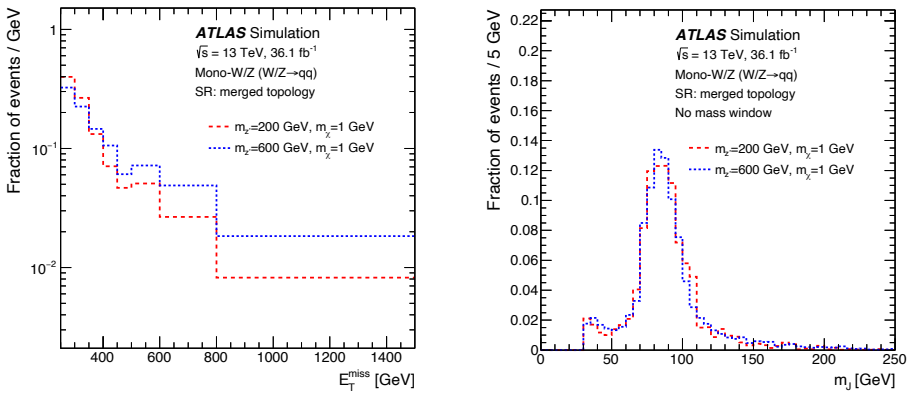



**Fig. 9.6.:** Distributions of $\min \Delta\varphi(\text{jets}_{1,2,3}, E_{\text{T}}^{\text{miss}})$, $\Delta\varphi(E_{\text{T}}^{\text{miss}}, V)$, and $\Delta\varphi(E_{\text{T}}^{\text{miss}}, E_{\text{T}}^{\text{miss, track}})$ after applying the 0 lepton SR merged baseline event selection requirements. The cut value is indicated by a red line and the region of selected events is indicated by the direction of the arrow. The data is shown overlaid on stacked histograms of the simulated background processes, including a MC sample of dijet events for illustration purposes.

substructure properties allow discriminating between the two-prong hadronic vector boson decay and combinatorial background.

Events with $E_{\text{T}}^{\text{miss}} > 250\,\text{GeV}$ and at least one reconstructed large-radius jet are considered for the merged event selection.

Figure 9.7 shows the expected distributions of missing transverse momentum $E_{\text{T}}^{\text{miss}}$ (left) and invariant mass of the most energetic large-radius jet $m_J$ in the merged topology, normalised to the unit area, for two representative signals. A larger $m_{\text{Z}'}$ mass corresponds to a harder $E_{\text{T}}^{\text{miss}}$ distribution and correspondingly to a larger signal efficiency. A large peak about the W/ Z mass can be seen in the $m_J$ distribution for both signals, whereas the combinatorial background processes (not shown) are expected to have comparatively flat distributions.




**(a)** $E_{\text{T}}^{\text{miss}}$ **(b)** Large-radius jet mass $m_J$

**Fig. 9.7.:** Expected distributions of missing transverse momentum $E_{\text{T}}^{\text{miss}}$ (left) and invariant mass $m_J$ (right), both normalised to the unit area, for two vector-mediator simplified model signals with $m_\chi = 1\,\text{GeV}$ and $m_{\text{Z}'} = 200\,\text{GeV}$ (red), $m_{\text{Z}'} = 600\,\text{GeV}$ (blue) after the full selection in the merged event topology.

Jet substructure observables are sensitive to the internal structure of large-radius jets and can identify the characteristic radiation pattern of two-prong vector boson decays [265]. A jet substructure observable with large discrimination power is the energy correlation ratio $D_2^{(\beta=1)}$, which is defined by

$$D_2^{(\beta)} = \frac{e_3^{(\beta)}}{\left(e_2^{(\beta)}\right)^3}. \tag{9.6}$$

It is based on the two- and three-point energy correlation functions

$$e_2^{(\beta)} = \frac{1}{\left(p_{\mathrm{T}}{}^J\right)^2} \sum_{i<j\in J} p_{\mathrm{T}}^i p_{\mathrm{T}}^j \left(R_{ij}\right)^\beta \tag{9.7}$$

$$e_3^{(\beta)} = \frac{1}{\left(p_{\mathrm{T}}{}^J\right)^3} \sum_{i<j<k\in J} p_{\mathrm{T}}^i p_{\mathrm{T}}^j p_{\mathrm{T}}^k \left(R_{ij} R_{jk} R_{ik}\right)^\beta, \tag{9.8}$$

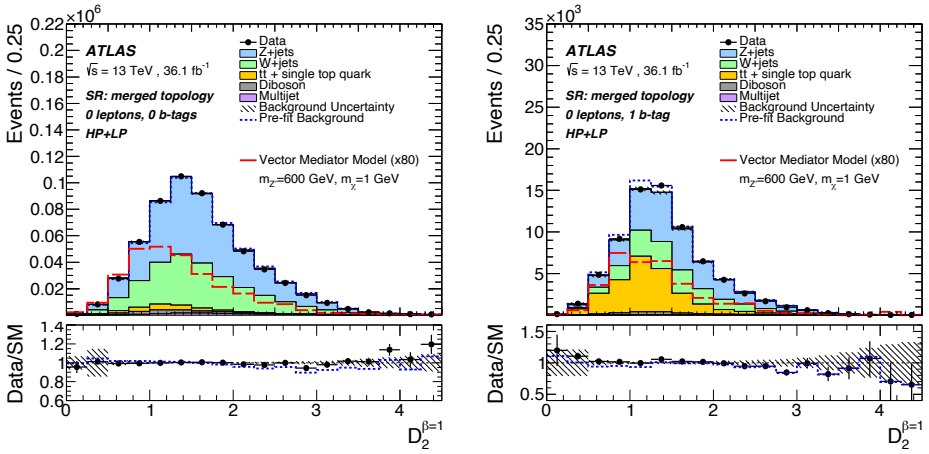
which are based on the transverse momenta $p_{\mathrm{T}}^i$ and pair-wise opening angles $R_{ij}$ of the constituents of the large-radius jet with transverse momentum $p_{\mathrm{T}}^J$. The $(N+1)$ energy correlation function is sensitive to $N$-prong jet substructure [274], therefore $D_2^{(\beta=1)}$ can discriminate the two-prong decays of vector bosons from pure strong interaction processes.

Figure 9.8 shows distributions of $D_2^{(\beta=1)}$ in events satisfying the full event selection with at most one $b$-tagged jet. Small values of $D_2^{(\beta=1)}$ correspond to large-radius jets originating from weak vector bosons, whereas large values indicate the jets originating from one-prong strong interaction processes. In the 1 $b$-tag selection, the separation between signal and background is less powerful due to the presence of W decays in $\mathrm{t\bar{t}}$ background events.

A dedicated boosted W/ Z boson tagger is used to identify large-radius jets originating from weak vector bosons. It is defined by a two-sided requirement on the jet mass $m_J$ and a one-sided requirement on $D_2^{(\beta=1)}$. Both requirements depend on the $p_{\mathrm{T}}$ of the large-radius jet, as shown in Figure 9.9 to ensure a fixed signal efficiency of $50\,\%$.

The track jets associated with the large radius jets are used to determine the quark-flavour of the vector boson decay products. In addition, events containing non-associated $b$-tagged track jets are rejected to suppress background processes involving heavy-flavour jets, such as top quark pair production. Three categories depending on the number of $b$-tagged track jets are defined with specific requirements on the vector boson candidate mass $m_J$ and jet substructure properties.

- **merged 0 *b*-tag**. Events selected for the merged 0 $b$-tag category satisfy the mass requirements of the boosted W/ Z tagger. In addition, the tagger's $D_2^{(\beta=1)}$ requirement is used to partition the events in a high-purity (HP) selection satisfying the requirement and a low-purity (LP) selection failing the requirement.




(a) 0 $b$-tag (b) 1 $b$-tag

**Fig. 9.8.:** Distributions of the energy correlation ratio $D_2^{(\beta=1)}$ of the most energetic large-radius jet in the event for data, simulated backgrounds and a representative vector mediator simplified model signal with $mZp = 600\,\text{GeV}$ and $m_\chi = 1\,\text{GeV}$. The distributions show events with 0 $b$-tagged jets (left) and 1 $b$-tagged jet (right).

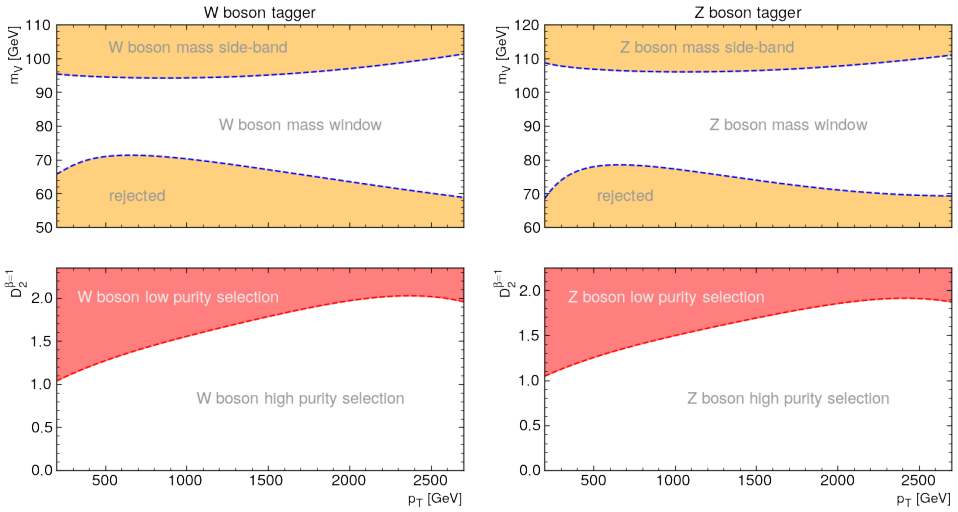


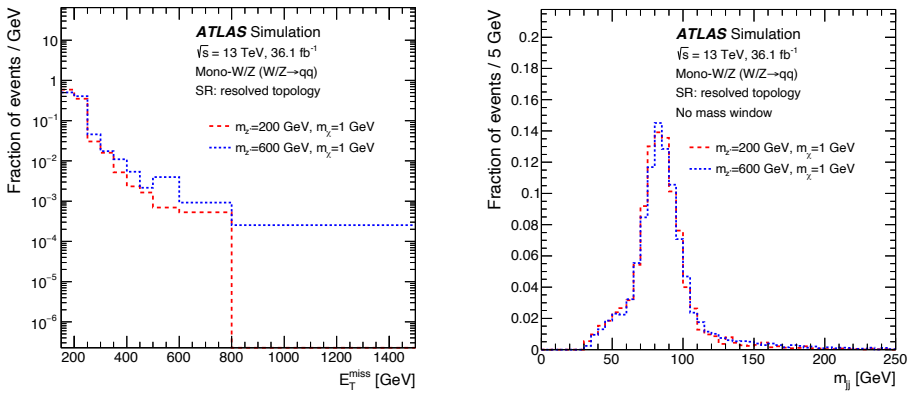

**Fig. 9.9.:** Selection requirements for the W boson tagger (left) and Z boson tagger (right). The upper panel shows the two-sided requirements on the combined jet mass $m_J$. The lower panel shows the upper cut on the energy correlation ratio $D_2^{(\beta=1)}$.

- **merged 1 *b*-tag**. Events selected for the merged 1 $b$-tag category are selected in the same way as for the merged 0 $b$-tag category and are partitioned in a HP and LP selection.
- **merged 2 *b*-tag**. Events selected for the merged 2 $b$-tag category are selected only by a mass window requirement $70\,\text{GeV} < m_J < 100\,\text{GeV}$, which is optimised for the $\text{Z} \to \text{b}\bar{\text{b}}$ signal process.

The **resolved event topology selection** is optimised for events with a moderately boosted weak vector boson, whose decay products can be resolved as well-separated small-radius jets.

Events with $E_{\text{T}}^{\text{miss}} > 150\,\text{GeV}$ and at least two reconstructed central jets are considered for the resolved event selection. The two highest-$p_{\text{T}}$ central jets in the event are used to reconstruct the vector boson candidate. Their invariant mass allows for the discrimination between signal and background processes.

Figure 9.10 shows the expected distributions of missing transverse momentum $E_{\text{T}}^{\text{miss}}$ (left) and invariant mass of the vector boson candidate in the resolved topology, normalised to the unit area, for two representative signals. The $E_{\text{T}}^{\text{miss}}$ distribution has a characteristic drop at $E_{\text{T}}^{\text{miss}} > 250\,\text{GeV}$, which is due to the priority given to the merged selection. Similar to the merged selection, the signals exhibit a large peak around the W/ Z mass.




(a) $E_{\text{T}}^{\text{miss}}$ (b) invariant mass $m_{jj}$

**Fig. 9.10.:** Expected distributions of missing transverse momentum $E_{\text{T}}^{\text{miss}}$ (left) and invariant mass $m_{jj}$ (right), both normalised to the unit area, for two vector-mediator simplified model signals with $m_\chi = 1\,\text{GeV}$ and $m_{\text{Z}'} = 200\,\text{GeV}$ (red), $m_{\text{Z}'} = 600\,\text{GeV}$ (blue) after the full selection in the resolved event topology.

The most energetic central jet is required to satisfy $p_{\text{T}} > 45\,\text{GeV}$. The modelling of the $E_{\text{T}}^{\text{miss}}$ trigger efficiency in simulations is improved by the requirement for events with exactly two central jets that their scalar transverse momentum sum is larger than $120\,\text{GeV}$. In events with three or more central jets, instead, the scalar transverse momentum sum of the three central jets with the highest $p_{\text{T}}$ is required to be larger than $150\,\text{GeV}$. An additional multijet-suppression requirement is imposed

for the resolved selection, which rejects events in which the azimuthal distance of the two most energetic central jets $\Delta\varphi(j_1, j_2)$ is larger than $140°$.

The $b$-tagging information of these jets is used to define three $b$-tag categories with specific requirements on the invariant mass of the vector boson candidate $m_{jj}$ and on the distance between the jets $\Delta R(j_1, j_2)$. Events containing three or more $b$-tagged jets are rejected.

- **resolved 0 *b*-tag**. Events selected for the resolved 0 $b$-tag category have to satisfy a mass window requirement of $65\,\text{GeV} < m_{jj} < 105\,\text{GeV}$ and $\Delta R(j_1, j_2) < 1.4$.

- **resolved 1 *b*-tag**. Events selected for the resolved 0 $b$-tag category have to satisfy a mass window requirement of $65\,\text{GeV} < m_{jj} < 105\,\text{GeV}$ and $\Delta R(j_1, j_2) < 1.25$.

- **resolved 2 *b*-tag**. Events selected for the resolved 0 $b$-tag category have to satisfy a mass window requirement of $65\,\text{GeV} < m_{jj} < 100\,\text{GeV}$ and $\Delta R(j_1, j_2) < 1.25$.

The full list of selection requirements used to define the SR of the $E_\text{T}^\text{miss} + V(q\bar{q})$ search is given in Table 9.4.

**Tab. 9.4.:** Signal region event selection requirements employed in the $E_\text{T}^\text{miss} + V(q\bar{q})$ search.

| SR selection | **Merged category** | | **Resolved category** |
|---|---|---|---|
| | baseline + multijet-suppression requirements<br>0 baseline e and 0 baseline $\mu$ | | |
| | $E_\text{T}^\text{miss} > 250\,\text{GeV}$<br>1 or more large-radius jets<br>no non-associated $b$-tagged track jets | | $E_\text{T}^\text{miss} > 150\,\text{GeV}$<br>not in merged category<br>2 or more central jets<br>$p_\text{T}^{j1} > 45\,\text{GeV}$<br>$\Delta\varphi(j_1, j_2) < 140°$<br>$\sum_i^{2(3)} p_\text{T}^{j_i} > 120\,\text{GeV}(150\,\text{GeV})$ |
| ***b*-tag category** | **High purity** | **Low purity** | **Inclusive** |
| 0 $b$-tag | W/ Z tagger<br>pass $m_J$ + pass $D_2^{(\beta=1)}$ | W/ Z tagger<br>pass $m_J$ + fail $D_2^{(\beta=1)}$ | $65\,\text{GeV} < m_{jj} < 105\,\text{GeV}$<br>$\Delta R(j_1, j_2) < 1.4$ |
| 1 $b$-tag | W/ Z tagger<br>pass $m_J$ + pass $D_2^{(\beta=1)}$ | W/ Z tagger<br>pass $m_J$ + fail $D_2^{(\beta=1)}$ | $65\,\text{GeV} < m_{jj} < 105\,\text{GeV}$<br>$\Delta R(j_1, j_2) < 1.25$ |
| 2 $b$-tag | $70\,\text{GeV} < m_J < 100\,\text{GeV}$ | | $65\,\text{GeV} < m_{jj} < 100\,\text{GeV}$<br>$\Delta R(j_1, j_2) < 1.25$ |

Figure 9.11 shows the product of acceptance and efficiency $\mathcal{A} \times \varepsilon$ for the simplified vector-mediator model signals with $m_\chi = 1\,\text{GeV}$ in dependence on the mediator mass $m_{Z'}$. Signals with higher $m_{Z'}$ are characterised by a higher $\mathcal{A} \times \varepsilon$, as they have a harder $E_\text{T}^\text{miss}$ spectrum and therefore a larger fraction of events can pass the $E_\text{T}^\text{miss}$ selection requirements.

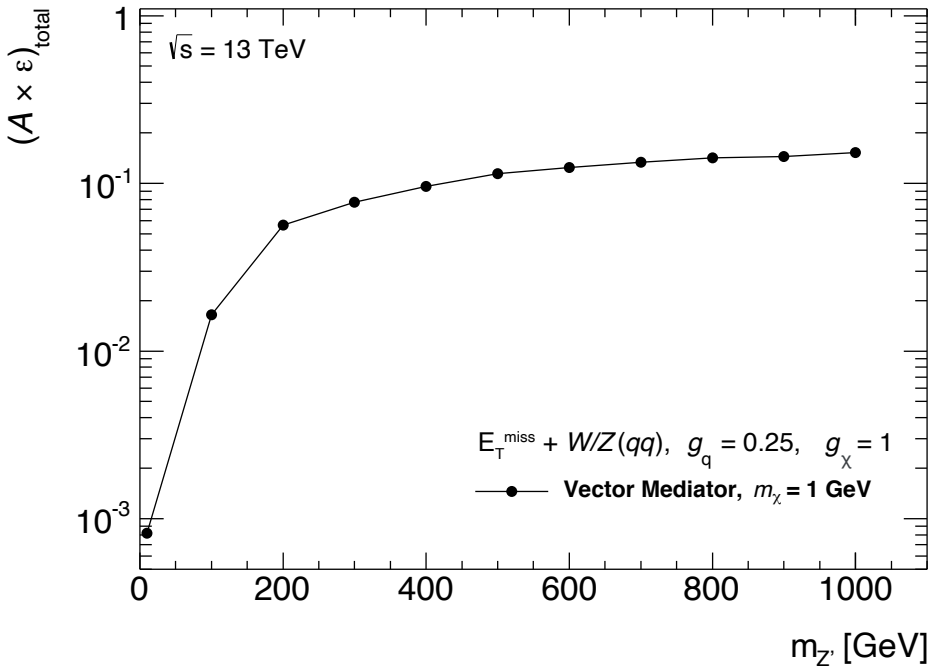



**Fig. 9.11.:** The product of acceptance and efficiency $\mathcal{A} \times \varepsilon$ for the process $pp \to Z'V \to \chi\overline{\chi}qq$, defined as the number of signal events satisfying the full set of selection criteria, divided by the total number of generated signal events for the simplified vector-mediator model signals, shown in dependence on the mediator mass $m_{Z'}$.

### 9.4.5 Validation region event selection

Complementary to the SR selection in the W/ Z mass window, the events in the W/ Z upper mass side-band are used to define a **validation region** (VR). The VR is similar to the SR in its background composition but has reduced contributions from signal processes. Therefore, it is used to verify the correct extrapolation of the background normalisation from the CRs to the 0 lepton event selection. In addition, the inclusion of the 0 lepton VR data in the statistical analysis has a similar effect as the CR data, as it provides additional information to constrain the background processes in the SR.

The VR selection is similar to the SR selection, except for the upper W/ Z mass side-band requirement instead of the W/ Z mass window requirement. The lower mass side-band is not considered in the search due to substantial modelling challenges when including both the high-mass and low-mass regions in the statistical analysis.

The full list of selection requirements used to define the VR of the $E_{\mathrm{T}}^{\mathrm{miss}} + V(q\bar{q})$ search is given in Table 9.5.

**Tab. 9.5.:** Validation region event selection requirements employed in the $E_{\mathrm{T}}^{\mathrm{miss}} + V(q\bar{q})$ search.

| VR selection | **Merged selection** | | **Resolved selection** |
|---|---|---|---|
| | baseline + multijet-suppression requirements<br>0 baseline e and 0 baseline $\mu$ | | |
| | $E_{\mathrm{T}}^{\mathrm{miss}} > 250\,\mathrm{GeV}$<br><br>1 or more large-radius jets<br>no non-associated $b$-tagged track jets | | $E_{\mathrm{T}}^{\mathrm{miss}} > 150\,\mathrm{GeV}$<br>not in merged selection<br>2 or more central jets<br>$p_{\mathrm{T}}^{j1} > 45\,\mathrm{GeV}$<br>$\Delta\varphi(j_1, j_2) < 140°$<br>$\sum_i^{2(3)} p_{\mathrm{T}}^{j_i} > 120\,\mathrm{GeV}(150\,\mathrm{GeV})$ |
| ***b*-tag category** | **High purity** | **Low purity** | **Inclusive** |
| 0 $b$-tag | W/ Z tagger<br>fail $m_J$ + pass $D_2^{(\beta=1)}$ | W/ Z tagger<br>fail $m_J$ + fail $D_2^{(\beta=1)}$ | $105\,\mathrm{GeV} < m_{jj} < 250\,\mathrm{GeV}$<br>$\Delta R(j_1, j_2) < 1.4$ |
| 1 $b$-tag | W/ Z tagger<br>fail $m_J$ + pass $D_2^{(\beta=1)}$ | W/ Z tagger<br>fail $m_J$ + fail $D_2^{(\beta=1)}$ | $105\,\mathrm{GeV} < m_{jj} < 250\,\mathrm{GeV}$<br>$\Delta R(j_1, j_2) < 1.25$ |
| 2 $b$-tag | $100\,\mathrm{GeV} < m_J < 250\,\mathrm{GeV}$ | | $100\,\mathrm{GeV} < m_{jj} < 250\,\mathrm{GeV}$<br>$\Delta R(j_1, j_2) < 1.25$ |

## 9.5 Background estimation

The dominant background processes of the $E_{\mathrm{T}}^{\mathrm{miss}} + V(q\bar{q})$ search are estimated in data of control regions, which are enhanced in the respective background processes. The kinematic similarity of the CRs to the SR is ensured by requiring almost the same selection as in the SR, except for the lepton multiplicity requirement and the

use of the $E_{\mathrm{T}}^{\mathrm{miss,no}\ell}$ and $E_{\mathrm{T}}^{\mathrm{miss,\ track,\ no}\ell}$ variable instead of $E_{\mathrm{T}}^{\mathrm{miss}}$ and $E_{\mathrm{T}}^{\mathrm{miss,\ track}}$. The contamination of the CR data by signal processes is expected to be negligible due to the stringent requirements in the lepton candidate definitions.

The normalisation parameters of the sub-dominant background processes are set to their predicted values based on theoretical predictions and can vary within the corresponding uncertainties.

However, this approach is not feasible for the multijet background. Due to the comparatively large cross-sections of pure QCD processes (c.f. Figure 4.4) and the small selection efficiency, an unreasonably large number of simulated events would be required for a reliable MC-based estimation. Therefore, a data-driven approach based on a template fit, which was developed for this analysis, is employed to evaluate the contribution of multijet background processes in the SR and VR.

### 9.5.1 1 muon control region

The 1 muon CR is defined to constrain W + jets and $\mathrm{t\bar{t}}$ processes using selected events, which contain exactly one tight signal muon candidate, no additional baseline muon candidates and no baseline electron candidates. The discrimination between the two processes is enabled by the different $b$-tag categories. The 0 $b$-tag category is mostly populated by W + jets background events, whereas the 1 or more $b$-tag categories are populated mostly by $\mathrm{t\bar{t}}$ background events. Events in the 1 muon CR are selected by $E_{\mathrm{T}}^{\mathrm{miss}}$ triggers.

Although the requirement of 1 muon substantially decreases the contribution of multijet background events, the multijet-suppression requirements are still applied to avoid biases in the kinematic properties of the selected events, using $E_{\mathrm{T}}^{\mathrm{miss,no}\ell}$ in the definition of the derived observables.

The remaining selection requirements are similar to that of the SR, except for the requirements on the vector boson candidate, which are relaxed to increase the number of selected events and thereby enhance the statistical precision. In the merged event selection, the requirement on the $D_2^{(\beta=1)}$ substructure is not considered. Similarly, in the resolved selection, the requirements on $\Delta R(j_1, j_2)$ are dropped from the event selection.

The full list of selection requirements used to define the 1 muon CR of the $E_{\mathrm{T}}^{\mathrm{miss}} + V(q\bar{q})$ search is given in Table 9.6.

### 9.5.2 2 lepton control region

The 2 lepton CR is designed to constrain the Z + jets background by selecting events with leptonically decaying Z bosons. The selected events have to contain either exactly two baseline electron candidates or exactly two baseline muon candidates.

Tab. 9.6.: 1 muon control region event selection requirements employed in the $E_{\mathrm{T}}^{\mathrm{miss}}+V(q\bar{q})$ search.

| 1 muon CR | **Merged selection** | **Resolved selection** |
|---|---|---|
| | baseline + multijet-suppression requirements<br>0 baseline e, 1 tight signal $\mu$ and no additional baseline $\mu$ | |
| | $E_{\mathrm{T}}^{\mathrm{miss,no}\ell} > 250\,\mathrm{GeV}$<br><br>1 or more large-radius jets<br>no non-associated $b$-tagged track jets | $E_{\mathrm{T}}^{\mathrm{miss,no}\ell} > 150\,\mathrm{GeV}$<br>not in merged selection<br>2 or more central jets<br>$p_{\mathrm{T}}^{j1} > 45\,\mathrm{GeV}$<br>$\Delta\varphi(j_1, j_2) < 140°$<br>$\sum_i^{2(3)} p_{\mathrm{T}}^{j_i} > 120\,\mathrm{GeV}(150\,\mathrm{GeV})$ |
| ***b*-tag category** | **Mass window / mass side-band** | **Mass window / mass side-band** |
| 0 $b$-tag | W/ Z tagger pass / fail $m_J$ | $65\,\mathrm{GeV} < m_{jj} < 105\,\mathrm{GeV}$ /<br>$105\,\mathrm{GeV} < m_{jj} < 250\,\mathrm{GeV}$ |
| 1 $b$-tag | W/ Z tagger pass / fail $m_J$ | $65\,\mathrm{GeV} < m_{jj} < 105\,\mathrm{GeV}$ /<br>$105\,\mathrm{GeV} < m_{jj} < 250\,\mathrm{GeV}$ |
| 2 $b$-tag | $70\,\mathrm{GeV} < m_J < 100\,\mathrm{GeV}$ /<br>$100\,\mathrm{GeV} < m_J < 250\,\mathrm{GeV}$ | $65\,\mathrm{GeV} < m_{jj} < 100\,\mathrm{GeV}$ /<br>$100\,\mathrm{GeV} < m_{jj} < 250\,\mathrm{GeV}$ |

At least one of the two electrons or muons must satisfy the signal muon or electron candidate definition. Events in the 2 lepton CR are selected by single lepton triggers.

The requirement of 2 leptons suppresses the multijet background contribution to a level that the multijet-suppression cuts are not urgently required. They are applied nevertheless to ensure kinematic similarity of the CR to the SR, using $E_{\mathrm{T}}^{\mathrm{miss,no}\ell}$ instead of $E_{\mathrm{T}}^{\mathrm{miss}}$. In addition, a requirement on the invariant mass of the two leptons $\ell$ to be consistent with the Z mass $66\,\mathrm{GeV} < m_{\ell\ell} < 106\,\mathrm{GeV}$ suppresses processes with non-resonantly produced leptons. Similar to the 1 muon CR, the requirements on the vector boson candidate are relaxed. The $D_2^{(\beta=1)}$ substructure requirement in the merged event selection is not considered. In the resolved event selection, the requirements on $\Delta R(j_1, j_2)$ are dropped.

The full list of selection requirements used to define the 2 lepton CR of the $E_{\mathrm{T}}^{\mathrm{miss}} + V(q\bar{q})$ search is given in Table 9.7.

### 9.5.3 Multijet background estimate

The multijet background is expected to be small in the SR and VR due to the multijet-suppression requirements and expected to be negligible in the CRs due to the additional lepton requirements. The multijet background is estimated in the 0 lepton SR and VR using a data-driven template method. The method consists of two steps, in which the shape and normalisation of the multijet $E_{\mathrm{T}}^{\mathrm{miss}}$ templates are determined. A sketch of the selections used in the procedure is shown in Section 9.5.3.

Tab. 9.7.: 2 lepton control region event selection requirements employed in the $E_{\mathrm{T}}^{\mathrm{miss}} + V(q\bar{q})$ search.

| 2 lepton CR | **Merged selection** | **Resolved selection** |
|---|---|---|
| | baseline + multijet-suppression requirements<br>exactly 2 baseline e/ $\mu$, among those at least 1 signal e/ $\mu$<br>$66\,\mathrm{GeV} < m_{\ell\ell} < 106\,\mathrm{GeV}$ | |
| | $E_{\mathrm{T}}^{\mathrm{miss,no}\ell} > 250\,\mathrm{GeV}$<br><br>1 or more large-radius jets<br>no non-associated $b$-tagged track jets | $E_{\mathrm{T}}^{\mathrm{miss,no}\ell} > 150\,\mathrm{GeV}$<br>not in merged selection<br>2 or more central jets<br>$p_{\mathrm{T}}^{j1} > 45\,\mathrm{GeV}$<br>$\Delta\varphi(j_1, j_2) < 140°$<br>$\sum_i^{2(3)} p_{\mathrm{T}}^{j_i} > 120\,\mathrm{GeV}(150\,\mathrm{GeV})$ |
| ***b*-tag category** | **Mass window / mass side-band** | **Mass window / mass side-band** |
| 0 $b$-tag | W/ Z tagger pass / fail $m_J$ | $65\,\mathrm{GeV} < m_{jj} < 105\,\mathrm{GeV}$ /<br>$105\,\mathrm{GeV} < m_{jj} < 250\,\mathrm{GeV}$ |
| 1 $b$-tag | W/ Z tagger pass / fail $m_J$ | $65\,\mathrm{GeV} < m_{jj} < 105\,\mathrm{GeV}$ /<br>$105\,\mathrm{GeV} < m_{jj} < 250\,\mathrm{GeV}$ |
| 2 $b$-tag | $70\,\mathrm{GeV} < m_J < 100\,\mathrm{GeV}$ /<br>$100\,\mathrm{GeV} < m_J < 250\,\mathrm{GeV}$ | $65\,\mathrm{GeV} < m_{jj} < 100\,\mathrm{GeV}$ /<br>$100\,\mathrm{GeV} < m_{jj} < 250\,\mathrm{GeV}$ |

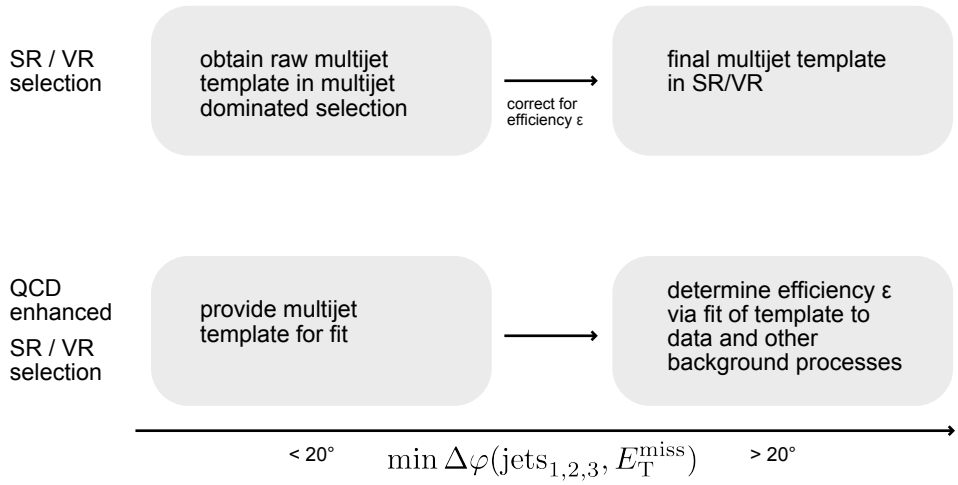



Fig. 9.12.: Sketch of the selections used in the multijet background estimate based on a template method. The $E_{\mathrm{T}}^{\mathrm{miss}}$ shape of the multijet background is obtained from a selection enriched in multijet events by inverting the $\min \Delta\varphi(\mathrm{jets}_{1,2,3}, E_{\mathrm{T}}^{\mathrm{miss}})$ requirement. The template is normalised by correcting for the efficiency of the $\min \Delta\varphi(\mathrm{jets}_{1,2,3}, E_{\mathrm{T}}^{\mathrm{miss}})$ cut. The efficiency is determined by a fit of a template and simulated backgrounds to the data in selections enhanced in multijet events.

In the first step, **template generation**, the templates for the $E_{\mathrm{T}}^{\mathrm{miss}}$ distribution are constructed using dedicated regions dominated by multijet processes. These regions are defined by selections similar to the SR/VR (c.f. Table 9.4 / Table 9.5) but with the dominant multijet-suppression requirement inverted, such that $\min \Delta\varphi(\mathrm{jets}_{1,2,3}, E_{\mathrm{T}}^{\mathrm{miss}}) < 20°$ for selected events. The multijet $E_{\mathrm{T}}^{\mathrm{miss}}$ shape template is generated by subtracting all simulated backgrounds from the data in the multijet-enriched region. This process is repeated for each of the eight categories in the SR, and similarly for the eight categories in the VR.

In the second step, **template normalisation**, the raw templates need to be corrected for the efficiency $\varepsilon_{\min \Delta\varphi(\mathrm{jets}_{1,2,3}, E_{\mathrm{T}}^{\mathrm{miss}})}$ of the $\min \Delta\varphi(\mathrm{jets}_{1,2,3}, E_{\mathrm{T}}^{\mathrm{miss}})$ requirement. The normalisation of the multijet $E_{\mathrm{T}}^{\mathrm{miss}}$ shape templates is determined using a profile likelihood fit to the data.

The fit is based on multijet-enhanced selections in the VR, as there are insufficient multijet events for the full VR event selections to provide meaningful fit results. The multijet-enhanced selections have a lowered $E_{\mathrm{T}}^{\mathrm{miss}}$ threshold of $E_{\mathrm{T}}^{\mathrm{miss}} > 150\,\mathrm{GeV}$ for the merged selection and allow for an overlap of events in the merged and resolved selections. Furthermore, the $\Delta\varphi(E_{\mathrm{T}}^{\mathrm{miss}}, E_{\mathrm{T}}^{\mathrm{miss,\,track}}) < 90°$ requirement is dropped from the event selection to increase the contribution of multijet events. The $\min \Delta\varphi(\mathrm{jets}_{1,2,3}, E_{\mathrm{T}}^{\mathrm{miss}})$ cut efficiency is determined using these multijet-enhanced selections.

The multijet $E_{\mathrm{T}}^{\mathrm{miss}}$ template, which is obtained from the corresponding selection with $\min \Delta\varphi(\mathrm{jets}_{1,2,3}, E_{\mathrm{T}}^{\mathrm{miss}}) < 20°$, is fitted to the data while considering also the other backgrounds in the selection with $\min \Delta\varphi(\mathrm{jets}_{1,2,3}, E_{\mathrm{T}}^{\mathrm{miss}}) > 20°$. In the fit, the simulated background processes are allowed to vary within the uncertainties listed in Table 9.8, including the uncertainty on the luminosity of $2.1\,\%$. These background normalisation uncertainties are loosely based on the studies described in Ref. [48].

**Tab. 9.8.:** Background process normalisation uncertainties and luminosity uncertainty in the profile likelihood fit used to determine the efficiency of the $\min \Delta\varphi(\mathrm{jets}_{1,2,3}, E_{\mathrm{T}}^{\mathrm{miss}})$ requirement.

| W + jets | Z + jets | $\mathrm{t\bar{t}}$ | Single top quark | Diboson | Luminosity |
|---|---|---|---|---|---|
| 20 % | 20 % | 6 % | 5 % | 25 % | 2.1 % |

The final multijet templates are obtained by scaling the templates obtained in the first step by the values of $\varepsilon_{\min \Delta\varphi(\mathrm{jets}_{1,2,3}, E_{\mathrm{T}}^{\mathrm{miss}})}$ obtained in the profile likelihood fit. Several justified assumptions enter the multijet estimate: the efficiency of the $\min \Delta\varphi(\mathrm{jets}_{1,2,3}, E_{\mathrm{T}}^{\mathrm{miss}})$ requirement, which is estimated in multijet enhanced VR selections, is assumed to be the same in SR and VR. In addition, $E_{\mathrm{T}}^{\mathrm{miss}}$ and $\varepsilon_{\min \Delta\varphi(\mathrm{jets}_{1,2,3}, E_{\mathrm{T}}^{\mathrm{miss}})}$ is assumed not to be strongly correlated with $E_{\mathrm{T}}^{\mathrm{miss}}$.

As the contribution of the multijet background is small, the multijet normalisation uncertainty was conservatively assigned a value of $100\,\%$ without compromising the sensitivity of the analysis to signals. In addition, a shape uncertainty is assigned to

the multijet $E_{\mathrm{T}}^{\mathrm{miss}}$ shape templates, which is based on variations of the multijet $E_{\mathrm{T}}^{\mathrm{miss}}$ distribution parametrised as an exponentially falling distribution.

## 9.6 Systematic uncertainties

Systematic uncertainties arise from biases in the reconstruction of physics objects and the description of the signal and background processes using MC simulation. These uncertainties can affect the total normalisation of signal and background processes, their relative distribution among the different SR, VR, and CR categories, and the shape of their $E_{\mathrm{T}}^{\mathrm{miss}}$ distribution. In this section, a general description of the considered systematic uncertainties is provided. The uncertainties are categorised in "experimental systematic uncertainties", which arise from the reconstruction, identification, and calibration of the physics objects, and in "theoretical systematic uncertainties", which are associated with the theoretical predictions of signal and background processes. The experimental systematic uncertainties are described in Section 9.6.1, while the theoretical systematic uncertainties are described in Section 9.6.2.

### 9.6.1 Experimental systematic uncertainties

The experimental systematic uncertainties, which arise from biases in the detector performance and physics object reconstruction, are listed below.

- **Trigger.** The $E_{\mathrm{T}}^{\mathrm{miss}}$ and single lepton triggers are corrected for discrepancies in the trigger efficiency between data and simulated events. These corrections are subject to uncertainties, as described in Section 8.2.3. The $E_{\mathrm{T}}^{\mathrm{miss}}$ trigger uncertainties are described by two components. The first component is obtained by comparing events with different flavour composition while the second component is obtained from the $1\sigma$ confidence interval of the trigger calibration fit. The single lepton uncertainties are derived in a similar manner. The single electron trigger efficiency is described by one component, while the single muon trigger efficiency is described by two components.
- **Luminosity.** The uncertainty on the measurement of the integrated luminosity, which is used for the absolute normalisation of the simulated physics processes to the data, is $2.1\,\%$ [56]. It is derived following a methodology similar to that detailed in Ref. [57].
- **Pile-up.** The pile-up conditions of the simulated events are reweighted to match those in data. This reweighting procedure is subject to uncertainty due to possible biases in the modelling of pile-up events.
- **Electrons.** The uncertainties associated with the reconstruction, identification, and isolation criteria of electrons can affect the normalisation of signal and background processes due to the electron-based veto in the SR and 1 muon CR, and the 2 electron requirement in the 2 lepton CR. In addition, the

uncertainties on the electron energy scale and resolution affect the electron $E_{\mathrm{T}}$ and consequently also the $E_{\mathrm{T}}^{\mathrm{miss,no}\ell}$ shape.

- **Muons.** The uncertainties associated with the reconstruction (including track-to-vertex association), identification, and isolation criteria of muons can affect the normalisation of signal and background processes due to the muon-based veto in the SR and the muon requirements in the CRs. The uncertainties on the muon $p_{\mathrm{T}}$ scale and resolution in the ID and the MS can affect the $E_{\mathrm{T}}^{\mathrm{miss,no}\ell}$ shape.

- **Small-radius jets.** The calibration of small-radius jets is subject to multiple sources of uncertainty. In total, the uncertainties on the JES calibration are parametrised by over 125 components which are derived from the in-situ calibration, the impact of pile-up, the jet flavour dependence and other effects [54]. These components are grouped into a strongly reduced set of four components so that the total uncertainty is preserved, but the correlations are not [52], since the JES uncertainties are expected to be sub-dominant for this search. The JER uncertainty is described by a single component.

- **Large-radius jets.** The large-radius jet uncertainties account for the modelling and the resolution of their energy, mass and $D_2^{(\beta=1)}$ substructure variable. The uncertainties on the modelling are correspondingly defined in three groups, each consisting of four components. These components account for the residual difference between data and MC simulation, the fragmentation modelling, uncertainties related to the use of tracking information, and the total statistical uncertainty in the calibration. The uncertainties on the resolution are described by one component for the jet energy, mass and $D_2^{(\beta=1)}$ substructure, respectively.

- ***b*-tagging.** The uncertainties associated with the identification of heavy-flavour jets are parametrised by separate components pertaining $b$-jets, $c$-jets, and light-flavour jets, as well as the extrapolation of $b$- and $c$-tagging efficiencies for high-$p_{\mathrm{T}}$ jets.

- **Missing transverse momentum.** The uncertainties associated with $E_{\mathrm{T}}^{\mathrm{miss}}$ arise from two contributions, related to the $E_{\mathrm{T}}^{\mathrm{miss}}$ hard term and soft term, respectively. The uncertainty related to the hard term is evaluated by propagating the uncertainties of all physics objects entering the hard term computation. The uncertainty related to the soft term is derived from measurements. In total, four components associated with the $E_{\mathrm{T}}^{\mathrm{miss}}$ uncertainty are considered.

### 9.6.2 Theoretical systematic uncertainties

The theoretical systematic uncertainties are associated with the description of signal and background processes. The specific choices of event generators, PDF sets, parton shower modelling, and values of the renormalisation and factorisation scales can introduce systematic biases, which affect the normalisation of signal and background

processes, their relative distribution among different categories, and the shape of their $E_{\mathrm{T}}^{\mathrm{miss}}$ distribution.

The normalisation uncertainties of the background processes are implemented as constraints on the normalisation of the respective distributions in the statistical model. The normalisation of the dominant background processes Z + jets, W + jets, and $\mathrm{t\bar{t}}$ is determined from the CR information and therefore unconstrained. However, the relative contribution of heavy-flavour and light-flavour processes in the $V$ + jets backgrounds is allowed to change within uncertainties. The simulated $V$ + jets background events are categorised depending on the flavour information of the weak vector boson candidate as $V + \mathrm{bb}$, $V + \mathrm{bc}$, $V + \mathrm{b}l$, $V + \mathrm{cc}$, $V + \mathrm{c}l$, and $V + ll$, where $l \in \{\mathrm{u}, \mathrm{d}, \mathrm{s}, \mathrm{g}\}$ denotes light flavour jets. The heavy-flavour processes $V + \mathrm{bb}$, $V + \mathrm{bc}$, and $V + \mathrm{b}l$, $V + \mathrm{cc}$ are grouped and referred to as $V +$ heavy flavour.

The normalisations of the sub-dominant background processes are constrained by the normalisation uncertainties, which are based on those described in Ref. [48]. They are estimated by comparing the acceptance of nominal and alternative simulated samples normalised to the same production cross-section on particle level while neglecting detector effects. In addition, comparisons to the data in control regions are considered. The normalisation uncertainties are listed in Table 9.9.

**Tab. 9.9.:** Theoretical systematic uncertainties on the normalisation of background processes in the $E_{\mathrm{T}}^{\mathrm{miss}} + V(q\bar{q})$ search. In the description of the jet flavour of $V$ + jets processes, light-flavour jets are abbreviated with $l \in \{\mathrm{u}, \mathrm{d}, \mathrm{s}\}$.

| Process | Uncertainty |
|---|---|
| Ratio of $V + \mathrm{bc}$ / $V +$ heavy flavour | 30 % |
| Ratio of $V + \mathrm{b}l$ / $V +$ heavy flavour | 30 % |
| Ratio of $V + \mathrm{cc}$ / $V +$ heavy flavour | 30 % |
| $V + \mathrm{c}l$ | 30 % |
| $V + ll$ | 20 % |
| $\mathrm{t\bar{t}}$ (resolved) | 30 % |
| Single top quark ($s$-channel) | 4.6 % |
| Single top quark ($t$-channel) | 4.4 % |
| Single top quark (W$t$-process) | 6.2 % |
| WW | 25 % |
| WZ | 26 % |
| ZZ | 20 % |

The uncertainties on the shape of the $E_{\mathrm{T}}^{\mathrm{miss}}$ and weak vector boson candidate mass distributions are also based on those described in Ref. [48]. They are defined in terms of the transverse momentum of the vector boson $p_{\mathrm{T}}^{V}$, which is highly correlated with $E_{\mathrm{T}}^{\mathrm{miss}}$, and the invariant mass of the two most energetic jets $m_{jj}$. The shape uncertainties are estimated in each of the $b-$tag categories separately by comparisons of nominal and alternative samples, which are scaled to have the same normalisation in each region.

The W+ jets and Z + jets uncertainties are estimated by comparing the nominal samples to alternative samples generated with MADGRAPH 5 + PYTHIA and to the data in a W/ Z-enriched selection. The $\pm 1\sigma$ shape variations are parametrised by an analytical function, which is fitted to the largest variations with respect to the nominal sample and is symmetrised. The uncertainties are derived separately for $V$ + jets processes with light-flavour jets and heavy-flavour jets to account for the different contributing processes, such as gluon splitting $g \to b\bar{b}$ in the 2 $b$-tag region.

The $t\bar{t}$ uncertainties are estimated by comparing the nominal samples to alternative samples with a different description of the hard scattering process based on MADGRAPH5_aMC@NLO + PYTHIA 8, samples with an alternative parton shower description based on POWHEG + HERWIG 7, and samples with increased and decreased parton radiation.

The single top quark uncertainties are estimated by comparing the nominal samples to alternative samples with an alternative parton shower description based on POWHEG + Herwig++, and samples with increased and decreased parton radiation. In addition, alternative descriptions of the hard scattering process are considered by comparing samples based on POWHEG + Herwig++ to samples based on MADGRAPH5_aMC@NLO + Herwig++.

The diboson uncertainties are estimated by comparing the nominal samples to alternative samples based on POWHEG + PYTHIA 8 and by comparing samples generated with POWHEG + PYTHIA 8 to those generated with POWHEG + Herwig++.

The theoretical uncertainties for the dark matter signals in the vector mediator simplified model are estimated by variations in the event generation and comparisons of the resulting $E_{\mathrm{T}}^{\mathrm{miss}}$ distributions on particle level neglecting detector effects. The uncertainties are defined in three components.

- The **scale** uncertainties are estimated by varying the renormalisation scale $\mu_{\mathrm{R}}$ and factorisation scale $\mu_{\mathrm{F}}$ coherently by factors of $0.5$ and $2$ on an event-by-event basis. The resulting $E_{\mathrm{T}}^{\mathrm{miss}}$ distributions are compared, and in each $E_{\mathrm{T}}^{\mathrm{miss}}$ bin, the largest variation with respect to the nominal value is taken as the scale uncertainty.
- The **PDF** uncertainty is estimated by replacing the nominal NNPDF23LO PDF set with the alternative MSTW2008LO [283] and CTEQ6L1 [305] PDF sets. The resulting $E_{\mathrm{T}}^{\mathrm{miss}}$ distributions are compared to the nominal distribution, and the largest deviation in each $E_{\mathrm{T}}^{\mathrm{miss}}$ bin is taken as the PDF uncertainty.
- The **tune** uncertainty is estimated by varying the amounts of initial state radiation, final state radiation, and multi-parton interactions. The $E_{\mathrm{T}}^{\mathrm{miss}}$ distributions obtained from different A14 variations are compared, and the largest variation with respect to the nominal in each $E_{\mathrm{T}}^{\mathrm{miss}}$ bin is taken as the tune uncertainty.

The relative scale, PDF, and tune uncertainties of signal events in the vector mediator simplified model, which are applied in each $E_{\mathrm{T}}^{\mathrm{miss}}$ bin are listed in Table 9.10. The uncertainties in the different $E_{\mathrm{T}}^{\mathrm{miss}}$ bins are fully correlated and described by a

single component in the statistical model for scale, PDF, and tune signal uncertainty, respectively.

**Tab. 9.10.:** Relative scale, PDF, and tune uncertainties of dark matter signals in the vector mediator simplified model, which are obtained from studied on generator level.

| $E_{\mathrm{T}}^{\mathrm{miss}}$ bin | Uncertainty | | |
|---|---|---|---|
| | Scale | PDF | Tune |
| 150 GeV to 250 GeV | 1.0 % | 1.0 % | 1.5 % |
| 250 GeV to 350 GeV | 2.0 % | 2.0 % | 3.0 % |
| 350 GeV to 500 GeV | 2.5 % | 3.0 % | 5.0 % |
| 500 GeV to 800 GeV | 3.0 % | 5.0 % | 7.0 % |
| 800 GeV to 1500 GeV | 6.0 % | 6.0 % | 8.5 % |

The theoretical uncertainties for the dark matter signals in the $a$-2HDM simplified model are estimated in a similar way on particle level neglecting detector effects.

- The **scale and parton shower** uncertainties are estimated by varying the renormalisation scale $\mu_{\mathrm{R}}$ and factorisation scale $\mu_{\mathrm{F}}$ coherently by factors of $0.5$ and $2$. In addition, samples generated with MADGRAPH + PYTHIA 8 are compared with samples generated with MADGRAPH + HERWIG 7 to estimate the uncertainty associated with the parton shower modelling.
- The **PDF** uncertainties are estimated by considering the parametrised uncertainty of the nominal NNPDF30LO PDF set and comparing it to the CT10 [270] and MMHT2014LO68CL [241] PDF sets.

For all signal points, a normalisation uncertainty of $9\,\%$ is applied to account for variations of the scale and parton shower uncertainties. An additional normalisation uncertainty of $1\,\%$ associated with the PDF set is considered.

## 9.7 Statistical model

The statistical model is based on the likelihood function Equation (6.11). The profile likelihood fit is based on the various $b$-tag and event topology categories of the SR, VR, and CRs and exploits the shape information provided by the $E_{\mathrm{T}}^{\mathrm{miss}}$ and $E_{\mathrm{T}}^{\mathrm{miss,no}\ell}$ distributions. A summary of all regions and kinematic distributions considered in the statistical model is provided in Table 9.11.

## 9.8 Results

The results of the $E_{\mathrm{T}}^{\mathrm{miss}} + V(q\bar{q})$ search are presented in this section. The observed results are presented in Section 9.8.1. The impact of groups of systematic uncertainty on the sensitivity of the search is discussed in Section 9.8.2. Finally, the results are

Tab. 9.11.: Summary of all regions and kinematic distributions considered in the statistical analysis of the $E_{\mathrm{T}}^{\mathrm{miss}} + V(q\bar{q})$ search.

| | 0 leptons | 1 muon | 2 leptons |
|---|---|---|---|
| Process of interest | signal | W + jets, $t\bar{t}$ | Z + jets |
| Fitted observable | $E_{\mathrm{T}}^{\mathrm{miss}}$ | $E_{\mathrm{T}}^{\mathrm{miss,no}\ell}$ | $E_{\mathrm{T}}^{\mathrm{miss,no}\ell}$ |
| Binning | merged topology: $[250, 350, 500, 800, 1500]$ GeV<br>resolved topology: $[150, 250, 350, 500, 800, 1500]$ GeV | | |
| Categories | 0, 1, and 2 $b$-tag categories<br>W/ Z mass window and upper mass side-band<br>HP / LP SR | | |

interpreted to constrain the parameter space of simplified models for dark matter production in Section 9.8.3 and Section 9.8.4.

### 9.8.1 Observed results

The background description by the statistical model is validated by performing a conditional background-only ($\mu = 0$) fit and investigating the corresponding distributions in the VR and the CRs. The $E_{\mathrm{T}}^{\mathrm{miss}}$ distributions in the validation region after the background-only ($\mu = 0$) fit to the data are shown in Figure 9.13.

Figure 9.14 and Figure 9.15 show the 1 muon and 2 lepton CRs, respectively. The observed data are in good agreement with the SM background prediction, thereby validating the background description.

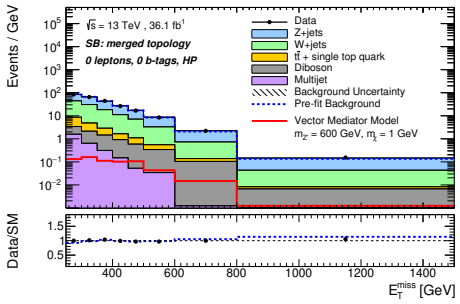
The results of the profile likelihood fit of the statistical model to the data are reported in terms of the discovery significance, which is listed for vector mediator simplified model dark matter signals with $m_{\chi} = 1\,\mathrm{GeV}$ and varying $m_{\mathrm{Z}'}$ in Table 9.12.

Tab. 9.12.: Expected median discovery significance $Z^{\mathrm{exp}}$ estimated with the Asimov dataset generated under the assumption of the nominal signal model ($\mu = 1$) and observed discovery significance $Z^{\mathrm{obs}}$ for vector mediator simplified model dark matter signals with $m_{\chi} = 1\,\mathrm{GeV}$ and the couplings $g_q = 0.25$, $g_{\chi} = 1$.

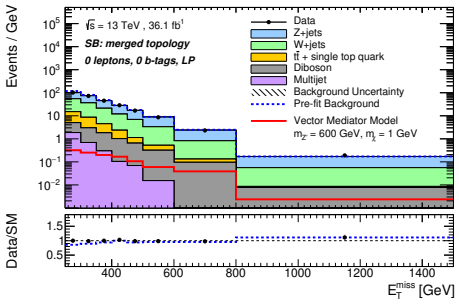
| $m_{\mathrm{Z}'}$ | 10 GeV | 100 GeV | 200 GeV | 300 GeV | 400 GeV | 500 GeV | 600 GeV | 700 GeV | 800 GeV | 900 GeV | 1000 GeV |
|---|---|---|---|---|---|---|---|---|---|---|---|
| $Z^{\mathrm{exp}}$ | 26.97 | 9.31 | 5.04 | 3.67 | 3.60 | 3.47 | 2.26 | 1.99 | 1.68 | 1.33 | 1.13 |
| $Z^{\mathrm{obs}}$ | 0 | 0.3 | 0.3 | 0 | 0 | 0.11 | 0 | 0 | 0.61 | 0.31 | 0 |

No significant deviations from the background-only hypothesis have been observed. Therefore, the results in SR are presented with the background normalisations scaled to the outcome of the conditional background-only ($\mu = 0$) fit.

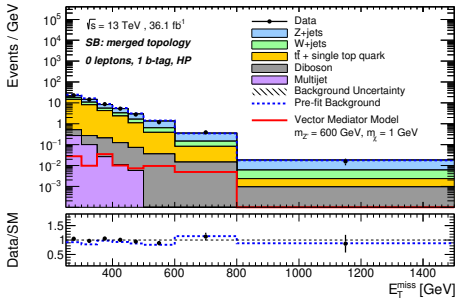
The observed number of events selected by the SR requirements in each category is shown in Table 9.13 for the merged event topology and in Table 9.14 for the resolved event topology. The expected number of events for a representative vector



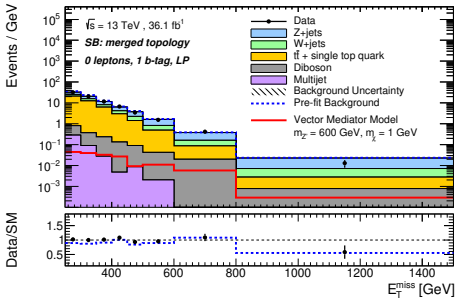

(a) merged 0 $b$-tag high purity



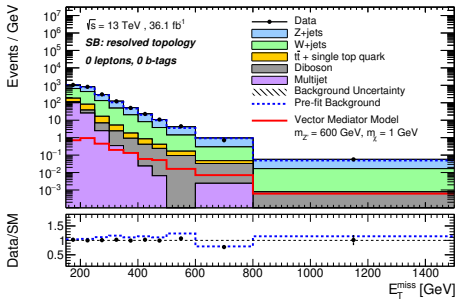

(b) merged 0 $b$-tag low purity



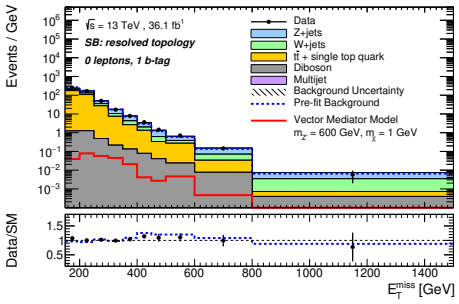

(c) merged 1 $b$-tag high purity



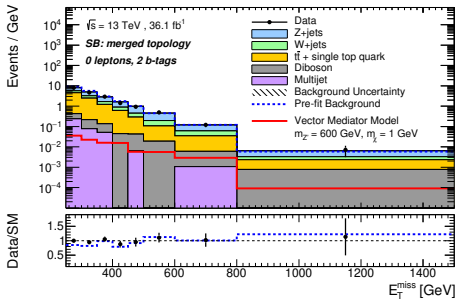

(d) merged 1 $b$-tag low purity



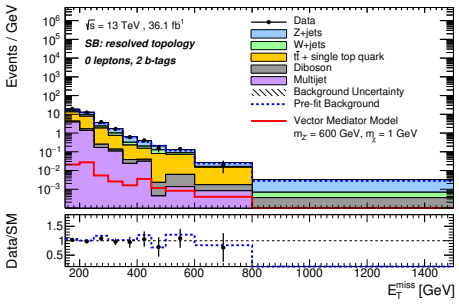

(e) resolved 0 $b$-tag




(f) resolved 1 $b$-tag

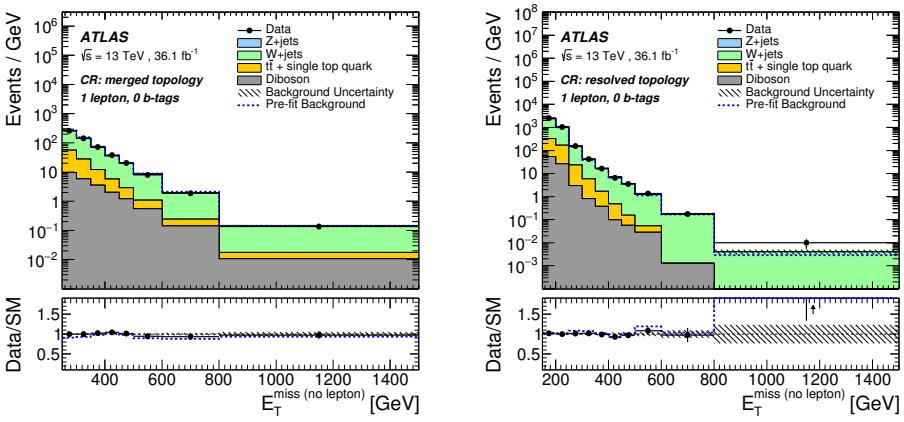



(g) merged 2 $b$-tag




(h) resolved 2 $b$-tag

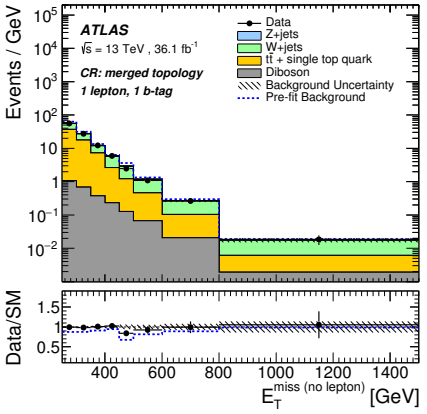
**Fig. 9.13.:** The $E_{\mathrm{T}}^{\mathrm{miss}}$ distributions in the 0 lepton VR after the background-only fit ($\mu = 0$) for data (dots) SM background prediction (histograms), shown separately for the merged-topology and resolved-topology event categories with 0 $b$-tags, 1 $b$-tag, and 2 $b$-tags. The expected distribution of a representative vector mediator simplified model with $m_{\chi} = 1\,\mathrm{GeV}$ and $m_{\mathrm{Z}'} = 600\,\mathrm{GeV}$ normalised to the theory prediction is overlaid. The total background contribution before the fit to the data is shown as a dotted blue line. The hatched area represents the total background uncertainty. The inset at the bottom of each plot shows the ratio of the data to the total post-fit (dots) and pre-fit (dotted blue line) background expectation.



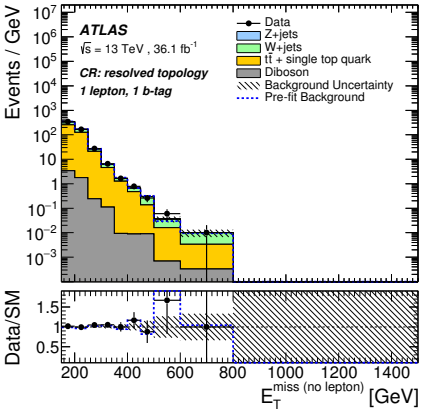

(a) merged 0 $b$-tag



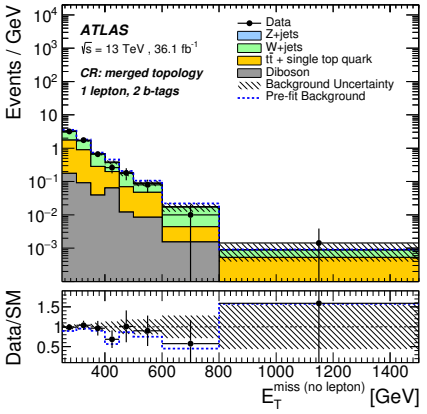

(b) resolved 0 $b$-tag



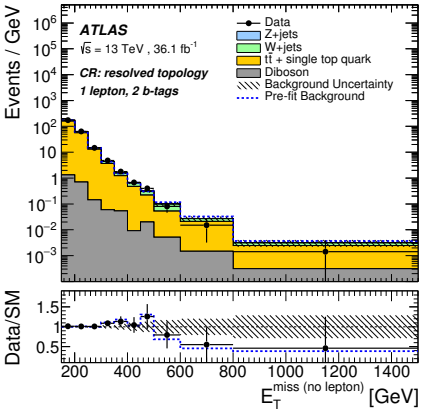

(c) merged 1 $b$-tag




(d) resolved 1 $b$-tag

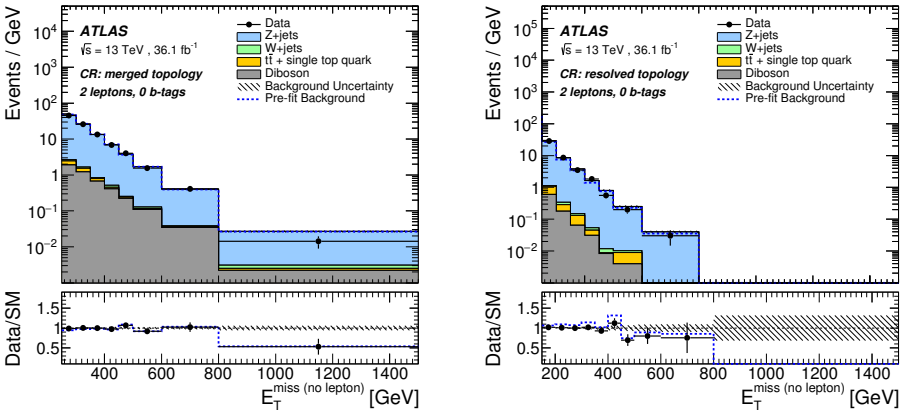



(e) merged 2 $b$-tag




(f) resolved 2 $b$-tag

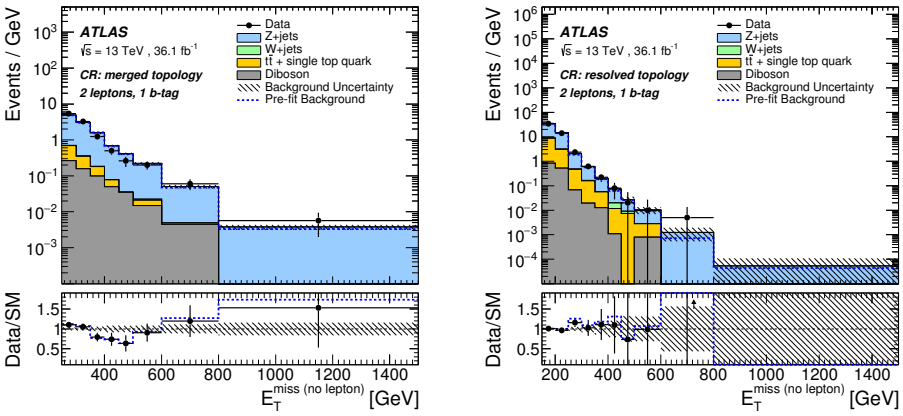
**Fig. 9.14.:** The $E_{\mathrm{T}}^{\mathrm{miss,no}\ell}$ distributions in the 1 muon CR (W/ Z mass window) after the background-only fit ($\mu = 0$) for data (dots) SM background prediction (histograms), shown separately for the merged-topology (left) and resolved-topology (right) event categories with 0 $b$-tags (top), 1 $b$-tag (middle), and 2 $b$-tags (bottom). The total background contribution before the fit to the data is shown as a dotted blue line. The hatched area represents the total background uncertainty. The inset at the bottom of each plot shows the ratio of the data to the total post-fit (dots) and pre-fit (dotted blue line) background expectation.




(a) merged 0 $b$-tag



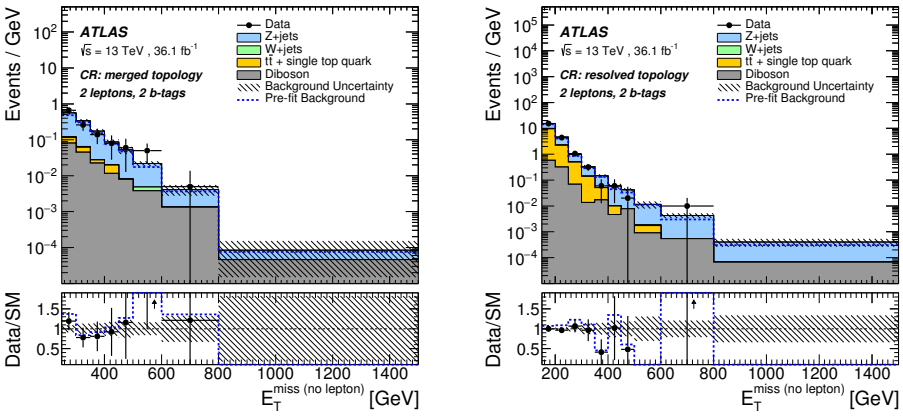

(b) resolved 0 $b$-tag




(c) merged 1 $b$-tag




(d) resolved 1 $b$-tag




(e) merged 2 $b$-tag




(f) resolved 2 $b$-tag

**Fig. 9.15.:** The $E_{\mathrm{T}}^{\mathrm{miss,no}\ell}$ distributions in the 2 lepton CR (W/ Z mass window) after the background-only fit ($\mu = 0$) for data (dots) SM background prediction (histograms), shown separately for the merged-topology (left) and resolved-topology (right) event categories with 0 $b$-tags (top), 1 $b$-tag (middle), and 2 $b$-tags (bottom). The total background contribution before the fit to the data is shown as a dotted blue line. The hatched area represents the total background uncertainty. The inset at the bottom of each plot shows the ratio of the data to the total post-fit (dots) and pre-fit (dotted blue line) background expectation.

mediator simplified signal model is shown together with the expected number of events for individual background processes, whose normalisation is determined by the background-only profile likelihood fit, and the observed events in data.

**Tab. 9.13.:** Expected and observed numbers of events in the merged event topology signal region for an integrated luminosity of $36.1\,\text{fb}^{-1}$ and $\sqrt{s} = 13\,\text{TeV}$. The background yields and uncertainties are shown after the profile-likelihood fit to the data. In addition, the expected event yield for a vector mediator model with $m_{Z'} = 600\,\text{GeV}$ and $m_\chi = 1\,\text{GeV}$ is shown. The quoted background uncertainties include both the statistical and systematic contributions.

| Process | Signal region merged topology | | | | |
|---|---|---|---|---|---|
| | 0 $b$-tag | | 1 $b$-tag | | 2 $b$-tag |
| | HP | LP | HP | LP | |
| Vector model signal | 285 ± 21 | 270 ± 18 | 31 ± 3.6 | 29.1 ± 2.7 | 17.0 ± 1.7 |
| W+ jets | 3 170 ± 130 | 10 000 ± 380 | 220 ± 28 | 890 ± 110 | 91.2 ± 12 |
| Z + jets | 4 750 ± 200 | 16 000 ± 590 | 470 ± 52 | 1 640 ± 180 | 186 ± 12 |
| $t\bar{t}$ | 775 ± 48 | 940 ± 60 | 630 ± 27 | 702 ± 35 | 50.2 ± 11 |
| Single top-quark | 159 ± 12 | 200 ± 13 | 89 ± 6.7 | 125 ± 8.7 | 16.1 ± 1.7 |
| Diboson | 774 ± 110 | 960 ± 140 | 88 ± 14 | 115 ± 18 | 54.0 ± 9.7 |
| Multijet | 11.9 ± 35 | 49 ± 140 | 3.7 ± 3.3 | 14.7 ± 13 | 9.32 ± 9.4 |
| Total background | 9 640 ± 87 | 28 000 ± 150 | 1 500 ± 31 | 3 490 ± 52 | 407 ± 15 |
| Data | 9 627 | 27 856 | 1 502 | 3 525 | 414 |

The corresponding $E_{\text{T}}^{\text{miss}}$ distributions are shown in Figure 9.16 for the merged and resolved event topologies. No significant excess over the SM background is observed.

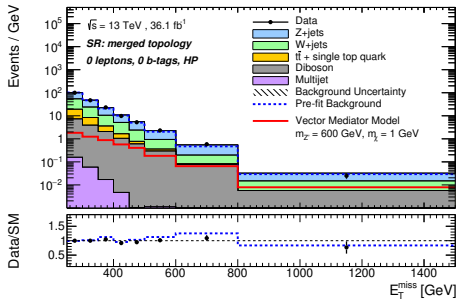
## 9.8.2 Impact of systematic uncertainties

The different sources of systematic uncertainty affect the sensitivity of the search. Their impact on the fitted signal strength $\mu$ is evaluated using the Asimov dataset (c.f. Section 6.2) including the signal process normalised to its theoretical expectation. The relevance of a certain NP $\theta_i$ can be estimated as a fractional uncertainty on the fitted signal strength by performing a fit with $\theta_i$ set to its nominal value, thereby excluding the NP from the fit, and subtracting in quadrature the resulting uncertainty on $\mu$ from the total uncertainty on $\mu$

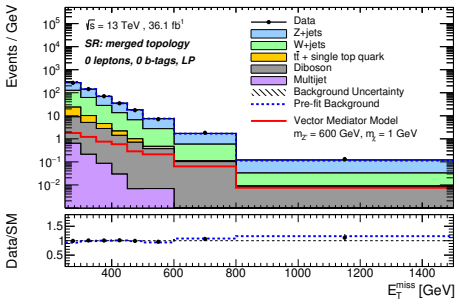
$$\sigma_{\theta_i} = \sqrt{\sigma^2_{\text{total}} - \sigma^2_{\theta_i\text{fixed}}}. \tag{9.9}$$

In practice, this procedure is not conducted for individual NPs but for groups of NPs to identify the sources of largest impact on the sensitivity. The total statistical uncertainty is evaluated by neglecting all groups of systematic uncertainties in the fit.

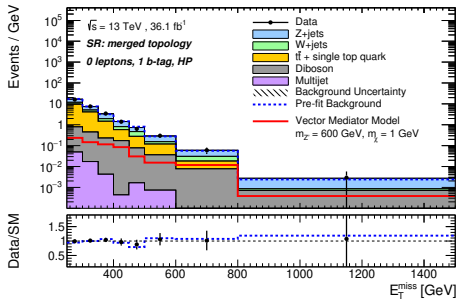
Table 9.15 shows a breakdown of the expected signal strength uncertainties for three representative vector mediator simplified model signals. The estimate is based on the Asimov data set generated under the assumption of the nominal signal model.



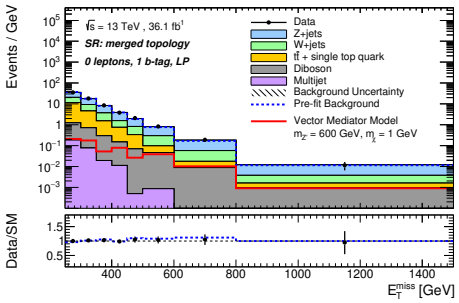

(a) merged 0 $b$-tag high purity



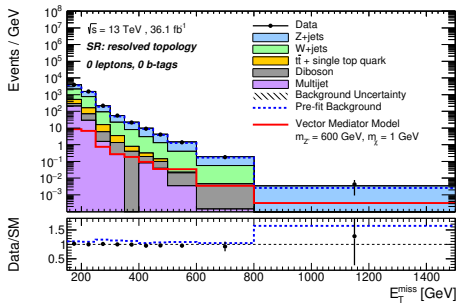

(b) merged 0 $b$-tag low purity



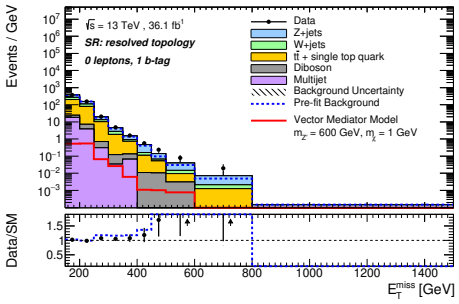

(c) merged 1 $b$-tag high purity



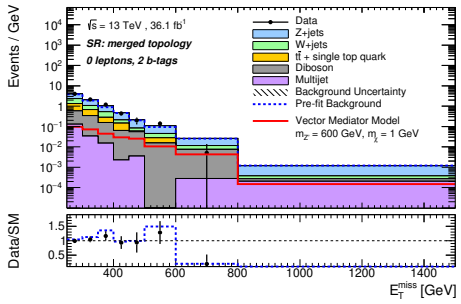

(d) merged 1 $b$-tag low purity



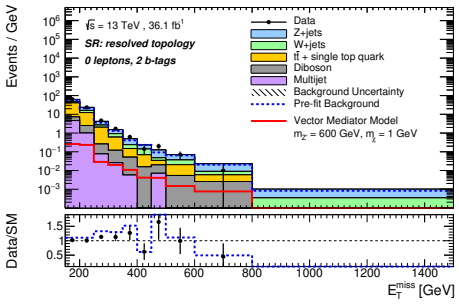

(e) resolved 0 $b$-tag




(f) resolved 1 $b$-tag




(g) merged 2 $b$-tag




(h) resolved 2 $b$-tag

**Fig. 9.16.:** The $E_{\mathrm{T}}^{\mathrm{miss}}$ distributions in the 0 lepton SR after the background-only fit ($\mu = 0$) for data (dots) SM background prediction (histograms), shown separately for the merged-topology and resolved-topology event categories with 0 $b$-tags, 1 $b$-tag, and 2 $b$-tags. The expected distribution of a representative vector mediator simplified model with $m_{\chi} = 1\,\mathrm{GeV}$ and $m_{\mathrm{Z}'} = 600\,\mathrm{GeV}$ normalised to the theory prediction is overlaid. The total background contribution before the fit to the data is shown as a dotted blue line. The hatched area represents the total background uncertainty. The inset at the bottom of each plot shows the ratio of the data to the total post-fit (dots) and pre-fit (dotted blue line) background expectation.

Tab. 9.14.: Expected and observed numbers of events in the resolved event topology signal region for an integrated luminosity of $36.1\,\text{fb}^{-1}$ and $\sqrt{s} = 13\,\text{TeV}$. The background yields and uncertainties are shown after the profile-likelihood fit to the data. In addition, the expected event yield for a vector mediator model with $m_{Z'} = 600\,\text{GeV}$ and $m_{\chi} = 1\,\text{GeV}$ is shown. The quoted background uncertainties include both the statistical and systematic contributions.

| Process | Signal region resolved topology | | |
|---|---|---|---|
| | 0 $b$-tag | 1 $b$-tag | 2 $b$-tag |
| Vector model signal | 845 ± 29 | 59.3 ± 3.4 | 27.1 ± 1.2 |
| W + jets | 117 000 ± 4 600 | 5 000 ± 680 | 598 ± 98 |
| Z + jets | 135 000 ± 5 600 | 7 710 ± 780 | 1 220 ± 67 |
| $t\bar{t}$ | 13 800 ± 780 | 12 100 ± 420 | 2 050 ± 70 |
| Single top-quark | 2 360 ± 140 | 1 150 ± 71 | 222 ± 14 |
| Diboson | 6 880 ± 950 | 514 ± 71 | 228 ± 34 |
| Multijet | 11 900 ± 2 300 | 1 130 ± 370 | 288 ± 150 |
| Total background | 288 000 ± 570 | 27 600 ± 170 | 4 600 ± 90 |
| Data | 287 722 | 27 586 | 4 642 |

The first signal with $m_{Z'} = 200\,\text{GeV}$ corresponds to a large production cross-section, which is clearly excluded, and a relatively soft $E_{\text{T}}^{\text{miss}}$ distribution. The second signal corresponds to a sizeable production cross-section, which is at the expected exclusion boundary, and a somewhat harder $E_{\text{T}}^{\text{miss}}$ distribution. The third signal corresponds to a very low production cross-section, which is scaled by a factor of 10, and a hard tail in the $E_{\text{T}}^{\text{miss}}$ distribution.

The dominant sources of uncertainty are due to large-radius jets, the normalisation of the irreducible Z + jets and diboson background processes, modelling uncertainties in signal and $V$ + jets processes, and the statistical uncertainty in the background prediction. The impact of large-radius jet and $E_{\text{T}}^{\text{miss}}$ uncertainties for the second and third signals increases because the harder $E_{\text{T}}^{\text{miss}}$ distributions, which increase the relevance of the merged topology. The statistical uncertainty in the background prediction is larger in the merged category. Therefore, its impact is increased for signals with harder $E_{\text{T}}^{\text{miss}}$ distributions.

### 9.8.3 Constraints on the spin-1 Z′ mediator simplified model

As no significant deviation from the SM background expectation is observed for any of the signal mass points, the parameter space of the spin-1 Z′ mediator simplified model can be constrained by computing upper limits on the signal strength $\mu$ at 95 % confidence level using the $\text{CL}_s$ method [307].

Tab. 9.15.: Breakdown of expected signal strength uncertainties for three vector mediator simplified model signals each with $m_\chi = 1\,\text{GeV}$ and (a) $m_{Z'} = 200\,\text{GeV}$, (b) $600\,\text{GeV}$, and (c) $2000\,\text{GeV}$. The estimate is based on the Asimov data set generated under the assumption of the nominal signal model. The production cross-section of signal (c) is scaled by a factor of 10. Each systematic uncertainty contribution is provided as the quadratic difference between the total uncertainty and the uncertainty obtained by setting the systematic uncertainty in question to its nominal value and excluding it thereby from the fit. Total denotes the quadrature sum of statistical and total systematic uncertainties.

| Source of uncertainty | Uncertainty on $\mu$ [%] (a) | (b) | (c) |
|---|---|---|---|
| Large-radius jets | 9 | 20 | 19 |
| Small-radius jets | 3 | 8 | 10 |
| Electrons | 4 | 9 | 12 |
| Muons | 6 | 7 | 4 |
| $E_{\text{T}}^{\text{miss}}$ | 1 | 4 | 7 |
| $b$-tagging (track jets) | 4 | 4 | 6 |
| $b$-tagging (small-radius jets) | 2 | 4 | 2 |
| Luminosity | 3 | 4 | 4 |
| Multijet normalisation | 7 | 11 | 10 |
| Diboson normalisation | 5 | 11 | 13 |
| Z + jets normalisation | 5 | 9 | 12 |
| W + jets normalisation | 3 | 4 | 5 |
| $\text{t}\bar{\text{t}}$ normalisation | 3 | 1 | 3 |
| Signal modelling | 7 | 9 | 10 |
| $V$ + jets modelling | 4 | 10 | 14 |
| $V$ + jets composition | 1 | 3 | 3 |
| $\text{t}\bar{\text{t}}$ modelling | 2 | 4 | 3 |
| Diboson modelling | 1 | 2 | 2 |
| Background MC stat. | 10 | 18 | 24 |
| Total syst. | 21 | 40 | 49 |
| Data stat. | 7 | 21 | 45 |
| Total | 22 | 45 | 67 |

The exclusion limits on the vector mediator signals, which were simulated at LO accuracy in QCD, are scaled to an implementation of the spin-1 Z′ mediator simplified model at next-to-leading-order (NLO) accuracy [115] for vector and axial-vector couplings of the mediator.

Samples based on the NLO implementation have been simulated at particle level neglecting detector effects using the MADGRAPH5_aMC@NLO 2.4.2 event generator [23] interfaced to the PYTHIA 8.186 [320] parton shower model with the NNPDF30 PDF set [118] at NLO accuracy in QCD and $\alpha_s(m_{\mathrm{Z}}^2) = 0.118$. These samples are used to re-weight the simulated vector mediator MC samples, following the procedure outlined in Ref. [333]. The re-weighting takes accounts for changes in the product of acceptance and efficiency and in the predicted cross-sections due to the implementation of the model at NLO accuracy and the modified couplings.

The limits are provided in the two-dimensional $m_{\mathrm{Z}'}$-$m_\chi$ plane for vector and axial-vector mediator couplings with the fixed choice of coupling parameters $g_q = 0.25$, $g_\ell = 0$, and $g_\chi = 1$. The corresponding exclusion contours are shown in Figure 9.17.

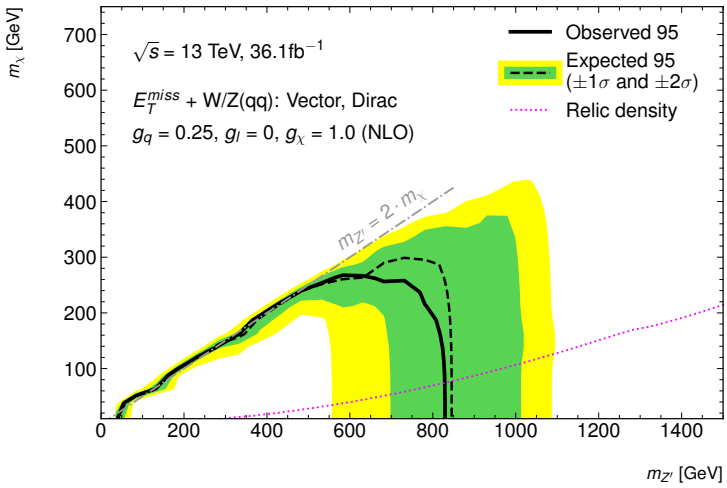
Signals with vector mediator masses $m_{\mathrm{Z}'}$ of up to $830\,\mathrm{GeV}$ and dark matter masses of up to $280\,\mathrm{GeV}$ are excluded at $95\,\%$ CL$_s$. The exclusion contour for axial-vector mediator signals has similar coverage in $m_{\mathrm{Z}'}$ but smaller coverage in the on-shell region, defined by the kinematic limit $2m_\chi < m_{\mathrm{Z}'}$, as the signal strength $\mu$ decreases more strongly for axial-vector mediators compared to vector mediators as $m_{\mathrm{Z}'}$ increases.

### 9.8.4 Constraints on the $a$-2HDM simplified model

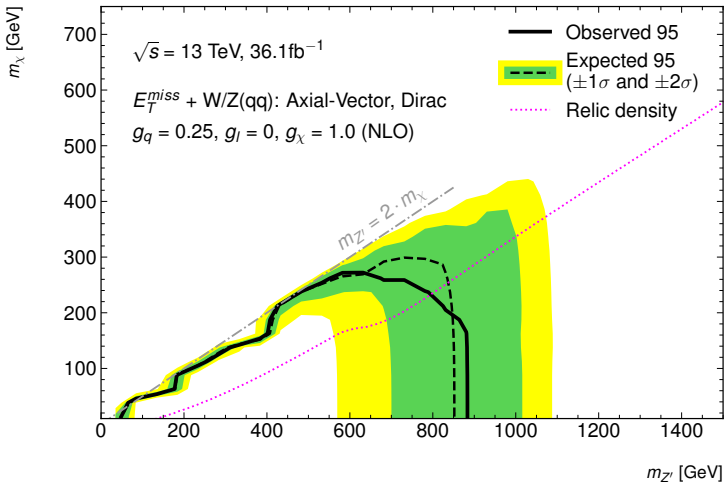
The signature of the $E_{\mathrm{T}}^{\mathrm{miss}} + V(q\bar{q})$ search allows placing limits also on the $a$-2HDM simplified model. The sensitivity of the $E_{\mathrm{T}}^{\mathrm{miss}}$+W channel is expected to be negligible for the $a$-2HDM model compared to the $E_{\mathrm{T}}^{\mathrm{miss}}$ + Z channel. Therefore, only the latter is considered for the interpretation in terms of this model.

The subset of the simulated signal samples with $m_{\mathrm{H}} < 800\,\mathrm{GeV}$ is generated using a simplified parametrisation of the calorimeter response, which is known to describe the jet substructure in simulated events inadequately. Therefore, only the resolved event topology selection, which does not consider large-radius jet substructure, is considered for calculating limits on these signal points.

Figure 9.18 shows the exclusion contour at at $95\,\%$ CL$_s$ in the $m_{\mathrm{H}}$-$m_a$ plane of the parameter space for the fixed choice of parameters $\tan\beta = 1.0$, $m_\chi = 10\,\mathrm{GeV}$, and $\sin\theta = 0.35$. The $a$-2HDM signals with heavy Higgs boson masses $m_H$ in the range $800\,\mathrm{GeV}$ to $1050\,\mathrm{GeV}$ and pseudo-scalar mediator masses of up to $200\,\mathrm{GeV}$ are excluded at $95\,\%$ CL$_s$. The observed limit extends to higher $m_H$ than the predicted ones.




(a) Vector mediator simplified model




(b) Axial-vector simplified model

**Fig. 9.17.:** Exclusion contours at $95\,\%$ $\mathrm{CL}_s$ for the $V/A$ simplified model at NLO accuracy for vector mediator (top) and axial-vector mediator (bottom) with couplings $g_q = 0.25$, $g_\ell = 0$, and $g_\chi = 1$. The black dashed line shows the median of the expected limit, whereas the solid line shows the observed limit. The dotted magenta curve corresponds to the set of points for which the relic density predicted by the vector mediator simplified model is consistent with the Planck [301] measurements, as computed with MADDM [25]. The region on the right of the curve corresponds to higher predicted relic density than these measurements.

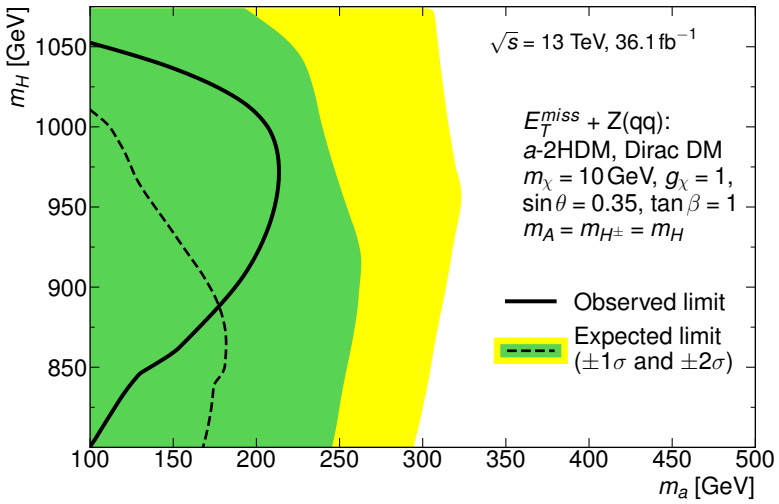


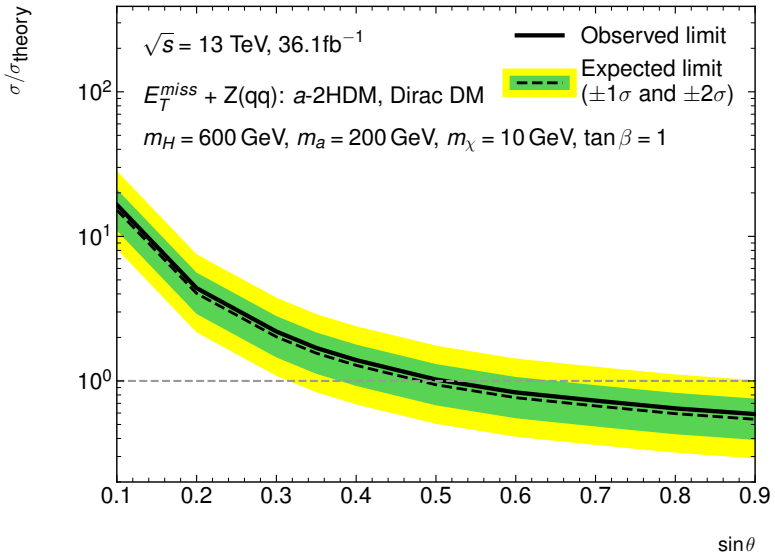

**Fig. 9.18.:** Exclusion contours at 95 % $CL_s$ for the $a$-2HDM model in the two-dimensional $m_H$-$m_a$ plane for the fixed choice of parameters $\tan\beta = 1.0$, $m_\chi = 10\,\text{GeV}$, and $\sin\theta = 0.35$.

Figure 9.19 shows the exclusion limits on the signal strength $\mu$ for the $a$-2HDM model as a function of $\sin\theta$ for the fixed parameter choices $\tan\beta = 1.0$, $m_\chi = 10\,\text{GeV}$, considering a low-mass scenario with $m_H = 600\,\text{GeV}$, $m_a = 200\,\text{GeV}$, and a high-mass scenario with $m_H = 1000\,\text{GeV}$, $m_a = 350\,\text{GeV}$. The sensitivity improves as a function of $\sin\theta$, as the cross-section increases with $\sin\theta$. Limits on $\sin\theta > 0.5$ can only be placed for the low-mass scenario, while the search is not yet sensitive to the high-mass scenario.

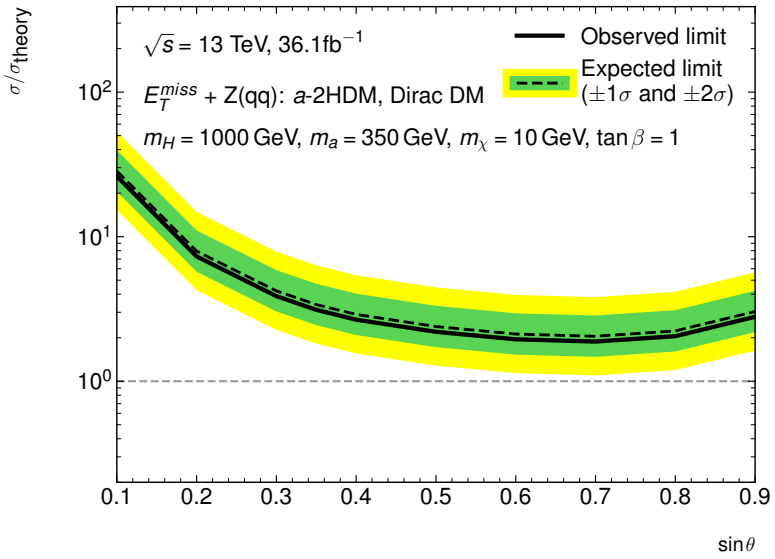
Figure 9.20 shows the exclusion limit on the signal strength $\mu$ in dependence of the dark matter mass $m_\chi$ for the fixed choices of the parameters $\tan\beta = 1.0$, $m_H = 600\,\text{GeV}$, $m_a = 250\,\text{GeV}$, and $\sin\theta = 0.35$. The limit is flat in the on-shell region $2m_\chi < m_a$, strongly increases around the threshold $2m_\chi = 250\,\text{GeV}$ through resonant enhancement, and steeply drops off in the off-shell region.

## 9.9 Conclusion of the $E_T^{miss} + V(q\bar{q})$ search

In conclusion, the $E_T^{miss} + V(q\bar{q})$ search is relevant for probing models of dark matter production at particle colliders with varying degrees of complexity. The use of large-radius jets and jet substructure allows exploring signatures with highly boosted weak vector bosons and is complementary to the reconstruction of weak vector boson candidates with a moderate boost. The signature of $E_T^{miss} + V(q\bar{q})$ is furthermore relevant for measurements of the invisible decays of the Higgs boson and has been used in a combination to place a 95 % $CL_s$ upper limit of 26 % on the branching fraction of invisible Higgs boson decays [39].




(a) Low-mass scenario $m_{\mathrm{H}} = 600\,\mathrm{GeV}$, $m_a = 200\,\mathrm{GeV}$




(b) High-mass scenario $m_{\mathrm{H}} = 1000\,\mathrm{GeV}$, $m_a = 350\,\mathrm{GeV}$

**Fig. 9.19.:** Observed exclusion limits at 95 % $\mathrm{CL}_s$ on the signal strength $\mu$ for the $a$-2HDM model as a function of $\sin\theta$, shown for parameters corresponding to a low-mass scenario (top) and a high-mass scenario (bottom).

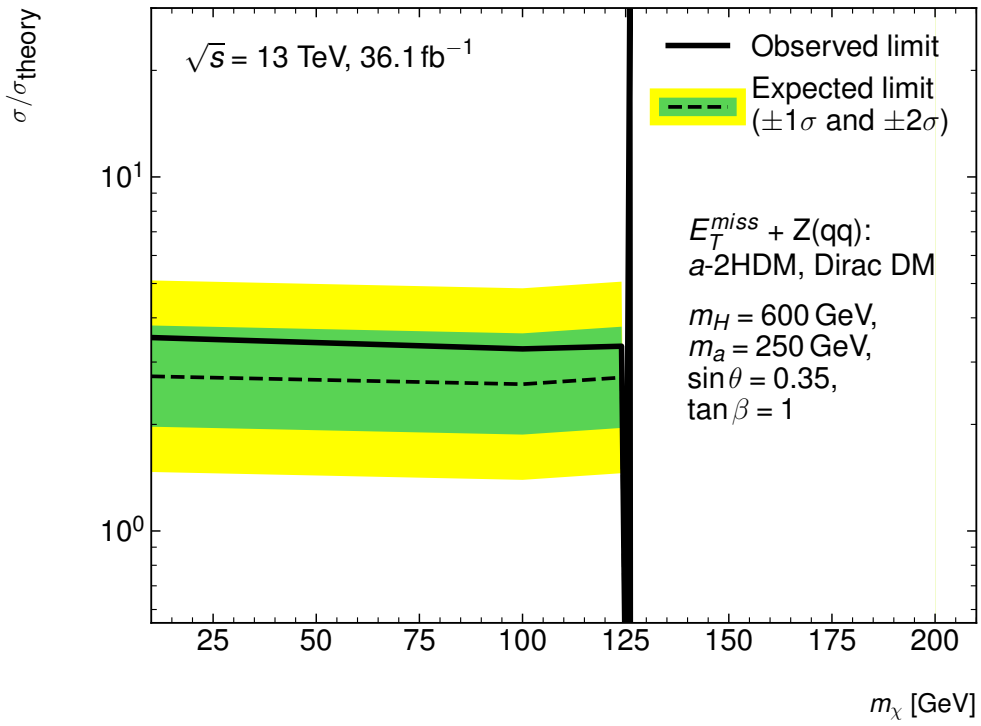



**Fig. 9.20.:** Exclusion limits at 95 % $\text{CL}_s$ on the signal strength $\mu$ for the $a$-2HDM model as a function of $m_\chi$ for the fixed choices of the parameters $\tan\beta = 1.0$, $m_\text{H} = 600\,\text{GeV}$, $m_a = 250\,\text{GeV}$, and $\sin\theta = 0.35$.

# 10 Search for dark matter in association with a Higgs boson decaying to $b$-quarks

## 10.1 Introduction

This chapter describes the search for dark matter in association with a Higgs boson h decaying to $b$-quarks, referred to as $E_{\mathrm{T}}^{\mathrm{miss}}+\mathrm{h}(\mathrm{b\bar{b}})$. The signature of the signal process is missing transverse momentum originating from the production of dark matter particles $\chi$ and a pair of $b$-tagged jets from the Higgs boson decay. Searches for dark matter produced in association with Higgs bosons enable a direct investigation of the interaction of dark matter with the Higgs boson, as the initial state radiation of Higgs bosons is strongly Yukawa-suppressed. The various decay modes of the Higgs boson allow for searches in final states with $b$-quarks, vector boson pairs, photons, and $\tau$ leptons. This search focuses on the Higgs boson decaying to $b$-quarks, as it is the decay mode with the largest branching fraction $\mathcal{B}=57\,\%$ [159].

Searches for dark matter in the $E_{\mathrm{T}}^{\mathrm{miss}}+\mathrm{h}(\mathrm{b\bar{b}})$ final state have been carried out by the ATLAS collaboration using $20.3\,\mathrm{fb}^{-1}$ pp collision data collected at a centre-of-mass energy $\sqrt{s}=8\,\mathrm{TeV}$ [93] and using up to $36.1\,\mathrm{fb}^{-1}$ pp collision data collected at a centre-of-mass energy $\sqrt{s}=13\,\mathrm{TeV}$ [85, 92]. Similar searches have been carried out also by the CMS collaboration [164, 170, 167].

This search is based on proton-proton collision data at a centre-of-mass energy of $13\,\mathrm{TeV}$ recorded in the years 2015 – 2017 with the ATLAS detector at the LHC, corresponding to an integrated luminosity of $79.8\,\mathrm{fb}^{-1}$.

Besides the more extensive data sample, the search benefits from two novel reconstruction techniques, which result in enhanced sensitivity to previous results. The improved identification of $b$-jets which is based on track jets with a variable radius parameter enhances the reconstruction efficiency of highly boosted Higgs boson candidates. The use of an object-based $E_{\mathrm{T}}^{\mathrm{miss}}$ significance, which fully accounts for the resolutions and correlations of the objects entering the $E_{\mathrm{T}}^{\mathrm{miss}}$ reconstruction, enables the efficient suppression of processes with fake $E_{\mathrm{T}}^{\mathrm{miss}}$. The results of this search have been presented in Ref. [91].

Section 10.2 introduces the signal and background processes in the $E_{\mathrm{T}}^{\mathrm{miss}}+\mathrm{h}(\mathrm{b\bar{b}})$ search. The analysis strategy is outlined in Section 10.3. The object and event selection, including the definition of the signal region, is described in Section 10.4, whereas the background estimation strategy and the definitions of the control regions are described in Section 10.5. The systematic uncertainties taken into account in the

statistical model are described in Section 10.6, while the statistical model itself is provided in Section 10.7. Finally, the observed results are presented and discussed in Section 10.8. A conclusion is given in Section 10.9.

## 10.2 Signal and background processes

The analysis investigates dark matter production in the framework of the Z′-2HDM simplified model, which is described in Section 10.2.1. The background processes are described in Section 10.2.2. The simulated signal and background samples are summarised in Section 10.2.3.

### 10.2.1 Z′-2HDM simplified model

The Z′-2HDM simplified model, a type-II two-Higgs-doublet model (2HDM) with an additional $\mathrm{U}(1)_{\mathrm{Z}'}$ gauge symmetry (c.f. Section 3.7.3), is considered for the optimisation of the search and the interpretation of its results. The process yielding the signature of $E_{\mathrm{T}}^{\mathrm{miss}} + \mathrm{h}(\mathrm{b\bar{b}})$ is illustrated in Figure 10.1.

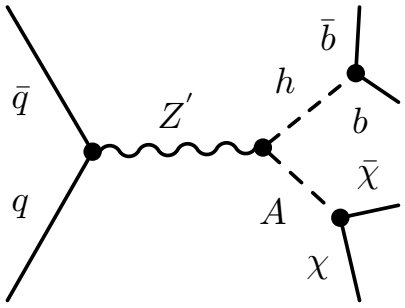



Fig. 10.1.: Production of dark matter particles $\chi$ and a Higgs boson h through a new Z′ mediator coupled to the CP-odd Higgs boson A, where the latter decays primarily to $\chi\bar{\chi}$.

A Z′ vector boson is produced in pp collisions and decays into the neutral Higgs boson h, which is identified with the SM Higgs boson in the alignment limit, and the CP-odd Higgs boson A. The latter decays into dark matter particles, which give rise to missing transverse momentum $E_{\mathrm{T}}^{\mathrm{miss}}$. A characteristic feature of the model is that for heavy Z′ boson masses, the predicted $E_{\mathrm{T}}^{\mathrm{miss}}$ spectra are much harder than for other models describing the $E_{\mathrm{T}}^{\mathrm{miss}} + \mathrm{h}(\mathrm{b\bar{b}})$ signature [7].

The relevant model parameters and their chosen values are listed in Table 10.1. These parameters include the masses of the involved particles $m_{\mathrm{A}}$, $m_{\mathrm{Z}'}$, $m_{\chi}$, and the gauge coupling of the Z′ boson to quarks $g_{\mathrm{Z}'}$. The dark matter particle mass $m_{\chi}$ has negligible impact on the results for $2m_{\chi} < m_{\mathrm{A}}$ and is set to $100\,\mathrm{GeV}$. The value of the ratio of the vacuum expectation values (VEV) of the two Higgs fields is chosen

as 1.0, thereby satisfying perturbativity requirements due to the top-quark Yukawa coupling [129]. As the alignment limit $\alpha = \beta - \pi/2$ is considered, the lightest neutral scalar boson is identified with the SM Higgs boson with $m_{\mathrm{h}} = 125\,\mathrm{GeV}$. The masses of the heavy scalar Higgs boson and of the charged Higgs bosons are set to $m_{\mathrm{H}} = m_{\mathrm{H}^{\pm}} = 300\,\mathrm{GeV}$.

The Z′-2HDM model is used as a benchmark to probe the $E_{\mathrm{T}}^{\mathrm{miss}} + \mathrm{h}(\mathrm{b\bar{b}})$ signature in a generic way. In particular, the discriminating variables deliberately do not exploit the characteristic features of the resonant production of $\mathrm{h}\chi\overline{\chi}$, such as the Jacobian peak in the Higgs boson's $p_{\mathrm{T}}$ distribution with an endpoint at

$$p_{\mathrm{T}}^{\mathrm{h,max.}} = \frac{\sqrt{(m_{\mathrm{Z}'}^2 - m_{\mathrm{h}}^2 - m_A^2)^2 - 4m_{\mathrm{h}}^2 m_A^2}}{2m_{\mathrm{Z}'}}. \tag{10.1}$$

Although the chosen value of $g_q = 0.8$, which was initially recommended by the LHC DM WG [7], is already excluded by dijet searches [40], it is adopted to allow for the direct performance comparison to the results of the previous iteration [92]. The branching fraction of the decay $\mathrm{A} \to \chi\overline{\chi}$ is assumed to be 100 % for the interpretation of the results.

The results of the search are interpreted for a scan over the two-dimensional $m_{\mathrm{Z}'}$-$m_{\mathrm{A}}$ plane for fixed choices of the other model parameters. The scan extends over the range 400 GeV to 3000 GeV in $m_{\mathrm{Z}'}$ and 300 GeV to 800 GeV in $m_{\mathrm{A}}$.

**Tab. 10.1.:** Parameters of the Z′-2HDM simplified model in the $E_{\mathrm{T}}^{\mathrm{miss}} + \mathrm{h}(\mathrm{b\bar{b}})$ search.

| Parameter | Description | Chosen value |
|---|---|---|
| $m_{\mathrm{h}}$ | light CP-event Higgs boson mass | 125 GeV |
| $m_{\mathrm{Z}'}$ | Z′ boson mass | free |
| $m_{\mathrm{A}}$ | CP-odd Higgs boson mass | free |
| $m_{\chi}$ | dark matter particle mass | 100 GeV |
| $m_{\mathrm{H}}$ | heavy Higgs boson mass | 300 GeV |
| $m_{\mathrm{H}^{\pm}}$ | charged Higgs boson mass | 300 GeV |
| $g_{\mathrm{Z}'}$ | Z′ gauge coupling to quarks | 0.8 |
| $\tan\beta$ | ratio of Higgs VEV | 1 |
| $\alpha$ | mixing of h and H | $-\pi/4$ |

### 10.2.2 Background processes

The dominant background processes with the signature of two $b$-jets and substantial $E_{\mathrm{T}}^{\mathrm{miss}}$ are $\mathrm{t\bar{t}}$ production (50 % background contribution), Z + jets production (33 % background contribution), and W + jets production (15 % background contribution).

Sub-dominant background processes include WW, WZ, and ZZ diboson production, single top quark production, SM $Vh, h \to b\bar{b}$ production, and multijet events.

The dominant background processes are estimated using simulated samples, whose normalisation is constrained by control region data. The smaller background processes are estimated purely by simulation. Based on a data-driven estimate, it will be shown in Section 10.5.3 that the multijet background is negligible.

### 10.2.3 Simulated Monte Carlo samples

The signal and background processes with the MC event generators, parton shower models and PDF sets used for their description are summarised in Table 10.2. Detailed descriptions of the background samples are provided in Section 8.2.2.

The signal process in the Z′-2HDM simplified model is simulated on a grid of 53 mass points defined by the mediator mass $m_{Z'}$ and the CP-odd Higgs boson mass $m_A$. The mass of the Z′ boson is scanned in the range 400 GeV to 3000 GeV in steps of 200 GeV and the mass of the CP-odd Higgs boson A is scanned in the range 300 GeV to 800 GeV in 100 GeV steps for the relevant regions of phase space.

The simulated events are generated at leading-order (LO) accuracy in QCD with the MadGraph5_aMC@NLO 2.2.3 event generator [23] interfaced to the Pythia 8.186 [320] parton shower and hadronisation model, using the NNPDF30 PDF set [119] and the A14 set of tuned parameters [37].

**Tab. 10.2.:** List of the signal and background processes with the MC event generators, sets of PDFs and tunes used for their description in the $E_T^{miss} + h(b\bar{b})$ search.

| Process | Generator | PDF / parton shower tune |
|---|---|---|
| **Signal** | | |
| Z′-2HDM simplified model | MadGraph5_aMC@NLO 2.2.3 + Pythia 8.212 | NNPDF30LO / A14 |
| **Top quark** | | |
| $t\bar{t}$ | Powheg-Box 2 + Pythia 8.230 | NNPDF30NLO / A14 |
| t ($s$-channel) | Powheg-Box 2 + Pythia 8.230 | NNPDF30NLO / A14 |
| t ($t$-channel) | Powheg-Box 2 + Pythia 8.230 | NNPDF30NLO / A14 |
| t (W$t$) | Powheg-Box 2 + Pythia 8.230 | NNPDF30NLO / A14 |
| ***V* + jets** | | |
| W + jets | Sherpa 2.2.1 | NNPDF30NNLO / Sherpa-tune |
| Z + jets | Sherpa 2.2.1 | NNPDF30NNLO / Sherpa-tune |
| **Diboson** | | |
| WW | Sherpa 2.2.1 | NNPDF30NLO / Sherpa-tune |
| WZ | Sherpa 2.2.1 | NNPDF30NLO / Sherpa-tune |
| ZZ | Sherpa 2.2.1 | NNPDF30NLO / Sherpa-tune |
| $Vh, h \to b\bar{b}$ | Powheg-Box 2 + Pythia 8.212 | NNPDF30NLO / AZNLO |

## 10.3 Analysis strategy

The signature of dark matter particle production in association with a Higgs boson is provided by missing transverse momentum $E_{\mathrm{T}}^{\mathrm{miss}}$ recoiling against a system of two $b$-jets resulting from the Higgs boson decay $\mathrm{h} \to \mathrm{b\bar{b}}$.

The signal region (SR) is defined by the requirement of substantial $E_{\mathrm{T}}^{\mathrm{miss}}$ and a Higgs boson candidate. In events with a moderately boosted Higgs boson, the Higgs boson candidate can be reconstructed using two well-separated $b$-tagged small-radius jets (resolved event topology). This approach fails for events with a highly boosted Higgs boson, as the smaller separation of the jets due to the Higgs boson's Lorentz boost does not allow for their individual reconstruction. Therefore, it is advantageous to reconstruct the Higgs boson candidate using a single large-radius jet, which is supplemented with sub-jets based on ID tracks to identify the two $b$-quarks.

Consequently, the signal region selection considers both the resolved and the merged event topologies. The distinction between these two categories is provided by $E_{\mathrm{T}}^{\mathrm{miss}}$, which is strongly correlated with the boost of the Higgs boson candidate. The boundary at $500\,\mathrm{GeV}$ is chosen to enhance the sensitivity of the search in the merged category, since for large $E_{\mathrm{T}}^{\mathrm{miss}}$ the SM backgrounds are strongly suppressed. The resolved category provides complementary sensitivity to signals with a moderate boost.

The two event topologies are similar to those considered in the $E_{\mathrm{T}}^{\mathrm{miss}} + V(q\bar{q})$ search, which are illustrated in Figure 9.4.

Further requirements on kinematic properties and the event topology reduce the contribution of background processes. The main discriminating variable in the statistical analysis is the invariant mass of the Higgs boson candidate. Additional information is provided by the coarsely binned $E_{\mathrm{T}}^{\mathrm{miss}}$ distribution. The resolved selection is defined for three $E_{\mathrm{T}}^{\mathrm{miss}}$ bins, which extend from $150\,\mathrm{GeV}$ to $200\,\mathrm{GeV}$, $200\,\mathrm{GeV}$ to $350\,\mathrm{GeV}$, and $350\,\mathrm{GeV}$ to $500\,\mathrm{GeV}$. The merged selection is defined for events with more than $500\,\mathrm{GeV}$.

The control regions (CRs) are defined by the lepton multiplicity in the event (c.f. Section 8.1) and cover a similar phase-space as the SR. As SR and CRs have different requirements on the lepton multiplicity, they do not overlap. The SR selection vetoes events containing electrons or muons. The control regions, in turn, require the presence of either one muon (1 muon CR) or two electrons or muons (2 lepton CR). Instead of $E_{\mathrm{T}}^{\mathrm{miss}}$, the 1 muon selection employs the $E_{\mathrm{T}}^{\mathrm{miss,no}\mu}$ variable, which is constructed by adding the muon momentum vector to $E_{\mathrm{T}}^{\mathrm{miss}}$. Similarly, the 2 muon selection uses the transverse momentum of the dilepton system $p_{\mathrm{T}}^{\ell\ell}$. These variables emulate the way how the background processes can enter the SR.

The SR and CRs considered in the analysis are

- 0 lepton SR with no electrons and no muons, requiring two $b$-jets, partitioned in three $E_{\mathrm{T}}^{\mathrm{miss}}$ bins in the resolved category and one in the merged category,

- 1 muon CR with one muon and no electrons, requiring two $b$-jets, partitioned in three $E_{\mathrm{T}}^{\mathrm{miss,no}\mu}$ bins in the resolved category and one in the merged category,
- 2 lepton CR with two same-flavour leptons, requiring two $b$-jets, partitioned in three $p_{\mathrm{T}}^{\ell\ell}$ bins in the resolved category and one in the merged category.

A graphical overview of all regions and categories considered in the analysis with their relative background composition is given in Figure 10.2.

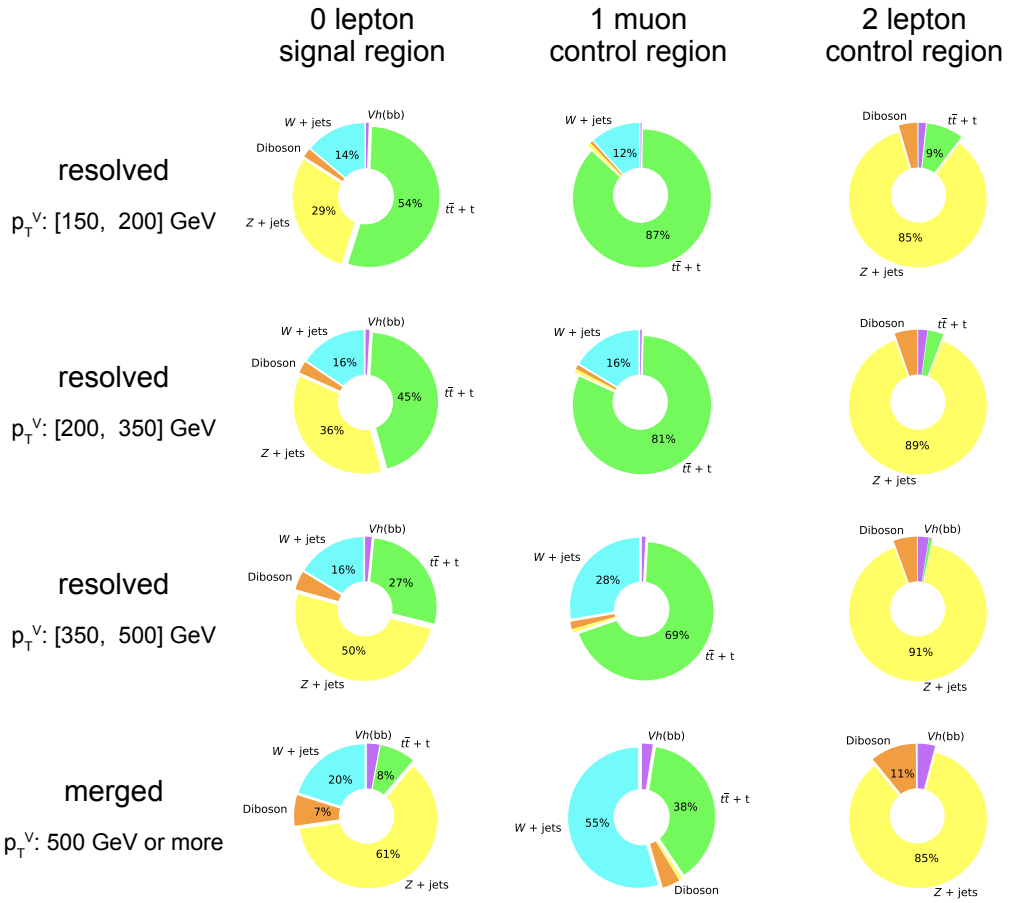



**Fig. 10.2.:** Overview of all regions and $p_{\mathrm{T}}^{V}$ bins considered in the $E_{\mathrm{T}}^{\mathrm{miss}} + \mathrm{h}(\mathrm{b\bar{b}})$ search with their relative background composition, where $p_{\mathrm{T}}^{V}$ denotes $E_{\mathrm{T}}^{\mathrm{miss}}$ in the signal region, $E_{\mathrm{T}}^{\mathrm{miss,no}\mu}$ in the 1 muon control region, and $p_{\mathrm{T}}^{\ell\ell}$ in the 2 lepton control region, respectively. Each region consists of three resolved event-topology $p_{\mathrm{T}}^{V}$ bins and the merged event-topology $p_{\mathrm{T}}^{V}$ bin.

## 10.4 Object and event selection

The event selection requirements for events considered in the SR are outlined below. The specific choices for physics object definitions are summarised in Section 10.4.1.

The common baseline selection used in SR and CRs is described in Section 10.4.2, while the SR event selection is described in Section 10.4.3.

### 10.4.1 Object selection

The physical compound objects used in the $E_{\mathrm{T}}^{\mathrm{miss}} + \mathrm{h}(\mathrm{b\bar{b}})$ search are based on the object definitions, which are introduced in Section 8.3.

Two novel object definitions are exploited — the variable radius track jets, which extend the sensitivity of the search in case of large boosts of the Higgs boson candidate, and an object-based $E_{\mathrm{T}}^{\mathrm{miss}}$ significance, which serves the rejection of background processes with fake $E_{\mathrm{T}}^{\mathrm{miss}}$.

Central jets and forward jets are used to define selection requirements on the event topology, which suppress background processes. The $b$-jets are identified by $b$-tagging algorithms, using the MV2 discriminant with a fixed-cut working point corresponding to $77\,\%$ $b$-tagging efficiency. The Higgs candidate reconstruction is based on the two most energetic $b$-jets in the resolved category and on the most energetic large-radius jet in the merged category.

The identification of the large-radius jet flavour content is based on track jets associated with the large-radius jet via ghost-matching. The track jets allow for maintaining high double $b$-tagging efficiency in the merged event topology. However, for substantially large Higgs boson momenta, even the track jets can overlap if they are reconstructed with a fixed radius parameter. The problem of track jet merging is overcome by the use of variable-radius (VR) track jets, as illustrated in Figure 10.3.

The use of the VR track jets allows maintaining a high double $b$-tagging efficiency over a broad Higgs boson momentum range, which overall is superior to conventional FR track jets. Therefore, the identification of $b$-jets in the merged category is based on VR track jets.

The charged lepton definitions are similar to those used in the $E_{\mathrm{T}}^{\mathrm{miss}} + V(qq)$ search (c.f. Section 9.4.1), except for the $E_{\mathrm{T}} > 27\,\mathrm{GeV}$ requirement in the signal electron candidate definition due to the increased single electron trigger threshold in 2017 data-taking. Baseline electron and muon candidates are used for the definition of lepton vetoes in the SR, as the baseline definition aims at providing a high reconstruction efficiency. Signal electron and muon candidates are used to select electron or muon pairs for the 2 lepton CR, where a high purity selection is desired. Tight signal muons are used to select muons in the 1 muon CR. In addition, baseline tau lepton candidates are used to define vetoes on tau leptons in the event selection.

The missing transverse momentum $E_{\mathrm{T}}^{\mathrm{miss}}$ is reconstructed from the calibrated physics objects in the event and the track-based soft term (TST) using the LOOSE working point. Closely related definitions are employed in the CRs to accommodate how background processes are contributing to the SR. In the 1 muon CR, the $E_{\mathrm{T}}^{\mathrm{miss,no}\mu}$

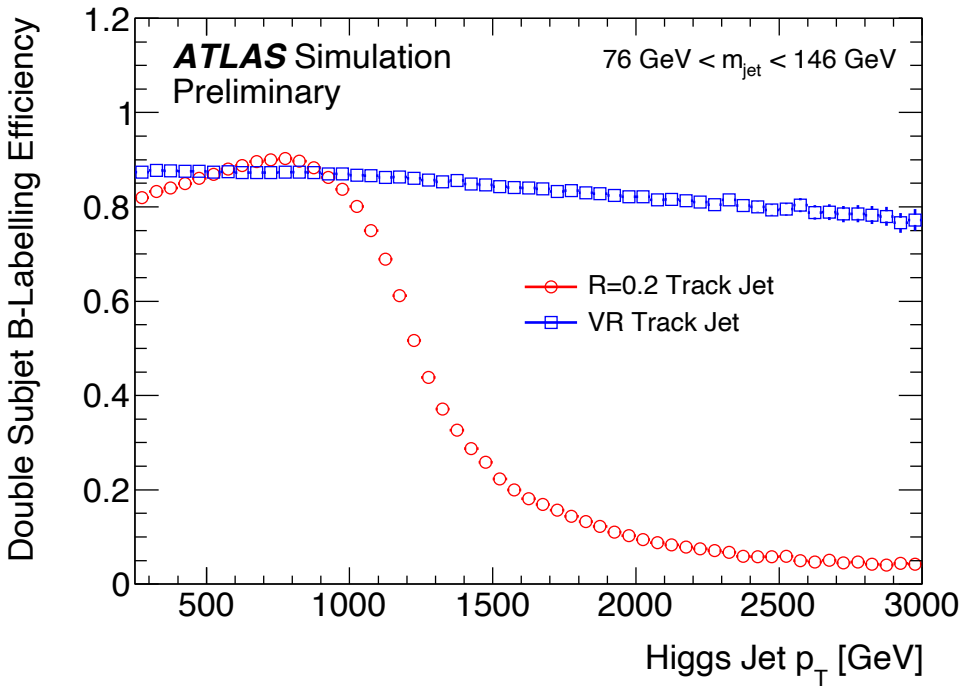



**Fig. 10.3.:** The efficiency for a large-radius jet from a $h \to b\bar{b}$ decay (referred to as Higgs jet) to have its two associated sub-jets with largest transverse momentum matched to truth B-hadrons in dependence of its $p_T$. The error bars include statistical uncertainties only. Figure modified from Ref. [110].

variable is used, which is reconstructed by excluding muons from the $E_T^{miss}$ calculation, thereby adding the muon momentum vector to $E_T^{miss}$. Similarly, in the 2 lepton CR, the transverse momentum of the dilepton system $p_T^{\ell\ell}$ is used.

The object-based $E_T^{miss}$ significance $\mathcal{S}$ is used to separate events in which the reconstructed missing transverse momentum $E_T^{miss}$ is genuinely coming from dark matter particles or neutrinos from events with fake $E_T^{miss}$ caused by resolution effects.

Figure 10.4 illustrates the performance of the object-based $E_T^{miss}$ significance in comparison to an event-based definition of $E_T^{miss}$ significance $E_T^{miss}/\sqrt{\sum E_T^{miss}}$ and $E_T^{miss}$ itself in the $E_T^{miss}+h(b\bar{b})$ search. The object-based $E_T^{miss}$ significance definition is clearly superior, as a requirement of $\mathcal{S} > 16$ can reject over $95\,\%$ of background processes with fake $E_T^{miss}$ while retaining a signal efficiency over $90\,\%$. In contrast, the event-based $E_T^{miss}$ significance achieves similar background rejection with a signal efficiency of $80\,\%$, while the use of $E_T^{miss}$ decreases the signal efficiency to $30\,\%$.

Potential ambiguities in the reconstruction, such as reconstructed objects matching multiple object hypotheses, must be resolved by an overlap removal procedure. The overlap removal procedure applies six stages in the order listed as follows.

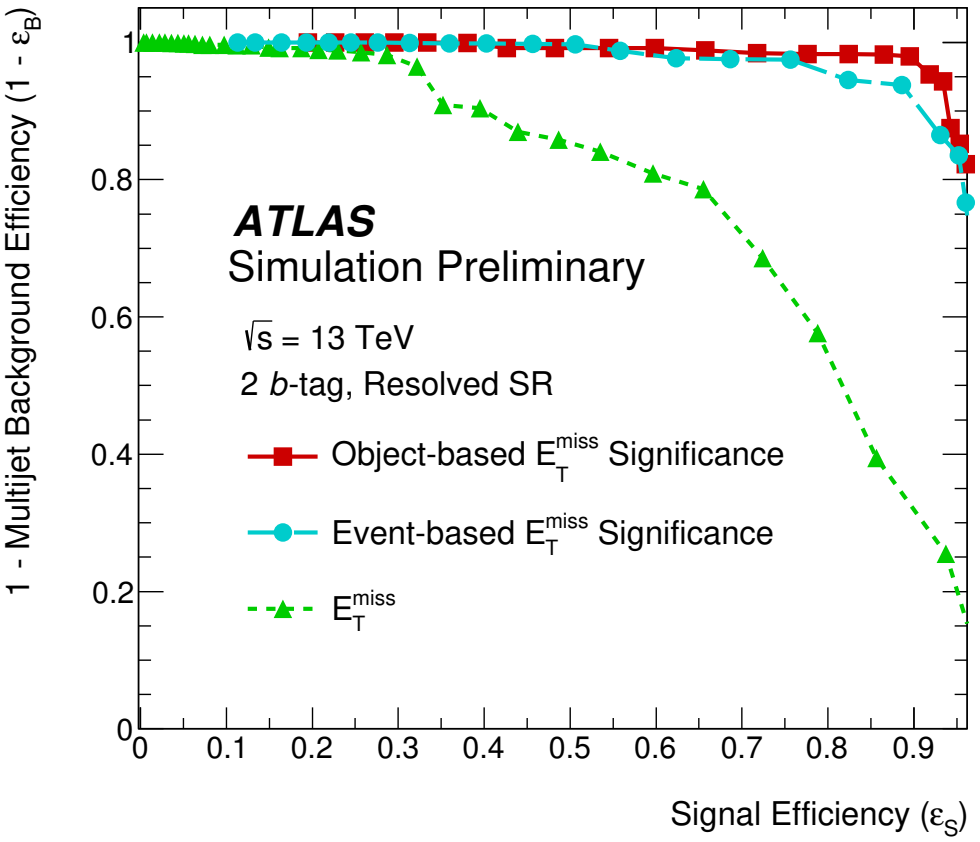



**Fig. 10.4.:** Performance of the $E_{\mathrm{T}}^{\mathrm{miss}}$ significance (line with square markers) in terms of the signal efficiency and multijet background rejection in the $E_{\mathrm{T}}^{\mathrm{miss}} + \mathrm{h}(\mathrm{b\bar{b}})$ search, compared to an event-based $E_{\mathrm{T}}^{\mathrm{miss}}$ significance definition $E_{\mathrm{T}}^{\mathrm{miss}}/\sqrt{\sum E_{\mathrm{T}}^{\mathrm{miss}}}$ (dashed line with circular markers), and on $E_{\mathrm{T}}^{\mathrm{miss}}$ itself (densely-dashed line with triangular markers). The signal efficiency is estimated with a Z′-2HDM signal sample with $m_{\mathrm{Z}'} = 400\,\mathrm{GeV}$ and $m_{\mathrm{A}} = 300\,\mathrm{GeV}$, which has a very soft $E_{\mathrm{T}}^{\mathrm{miss}}$ distribution, whereas the background rejection is estimated with a sample of simulated dijet events. The events used for the comparison are selected by the $E_{\mathrm{T}}^{\mathrm{miss}} + \mathrm{h}(\mathrm{b\bar{b}})$ baseline selection requirements, including a requirement on the angular separation between the $E_{\mathrm{T}}^{\mathrm{miss}}$ vector and the three jets with highest $p_{\mathrm{T}}$.

1. Electron-electron overlap removal. If an event contains two reconstructed electrons sharing a track, the electron candidate with lower $p_{\mathrm{T}}$ is removed from the event.

2. Tau-electron and tau-muon overlap removal. If an event contains a reconstructed tau lepton within the distance $\Delta R < 0.2$ of any reconstructed electron or muon, the tau candidate is removed from the event.

3. Electron-muon overlap removal. If an event contains a reconstructed electron and a reconstructed muon sharing the same track, the electron candidate is removed from the event.

4. Electron-jet overlap removal. All jets within the distance[1] $\Delta R = \sqrt{\Delta y^2 + \Delta\varphi^2} < 0.2$ of electrons surviving the previous stage of the overlap removal procedure are removed from the event. Then, all reconstructed electrons of transverse energy $E_{\mathrm{T}}$ within the distance $\min\{0.4, 0.04 + 10\,\mathrm{GeV}/E_{\mathrm{T}}\}$ of jets are removed from the event.

5. Muon-jet overlap removal. All jets within the distance $\Delta R < 0.2$ of any reconstructed muon are removed, if they either have fewer than three associated tracks or if the muon $p_{\mathrm{T}}$ is greater than $\max\{0.5\,p_{\mathrm{T}}^{\mathrm{jet}}, 0.7\sum_i p_{\mathrm{T}}^{\mathrm{track,\,i}}\}$, where $p_{\mathrm{T}}^{\mathrm{track}}$ denotes the transverse momentum of tracks associated to the jet. Then, all reconstructed muons of transverse momentum $p_{\mathrm{T}}$ within the distance $\min\{0.4, 0.04 + 10\,\mathrm{GeV}/p_{\mathrm{T}}\}$ of jets are removed from the event.

6. Overlap removal between large-radius-jets and electrons. If an event contains a large-radius jet within the distance $\Delta R < 0.1$ of an electron, the large-radius jet is removed from the event.

### 10.4.2 Baseline selection

The SR and CR definition is based on a common baseline selection and common requirements to suppress the multijet background. These selection requirements are almost identical to the those used in the $E_{\mathrm{T}}^{\mathrm{miss}} + V(qq)$ search, which are presented in Section 9.4.2 and Section 9.4.3, respectively. There are three exceptions, which concern the jet cleaning requirement in the baseline selection and the definition of the multijet-suppression requirements.

- The jet cleaning selection requirement is solely based on the BADLOOSE definition. No additional requirement based on the TIGHT jet cleaning definition is made.

- Only the $\min\Delta\varphi(\mathrm{jets}_{1,2,3}, E_{\mathrm{T}}^{\mathrm{miss}}) > 20°$ and the $\Delta\varphi(E_{\mathrm{T}}^{\mathrm{miss}}, E_{\mathrm{T}}^{\mathrm{miss,\,track}}) < 90°$ multijet-suppression requirements are applied. The requirement that the azimuthal distance between $E_{\mathrm{T}}^{\mathrm{miss}}$ and the boson candidate has to exceed $120°$

[1] The distance measure employed for the overlap removal procedure is based on the rapidity distance $\Delta y$ instead of the pseudorapidity distance $\Delta\eta$.

and the requirement on $E_{\mathrm{T}}^{\mathrm{miss,\,track}} > 30\,\mathrm{GeV}$ are no longer part of the common baseline selection.

- These multijet-suppression requirements are only applied in the SR and in the 1 muon CR selection but not in the 2 lepton CR. The 2 lepton CR selection sufficiently suppresses potential contamination through multijet events and would suffer from large statistical uncertainty if the multijet-suppression requirements were applied.

The baseline selection requirements are summarised in Table 10.3.

**Tab. 10.3.:** List of the baseline event selection requirements employed in the $E_{\mathrm{T}}^{\mathrm{miss}} + \mathrm{h}(\mathrm{b\bar{b}})$ search.

| Baseline selection | 0 lepton SR | 1 muon CR | 2 lepton CR |
|---|---|---|---|
| Data quality | basic requirements vetoing corrupted data or incomplete events | | |
| Vertex reconstruction | primary vertex with at least two associated tracks | | |
| Jet cleaning | veto on events containing jets flagged as BADLOOSE jets | | |
| Trigger | $E_{\mathrm{T}}^{\mathrm{miss}}$ trigger | $E_{\mathrm{T}}^{\mathrm{miss}}$ trigger | single lepton trigger |
| Multijet suppression | $\min \Delta\varphi(\mathrm{jets}_{1,2,3}, E_{\mathrm{T}}^{\mathrm{miss}}) > 20°$ | $\min \Delta\varphi(\mathrm{jets}_{1,2,3}, E_{\mathrm{T}}^{\mathrm{miss,no}\mu}) > 20°$ | no |
| | $\Delta\varphi(E_{\mathrm{T}}^{\mathrm{miss}}, E_{\mathrm{T}}^{\mathrm{miss,\,track}}) < 90°$ | $\Delta\varphi(E_{\mathrm{T}}^{\mathrm{miss,no}\mu}, E_{\mathrm{T}}^{\mathrm{miss,\,track,\,no}\mu}) < 90°$ | no |

### 10.4.3 Signal region selection

As the signature sought by the $E_{\mathrm{T}}^{\mathrm{miss}} + \mathrm{h}(\mathrm{b\bar{b}})$ search does not involve leptons, a veto on events containing baseline muons or baseline electrons is employed in the SR event selection.

Following the baseline selection requirements, events are separated into the resolved and merged categories using a single selection requirement on $E_{\mathrm{T}}^{\mathrm{miss}}$.

The **resolved category** event selection is optimised for events with a moderate amount of missing transverse momentum $150\,\mathrm{GeV} < E_{\mathrm{T}}^{\mathrm{miss}} < 500\,\mathrm{GeV}$ and a Higgs boson candidate, whose decay products can be resolved by two $b$-tagged small-radius jets. The jets used for the Higgs boson candidate reconstruction are the two $b$-jets with highest $p_{\mathrm{T}}$ in the event and are referred to as $j_1$ and $j_2$. The invariant mass of the dijet system composed out of these jets, which is referred to as $m_{jj}$, provides strong discrimination between signal and background processes, as Higgs boson candidates exhibit a characteristic mass peak at the Higgs boson mass.

The remaining selection requirements are similar to those of the $E_{\mathrm{T}}^{\mathrm{miss}} + V(q\bar{q})$ search, as a similar event topology is targeted. In events with exactly two central jets, their scalar transverse momentum sum is required to be larger than $120\,\mathrm{GeV}$, whereas in events with three or more central jets, instead the scalar transverse momentum sum of the three central jets with highest $p_{\mathrm{T}}$ is required to be larger than $150\,\mathrm{GeV}$. At least one of the jets used to reconstruct the Higgs boson candidate is required to have a transverse momentum greater than $45\,\mathrm{GeV}$.

In addition to the multijet-suppression requirements outlined in Section 10.4.2, four requirements are explicitly introduced for the resolved category to reduce the contribution of multijet processes. The jets used for the Higgs boson candidate reconstruction often are in a back-to-back topology for multijet events, whereas they are in close proximity for the signal process. Therefore, the requirements on the separation of the Higgs boson candidate jets $\Delta\varphi(j_1, j_2) < 140°$ and $\Delta R(j_1, j_2) < 1.8$ are introduced. In signal-like events the missing transverse momentum is expected to be in a back-to-back topology with the Higgs boson candidate, motivating the requirement on the azimuthal distance between $E_{\mathrm{T}}^{\mathrm{miss}}$ and the Higgs boson candidate $\Delta\varphi(E_{\mathrm{T}}^{\mathrm{miss}}, \mathrm{h}) > 120°$. The specific values used in these requirements are chosen by examining distributions of these observables for excesses of data over the simulated non-multijet backgrounds, which are attributed to multijet backgrounds. These studies were validated with simulated multijet events. Finally, a requirement based on the object-based $E_{\mathrm{T}}^{\mathrm{miss}}$ significance $\mathcal{S} > 16$ suppresses the remaining contributions of backgrounds with fake $E_{\mathrm{T}}^{\mathrm{miss}}$ (c.f. Section 10.4.1).

Although the $\mathrm{t\bar{t}}$, $\mathrm{t} \to \mathrm{Wb}$ background processes with W bosons decaying to electrons and muons are suppressed by the lepton vetoes, those with hadronically decaying tau leptons can still pass the event selection. Therefore, an additional veto on tau leptons is introduced. It is based on the rejection of events containing baseline tau lepton candidates and improved by an extended tau veto definition, also rejecting events containing small-radius jets with $1$ to $4$ associated tracks and satisfying the requirement $\Delta\varphi(\text{jet}, E_{\mathrm{T}}^{\mathrm{miss}}) < 22.5°$.

The contribution of the $\mathrm{t\bar{t}}$ background is further reduced by imposing a veto on events containing more than 2 $b$-jets and imposing a requirement on the hadronic activity ratio $H_{\mathrm{T}}^{\mathrm{resolved}} < 0.37$. The latter quantity relates the scalar sum of the $p_{\mathrm{T}}$ of the Higgs boson candidate jets and up to one additional high-$p_{\mathrm{T}}$ jet to the scalar sum of the transverse momenta of additional jets in the event. It is defined as

$$H_{\mathrm{T}}^{\mathrm{resolved}} = 1 - \frac{H_{\mathrm{T}}(\text{Higgs candidate + ISR jet})}{H_{\mathrm{T}}(\text{all jets})} = 1 - \frac{\sum_{i=1}^{3} p_{\mathrm{T}}^{\mathrm{j}_i}}{\sum_{i=1}^{N(\text{jets})} p_{\mathrm{T}}^{\mathrm{j}_i}}. \tag{10.2}$$

In events with a Higgs boson, $H_{\mathrm{T}}^{\mathrm{resolved}}$ is relatively small because the high-$p_{\mathrm{T}}$ jets originate from the Higgs decay and the additional hadronic activity, which mostly originates from ISR processes, occurs with low $p_{\mathrm{T}}$. In events with semi-leptonic $\mathrm{t\bar{t}}$ processes on the other hand, additional high-$p_{\mathrm{T}}$ jets can originate from the hadronic decays of W bosons or from the $b$-quarks in the $\mathrm{t} \to \mathrm{Wb}$ decays, resulting in high values of $H_{\mathrm{T}}^{\mathrm{resolved}}$.

The signal-to-background ratio of dark matter production characteristically is larger at high $E_{\mathrm{T}}^{\mathrm{miss}}$. In order to profit from the increased sensitivity of the high $E_{\mathrm{T}}^{\mathrm{miss}}$ region while retaining high signal efficiency for signals with lower $E_{\mathrm{T}}^{\mathrm{miss}}$, the events in the resolved regime are further categorised in three $E_{\mathrm{T}}^{\mathrm{miss}}$ bins with $150\,\mathrm{GeV}$ to $200\,\mathrm{GeV}$, $200\,\mathrm{GeV}$ to $350\,\mathrm{GeV}$, and $350\,\mathrm{GeV}$ to $500\,\mathrm{GeV}$.

Events with the Higgs boson candidate invariant mass in the range $50\,\mathrm{GeV} < m_{jj} < 280\,\mathrm{GeV}$ are considered in the statistical analysis.

The events comprising the **merged category** are selected by applying the baseline selections and increasing the $E_{\mathrm{T}}^{\mathrm{miss}}$ cut to $500\,\mathrm{GeV}$. The Higgs boson candidate in the merged category is reconstructed using the large-radius jet with highest $p_{\mathrm{T}}$ in the event. Its invariant mass is referred to as $m_J$.

Consequently, the merged category selection requires the presence of at least one large-radius jet with two associated VR track jets, which are identified as $b$-jets. Similar as in the resolved category selection, events with less than two $b$-tagged VR track jets are considered for optimisation studies but not for the statistical analysis.

Figure 10.5 shows the product of detector acceptance $\times$ selection efficiency in dependence of $m_{\mathrm{Z}'}$ for a Z′-2HDM signal sample with fixed $m_{\mathrm{A}} = 500\,\mathrm{GeV}$ in the SR merged category. The use of VR track jets strongly improves the double $b$-tagging efficiency for signal processes with $m_{\mathrm{Z}'} > 2.5\,\mathrm{TeV}$, which corresponds to event topologies with a highly boosted Higgs boson candidate. Although for lower $m_{\mathrm{Z}'}$ FR track jets appear to have a better double $b$-tagging performance for the signal process, their use also results in the reconstruction of more background events. Hence, the VR track jet algorithm results in a better signal to background ratio.

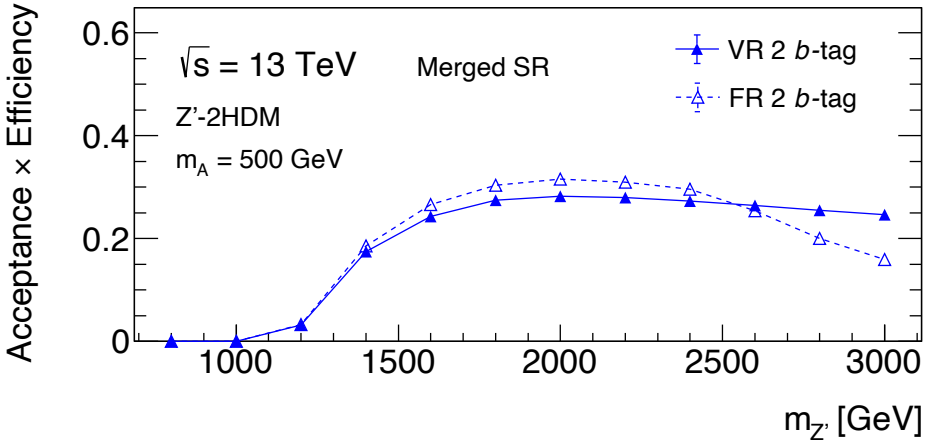



**Fig. 10.5.:** Product of detector acceptance $\times$ selection efficiency in the signal region merged category shown in dependence of $m_{\mathrm{Z}'}$ for a Z′-2HDM signal sample with fixed $m_{\mathrm{A}} = 500\,\mathrm{GeV}$. The performance for VR track jets (filled triangles, solid lines) is compared to that of FR track jets (open triangles, dashed lines).

No additional requirements to suppress the multijet background besides the baseline selection and $E_{\mathrm{T}}^{\mathrm{miss}} > 500\,\mathrm{GeV}$ are required for the merged category selection.

Similar as in the resolved category, the $\mathrm{t\bar{t}}$ background contribution is suppressed by dedicated requirements. Events containing $b$-tagged VR track jets, which are not associated to the Higgs boson candidate, are rejected. Furthermore, events have to satisfy a requirement on the hadronic activity ratio $H_{\mathrm{T}}^{\mathrm{merged}} < 0.57$. In the merged

category, it is defined by the Higgs boson candidate $p_{\mathrm{T}}^{\mathrm{J}}$ and the momenta of the central jets which do not overlap with the Higgs boson candidate $p_{\mathrm{T}}^{\mathrm{j}_i}$ as

$$H_{\mathrm{T}}^{\text{merged}} = 1 - \frac{\text{Higgs candidate}}{\text{all jets}} = 1 - \frac{p_{\mathrm{T}}^{\mathrm{J}}}{\left(\sum_{i=1}^{N(\text{jets})} p_{\mathrm{T}}^{\mathrm{j}_i} + p_{\mathrm{T}}^{\mathrm{J}}\right)}. \tag{10.3}$$

Events with the Higgs boson candidate invariant mass in the range $50\,\mathrm{GeV} < m_J < 270\,\mathrm{GeV}$ are considered in the statistical analysis.

A summary of the SR selection requirements is presented in Table 10.4.

**Tab. 10.4.:** Signal region event selection requirements employed in the $E_{\mathrm{T}}^{\text{miss}}+\mathrm{h}(\mathrm{b\bar{b}})$ search.

| **Common selection requirements** | |
|---|---|
| baseline selection requirements<br>multijet-suppression requirements<br>0 baseline e and 0 baseline $\mu$<br>extended tau lepton veto | |
| **Resolved category** | **Merged category** |
| $150\,\mathrm{GeV} < E_{\mathrm{T}}^{\text{miss}} < 500\,\mathrm{GeV}$<br>2 $b$-tagged central jets | $E_{\mathrm{T}}^{\text{miss}} > 500\,\mathrm{GeV}$<br>at least 1 large-radius jet<br>associated with 2 $b$-tagged VR track jets |
| $\max\left\{p_{\mathrm{T}}^{j1}, p_{\mathrm{T}}^{j2}\right\} > 45\,\mathrm{GeV}$ | no non-associated $b$-tagged track jets |
| $H_{\mathrm{T}}^{\text{resolved}} < 0.37$ | $H_{\mathrm{T}}^{\text{merged}} < 0.57$ |
| $\sum_i^{2(3)} p_{\mathrm{T}}^{j_i} > 120\,\mathrm{GeV}(150\,\mathrm{GeV})$ | |
| $\mathcal{S} > 16$ | |
| $\Delta\varphi(\text{jet}_1, \text{jet}_2) < 140°$ | |
| $\Delta R(j_1, j_2) < 1.8$ | |
| $\Delta\varphi(E_{\mathrm{T}}^{\text{miss}}, \mathrm{h}) > 120°$ | |

The complementarity of resolved and merged signal categories is demonstrated in Figure 10.6. The combined acceptance $\times$ efficiency is shown by black filled points, and the acceptance $\times$ efficiency of individual resolved and merged selections is indicated by open and filled blue triangles, respectively. High signal efficiency is maintained over a broad range by employing both resolved and merged selection requirements.

## 10.5 Background estimation

The estimation of the dominant background processes in the $E_{\mathrm{T}}^{\text{miss}} + \mathrm{h}(\mathrm{b\bar{b}})$ search via MC simulation is improved by control region data. In contrast to the signal process, the dominant background processes have no characteristic peak in the

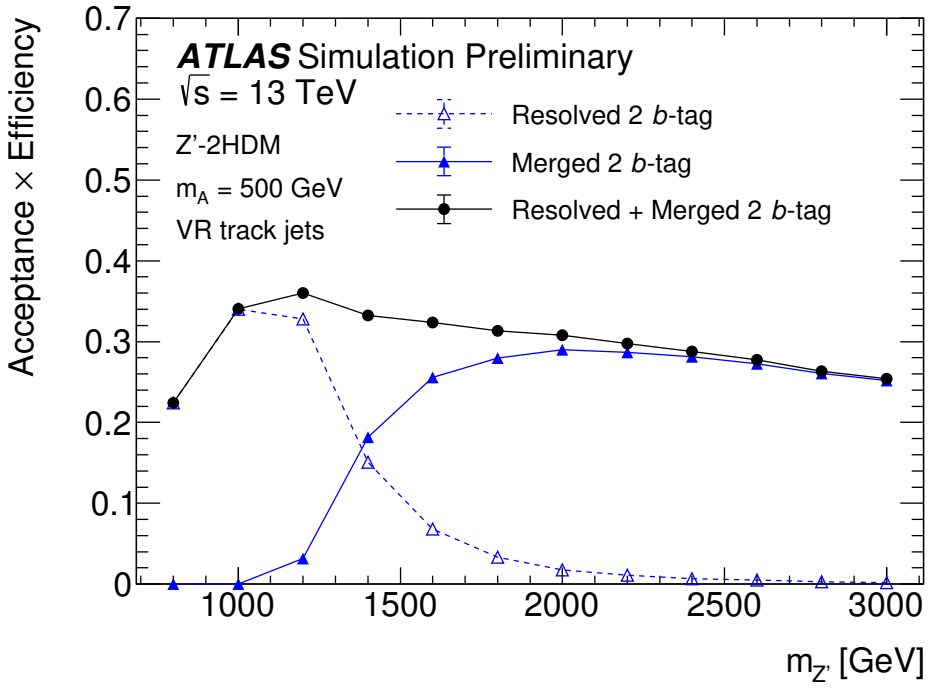



**Fig. 10.6.:** Product of detector acceptance $\times$ selection efficiency for events with 2 $b$-tagged jets as a function of $m_{Z'}$ for a Z′-2HDM signal sample with fixed $m_{\mathrm{A}} = 500\,\mathrm{GeV}$. The values obtained for the resolved category are shown in blue with open triangles and a dashed line, the ones for the merged category with filled triangles and a solid line. The combined selection efficiency is shown in black.

Higgs candidate mass distributions. As the CRs have a high purity in the specific background processes, no additional $m_J$ / $m_{jj}$ information is used.

The normalisation parameters of the sub-dominant background processes are set to their predicted values based on theoretical predictions and can vary within the corresponding uncertainties. The multijet background is found to be negligible based on a data-driven estimate, which is described in Section 10.5.3.

### 10.5.1 1 muon control region

The 1 muon CR is defined to constrain W + jets and $\mathrm{t\bar{t}}$ processes. These background processes can contribute to the SR event selection by inefficiencies in the lepton reconstruction and muons outside of the detector acceptance. Consequently, the selected events contain exactly one tight signal muon, no additional baseline muons and no baseline electrons. The variable $E_{\mathrm{T}}^{\mathrm{miss,no}\mu}$ is introduced, which is defined as the missing transverse momentum reconstructed by neglecting the muon in the event with the highest $p_{\mathrm{T}}$. Events in the 1 muon CR are selected by $E_{\mathrm{T}}^{\mathrm{miss}}$ triggers.

The other event selection requirements, such as the tau lepton veto, the requirements on the jet multiplicity and the event topology, are similar to the SR selection. In

addition to the $E_{\mathrm{T}}^{\mathrm{miss,no}\mu}$ information, the electrical charge of the muon is used in the statistical analysis to distinguish between $\mathrm{t\bar{t}}$ and W + jets processes. The fact that the LHC delivers proton-proton collisions results in a larger fraction of positively charged $\mathrm{W}^{+}$ bosons produced in W+ jets processes [267] because of the larger u parton luminosity with respect to the d parton luminosity (c.f. Figure 4.2). In contrast, the fractions of positively and negatively charged W bosons are equal in $\mathrm{t\bar{t}}$ processes.

The four $E_{\mathrm{T}}^{\mathrm{miss,no}\mu}$ bins provide additional discrimination power, as the $\mathrm{t\bar{t}}$ background accumulates in the lower $E_{\mathrm{T}}^{\mathrm{miss,no}\mu}$ bins, whereas the W+ jets background accumulates in higher $E_{\mathrm{T}}^{\mathrm{miss,no}\mu}$ bins. A summary of the 1 muon CR selection requirements is presented in Table 10.5.

**Tab. 10.5.:** 1 muon control region event selection requirements employed in the $E_{\mathrm{T}}^{\mathrm{miss}}$ + $\mathrm{h(b\bar{b})}$ search.

| **Common selection requirements** | |
|---|---|
| baseline selection requirements<br>multijet-suppression requirements<br>0 baseline e, 1 tight signal $\mu$ and no additional baseline $\mu$<br>extended tau lepton veto | |
| **Resolved category** | **Merged category** |
| $150\,\mathrm{GeV} < E_{\mathrm{T}}^{\mathrm{miss,no}\mu} < 500\,\mathrm{GeV}$<br>2 $b$-tagged central jets | $E_{\mathrm{T}}^{\mathrm{miss,no}\mu} > 500\,\mathrm{GeV}$<br>at least 1 large-radius jet<br>associated with 2 $b$-tagged VR track jets |
| $\max\left\{p_{\mathrm{T}}^{j1}, p_{\mathrm{T}}^{j2}\right\} > 45\,\mathrm{GeV}$ | no non-associated $b$-tagged track jets |
| $H_{\mathrm{T}}^{\mathrm{resolved}} < 0.37$ | $H_{\mathrm{T}}^{\mathrm{merged}} < 0.57$ |
| $\sum_{i}^{2(3)} p_{\mathrm{T}}^{j_i} > 120\,\mathrm{GeV}(150\,\mathrm{GeV})$ | |
| $\mathcal{S}^{\mathrm{no}\,\mu} > 16$ | |
| $\Delta\varphi(\mathrm{jet}_1, \mathrm{jet}_2) < 140°$ | |
| $\Delta R(j_1, j_2) < 1.8$ | |
| $\Delta\varphi(E_{\mathrm{T}}^{\mathrm{miss,no}\mu}, \mathrm{h}) > 120°$ | |

### 10.5.2 2 lepton control region

The 2 lepton CR is designed to constrain the Z + jets background using leptonically decaying Z + jets events in the 2 lepton control region. The dilepton transverse momentum $p_{\mathrm{T}}^{\ell\ell}$ serves as a proxy of the missing transverse momentum. The selected events contain either exactly two baseline electrons ee or exactly two baseline muons $\mu\mu$. At least one of the two electrons must satisfy the requirement $p_{\mathrm{T}} > 27\,\mathrm{GeV}$. Similarly, at least one of the two muons must satisfy the requirements $p_{\mathrm{T}} > 25\,\mathrm{GeV}$ and $|\eta| < 2.5$. Events containing two muons are only selected if these are of opposite charge. A similar requirement is not applied for events containing two electrons due

to the higher rate of electron charge misidentification. Events in the 2 lepton CR are selected by single lepton triggers.

A requirement on the invariant mass of the dilepton system ensures high purity in Z + jets processes by suppressing backgrounds with a non-resonantly produced lepton-pair. The requirement for events containing two muons is $71\,\text{GeV} < m_{\mu\mu} < 106\,\text{GeV}$, whereas for events containing two electrons the requirement is $83\,\text{GeV} < m_{\text{ee}} < 99\,\text{GeV}$, due to the better mass resolution of the EM calorimeter at high electron energies compared to the MS momentum resolution for high-$p_{\text{T}}$ muons (c.f. Section 5.3.4). No multijet-suppression requirements are part of the baseline selection for the 2 lepton CR, similarly the requirements on $\Delta\varphi(j_1, j_2)$ and $\Delta R(j_1, j_2)$ are not included in the 2 lepton CR selection. Top quark background processes are suppressed by a requirement on the ratio of $E_{\text{T}}^{\text{miss}}$ and the square root of the scalar sum of lepton and jet transverse momenta in the event, which is required to be $E_{\text{T}}^{\text{miss}}/\sqrt{\sum(p_{\text{T}}^{\text{jets}} + p_{\text{T}}^{\text{leptons}})} < 3.5\,\sqrt{\text{GeV}}$.

Because of these selection requirements, the purity of the 2 lepton control region selection is sufficiently high to use the event yield in four $p_{\text{T}}^{\ell\ell}$ bins directly as the observable in the statistical analysis. A summary of the 2 lepton CR selection requirements is presented in Table 10.6.

**Tab. 10.6.:** 2 lepton control region event selection requirements employed in the $E_{\text{T}}^{\text{miss}} + \text{h}(\text{b}\bar{\text{b}})$ search.

| **Common selection requirements** | |
|---|---|
| baseline selection requirements | |
| exactly 2 baseline e/ $\mu$, among which 1 signal e/ $\mu$ | |
| extended tau lepton veto | |
| $71\,\text{GeV} < m_{\mu\mu} < 106\,\text{GeV}$ or $83\,\text{GeV} < m_{\text{ee}} < 99\,\text{GeV}$ | |
| $E_{\text{T}}^{\text{miss}}/\sqrt{\sum(p_{\text{T}}^{\text{jets}} + p_{\text{T}}^{\text{leptons}})} < 3.5\,\sqrt{\text{GeV}}$ | |
| **Resolved category** | **Merged category** |
| $150\,\text{GeV} < p_{\text{T}}^{\ell\ell} < 500\,\text{GeV}$ | $p_{\text{T}}^{\ell\ell} > 500\,\text{GeV}$ |
| 2 $b$-tagged central jets | at least 1 large-radius jet associated with 2 $b$-tagged VR track jets |
| $\max\left\{p_{\text{T}}^{j1}, p_{\text{T}}^{j2}\right\} > 45\,\text{GeV}$ | no non-associated $b$-tagged track jets |
| $H_{\text{T}}^{\text{resolved}} < 0.37$ | $H_{\text{T}}^{\text{merged}} < 0.57$ |
| $\sum_i^{2(3)} p_{\text{T}}^{j_i} > 120\,\text{GeV}(150\,\text{GeV})$ | |
| $\Delta R(j_1, j_2) < 1.8$ | |

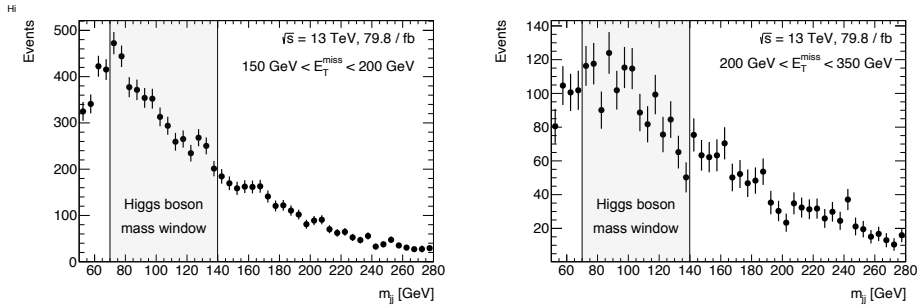
### 10.5.3 Multijet background estimate

The multijet background is expected to be small in the SR resolved category due to the multijet-suppression requirements. It is expected to be negligible in the SR

merged category as well as in the CRs due to the requirement of large $E_{\mathrm{T}}^{\mathrm{miss}}$ and the additional lepton requirements, respectively.

The multijet background is estimated using a data-driven factorisation method, also referred to as "ABCD" method. The number of multijet events in the SR is determined by extrapolation from a multijet-enriched selection (region A), which is defined by the SR event selection with the two most powerful multijet-suppression requirements inverted, such that $\min \Delta\varphi(\text{jets}_{1,2,3}, E_{\mathrm{T}}^{\mathrm{miss}}) < 20°$ and $\mathcal{S} < 16$.

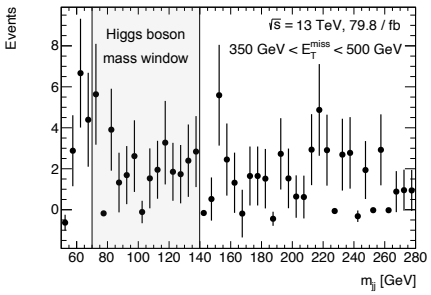
In this multijet-enriched selection, the number of multijet events is obtained from the difference between the data and the other simulated background processes. The corresponding distributions of the Higgs boson candidate mass $m_{jj}$ are shown in Figure 10.7.




(a) $150 < E_{\mathrm{T}}^{\mathrm{miss}} < 200\,\mathrm{GeV}$




(b) $200 < E_{\mathrm{T}}^{\mathrm{miss}} < 350\,\mathrm{GeV}$




(c) $350 < E_{\mathrm{T}}^{\mathrm{miss}} < 500\,\mathrm{GeV}$

**Fig. 10.7.:** Distributions of the Higgs boson candidate invariant mass $m_{jj}$ for multijet background processes in the multijet-enriched region with 2 $b$-tagged jets, obtained by subtracting all other simulated background processes from the data. The distributions are shown in the bins $150\,\mathrm{GeV} < E_{\mathrm{T}}^{\mathrm{miss}} < 200\,\mathrm{GeV}$ (left), $150\,\mathrm{GeV} < E_{\mathrm{T}}^{\mathrm{miss}} < 200\,\mathrm{GeV}$ (right), $150\,\mathrm{GeV} < E_{\mathrm{T}}^{\mathrm{miss}} < 200\,\mathrm{GeV}$ (bottom). The error bars represent the statistical uncertainty only.

The multijet event yield in the SR (D) can be estimated by correcting for the efficiency of the $\min \Delta\varphi(\text{jets}_{1,2,3}, E_{\mathrm{T}}^{\mathrm{miss}})$ and $\mathcal{S}$ selection requirements. To this end, two additional selections — region B and region C — are defined, in which only one of the two selection requirements is inverted. Together with the multijet-enriched selection and the SR, four regions are defined in total, which is illustrated in Figure 10.8.

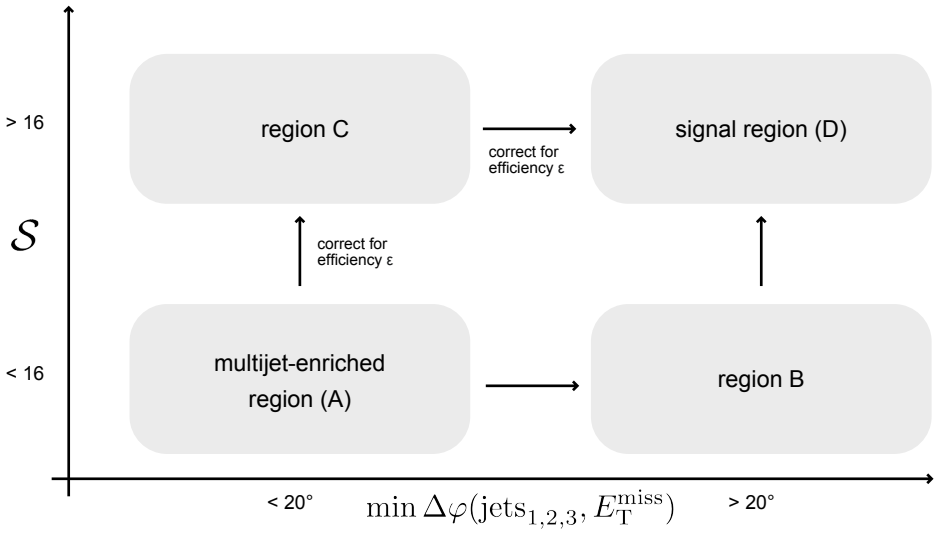



**Fig. 10.8.:** Sketch of the regions used in the multijet background estimate based on a factorisation method. The multijet-enriched region A is defined by inverting both the $\min \Delta\varphi(\text{jets}_{1,2,3}, E_{\text{T}}^{\text{miss}})$ and $\mathcal{S}$ requirements. The regions B and C are defined by inverting only one of those requirements, whereas both requirements are applied in the signal region D.

If $\min \Delta\varphi(\text{jets}_{1,2,3}, E_{\text{T}}^{\text{miss}})$ and $\mathcal{S}$ are not strongly correlated, the amount of multijet events in the signal region can be estimated as

$$\hat{N}_{\text{D}(\mathcal{S}>16, \min\Delta\varphi>20°)} = \frac{N_{\text{B}(\mathcal{S}<16, \min\Delta\varphi>20°)}}{N_{\text{A}(\mathcal{S}<16, \min\Delta\varphi<20°)}} \times N_{\text{C}(\mathcal{S}>16, \min\Delta\varphi<20°)}, \tag{10.4}$$

where $N_{R(\mathcal{S}, \min\Delta\varphi)}$ denotes the number of multijet events in the respective region $R$, which is obtained as the difference between the data and the other simulated background processes.

Figure 10.9 compares the shape of $\mathcal{S}$ for different selections in $\min \Delta\varphi(\text{jets}_{1,2,3}, E_{\text{T}}^{\text{miss}})$. As the $\mathcal{S}$ shape is independent of $\min \Delta\varphi(\text{jets}_{1,2,3}, E_{\text{T}}^{\text{miss}})$, the assumption of the two variables being uncorrelated is justified. The corresponding two-dimensional distributions of $\mathcal{S}$ and $\min \Delta\varphi(\text{jets}_{1,2,3}, E_{\text{T}}^{\text{miss}})$ are shown in Figure 10.10.

The estimate is performed by excluding events in the Higgs boson mass window $70\,\text{GeV} < m_{jj} < 140\,\text{GeV}$ to avoid the contamination by potential signals. The corresponding event yields for the observed data and the total simulated background processes (excluding the multijet background) are shown in Table 10.7. The multijet background reported in the regions A, B, and C is the difference between the data and the simulated background processes. The corresponding errors account only for the statistical uncertainty.

The estimated multijet event yield in the SR Higgs boson mass side-band is

- $20.0 \pm 3.3$ events for $150\,\text{GeV} < E_{\text{T}}^{\text{miss}} < 200\,\text{GeV}$,

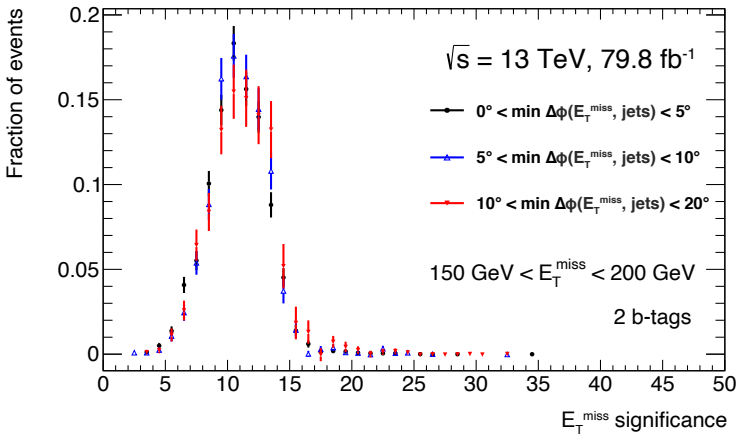
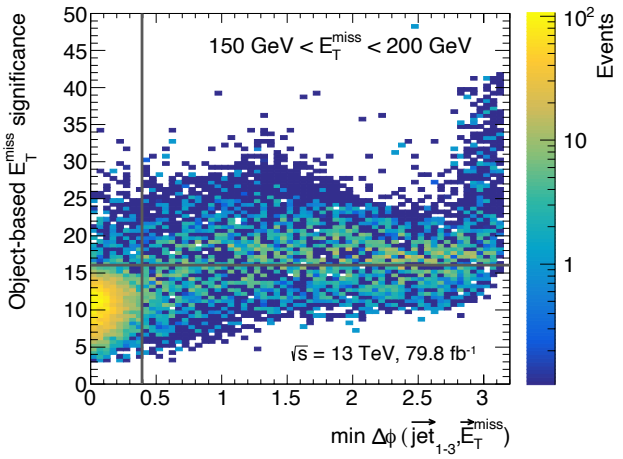


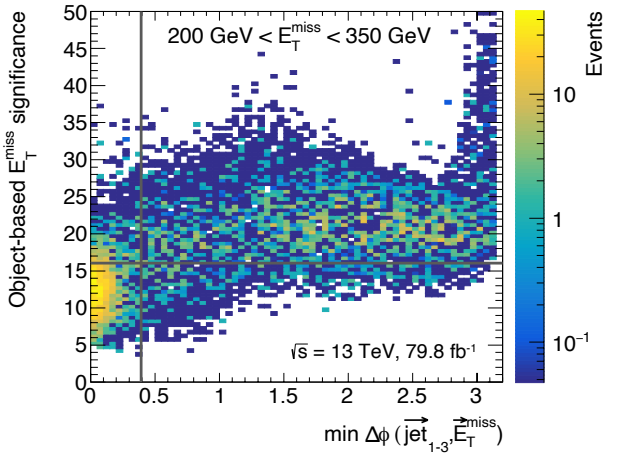

**Fig. 10.9.:** Shape of the object-based $E_{\mathrm{T}}^{\mathrm{miss}}$ significance $\mathcal{S}$ shown for the difference between the data and the other simulated background processes in different selections of $\min \Delta\varphi(\mathrm{jets}_{1,2,3}, E_{\mathrm{T}}^{\mathrm{miss}})$. The selected events have two $b$-tagged jets and satisfy $150\,\mathrm{GeV} < E_{\mathrm{T}}^{\mathrm{miss}} < 200\,\mathrm{GeV}$.

**Tab. 10.7.:** Event yields of the observed data, the simulated background processes, and their difference in the regions A, B, C, and D.

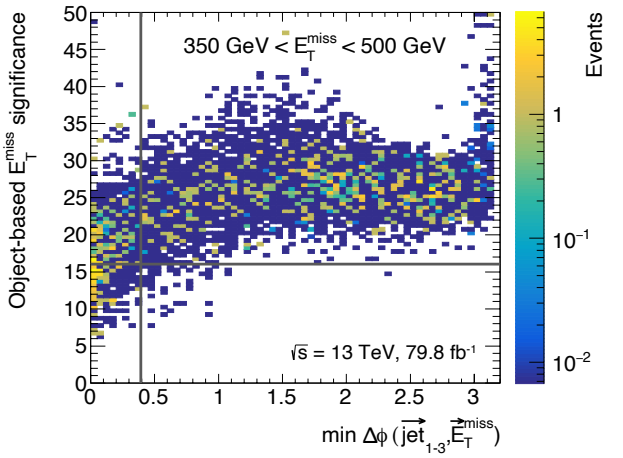
| Sample | $E_{\mathrm{T}}^{\mathrm{miss}}$ range | $N_{\mathrm{A}}$ | $N_{\mathrm{B}}$ | $N_{\mathrm{C}}$ | $N_{\mathrm{D}}$ |
|---|---|---|---|---|---|
| Data | 150 GeV to 200 GeV | 4 570 ± 68 | 3 450 ± 59 | 129 ± 11 | 7 700 ± 88 |
| Other bkg. | 150 GeV to 200 GeV | 595 ± 13 | 2 440 ± 28 | 50 ± 3 | 6 400 ± 45 |
| Multijet | 150 GeV to 200 GeV | 3 980 ± 69 | 1 020 ± 65 | 79 ± 12 | n.a. |
| Data | 200 GeV to 350 GeV | 1 710 ± 41 | 381 ± 20 | 355 ± 19 | 5 430 ± 74 |
| Other bkg. | 200 GeV to 350 GeV | 282 ± 9 | 317 ± 10 | 174 ± 7 | 4 730 ± 36 |
| Multijet | 200 GeV to 350 GeV | 1 420 ± 42 | 64 ± 22 | 181 ± 20 | n.a. ± |
| Data | 350 GeV to 500 GeV | 66 ± 8 | 1 ± 1 | 94 ± 10 | 484 ± 22 |
| Other bkg. | 350 GeV to 500 GeV | 9 ± 1 | 0.90 ± 0.20 | 52 ± 4 | 434 ± 9 |
| Multijet | 350 GeV to 500 GeV | 57 ± 8 | 0.10 ± 1 | 42 ± 11 | n.a. ± |




(a) $150 < E_{\mathrm{T}}^{\mathrm{miss}} < 200\,\mathrm{GeV}$




(b) $200 < E_{\mathrm{T}}^{\mathrm{miss}} < 350\,\mathrm{GeV}$



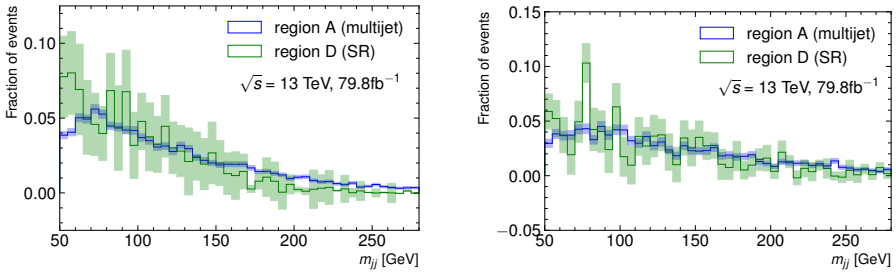

(c) $350 < E_{\mathrm{T}}^{\mathrm{miss}} < 500\,\mathrm{GeV}$

**Fig. 10.10.:** Two-dimensional distributions of $\mathcal{S}$ and $\min\Delta\varphi(\mathrm{jets}_{1,2,3}, E_{\mathrm{T}}^{\mathrm{miss}})$ for multijet background processes, obtained by subtracting all other simulated background processes from the data. The grey lines indicate the regions used in the multijet estimate. The distributions are shown in the bins $150\,\mathrm{GeV} < E_{\mathrm{T}}^{\mathrm{miss}} < 200\,\mathrm{GeV}$ (left), $150\,\mathrm{GeV} < E_{\mathrm{T}}^{\mathrm{miss}} < 200\,\mathrm{GeV}$ (right), $150\,\mathrm{GeV} < E_{\mathrm{T}}^{\mathrm{miss}} < 200\,\mathrm{GeV}$ (bottom).

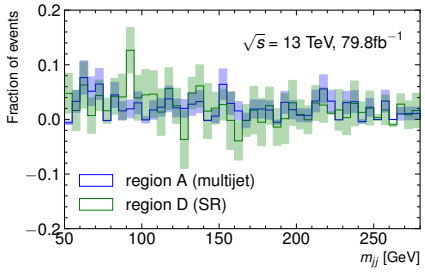
- $8.0 \pm 2.9$ events for $200\,\text{GeV} < E_\text{T}^\text{miss} < 350\,\text{GeV}$, and
- $0.0 \pm 0.8$ events for $350\,\text{GeV} < E_\text{T}^\text{miss} < 500\,\text{GeV}$.

It is substantially smaller than the statistical uncertainty of the observed data and thus can be safely neglected.

In order to draw a similar conclusion for the full $m_{jj}$ range in the SR, the predicted multijet event yield in the SR Higgs boson mass side-bands needs to be corrected for the events in the Higgs boson mass window. A rough estimate for this correction factor is obtained from the multijet $m_{jj}$ distributions in the multijet-enriched region D, which are shown in Figure 10.7. Their shape corresponds to that of the multijet background in the SR, although the latter is afflicted with sizeable statistical uncertainty, as shown in Figure 10.11.




(a) $150 < E_\text{T}^\text{miss} < 200\,\text{GeV}$ (b) $200 < E_\text{T}^\text{miss} < 350\,\text{GeV}$




(c) $350 < E_\text{T}^\text{miss} < 500\,\text{GeV}$

**Fig. 10.11.:** Comparison of the shapes of the Higgs boson candidate invariant mass $m_{jj}$ for the multijet background in the multijet-enriched region and the signal region. The shapes are obtained by subtracting all other simulated background processes from the data. The distributions are shown in the bins $150\,\text{GeV} < E_\text{T}^\text{miss} < 200\,\text{GeV}$ (left), $150\,\text{GeV} < E_\text{T}^\text{miss} < 200\,\text{GeV}$ (right), $150\,\text{GeV} < E_\text{T}^\text{miss} < 200\,\text{GeV}$ (bottom). The error bands represent the statistical uncertainty only.

Therefore, the correction factor is obtained in the multijet-enriched region D as the ratio of the multijet events in the full mass range and the multijet events outside of the Higgs boson mass window. Thus, the total predicted multijet yield is smaller than

- $38 \pm 17$ events for $150\,\text{GeV} < E_\text{T}^\text{miss} < 200\,\text{GeV}$,
- $14 \pm 22$ events for $200\,\text{GeV} < E_\text{T}^\text{miss} < 350\,\text{GeV}$, and

- $0 \pm 80$ events for $350\,\text{GeV} < E_{\text{T}}^{\text{miss}} < 500\,\text{GeV}$.

Although the prediction in the highest $E_{\text{T}}^{\text{miss}}$ bin is afflicted with large statistical uncertainty, an extrapolation from the two lower $E_{\text{T}}^{\text{miss}}$ bins shows that it is negligible. Multijet processes typically decrease exponentially in $E_{\text{T}}^{\text{miss}}$. Therefore, comparing the event yields between bins shows that multijet background falls off much steeper than the observed data outside the Higgs peak.

The estimated total multijet background event yield in the SR is substantially smaller than the statistical uncertainty on the total data. Therefore, it is neglected in the background model.

## 10.6 Systematic uncertainties

Systematic uncertainties arise from the biases in the reconstruction of physics objects and the description of the signal and background processes using MC simulation. The experimental systematic uncertainties are described in Section 10.6.1, while the theoretical systematic uncertainties are described in Section 10.6.2.

### 10.6.1 Experimental systematic uncertainties

The experimental systematic uncertainties in the $E_{\text{T}}^{\text{miss}} + \text{h}(\text{b}\bar{\text{b}})$ search, which arise from biases in the reconstruction of physics objects, resemble those of the $E_{\text{T}}^{\text{miss}} + V(q\bar{q})$ search. The shared uncertainties include the trigger uncertainties, the uncertainties related to the pile-up modelling, the uncertainties on the reconstruction and calibration of electrons, muons, small-radius jets, $b$-tagging uncertainties, and the $E_{\text{T}}^{\text{miss}}$ soft term uncertainties. The differences in the experimental uncertainties are listed below.

- **Luminosity.** The uncertainty on the measurement of the integrated luminosity is $2.0\,\%$ [56].

- **Large-radius jets.** The large-radius jet uncertainties are defined for their energy and mass resolution, and their mass and $p_{\text{T}}$ scale. The latter uncertainties are described by four components, which account for the residual difference between data and MC simulation, the fragmentation modelling, uncertainties related to the use of tracking information, and the total statistical uncertainty in the calibration. The uncertainties on the resolution are described by one component for the jet energy and mass, each.

### 10.6.2 Theoretical systematic uncertainties

The theoretical systematic uncertainties arise from specific choices of event generators, PDF sets, parton shower modelling, and values of the renormalisation and factorisation scales in the modelling of signal and background processes. The evaluation of the theoretical systematic uncertainties follows the same strategy as described in Ref. [66].

In the description of the $V$ + jets background processes, the contributions of different jet flavour are accounted for individually. The simulated $V$ + jets background events are categorised as $V + \mathrm{bb}$, $V + \mathrm{bc}$, $V + \mathrm{b}l$, $V + \mathrm{cc}$, $V + \mathrm{c}l$, and $V + ll$, where $l \in \{\mathrm{u}, \mathrm{d}, \mathrm{s}, \mathrm{g}\}$ denotes light flavour jets. The heavy-flavour processes $V + \mathrm{bb}$, $V + \mathrm{bc}$, and $V + \mathrm{b}l$, $V + \mathrm{cc}$ are grouped and referred to as $V + \mathrm{hf}$.

The total normalisations of the dominant background processes — $\mathrm{t\bar{t}}$, $\mathrm{Z} + \mathrm{hf}$, and $\mathrm{W} + \mathrm{hf}$ — are determined by the control region data. The relative contributions of the individual heavy-flavour processes are allowed to change within their theoretical uncertainties. These uncertainties are determined by comparing the nominal SHERPA MC samples to alternative samples generated with MADGRAPH 5 (c.f. Section 9.6.2) and taking the largest difference as the uncertainty. The normalisation of the Z + jets and W+ jets background processes is decorrelated by $20\,\%$ among SR and CRs, as the varied kinematic distributions of leptons due to scale and PDF uncertainties introduce selection efficiency biases due to the limited detector acceptance for leptons. These uncertainties have been studied in Ref. [66] and have been adopted here.

The normalisations of the sub-dominant background processes — $V + \mathrm{c}l$, $V + ll$, single top quark production, $V\mathrm{h}, \mathrm{h} \to \mathrm{b\bar{b}}$ production, and diboson processes —are constrained by the normalisation uncertainties, which are estimated from theoretical expectations. The normalisation uncertainties of single top-quark production include scale variations and PDF uncertainties, whereas the diboson uncertainties include scale variations as well as parton shower uncertainties. The $V\mathrm{h}, \mathrm{h} \to \mathrm{b\bar{b}}$ uncertainty is taken from the ATLAS measurement presented in Ref. [48]. The normalisation uncertainties are listed in Table 10.8.

In addition, shape uncertainties on both the $E_{\mathrm{T}}^{\mathrm{miss}}$ (or $E_{\mathrm{T}}^{\mathrm{miss,no}\mu}$/ $p_{\mathrm{T}}^{\ell\ell}$) and Higgs boson candidate invariant mass distributions are considered, which are obtained by comparing samples generated with different event generator settings, as well as comparisons to events in data in a selection enriched in Z + jets events. Their estimation follows the procedure described in Section 9.6.2.

The theoretical uncertainties for the dark matter signals in the Z′-2HDM model are estimated by variations in the event generation and comparing the event yields at particle level neglecting detector effects. The uncertainties are defined in three components.

- The **scale** uncertainties are estimated by varying the renormalisation scale $\mu_{\mathrm{R}}$ and factorisation scale $\mu_{\mathrm{F}}$ coherently by factors of $0.5$ and $2$ on an event-by-

Tab. 10.8.: Theoretical systematic uncertainties on the normalisation of background processes in the $E_{\mathrm{T}}^{\mathrm{miss}} + \mathrm{h}(\mathrm{b\bar{b}})$ search.

| Process | Uncertainty |
|---|---|
| Ratio of $V + \mathrm{bc}$ / $V +$ heavy flavour | 20 % |
| Ratio of $V + \mathrm{b}l$ / $V +$ heavy flavour | 20 % |
| Ratio of $V + \mathrm{cc}$ / $V +$ heavy flavour | 20 % |
| Ratio of W + hf in SR and 1 muon CR | 20 % |
| Ratio of Z + hf in SR and 2 lepton CR | 20 % |
| $V + \mathrm{c}l$ | 30 % |
| $V + l$ | 10 % |
| Single top quark ($s$-channel) | 4.6 % |
| Single top quark ($t$-channel) | 4.4 % |
| Single top quark (W$t$-process) | 6.2 % |
| WW | 25 % |
| WZ | 26 % |
| ZZ | 20 % |
| $V\mathrm{h}, \mathrm{h} \to \mathrm{b\bar{b}}$ | 30 % |

event basis. The largest variation with respect to the nominal value is taken as the scale uncertainty.

- The **PDF** uncertainty is estimated by replacing the nominal NNPDF30LO PDF set with the alternative MSTW2008LO [283] and CTEQ6L1 [305] PDF sets. The largest deviation between the nominal and alternative PDF sets is taken as the signal PDF uncertainty.
- The **tune** uncertainty is estimated by varying the amounts of initial state radiation, final state radiation, and multi-parton interactions.

The average size of the signal acceptance uncertainties is below 1 %, except for a few signal mass points with lower acceptance. The signal acceptance uncertainties are correlated over the $E_{\mathrm{T}}^{\mathrm{miss}}$ bins by considering a single nuisance parameter for each type of systematic uncertainty.

## 10.7 Statistical model

The statistical model is based on the likelihood function Equation (6.11). The profile likelihood fit is based on the $E_{\mathrm{T}}^{\mathrm{miss}}$ bins and the invariant mass of the Higgs boson candidate in the SR, the muon charge and the $E_{\mathrm{T}}^{\mathrm{miss,no}\mu}$ bins in the 1 muon CR, and the $p_{\mathrm{T}}^{\ell\ell}$ bins in the 2 lepton CR. While the Higgs boson candidate mass information in the SR is provided in bin sizes ranging from 5 GeV to 20 GeV, the $E_{\mathrm{T}}^{\mathrm{miss}}$ information is provided more coarsely, using three bins in the resolved signal region and a single bin in the merged signal region. The $E_{\mathrm{T}}^{\mathrm{miss,no}\mu}$ and $p_{\mathrm{T}}^{\ell\ell}$ distributions employ

the same binning as the SR $E_{\mathrm{T}}^{\mathrm{miss}}$ distribution. The 1 muon CR exploits the muon charge information, which is naturally provided in two bins. A summary of all regions and kinematic distributions considered in the statistical model is provided in Table 10.9.

**Tab. 10.9.:** Summary of all regions and kinematic distributions considered in the statistical analysis of the $E_{\mathrm{T}}^{\mathrm{miss}} + \mathrm{h}(\mathrm{b\bar{b}})$ search.

| | **0 leptons** | **1 muon** | **2 leptons** |
|---|---|---|---|
| Process of interest | signal | W + jets, $\mathrm{t\bar{t}}$ | Z + jets |
| Primary fitted observable | $m_J$ / $m_{jj}$ | muon charge | event yield |
| Auxiliary fitted observable | $E_{\mathrm{T}}^{\mathrm{miss}}$ | $E_{\mathrm{T}}^{\mathrm{miss,no}\mu}$ | $p_{\mathrm{T}}^{\ell\ell}$ |
| Binning | resolved topology: $[150, 200, 350, 500]$ GeV<br>merged topology: 500 GeV or more | | |

## 10.8 Results

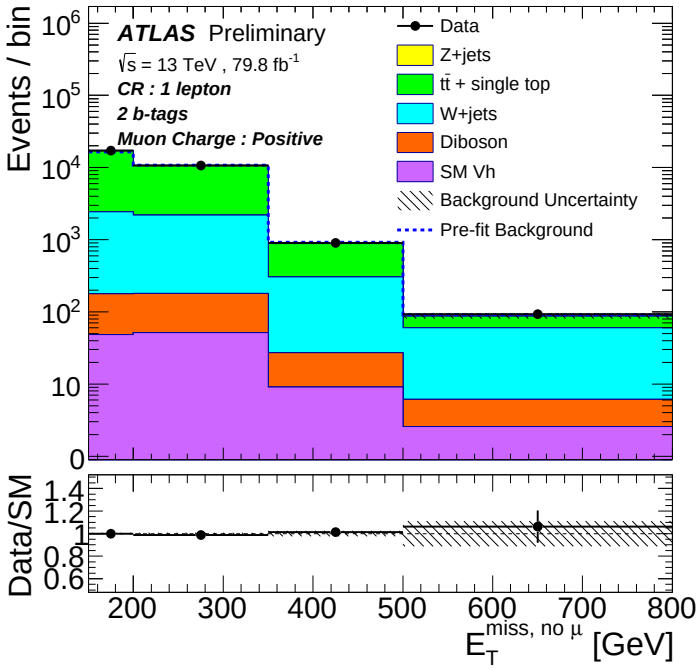
The results of the $E_{\mathrm{T}}^{\mathrm{miss}} + \mathrm{h}(\mathrm{b\bar{b}})$ search are presented in this section. The observed results are presented in Section 10.8.1. The impact of groups of systematic uncertainty on the sensitivity of the search is discussed in Section 10.8.2. Finally, the results are interpreted to constrain the parameter space of the Z′-2HDM simplified model in Section 10.8.3.

### 10.8.1 Observed results

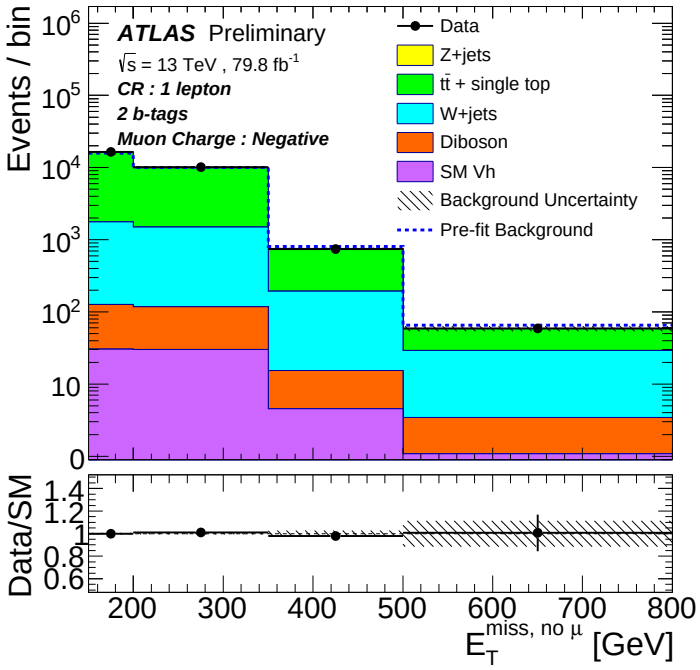
The background description by the statistical model is validated by performing a conditional background-only ($\mu = 0$) fit and investigating the corresponding distributions in the CRs. Figure 10.12 shows the $E_{\mathrm{T}}^{\mathrm{miss,no}\mu}$ distributions for the 1 muon CR for events with positively and negatively charged muon. Figure 10.13 shows the $p_{\mathrm{T}}^{\ell\ell}$ distribution for the 2 lepton CR. The observed data in the CRs are in good agreement with the SM background prediction, thereby validating the background description.

The results of the profile likelihood fit of the statistical model to the data are reported in terms of the discovery significance for Z′-2HDM simplified model signals in dependence of $m_{\mathrm{Z'}}$ and $m_{\mathrm{A}}$ in Figure 10.14.

No significant deviations from the background-only hypothesis have been observed. Therefore, the results in SR are presented with the background normalisations scaled to the outcome of the conditional background-only ($\mu = 0$) fit.




(a) 1 muon CR $E_{\mathrm{T}}^{\mathrm{miss,no}\mu}$ distribution (positive muon charge)




(b) 1 muon CR $E_{\mathrm{T}}^{\mathrm{miss,no}\mu}$ distribution (negative muon charge)

**Fig. 10.12.:** $E_{\mathrm{T}}^{\mathrm{miss,no}\mu}$ distributions for the 1 muon CR, positive (top) and negative (bottom) muon charge shown separately. The upper panel shows the comparison of data to the SM background expectation before (dashed lines) and after the background-only fit (solid histograms). The lower panel shows the ratio of the data to SM background expectations after the background-only fit, with the hatched band showing the systematic uncertainty.

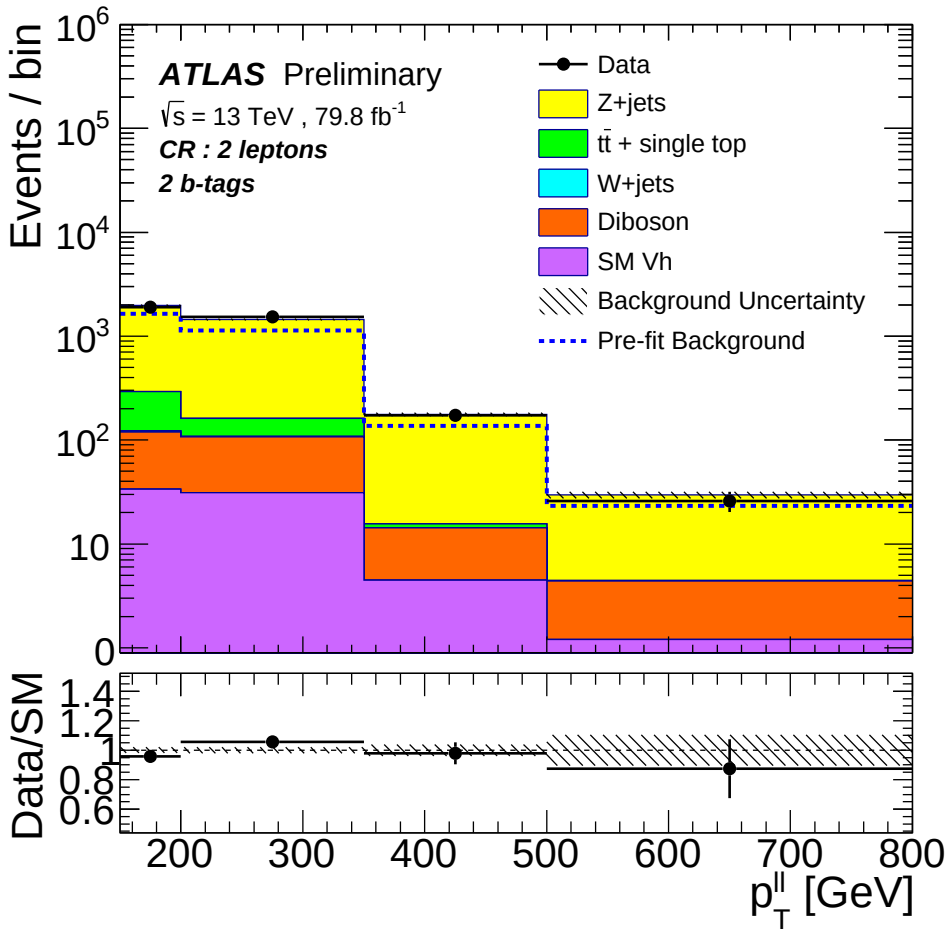
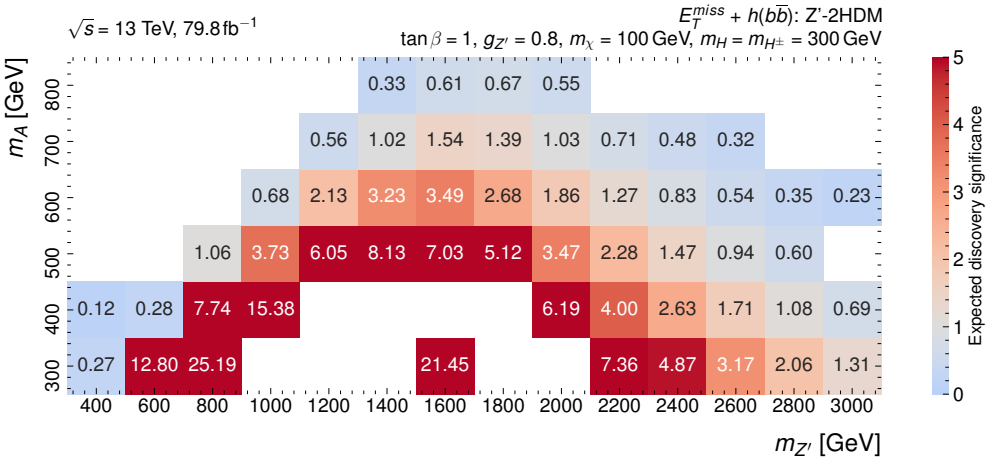
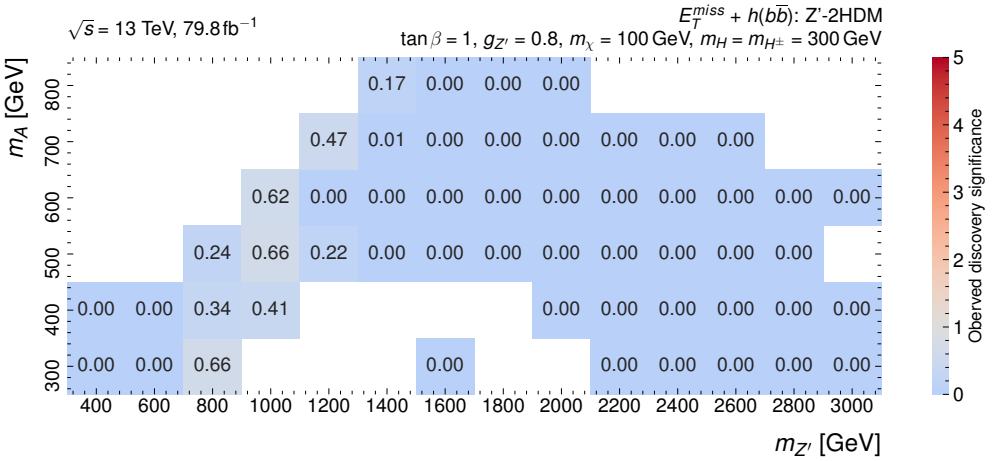



Fig. 10.13.: $p_{\mathrm{T}}^{\ell\ell}$ distribution for the 2 lepton CR. The upper panel shows the comparison of data to the SM background expectation before (dashed lines) and after the background-only fit (solid histograms). The lower panel shows the ratio of the data to SM background expectations after the background-only fit, with the hatched band showing the systematic uncertainty.




(a) Expected median discovery significance




(b) Observed discovery significance

**Fig. 10.14.:** Expected median discovery significance $Z^{\text{exp}}$ (top) estimated with the Asimov dataset generated under the assumption of the nominal signal model ($\mu = 1$) and observed discovery significance (bottom) for the Z′-2HDM simplified model signals in dependence of Z′ mediator mass $m_{Z'}$ and CP-odd Higgs boson mass $m_{\text{A}}$.

The observed number of events in the SR event selection for each $E_{\mathrm{T}}^{\mathrm{miss}}$ bin is shown in Table 10.10. The expected number of events for the individual background processes, whose normalisation is determined by the background-only profile likelihood fit, and the observed events in data are shown.

**Tab. 10.10.:** Expected and observed numbers of events in the signal region for an integrated luminosity of $79.8\,\mathrm{fb}^{-1}$ and $\sqrt{s} = 13\,\mathrm{GeV}$. The background yields and uncertainties are shown after the profile-likelihood fit to the data. The quoted background uncertainties include both the statistical and the systematic contributions.

| Process | Range in $E_{\mathrm{T}}^{\mathrm{miss}}$ [GeV] | | | |
|---|---|---|---|---|
| | $[150, 200)$ | $[200, 350)$ | $[350, 500)$ | $[500, \infty)$ |
| $\mathrm{t\bar{t}}$ + single top quark | 11 800 ± 350 | 6 450 ± 200 | 308 ± 25 | 10.8 ± 2.5 |
| W + jets | 3 020 ± 530 | 2 240 ± 360 | 184 ± 32 | 26.4 ± 5.7 |
| Z + jets | 6 330 ± 450 | 5 180 ± 340 | 565 ± 37 | 80.5 ± 6.3 |
| Diboson | 438 ± 67 | 400 ± 59 | 49.0 ± 11 | 9.37 ± 1.7 |
| $V\mathrm{h}, \mathrm{h} \to \mathrm{b\bar{b}}$ | 136 ± 39 | 129 ± 37 | 17.3 ± 5.0 | 3.86 ± 1.1 |
| Background | 21 700 ± 140 | 14 400 ± 110 | 1 120 ± 25 | 131 ± 7.2 |
| Data | 21 818 | 14 350 | 1 128 | 119 |

The corresponding $E_{\mathrm{T}}^{\mathrm{miss}}$ distribution is shown in Figure 10.15. No significant excess over the SM background is observed.

The invariant mass distributions in the SR are shown in Figure 10.16. The signal process is characterised by a large Higgs boson mass peak, which is most evident in the merged category due to the relatively low contribution of background processes.

## 10.8.2 Impact of systematic uncertainties

The impact of the various sources of systematic uncertainty on the fitted signal strength $\mu$ is evaluated using the procedure presented in Section 9.8.2.

Table 10.11 shows a breakdown of the expected signal strength uncertainties for three representative Z′-2HDM simplified model signals. The first signal corresponds to events selected primarily in the resolved category. The second signal corresponds to equal contributions of the merged and resolved categories. The third signal corresponds to events selected primarily in the merged category. The dominant sources of uncertainty are due to the identification of $b$-tagged jets, modelling uncertainties in $\mathrm{t\bar{t}}$ and $V$ + jets processes, and statistical uncertainty in the background prediction. The impact of large-radius jet uncertainties and the statistical uncertainty in the background prediction increases for the second and third signals because of a larger fraction of events in the merged category. For signals with heavy $m_{Z'}$, the total uncertainty is dominated by the statistical uncertainty of data.

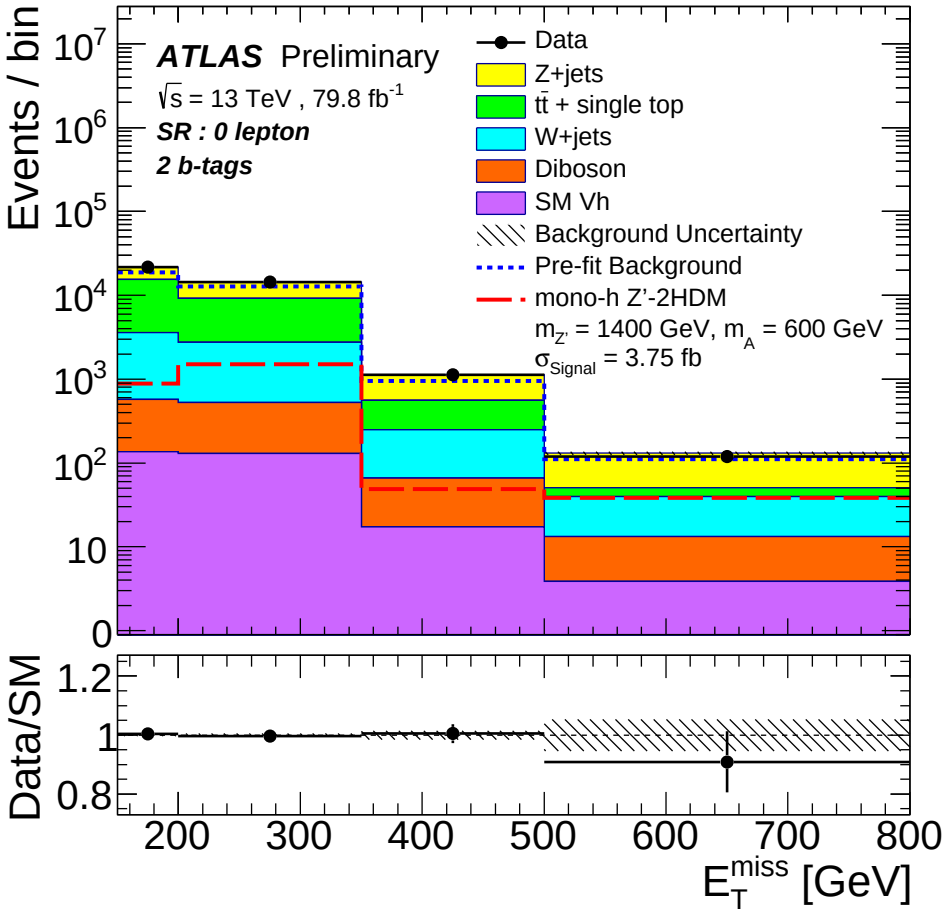
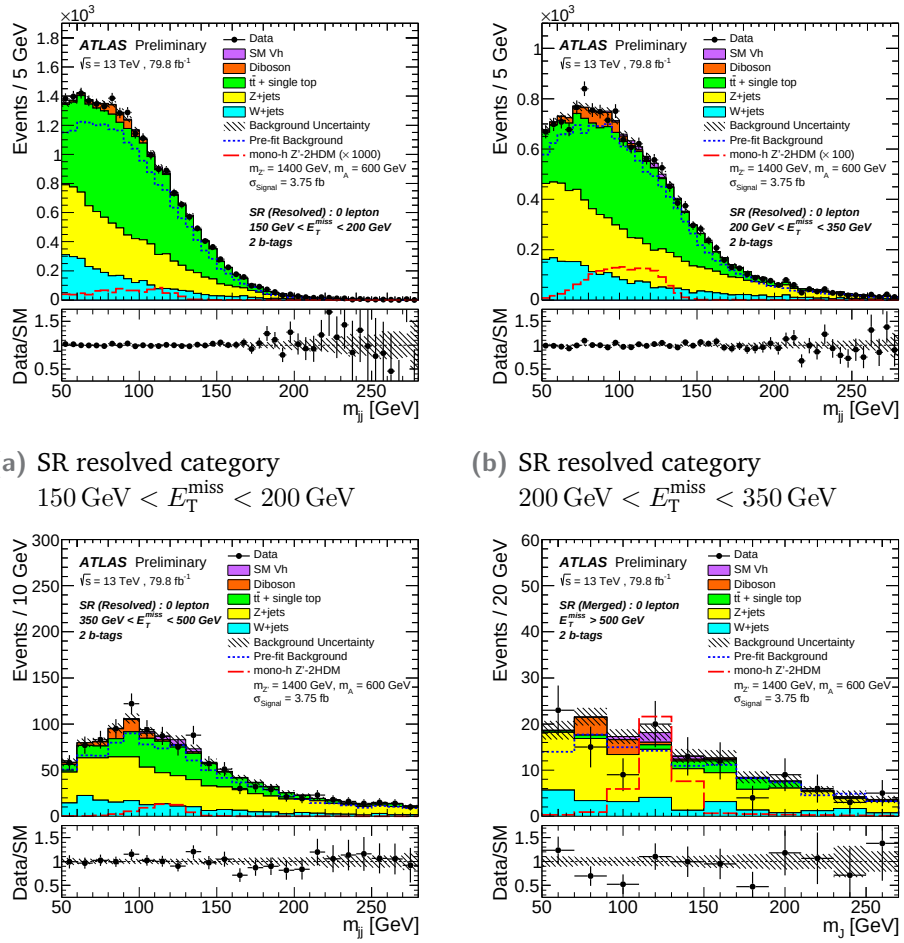



Fig. 10.15.: $E_{\mathrm{T}}^{\mathrm{miss}}$ distribution for the SR. The upper panel shows the comparison of data to the SM background expectation before (dashed lines) and after the background-only fit (solid histograms). The expected distribution for a representative Z′-2HDM signal is overlaid (long-dashed line). The lower panel shows the ratio of the data to SM background expectations after the background-only fit, with the hatched band showing the systematic uncertainty.




(a) SR resolved category $150\,\text{GeV} < E_{\text{T}}^{\text{miss}} < 200\,\text{GeV}$

(b) SR resolved category $200\,\text{GeV} < E_{\text{T}}^{\text{miss}} < 350\,\text{GeV}$

(c) SR resolved category $350\,\text{GeV} < E_{\text{T}}^{\text{miss}} < 500\,\text{GeV}$

(d) SR merged category $E_{\text{T}}^{\text{miss}} > 500\,\text{GeV}$

**Fig. 10.16.:** Distributions of the Higgs boson candidate invariant mass $m_{jj}$ (resolved) and $m_J$ (merged) in the SR for the four $E_{\text{T}}^{\text{miss}}$ bins. The upper panels show a comparison of data to the SM expectation before (dashed lines) and after the background-only fit (solid histograms). The expected distribution for a representative Z′-2HDM signal is overlaid (long-dashed line) and scaled by factors of 1000 and 100 in the two lowest $E_{\text{T}}^{\text{miss}}$ bins. The lower panels show the ratio of the data to SM background expectations after the background-only fit, with the hatched band indicating the systematic uncertainty.

**Tab. 10.11.:** Breakdown of expected signal strength uncertainties for three representative Z′-2HDM signal samples (a) $(m_{Z'}, m_A) = (0.6\,\text{TeV}, 0.3\,\text{TeV})$, (b) $(m_{Z'}, m_A) = (1.4\,\text{TeV}, 0.6\,\text{TeV})$, and (c) $(m_{Z'}, m_A) = (2.6\,\text{TeV}, 0.3\,\text{TeV})$. The effect is expressed as the relative uncertainty on the signal strength, assuming total cross-sections of (a) $452\,\text{fb}$, (b) $3.75\,\text{fb}$, and (c) $2.03\,\text{fb}$. Each systematic uncertainty contribution is provided as the quadratic difference between the total uncertainty and the uncertainty obtained by setting the systematic uncertainty in question to its nominal value and excluding it thereby from the fit. Total denotes the quadrature sum of statistical and total systematic uncertainties.

| Source of uncertainty | Uncertainty on $\mu$ [%] (a) | (b) | (c) |
|---|---|---|---|
| $b$-tagging | 4.0 | 8.0 | 10 |
| Large-radius jets | 0.2 | 1.0 | 2.0 |
| Small-radius jets | 1.4 | 3.0 | 2.0 |
| $E_T^{miss}$ | 1.2 | 1.7 | 1.1 |
| Leptons | 0.2 | 0.8 | 0.7 |
| Luminosity | 2.0 | 2.5 | 2.5 |
| Signal modelling | 3.0 | 2.5 | 1.5 |
| Top quark modelling | 3.7 | 4.8 | 4.5 |
| $V$ + jets modelling | 3.5 | 6.0 | 5.0 |
| SM $Vh, h \to b\bar{b}$ modelling | 0.8 | 3.2 | 2.1 |
| Diboson modelling | 0.8 | 1.5 | 1.1 |
| Background MC stat. | 1.8 | 5.4 | 4.9 |
| Total syst. | 6.5 | 13 | 13 |
| Data stat. | 2.3 | 20 | 22 |
| Total | 7 | 24 | 25 |

### 10.8.3 Constraints on the Z′-2HDM simplified model

As no significant deviation from the SM background expectation is observed for any of the signal mass points, the parameter space of the Z′-2HDM simplified model can be constrained by computing upper limits on the signal strength $\mu$ at $95\,\%$ confidence level using the $\mathrm{CL}_s$ method [307].

The exclusion limit contour, which is provided in the two-dimensional $m_{\mathrm{Z}'}$-$m_{\mathrm{A}}$ plane for the fixed set of parameters $g_{\mathrm{Z}'} = 0.8$, $\tan\beta = 1$, $m_\chi = 100\,\mathrm{GeV}$, and $m_{\mathrm{H}} = m_{\mathrm{H}^\pm} = 300\,\mathrm{GeV}$, is shown in Figure 10.17. The signal points in the Z′-2HDM model with $m_{\mathrm{Z}'}$ of up to $2.85\,\mathrm{TeV}$ and $m_{\mathrm{A}}$ up to $670\,\mathrm{GeV}$ are excluded at $95\,\%$ $\mathrm{CL}_s$, slightly exceeding the expected exclusion of the Z′ masses of up to $2.7\,\mathrm{TeV}$.

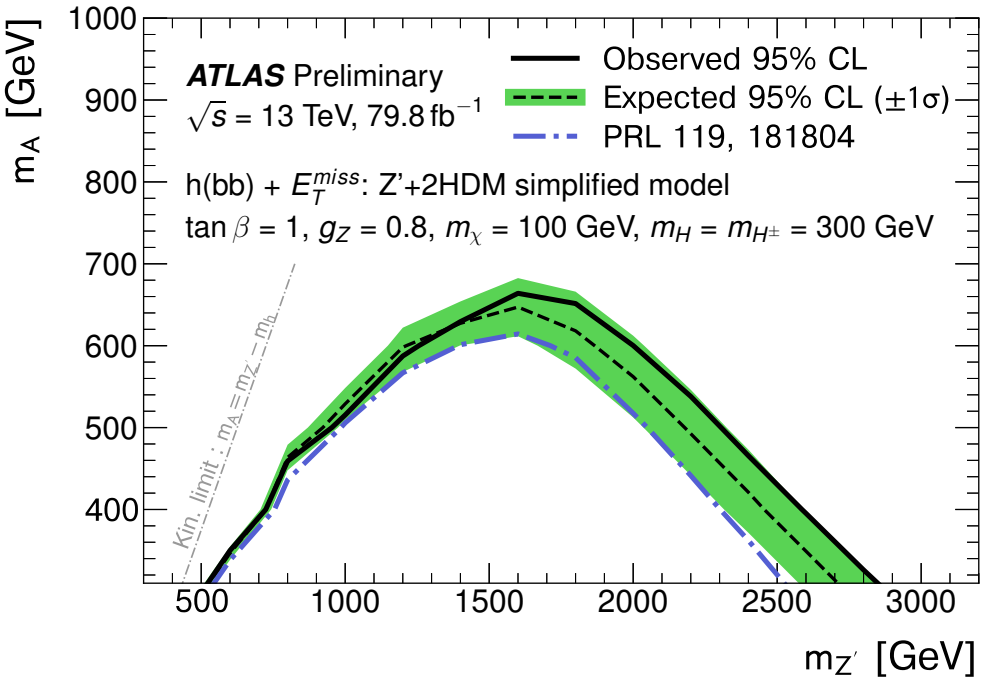



**Fig. 10.17.:** Exclusion contours at $95\,\%$ $\mathrm{CL}_s$ for the Z′-2HDM simplified model in the $m_{\mathrm{Z}'}$-$m_{\mathrm{A}}$ plane for the fixed set of parameters $\tan\beta = 1.0$, $g_{\mathrm{Z}'} = 0.8$, and $m_\chi = 100\,\mathrm{GeV}$. The observed limits (solid line) are consistent with the expectation under the SM-only hypothesis (densely dashed line) within uncertainties (filled band). The observed exclusion contour from a previous ATLAS publication at $\sqrt{s} = 13\,\mathrm{TeV}$ (dash-dotted line) [92] is overlaid.

The improvement from using VR track jets instead of FR track jets is demonstrated in Figure 10.18. The expected upper limits on the signal strength $\mu$ obtained with VR track jets is compared against that of the search presented in Ref. [92], which is obtained using fixed-radius (FR) track jets. The latter is scaled to $79.8\,\mathrm{fb}$ and computed by only considering events with two $b$-jets. Other differences between the two searches include the suppression of the multijet background using the object-based $E_{\mathrm{T}}^{\mathrm{miss}}$ significance, reduced statistical uncertainties from the MC background

simulation, and an improved $b$-tagging calibration for VR track jets. The expected limits for Z′-2HDM signals with highly boosted Higgs bosons show a significant improvement of up to a factor of three. Thus, this search based on VR track jets outperforms its predecessor considerably.

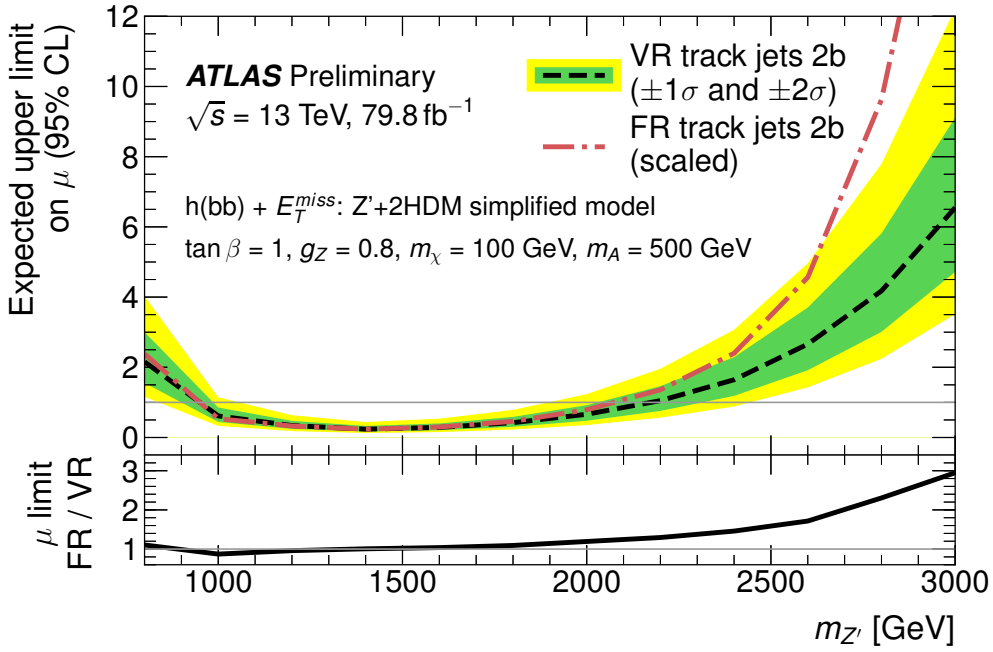



**Fig. 10.18.:** Expected exclusion limit on the signal strength $\mu$ at 95 % $\mathrm{CL}_s$ in dependence of $m_{\mathrm{Z}'}$ for the Z′-2HDM simplified model for the fixed set of parameters $m_{\mathrm{A}} = 500\,\mathrm{GeV}$, $\tan\beta = 1.0$, $g_{\mathrm{Z}'} = 0.8$, and $m_{\chi} = 100\,\mathrm{GeV}$. The expected limit of this search (dashed line) using variable-radius (VR) track jets is compared against that of the search presented in Ref. [92] using fixed-radius (FR) track jets. The latter is scaled to $79.8\,\mathrm{fb}$ and computed by only considering events with two $b$-jets. Other differences between the two searches include the suppression of the multijet background using the object-based $E_{\mathrm{T}}^{\mathrm{miss}}$ significance, reduced statistical uncertainties from the MC background simulation, and an improved $b$-tagging calibration for VR track jets. The lower panel shows the ratio of the expected limit obtained with VR track jets and FR track jets.

## 10.9 Conclusion of the $E_{\mathrm{T}}^{\mathrm{miss}} + \mathrm{h}(\mathrm{b\bar{b}})$ search

In conclusion, the novelty of VR track jets is applied in this search, and its superior performance in events with highly boosted Higgs candidates is established. The null results push the viable parameter space for yet unobserved resonances to yet higher masses, thereby increasing the relevance of event topologies with highly boosted objects. The VR track jet technique enables searches targeting these event topologies and is eagerly adopted by the experimental community [81, 79, 59, 95].

# 11 Search for dark matter in association with a dark Higgs boson decaying to $b$-quarks

## 11.1 Introduction

This chapter describes the search for dark matter in association with a dark Higgs boson $s$. The signature of missing transverse momentum and a hypothetical dark Higgs boson is predicted by the 2MDM simplified model (c.f. Section 3.7.4). The presence of such a dark Higgs boson is motivated both by the need to generate the masses of dark matter particles and the Z′ boson mediator and by constraints on models of dark matter production due to the observed dark matter relic density [211].

The dark Higgs boson can mix with the SM Higgs boson and thereby shares its decay modes. Consequently, the dark Higgs boson can be sought by searches in various final states, which probe a broad dark Higgs boson mass range. The search presented in this chapter focuses on the dark Higgs boson decay to $b$-quarks and is sensitive to dark Higgs bosons in the mass range below $160\,\mathrm{GeV}$, while Chapter 12 focuses on the decay to pairs of weak vector bosons and extends the coverage towards heavier dark Higgs boson signals.

The production of dark matter particles $\chi$ in association with a dark Higgs boson decaying to $b$-quarks shares the signature of $E_\mathrm{T}^\mathrm{miss}$ and two $b$-tagged jets with the $E_\mathrm{T}^\mathrm{miss} + \mathrm{h}(\mathrm{b\bar{b}})$ search, except for the mass of the Higgs boson candidate. The primary discriminating variable of the $E_\mathrm{T}^\mathrm{miss} + \mathrm{h}(\mathrm{b\bar{b}})$ search is the invariant mass of the Higgs candidate, which extends from $50\,\mathrm{GeV}$ to $280\,\mathrm{GeV}$. Therefore, the search presented in Chapter 10 can be reinterpreted in terms of the 2MDM simplified model for a dark Higgs boson signal with mass $m_s$.

The reinterpretation is performed using the RECAST framework (c.f. Section 6.3). It is based on the 2015–2017 pp dataset corresponding to an integrated luminosity of $79.8\,\mathrm{fb}^{-1}$. Constraints on the 2MDM model are obtained by combining the preserved background model and observed data of the $E_\mathrm{T}^\mathrm{miss} + \mathrm{h}(\mathrm{b\bar{b}})$ search with distributions of the discriminating variables for the simulated 2MDM signal model points. While previous efforts already demonstrated capturing the analysis software in containers to be feasible [103, 42, 40, 77], this reinterpretation also captures the analysis workflow and thereby is fully automated. The results of this reinterpretation have been presented in Ref. [76].

Section 11.2 introduces the signal process in the search for dark matter and dark Higgs bosons decaying to $b$-quarks. As this search is a reinterpretation of the

$E_{\mathrm{T}}^{\mathrm{miss}} + \mathrm{h}(\mathrm{b\bar{b}})$ search, the background processes are the same as those described in Section 10.2.2. The systematic uncertainties on the signal are discussed in Section 11.3. The technical implementation in the RECAST framework is described in Section 11.4, while the results are presented in Section 11.5. A conclusion is given in Section 11.6.

## 11.2 Signal processes

The analysis investigates dark matter production in the framework of the 2MDM simplified model, which is described in Section 11.2.1. The simulated signal samples are summarised in Section 11.2.2.

### 11.2.1 2MDM simplified model

The 2MDM simplified model is considered for the reinterpretation of the $E_{\mathrm{T}}^{\mathrm{miss}}+\mathrm{h}(\mathrm{b\bar{b}})$ search. It is a simplified model in which a $\mathrm{Z}'$ spin-1 mediator and a dark Higgs boson $s$ arise from a spontaneously broken $\mathrm{U}(1)_{\mathrm{Z}'}$ gauge symmetry and an additional complex Higgs field (c.f. Section 3.7.4).

The processes yielding the signature of $E_{\mathrm{T}}^{\mathrm{miss}} + s(\mathrm{b\bar{b}})$ are illustrated by the two example Feynman graphs in Figure 11.1.

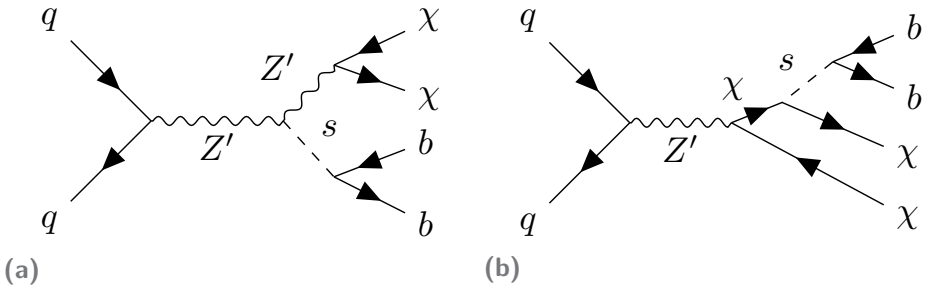



Fig. 11.1.: Production of dark matter particles $\chi$ and a dark Higgs boson $s$ through $s$-channel exchange of a new $\mathrm{Z}'$ mediator. The dark Higgs boson is decaying to $b$-quarks.

A $\mathrm{Z}'$ vector boson is produced in pp collisions, which couples both to dark matter particles and the dark Higgs boson. The dark Higgs boson can be radiated off either from the $\mathrm{Z}'$ boson or from a dark matter particle in the final state. Through mixing with the SM Higgs boson, the dark Higgs boson decays to visible particles, such as $b$-quarks or weak vector bosons.

The relevant model parameters and their chosen values are listed in Table 11.1. These parameters include the masses of the involved particles $m_{\mathrm{Z}'}$, $m_s$, $m_\chi$, the gauge couplings of the $\mathrm{Z}'$ boson to quarks $g_q$ and the dark sector $g_\chi$, and the mixing angle between the SM Higgs boson and the dark Higgs boson. The dark matter

particle mass $m_\chi$ is set to 200 GeV. The chosen values of the couplings $g_q = 0.25$ and $g_\chi = 1$ are adopted to allow for comparisons with other simplified models, despite stringent constraints on $g_q$ from dijet searches [40]. The mixing angle between the dark Higgs boson and the SM Higgs boson is set to $\theta = 0.01$, following the choice adopted in Ref. [211].

The interpretation of the results of the search is performed via a scan over the two-dimensional $m_{Z'}$-$m_s$ plane for fixed choices of the coupling parameters and the dark matter mass $m_\chi = 200$ GeV. The scan extends over the range 500 GeV to 3500 GeV in $m_{Z'}$ and 50 GeV to 150 GeV in $m_s$.

**Tab. 11.1.:** Parameters of the 2MDM simplified model in the searches for dark matter in association with a dark Higgs boson.

| Parameter | Description | Chosen value |
|---|---|---|
| $m_{Z'}$ | $Z'$ boson mass | free |
| $m_s$ | dark Higgs boson mass | free |
| $m_\chi$ | dark matter particle mass | 200 GeV |
| $g_q$ | $Z'$ gauge coupling to quarks | 0.25 |
| $g_\chi$ | $Z'$ gauge coupling to the dark sector | 1 |
| $\theta$ | mixing angle between the SM Higgs boson and the dark Higgs boson | 0.01 |

### 11.2.2 Simulated Monte Carlo samples for signal processes

Signals of the process $pp \to Z' \to \chi\overline{\chi} + b\bar{b}$ are simulated by scanning the mass of the $Z'$ boson in the range 500 GeV to 3500 GeV in steps of 500 GeV and the mass of the dark Higgs boson $m_s$ in the range 50 GeV to 150 GeV in 20 GeV steps.

The simulated events are generated at leading-order (LO) accuracy with the MADGRAPH5_aMC@NLO 2.6.2 event generator [23] interfaced to the PYTHIA 8.230 [320] parton shower and hadronisation model, using the NNPDF23 PDF set [118] and the A14 set of tuned parameters [37]. To remove the overlap between the hard scattering and the parton shower model, the CKKW-L merging procedure [276, 277] is applied with the matching scale set to 40 GeV.

## 11.3 Systematic uncertainties on the signal process

Only the systematic uncertainties associated with the signal process need to be estimated, as the preserved background model of the $E_T^{miss} + h(b\bar{b})$ search already contains all systematic uncertainties on the background.

The experimental systematic uncertainties on the signal process are estimated similarly to those on the background process, using the calibration tools which are part of the preserved analysis software.

The theoretical systematic uncertainties on the signal process are estimated by varying the model parameters and comparing the event yield after applying the analysis selection at particle level neglecting detector effects. Renormalisation and factorisation scale uncertainties and variations of parton distribution functions (PDFs) are considered in the four $E_{\mathrm{T}}^{\mathrm{miss}}$ bins of the search. The scale uncertainties in individual $E_{\mathrm{T}}^{\mathrm{miss}}$ bins range from $6.2\,\%$ to $22.2\,\%$, while the uncertainty on PDFs ranges from $3.8\,\%$ to $16.4\,\%$. The signal acceptance uncertainties are correlated over the $E_{\mathrm{T}}^{\mathrm{miss}}$ bins by considering a single nuisance parameter for each type of systematic uncertainty.

## 11.4 Technical implementation

The reinterpretation requires the simulated events for the 2MDM simplified model signals to be processed by the analysis workflow, which consists of two steps. The first step involves processing the simulated events for the signal process to obtain fit inputs for the statistical inference. The second step combines these inputs with the preserved background estimate and the observed data of the $E_{\mathrm{T}}^{\mathrm{miss}} + \mathrm{h}(\mathrm{b\bar{b}})$ search to compute upper limits on the signal strength of the 2MDM simplified model signals. Figure 11.2 illustrates the workflow, which consists of the following steps:

- **Signal preparation**. The signal events are sampled using the standard tools as described in Section 8.2.2, which are centrally maintained and thus do not require the expert knowledge encoded in RECAST.
- **Signal analysis**. The event processing stage involves the calibration of physics objects, object and event selection, as well as the variation of the latent parameters in the simulation to account for systematic uncertainties. In addition, the pile-up profile of the simulated events is corrected to match the data, and the simulated events are weighted according to the integrated luminosity. This step is performed using a DOCKER image of the event processing software, which is maintained on the CERN GitLab [245] platform. The output of the signal analysis step is the expected number of events in each SR $E_{\mathrm{T}}^{\mathrm{miss}}$ bin, including the systematic uncertainty in the expected event yield.
- **Inference**. The statistical inference involves the construction of a binned likelihood following Equation (6.11). The preserved background and data inputs are combined with the newly derived signal estimates. As the predicted signal yields are estimated using simulation, they are subject to systematic uncertainties on the acceptance. The likelihood function accounts for this through the addition of nuisance parameters and corresponding constraint terms. Upper limits on the signal cross-section normalised to the theoretical expectation are derived from the constructed likelihood.

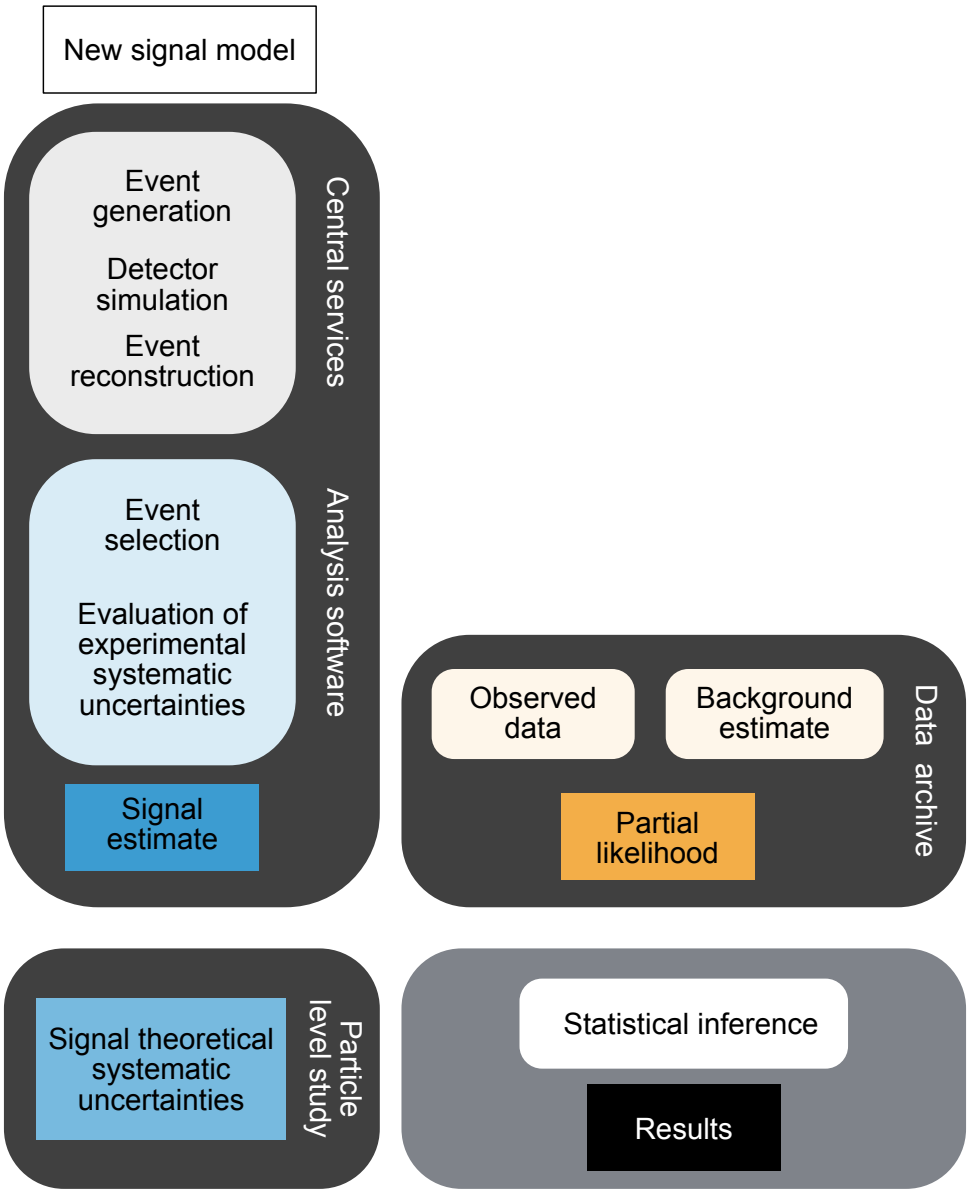



**Fig. 11.2.:** Workflow for the RECAST reinterpretation of the $E_{\mathrm{T}}^{\mathrm{miss}} + \mathrm{h}(\mathrm{b\bar{b}})$ search. The signal preparation step is performed using centrally provided services for MC event generation, detector simulation, and event reconstruction of the new signal sample. The signal analysis is based on the RECAST framework services by capturing the analysis software and the associated workflow for performing the event selection and the evaluation of experimental systematic uncertainties on the signal estimate. The statistical inference combines the partial likelihood, which is constructed using the preserved data and background estimate, the signal estimate, and the theoretical systematic uncertainties on the signal. The latter are estimated using a simplified implementation of the analysis on particle level neglecting detector effects.

## 11.5 Results

The results of the $E_{\mathrm{T}}^{\mathrm{miss}} + \mathrm{h}(\mathrm{b\bar{b}})$ search established that the observed data is compatible with the SM background, and no significant excess has been observed. Therefore, exclusion limits on the 2MDM signal model are placed in the statistical inference step of the reinterpretation, which is based on the same combined profile likelihood fit as in the $E_{\mathrm{T}}^{\mathrm{miss}} + \mathrm{h}(\mathrm{b\bar{b}})$ search, only with the signal and its associated uncertainties replaced.

Figure 11.3 shows the $E_{\mathrm{T}}^{\mathrm{miss}}$ distribution for the observed data corresponding to an integrated luminosity of $79.8\,\mathrm{fb}^{-1}$ and the expected SM background before and after the background-only fit.

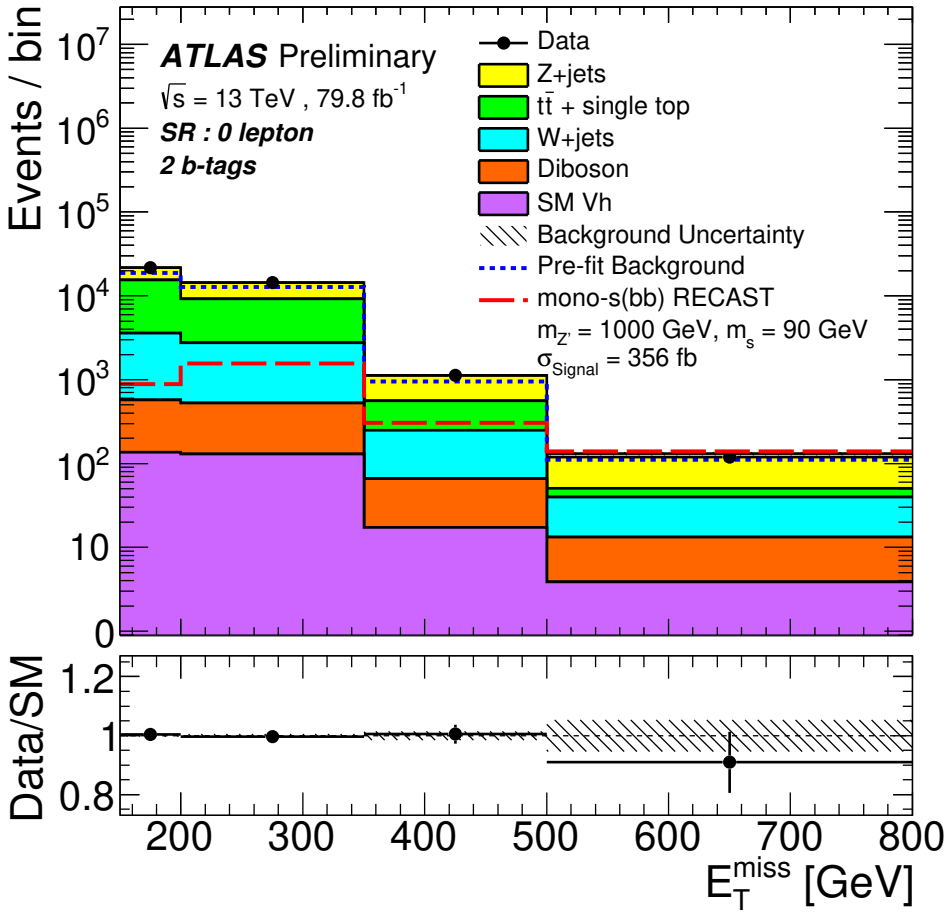



**Fig. 11.3.:** $E_{\mathrm{T}}^{\mathrm{miss}}$ distribution for the SR. The upper panel shows the comparison of data to the SM background expectation before (dashed lines) and after the background-only fit (solid histograms). The expected distribution for a representative 2MDM signal with $m_{Z'} = 1\,\mathrm{TeV}$ and $m_s = 90\,\mathrm{GeV}$ is overlaid (long-dashed line). The signal is scaled to an arbitrary cross-section of $356\,\mathrm{fb}$ for visualisation. The lower panel shows the ratio of data to SM background expectations after the background-only fit, with the hatched band showing the systematic uncertainty.

The invariant mass distributions in the SR are shown in Figure 11.4. The distributions are exactly the same as those shown in Figure 10.15, except for the new signal process (red dashed line), which corresponds to the production of a dark Higgs boson with mass $m_s = 90\,\text{GeV}$ via a Z′ boson mediator with $m_{Z'} = 1\,\text{TeV}$. The signal process is characterised by a mass peak at ($m_{jj}$ and $m_J = 90\,\text{GeV}$, which becomes more evident with increasing $E_\text{T}^\text{miss}$ due to the decreasing contribution of background processes.

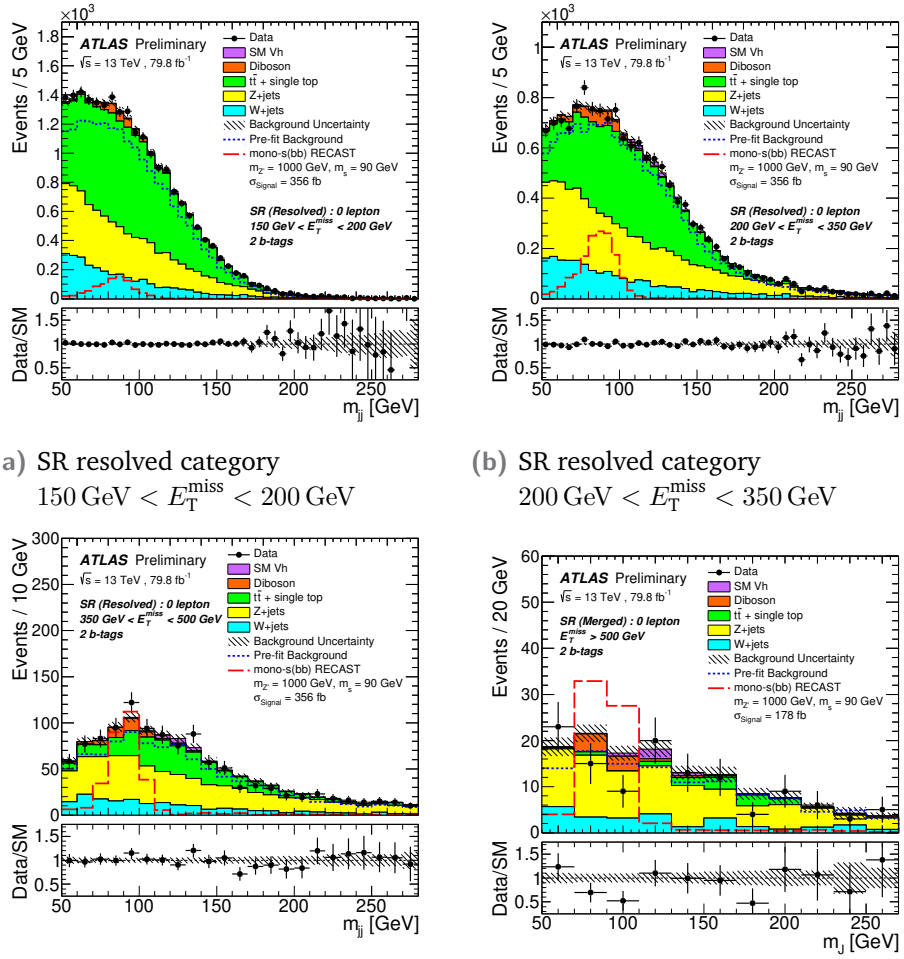
The expected and observed upper $95\,\%$ $\text{CL}_s$ limits on the signal strength $\mu$ as a function of $m_{Z'}$ and $m_s$ are shown in Figure 11.5 for the fixed choice of parameters $m_\chi = 200\,\text{GeV}$, $g_q = 0.25$, and $g_\chi = 1$. If the upper limit is below one, the specific model configuration is excluded at $95\,\%$ $\text{CL}_s$.

The exclusion limits can also be presented as a corresponding exclusion contour in the $m_{Z'}$-$m_s$ plane, as shown in Figure 11.6. The region to the left of the observed $95\,\%$ $\text{CL}_s$ exclusion contour, which is indicated by the black line, is excluded. The expected exclusion contour is indicated by the dashed line, while the green and yellow bands represent the $\pm1\sigma$ and $\pm2\sigma$ uncertainty, respectively.

The expected exclusion of the 2MDM parameter space for the fixed choice of parameters $m_\chi = 200\,\text{GeV}$, $g_q = 0.25$, and $g_\chi = 1$ extends in $m_{Z'}$ up to $2.3\,\text{TeV}$ for $m_s = 50\,\text{GeV}$ and up to $2.8\,\text{TeV}$ for $70\,\text{GeV} < m_s < 110\,\text{GeV}$. The reduced sensitivity for lower $m_s$ is because of the larger contribution of SM backgrounds. The sensitivity for $m_s > 130\,\text{GeV}$ decreases because of the diminishing branching fraction of the $s \to \text{b}\bar{\text{b}}$ process for larger $m_s$ (c.f. Figure 3.11). The observed exclusion extends up to $3.2\,\text{TeV}$ in $m_{Z'}$. The exclusion for model configurations with high $m_{Z'}$ is almost entirely driven by the merged category. For $70\,\text{GeV} < m_s < 130\,\text{GeV}$, the observed limits are stronger than the expected ones. This is caused by the under-fluctuation in data visible in Figure 11.4d for $70\,\text{GeV} < m_J < 110\,\text{GeV}$. In addition to the exclusion contours, a purple dotted line indicates the region of the 2MDM simplified model's parameter space which is compatible with the dark matter relic density measurements performed by the PLANCK collaboration [301]. The region to the right of this line corresponds to a predicted relic density, which is higher than these measurements. In conclusion, the whole region of parameter space in $m_{Z'}$ for the fixed choice of parameters $m_\chi = 200\,\text{GeV}$, $g_q = 0.25$, and $g_\chi = 1$ is excluded for $50\,\text{GeV} < m_s < 150\,\text{GeV}$.

## 11.6 Conclusion of the $E_\text{T}^\text{miss} + s(\text{b}\bar{\text{b}})$ search

This reinterpretation provided a first demonstration of using the RECAST framework to constrain new models with a faithful re-execution of a preserved search with similar signature. The analysis preservation strategies employed by RECAST have more widely influenced the CERN Analysis Preservation efforts [197] and are an integral part of the preservation of full Run-2 ATLAS searches for dark matter and other Beyond-the-Standard-Model phenomena.



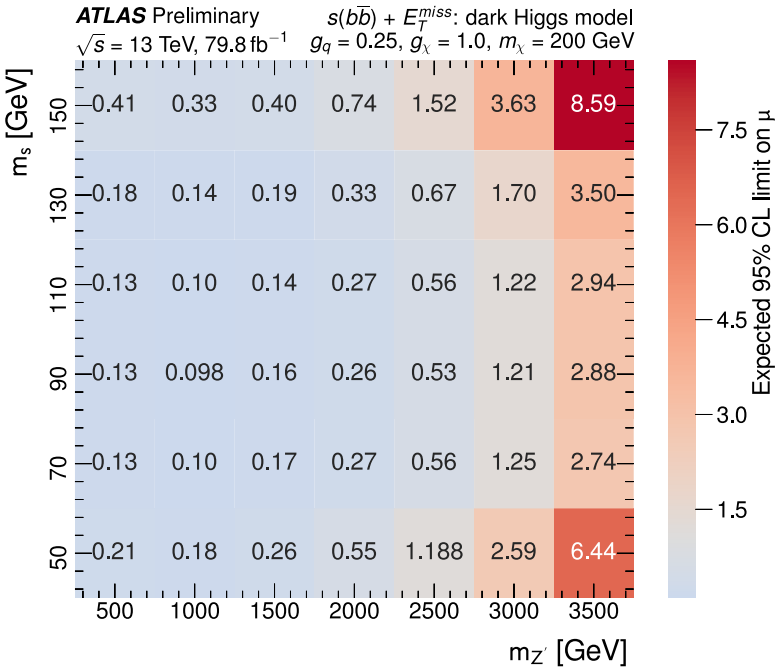

(a) SR resolved category $150\,\text{GeV} < E_{\text{T}}^{\text{miss}} < 200\,\text{GeV}$

(b) SR resolved category $200\,\text{GeV} < E_{\text{T}}^{\text{miss}} < 350\,\text{GeV}$

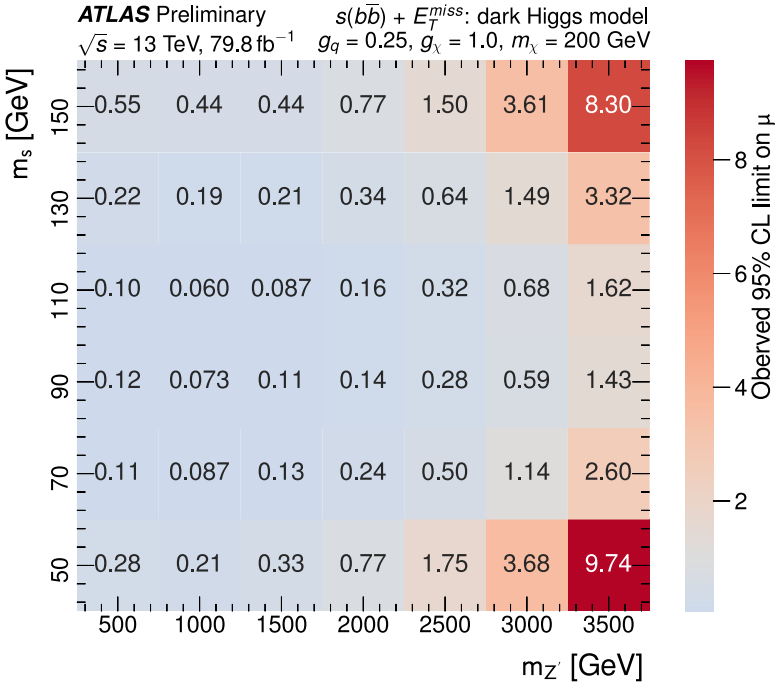
(c) SR resolved category $350\,\text{GeV} < E_{\text{T}}^{\text{miss}} < 500\,\text{GeV}$

(d) SR merged category

**Fig. 11.4.:** Distributions of the Higgs boson candidate invariant mass $m_{jj}$ (resolved), $m_J$ (merged) in the SR for the four $E_{\text{T}}^{\text{miss}}$ bins. The upper panels show a comparison of data to the SM expectation before (dashed lines) and after the background-only fit (solid histograms). The expected distribution for a representative 2MDM signal with $m_{Z'} = 1\,\text{TeV}$ and $m_s = 90\,\text{GeV}$ is overlaid (long-dashed line). The signal is scaled to an arbitrary cross-section of $356\,\text{fb}$ in the resolved category and $178\,\text{fb}$ in the merged category for visualisation. The lower panels show the ratio of data to SM background expectations after the background-only fit, with the hatched band indicating the systematic uncertainty.




(a) Expected upper limits on the signal strength $\mu$




(b) Observed upper limits on the signal strength $\mu$

**Fig. 11.5.:** Upper 95 % $CL_s$ exclusion limits on the signal strength $\mu$ for the 2MDM simplified model with parameters $m_\chi = 200\,\text{GeV}$, $g_q = 0.25$, and $g_\chi = 1$ for different values of $m_{Z'}$ and $m_s$. The expected exclusion limits are shown at the top, while the observed exclusion limits are shown at the bottom.

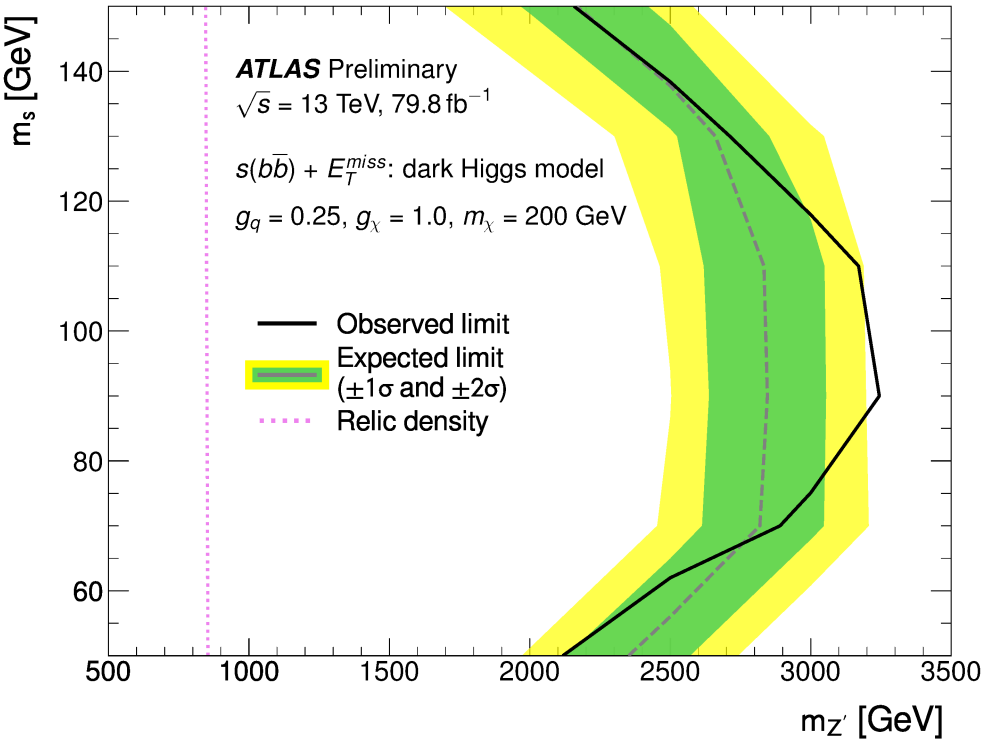



Fig. 11.6.: Exclusion contours at 95 % $CL_s$ for the 2MDM simplified model in the $m_{Z'}$-$m_s$ plane for the fixed set of parameters $m_\chi = 200\,\text{GeV}$, $g_q = 0.25$, and $g_\chi = 1$. The observed limits (solid line) are consistent with the expectation under the SM-only hypothesis (densely dashed line) mostly within $\pm 2\sigma$ uncertainties (filled bands).

# 12 Search for dark matter in association with a dark Higgs boson decaying to a pair of weak vector bosons

## 12.1 Introduction

This chapter describes the search for dark matter in association with a dark Higgs boson $s$ decaying to a pair of weak vector bosons, which is referred to as the $E_{\mathrm{T}}^{\mathrm{miss}} + s(VV)$ search. The results presented in this chapter complement those presented in Chapter 11 by extending the dark Higgs boson mass reach.

The $E_{\mathrm{T}}^{\mathrm{miss}} + s(VV)$ signature is explored by a search in the fully hadronic channel, as the hadronic decays of weak vector bosons have the largest branching fraction [335]. The search makes use of the full ATLAS Run-2 pp dataset, corresponding to an integrated luminosity of $139\,\mathrm{fb}^{-1}$.

The $E_{\mathrm{T}}^{\mathrm{miss}} + s(VV)$ search investigates the yet uncharted signature of missing transverse momentum and the resonant production of a pair of hadronically decaying weak vector bosons, whose decays give rise to a system of up to four jets. The challenging event topology is addressed with the novel reconstruction technique of the Track-Assisted-Reclustering (TAR) jet algorithm [109], which enables the reconstruction of large-radius jets from calibrated small-radius jets and ID tracks. The results of this search have been presented in Ref. [89].

Section 12.2 introduces the signal and background processes in the $E_{\mathrm{T}}^{\mathrm{miss}} + s(VV)$ search. The analysis strategy is outlined in Section 12.3. The corresponding object and event selection, including the definition of the signal region is described in Section 12.4, whereas the background estimation strategy and the definitions of the control regions are described in Section 12.5. The systematic uncertainties taken into account in the statistical model are described in Section 12.6, while the statistical model itself is provided in Section 12.7. The observed results are presented and discussed in Section 12.8. A conclusion is given in Section 12.9.

## 12.2 Signal and background processes

The analysis investigates dark matter production in the framework of the 2MDM simplified model, using the configuration which is described in Section 11.2.1. The

background processes are outlined in Section 12.2.1. The simulated signal and background samples are summarised in Section 12.2.2.

### 12.2.1 Background processes

The dominant background processes resulting in the signature of two weak vector bosons and substantial $E_{\mathrm{T}}^{\mathrm{miss}}$ are Z + jets production ($61\,\%$ background contribution) and W + jets production ($32\,\%$ background contribution). Sub-dominant background processes include $\mathrm{t\bar{t}}$ production, WW, WZ, and ZZ diboson production, single top quark production, SM $V\mathrm{h}, \mathrm{h} \to \mathrm{b\bar{b}}$ production, and multijet events.

The dominant background processes are estimated using simulated samples, whose normalisation is constrained by control region data. The smaller background processes are estimated purely by simulation. The multijet background is estimated to be negligible based on a data-driven estimate.

### 12.2.2 Simulated Monte Carlo samples

The signal and background processes with the MC event generators, parton shower models and PDF sets used for their description are summarised in Table 12.1. Detailed descriptions of the background samples are provided in Section 8.2.2.

The signal process in the 2MDM simplified model is simulated on grids defined by the mediator mass $m_{\mathrm{Z}'}$ and the dark Higgs boson mass $m_s$ for a fixed dark matter particle mass $m_\chi = 200\,\mathrm{GeV}$. The signals are simulated by scanning the mass of the dark Higgs boson $m_s$ in the range $160\,\mathrm{GeV}$ to $360\,\mathrm{GeV}$ in $25\,\mathrm{GeV}$ steps considering $\mathrm{Z}'$ boson masses of $0.5\,\mathrm{TeV}$, $1\,\mathrm{TeV}$, $1.7\,\mathrm{TeV}$, and $2.1\,\mathrm{TeV}$.

The coverage in the $m_{\mathrm{Z}'}$-$m_s$ plane of the parameter space is extended by an interpolation procedure. The interpolation is based on reweighting the simulated samples to signal configurations with different $m_{\mathrm{Z}'}$ using events generated at particle level neglecting detector effects [309]. The interpolation procedure provides the exclusion contour with a $\Delta m_{\mathrm{Z}'} = 100\,\mathrm{GeV}$ spacing.

The simulated events are generated at leading-order (LO) accuracy with the MADGRAPH5_aMC@NLO 2.6.2 event generator [23] interfaced to the PYTHIA 8.230 [320] parton shower and hadronisation model, using the NNPDF23 PDF set [118] and the A14 set of tuned parameters [37]. To remove the overlap between the hard scattering and the parton shower model, the CKKW-L merging procedure [276, 277] is applied with the matching scale set to $40\,\mathrm{GeV}$.

Tab. 12.1.: List of the signal and background processes with the MC event generators, sets of PDFs and tunes used for their description in the $E_{\mathrm{T}}^{\mathrm{miss}} + s(VV)$ search.

| Process | Generator | PDF / parton shower tune |
|---|---|---|
| **Signal** | | |
| 2MDM simplified model | MadGraph5_aMC@NLO 2.6.2 + Pythia 8.230 | NNPDF23LO / A14 |
| **Top quark** | | |
| $t\bar{t}$ | Powheg-Box 2 + Pythia 8.230 | NNPDF30NLO / A14 |
| t ($s$-channel) | Powheg-Box 2 + Pythia 8.230 | NNPDF30NLO / A14 |
| t ($t$-channel) | Powheg-Box 2 + Pythia 8.230 | NNPDF30NLO / A14 |
| t (W$t$) | Powheg-Box 2 + Pythia 8.230 | NNPDF30NLO / A14 |
| ***V*** **+ jets** | | |
| W + jets | Sherpa 2.2.1 | NNPDF30NNLO / Sherpa-tune |
| Z + jets | Sherpa 2.2.1 | NNPDF30NNLO / Sherpa-tune |
| **Diboson** | | |
| WW | Sherpa 2.2.1 | NNPDF30NLO / Sherpa-tune |
| WZ | Sherpa 2.2.1 | NNPDF30NLO / Sherpa-tune |
| ZZ | Sherpa 2.2.1 | NNPDF30NLO / Sherpa-tune |
| $V\mathrm{h}, \mathrm{h} \to \mathrm{b\bar{b}}$ | Powheg-Box 2 + Pythia 8.212 | NNPDF30NLO / AZNLO |

## 12.3 Analysis strategy

The signature of dark matter particle production in association with a dark Higgs boson $s$ decaying to pairs of weak vector bosons in the hadronic decay channel is provided by missing transverse momentum $E_{\mathrm{T}}^{\mathrm{miss}}$ recoiling against a system of up to four jets resulting from the $s \to V(qq)V(qq)$ decay.

The signal region (SR) is defined by the requirement of substantial missing transverse momentum and a dark Higgs boson candidate. The sensitivity of the search is optimised over a broad range of dark Higgs boson candidate momenta by considering two event topologies for the dark Higgs boson candidate reconstruction.

In events with a highly boosted dark Higgs boson candidate, the dark Higgs boson decay products become collimated and can be fully captured within a single TAR jet. This event topology is referred to as the merged category.

Moderately boosted dark Higgs boson candidates result in less collimated decay products, which might be captured only partially by a single TAR jet. Therefore, a dedicated algorithm is employed to reconstruct dark Higgs boson candidates from TAR jets augmented with one or two small-radius jets. This event topology is referred to as the intermediate category.

In contrast to the other searches discussed in this dissertation, no resolved category is considered, as the sensitivity in the $E_{\mathrm{T}}^{\mathrm{miss}} + s(VV)$ signature is driven by highly boosted boson decays.

Potential ambiguities in the selection are resolved by giving preference to the merged category, which has better sensitivity. Figure 12.1 illustrates the two event topologies in the transverse plane of the detector.

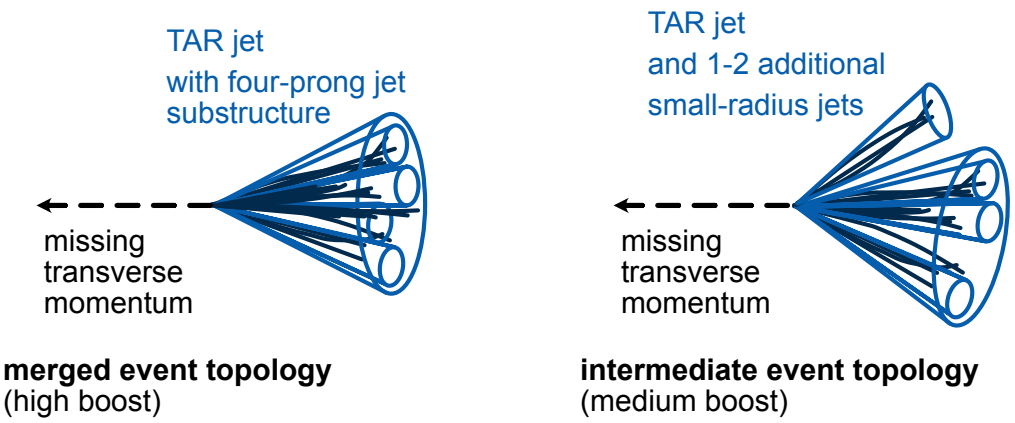



**Fig. 12.1.:** Illustrations of the merged and intermediate event topologies in the $E_{\mathrm{T}}^{\mathrm{miss}}+s(VV)$ search.

Additional requirements on kinematic properties and the event topology further increase the sensitivity of the search. The primary discriminating variable in the statistical analysis is the invariant mass of the dark Higgs boson candidate. Moreover, the merged category SR is further classified in the two $E_{\mathrm{T}}^{\mathrm{miss}}$ bins $300\,\mathrm{GeV}$ to $500\,\mathrm{GeV}$ and $500\,\mathrm{GeV}$ or more to benefit from the increased signal sensitivity with higher $E_{\mathrm{T}}^{\mathrm{miss}}$.

The SR selection vetoes events containing electrons or muons. The control regions (CRs) require the presence of either one muon (1 muon CR) or two electrons or muons (2 lepton CR). As SR and CRs have different requirements on the lepton multiplicity, they do not overlap. Similar to the $E_{\mathrm{T}}^{\mathrm{miss}} + \mathrm{h}(\mathrm{b\bar{b}})$ search, the CR selections do not employ $E_{\mathrm{T}}^{\mathrm{miss}}$ but instead the $E_{\mathrm{T}}^{\mathrm{miss,no}\mu}$ variable in the 1 muon CR and the transverse momentum of the dilepton system $p_{\mathrm{T}}^{\ell\ell}$ in the 2 lepton CR.

The SR and CRs considered in the analysis are

- 0 lepton SR with no electrons and no muons, including the “merged” category with two $E_{\mathrm{T}}^{\mathrm{miss}}$ bins and the intermediate category,
- 1 muon CR with one muon and no electrons, including the merged category with two $E_{\mathrm{T}}^{\mathrm{miss,no}\mu}$ bins and the intermediate category,
- 2 lepton CR with two same-flavour leptons, including the merged category with two $p_{\mathrm{T}}^{\ell\ell}$ bins and the intermediate category,

A graphical overview of all regions and categories considered in the analysis with their relative background composition is given in Figure 12.2.

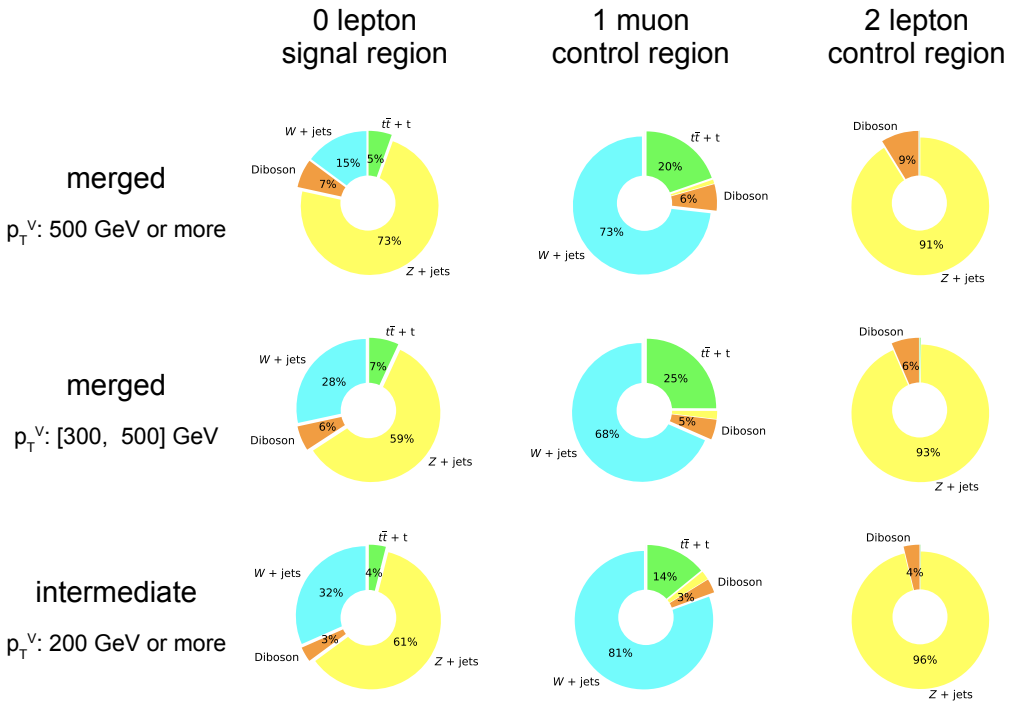



**Fig. 12.2.:** Overview of all regions and categories considered in the $E_{\mathrm{T}}^{\mathrm{miss}} + s(VV)$ search with their relative background composition. Each region is composed of the merged event topology category and the intermediate event topology category. The merged category is further divided in two $p_{\mathrm{T}}^{V}$ bins, where $p_{\mathrm{T}}^{V}$ denotes $E_{\mathrm{T}}^{\mathrm{miss}}$ in the signal region, $E_{\mathrm{T}}^{\mathrm{miss,no}\mu}$ in the 1 muon CR, and $p_{\mathrm{T}}^{\ell\ell}$ in the 2 lepton CR, respectively.

## 12.4 Object and event selection

The selection requirements for events considered in the signal region are outlined below. The specific choices for physics object definitions are summarised in Section 12.4.1. The common baseline selection used in the SR and CRs is described in Section 12.4.2, while the SR event selection is described in Section 12.4.3.

### 12.4.1 Object selection

The physical objects used in the $E_{\mathrm{T}}^{\mathrm{miss}} + s(VV)$ search are based on the object definitions, which are introduced in Section 8.3.

The novel TAR jet algorithm is exploited to reconstruct the dark Higgs boson candidates. The TAR jet algorithm provides superior jet substructure resolution even in dense event topologies by supplementing reclustered jets with precision tracking information. The steps involved in the reconstruction of TAR jets are shown in Figure 12.3.

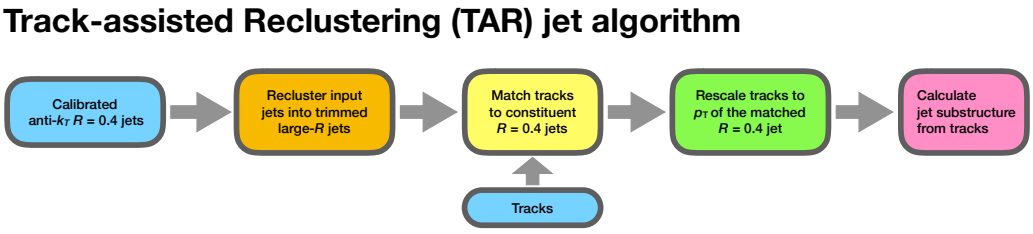



Fig. 12.3.: Flowchart illustrating the TAR jet algorithm. The input objects to the algorithm are shown in blue boxes. Figure adapted from Ref. [109].

1. **Jet reclustering.** The calibrated small-radius jets are used as inputs to the anti-$k_t$ algorithm with radius parameter $R = 0.8$. The resulting jets with large-radius parameter are processed with the trimming algorithm (c.f. Section 6.1.5) using the parameters $f_{\mathrm{cut}} = 0.05$ and $R_{\mathrm{sub}} = 0.2$ to remove sub-jets originating from pile-up.

2. **Track matching.** The ID tracks are matched to the reclustered jet's constituent small-radius jets. This is done using first the ghost-association technique (c.f. Section 6.1.5) and then matching the remaining not yet associated tracks to the small-radius jets within $\Delta R(\text{sub-jet}, \text{track}) = \sqrt{\Delta\eta^2 + \Delta\varphi^2} = 0.5$.

3. **Scaling of track transverse momenta.** As the ID is only sensitive to charged particles, the track momenta need to be corrected for the presence of neutral hadrons in the jet. Consequently, the transverse momenta of the constituent tracks of the small-radius jets are scaled with a correction factor, which is defined as the ratio of the $p_{\mathrm{T}}$ of the small-radius jet to which the tracks were

matched over the sum of all its constituent tracks. As a result, the scaled track transverse momenta are

$$p_{\mathrm{T}}^{\text{track, new}} = \frac{p_{\mathrm{T}}^{\text{track}}}{\sum_{\text{tracks in jet}} p_{\mathrm{T}}^{\text{track}}} \times p_{\mathrm{T}}^{\text{jet}}. \tag{12.1}$$

4. **Jet substructure from tracking information.** The TAR jet mass $m^{\text{TAR}}$ and jet substructure observables are computed using the re-scaled constituent tracks of the TAR jet.

The major advantage of the TAR jet algorithm is the improved jet mass and substructure resolution, which is demonstrated in Figure 12.4. Considering event topologies with hadronically decaying W bosons, the resolution of the jet mass and the $D_2^{(\beta=1)}$ energy correlation ratio (c.f. Equation (9.6)) computed with TAR jets is compared against conventional large-radius jets (c.f. Section 6.1.5). The best resolution for $m^{\text{TAR}}$ is achieved for jets with $p_{\mathrm{T}} < 800\,\mathrm{GeV}$ with relative gains with respect to conventional large-radius jets of up to $35\,\%$. Also for the high-$p_{\mathrm{T}}$ regime $p_{\mathrm{T}} > 1500\,\mathrm{GeV}$, TAR jets have the best performance. Similarly, the $D_2^{(\beta=1)}$ resolution achieved with TAR jets provides a relative gain of $50\,\%$ over the conventional large-radius jet substructure and deteriorates more slowly with increasing jet $p_{\mathrm{T}}$.

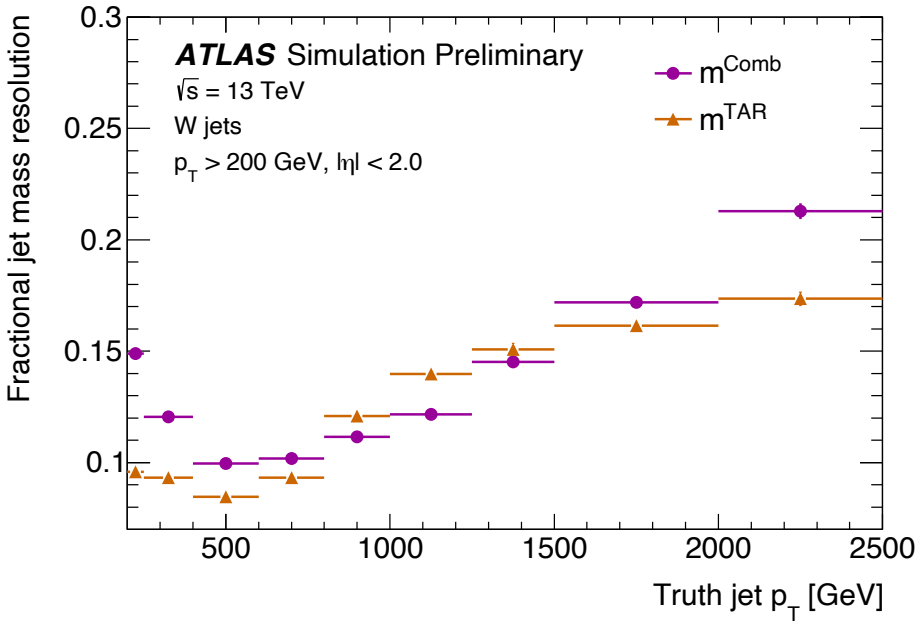
Furthermore, the algorithm provides flexibility in the jet definition by using already calibrated objects as inputs to the jet reclustering. The propagation of the small-radius jet and tracking uncertainties allows avoiding a dedicated TAR jet calibration, as the TAR jet uncertainties can be derived from its constituent objects.

The TAR jets employed in this search have to satisfy $p_{\mathrm{T}} > 100\,\mathrm{GeV}$ and $|\eta| < 2.0$. The TAR jet definition is summarised in Table 12.2.

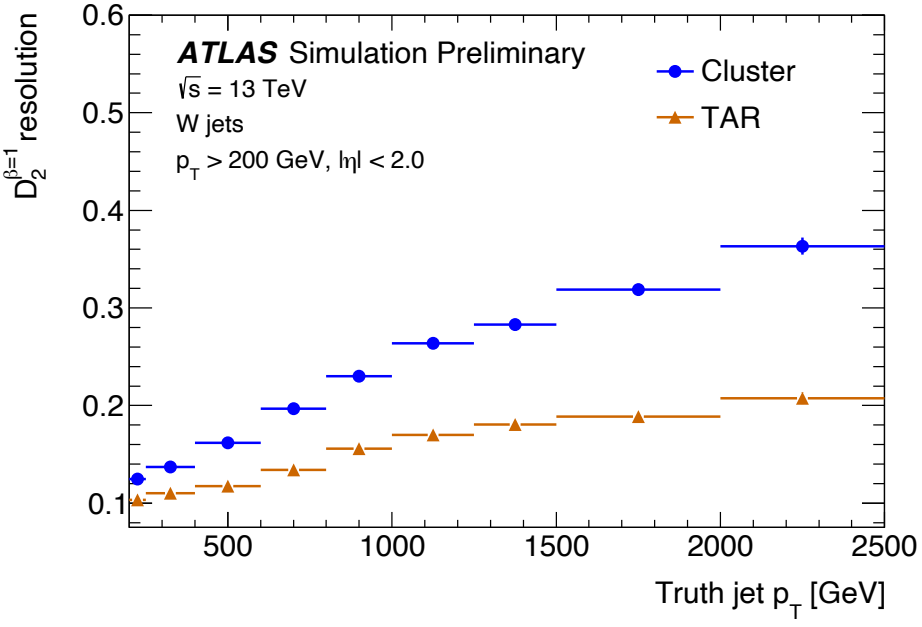
**Tab. 12.2.:** TAR jet definition in the $E_{\mathrm{T}}^{\text{miss}} + s(VV)$ search

| | TAR jets |
|---|---|
| Jet algorithm | anti-$k_t$ |
| $R$-parameter | 0.8 |
| Grooming algorithm | trimming |
| $R_{\text{sub}}$ | 0.2 |
| $f_{cut}$ | 0.05 |
| Input constituents | small-radius jets and ID tracks |
| $\Delta R(\text{sub-jet}, \text{track})$ | 0.5 |
| Pseudorapidity range | $\|\eta\| < 2.0$ |
| Transverse momentum | $p_{\mathrm{T}} > 100\,\mathrm{GeV}$ |

The contributions of background processes are suppressed further by additional requirements on small-radius jets. Variable radius (VR) track jets are used to identify $b$-jets using the MV2 discriminant with a fixed-cut working point corresponding to a $b$-tagging efficiency of $77\,\%$.




(a) Jet mass resolution




(b) $D_2^{(\beta=1)}$ energy correlation ratio resolution

**Fig. 12.4.:** Jet mass resolution (top) and $D_2^{(\beta=1)}$ energy correlation ratio resolution (bottom) in simulated events with hadronically decaying W bosons. The resolution of TAR jet observables is compared to that of conventional large-radius jets. Figures adapted from Ref. [109].

The lepton definitions are the same as those used in the $E_{\mathrm{T}}^{\mathrm{miss}} + \mathrm{h}(\mathrm{b\bar{b}})$ search (c.f. Section 10.4.1).

The missing transverse momentum $E_{\mathrm{T}}^{\mathrm{miss}}$ is reconstructed from the calibrated physics objects in the event and the track-based soft term (TST) using the TIGHT working point due to the increased pile-up in the 2017–2018 data-taking. In the CRs, the $E_{\mathrm{T}}^{\mathrm{miss,no}\mu}$ and $p_{\mathrm{T}}^{\ell\ell}$ substitute observables are used, which describe how background processes are contributing to the signal region. Their definition is the same as in the $E_{\mathrm{T}}^{\mathrm{miss}} + \mathrm{h}(\mathrm{b\bar{b}})$ search (c.f. Section 10.4.1). The object-based $E_{\mathrm{T}}^{\mathrm{miss}}$ significance is used to suppress events with fake $E_{\mathrm{T}}^{\mathrm{miss}}$ caused by resolution effects.

Potential ambiguities in the reconstruction, such as reconstructed objects matching multiple object hypotheses, must be resolved by an overlap removal procedure. The overlap removal procedure is identical to that described in Section 10.4.1 except for the overlap removal step for large-radius jets and electrons, which is not applied.

### 12.4.2 Baseline selection

The SR and CR definition is based on a common baseline selection and common requirements to suppress the multijet background. These selection requirements share similarities with those employed in the $E_{\mathrm{T}}^{\mathrm{miss}} + V(q\bar{q})$ and $E_{\mathrm{T}}^{\mathrm{miss}} + \mathrm{h}(\mathrm{b\bar{b}})$ searches, which are presented in Section 9.4.2, Section 9.4.3, and Section 10.4.2.

In addition to the requirements on data quality, vertex reconstruction, jet cleaning, and the trigger, which are the same as in the $E_{\mathrm{T}}^{\mathrm{miss}} + \mathrm{h}(\mathrm{b\bar{b}})$ search, vetoes on events containing $b$-tagged VR track jets or baseline tau lepton candidates are applied to reduce the background contribution of $\mathrm{t\bar{t}}$ and $V$ + jets processes.

Selected events in the SR have to satisfy $E_{\mathrm{T}}^{\mathrm{miss}} > 200\,\mathrm{GeV}$, thereby ensuring operation in the region of full $E_{\mathrm{T}}^{\mathrm{miss}}$ trigger efficiency and avoiding the need for an $E_{\mathrm{T}}^{\mathrm{miss}}$ trigger calibration.

The multijet background is suppressed by applying two multijet-suppression requirements.

- Selected events have to pass a requirement on the minimum azimuthal distance between the three highest-$p_{\mathrm{T}}$ central jets $\min \Delta\varphi(\mathrm{jets}_{1,2,3}, E_{\mathrm{T}}^{\mathrm{miss}}) > 20°$.
- Selected events also have to satisfy a requirement on the object-based $E_{\mathrm{T}}^{\mathrm{miss}}$ significance $\mathcal{S} > 15$ in the SR. In the 1 muon CR, the requirement is based on a modified object-based $E_{\mathrm{T}}^{\mathrm{miss}}$ significance $\mathcal{S}^{\mathrm{no}\,\mu}$, neglecting the highest-$p_{\mathrm{T}}$ muon in the $E_{\mathrm{T}}^{\mathrm{miss}}$ reconstruction.

Similarly to the $E_{\mathrm{T}}^{\mathrm{miss}} + \mathrm{h}(\mathrm{b\bar{b}})$ search, the multijet-suppression requirements are not applied in the 2 lepton CR to increase the statistical precision of the CR. The requirement of 2 leptons already strongly suppresses potential contamination through multijet processes. Instead, a requirement on the object-based $E_{\mathrm{T}}^{\mathrm{miss}}$ significance $\mathcal{S} < 15$ is applied to reject potential signal processes with a $E_{\mathrm{T}}^{\mathrm{miss}} + s \to Z(\ell\ell)V(qq)$ signature.

The baseline selection requirements are summarised in Table 12.3.

**Tab. 12.3.:** List of the baseline selection requirements employed in the $E_{\mathrm{T}}^{\mathrm{miss}}+s(VV)$ search.

| Baseline selection | **0 lepton SR** | **1 muon CR** | **2 lepton CR** |
|---|---|---|---|
| Data quality | basic requirements vetoing corrupted data or incomplete events | | |
| Vertex reconstruction | primary vertex with at least two associated tracks | | |
| Jet cleaning | veto on events containing jets flagged as BADLOOSE jets | | |
| Trigger | $E_{\mathrm{T}}^{\mathrm{miss}}$ trigger | $E_{\mathrm{T}}^{\mathrm{miss}}$ trigger | single lepton trigger |
| $b$-jet veto | 0 $b$-tagged VR track jets in the event | | |
| Tau lepton veto | 0 baseline tau lepton candidates in the event | | |
| Missing transverse momentum | $E_{\mathrm{T}}^{\mathrm{miss}} > 200\,\mathrm{GeV}$ | $E_{\mathrm{T}}^{\mathrm{miss,no}\mu} > 200\,\mathrm{GeV}$ | $p_{\mathrm{T}}^{\ell\ell} > 200\,\mathrm{GeV}$ |
| Multijet suppression | $\min\Delta\varphi(\mathrm{jets}_{1,2,3}, E_{\mathrm{T}}^{\mathrm{miss}}) > 20°$<br>$E_{\mathrm{T}}^{\mathrm{miss}}$ significance $\mathcal{S} > 15$ | $\min\Delta\varphi(\mathrm{jets}_{1,2,3}, E_{\mathrm{T}}^{\mathrm{miss,no}\mu}) > 20°$<br>$E_{\mathrm{T}}^{\mathrm{miss,no}\mu}$ significance $\mathcal{S}^{\mathrm{no}\,\mu} > 15$ | no<br>no |
| Signal suppression | no | no | $E_{\mathrm{T}}^{\mathrm{miss}}$ significance $\mathcal{S} < 15$ |

### 12.4.3 Signal region selection

The SR event selection employs a veto on events containing baseline electrons or baseline muons, as the $E_{\mathrm{T}}^{\mathrm{miss}} + s(VV)$ search targets the hadronic decay mode of the weak vector bosons $V$. Two complementary selection categories are considered to cover the merged and intermediate event topologies, with priority given to the merged category in case of ambiguities.

The events comprising the **merged category** are selected by applying the baseline selections and requiring $E_{\mathrm{T}}^{\mathrm{miss}} > 300\,\mathrm{GeV}$. The dark Higgs boson candidate in the merged category is reconstructed using the TAR jet with the highest transverse momentum. The dark Higgs boson candidate $p_{\mathrm{T}}$ is strongly correlated with $E_{\mathrm{T}}^{\mathrm{miss}}$. Therefore, its transverse momentum is required to be larger than $300\,\mathrm{GeV}$ as well.

The TAR jet substructure is used to identify the four-prong dark Higgs boson decay. To this end, the set of $N$-subjettiness [338, 339] jet substructure observables, denoted $\tau_N$, is employed. $N$-subjettiness allows quantifying how well jets can be described as containing $N$ or fewer sub-jets.

The calculation of $\tau_N$ begins with the definition of $N$ sub-jet axes within the TAR jet by using the exclusive $k_{\mathrm{T}}$ clustering algorithm, which reconstructs jets by approximately inverting the QCD parton shower evolution and continues with the jet reconstruction until a desired number of jets is found. The $N$-subjettiness is calculated via

$$\tau_0 = \sum_k p_{\mathrm{T},k} \times R_0, \tag{12.2}$$

$$\tau_N = \frac{1}{\tau_0} \times \left( \sum_k p_{\mathrm{T},k} \times R_k^{\mathrm{min}} \right), \tag{12.3}$$

where $R_0 = 0.8$ is radius of the TAR jet, $k$ runs over the constituent tracks in a given TAR jet, $p_{\mathrm{T},k}$ are their transverse momenta, and $R_k^{\mathrm{min}}$ is the distance in the

rapidity-azimuth plane between the constituent track $k$ and the axis of the closest sub-jet.

In this search, the winner-takes-all scheme [132, 273] is employed, in which the sub-jet axis is taken to be parallel with the momentum of the hardest sub-jet constituent, as it provides increased discrimination power.

Small values of $\tau_{42}$ and $\tau_{43}$ correspond to TAR jets with signal-like four-prong substructure, whereas large values indicate the jets originating from background processes.

Therefore, the $N$-subjettiness ratios $\tau_{42} = \tau_4/\tau_2$ and $\tau_{43} = \tau_4/\tau_3$ provide strong discrimination of four-prong decays against two- or three-prong decays. The dark Higgs boson candidate TAR jet is required to satisfy the requirements on the $N$-subjettiness ratios $0 < \tau_{42} < 0.3$ and $0 < \tau_{43} < 0.6$. The distributions of the $N$-subjettiness ratios for signal and background processes are shown in Figure 12.5.

As the jets are more collimated for signals with lower $m_s$, the corresponding $\tau_{42}$ and $\tau_{43}$ distributions accumulate at lower values than for signals with larger $m_s$.

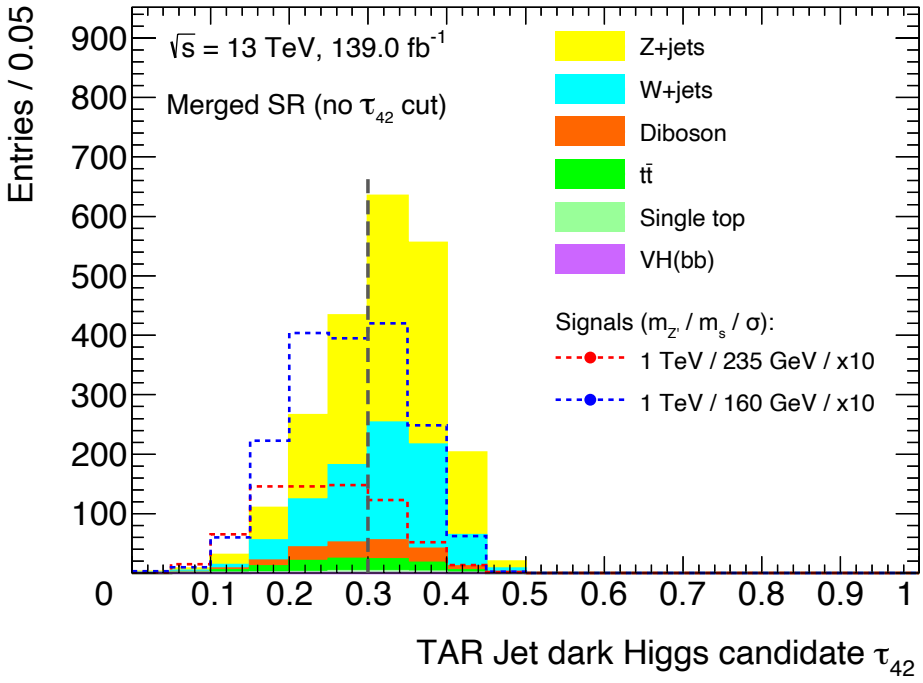
Figure 12.6 shows correlations between the dark Higgs boson candidate mass $m_{VV}$ and the $N$-subjettiness ratio variables for a representative signal process with $m_{Z'} = 1.7\,\text{TeV}$ and $m_s = 160\,\text{GeV}$, depending on the number of partons matched to the TAR jet using the $\Delta R$ distance measure.

The dark Higgs boson candidate mass is reconstructed deficiently if not all four partons are contained within the TAR jet. Therefore, the tight requirements on the jet substructure variables $\tau_{42}$ and $\tau_{43}$ not only provide discrimination against background processes but also improve the signal reconstruction by restricting the merged selection to events in which the full dark Higgs decay is most likely contained in the TAR jet.

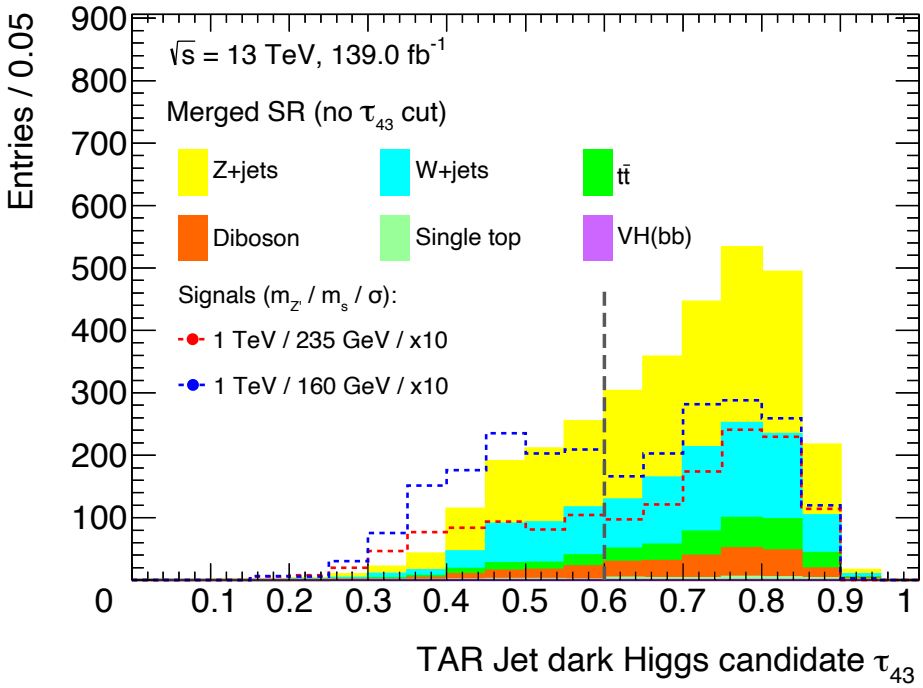
The invariant mass of the TAR jet, denoted $m_{VV}$, is used as the primary discriminating variable in the statistical analysis. Additionally, the merged event selection considers two $E_{\text{T}}^{\text{miss}}$ bins.

The event selection of the **intermediate category** is optimised for events with moderate amount of missing transverse momentum $E_{\text{T}}^{\text{miss}} > 200\,\text{GeV}$, which are not selected in the merged category. The resulting event topology consists of one highly boosted weak vector boson whose decay products are contained within a single TAR jet and another weak vector boson whose smaller boost enables the reconstruction of its decay products with small-radius jets. The intermediate category selection is particularly relevant for signal processes with large $m_s$, as the separation of the weak vector bosons increases with it.

A dedicated algorithm is developed to address this scenario, which exploits both the TAR jet mass and the TAR jet substructure to identify weak vector boson candidates. As W and Z bosons are almost indistinguishable given the coarse jet mass resolution $\sigma(m) > |m_W - m_Z|$, the algorithm employs the W boson mass to define weak vector boson candidates. Choosing the W boson mass instead of the Z boson mass is

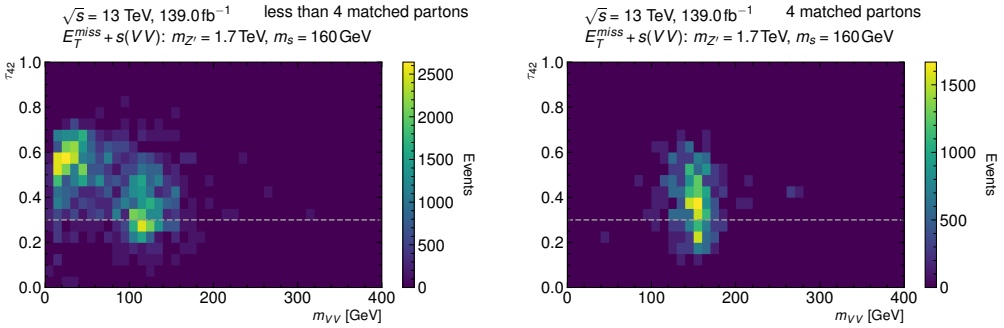



(a) $\tau_{42}$ distribution of the highest-$p_{\mathrm{T}}$ TAR jet



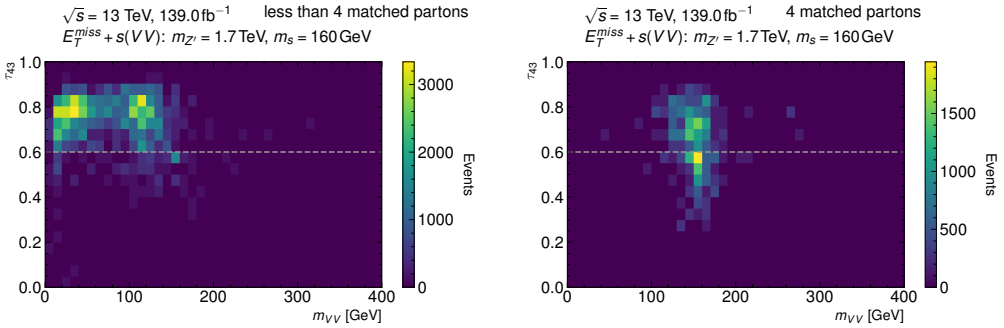

(b) $\tau_{43}$ distribution of the highest-$p_{\mathrm{T}}$ TAR jet

**Fig. 12.5.:** Dark Higgs boson candidate TAR jet substructure variables $\tau_{42}$ (top) and $\tau_{43}$ (bottom) for two $E_{\mathrm{T}}^{\mathrm{miss}} + s(VV)$ signal processes with $m_{Z'} = 1\,\mathrm{TeV}$ and $m_s = 160\,\mathrm{GeV}$ or $235\,\mathrm{GeV}$ and background processes. The simulated background processes are normalised to the theoretical prediction. The requirements on the SR merged category event selection are applied, except for the requirement on the variable which is shown. The cut value is indicated by a long-dashed line.




(a) $\tau_{42}$, less than four matched partons

(b) $\tau_{42}$, four matched partons




(c) $\tau_{43}$, less than four matched partons

(d) $\tau_{43}$, four matched partons

**Fig. 12.6.:** Correlation between the dark Higgs boson candidate mass $m_{VV}$ and the $N$-subjettiness ratio variables $\tau_{42}$ (top) and $\tau_{43}$ (bottom). The distributions are shown separately for events in which not all four partons are contained within the dark Higgs boson candidate TAR jet (left) and events in which all four partons are contained (right). The cut value used in the substructure requirements is indicated by a dashed line.

favourable because of the larger branching fraction for the dark Higgs boson decay to W bosons as opposed to Z bosons.

The so-called TAR+COMB algorithm is described below.

1. **Decision based on TAR jet**. The highest-$p_{\mathrm{T}}$ TAR jet is considered. If its mass $m^{\mathrm{TAR}}$ is in the range $60\,\mathrm{GeV}$ to $100\,\mathrm{GeV}$ and the energy correlation ratio $D_2^{(\beta=1)}$ computed with TAR jet substructure satisfies $D_2^{(\beta=1)} < 1.5$, the TAR jet is considered as a weak vector boson candidate and the second weak vector boson candidate is reconstructed with small-radius jets. Otherwise, if $m^{\mathrm{TAR}} > 100\,\mathrm{GeV}$, the majority of the dark Higgs decay is contained within the TAR jet and it is considered as an "incomplete" dark Higgs boson candidate and the missing components of the dark Higgs boson candidate are supplemented by small-radius jets.

2.1 **Case 1: weak vector boson candidate**, $60\,\mathrm{GeV} < m^{\mathrm{TAR}} < 100\,\mathrm{GeV}$.

- The small-radius jets within $\Delta R < 2.5$ of the weak vector boson candidate are considered unless they overlap with it based on the $\Delta R$ distance measure.
- All possible combinations of small-radius jet pairs are formed and ordered by the difference of their invariant mass to the W boson mass.
- The jet pair closest in mass to the W boson mass is considered as the second weak vector boson candidate.
- The dark Higgs boson TAR+COMB candidate is defined by the combined four-momentum of the two weak vector boson candidates.

2.2 **Case 2: "incomplete" dark Higgs boson candidate**, $m^{\mathrm{TAR}} > 100\,\mathrm{GeV}$.

- The small-radius jets within $\Delta R < 2.5$ of the weak vector boson candidate are considered even if they overlap with the TAR jet. Small-radius jets are discarded if their transverse momentum is below $5\,\%$ of the TAR jet's $p_{\mathrm{T}}$.
- All possible combinations of small-radius jet pairs are formed and ordered by the difference of their invariant mass to the W boson mass.
- The jet pair which overlaps with the TAR jet, whose invariant mass is in the range $60\,\mathrm{GeV}$ to $100\,\mathrm{GeV}$, and which is closest in mass to the W boson mass is considered as the first weak vector boson candidate. If such a jet pair exists, it is not considered further.
- The jet pair with exactly one small-radius jet overlapping with the TAR jet, whose invariant mass is in the range $60\,\mathrm{GeV}$ to $100\,\mathrm{GeV}$, and which is closest in mass to the W boson mass is considered as the second weak vector boson candidate. If no such second weak vector boson candidate is present, the algorithm is aborted.
- The dark Higgs boson TAR+COMB candidate is defined by the combined four-momentum of the TAR jet and the non-overlapping jet of the second weak vector boson candidate.

Events with a dark Higgs boson candidate invariant mass in the range $100\,\text{GeV} < m_{VV} < 400\,\text{GeV}$ are considered in the statistical analysis.

A summary of the SR event selection requirements is presented in Table 12.4.

**Tab. 12.4.:** List of the SR event selection requirements employed in the $E_{\text{T}}^{\text{miss}} + s(VV)$ search.

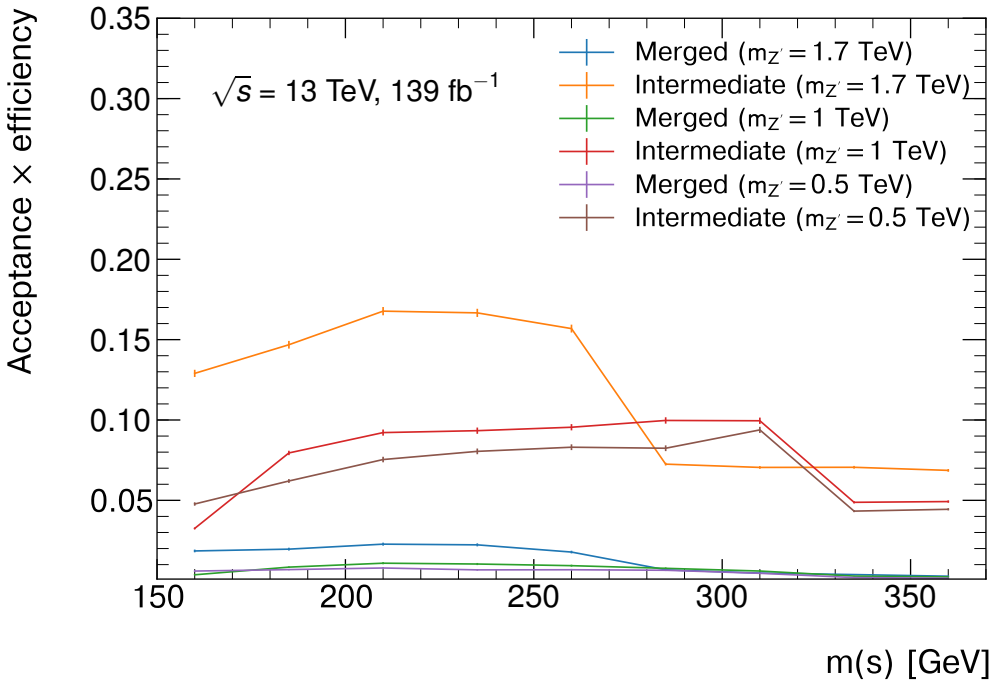
| **Common selection requirements** | | |
|---|---|---|
| baseline selection requirements<br>multijet-suppression requirements<br>0 baseline e and 0 baseline $\mu$ | | |
| **Merged category**<br>$E_{\text{T}}^{\text{miss}} > 500\,\text{GeV}$ | **Merged category**<br>$300\,\text{GeV} < E_{\text{T}}^{\text{miss}} < 500\,\text{GeV}$ | **Intermediate category**<br>$E_{\text{T}}^{\text{miss}} > 200\,\text{GeV}$ |
| at least one dark Higgs boson candidate TAR jet<br>with $100\,\text{GeV} < m_{VV} < 400\,\text{GeV}$,<br>$p_{\text{T}} > 300\,\text{GeV}$,<br>$0 < \tau_{42} < 0.3$,<br>$0 < \tau_{43} < 0.6$ | | not in merged category<br>one dark Higgs TAR+COMB candidate<br>with $100\,\text{GeV} < m_{VV} < 400\,\text{GeV}$ |

The product of acceptance and efficiency $\mathcal{A} \times \varepsilon$ for $s \to$ WW and $s \to$ ZZ signal processes is shown in dependence of $m_s$ for various $m_{Z'}$ in Figure 12.7. The merged category has smaller $\mathcal{A} \times \varepsilon$ in comparison to the intermediate category because of its tight jet substructure requirements. It is optimised for the reconstruction of dark Higgs boson candidates with low $m_s > 160\,\text{GeV}$, which can be fully contained within a single TAR jet. The intermediate category, on the other hand, is optimised for the reconstruction of dark Higgs boson candidates with large $m_s$, thereby providing complementarity. The combined use of both categories allows the reconstruction of dark Higgs boson candidates over a broad $m_s$ range from $160\,\text{GeV}$ to $360\,\text{GeV}$.

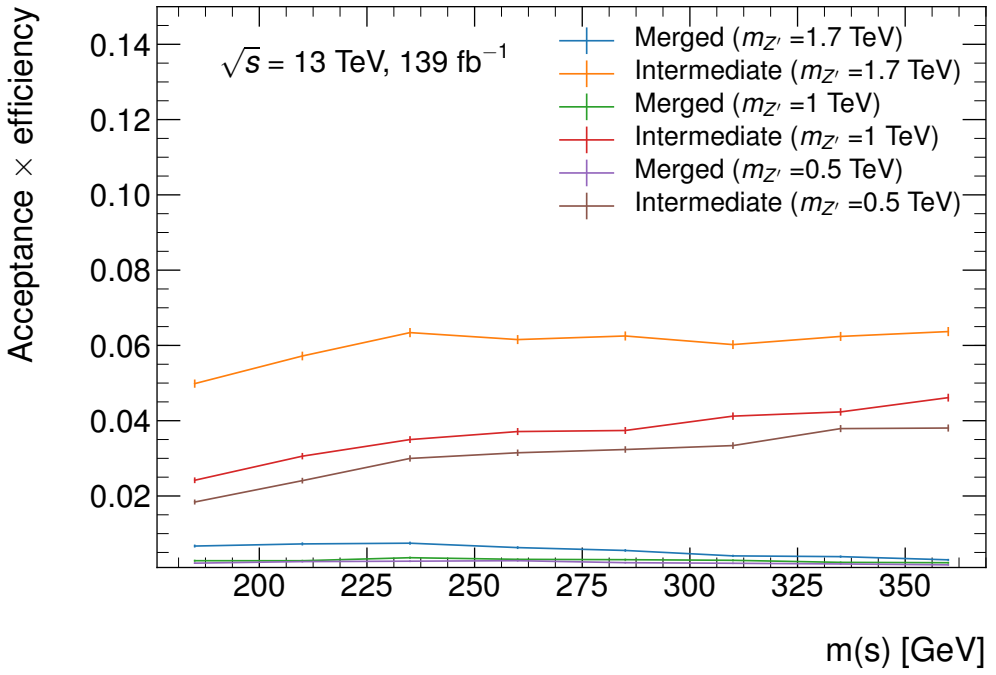
## 12.5 Background estimation

The estimation of the dominant background processes in the $E_{\text{T}}^{\text{miss}} + s(VV)$ search is improved by control region data. The CR event selections are defined by requirements on the lepton multiplicity and therefore do not overlap with the SR selection. The CRs have a high purity in the specific background processes. In contrast to the signal process, the dominant background processes have no characteristic peak in the dark Higgs boson candidate mass distributions. Therefore, only $E_{\text{T}}^{\text{miss,no}\mu}$ and $p_{\text{T}}^{\ell\ell}$ information is used.

The normalisation parameters of the sub-dominant background processes are set to their predicted values based on theoretical predictions and can vary within the corresponding uncertainties.




(a) $(\mathcal{A} \times \varepsilon)$ for $s \to$ WW signal processes.




(b) $(\mathcal{A} \times \varepsilon)$ for $s \to$ ZZ signal processes.

**Fig. 12.7.:** The product of detector acceptance and selection efficiency $(\mathcal{A} \times \varepsilon)$ for the $s \to$ WW (top) and $s \to$ ZZ (bottom) signal processes with the Z′ boson mass $m_{Z'} = 0.5\,\text{TeV}, 1\,\text{TeV}, 1.7\,\text{TeV}$, shown in dependence on the dark Higgs boson mass $m_s$. The points are connected in order to guide the eye.

### 12.5.1 1 muon control region

The 1 muon CR is defined to constrain W+ jets processes, which can contribute to the SR through inefficiencies in the lepton reconstruction and due to the limited detector acceptance. Consequently, the selected events contain exactly one tight signal muon, no additional baseline muons and no baseline electrons. The variable $E_{\mathrm{T}}^{\mathrm{miss,no}\mu}$ is introduced, which is reconstructed by neglecting muons in the $E_{\mathrm{T}}^{\mathrm{miss}}$ calculation. Events in the 1 muon CR are selected by $E_{\mathrm{T}}^{\mathrm{miss}}$ triggers. The selection requirements are identical to those of the SR which are listed in Table 12.4, except for the use of $E_{\mathrm{T}}^{\mathrm{miss,no}\mu}$ instead of $E_{\mathrm{T}}^{\mathrm{miss}}$.

### 12.5.2 2 lepton control region

The 2 lepton CR is designed to constrain the Z + jets background using leptonically decaying Z + jets events. The dilepton transverse momentum $p_{\mathrm{T}}^{\ell\ell}$ serves as a proxy of the missing transverse momentum. Events in the 2 lepton CR are selected by single lepton triggers. The selected events contain either exactly two baseline electrons ee or exactly two baseline muons $\mu\mu$. At least one of the two electrons must satisfy $p_{\mathrm{T}}^{\mathrm{e}} > 27\,\mathrm{GeV}$. Similarly, at least one of the two muons must satisfy $p_{\mathrm{T}}^{\mu} > 25\,\mathrm{GeV}$ and $\left|\eta^{\mu}\right| < 2.5$. Events containing two muons are only selected if these are of opposite charge. A similar requirement is not applied for events containing two electrons due to higher rate of electron charge misidentification.

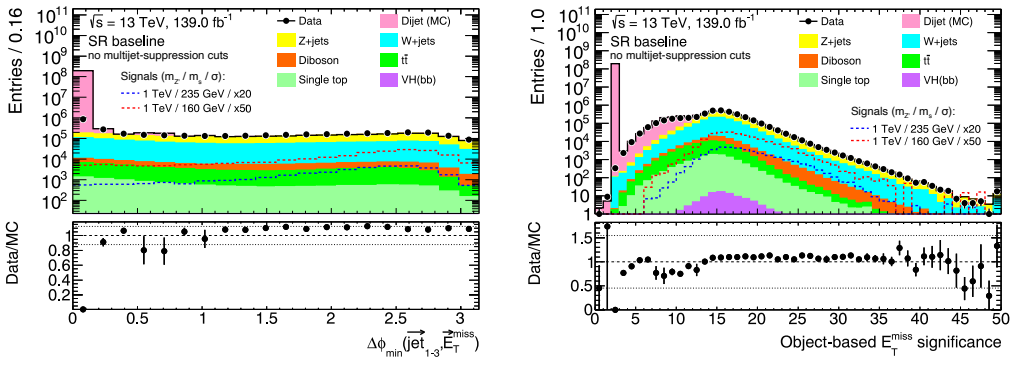
A requirement on the invariant mass of the dilepton system $83\,\mathrm{GeV} < m_{\ell\ell} < 99\,\mathrm{GeV}$ ensures high purity in Z + jets processes by suppressing backgrounds with a non-resonantly produced lepton-pair.

The selection requirements are otherwise identical to those of the SR which are listed in Table 12.4, except for the use of $p_{\mathrm{T}}^{\ell\ell}$ instead of $E_{\mathrm{T}}^{\mathrm{miss}}$ and the absence of the multijet-suppression requirements.

### 12.5.3 Multijet background estimate

The multijet background is negligible in the SR selection due to the stringent multijet-suppression requirements and the $E_{\mathrm{T}}^{\mathrm{miss}} > 200\,\mathrm{GeV}$ requirement. Similarly, its contribution to the CR selection is vanishing due to the additional requirements on leptons.

Based on an MC-based estimation using the simulated PYTHIA dijet sample, this background is suppressed to a similar order of magnitude as the statistical uncertainty of the observed data or below. Figure 12.8 shows the distributions $\min \Delta\varphi(\mathrm{jets}_{1,2,3}, E_{\mathrm{T}}^{\mathrm{miss}})$ and the object-based $E_{\mathrm{T}}^{\mathrm{miss}}$ significance for the baseline selection without the multijet-suppression requirements applied.




**(a)** $\min \Delta\varphi(\text{jets}_{1,2,3}, E_{\text{T}}^{\text{miss}})$ **(b)** Object-based $E_{\text{T}}^{\text{miss}}$ significance

**Fig. 12.8.:** Distributions of the $\min \Delta\varphi(\text{jets}_{1,2,3}, E_{\text{T}}^{\text{miss}})$ (left) and object-based $E_{\text{T}}^{\text{miss}}$ significance (right) variables, which define the multijet-suppression requirements, shown for the observed data (black dots), background processes (stacked histograms) scaled to their theoretical expectation, and two representative signal processes (red and blue dashed lines). The multijet background is estimated with MC simulated events.

The simulated multijet events are rejected by the multijet-suppression requirements and are thus neglected in the statistical model. A rough data-driven estimate is performed to express certainty.

Multijet-enriched selections are defined for the merged and intermediate categories by removing the $\min \Delta\varphi(\text{jets}_{1,2,3}, E_{\text{T}}^{\text{miss}}) > 20°$ requirement and modifying the requirement on $E_{\text{T}}^{\text{miss}}$ to $150\,\text{GeV} < E_{\text{T}}^{\text{miss}} < 200\,\text{GeV}$.

In these multijet-enriched selections, a scale factor for the simulation-based multijet event yield is determined as the ratio of the number of multijet events in data to the multijet events in simulation

$$\text{SF}^{\text{multijet}} = \frac{N(\text{data}) - N(\text{other backgrounds})}{N(\text{simulated multijet background})}, \tag{12.4}$$

where the number of multijet events in data is roughly estimated by subtracting the event yields of the other background processes normalised to their prediction while neglecting uncertainties. This results in $\text{SF}^{\text{multijet}}$ of $2.24$ in the SR merged category and $1.44$ in the SR intermediate category, respectively. The scale-factors differ from unity because of the various reasons, the most important being imperfections in the description of the multijet background with LO accuracy in QCD and the notoriously difficult modelling of tails in the jet energy resolution.

The product of the simulation-based multijet event yield and $\text{SF}^{\text{multijet}}$ provides an upper estimate in the order of magnitude for the contribution of multijet events in the SR. The results of the estimate are shown in Table 12.5.

Tab. 12.5.: Event yields for the simulated multijet background (dijet MC) and their product with the scale factor $SF^{multijet}$ in the SR merged and intermediate categories. The observed data and the corresponding statistical uncertainty are shown in comparison.

| Signal region | **Merged** | **Intermediate** |
|---|---|---|
| Dijet MC | $2.4 \pm 2.4$ | $300 \pm 160$ |
| Scaled dijet MC | $5.4 \pm 5.4$ | $440 \pm 230$ |
| Observed data | $825 \pm 29$ | $80519 \pm 280$ |

## 12.6 Systematic uncertainties

Systematic uncertainties arise from biases in the reconstruction of compound physics objects and the description of the signal and background processes using MC simulation.

### 12.6.1 Experimental systematic uncertainties

The experimental systematic uncertainties in the $E_{\mathrm{T}}^{\mathrm{miss}} + s(VV)$ search due to biases in the reconstruction of physics objects resemble those of the $E_{\mathrm{T}}^{\mathrm{miss}} + \mathrm{h}(\mathrm{b\bar{b}})$ search. The uncertainties which are similar pertain to the trigger, the pile-up modelling, the reconstruction and calibration of electrons, muons, small-radius jets, $b$-tagging, and the $E_{\mathrm{T}}^{\mathrm{miss}}$ reconstruction. The differences in the experimental uncertainties between the two searches are listed below.

- **Luminosity.** The uncertainty on the measurement of the integrated luminosity is $1.7\,\%$ [56].
- **Large-radius jets.** No uncertainties on large-radius jets are considered, as TAR jets are used instead to reconstruct the dark Higgs boson candidates.
- **Small-radius jets.** The calibration of small-radius jets is subject to multiple sources of uncertainty [55]. In total, the uncertainties on the JES calibration are parametrised by over 125 components. These components are grouped into a reduced set of 30 components which are derived from the in-situ calibration, pile-up effects, the jet-flavour dependence, and other effects. The JER uncertainties are described by a set of 8 components which are derived from the in-situ calibration.
- **Tracking.** The track reconstruction systematic uncertainties describe the residual alignment uncertainties in the impact parameters $d_0$ and $z_0$, the impact parameter resolution, uncertainties on the tracking efficiency and on the track fake rate and a dedicated uncertainty for tracking in dense environments [44]. These systematic uncertainties are parametrised by 12 components.

### 12.6.2 Theoretical systematic uncertainties

The theoretical systematic uncertainties arise from the description of the signal and background processes, in which the specific choices of event generators, PDF sets, parton shower modelling, and values of the renormalisation and factorisation scales can introduce systematic biases.

The total normalisations of the dominant background processes Z + jets and W + jets are constrained by the control region data. The normalisations of the sub-dominant background processes are constrained by the theoretical normalisation uncertainties, which are listed in Table 12.6.

**Tab. 12.6.:** Theoretical systematic uncertainties on the normalisation of background processes in the $E_{\mathrm{T}}^{\mathrm{miss}} + s(VV)$ search.

| **Process** | **Uncertainty** |
|---|---|
| $\mathrm{t\bar{t}}$ | 5 % |
| Single top quark ($s$-channel) | 4.6 % |
| Single top quark ($t$-channel) | 4.4 % |
| Single top quark (W$t$-process) | 6.2 % |
| WW | 25 % |
| WZ | 26 % |
| ZZ | 20 % |
| $V\mathrm{h}, \mathrm{h} \to \mathrm{b\bar{b}}$ | 30 % |

In addition, shape uncertainties on the dark Higgs boson candidate mass and $E_{\mathrm{T}}^{\mathrm{miss}}$ distributions are considered for the dominant background processes, as well as acceptance uncertainties which account for the migration of events among the merged and intermediate categories. The $E_{\mathrm{T}}^{\mathrm{miss}}$ shape uncertainty allows for relative changes in the event yield in the two merged category $E_{\mathrm{T}}^{\mathrm{miss}}$ bins, leaving the total event yield unchanged. Similarly, the acceptance uncertainties allow for relative variations in the population of merged and intermediate categories, keeping the event yield sum of both categories constant. These uncertainties are obtained by comparing samples simulated with different event generator settings.

In contrast to the other searches discussed in this dissertation, the uncertainties are evaluated with simulated samples considering the full detector simulation. The stringent TAR jet substructure requirements applied in the event selection have no equivalent description on particle level. Therefore, the evaluation of the theoretical systematic uncertainties on particle level is not possible.

Three sources of theoretical systematic uncertainty are considered for the dominant $V$ + jets background processes, which are listed below.

- The **scale** uncertainties are estimated by varying the renormalisation scale $\mu_{\mathrm{R}}$ and factorisation scale $\mu_{\mathrm{F}}$ coherently by factors of $0.5$ and $2$ on an event-by-event basis. The largest variation with respect to the nominal value is taken as the scale uncertainty.

- The **PDF** uncertainty is estimated using the set of 100 eigen-variations of the NNPDF30NLO PDF set [119] via the standard deviation approach, in which the uncertainty is computed as

$$\Delta X = \sqrt{\frac{1}{N-1}\sum_{i=1}^{N}(X_i - X_0)^2}. \tag{12.5}$$

  Here, $N = 100$ is the number of PDF replicas, $X_i$ is the event yield for the $i$-th PDF variation, and $X_0$ is the mean value of the event yield over all PDF variations. It is added in quadrature with variations of the coupling strength of the strong interaction $\Delta\alpha_s = \pm 0.01$, following the PDF4LHC recommendations [148].

- The uncertainties related to the choices of **event generator** and **parton shower + hadronisation** model are evaluated using alternative MC samples. These are generated with MADGRAPH5_aMC@NLO 2.6.2 at LO with up to four final-state partons using the NNPDF23LO PDF set and interfaced to PYTHIA 8.230. The CKKW-L merging procedure [276, 277] is used with a matching scale of $30\,\text{GeV}$ to remove the overlap in the description of final-state partons by the hard scattering and the parton shower modelling. As the uncertainties on the $m_{VV}$ shape are subject to large statistical fluctuations, the distributions were smoothed by cubic spline fits.

The average size of the $m_{VV}$ shape uncertainties is in the range $1\,\%$ to $20\,\%$, with the largest uncertainty coming from the scale variations and the choice of the event generator and the parton shower + hadronisation model.

The theoretical uncertainties for the dark matter signals in the 2MDM model are estimated by variations in the event generation, considering two sources of uncertainty which are listed below.

- The **scale** uncertainties are estimated by varying the renormalisation scale $\mu_\text{R}$ and factorisation scale $\mu_\text{F}$ coherently by factors of $0.5$ and $2$ on an event-by-event basis. The largest variation with respect to the nominal value is taken as the scale uncertainty.

- The **PDF** uncertainty is estimated using the standard deviation approach described above, except that no variations of the strong coupling are considered.

The average size of the signal uncertainties due to scale variations is of the order of $10\,\%$, while the PDF uncertainties are typically smaller with values in the range of $3\,\%$ to $4\,\%$.

## 12.7 Statistical model

The statistical model is based on the likelihood function Equation (6.11). The profile likelihood fit is based on the invariant mass of the dark Higgs boson candidate in

the three SR categories based on $E_{\mathrm{T}}^{\mathrm{miss}}$ and the event topology. In the 1 muon CR and the 2 lepton CR, it is based on the event yield in similar categories, which are defined by $E_{\mathrm{T}}^{\mathrm{miss,no}\mu}$ and $p_{\mathrm{T}}^{\ell\ell}$, respectively. A summary of all regions and kinematic distributions considered in the statistical model is provided in Table 12.7.

**Tab. 12.7.:** Summary of all regions and kinematic distributions considered in the statistical analysis of the $E_{\mathrm{T}}^{\mathrm{miss}} + s(VV)$ search.

| | **0 leptons** | **1 muon** | **2 leptons** |
|---|---|---|---|
| Process of interest | signal | W + jets | Z + jets |
| Primary fitted observable | $m_{VV}$ | event yield | event yield |
| Auxiliary fitted observable | $E_{\mathrm{T}}^{\mathrm{miss}}$ | $E_{\mathrm{T}}^{\mathrm{miss,no}\mu}$ | $p_{\mathrm{T}}^{\ell\ell}$ |
| Binning | merged category: 300 GeV to 500 GeV, 500 GeV or more<br>intermediate category: 200 GeV or more | | |

## 12.8 Results

The results of the $E_{\mathrm{T}}^{\mathrm{miss}} + s(VV)$ search are presented in this section. The observed results are presented in Section 12.8.1. The impact of groups of systematic uncertainty on the sensitivity of the search is discussed in Section 12.8.2. Finally, the results are interpreted to constrain the parameter space of the 2MDM simplified model in Section 12.8.3.

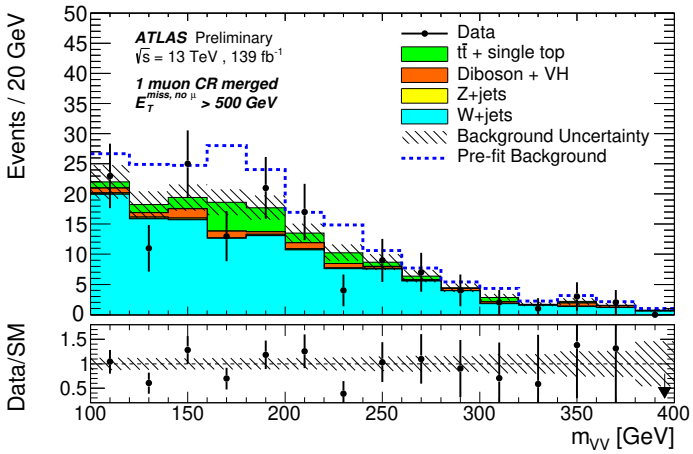
### 12.8.1 Observed results

The background description by the statistical model is validated by performing a conditional background-only ($\mu = 0$) fit and investigating the corresponding distributions in the CRs.

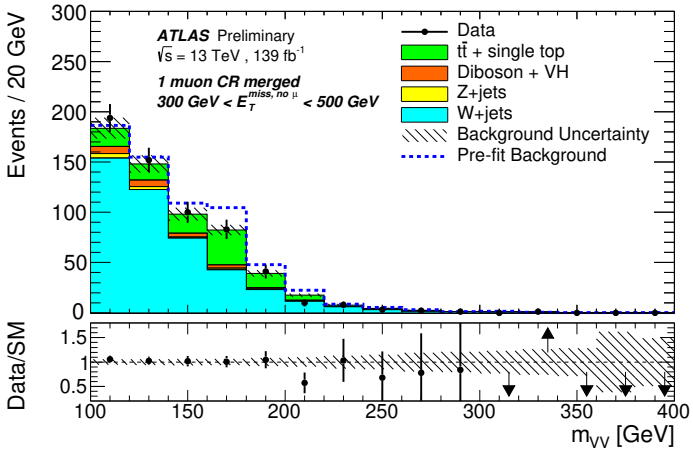
Figure 12.9 and Figure 12.10 show the dark Higgs boson candidate mass distributions in the 1 muon CR and in the 2 lepton CR, respectively. Although only the CR event yield is used in the statistical analysis, the mass distributions are shown to demonstrate adequate modelling in the merged and intermediate categories. The observed data in the CRs are in good agreement with the SM background prediction, thereby validating the background description.

The results of the profile likelihood fit of the statistical model to the data are reported in terms of the discovery significance for 2MDM simplified model signals in dependence of $m_{\mathrm{Z}'}$ and $m_s$ in Figure 12.11.

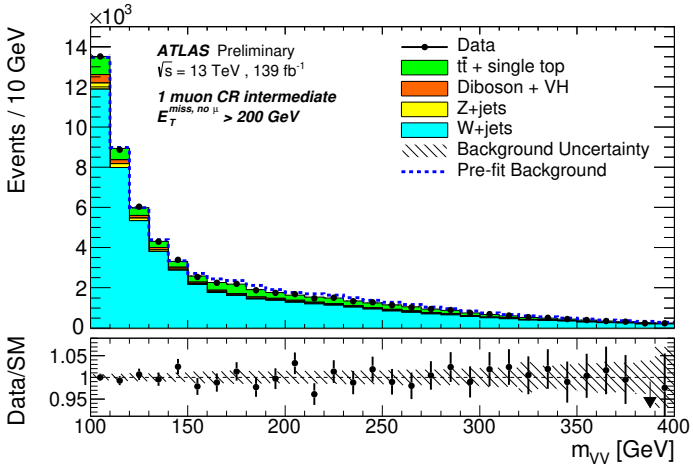
No significant deviations from the background-only hypothesis have been observed. Therefore, the results in the SR are presented with the background normalisations scaled to the outcome of the conditional background-only ($\mu = 0$) fit.




(a) 1 muon CR merged category $E_{\mathrm{T}}^{\mathrm{miss,no}\mu} > 500\,\mathrm{GeV}$

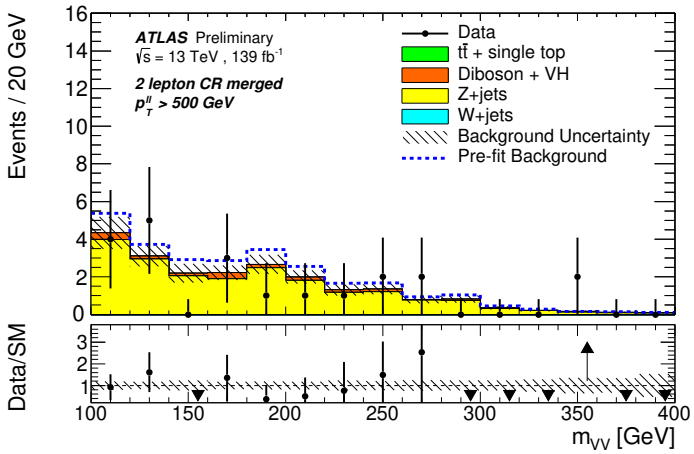



(b) 1 muon CR merged category $300\,\mathrm{GeV} < E_{\mathrm{T}}^{\mathrm{miss,no}\mu} < 500\,\mathrm{GeV}$

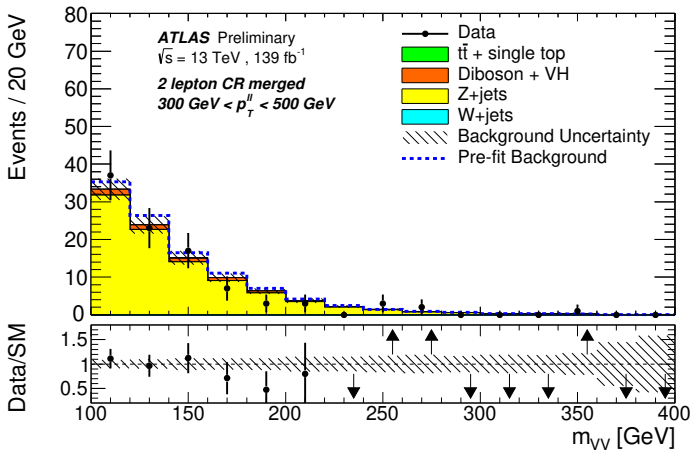



(c) 1 muon CR intermediate category $E_{\mathrm{T}}^{\mathrm{miss,no}\mu} > 200\,\mathrm{GeV}$

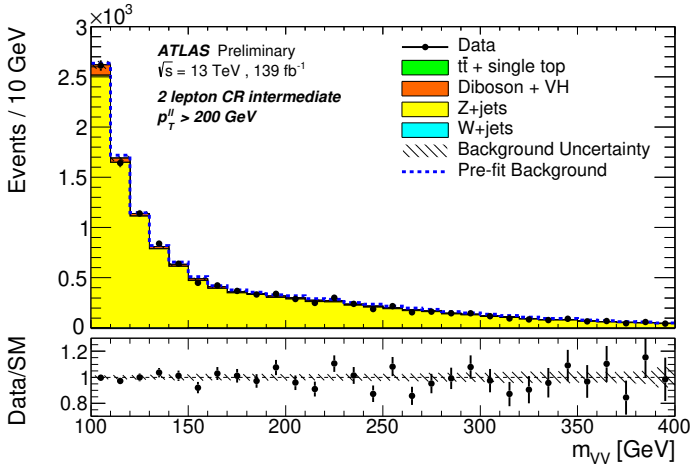
**Fig. 12.9.:** Distributions of the dark Higgs boson candidate invariant mass in the 1 muon CR merged and intermediate categories after the background-only fit to the data. The upper panel shows the comparison of data to the SM background expectation before (dashed lines) and after the background-only fit (solid histograms). The lower panels display the ratio of data to SM expectations after the fit, with the hatched band expressing the systematic uncertainty. No $m_{VV}$ shape information in the CRs is considered in the fit.




(a) 2 lepton CR merged category $E_{\mathrm{T}}^{\mathrm{miss,no}\mu} > 500\,\mathrm{GeV}$

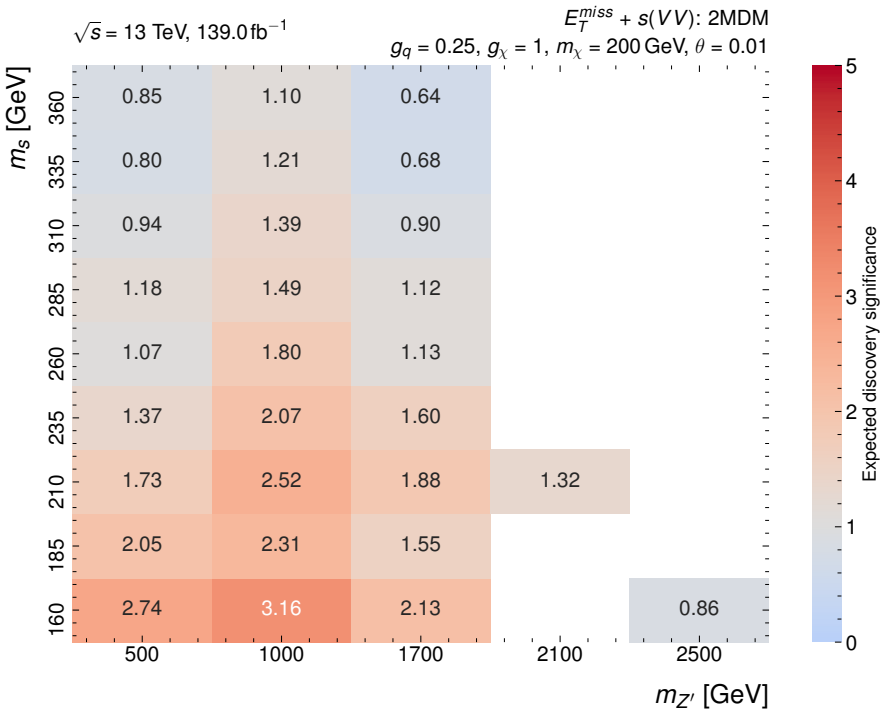



(b) 2 lepton CR merged category $300\,\mathrm{GeV} < E_{\mathrm{T}}^{\mathrm{miss,no}\mu} < 500\,\mathrm{GeV}$

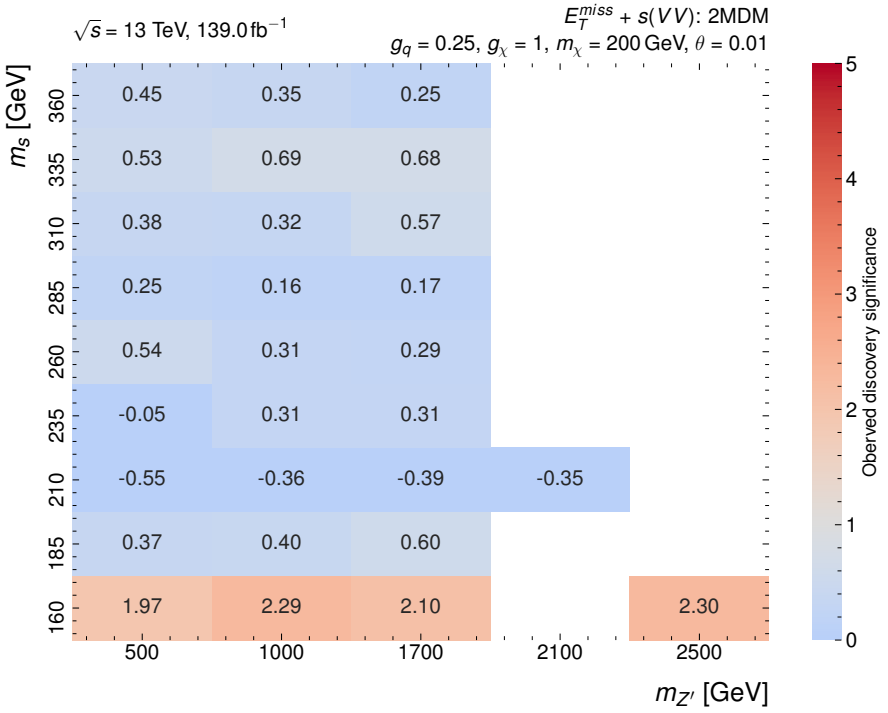



(c) 2 lepton CR intermediate category $E_{\mathrm{T}}^{\mathrm{miss,no}\mu} > 200\,\mathrm{GeV}$

**Fig. 12.10.:** Distributions of the dark Higgs boson candidate invariant mass in the 2 lepton CR merged and intermediate categories after the background-only fit to the data. The upper panel shows the comparison of data to the SM background expectation before (dashed lines) and after the background-only fit (solid histograms). The lower panels display the ratio of data to SM expectations after the fit, with the hatched band expressing the systematic uncertainty. No $m_{VV}$ shape information in the CRs is considered in the fit.




(a) Expected median discovery significance




(b) Observed discovery significance

**Fig. 12.11.:** Expected median discovery significance $Z^{\text{exp}}$ (top) estimated with the Asimov dataset generated under the assumption of the nominal signal model ($\mu = 1$) and observed discovery significance (bottom) for the 2MDM simplified model signals in dependence of the Z′ mediator mass $m_{Z'}$ and the dark Higgs boson mass $m_s$.

The observed number of events in the SR event selection for each category is shown in Table 12.8, together with the expected number of events for the individual background processes, whose normalisation is determined by the background-only profile likelihood fit.

**Tab. 12.8.:** Expected and observed numbers of events in the merged event topology signal region with an integrated luminosity of $139\,\text{fb}^{-1}$ and $\sqrt{s} = 13\,\text{GeV}$. The background yields and uncertainties are shown after the profile-likelihood fit to the data. The quoted background uncertainties include both the statistical and systematic contributions.

| Process | Range in $E_{\text{T}}^{\text{miss}}$ [GeV] | | |
|---|---|---|---|
| | merged $[300, 500)$ | merged $[500, \infty)$ | intermediate $[200, \infty)$ |
| Z + jets | $384 \pm 27$ | $117 \pm 10$ | $49\,100 \pm 720$ |
| W + jets | $185 \pm 20$ | $24 \pm 6$ | $25\,500 \pm 800$ |
| $t\bar{t}$ | $40 \pm 9$ | $7 \pm 5$ | $2\,530 \pm 400$ |
| Single top-quark | $5 \pm 3$ | $1 \pm 1$ | $631 \pm 89$ |
| Diboson | $38 \pm 8$ | $11 \pm 3$ | $2\,810 \pm 450$ |
| Bkg | $653 \pm 23$ | $160 \pm 11$ | $80\,500 \pm 290$ |
| Data | 647 | 178 | 80 519 |

The overall event yields in the CRs and the SR are shown in Figure 12.12. They are found to be well described by SM processes within uncertainties. In particular, the $E_{\text{T}}^{\text{miss,no}\mu}$ and $p_{\text{T}}^{\ell\ell}$ shape information of the W + jets and Z + jets backgrounds provided by the CRs are propagated to the SR.

The dark Higgs boson candidate mass distributions in the SR are shown in Figure 12.13. The signal process is characterised by a large mass peak, which is most evident in the merged category with $E_{\text{T}}^{\text{miss}} > 500\,\text{GeV}$ due to the relatively low contribution of background processes. The observed results indicate that the data are overall well described by SM predictions. A mild excess in data around $m_{VV} = 160\,\text{GeV}$ is observed. The excess corresponds to a local significance of $2.3\sigma$ and a global significance of $1.3\sigma$ when considering the nine independent $m_s$ hypotheses under consideration. Although the excess seems to be most prominent in the intermediate category, it is narrower than the experimental resolution for $m_s$ in this category.

## 12.8.2 Impact of systematic uncertainties

The impact of the various sources of systematic uncertainty on the fitted signal strength $\mu$ is evaluated using the procedure presented in Section 9.8.2.

Table 12.9 shows a breakdown of the expected signal strength uncertainties for three representative 2MDM simplified model signals with different $m_s$. The three 2MDM scenarios are chosen to represent different event topologies. The first signal corresponds to events selected primarily in the merged category, while the third

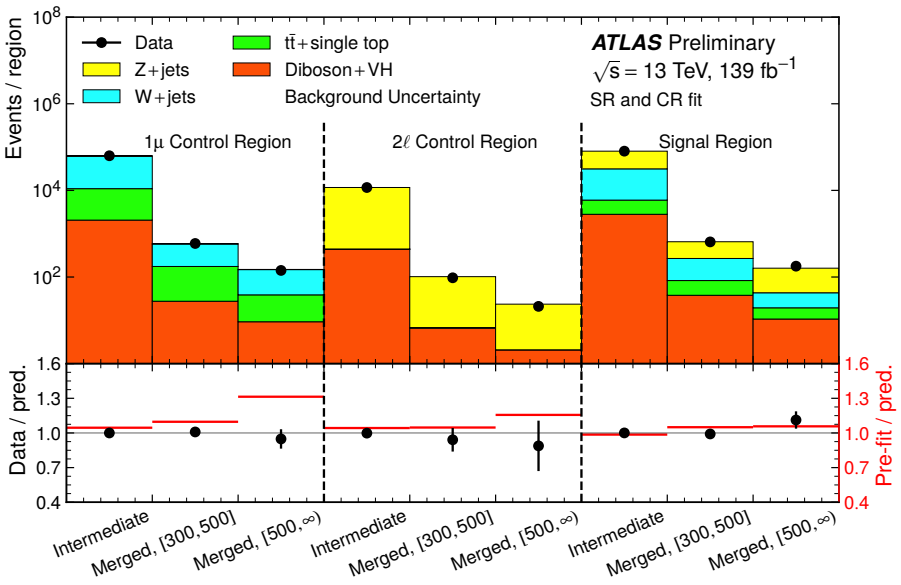
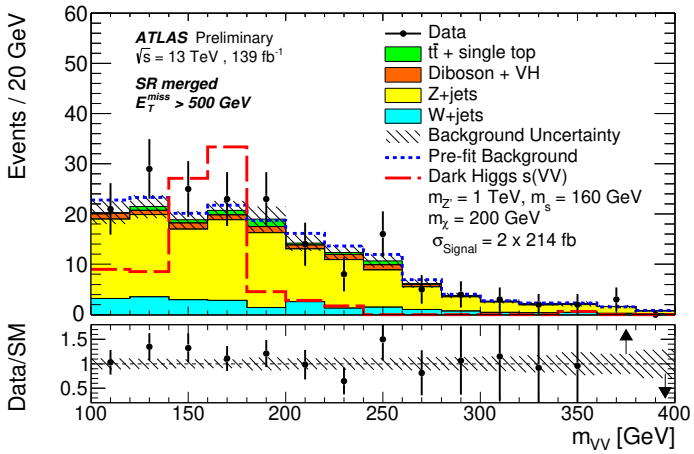
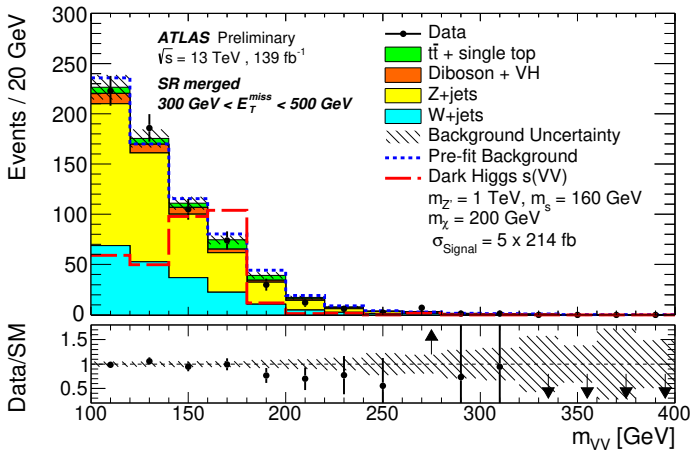


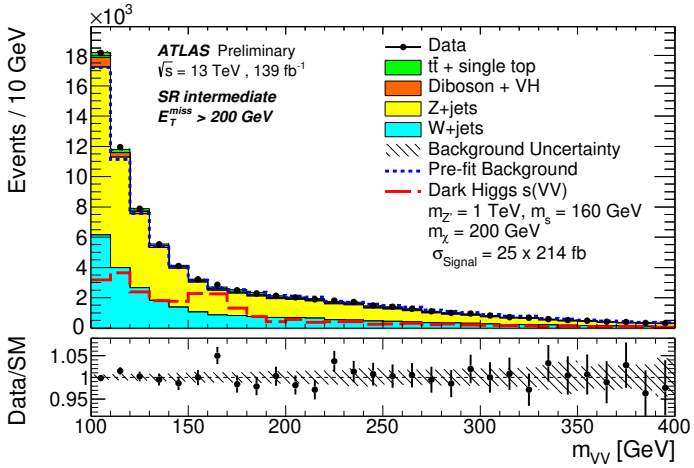

Fig. 12.12.: Data and SM background post-fit yields stacked in each SR and CR category with the maximum likelihood estimators set to the conditional values of the combined signal and control region fit. The hatched uncertainty band includes simulation statistical uncertainties, experimental systematic uncertainties, and $V$ + jets theory modelling systematic uncertainties. The red line in the lower panel shows the ratio of the pre-fit to the post-fit background prediction.




(a) SR merged category $E_{\mathrm{T}}^{\mathrm{miss,no}\mu} > 500\,\mathrm{GeV}$




(b) SR merged category $300\,\mathrm{GeV} < E_{\mathrm{T}}^{\mathrm{miss,no}\mu} < 500\,\mathrm{GeV}$




(c) SR intermediate category $E_{\mathrm{T}}^{\mathrm{miss,no}\mu} > 200\,\mathrm{GeV}$

**Fig. 12.13.:** Distributions of the dark Higgs boson candidate invariant mass in the SR merged and intermediate categories, after the background-only fit to the data. The upper panel shows the comparison of data to the SM background expectation before (dashed lines) and after the background-only fit (solid histograms). The lower panels display the ratio of data to SM expectations after the fit, with the hatched band expressing the systematic uncertainty. A representative 2MDM simplified model signal with $m_{Z'} = 1\,\mathrm{TeV}$, $m_s = 160\,\mathrm{GeV}$, $g_q = 0.25$, $g_\chi = 1$, and $m_\chi = 200\,\mathrm{GeV}$ is overlaid.

signal corresponds to events selected primarily in the intermediate category. The second signal corresponds to events selected by both categories.

The dominant sources of experimental uncertainty arise from the scale and resolution of the energy of jets, tracking efficiencies, as well as the calibration of the lepton identification. Dominant theoretical systematic uncertainties originate from the modelling of the signal and the W + jets and Z + jets background processes, which encompass uncertainties from the choice of PDFs and factorisation and renormalisation scales. Other large systematic uncertainties arise from the statistical uncertainty of the MC simulated events.

As systematic uncertainties dominate the search, a future iteration would strongly benefit from improvements in the jet energy calibration and an improved description of the background processes.

**Tab. 12.9.:** Breakdown of expected signal strength uncertainties for three representative 2MDM signal samples with $m_{Z'} = 1\,\text{TeV}$ and (a) $m_s = 160\,\text{GeV}$, (b) $m_s = 235\,\text{GeV}$, and (c) $m_s = 310\,\text{GeV}$. The effect is expressed as the relative uncertainty on the signal strength, assuming total cross-sections of (a) $214\,\text{fb}$, (b) $53\,\text{fb}$ fb, and (c) $19\,\text{fb}$. Each systematic uncertainty contribution is provided as the quadratic difference between the total uncertainty and the uncertainty obtained by setting the systematic uncertainty in question to its nominal value and excluding it thereby from the fit. Total denotes the quadrature sum of statistical and total systematic uncertainties.

| Source of uncertainty | Uncertainty on $\mu$ [%] (a) | (b) | (c) |
|---|---|---|---|
| Signal modelling | 11 | 10 | 10 |
| W + jets modelling | 9 | 21 | 14 |
| Z + jets modelling | 7 | 12 | 13 |
| Diboson modelling | 1.1 | 1.0 | 1.5 |
| $t\bar{t}$/ single t modelling | 0.3 | 0.5 | 0.7 |
| Pile-up modelling | 0.2 | 1.1 | 2.3 |
| MC statistics | 11 | 14 | 23 |
| $E_{\text{T}}^{\text{miss}}$ | 5.2 | 0.6 | 2.1 |
| Jet energy scale | 8 | 17 | 24 |
| Jet energy resolution | 11 | 18 | 15 |
| Lepton reconstruction | 8 | 9 | 5 |
| Flavour tagging | 1.3 | 1.7 | 8.5 |
| Track reconstruction | 6 | 7 | 5 |
| Luminosity | 1.6 | 2.0 | 1.3 |
| Systematic uncertainty | 30 | 42 | 55 |
| Statistical uncertainty | 16 | 25 | 50 |
| Total uncertainty | 34 | 49 | 74 |

### 12.8.3 Constraints on the 2MDM simplified model

As no large deviation from the SM background expectation is observed for any of the signal mass points, the parameter space of the 2MDM simplified model can be constrained by computing upper limits on the signal strength $\mu$ at $95\,\%$ confidence level using the $\mathrm{CL}_s$ method [307].

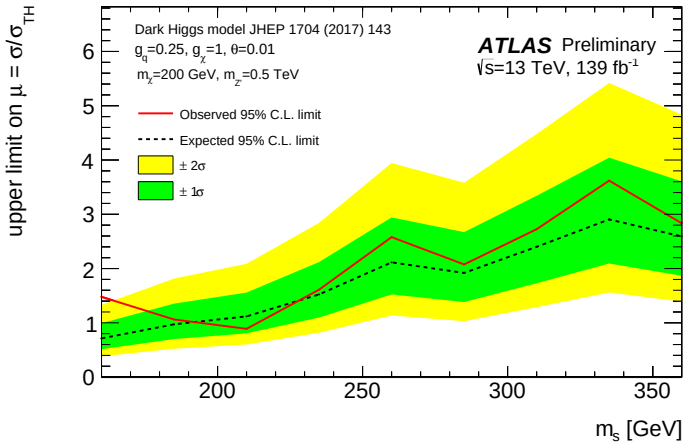
Figure 12.14 shows the exclusion limits on the signal strength $\mu$ for signals in the 2MDM simplified model with $m_{Z'} = 0.5\,\mathrm{TeV}$, $m_{Z'} = 1.0\,\mathrm{TeV}$, and $m_{Z'} = 1.7\,\mathrm{TeV}$ in dependence of $m_s$.

The corresponding exclusion limit contour, which is provided in the $m_{Z'}$-$m_s$ plane for the fixed set of parameters $g_q = 0.25$, $g_\chi = 1$, and $m_\chi = 200\,\mathrm{GeV}$, is shown in Figure 12.15. The signal points in the 2MDM simplified model with $m_{Z'}$ of up to $1.6\,\mathrm{TeV}$ are excluded at $95\,\%$ $\mathrm{CL}_s$ for $m_s = 210\,\mathrm{GeV}$. The observed exclusion range in $m_{Z'}$ becomes narrower than expected at low $m_s$ owing to the small excess in data close to $m_{VV} = 160\,\mathrm{GeV}$ as discussed above.

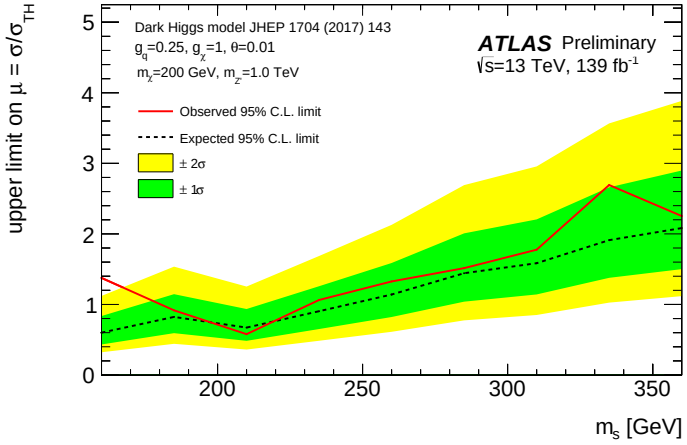
## 12.9 Conclusion of the $E_{\mathrm{T}}^{\mathrm{miss}} + s(VV)$ search

In conclusion, the signature of $E_{\mathrm{T}}^{\mathrm{miss}}$ and resonant production of weak vector boson pairs is explored for the first time at the LHC. The novelty of TAR jets is applied in this search to reconstruct dark Higgs boson candidates in dense event topologies using $s \to V(qq)V(qq)$ decays. The TAR jet algorithm improves the sensitivity of the search by a factor of up to 2.5 regarding the expected median discovery significance compared to the conventional large-R jet approach, assuming similar impact of the systematic uncertainties as suggested by the comparison of Table 9.15 and Table 12.9.

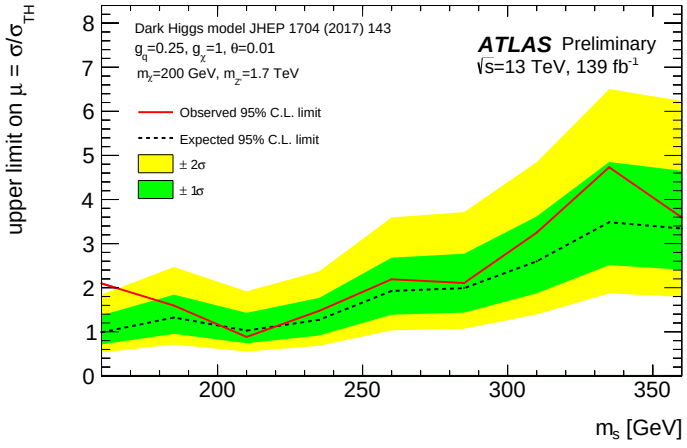
The minor excess invites further investigation, for instance by searches targeting the (semi-)leptonic decay channel of the weak vector bosons. The 2MDM model can be further explored in the various decay modes of the dark Higgs boson. Heavy dark Higgs bosons decay to pairs of SM Higgs bosons, which can be probed using the $E_{\mathrm{T}}^{\mathrm{miss}} + \mathrm{h}(\mathrm{b\bar{b}})\mathrm{h}(\mathrm{b\bar{b}})$ signature. Very light dark Higgs bosons can be searched for using the $E_{\mathrm{T}}^{\mathrm{miss}} + s(\mathrm{b\bar{b}})$ signature, which awaits further exploration for $m_s < 50\,\mathrm{GeV}$.




(a) Exclusion limits for 2MDM signals with $m_{Z'} = 0.5\,\text{TeV}$




(b) Exclusion limits for 2MDM signals with $m_{Z'} = 1.0\,\text{TeV}$




(c) Exclusion limits for 2MDM signals with $m_{Z'} = 1.7\,\text{TeV}$

**Fig. 12.14.:** Upper 95 % $\text{CL}_s$ limits on the signal strength $\mu$ of 2MDM simplified model signals in dependence of the dark Higgs boson mass $m_s$ for the fixed set of parameters $g_q = 0.25$, $g_\chi = 1$, and $m_\chi = 200\,\text{GeV}$ in the scenarios with Z′ boson mediator masses $m_{Z'} = 0.5\,\text{TeV}$ (top), $m_{Z'} = 1.0\,\text{TeV}$ (middle), and $m_{Z'} = 1.7\,\text{TeV}$ (bottom). The observed limits (solid line) are consistent with the expectation under the background-only hypothesis (dashed line) within the uncertainties (filled band), except for a small excess at $m_s = 160\,\text{GeV}$.

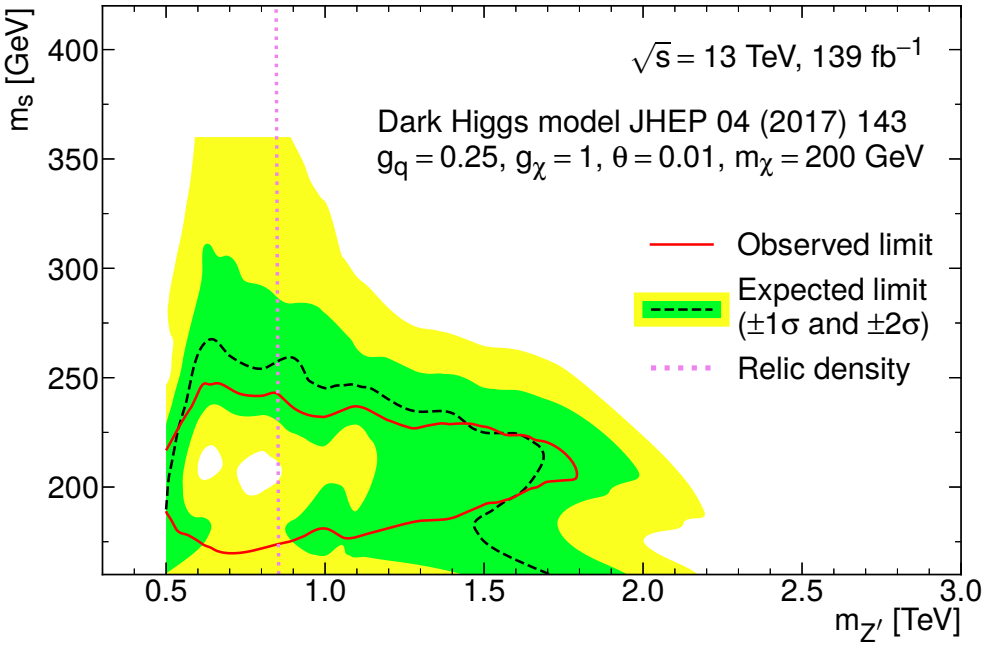



**Fig. 12.15.:** Exclusion contours at 95 % $CL_s$ for the 2MDM simplified model in the $m_{Z'}$-$m_s$ plane for the fixed set of parameters $g_q = 0.25$, $g_\chi = 1$, and $m_\chi = 200\,\text{GeV}$. The observed limits are encircled by the solid line, whereas the expected limits are indicated by the dashed line. The expected $\pm 1\sigma$ and $\pm 2\sigma$ uncertainties are shown as filled green and yellow bands. The observed value of the relic density from the Planck [301] measurements is obtained for $m_{Z'} = 850\,\text{GeV}$ (dotted line). The region on the right of the line corresponds to higher predicted relic density than these measurements.

# 13 Status of dark matter searches with ATLAS

## 13.1 Introduction

This chapter relates the results presented in this dissertation to the broader picture and aims to provide an overview of the experimental status of ATLAS mediator-based dark matter searches.

The public ATLAS results based on the pp collision data collected in the Run-2 data-taking during 2015–2018 are summarised in the context provided by models for dark matter production. As no significant excess over the expected SM background was observed in any of these searches, constraints on the parameter space of three classes of dark matter models are presented.

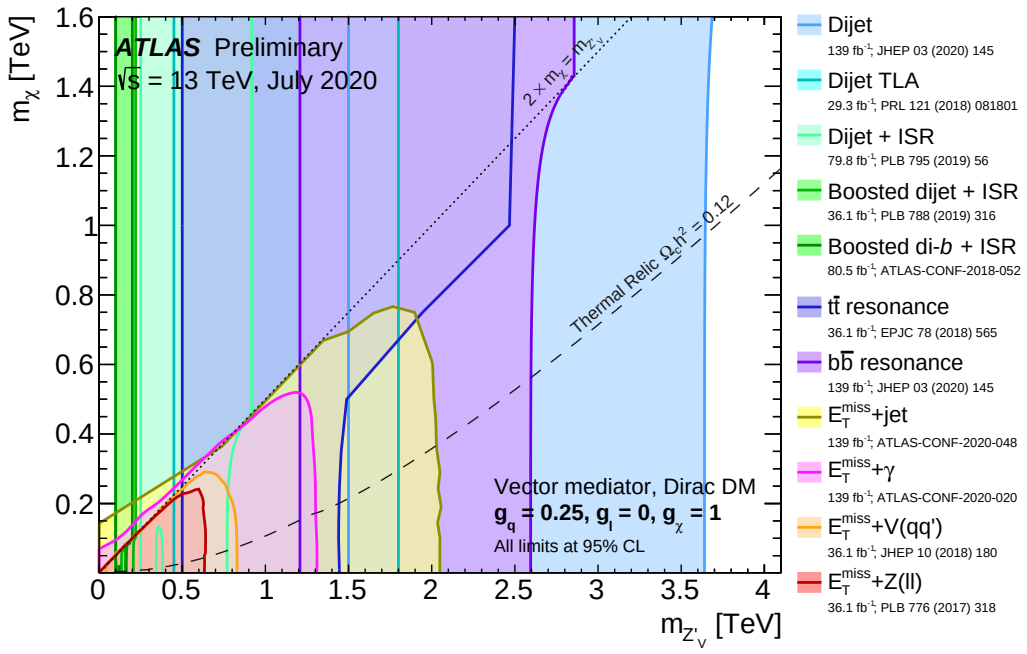
Section 13.2 discusses limits on simplified models with spin-1 $\mathrm{Z}'$ mediators. Section 13.3 discusses the limits on simplified models with extended Higgs sector. Finally, Section 13.4 discusses the limits on simplified models with two mediators.

## 13.2 Simplified models with spin-1 $\mathrm{Z}'$ mediators

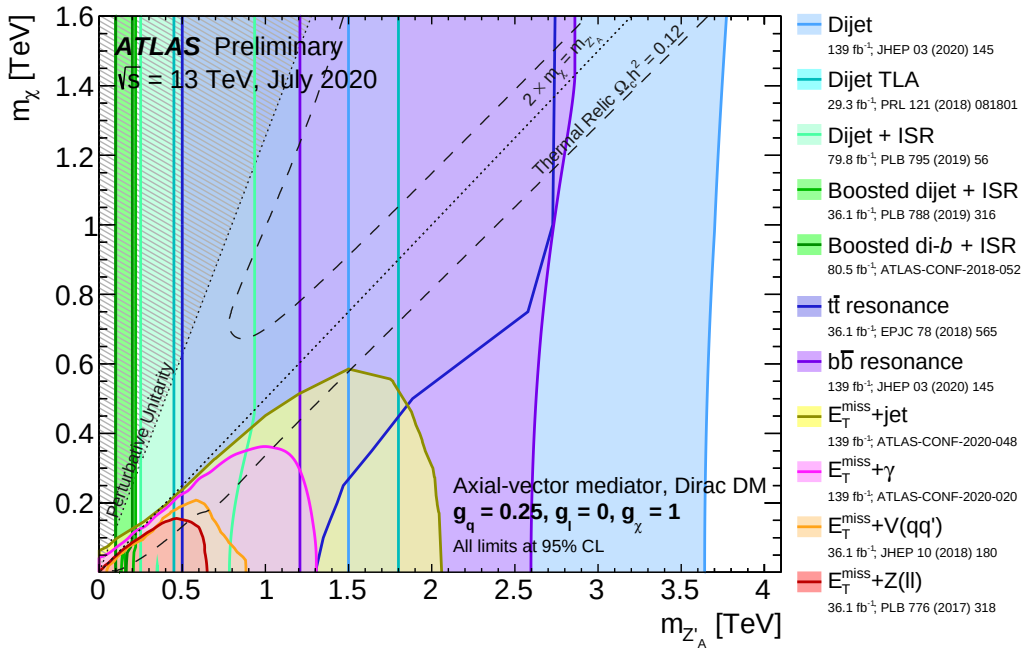
The $V/A$ simplified model (c.f. Section 3.7.1) is strongly constrained by searches for the associated production of dark matter particles with ISR objects and by searches for high-mass resonances decaying into pairs of fermions. The resonance searches can place limits on the $V/A$ simplified model, as the production of dark matter via a mediator produced from quarks also establishes the inverse process of the mediator decaying to quarks. Therefore, these limits have very little dependence on $m_\chi$ and can exclude large regions of parameter space.

Figure 13.1 shows the constraints on the $\mathrm{Z}'$ boson vector and axial-vector mediator scenarios for the parameters $g_q = 0.25$, $g_\ell = 0$, $g_\chi = 1$ in the $m_{\mathrm{Z}'}$-$m_\chi$ plane.

The combinations of $m_{\mathrm{Z}'}$ and $m_\chi$, which result in the observed relic density $\Omega h^2 = 0.12$ from Planck [301] measurements are indicated by dashed curves labelled with *thermal relic*. The kinematic threshold where on-shell decays of the mediator to dark matter particles become possible is indicated by a dotted line. Also, the regions which are in tension with considerations of perturbative unitarity [257] are indicated by shading.




(a) Vector mediator




(b) Axial-vector mediator

**Fig. 13.1.:** Regions in the $m_{Z'}$-$m_\chi$ plane in the parameter space of the spin-1 Z′ mediator simplified model excluded at 95 % $CL_s$ for the choice of vector (top) and axial-vector (bottom) mediator mediator couplings $g_q = 0.25$, $g_\chi = 1$, $g_\ell = 0$. The dashed curve indicates combinations of mediator mass $m_{Z'}$ and dark matter particle mass $m_\chi$ which are consistent with the Planck [301] dark matter relic density measurements. The dotted line indicates the kinematic threshold where the mediator can decay on-shell into dark matter particles. The shading in the upper left corner indicates regions which are in tension with perturbative unitary considerations. Figures reproduced from Ref. [180].

The most stringent limits for the chosen benchmark scenario with $g_q = 0.25$ are placed by the dijet search, with exclusion up to $m_{Z'} = 3.6\,\text{TeV}$. Its lower mass reach down to $460\,\text{GeV}$ is limited by the jet trigger threshold. Therefore, two alternative search strategies are employed to circumvent this limitation. The trigger-level-analysis (TLA) stores event information at trigger-level with reduced detector information to allow for a lower mass threshold. The searches in the dijet + ISR family trigger on additional ISR objects and can therefore set limits on mediator masses as low as $100\,\text{GeV}$. In addition, the searches for di-$b$-jet and top quark pair resonances place complementary exclusion limits.

The $E_{\text{T}}^{\text{miss}} + X$ family of searches are most sensitive in the on-shell region $2m_\chi < m_{Z'}$. Their sensitivity decreases in the off-shell region due to a strong decrease in the production cross-section. Therefore, only the $E_{\text{T}}^{\text{miss}}$ + jet and $E_{\text{T}}^{\text{miss}} + \gamma$ searches can probe this region and only for low $m_{Z'}$ and $m_\chi$. In addition to the limit of the $E_{\text{T}}^{\text{miss}} + V(q\bar{q})$ search, the results of the $E_{\text{T}}^{\text{miss}} + \text{Z}(\ell\ell)$ search is shown, which is also based on $36.1\,\text{fb}^{-1}$ pp collision data. The $E_{\text{T}}^{\text{miss}} + V(q\bar{q})$ search is more sensitive than the $E_{\text{T}}^{\text{miss}} + \text{Z}(\ell\ell)$ search because it targets both W and Z weak vector bosons and because of the larger weak vector boson branching fraction to hadronic decays. The $E_{\text{T}}^{\text{miss}} + \gamma$ search is based on the full Run-2 dataset and benefits from the larger production cross-section of photon ISR. Therefore, the reach of the exclusion extends up to $1.3\,\text{TeV}$, which is more than twice the reach of the $E_{\text{T}}^{\text{miss}} + V(q\bar{q})$ search. The largest exclusion of up to $2.0\,\text{TeV}$ in $m_{Z'}$ and $750\,\text{GeV}$ in $m_\chi$ is provided by the $E_{\text{T}}^{\text{miss}}$ + jet search, which benefits also from the full Run-2 dataset and from the largest production cross-section.

Large regions of the viable parameter space for the $V/A$ simplified model are ruled out for the mediator couplings under consideration. However, alternative coupling scenarios correspond to different regions of excluded parameter space. A reduced coupling of the mediator to quarks results in smaller reach of the dijet searches and gives more emphasis to the $E_{\text{T}}^{\text{miss}} + X$ limits, thereby demonstrating the interplay of the two approaches.

Collider experiments provide a complementary approach to direct and in-direct detection experiments (c.f. Section 3.6). The $V/A$ simplified model allows comparing the collider-based limits with those of direct detection experiments. Figure 13.2 shows the limits on the spin-independent $\chi$-nucleon scattering cross-sections as a function of the dark matter mass $m_\chi$.

The direct detection experiments dominate the sensitivity by a few orders of magnitude for $m_\chi > 6\,\text{GeV}$. In the low $m_\chi$ range, the direct detection experiments have reduced sensitivity due to the very low energy recoil that light dark dark matter particles would induce. In this region, the resonance searches complement the direct detection limits.

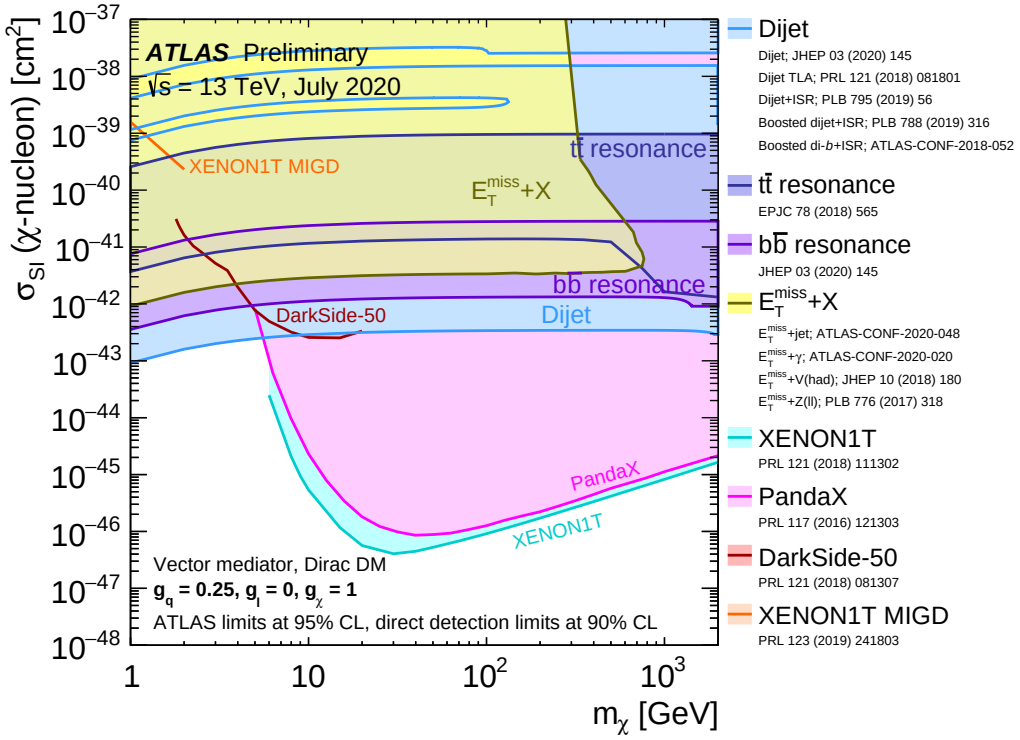



**Fig. 13.2.:** Regions in the $m_{Z'}$-$m_\chi$ plane in the parameter space of the spin-1 Z′ axial-vector mediator simplified model excluded at 95 % $CL_s$ for the choice of mediator couplings $g_q = 0.25$, $g_\chi = 1$, $g_\ell = 0$. The dashed curve indicates combinations of mediator mass $m_{Z'}$ and dark matter particle mass $m_\chi$ which are consistent with the Planck [301] dark matter relic density measurements. The dotted line indicates the kinematic threshold where the mediator can decay on-shell into dark matter particles. The shaded region in the upper left corner indicates combinations of mediator mass $m_{Z'}$ and dark matter particle mass $m_\chi$ which are in tension with the perturbative unitary considerations. Figure reproduced from Ref. [180].

## 13.3 Simplified models with extended Higgs sector

Two models with an extended Higgs sector are considered in this dissertation. These models are the simplest extensions of the simplified models describing only dark matter particles and mediators. They address some of the shortcomings of these elementary simplified models, such as lacking the ingredients of UV-complete theories and consequently missing signatures which are contained in the broader phenomenology of more sophisticated models [257].

The Z′-2HDM model, which is probed by the $E_{\mathrm{T}}^{\mathrm{miss}} + \mathrm{h}(\mathrm{b\bar{b}})$ search, is strongly constrained by dijet searches and is subjected to additional indirect constraints from flavour-physics [243, 288] and electro-weak precision measurements [129], leaving very little viable parameter space. Therefore, the following discussion is focused on the $a$-2HDM simplified model (c.f. Section 3.7.2).

The $a$-2HDM simplified model describes the interaction between SM particles and dark matter particles which is mediated by a pseudo-scalar mediator. Consequentially, not only the constraints from most resonance searches but also from direct-detection experiments are avoided. Therefore, collider-based searches are particularly important to test this class of models.

Figure 13.3 shows the exclusion contours at at $95\,\%$ $\mathrm{CL}_s$ in the $m_{\mathrm{A}}$-$m_a$ plane of the parameter space for the fixed choice of parameters $\tan\beta = 1.0$, $m_\chi = 10\,\mathrm{GeV}$, and $\sin\theta = 0.35$.

In addition to the $E_{\mathrm{T}}^{\mathrm{miss}} + Z(qq)$ contour, the limits placed by the $E_{\mathrm{T}}^{\mathrm{miss}} + Z(\ell\ell)$ search [80], the $E_{\mathrm{T}}^{\mathrm{miss}} + \mathrm{h}(\mathrm{b\bar{b}})$ search [92], the $E_{\mathrm{T}}^{\mathrm{miss}} + \mathrm{H} \to \gamma\gamma$ search [86], the $E_{\mathrm{T}}^{\mathrm{miss}} + \mathrm{t\bar{t}}$ search [94], and searches for invisible decays of the Higgs boson (H + invisible) [41] are displayed. The exclusion sensitivity is vastly dominated by the $E_{\mathrm{T}}^{\mathrm{miss}} + Z(\ell\ell)$ and $E_{\mathrm{T}}^{\mathrm{miss}} + \mathrm{h}(\mathrm{b\bar{b}})$ searches. In contrast to the $V/A$ simplified model, the most relevant signal processes involve the resonant production of Z and Higgs bosons, therefore the experimentally much cleaner $E_{\mathrm{T}}^{\mathrm{miss}} + \mathrm{Z}(\ell\ell)$ signature provides better sensitivity than the $E_{\mathrm{T}}^{\mathrm{miss}} + \mathrm{Z}(qq)$ signature.

Figure 13.4 shows the exclusion limits on the signal strength $\mu$ for the $a$-2HDM simplified model as a function of $\sin\theta$ for the fixed parameter choices $\tan\beta = 1.0$, $m_\chi = 10\,\mathrm{GeV}$, considering a low-mass scenario with $m_{\mathrm{H}} = 600\,\mathrm{GeV}$, $m_a = 200\,\mathrm{GeV}$, and a high-mass scenario with $m_{\mathrm{H}} = 1000\,\mathrm{GeV}$, $m_a = 350\,\mathrm{GeV}$.

The strongest exclusion again is provided by the $E_{\mathrm{T}}^{\mathrm{miss}} + \mathrm{Z}(\ell\ell)$ and $E_{\mathrm{T}}^{\mathrm{miss}} + \mathrm{h}(\mathrm{b\bar{b}})$ searches. While the sensitivity of the $E_{\mathrm{T}}^{\mathrm{miss}} + \mathrm{Z}$ searches improves monotonically as a function of $\sin\theta$, the sensitivity of the $E_{\mathrm{T}}^{\mathrm{miss}} + \mathrm{h}$ searches varies due to the non-trivial dependence of the Higgs boson $p_{\mathrm{T}}$ distribution on the mixing angle. The heavy-flavour signatures are presented for the different parameter choices $\tan\beta = 0.5$ ($E_{\mathrm{T}}^{\mathrm{miss}} + \mathrm{t\bar{t}}$, $\mathrm{t\bar{t}}\ \mathrm{t\bar{t}}$) and $\tan\beta = 50$ ($E_{\mathrm{T}}^{\mathrm{miss}} + \mathrm{b\bar{b}}$), which result in enhanced coupling of the pseudo-scalar mediator to up-type or down-type quarks, respectively.

Figure 13.5 shows the exclusion limits on the dark matter mass $m_\chi$ for the fixed choices of the parameters $\tan\beta = 1.0$, $m_{\mathrm{H}} = 600\,\mathrm{GeV}$, $m_a = 250\,\mathrm{GeV}$, and $\sin\theta =$

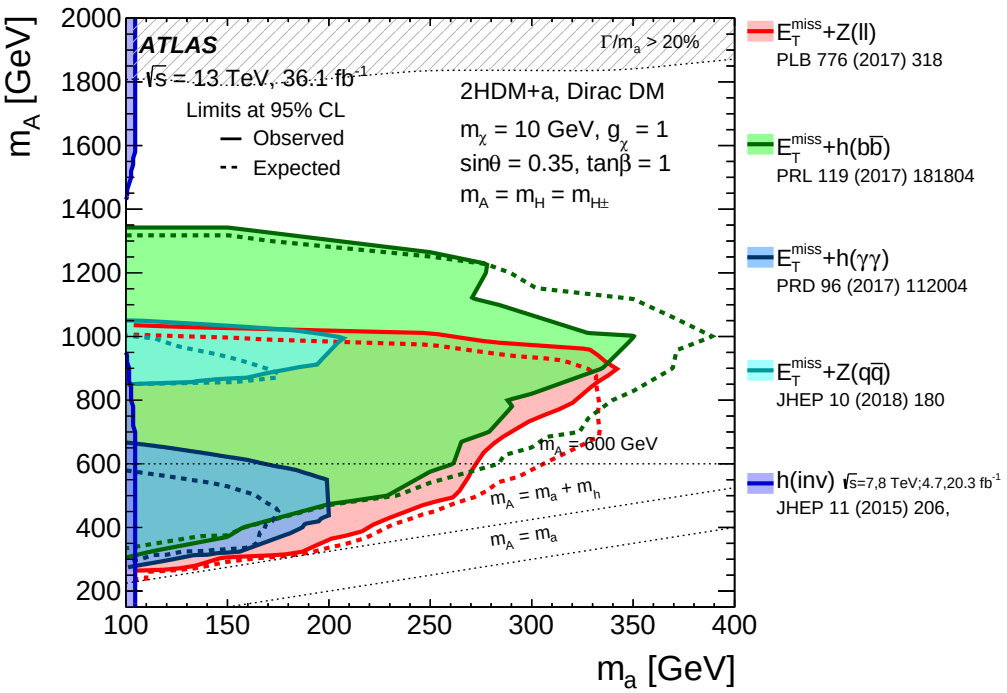
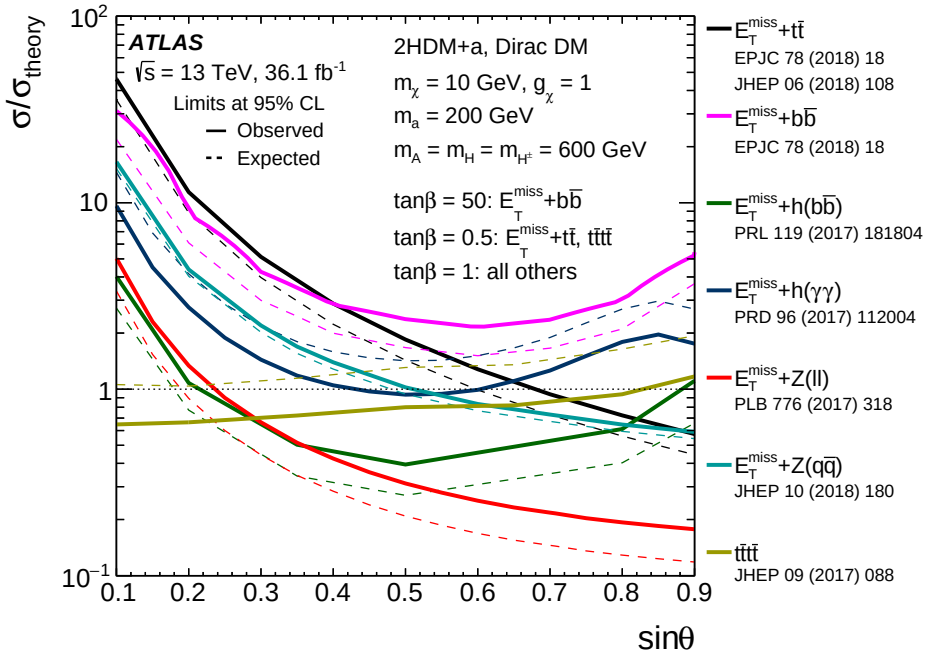
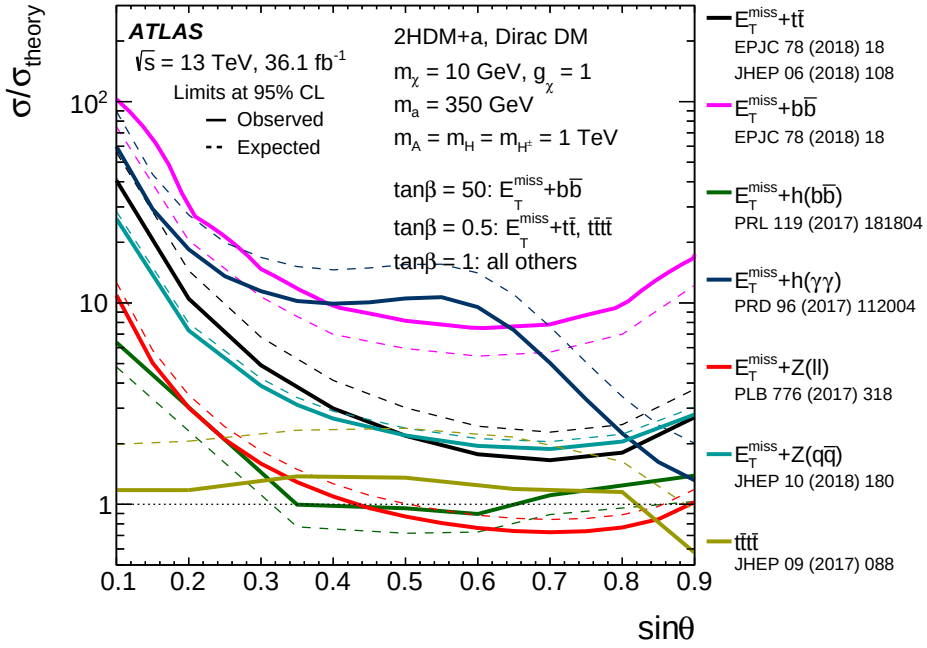



**Fig. 13.3.:** Exclusion contours at $95\,\%$ $\mathrm{CL}_s$ for the $a$-2HDM simplified model in the two-dimensional $m_{\mathrm{H}}$-$m_a$ plane for the fixed choice of parameters $\tan\beta = 1.0$, $m_\chi = 10\,\mathrm{GeV}$, and $\sin\theta = 0.35$, due to various $E_{\mathrm{T}}^{\mathrm{miss}} + X$ searches and searches for invisible decays of the Higgs boson (H + invisible). The dashed grey regions at the top indicate the region where the width of any of the Higgs bosons exceeds $20\,\%$ of its mass. Figure reproduced from Ref. [40].




(a) Low-mass scenario $m_{\mathrm{H}} = 600\,\mathrm{GeV}$, $m_a = 200\,\mathrm{GeV}$




(b) High-mass scenario $m_{\mathrm{H}} = 1000\,\mathrm{GeV}$, $m_a = 350\,\mathrm{GeV}$

**Fig. 13.4.:** Observed exclusion limits at 95 % $\mathrm{CL}_s$ on the signal strength $\mu$ for the $a$-2HDM simplified model as a function of $\sin\theta$, shown for parameters corresponding to a low-mass scenario (top) and a high-mass scenario (bottom). Figures reproduced from Ref. [40].

0.35. The dark matter mass is the parameter with the strongest impact on the relic density $\Omega h^2$, which is overlaid as a blue long-dashed curve.

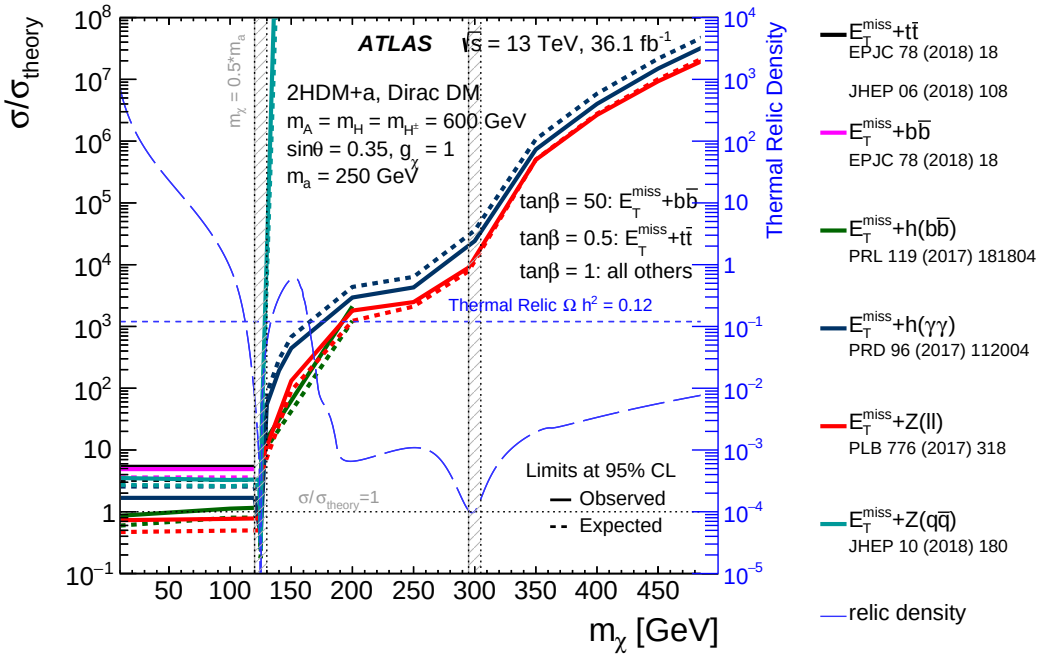



**Fig. 13.5.:** Exclusion limits at 95 % $CL_s$ on the signal strength $\mu$ for the $a$-2HDM simplified model as a function of $m_\chi$ for the fixed choices of the parameters $\tan\beta = 1.0$, $m_H = 600\,\text{GeV}$, $m_a = 250\,\text{GeV}$, and $\sin\theta = 0.35$. The relic density prediction by the $a$-2HDM simplified model is superimposed (long-dashed line). Figure reproduced from Ref. [40].

For dark matter masses close to $m_a/2$ or $m_\chi > 170\,\text{GeV}$, the predicted value of the relic density is equal to or below the observed value from Planck [301] measurements. The sensitivity of all $E_T^{miss} + X$ signatures under consideration is independent of $m_\chi$ in the on-shell region $2m_\chi < m_a$. The $E_T^{miss} + Z(\ell\ell)$ search excludes this parameter space. The sensitivity of these searches is resonantly enhanced close to the threshold $m_\chi = m_a/2 = 125\,\text{GeV}$. For higher dark matter masses, the sensitivity strongly decreases, leaving the parameter choices for $m_\chi > m_a/2$ which are not in conflict with the relic density measurements unconstrained.

The $a$-2HDM simplified model is probed by several ATLAS dark matter searches [40, 83]. As it is the benchmark next-generation spin-0 dark matter model by the LHC DM WG [6], its investigation is central to the ATLAS full Run-2 dark matter research programme.

## 13.4 Simplified models with two mediators

The simplified model containing both a spin-1 Z′ and a spin-0 dark Higgs boson mediator extends the elementary simplified models in complexity by explicitly

describing elements of their potential UV-completion. Consequentially, the model predicts additional signatures which were not considered in searches motivated by elementary simplified models. One such neglected signature is the resonant production of a dark Higgs boson of unknown mass $m_s$ in association with dark matter particles, which manifest as missing transverse momentum and result in boosted dark Higgs boson candidates. The dark Higgs boson hypothesis can be probed in different final states, depending on the branching fraction of the dark Higgs boson decays (c.f. Figure 3.11) which is contingent on $m_s$.

Figure 13.6 shows the $95\,\%$ $\mathrm{CL}_s$ on the signal strength $\mu$ for the 2MDM simplified model as a function of $m_s$ for the fixed choices of the parameters $m_{\mathrm{Z}'} = 1\,\mathrm{TeV}$, $m_\chi = 200\,\mathrm{GeV}$, $g_q = 0.25$, $g_\chi = 1$, and $\theta = 0.01$.

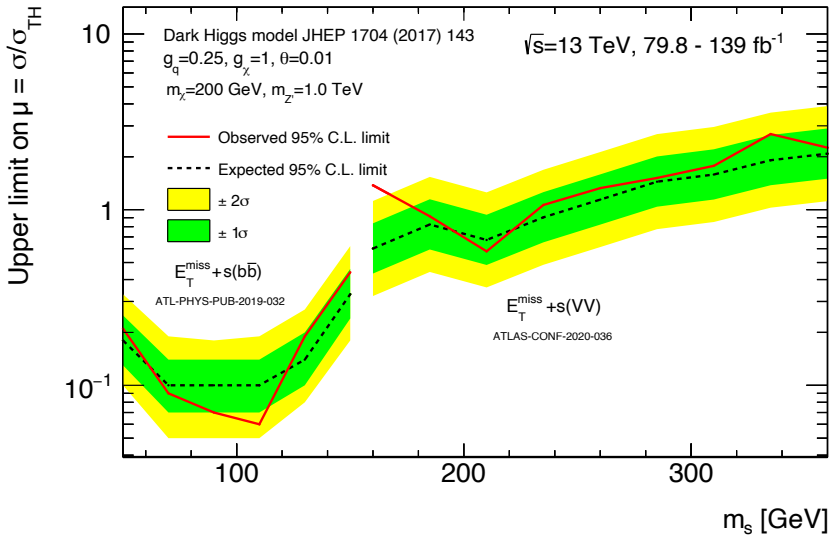



**Fig. 13.6.:** Exclusion limits at $95\,\%$ $\mathrm{CL}_s$ on the signal strength $\mu$ for the 2MDM simplified model as a function of $m_s$ for the fixed choices of the parameters $m_{\mathrm{Z}'} = 1\,\mathrm{TeV}$, $m_\chi = 200\,\mathrm{GeV}$, $g_q = 0.25$, $g_\chi = 1$, and $\theta = 0.01$.

For low $m_s$, the $E_{\mathrm{T}}^{\mathrm{miss}} + s(\mathrm{b\bar{b}})$ search places stringent limits on the signal strength $\mu$. For heavier $m_s$, the $E_{\mathrm{T}}^{\mathrm{miss}} + s(VV)$ search is able to probe the parameter space. The mild excess at $m_s = 160\,\mathrm{GeV}$ which is observed by the $E_{\mathrm{T}}^{\mathrm{miss}} + s(VV)$ search invites corroboration by further investigation of the $E_{\mathrm{T}}^{\mathrm{miss}} + s(\mathrm{b\bar{b}})$ final state or by searches targeting the semi-leptonic $E_{\mathrm{T}}^{\mathrm{miss}} + s(VV)$ signature.

In summary, the 2MDM simplified model can avoid constraints from perturbative unitarity considerations, dark matter relic density measurements, and from direct detection experiments, thereby leading towards previously neglected signatures. Interestingly, the 2MDM simplified model also predicts $E_{\mathrm{T}}^{\mathrm{miss}} + \mathrm{Z}'$ signatures if the dark Higgs boson decays into invisible states and the $\mathrm{Z}'$ boson decays hadronically, which are probed in similar final states as those considered in the $E_{\mathrm{T}}^{\mathrm{miss}} + V(q\bar{q})$ search [88, 26]. Further exploration of this model's viable parameter space by a combination of searches in different final states seems promising.

# 14 Conclusion

The investigation of the particle nature of dark matter is among the central research problems of the LHC physics programme. The unprecedented Run-2 pp collision dataset collected at a centre-of-mass energy of $13\,\text{TeV}$ enables searches for associated dark matter production in various final states and event topologies. This thesis investigates the production of dark matter in signatures of missing transverse momentum $E_{\text{T}}^{\text{miss}}$ and hadronically decaying bosons.

The MC-based background estimation in these searches is improved by auxiliary measurements in control regions, which rely on efficient identification of leptons. As these measurements are ultimately limited by the trigger, improvements in the trigger selectivity directly impact the recorded data. An **optimisation of the low-$p_{\text{T}}$ L1 muon trigger coincidence logic** results in a reduction of the L1MU4 trigger rate of $20\,\%$ while maintaining a muon efficiency of $99\,\%$ in the forward region of the detector in the range $2.0 < |\eta| < 2.4$.

In addition to the trigger optimisation study, four **searches for dark matter produced in association with hadronically decaying heavy bosons** are presented in this dissertation. In all searches, the signature of the signal process is $E_{\text{T}}^{\text{miss}}$ arising from the elusive dark matter particles and jets from the heavy boson decay. The searches are motivated by simplified models for mediator-based dark matter production with varying degrees of complexity, which are used for the interpretation of the results by expressing constraints on the parameter space of these models.

The $\boldsymbol{E_{\text{T}}^{\text{miss}} + V(q\bar{q})}$ **search** investigates signatures with weak vector boson candidates, which are reconstructed either as a single large-radius jet if they are boosted or as a pair of small-radius jets otherwise. The weak vector boson candidates are required to be compatible with the W and Z mass and jet substructure of their hadronic decays. The ATLAS pp collision data recorded in the years 2015–2016, corresponding to an integrated luminosity of $36.1\,\text{fb}^{-1}$ are analysed by selecting events in categories defined by the event topology and the $b$-jet multiplicity. The backgrounds estimate based on MC simulation is improved by the use of control region measurements for the dominant background processes Z + jets, W + jets, and $\text{t}\bar{\text{t}}$ production. A combined likelihood-based statistical analysis of all regions is performed with $E_{\text{T}}^{\text{miss}}$ as the discriminating variable. Two simplified models, a spin-1 $\text{Z}'$ boson mediator model and a model with extended Higgs sector and a pseudo-scalar mediator, are probed by comparing the hypothesis of dark matter signals on top of the SM backgrounds against the null hypothesis. The statistical model takes into account various sources of experimental and theoretical systematic uncertainty. No significant excess over the SM prediction is observed. Therefore, exclusion limits on dark matter production in the simplified models under consideration are derived for model parameters recommended by the LHC DM WG. In the spin-1 $\text{Z}'$ boson

mediator model, limits are set in the $m_{Z'}$-$m_\chi$ plane with fixed mediator couplings $g_q = 0.25$, $g_\chi = 0.25$, and $g_\ell = 0$. Dark matter production via the $s$-channel exchange of a Z′ boson with vector couplings is excluded at 95 % $\mathrm{CL}_s$ for $m_{Z'}$ up to 830 GeV and $m_\chi$ up to 280 GeV. The limits on Z′ boson mediators with axial-vector couplings have similar reach in $m_{Z'}$ but cover a smaller region of the on-shell region. Only the $E_{\mathrm{T}}^{\mathrm{miss}} + \mathrm{Z}(qq)$ signature is relevant for setting limits on the simplified model with an extended Higgs sector and a pseudo-scalar mediator, which is therefore only mildly constrained. For the parameter choices $\tan\beta = 1.0$, $m_\chi = 10$ GeV, and $\sin\theta = 0.35$, configurations with heavy Higgs boson masses $m_H$ in the range 800 GeV to 1050 GeV and pseudo-scalar mediator masses of up to 200 GeV are excluded at 95 % $\mathrm{CL}_s$. Similarly, values of $\sin\theta > 0.5$ are excluded for a model configuration with $m_{\mathrm{H}} = 600$ GeV, $m_a = 200$ GeV, $\tan\beta = 1.0$, and $m_\chi = 10$ GeV.

The $\boldsymbol{E_{\mathrm{T}}^{\mathrm{miss}} + \mathrm{h}(\mathrm{b\bar{b}})}$ **search** investigates signatures with Higgs boson candidates in the $\mathrm{b\bar{b}}$ final state, which are reconstructed as a single large-radius jet with two $b$-tagged sub-jets or as a pair of $b$-jets. The search is sensitive to highly boosted Higgs boson candidates by employing a track-based sub-jet reconstruction algorithm with a variable radius size, which adapts to the momentum of the Higgs boson candidate (VR track jets). The ATLAS pp collision data recorded in the years 2015–2017, corresponding to an integrated luminosity of 79.8 $\mathrm{fb}^{-1}$ is analysed by selecting events in four $E_{\mathrm{T}}^{\mathrm{miss}}$ bins. The background estimate of the dominant $\mathrm{t\bar{t}}$, Z + jets and W + jets backgrounds is improved by dedicated control regions. The combined likelihood-based statistical analysis, which is based on the Higgs candidate mass as the primary discriminating variable, probes a simplified model with an extended Higgs sector and a Z′ mediator. As no significant excess over the SM background is observed, exclusion limits on the simplified model are derived, which exclude large regions in the two-dimensional $m_{Z'}$-$m_{\mathrm{A}}$ plane for the fixed set of parameters $g_{Z'} = 0.8$, $\tan\beta = 1$, $m_\chi = 100$ GeV, and $m_{\mathrm{H}} = m_{\mathrm{H}^\pm} = 300$ GeV with $m_{Z'}$ of up to 2.85 TeV and $m_{\mathrm{A}}$ up to 670 GeV. The model, which is already strongly constrained by dijet searches, is chosen as a benchmark to compare the performance of the novel VR track technique to a previous iteration of the search. For configurations with $m_{Z'} > 2.5$ TeV, which correspond to event topologies with highly boosted Higgs candidates, the performance is improved up to a factor of 3, thereby establishing the advantage of VR track jets in future boosted resonances searches.

The $\boldsymbol{E_{\mathrm{T}}^{\mathrm{miss}} + s(\mathrm{b\bar{b}})}$ **search** investigates signatures with a hypothetical dark Higgs boson decaying to $b$-quarks. As the final state of $E_{\mathrm{T}}^{\mathrm{miss}}$ and $b$-jets is shared with the $E_{\mathrm{T}}^{\mathrm{miss}} + \mathrm{h}(\mathrm{b\bar{b}})$ search, the latter is reinterpreted using the RECAST framework to place limits on a simplified model with a spin-1 Z′ boson mediator and a spin-0 dark Higgs boson mediator. The RECAST framework enables faithful and automated reinterpretations by preserving not only the observed data and the background model of the original search but also the analysis software and the full analysis workflow. The reinterpretation places stringent limits on the model under consideration for the fixed choice of parameters $m_\chi = 200$ GeV, $g_q = 0.25$, and $g_\chi = 1.0$ by excluding the configurations compatible with relic density measurements in the region $50\,\mathrm{GeV} < m_s < 150\,\mathrm{GeV}$. The search demonstrates the feasibility of

RECAST-based reinterpretations, which are of paramount importance for exploiting the full potential of searches given the increasing number of models being proposed. RECAST is becoming an integral part in the preservation efforts of full Run-2 ATLAS searches.

The $\boldsymbol{E_{\mathrm{T}}^{\mathrm{miss}} + s(VV)}$ **search** investigates signatures with a hypothetical dark Higgs boson decaying to pairs of weak vector boson in their hadronic decay mode. The novel Track-Assisted-Reclustering (TAR) jet algorithm is employed to reconstruct the collimated $s(VV)$ system, using small-radius jets augmented with precision tracking information to form TAR jets with jet substructure resolution superior to conventional jet reconstruction techniques. The dark Higgs boson candidate is reconstructed either as a single TAR jet or as a TAR jet supplemented with one or two small-radius jets in event topologies with less boosted dark Higgs boson candidates. The search is based on the full Run-2 ATLAS pp collision data recorded in the years 2015–2018, corresponding to an integrated luminosity of $139\,\mathrm{fb}^{-1}$. Again, control regions improve the MC-based background estimate of the dominant background processes Z + jets and W + jets production. The statistical analysis is performed using the dark Higgs candidate mass as the discriminating variable in three categories, which are based on the event topology and $E_{\mathrm{T}}^{\mathrm{miss}}$. The simplified model with two mediators which is also probed by the $E_{\mathrm{T}}^{\mathrm{miss}} + s(\mathrm{b\bar{b}})$ search is considered for the interpretation of the results, focusing on dark Higgs masses $m_s > 160\,\mathrm{GeV}$ where decays to weak vector boson pairs become relevant. A mild localised excess in data is observed, which corresponds to a local significance of $2.3\sigma$ for the dark Higgs boson hypothesis with $m_s = 160\,\mathrm{GeV}$ and a global significance of $1.3\sigma$ when considering the nine independent $m_s$ hypotheses under consideration. As no large deviations from the SM background are observed, limits for the fixed choice of parameters $m_\chi = 200\,\mathrm{GeV}$, $g_q = 0.25$, and $g_\chi = 1.0$ are computed in the $m_{\mathrm{Z}'}$-$m_s$ plane. Signal configurations with $m_{\mathrm{Z}'}$ of up to $1.8\,\mathrm{TeV}$ and $m_s$ in the range $170\,\mathrm{GeV}$ to $230\,\mathrm{GeV}$ are excluded at $95\,\%$ $\mathrm{CL}_s$.

Although no significant evidence of dark matter production was observed in these searches, these null results fit in the larger **puzzle of dark matter**, whose pieces are unveiled by the combined efforts of experiments probing its microscopic and macroscopic interactions and by theorists exploring the viable models of dark matter. The searches for dark matter at particle colliders — windows on the microscopic interactions of dark matter – are an integral part of solving the dark matter puzzle. The ATLAS detector will continue to collect pp collision data in the upcoming LHC runs over the next decade, eventually increasing the size of the dataset by order of magnitude. The novel reconstruction techniques employed in the searches presented in this dissertation improve the sensitivity to boosted resonances in dense environments and enable the exploration of yet uncovered signatures. As the increasingly involved reconstruction techniques render these searches more complex and challenging, an automated framework enabling faithful reinterpretations like RECAST is required to exploit the dataset sustainably and fully. The search for dark matter is still ongoing, leaving the scientific community in shared wonder about the true nature of dark matter. May the results of this work benefit future searches for new phenomena and testify the joy of curious enquiry.

# Bibliography


[1] M. G. Aartsen, R. Abbasi, Y. Abdou, et al. “Search for Dark Matter Annihilations in the Sun with the 79-String IceCube Detector”. In: *Physical Review Letters* 110.13 (Mar. 2013).

[2] B. Abbott, J. Albert, F. Alberti, et al. “Production and integration of the ATLAS Insertable B-Layer”. In: *Journal of Instrumentation* 13.05 (May 2018), T05008–T05008.

[3] Jalal Abdallah, Henrique Araujo, Alexandre Arbey, et al. “Simplified models for dark matter searches at the LHC”. In: *Physics of the Dark Universe* 9-10 (Sept. 2015), pp. 8–23.

[4] A. H. Abdelhameed, G. Angloher, P. Bauer, et al. “First results from the CRESST-III low-mass dark matter program”. In: *Physical Review D* 100.10 (Nov. 2019).

[5] Hanadi M. AbdelSalam, Prasenjit Saha, and Liliya L. R. Williams. “Nonparametric Reconstruction of Abell 2218 from Combined Weak and Strong Lensing”. In: *The Astronomical Journal* 116.4 (Oct. 1998), pp. 1541–1552.

[6] Tomohiro Abe, Yoav Afik, Andreas Albert, et al. “LHC Dark Matter Working Group: Next-generation spin-0 dark matter models”. In: *Physics of the Dark Universe* 27 (Jan. 2020), p. 100351.

[7] Daniel Abercrombie, Nural Akchurin, Ece Akilli, et al. “Dark Matter benchmark models for early LHC Run-2 Searches: Report of the ATLAS/CMS Dark Matter Forum”. In: *Physics of the Dark Universe* (Sept. 2019), p. 100371.

[8] A.U. Abeysekara, A. Albert, R. Alfaro, et al. “A search for dark matter in the Galactic halo with HAWC”. In: *Journal of Cosmology and Astroparticle Physics* 2018.02 (Feb. 2018), pp. 049–049.

[9] “Account of the Discovery of the Planet of Le Verrier at Berlin”. In: *Monthly Notices of the Royal Astronomical Society* 7.9 (Nov. 1846), pp. 153–153.

[10] O. Adriani, G. C. Barbarino, G. A. Bazilevskaya, et al. “An anomalous positron abundance in cosmic rays with energies 1.5–100 GeV”. In: *Nature* 458.7238 (Apr. 2009), pp. 607–609.

[11] P. Agnes, I. F. M. Albuquerque, T. Alexander, et al. “DarkSide-50 532-day dark matter search with low-radioactivity argon”. In: *Physical Review D* 98.10 (Nov. 2018).

[12] R. Agnese, T. Aralis, T. Aramaki, et al. “Search for low-mass dark matter with CDMSlite using a profile likelihood fit”. In: *Physical Review D* 99.6 (Mar. 2019).

[13]R. Agnese, T. Aramaki, I. J. Arnquist, et al. “Results from the Super Cryogenic Dark Matter Search Experiment at Soudan”. In: *Physical Review Letters* 120.6 (Feb. 2018).

[14]S. Agostinelli et al. “GEANT4 – a simulation toolkit”. In: *Nucl. Instrum. Meth. A* 506 (2003), p. 250.

[15]M. Aguilar, G. Alberti, B. Alpat, et al. “First Result from the Alpha Magnetic Spectrometer on the International Space Station: Precision Measurement of the Positron Fraction in Primary Cosmic Rays of 0.5–350 GeV”. In: *Physical Review Letters* 110.14 (Apr. 2013).

[16]F. Aharonian, A. G. Akhperjanian, A. R. Bazer-Bachi, et al. “HESS Observations of the Galactic Center Region and Their Possible Dark Matter Interpretation”. In: *Physical Review Letters* 97.22 (Nov. 2006).

[17]M. Aker, K. Altenmüller, M. Arenz, et al. “Improved Upper Limit on the Neutrino Mass from a Direct Kinematic Method by KATRIN”. In: *Physical Review Letters* 123.22 (Nov. 2019).

[18]D.S. Akerib, X. Bai, S. Bedikian, et al. “The Large Underground Xenon (LUX) experiment”. In: *Nuclear Instruments and Methods in Physics Research Section A: Accelerators, Spectrometers, Detectors and Associated Equipment* 704 (Mar. 2013), pp. 111–126.

[19]Andreas Albert, Mihailo Backović, Antonio Boveia, et al. “Recommendations of the LHC Dark Matter Working Group: Comparing LHC searches for dark matter mediators in visible and invisible decay channels and calculations of the thermal relic density”. In: *Physics of the Dark Universe* 26 (2019), p. 100377.

[20]J. Aleksić, S. Ansoldi, L.A. Antonelli, et al. “The major upgrade of the MAGIC telescopes, Part I: The hardware improvements and the commissioning of the system”. In: *Astroparticle Physics* 72 (Jan. 2016), pp. 61–75.

[21]Simone Alioli, Paolo Nason, Carlo Oleari, and Emanuele Re. “A general framework for implementing NLO calculations in shower Monte Carlo programs: the POWHEG BOX”. In: *JHEP* 06 (2010), p. 043. arXiv: 1002.2581 [hep-ph].

[22]G. Altarelli and G. Parisi. “Asymptotic freedom in parton language”. In: *Nuclear Physics B* 126.2 (Aug. 1977), pp. 298–318.

[23]J. Alwall, R. Frederix, S. Frixione, et al. “The automated computation of tree-level and next-to-leading order differential cross sections, and their matching to parton shower simulations”. In: *JHEP* 07 (2014), p. 079. arXiv: 1405.0301 [hep-ph].

[24]P.-A. Amaudruz, M. Baldwin, M. Batygov, et al. “First Results from the DEAP-3600 Dark Matter Search with Argon at SNOLAB”. In: *Physical Review Letters* 121.7 (Aug. 2018).

[25]Federico Ambrogi, Chiara Arina, Mihailo Backović, et al. “MadDM v.3.0: A comprehensive tool for dark matter studies”. In: *Physics of the Dark Universe* 24 (Mar. 2019), p. 100249.

[26] Paul Philipp Gadow and. "Search for dark matter produced in association with a hadronically decaying Z' vector boson with the ATLAS detector at the LHC". In: *Proceedings of Sixth Annual Conference on Large Hadron Collider Physics — PoS(LHCP2018)*. Sissa Medialab, Sept. 2018.

[27] B. Andersson, G. Gustafson, G. Ingelman, and T. Sjöstrand. "Parton fragmentation and string dynamics". In: *Physics Reports* 97.2-3 (July 1983), pp. 31–145.

[28] E. Aprile, J. Aalbers, F. Agostini, et al. "The XENON1T dark matter experiment". In: *The European Physical Journal C* 77.12 (Dec. 2017).

[29] S. Archambault, A. Archer, W. Benbow, et al. "Dark matter constraints from a joint analysis of dwarf Spheroidal galaxy observations with VERITAS". In: *Physical Review D* 95.8 (Apr. 2017).

[30] Akitaka Ariga, Tomoko Ariga, Jamie Boyd, et al. *TECHNICAL PROPOSAL: FASER, THE FORWARD SEARCH EXPERIMENT AT THE LHC*. Tech. rep. arXiv:1812.09139. LHCC-P-013. 82 pages, 62 figures; submitted to the CERN LHCC on 7 November 2018. Geneva: CERN, Dec. 2018.

[31] G. Arnison, A. Astbury, B. Aubert, et al. "Experimental observation of isolated large transverse energy electrons with associated missing energy at $\sqrt{s}$=540 GeV". In: *Physics Letters B* 122.1 (Feb. 1983), pp. 103–116.

[32] G. Arnison, A. Astbury, B. Aubert, et al. "Experimental observation of lepton pairs of invariant mass around 95 GeV/c$^2$ at the CERN SPS collider". In: *Physics Letters B* 126.5 (July 1983), pp. 398–410.

[33] Pierre Artoisenet, Rikkert Frederix, Olivier Mattelaer, and Robbert Rietkerk. "Automatic spin-entangled decays of heavy resonances in Monte Carlo simulations". In: *JHEP* 03 (2013), p. 015. arXiv: 1212.3460 [hep-ph].

[34] ATLAS Collaboration. *$E_T^{miss}$ performance in the ATLAS detector using 2015–2016 LHC $pp$ collisions*. ATLAS-CONF-2018-023. 2018.

[35] ATLAS Collaboration. "ATLAS $b$-jet identification performance and efficiency measurement with $t\bar{t}$ events in $pp$ collisions at $\sqrt{s} = 13$ TeV". In: *Eur. Phys. J. C* 79 (2019), p. 970. arXiv: 1907.05120 [hep-ex].

[36] ATLAS Collaboration. "ATLAS data quality operations and performance for 2015–2018 data-taking". In: *JINST* 15 (2020), P04003. arXiv: 1911.04632 [physics.ins-det].

[37] ATLAS Collaboration. *ATLAS Pythia 8 tunes to 7 TeV data*. ATL-PHYS-PUB-2014-021. 2014.

[38] ATLAS Collaboration. *ATLAS simulation of boson plus jets processes in Run 2*. ATL-PHYS-PUB-2017-006. 2017.

[39] ATLAS Collaboration. "Combination of Searches for Invisible Higgs Boson Decays with the ATLAS Experiment". In: *Phys. Rev. Lett.* 122 (2019), p. 231801. arXiv: 1904.05105 [hep-ex].

[40] ATLAS Collaboration. "Constraints on mediator-based dark matter and scalar dark energy models using $\sqrt{s} = 13$ TeV $pp$ collision data collected by the ATLAS detector". In: *JHEP* 05 (2019), p. 142. arXiv: 1903.01400 [hep-ex].

[41] ATLAS Collaboration. "Constraints on new phenomena via Higgs boson couplings and invisible decays with the ATLAS detector". In: *JHEP* 11 (2015), p. 206. arXiv: 1509.00672 [hep-ex].

[42] ATLAS Collaboration. "Dark matter interpretations of ATLAS searches for the electroweak production of supersymmetric particles in $\sqrt{s} = 8$ TeV proton–proton collisions". In: *JHEP* 09 (2016), p. 175. arXiv: 1608.00872 [hep-ex].

[43] ATLAS Collaboration. "Determination of jet calibration and energy resolution in proton–proton collisions at $\sqrt{s} = 8$ TeV using the ATLAS detector". In: (2019). arXiv: 1910.04482 [hep-ex].

[44] ATLAS Collaboration. *Early Inner Detector Tracking Performance in the 2015 Data at $\sqrt{s} = 13$ TeV*. ATL-PHYS-PUB-2015-051. 2015.

[45] ATLAS Collaboration. "Electron and photon performance measurements with the ATLAS detector using the 2015–2017 LHC proton–proton collision data". In: *JINST* 14 (2019), P12006. arXiv: 1908.00005 [hep-ex].

[46] ATLAS Collaboration. *Electron and photon reconstruction and performance in ATLAS using a dynamical, topological cell clustering-based approach*. ATL-PHYS-PUB-2017-022. 2017.

[47] ATLAS Collaboration. "Electron reconstruction and identification in the ATLAS experiment using the 2015 and 2016 LHC proton–proton collision data at $\sqrt{s} = 13$ TeV". In: *Eur. Phys. J. C* 79 (2019), p. 639. arXiv: 1902.04655 [hep-ex].

[48] ATLAS Collaboration. "Evidence for the $H \to b\bar{b}$ decay with the ATLAS detector". In: *JHEP* 12 (2017), p. 024. arXiv: 1708.03299 [hep-ex].

[49] ATLAS Collaboration. *Improved electron reconstruction in ATLAS using the Gaussian Sum Filter-based model for bremsstrahlung*. ATLAS-CONF-2012-047. 2012.

[50] ATLAS Collaboration. *Improvements in $t\bar{t}$ modelling using NLO+PS Monte Carlo generators for Run 2*. ATL-PHYS-PUB-2018-009. 2018.

[51] ATLAS Collaboration. "In situ calibration of large-radius jet energy and mass in 13 TeV proton–proton collisions with the ATLAS detector". In: *Eur. Phys. J. C* 79 (2019), p. 135. arXiv: 1807.09477 [hep-ex].

[52] ATLAS Collaboration. "Jet energy measurement and its systematic uncertainty in proton–proton collisions at $\sqrt{s} = 7$ TeV with the ATLAS detector". In: *Eur. Phys. J. C* 75 (2015), p. 17. arXiv: 1406.0076 [hep-ex].

[53] ATLAS Collaboration. "Jet energy measurement with the ATLAS detector in proton–proton collisions at $\sqrt{s} = 7$ TeV". In: *Eur. Phys. J. C* 73 (2013), p. 2304. arXiv: 1112.6426 [hep-ex].

[54] ATLAS Collaboration. "Jet energy scale and resolution measured in proton–proton collisions at $\sqrt{s} = 13,$ TeV with the ATLAS detector". In: (2020). arXiv: 2007.02645 [hep-ex].

[55] ATLAS Collaboration. "Jet energy scale measurements and their systematic uncertainties in proton–proton collisions at $\sqrt{s} = 13$ TeV with the ATLAS detector". In: *Phys. Rev. D* 96 (2017), p. 072002. arXiv: 1703.09665 [hep-ex].

[56] ATLAS Collaboration. *Luminosity determination in $pp$ collisions at $\sqrt{s} = 13$ TeV using the ATLAS detector at the LHC*. ATLAS-CONF-2019-021. 2019.

[57] ATLAS Collaboration. "Luminosity determination in $pp$ collisions at $\sqrt{s} = 8$ TeV using the ATLAS detector at the LHC". In: *Eur. Phys. J. C* 76 (2016), p. 653. arXiv: 1608.03953 [hep-ex].

[58] ATLAS Collaboration. "Measurement of the $Z/\gamma^*$ boson transverse momentum distribution in $pp$ collisions at $\sqrt{s} = 7$ TeV with the ATLAS detector". In: *JHEP* 09 (2014), p. 145. arXiv: 1406.3660 [hep-ex].

[59] ATLAS Collaboration. "Measurement of the associated production of a Higgs boson decaying into $b$-quarks with a vector boson at high transverse momentum in $pp$ collisions at $\sqrt{s} = 13$ TeV with the ATLAS detector". In: (2020). arXiv: 2008.02508 [hep-ex].

[60] ATLAS Collaboration. "Measurement of the Inelastic Proton–Proton Cross Section at $\sqrt{s} = 13$ TeV with the ATLAS Detector at the LHC". In: *Phys. Rev. Lett.* 117 (2016), p. 182002. arXiv: 1606.02625 [hep-ex].

[61] ATLAS Collaboration. "Measurements of $b$-jet tagging efficiency with the ATLAS detector using $t\bar{t}$ events at $\sqrt{s} = 13$ TeV". In: *JHEP* 08 (2018), p. 089. arXiv: 1805.01845 [hep-ex].

[62] ATLAS Collaboration. *Multi-Boson Simulation for 13 TeV ATLAS Analyses*. ATL-PHYS-PUB-2017-005. 2017.

[63] ATLAS Collaboration. *Muon reconstruction and identification efficiency in ATLAS using the full Run 2 $pp$ collision data set at $\sqrt{s} = 13$ TeV*. ATLAS-CONF-2020-030. 2020.

[64] ATLAS Collaboration. "Muon reconstruction performance of the ATLAS detector in proton–proton collision data at $\sqrt{s} = 13$ TeV". In: *Eur. Phys. J. C* 76 (2016), p. 292. arXiv: 1603.05598 [hep-ex].

[65] ATLAS Collaboration. *Object-based missing transverse momentum significance in the ATLAS Detector*. ATLAS-CONF-2018-038. 2018.

[66] ATLAS Collaboration. "Observation of $H \to b\bar{b}$ decays and $VH$ production with the ATLAS detector". In: *Phys. Lett. B* 786 (2018), p. 59. arXiv: 1808.08238 [hep-ex].

[67] ATLAS Collaboration. "Observation of a new particle in the search for the Standard Model Higgs boson with the ATLAS detector at the LHC". In: *Phys. Lett. B* 716 (2012), p. 1. arXiv: 1207.7214 [hep-ex].

[68] ATLAS Collaboration. *Optimisation and performance studies of the ATLAS $b$-tagging algorithms for the 2017-18 LHC run*. ATL-PHYS-PUB-2017-013. 2017.

[69] ATLAS Collaboration. "Performance of electron and photon triggers in ATLAS during LHC Run 2". In: *Eur. Phys. J. C* 80 (2020), p. 47. arXiv: 1909.00761 [hep-ex].

[70] ATLAS Collaboration. "Performance of jet substructure techniques for large-$R$ jets in proton–proton collisions at $\sqrt{s} = 7$ TeV using the ATLAS detector". In: *JHEP* 09 (2013), p. 076. arXiv: 1306.4945 [hep-ex].

[71] ATLAS Collaboration. *Performance of the ATLAS Inner Detector Track and Vertex Reconstruction in High Pile-Up LHC Environment*. ATLAS-CONF-2012-042. 2012.

[72] ATLAS Collaboration. *Performance of the ATLAS muon trigger in 2011*. ATLAS-CONF-2012-099. 2012.

[73] ATLAS Collaboration. "Performance of the ATLAS muon triggers in Run 2". In: (2020). arXiv: 2004.13447 [hep-ex].

[74] ATLAS Collaboration. "Performance of the ATLAS track reconstruction algorithms in dense environments in LHC Run 2". In: *Eur. Phys. J. C* 77 (2017), p. 673. arXiv: 1704.07983 [hep-ex].

[75] ATLAS Collaboration. "Performance of the missing transverse momentum triggers for the ATLAS detector during Run-2 data taking". In: *JHEP* 08 (2020), p. 80. arXiv: 2005.09554 [hep-ex].

[76] ATLAS Collaboration. *RECAST framework reinterpretation of an ATLAS Dark Matter Search constraining a model of a dark Higgs boson decaying to two $b$-quarks*. ATL-PHYS-PUB-2019-032. 2019.

[77] ATLAS Collaboration. *Reinterpretation of searches for supersymmetry in models with variable $R$-parity-violating coupling strength and long-lived $R$-hadrons*. ATLAS-CONF-2018-003. 2018.

[78] ATLAS Collaboration. *Reinterpretation of the ATLAS Search for Displaced Hadronic Jets with the RECAST Framework*. ATL-PHYS-PUB-2020-007. 2020.

[79] ATLAS Collaboration. "Search for $t\bar{t}$ resonances in fully hadronic final states in $pp$ collisions at $\sqrt{s} = 13$ TeV with the ATLAS detector". In: (2020). arXiv: 2005.05138 [hep-ex].

[80] ATLAS Collaboration. "Search for an invisibly decaying Higgs boson or dark matter candidates produced in association with a $Z$ boson in $pp$ collisions at $\sqrt{s} = 13$ TeV with the ATLAS detector". In: *Phys. Lett. B* 776 (2018), p. 318. arXiv: 1708.09624 [hep-ex].

[81] ATLAS Collaboration. *Search for boosted resonances decaying to two $b$-quarks and produced in association with a jet at $\sqrt{s} = 13$ TeV with the ATLAS detector*. ATLAS-CONF-2018-052. 2018.

[82] ATLAS Collaboration. "Search for dark matter and other new phenomena in events with an energetic jet and large missing transverse momentum using the ATLAS detector". In: *JHEP* 01 (2018), p. 126. arXiv: 1711.03301 [hep-ex].

[83] ATLAS Collaboration. *Search for dark matter associated production with a single top quark in $\sqrt{s} = 13$ TeV $pp$ collisions with the ATLAS detector*. ATLAS-CONF-2020-034. 2020.

[84] ATLAS Collaboration. "Search for dark matter at $\sqrt{s} = 13$ TeV in final states containing an energetic photon and large missing transverse momentum with the ATLAS detector". In: *Eur. Phys. J. C* 77 (2017), p. 393. arXiv: 1704.03848 [hep-ex].

[85] ATLAS Collaboration. "Search for dark matter in association with a Higgs boson decaying to $b$-quarks in $pp$ collisions at $\sqrt{s} = 13$ TeV with the ATLAS detector". In: *Phys. Lett. B* 765 (2017), p. 11. arXiv: 1609.04572 [hep-ex].

[86] ATLAS Collaboration. "Search for dark matter in association with a Higgs boson decaying to two photons at $\sqrt{s} = 13$ TeV with the ATLAS detector". In: *Phys. Rev. D* 96 (2017), p. 112004. arXiv: 1706.03948 [hep-ex].

[87] ATLAS Collaboration. "Search for dark matter in events with a hadronically decaying $W$ or $Z$ boson and missing transverse momentum in $pp$ collisions at $\sqrt{s} = 8$ TeV with the ATLAS detector". In: *Phys. Rev. Lett.* 112 (2014), p. 041802. arXiv: 1309.4017 [hep-ex].

[88] ATLAS Collaboration. "Search for dark matter in events with a hadronically decaying vector boson and missing transverse momentum in $pp$ collisions at $\sqrt{s} = 13$ TeV with the ATLAS detector". In: *JHEP* 10 (2018), p. 180. arXiv: 1807.11471 [hep-ex].

[89] ATLAS Collaboration. *Search for dark matter produced in association with a dark Higgs boson decaying to $W^{\pm}W^{\mp}$ or $ZZ$ in fully hadronic final states using $pp$ collisions at $\sqrt{s} = 13$ TeV recorded with the ATLAS detector*. ATLAS-CONF-2020-036. 2020.

[90] ATLAS Collaboration. "Search for dark matter produced in association with a hadronically decaying vector boson in $pp$ collisions at $\sqrt{s} = 13$ TeV with the ATLAS detector". In: *Phys. Lett. B* 763 (2016), p. 251. arXiv: 1608.02372 [hep-ex].

[91] ATLAS Collaboration. *Search for Dark Matter Produced in Association with a Higgs Boson decaying to $b\bar{b}$ at $\sqrt{s} = 13$ TeV with the ATLAS Detector using $79.8$ fb$^{-1}$ of proton–proton collision data*. ATLAS-CONF-2018-039. 2018.

[92] ATLAS Collaboration. "Search for Dark Matter Produced in Association with a Higgs Boson Decaying to $b\bar{b}$ using $36$ fb$^{-1}$ of $pp$ collisions at $\sqrt{s} = 13$ TeV with the ATLAS Detector". In: *Phys. Rev. Lett.* 119 (2017), p. 181804. arXiv: 1707.01302 [hep-ex].

[93] ATLAS Collaboration. "Search for dark matter produced in association with a Higgs boson decaying to two bottom quarks in $pp$ collisions at $\sqrt{s} = 8$ TeV with the ATLAS detector". In: *Phys. Rev. D* 93 (2016), p. 072007. arXiv: 1510.06218 [hep-ex].

[94] ATLAS Collaboration. "Search for dark matter produced in association with bottom or top quarks in $\sqrt{s} = 13$ TeV $pp$ collisions with the ATLAS detector". In: *Eur. Phys. J. C* 78 (2018), p. 18. arXiv: 1710.11412 [hep-ex].

[95] ATLAS Collaboration. *Search for heavy resonances decaying into a $Z$ boson and a Higgs boson in final states with leptons and $b$-jets in $139$ fb$^{-1}$ of $pp$ collisions at $\sqrt{s} = 13$ TeV with the ATLAS detector*. ATLAS-CONF-2020-043. 2020.

[96] ATLAS Collaboration. "Search for high-mass dilepton resonances using $139\,\text{fb}^{-1}$ of $pp$ collision data collected at $\sqrt{s} = 13\,\text{TeV}$ with the ATLAS detector". In: *Phys. Lett. B* 796 (2019), p. 68. arXiv: 1903.06248 [hep-ex].

[97] ATLAS Collaboration. "Search for Low-Mass Dijet Resonances Using Trigger-Level Jets with the ATLAS Detector in $pp$ Collisions at $\sqrt{s} = 13\,\text{TeV}$". In: *Phys. Rev. Lett.* 121 (2018), p. 081801. arXiv: 1804.03496 [hep-ex].

[98] ATLAS Collaboration. "Search for low-mass resonances decaying into two jets and produced in association with a photon using $pp$ collisions at $\sqrt{s} = 13\,\text{TeV}$ with the ATLAS detector". In: *Phys. Lett. B* 795 (2019), p. 56. arXiv: 1901.10917 [hep-ex].

[99] ATLAS Collaboration. "Search for new resonances in mass distributions of jet pairs using $139\,\text{fb}^{-1}$ of $pp$ collisions at $\sqrt{s} = 13\,\text{TeV}$ with the ATLAS detector". In: *JHEP* 03 (2019), p. 145. arXiv: 1910.08447 [hep-ex].

[100] ATLAS Collaboration. *Secondary vertex finding for jet flavour identification with the ATLAS detector*. ATL-PHYS-PUB-2017-011. 2017.

[101] ATLAS Collaboration. *Selection of jets produced in 13 TeV proton–proton collisions with the ATLAS detector*. ATLAS-CONF-2015-029. 2015.

[102] ATLAS Collaboration. *Standard Model Summary Plots Spring 2020*. ATL-PHYS-PUB-2020-010. 2020.

[103] ATLAS Collaboration. "Summary of the ATLAS experiment's sensitivity to supersymmetry after LHC Run 1 — interpreted in the phenomenological MSSM". In: *JHEP* 10 (2015), p. 134. arXiv: 1508.06608 [hep-ex].

[104] ATLAS Collaboration. "The ATLAS Simulation Infrastructure". In: *Eur. Phys. J. C* 70 (2010), p. 823. arXiv: 1005.4568 [physics.ins-det].

[105] ATLAS Collaboration. *The Pythia 8 A3 tune description of ATLAS minimum bias and inelastic measurements incorporating the Donnachie–Landshoff diffractive model*. ATL-PHYS-PUB-2016-017. 2016.

[106] ATLAS Collaboration. *The simulation principle and performance of the ATLAS fast calorimeter simulation FastCaloSim*. ATL-PHYS-PUB-2010-013. 2010.

[107] ATLAS Collaboration. *Topological $b$-hadron decay reconstruction and identification of $b$-jets with the JetFitter package in the ATLAS experiment at the LHC*. ATL-PHYS-PUB-2018-025. 2018.

[108] ATLAS Collaboration. "Topological cell clustering in the ATLAS calorimeters and its performance in LHC Run 1". In: *Eur. Phys. J. C* 77 (2017), p. 490. arXiv: 1603.02934 [hep-ex].

[109] ATLAS Collaboration. *Track assisted techniques for jet substructure*. ATL-PHYS-PUB-2018-012. 2018.

[110] ATLAS Collaboration. *Variable Radius, Exclusive-$k_T$, and Center-of-Mass Subjet Reconstruction for Higgs($\to b\bar{b}$) Tagging in ATLAS*. ATL-PHYS-PUB-2017-010. 2017.

[111]*ATLAS Insertable B-Layer Technical Design Report Addendum*. Tech. rep. CERN-LHCC-2012-009. ATLAS-TDR-19-ADD-1. Addendum to CERN-LHCC-2010-013, ATLAS-TDR-019. May 2012.

[112]*ATLAS level-1 trigger: Technical Design Report*. Technical Design Report ATLAS. Geneva: CERN, 1998.

[113]W. B. Atwood, A. A. Abdo, M. Ackermann, et al. "The Large Area Telescope on the Fermi Gamma-ray Space Telescope mission". In: *The Astrophysical Journal* 697.2 (May 2009), pp. 1071–1102.

[114]Benjamin Audren, Julien Lesgourgues, Gianpiero Mangano, Pasquale Dario Serpico, and Thomas Tram. "Strongest model-independent bound on the lifetime of Dark Matter". In: *Journal of Cosmology and Astroparticle Physics* 2014.12 (Dec. 2014), pp. 028–028.

[115]Mihailo Backović, Michael Krämer, Fabio Maltoni, et al. "Higher-order QCD predictions for dark matter production at the LHC in simplified models with s-channel mediators". In: *The European Physical Journal C* 75.10 (Oct. 2015).

[116]P. Bagnaia, M. Banner, R. Battiston, et al. "Evidence for $Z^0 \to e^+e^-$ at the CERN pp collider". In: *Physics Letters B* 129.1-2 (Sept. 1983), pp. 130–140.

[117]R. Bailey. "An Application for Research: the Large Hadron Collider". In: (Apr. 2014), 565–574. 10 p.

[118]Richard D. Ball et al. "Parton distributions with LHC data". In: *Nucl. Phys. B* 867 (2013), p. 244. arXiv: 1207.1303 [hep-ph].

[119]Richard D. Ball, Valerio Bertone, Stefano Carrazza, et al. "Parton distributions for the LHC run II". In: *Journal of High Energy Physics* 2015.4 (Apr. 2015).

[120]M. Banner, R. Battiston, Ph. Bloch, et al. "Observation of single isolated electrons of high transverse momentum in events with missing transverse energy at the CERN pp collider". In: *Physics Letters B* 122.5-6 (Mar. 1983), pp. 476–485.

[121]Matthias Bartelmann. "Gravitational lensing". In: *Classical and Quantum Gravity* 27.23 (Nov. 2010), p. 233001.

[122]Matthias Bartelmann and Matteo Maturi. "Weak gravitational lensing". In: Dec. 2016. arXiv: 1612.06535 [astro-ph.CO].

[123]Martin Bauer, Ulrich Haisch, and Felix Kahlhoefer. "Simplified dark matter models with two Higgs doublets: I. Pseudoscalar mediators". In: *Journal of High Energy Physics* 2017.5 (May 2017).

[124]Daniel Baumann. *Lecture notes in Cosmology*. June 2018.

[125]Johannes Bellm et al. "Herwig 7.0/Herwig++ 3.0 release note". In: *Eur. Phys. J. C* 76.4 (2016), p. 196. arXiv: 1512.01178 [hep-ph].

[126]M. Benedikt, P. Collier, V. Mertens, J. Poole, and K. Schindl. "LHC Design Report Vol.3: The LHC injector chain". In: (2004).

[127]C. L. Bennett, M. Halpern, G. Hinshaw, et al. “First-Year Wilkinson Microwave Anisotropy Probe (WMAP) Observations: Preliminary Maps and Basic Results”. In: *The Astrophysical Journal Supplement Series* 148.1 (Sept. 2003), pp. 1–27.

[128]Lars Bergström. “Non-baryonic dark matter: observational evidence and detection methods”. In: *Reports on Progress in Physics* 63.5 (Apr. 2000), pp. 793–841.

[129]Asher Berlin, Tongyan Lin, and Lian-Tao Wang. “Mono-Higgs detection of dark matter at the LHC”. In: *Journal of High Energy Physics* 2014.6 (June 2014).

[130]R. Bernabei et al. “First model independent results from DAMA/LIBRA-phase2”. In: *Nucl. Phys. Atom. Energy* 19.4 (2018), pp. 307–325. arXiv: 1805.10486 [hep-ex].

[131]D. Bernstein. “Containers and Cloud: From LXC to Docker to Kubernetes”. In: *IEEE Cloud Computing* 1.03 (Sept. 2014), pp. 81–84.

[132]Daniele Bertolini, Tucker Chan, and Jesse Thaler. “Jet observables without jet algorithms”. In: *Journal of High Energy Physics* 2014.4 (Apr. 2014).

[133]Gianfranco Bertone and Dan Hooper. “History of dark matter”. In: *Reviews of Modern Physics* 90.4 (Oct. 2018), p. 045002.

[134]Gianfranco Bertone, Dan Hooper, and Joseph Silk. “Particle dark matter: evidence, candidates and constraints”. In: *Physics Reports* 405.5 (2005), pp. 279–390.

[135]Andreas Birkedal, Andrew Noble, Maxim Perelstein, and Andrew Spray. “Little Higgs dark matter”. In: *Physical Review D* 74.3 (Aug. 2006).

[136]George R. Blumenthal, S. M. Faber, Joel R. Primack, and Martin J. Rees. “Formation of galaxies and large-scale structure with cold dark matter”. In: *Nature* 311.5986 (Oct. 1984), pp. 517–525.

[137]Wim de Boer, Léo Bosse, Iris Gebauer, Alexander Neumann, and Peter L. Biermann. “Molecular clouds as origin of the Fermi gamma-ray GeV excess”. In: *Physical Review D* 96.4 (Aug. 2017).

[138]Enrico Bothmann, Gurpreet Singh Chahal, Stefan Höche, et al. “Event generation with Sherpa 2.2”. In: *SciPost Physics* 7.3 (Sept. 2019).

[139]S Boutle, D Casper, B Hooberman, et al. “Primary vertex reconstruction at the ATLAS experiment”. In: *Journal of Physics: Conference Series* 898 (Oct. 2017), p. 042056.

[140]A. Boyarsky, M. Drewes, T. Lasserre, S. Mertens, and O. Ruchayskiy. “Sterile neutrino Dark Matter”. In: *Progress in Particle and Nuclear Physics* 104 (Jan. 2019), pp. 1–45.

[141]G.C. Branco, P.M. Ferreira, L. Lavoura, et al. “Theory and phenomenology of two-Higgs-doublet models”. In: *Physics Reports* 516.1-2 (July 2012), pp. 1–102.

[142]O. Bruning, P. Collier, P. Lebrun, et al. “LHC Design Report Vol.2: The LHC infrastructure and general services”. In: (2004).

[143]Oliver S. Bruning, P. Collier, P. Lebrun, et al. “LHC Design Report Vol.1: The LHC Main Ring”. In: (2004).

[144]Oliver Buchmueller, Caterina Doglioni, and Lian-Tao Wang. “Search for dark matter at colliders”. In: *Nature Physics* 13.3 (Mar. 2017), pp. 217–223.

[145]Andy Buckley, Jonathan Butterworth, Stefan Gieseke, et al. “General-purpose event generators for LHC physics”. In: *Physics Reports* 504.5 (July 2011), pp. 145–233.

[146]Andy Buckley, James Ferrando, Stephen Lloyd, et al. “LHAPDF6: parton density access in the LHC precision era”. In: *The European Physical Journal C* 75.3 (Mar. 2015).

[147]E. M. Burbidge, G. R. Burbidge, D. J. Crampin, V. C. Rubin, and K. H. Prendergast. “The rotation and mass of NGC 6503”. In: *Astrophys. J.* 139 (1964), pp. 539–544.

[148]Jon Butterworth et al. “PDF4LHC recommendations for LHC Run II”. In: *J. Phys. G* 43 (2016), p. 023001. arXiv: 1510.03865 [hep-ph].

[149]Jon Butterworth, Stefano Carrazza, Amanda Cooper-Sarkar, et al. “PDF4LHC recommendations for LHC Run II”. In: *Journal of Physics G: Nuclear and Particle Physics* 43.2 (Jan. 2016), p. 023001.

[150]Jonathan M. Butterworth, Adam R. Davison, Mathieu Rubin, and Gavin P. Salam. “Jet Substructure as a New Higgs-Search Channel at the Large Hadron Collider”. In: *Physical Review Letters* 100.24 (June 2008).

[151]Nicola Cabibbo. “Unitary Symmetry and Leptonic Decays”. In: *Physical Review Letters* 10.12 (June 1963), pp. 531–533.

[152]Matteo Cacciari, Gavin P. Salam, and Gregory Soyez. “FastJet user manual”. In: *The European Physical Journal C* 72.3 (Mar. 2012).

[153]Matteo Cacciari, Gavin P Salam, and Gregory Soyez. “The anti-ktjet clustering algorithm”. In: *Journal of High Energy Physics* 2008.04 (Apr. 2008), pp. 063–063.

[154]Matteo Cacciari, Gavin P Salam, and Gregory Soyez. “The catchment area of jets”. In: *Journal of High Energy Physics* 2008.04 (Apr. 2008), pp. 005–005.

[155]John Campbell, Joey Huston, and Frank Krauss. *The Black Book of Quantum Chromodynamics*. Oxford University Press, Mar. 2018.

[156]M Capeans, G Darbo, K Einsweiller, et al. *ATLAS Insertable B-Layer Technical Design Report*. Tech. rep. CERN-LHCC-2010-013. ATLAS-TDR-19. Sept. 2010.

[157]Fabio Cascioli, Philipp Maierhöfer, and Stefano Pozzorini. “Scattering Amplitudes with Open Loops”. In: *Phys. Rev. Lett.* 108 (2012), p. 111601. arXiv: 1111.5206 [hep-ph].

[158]S. Catani, Yu.L. Dokshitzer, M.H. Seymour, and B.R. Webber. “Longitudinally-invariant k⊥-clustering algorithms for hadron-hadron collisions”. In: *Nuclear Physics B* 406.1-2 (Sept. 1993), pp. 187–224.

[159]CERN. *CERN Yellow Reports: Monographs, Vol 2 (2017): Handbook of LHC Higgs cross sections: 4. Deciphering the nature of the Higgs sector*. en. 2017.

[160]Hsin-Chia Cheng, Jonathan L. Feng, and Konstantin T. Matchev. “Kaluza-Klein Dark Matter”. In: *Physical Review Letters* 89.21 (Oct. 2002).

[161]G. M. Clemence. “The Relativity Effect in Planetary Motions”. In: *Reviews of Modern Physics* 19.4 (Oct. 1947), pp. 361–364.

[162]Douglas Clowe, Maruša Bradač, Anthony H. Gonzalez, et al. “A Direct Empirical Proof of the Existence of Dark Matter”. In: *The Astrophysical Journal* 648.2 (Aug. 2006), pp. L109–L113.

[163]CMS Collaboration. “Observation of a new boson at a mass of 125 GeV with the CMS experiment at the LHC”. In: *Phys. Lett. B* 716 (2012), p. 30. arXiv: 1207.7235 [hep-ex].

[164]CMS Collaboration. “Search for associated production of dark matter with a Higgs boson decaying to $b\bar{b}$ or $\gamma\gamma$ at $\sqrt{s} = 13\,\text{TeV}$”. In: *JHEP* 10 (2017), p. 180. arXiv: 1703.05236 [hep-ex].

[165]CMS Collaboration. “Search for dark matter in events with energetic, hadronically decaying top quarks and missing transverse momentum at $\sqrt{s} = 13\,\text{TeV}$”. In: *JHEP* 06 (2018), p. 027. arXiv: 1801.08427 [hep-ex].

[166]CMS Collaboration. “Search for dark matter in proton–proton collisions at $8\,\text{TeV}$ with missing transverse momentum and vector boson tagged jets”. In: *JHEP* 12 (2016), p. 083. arXiv: 1607.05764 [hep-ex].

[167]CMS Collaboration. “Search for dark matter particles produced in association with a Higgs boson in proton–proton collisions at $\sqrt{s} = 13\,\text{TeV}$”. In: (2019). arXiv: 1908.01713 [hep-ex].

[168]CMS Collaboration. “Search for Dark Matter Particles Produced in Association with a Top Quark Pair at $\sqrt{s} = 13\,\text{TeV}$”. In: *Phys. Rev. Lett.* 122 (2019), p. 011803. arXiv: 1807.06522 [hep-ex].

[169]CMS Collaboration. “Search for dark matter produced in association with a Higgs boson decaying to $\gamma\gamma$ or $\tau^+\tau^-$ at $\sqrt{s} = 13\,\text{TeV}$”. In: *JHEP* 09 (2018), p. 046. arXiv: 1806.04771 [hep-ex].

[170]CMS Collaboration. “Search for dark matter produced in association with a Higgs boson decaying to a pair of bottom quarks in proton–proton collisions at $\sqrt{s} = 13\,\text{TeV}$”. In: *Eur. Phys. J. C* 79 (2019), p. 280. arXiv: 1811.06562 [hep-ex].

[171]CMS Collaboration. “Search for dark matter produced in association with a single top quark or a top quark pair in proton–proton collisions at $\sqrt{s} = 13\,\text{TeV}$”. In: *JHEP* 03 (2019), p. 141. arXiv: 1901.01553 [hep-ex].

[172]CMS Collaboration. “Search for dark matter produced with an energetic jet or a hadronically decaying $W$ or $Z$ boson at $\sqrt{s} = 13\,\text{TeV}$”. In: *JHEP* 07 (2017), p. 014. arXiv: 1703.01651 [hep-ex].

[173]CMS Collaboration. “Search for dijet resonances in proton–proton collisions at $\sqrt{s} = 13\,\text{TeV}$ and constraints on dark matter and other models”. In: *Phys. Lett. B* 769 (2017), p. 520. arXiv: 1611.03568 [hep-ex].

[174]CMS Collaboration. “Search for narrow and broad dijet resonances in proton–proton collisions at $\sqrt{s} = 13\,\text{TeV}$ and constraints on dark matter mediators and other new particles”. In: *JHEP* 08 (2018), p. 130. arXiv: 1806.00843 [hep-ex].

[175] CMS Collaboration. "Search for new physics in final states with an energetic jet or a hadronically decaying $W$ or $Z$ boson and transverse momentum imbalance at $\sqrt{s} = 13\,\text{TeV}$". In: *Phys. Rev. D* 97 (2018), p. 092005. arXiv: 1712.02345 [hep-ex].

[176] CMS Collaboration. "Search for new physics in the monophoton final state in proton–proton collisions at $\sqrt{s} = 13\,\text{TeV}$". In: *JHEP* 10 (2017), p. 073. arXiv: 1706.03794 [hep-ex].

[177] ALICE Collaboration. "The ALICE experiment at the CERN LHC". In: *Journal of Instrumentation* 3.08 (Aug. 2008), S08002–S08002.

[178] ATLAS Collaboration. "The ATLAS Experiment at the CERN Large Hadron Collider". In: *Journal of Instrumentation* 3.08 (Aug. 2008), S08003–S08003.

[179] ATLAS collaboration. *ATLAS Combined Mass resolution and W mass reconstruction performance*. https://atlas.web.cern.ch/Atlas/GROUPS/PHYSICS/PLOTS/JETM-2017-002/. Feb. 2017.

[180] ATLAS collaboration. *Dark matter summary plots*. https://atlas.web.cern.ch/Atlas/GROUPS/PHYSICS/PUBNOTES/ATL-PHYS-PUB-2020-021/. July 2020.

[181] ATLAS collaboration. *Impact Parameter resolutions in di-jet events*. https://atlas.web.cern.ch/Atlas/GROUPS/PHYSICS/PLOTS/IDTR-2018-008/. 2018.

[182] CDF Collaboration. "Observation of Top Quark Production in $\bar{p}p$ Collisions with the Collider Detector at Fermilab". In: *Physical Review Letters* 74.14 (Apr. 1995), pp. 2626–2631.

[183] CMS Collaboration. "The CMS experiment at the CERN LHC". In: *Journal of Instrumentation* 3.08 (Aug. 2008), S08004–S08004.

[184] D0 Collaboration. "Observation of the Top Quark". In: *Physical Review Letters* 74.14 (Apr. 1995), pp. 2632–2637.

[185] KATRIN Collaboration. "First operation of the KATRIN experiment with tritium". In: *The European Physical Journal C* 80.3 (Mar. 2020).

[186] LHCb Collaboration. "Observation of $J/\psi\phi$ Structures Consistent with Exotic States from Amplitude Analysis of $B^+ \to J/\psi\phi K^+$ Decays". In: *Physical Review Letters* 118.2 (Jan. 2017).

[187] LHCb Collaboration. "Observation of $J/\psi p$ Resonances Consistent with Pentaquark States in $\Lambda_b^0 \to J/\psi K^- p$ Decays". In: *Physical Review Letters* 115.7 (Aug. 2015).

[188] LHCb Collaboration. "Observation of structure in the $J/\psi$-pair mass spectrum". In: (June 2020). arXiv: 2006.16957 [hep-ex].

[189] LHCb Collaboration. "The LHCb Detector at the LHC". In: *Journal of Instrumentation* 3.08 (Aug. 2008), S08005–S08005.

[190] LHCf Collaboration. "The LHCf detector at the CERN Large Hadron Collider". In: *Journal of Instrumentation* 3.08 (Aug. 2008), S08006–S08006.

[191] TOTEM Collaboration. "The TOTEM Experiment at the CERN Large Hadron Collider". In: *Journal of Instrumentation* 3.08 (Aug. 2008), S08007–S08007.

[192]John C. Collins, Davison E. Soper, and George Sterman. “FACTORIZATION OF HARD PROCESSES IN QCD”. In: *Perturbative QCD*. WORLD SCIENTIFIC, July 1989, pp. 1–91.

[193]Jan Conrad and Olaf Reimer. “Indirect dark matter searches in gamma and cosmic rays”. In: *Nature Physics* 13.3 (Mar. 2017), pp. 224–231.

[194]T G Cornelissen, N Van Eldik, M Elsing, et al. *Updates of the ATLAS Tracking Event Data Model (Release 13)*. Tech. rep. ATL-SOFT-PUB-2007-003. ATL-COM-SOFT-2007-008. Geneva: CERN, June 2007.

[195]Glen Cowan, Kyle Cranmer, Eilam Gross, and Ofer Vitells. In: *Eur. Phys. J. C* 73 (2013), p. 2501.

[196]Glen Cowan, Kyle Cranmer, Eilam Gross, and Ofer Vitells. “Asymptotic formulae for likelihood-based tests of new physics”. In: *Eur. Phys. J. C* 71 (2011), p. 1554. arXiv: 1007.1727 [physics.data-an]. Erratum: in: *Eur. Phys. J. C* 73 (2013), p. 2501.

[197]Kyle Cranmer and Lukas Heinrich. “Analysis Preservation and Systematic Reinterpretation within the ATLAS experiment”. In: *J. Phys. Conf. Ser.* 1085.4 (2018), p. 042011.

[198]Kyle Cranmer and Lukas Heinrich. “Yadage and Packtivity – analysis preservation using parametrized workflows”. In: *Journal of Physics: Conference Series* 898 (Oct. 2017), p. 102019.

[199]Kyle Cranmer, George Lewis, Lorenzo Moneta, Akira Shibata, and Wouter Verkerke. *HistFactory: A tool for creating statistical models for use with RooFit and RooStats*. Tech. rep. CERN-OPEN-2012-016. New York: New York U., Jan. 2012.

[200]Kyle Cranmer and Itay Yavin. “RECAST — extending the impact of existing analyses”. In: *Journal of High Energy Physics* 2011.4 (Apr. 2011).

[201]Michał Czakon, Paul Fiedler, and Alexander Mitov. “Total Top-Quark Pair-Production Cross Section at Hadron Colliders Through $O(\alpha_S^4)$”. In: *Physical Review Letters* 110.25 (June 2013).

[202]G. D’Ambrosio, G.F. Giudice, G. Isidori, and A. Strumia. “Minimal flavour violation: an effective field theory approach”. In: *Nuclear Physics B* 645.1-2 (Nov. 2002), pp. 155–187.

[203]Mrinal Dasgupta, Alessandro Fregoso, Simone Marzani, and Gavin P. Salam. “Towards an understanding of jet substructure”. In: *Journal of High Energy Physics* 2013.9 (Sept. 2013).

[204]Bryce S. DeWitt. “Quantum Theory of Gravity. I. The Canonical Theory”. In: *Physical Review* 160.5 (Aug. 1967), pp. 1113–1148.

[205]Bryce S. DeWitt. “Quantum Theory of Gravity. II. The Manifestly Covariant Theory”. In: *Physical Review* 162.5 (Oct. 1967), pp. 1195–1239.

[206]Bryce S. DeWitt. “Quantum Theory of Gravity. III. Applications of the Covariant Theory”. In: *Physical Review* 162.5 (Oct. 1967), pp. 1239–1256.

[207] Scott Dodelson and Lawrence M. Widrow. “Sterile neutrinos as dark matter”. In: *Physical Review Letters* 72.1 (Jan. 1994), pp. 17–20.

[208] Yu.L Dokshitzer, G.D Leder, S Moretti, and B.R Webber. “Better jet clustering algorithms”. In: *Journal of High Energy Physics* 1997.08 (Aug. 1997), pp. 001–001.

[209] Yuri L. Dokshitzer. “Calculation of the Structure Functions for Deep Inelastic Scattering and $e^+ e^-$ Annihilation by Perturbation Theory in Quantum Chromodynamics.” In: *Sov. Phys. JETP* 46 (1977), pp. 641–653.

[210] Frédéric A. Dreyer, Lina Necib, Gregory Soyez, and Jesse Thaler. “Recursive Soft Drop”. In: *Journal of High Energy Physics* 2018.6 (June 2018).

[211] Michael Duerr, Alexander Grohsjean, Felix Kahlhoefer, et al. “Hunting the dark Higgs”. In: *Journal of High Energy Physics* 2017.4 (Apr. 2017).

[212] Michael Duerr, Felix Kahlhoefer, Kai Schmidt-Hoberg, Thomas Schwetz, and Stefan Vogl. “How to save the WIMP: global analysis of a dark matter model with two s-channel mediators”. In: *Journal of High Energy Physics* 2016.9 (Sept. 2016).

[213] Pierre Duhem. *The Aim and Structure of Physical Theory*. Princeton: Princeton University Press, 1954.

[214] Sayipjamal Dulat, Tie-Jiun Hou, Jun Gao, et al. “New parton distribution functions from a global analysis of quantum chromodynamics”. In: *Physical Review D* 93.3 (Feb. 2016).

[215] Albert Einstein. “Lens-like action of a star by the deviation of light in the gravitational field”. In: *Science* 84.2188 (1936), pp. 506–507. eprint: `https://science.sciencemag.org/content/84/2188/506.full.pdf`.

[216] Stephen D. Ellis and Davison E. Soper. “Successive combination jet algorithm for hadron collisions”. In: *Physical Review D* 48.7 (Oct. 1993), pp. 3160–3166.

[217] Stephen D. Ellis, Christopher K. Vermilion, and Jonathan R. Walsh. “Recombination algorithms and jet substructure: Pruning as a tool for heavy particle searches”. In: *Physical Review D* 81.9 (May 2010).

[218] F. Englert and R. Brout. “Broken Symmetry and the Mass of Gauge Vector Mesons”. In: *Physical Review Letters* 13.9 (Aug. 1964), pp. 321–323.

[219] Lyndon Evans and Philip Bryant. “LHC Machine”. In: *JINST* 3 (2008), S08001.

[220] Richard Feynman. *Feynman Lectures on Gravitation*. CRC Press, May 2018.

[221] D. J. Fixsen. “The temperature of the cosmic microwave background”. In: *The Astrophysical Journal* 707.2 (Nov. 2009), pp. 916–920.

[222] Patrick J Fox. “TASI Lectures on WIMPs and Supersymmetry”. In: *Proceedings of Theoretical Advanced Study Institute Summer School 2018 "Theory in an Era of Data" — PoS(TASI2018)*. Sissa Medialab, July 2019.

[223] Katherine Freese. “Review of Observational Evidence for Dark Matter in the Universe and in upcoming searches for Dark Stars”. In: *EAS Publ. Ser.* 36 (2009), pp. 113–126. arXiv: `0812.4005 [astro-ph]`.

[224]H. Fritzsch, M. Gell-Mann, and H. Leutwyler. “Advantages of the color octet gluon picture”. In: *Physics Letters B* 47.4 (Nov. 1973), pp. 365–368.

[225]R. Frühwirth. “Application of Kalman filtering to track and vertex fitting”. In: *Nuclear Instruments and Methods in Physics Research Section A: Accelerators, Spectrometers, Detectors and Associated Equipment* 262.2-3 (Dec. 1987), pp. 444–450.

[226]Thomas K. Gaisser, Ralph Engel, and Elisa Resconi. *Cosmic Rays and Particle Physics*. 2nd ed. Cambridge University Press, 2016.

[227]Hans Geiger and Ernest Rutherford. “On the scattering of the $\alpha$-particles by matter”. In: *Proceedings of the Royal Society of London. Series A, Containing Papers of a Mathematical and Physical Character* 81.546 (1908), pp. 174–177.

[228]M. Gell-Mann. “The interpretation of the new particles as displaced charge multiplets”. In: *Il Nuovo Cimento* 4.S2 (Apr. 1956), pp. 848–866.

[229]Sheldon L. Glashow. “Partial-symmetries of weak interactions”. In: *Nuclear Physics* 22.4 (Feb. 1961), pp. 579–588.

[230]T. Gleisberg, S. Höche, F. Krauss, et al. “Event generation with SHERPA 1.1”. In: *JHEP* 02 (2009), p. 007. arXiv: 0811.4622 [hep-ph].

[231]Tanju Gleisberg and Stefan Höche. “Comix, a new matrix element generator”. In: *JHEP* 12 (2008), p. 039. arXiv: 0808.3674 [hep-ph].

[232]M.C. Gonzalez-Garcia and Michele Maltoni. “Phenomenology with massive neutrinos”. In: *Physics Reports* 460.1-3 (Apr. 2008), pp. 1–129.

[233]Peter W. Graham, Igor G. Irastorza, Steven K. Lamoreaux, Axel Lindner, and Karl A. van Bibber. “Experimental Searches for the Axion and Axion-Like Particles”. In: *Annual Review of Nuclear and Particle Science* 65.1 (Oct. 2015), pp. 485–514.

[234]V.N. Gribov and L.N. Lipatov. “Deep inelastic $ep$ scattering in perturbation theory”. In: *Sov. J. Nucl. Phys.* 15 (1972), pp. 438–450.

[235]Kim Griest. “The Search for the Dark Matter: WIMPs and MACHOs”. In: *Annals of the New York Academy of Sciences* 688.1 (June 1993), pp. 390–407.

[236]Kim Griest and Marc Kamionkowski. “Unitarity limits on the mass and radius of dark-matter particles”. In: *Physical Review Letters* 64.6 (Feb. 1990), pp. 615–618.

[237]David J. Gross and Frank Wilczek. “Asymptotically Free Gauge Theories. I”. In: *Physical Review D* 8.10 (Nov. 1973), pp. 3633–3652.

[238]David J. Gross and Frank Wilczek. “Ultraviolet Behavior of Non-Abelian Gauge Theories”. In: *Physical Review Letters* 30.26 (June 1973), pp. 1343–1346.

[239]G. S. Guralnik, C. R. Hagen, and T. W. B. Kibble. “Global Conservation Laws and Massless Particles”. In: *Physical Review Letters* 13.20 (Nov. 1964), pp. 585–587.

[240]F. Halzen and Alan D. Martin. *Quarks and leptons: and introductory course in modern particle physics*. Wiley, 1984.

[241] L. A. Harland-Lang, A. D. Martin, P. Motylinski, and R. S. Thorne. "Parton distributions in the LHC era: MMHT 2014 PDFs". In: *The European Physical Journal C* 75.5 (May 2015).

[242] Carsten Hensel and Kevin Kröninger. "Statistical Methods Commonly Used in High Energy Physics". In: *Data Analysis in High Energy Physics*. John Wiley and Sons, Ltd, 2013. Chap. 10, pp. 329–356. eprint: https://onlinelibrary.wiley.com/doi/pdf/10.1002/9783527653416.ch10.

[243] Thomas Hermann, Mikolaj Misiak, and Matthias Steinhauser. "$\overline{B} \to X_s\gamma$ in the Two Higgs Doublet Model up to next-to-next-to-leading order in QCD". In: *Journal of High Energy Physics* 2012.11 (Nov. 2012).

[244] Carlos Pérez de los Heros. "Status of direct and indirect dark matter searches". In: *2019 European Physical Society Conference on High Energy Physics*. Jan. 2020. arXiv: 2001.06193 [astro-ph.HE].

[245] J.M. Hethey. *GitLab Repository Management*. Packt Publishing, 2013.

[246] P.W. Higgs. "Broken symmetries, massless particles and gauge fields". In: *Physics Letters* 12.2 (Sept. 1964), pp. 132–133.

[247] Peter W. Higgs. "Broken Symmetries and the Masses of Gauge Bosons". In: *Physical Review Letters* 13.16 (Oct. 1964), pp. 508–509.

[248] Peter W. Higgs. "Spontaneous Symmetry Breakdown without Massless Bosons". In: *Physical Review* 145.4 (May 1966), pp. 1156–1163.

[249] Stefan Höche, Frank Krauss, Marek Schönherr, and Frank Siegert. "QCD matrix elements + parton showers. The NLO case". In: *JHEP* 04 (2013), p. 027. arXiv: 1207.5030 [hep-ph].

[250] Henk Hoekstra, H.K.C Yee, and Michael D Gladders. "Current status of weak gravitational lensing". In: *New Astronomy Reviews* 46.12 (2002). An Alternative to Dark Matter: MOND, pp. 767–781.

[251] Christophe Grojean and Maria Spiropulu, eds. *High-energy physics. Proceedings, 17th European School, ESHEP 2009, Bautzen, Germany, June 14-27, 2009*. CERN Yellow Reports: School Proceedings. Geneva: CERN, 2010, pp. 1–44. arXiv: 1012.4643 [hep-ph].

[252] G. 't Hooft and M. Veltman. "Regularization and renormalization of gauge fields". In: *Nuclear Physics B* 44.1 (July 1972), pp. 189–213.

[253] Dan Hooper and Lisa Goodenough. "Dark matter annihilation in the Galactic Center as seen by the Fermi Gamma Ray Space Telescope". In: *Physics Letters B* 697.5 (Mar. 2011), pp. 412–428.

[254] Alejandro Ibarra. "Dark Matter Theory". In: *Nuclear and Particle Physics Proceedings* 267-269 (Oct. 2015), pp. 323–331.

[255] "IX. On the problem of the most efficient tests of statistical hypotheses". In: *Philosophical Transactions of the Royal Society of London. Series A, Containing Papers of a Mathematical or Physical Character* 231.694-706 (Feb. 1933), pp. 289–337.

[256]Neal Jackson. “The Hubble Constant”. In: *Living Reviews in Relativity* 18.1 (Sept. 2015).

[257]Felix Kahlhoefer, Kai Schmidt-Hoberg, Thomas Schwetz, and Stefan Vogl. “Implications of unitarity and gauge invariance for simplified dark matter models”. In: *Journal of High Energy Physics* 2016.2 (Feb. 2016).

[258]Kimmo Kainulainen, Kimmo Tuominen, and Jussi Virkajärvi. “Weakly interacting dark matter particle of a minimal technicolor theory”. In: *Physical Review D* 75.8 (Apr. 2007).

[259]Jacobus Cornelius Kapteyn. “First Attempt at a Theory of the Arrangement and Motion of the Sidereal System”. In: *Astrophysical Journal* 55 (May 1922), p. 302.

[260]Christopher Karwin, Simona Murgia, Tim M. P. Tait, Troy A. Porter, and Philip Tanedo. “Dark matter interpretation of the Fermi-LAT observation toward the Galactic Center”. In: *Physical Review D* 95.10 (May 2017).

[261]Masahiro Kawasaki, Kazunori Kohri, Takeo Moroi, and Yoshitaro Takaesu. “Revisiting big-bang nucleosynthesis constraints on dark-matter annihilation”. In: *Physics Letters B* 751 (Dec. 2015), pp. 246–250.

[262]T. W. B. Kibble. “Symmetry Breaking in Non-Abelian Gauge Theories”. In: *Physical Review* 155.5 (Mar. 1967), pp. 1554–1561.

[263]Nikolaos Kidonakis. “Top Quark Production”. In: *Helmholtz International Summer School on Physics of Heavy Quarks and Hadrons*. 2014, pp. 139–168. arXiv: 1311.0283 [hep-ph].

[264]Makoto Kobayashi and Toshihide Maskawa. “CP-Violation in the Renormalizable Theory of Weak Interaction”. In: *Progress of Theoretical Physics* 49.2 (Feb. 1973), pp. 652–657.

[265]Roman Kogler, Benjamin Nachman, Alexander Schmidt, et al. “Jet substructure at the Large Hadron Collider”. In: *Reviews of Modern Physics* 91.4 (Dec. 2019).

[266]Edward W. Kolb and Michael S. Turner. *The Early Universe*. CRC Press, 1990.

[267]Chun-Hay Kom and W. James Stirling. “Charge asymmetry in $W$ + jets production at the LHC”. In: *The European Physical Journal C* 69.1-2 (June 2010), pp. 67–73.

[268]David Krohn, Jesse Thaler, and Lian-Tao Wang. “Jet trimming”. In: *Journal of High Energy Physics* 2010.2 (Feb. 2010).

[269]David Krohn, Jesse Thaler, and Lian-Tao Wang. “Jets with variable R”. In: *Journal of High Energy Physics* 2009.06 (June 2009), pp. 059–059.

[270]Hung-Liang Lai, Marco Guzzi, Joey Huston, et al. “New parton distributions for collider physics”. In: *Physical Review D* 82.7 (Oct. 2010).

[271]Imre Lakatos. “Falsification and the Methodology of Scientific Research Programmes”. In: *Can Theories be Refuted? Essays on the Duhem-Quine Thesis*. Ed. by Sandra G. Harding. Dordrecht: Springer Netherlands, 1976, pp. 205–259.

[272]D. J. Lange. “The EvtGen particle decay simulation package”. In: *Nucl. Instrum. Meth. A* 462 (2001), p. 152.

[273]Andrew J. Larkoski, Simone Marzani, Gregory Soyez, and Jesse Thaler. “Soft drop”. In: *Journal of High Energy Physics* 2014.5 (May 2014).

[274]Andrew J. Larkoski, Gavin P. Salam, and Jesse Thaler. “Energy correlation functions for jet substructure”. In: *Journal of High Energy Physics* 2013.6 (June 2013).

[275]Jianglai Liu, Xun Chen, and Xiangdong Ji. “Current status of direct dark matter detection experiments”. In: *Nature Physics* 13.3 (Mar. 2017), pp. 212–216.

[276]Leif Lönnblad. “Correcting the Colour-Dipole Cascade Model with Fixed Order Matrix Elements”. In: *Journal of High Energy Physics* 2002.05 (May 2002), pp. 046–046.

[277]Leif Lönnblad and Stefan Prestel. “Matching tree-level matrix elements with interleaved showers”. In: *Journal of High Energy Physics* 2012.3 (Mar. 2012).

[278]Arthur Loureiro, Andrei Cuceu, Filipe B. Abdalla, et al. “Upper Bound of Neutrino Masses from Combined Cosmological Observations and Particle Physics Experiments”. In: *Physical Review Letters* 123.8 (Aug. 2019).

[279]Michele Maggiore. *A Modern introduction to quantum field theory*. Oxford University Press, 2005.

[280]Ziro Maki, Masami Nakagawa, and Shoichi Sakata. “Remarks on the Unified Model of Elementary Particles”. In: *Progress of Theoretical Physics* 28.5 (Nov. 1962), pp. 870–880.

[281]G. Marchesini and B.R. Webber. “Monte Carlo simulation of general hard processes with coherent QCD radiation”. In: *Nuclear Physics B* 310.3-4 (Dec. 1988), pp. 461–526.

[282]G. Marchesini, B.R. Webber, G. Abbiendi, et al. “HERWIG 5.1 - a Monte Carlo event generator for simulating hadron emission reactions with interfering gluons”. In: *Computer Physics Communications* 67.3 (Jan. 1992), pp. 465–508.

[283]A. D. Martin, W. J. Stirling, R. S. Thorne, and G. Watt. “Parton distributions for the LHC”. In: *The European Physical Journal C* 63.2 (July 2009), pp. 189–285.

[284]Samuel D. McDermott, Hai-Bo Yu, and Kathryn M. Zurek. “Turning off the lights: How dark is dark matter?” In: *Physical Review D* 83.6 (Mar. 2011).

[285]S van der Meer. *Calibration of the effective beam height in the ISR*. Tech. rep. CERN-ISR-PO-68-31. ISR-PO-68-31. Geneva: CERN, 1968.

[286]Kirill Melnikov and Frank Petriello. “Electroweak gauge boson production at hadron colliders through $\mathcal{O}(\alpha_s^2)$”. In: *Phys. Rev. D* 74 (2006), p. 114017. arXiv: `hep-ph/0609070`.

[287]Dirk Merkel. “Docker: Lightweight Linux Containers for Consistent Development and Deployment”. In: *Linux J.* 2014.239 (Mar. 2014).

[288]M. Misiak, H. M. Asatrian, R. Boughezal, et al. “Updated Next-to-Next-to-Leading-Order QCD Predictions for the Weak Radiative $B$-Meson Decays”. In: *Physical Review Letters* 114.22 (June 2015).

[289]Vasiliki A Mitsou. “The MoEDAL experiment at the LHC: status and results”. In: *Journal of Physics: Conference Series* 873 (July 2017), p. 012010.

[290]Esma Mobs. “The CERN accelerator complex. Complexe des accélérateurs du CERN”. In: (July 2016). General Photo.

[291]Hitoshi Murayama. “Supersymmetry phenomenology”. In: *ICTP Summer School in Particle Physics*. Feb. 2000, pp. 296–335. arXiv: `hep-ph/0002232`.

[292]and N. Aghanim, Y. Akrami, F. Arroja, et al. “Planck 2018 results. I. Overview and the cosmological legacy of Planck”. In: *Astronomy & Astrophysics* (Oct. 2019).

[293]Tadao Nakano and Kazuhiko Nishijima. “Charge Independence for V-particles”. In: *Progress of Theoretical Physics* 10.5 (Nov. 1953), pp. 581–582.

[294]Isaac Newton. *Opticks*. Dover Press, 1704.

[295]Rosy Nicolaidou and Bernardo Resende. “Muon track reconstruction in the ATLAS experiment”. In: *2008 IEEE Nuclear Science Symposium Conference Record*. IEEE, Oct. 2008.

[296]Abraham Pais. *Inward Bound: Of Matter and Forces in the Physical World*. Oxford paperbacks. Clarendon Press, 1988.

[297]*Particle Dark Matter: Observations, Models and Searches*. Cambridge University Press, 2010.

[298]R. D. Peccei and Helen R. Quinn. “CPConservation in the Presence of Pseudoparticles”. In: *Physical Review Letters* 38.25 (June 1977), pp. 1440–1443.

[299]A. A. Penzias and R. W. Wilson. “A Measurement of Excess Antenna Temperature at 4080 Mc/s.” In: *The Astrophysical Journal* 142 (July 1965), p. 419.

[300]Michael E. Peskin and Daniel V. Schroeder. *An Introduction to quantum field theory*. Addison-Wesley, 1995.

[301]“Planck 2018 results. VI. Cosmological parameters”. In: *Astronomy & Astrophysics* (Apr. 2020).

[302]H. David Politzer. “Reliable Perturbative Results for Strong Interactions?” In: *Physical Review Letters* 30.26 (June 1973), pp. 1346–1349.

[303]Bruno Pontecorvo. “Neutrino Experiments and the Problem of Conservation of Leptonic Charge”. In: *Sov. Phys. JETP* 26 (1968), pp. 984–988.

[304]Karolos Potamianos. “The upgraded Pixel detector and the commissioning of the Inner Detector tracking of the ATLAS experiment for Run-2 at the Large Hadron Collider”. In: *PoS* EPS-HEP2015 (2015), p. 261. arXiv: `1608.07850 [physics.ins-det]`.

[305]J. Pumplin et al. “New Generation of Parton Distributions with Uncertainties from Global QCD Analysis”. In: *JHEP* 07 (2002), p. 012. arXiv: `hep-ph/0201195`.

[306] Scott W. Randall, Maxim Markevitch, Douglas Clowe, Anthony H. Gonzalez, and Marusa Bradač. “Constraints on the Self-Interaction Cross Section of Dark Matter from Numerical Simulations of the Merging Galaxy Cluster 1E 0657-56”. In: *The Astrophysical Journal* 679.2 (June 2008), pp. 1173–1180.

[307] Alexander L. Read. “Presentation of search results: the $CL_S$ technique”. In: *J. Phys. G* 28 (2002), p. 2693.

[308] C. L. Reichardt, P. A. R. Ade, J. J. Bock, et al. “High-resolution CMB power spectrum from the complete ACBAR data set”. In: *The Astrophysical Journal* 694.2 (Mar. 2009), pp. 1200–1219.

[309] Alex Rogozhnikov. “Reweighting with Boosted Decision Trees”. In: *Journal of Physics: Conference Series* 762 (Oct. 2016), p. 012036.

[310] Aranzazu Ruiz-Martinez and ATLAS Collaboration. *The Run-2 ATLAS Trigger System*. Tech. rep. ATL-DAQ-PROC-2016-003. Geneva: CERN, Feb. 2016.

[311] Andrei D Sakharov. “Violation ofCPin variance, Casymmetry, and baryon asymmetry of the universe”. In: *Soviet Physics Uspekhi* 34.5 (May 1991), pp. 392–393.

[312] Abdus Salam. “Weak and electromagnetic interactions”. In: *Selected Papers of Abdus Salam*. WORLD SCIENTIFIC, May 1994, pp. 244–254.

[313] Gavin P Salam and Grégory Soyez. “A practical seedless infrared-safe cone jet algorithm”. In: *Journal of High Energy Physics* 2007.05 (May 2007), pp. 086–086.

[314] Marc Schumann. “Direct detection of WIMP dark matter: concepts and status”. In: *Journal of Physics G: Nuclear and Particle Physics* 46.10 (Aug. 2019), p. 103003.

[315] Steffen Schumann and Frank Krauss. “A parton shower algorithm based on Catani–Seymour dipole factorisation”. In: *JHEP* 03 (2008), p. 038. arXiv: 0709.1027 [hep-ph].

[316] Matthew D. Schwartz. *Quantum Field Theory and the Standard Model*. Cambridge University Press, 2014.

[317] Pat Scott, Malcolm Fairbairn, and Joakim Edsjo. “Impacts of WIMP dark matter upon stellar evolution: main-sequence stars”. In: *Proceedings of Identification of dark matter 2008 — PoS(idm2008)*. Sissa Medialab, Aug. 2009.

[318] Vimal Simha and Gary Steigman. “Constraining the early-Universe baryon density and expansion rate”. In: *Journal of Cosmology and Astroparticle Physics* 2008.06 (June 2008), p. 016.

[319] Torbjorn Sjostrand. “Status and developments of event generators”. In: *Proceedings of Fourth Annual Large Hadron Collider Physics — PoS(LHCP2016)*. Sissa Medialab, Sept. 2016.

[320] Torbjörn Sjöstrand, Stefan Ask, Jesper R. Christiansen, et al. “An introduction to PYTHIA 8.2”. In: *Comput. Phys. Commun.* 191 (2015), p. 159. arXiv: 1410.3012 [hep-ph].

[321] Torbjorn Sjöstrand, Stephen Mrenna, and Peter Z. Skands. "PYTHIA 6.4 Physics and Manual". In: *JHEP* 05 (2006), p. 026. arXiv: hep-ph/0603175.

[322] Peter Zeiler Skands. "Tuning Monte Carlo generators: The Perugia tunes". In: *Phys. Rev. D* 82 (2010), p. 074018. arXiv: 1005.3457 [hep-ph].

[323] Martin C. Smith and Scott S. Willenbrock. "QCD and Yukawa corrections to single-top-quark production via$qq^- \to tb^-$". In: *Physical Review D* 54.11 (Dec. 1996), pp. 6696–6702.

[324] G. F. Smoot, C. L. Bennett, A. Kogut, et al. "Structure in the COBE differential microwave radiometer first-year maps". In: *The Astrophysical Journal* 396 (Sept. 1992), p. L1.

[325] D. N. Spergel, R. Bean, O. Dore, et al. "Three-Year Wilkinson Microwave Anisotropy Probe (WMAP) Observations: Implications for Cosmology". In: *The Astrophysical Journal Supplement Series* 170.2 (June 2007), pp. 377–408.

[326] D. N. Spergel, L. Verde, H. V. Peiris, et al. "First-Year Wilkinson Microwave Anisotropy Probe (WMAP) Observations: Determination of Cosmological Parameters". In: *The Astrophysical Journal Supplement Series* 148.1 (Sept. 2003), pp. 175–194.

[327] Mark Srednicki, Richard Watkins, and Keith A. Olive. "Calculations of relic densities in the early universe". In: *Nuclear Physics B* 310.3-4 (Dec. 1988), pp. 693–713.

[328] T. Stelzer, Z. Sullivan, and S. Willenbrock. "Single-top-quark production at hadron colliders". In: *Physical Review D* 58.9 (Oct. 1998).

[329] T. Stelzer, Z. Sullivan, and S. Willenbrock. "Single-top-quark production viaW-gluon fusion at next-to-leading order". In: *Physical Review D* 56.9 (Nov. 1997), pp. 5919–5927.

[330] George Sterman and Steven Weinberg. "Jets from Quantum Chromodynamics". In: *Physical Review Letters* 39.23 (Dec. 1977), pp. 1436–1439.

[331] W. J. Stirling. private communication. 2012.

[332] Louis E Strigari. "Dark matter in dwarf spheroidal galaxies and indirect detection: a review". In: *Reports on Progress in Physics* 81.5 (Mar. 2018), p. 056901.

[333] Stanislav Suchek. "Search for Dark Matter produced in association with hadronically decaying Standard Model bosons using $36\,\mathrm{fb}^{-1}$ of $pp$ collisions at the ATLAS detector". PhD thesis. University of Heidelberg, 2018.

[334] Andi Tan, Mengjiao Xiao, Xiangyi Cui, et al. "Dark Matter Results from First 98.7 Days of Data from the PandaX-II Experiment". In: *Physical Review Letters* 117.12 (Sept. 2016).

[335] M. Tanabashi et al. "Review of Particle Physics". In: *Phys. Rev. D* 98.3 (2018), p. 030001.

[336] Marco Taoso, Gianfranco Bertone, and Antonio Masiero. "Dark matter candidates: a ten-point test". In: *Journal of Cosmology and Astroparticle Physics* 2008.03 (Mar. 2008), p. 022.

[337] Max Tegmark, Michael A. Strauss, Michael R. Blanton, et al. “Cosmological parameters from SDSS and WMAP”. In: *Physical Review D* 69.10 (May 2004).

[338] Jesse Thaler and Ken Van Tilburg. “Identifying boosted objects with N-subjettiness”. In: *Journal of High Energy Physics* 2011.3 (Mar. 2011).

[339] Jesse Thaler and Ken Van Tilburg. “Maximizing boosted top identification by minimizing N-subjettiness”. In: *Journal of High Energy Physics* 2012.2 (Feb. 2012).

[340] “The Discovery of Neptune Leverrier’s Letter to Galle”. In: *Nature* 85.2145 (Dec. 1910), pp. 184–185.

[341] Mark Thomson. *Modern Particle Physics*. Cambridge University Press, 2013.

[342] W. Tucker, P. Blanco, S. Rappoport, et al. “1E 0657-56: A Contender for the Hottest Known Cluster of Galaxies”. In: *The Astrophysical Journal* 496.1 (Mar. 1998), pp. L5–L8.

[343] Sean Tulin and Hai-Bo Yu. “Dark matter self-interactions and small scale structure”. In: *Physics Reports* 730 (Feb. 2018), pp. 1–57.

[344] Matthew Walker. “Dark Matter in the Galactic Dwarf Spheroidal Satellites”. In: *Planets, Stars and Stellar Systems: Volume 5: Galactic Structure and Stellar Populations*. Ed. by Terry D. Oswalt and Gerard Gilmore. Dordrecht: Springer Netherlands, 2013, pp. 1039–1089.

[345] B.R. Webber. “A QCD model for jet fragmentation including soft gluon interference”. In: *Nuclear Physics B* 238.3 (June 1984), pp. 492–528.

[346] Steven Weinberg. “A Model of Leptons”. In: *Physical Review Letters* 19.21 (Nov. 1967), pp. 1264–1266.

[347] Simon D.M. White, C.S. Frenk, and M. Davis. “Clustering in a Neutrino Dominated Universe”. In: *Astrophys. J. Lett.* 274 (1983). Ed. by M.A. Srednicki, pp. L1–L5.

[348] C. N. Yang and R. L. Mills. “Conservation of Isotopic Spin and Isotopic Gauge Invariance”. In: *Physical Review* 96.1 (Oct. 1954), pp. 191–195.

[349] F. Zwicky. “Nebulae as Gravitational Lenses”. In: *Phys. Rev.* 51 (4 Feb. 1937), pp. 290–290.

# List of Figures


2.1 Schematic overview of quarks and leptons, grouped by affiliation to generation and electric charge. The size of the circles is proportional to the fermion mass. . . . . 11

2.2 The Higgs potential $V(\phi)$ with parameters $\mu^2 = -(125\,\mathrm{GeV})^2/2$ and $\lambda = 0.13$ is shown in dependency of the real and imaginary part of $\phi$. For this choice of parameters $\mu^2 < 0$ and $\lambda > 0$ the potential assumes its minimum at the circle with radius $v/\sqrt{2} = 246\,\mathrm{GeV}/\sqrt{2}$, which is defined by the vacuum expectation value $v$. . . . . 15

2.3 Summary of several Standard Model total production cross-section measurements, corrected for branching fractions, compared to the corresponding theoretical expectations and ratio with respect to best theory prediction. Figure reproduced from Ref. [102]. . . . . 19

3.1 Evolution of the energy densities in the universe. Figure reproduced from Ref. [124]. . . . . 25

3.2 Abundance of dark matter particles $N_X$ in dependence of the dimensionless parameter $x = m_\chi/T$. The freeze-out occurs at the point, where the temperature $T$ drops below the dark matter particle mass $m_\chi$. The annihilation cross-section is expressed as $\lambda = \frac{2\pi^2}{45} g^\star \frac{m_\chi \langle \sigma_{\mathrm{ann}} v \rangle}{H(m_\chi)}$, where $g_{S\star}$ denotes the effective number of degrees of freedom in entropy. Figure reproduced from Ref. [124]. . . . . 27

3.3 Galactic rotation curve for NGC 6503 (observed data taken from Ref. [147]). The decomposition of the rotation curve in contributions from disk and gas potentials shows that an additional contribution due to the dark matter halo is required to match the data. Figure reproduced from Ref. [223]. . . . . 29

3.4 Image of the galaxy cluster Abell 2218 and its gravitational lenses, taken by the Hubble space telescope in 1999. Image by Andrew Fruchter (STScI) et al., WFPC2, HST, NASA / Public domain. . . . . 31

3.5 Images of 1E657-558 based on optical (top) and X-ray observations (bottom). The green contours of the reconstructed cluster surface mass density $\kappa$ obtained from weak gravitational lensing are overlaid in both images. The three white contours show the uncertainty in the position of the two primary galaxy concentration centres, corresponding to $1\sigma$, $2\sigma$, and $3\sigma$ confidence levels. Figures reproduced from Ref. [162]. . . . 33

3.6 Planck (2018) observations of the CMB. Figures reproduced from Refs. [292] (top) and [301] (bottom). . . . . 35

3.7 Range of momentum transfers probed by direct detection experiments, indirect detection experiments and collider searches with prototypical Feynman graphs illustrating the underlying processes. Figure reproduced from Ref. [6]. . . . . 39
3.8 Constraints placed on the SI WIMP-nucleon cross-section for WIMPs with mass $m_\chi$ by direct detection experiments. Figure reproduced from Ref. [314]. . . . . 41
3.9 Constraints placed on the self-annihilation cross-section for WIMPs with mass $m_\chi$ by indirect detection experiments. Figure reproduced from Ref. [335]. . . . . 43
3.10 Overview of theoretical frameworks describing dark matter production at particle colliders. The models range from dark matter effective field theory, over various simplified models, to complete dark matter models. Figure reproduced from Ref. [3]. . . . . 45
3.11 Branching fractions of dark Higgs boson decays to SM particles (produced on-shell) in dependence of $m_s$. . . . . 51

4.1 Sketch of a proton-proton collision event in which a top quark pair and a Higgs boson are produced in the hard scattering process. The incoming protons are shown as the central green ellipses with three incoming valence quark lines. The hard scattering process is depicted as the central red blob. The initial and final state radiation processes are shown in blue and red, respectively. The underlying event of other partons scattering and producing further activity is shown in purple. All emerging partons undergo hadronisation, resulting in cascading showers of hadrons, which are shown in green. Figure reproduced from Ref. [155]. . . . . 54
4.2 The CT14 parton distribution functions at the scales of $2\,\mathrm{GeV}$ (top) and $100\,\mathrm{GeV}$ (bottom) for u $\bar{\mathrm{u}}$, d, $\bar{\mathrm{d}}$, $\bar{\mathrm{s}}$, and g. Figure reproduced from Ref. [214]. . . . . 57
4.3 Comparison of the gluon (top) and up quark (bottom) PDFs from the CT14, MMHT14 and NNNPDF3.0 sets at next-to-next-to-leading order (NNLO ) at a scale of $Q^2 = 100\,\mathrm{GeV}^2$. The results are shown relative to the central value of CT14. Figure reproduced from Ref. [149]. . . . . 58
4.4 Cross-sections and event rates for various centre-of-mass energies $\sqrt{s}$ in antiproton-proton (Tevatron, $\sqrt{s} < 4\,\mathrm{GeV}$) and proton-proton (LHC, $\sqrt{s} > 4\,\mathrm{GeV}$) collisions. The cross-sections have been calculated in perturbative QCD at NLO and NNLO using the MSTW2008 PDF set [283]. Figure reproduced from Ref. [331]. . . . . 60
4.5 Clustering of a sample parton-level event with four different jet algorithms, illustrated by the active catchment area of the resulting hard jets. Figure reproduced from Ref. [153]. . . . . 62

5.1 The CERN accelerator complex. The illustration shows the LHC ring and the associated pre-accelerator chain relevant for producing pp collisions. Figure adapted from Ref. [290]. . . . . 66

5.2 Schematic representation of the ATLAS detector and its various subsystems. Figure reproduced from Ref. [178]. . . . . 69
5.3 Illustrations of the ID layout and its spatial dimensions. . . . . 72
5.4 The ATLAS calorimeter system with its various components. Figure reproduced from Ref. [178]. . . . . 75
5.5 The ATLAS muon spectrometer with its various components. Figure reproduced from Ref. [178]. . . . . 77
5.6 The ATLAS trigger logic in Run-2. Figure reproduced from Ref. [310]. . 79

6.1 A track parametrised with respect to the nominal $z$-axis through the azimuthal angle $\varphi$, the polar angle $\theta$, the charged inverse momentum $q/p$, and the transverse and longitudinal impact parameters $d_0$ and $z_0$. Figure reproduced from Ref. [194]. . . . . 83
6.2 Resolution of the transverse impact parameter $d_0$ and the longitudinal impact parameter $z_0$ of tracks associated with jets with $p_{\mathrm{T}} > 20\,\mathrm{GeV}$, measured in pp collision data recorded in 2017 and 2018 with dijet triggers. Figure reproduced from Ref. [181]. . . . . 83
6.3 Vertex performance in 2018 pp data, indicated by the number of reconstructed vertices in dependence of the average number of interactions per bunch crossing. Figure reproduced from Ref. [181]. . . . . 84
6.4 Schematic illustration of an electron's trajectory (red) through the detector, first traversing the tracking system comprised of PXD detectors, SCT detectors and lastly the TRT, and then enters the EM calorimeters. The dashed trajectory (red) illustrates the path of a photon radiated off the electron due to interactions with the detector material. Figure reproduced from Ref. [47]. . . . . 85
6.5 Electron identification efficiencies for the different operating points LOOSE, MEDIUM, and TIGHT. Figures reproduced from Ref. [45]. . . . 87
6.6 Electron isolation efficiencies for the fixed cut OPs "Loose", "Tight", and "HighPtCaloOnly", as well as for the "Gradient" OP. Figures reproduced from Ref. [45]. . . . . 89
6.7 Muon reconstruction and identification efficiencies for MEDIUM muons with $p_{\mathrm{T}} > 10\,\mathrm{GeV}$. Figures reproduced from Ref. [63]. . . . . 92
6.8 Muon isolation efficiency in bins of $p_{\mathrm{T}}$ for the LOOSE and TIGHT fixed cut OPs. Figures reproduced from Ref. [63]. . . . . 93
6.9 Stages of jet energy scale calibrations. Each one is applied to the four-momentum of the jet. Figure reproduced from Ref. [54] . . . . . 94
6.10 Dependence of jet $p_{\mathrm{T}}$ on in-time pile-up (left) and out-of-time pile-up (right) as a function of $|\eta|$ for truth jet $p_{\mathrm{T}} = 25\,\mathrm{GeV}$. Figures reproduced from Ref. [55]. . . . . 95
6.11 The average jet energy response (left) and the signed difference between the truth and the reconstructed jet pseudorapidity (right) as functions of $\eta_{\mathrm{det}}$ for jets with truth energy of 30, 60, 110, 400, and $1200\,\mathrm{GeV}$. Figures reproduced from Ref. [55]. . . . . 96

6.12 Binned ratio (open circles) of the jet response in simulated events to that in data as a function of $\eta_{\text{det}}$ for jets at the EM+JES and GSC scale with $40\,\text{GeV} < p_{\text{T}}^{\text{avg}} < 55\,\text{GeV}$. The smoothed correction (black line) with corresponding statistical (dark blue) and total (light green) uncertainty bands is overlaid, together with horizontal dotted lines to guide the eye. Figure reproduced from Ref. [55]. . . . . 97

6.13 Distribution of the output discriminant of the MV2 $b$-tagging algorithm for $b$-jets (blue), $c$-jets (green) and light-flavour jets (red) in a sample of MC simulated $\text{t}\bar{\text{t}}$ events. Figure adapted from Ref. [35]. . . . . 99

6.14 The $b$-tagging efficiency (left) and $b$-tagging efficiency simulation-to-data scale factors (right) for the $70\,\%$ single-cut OP of the MV2 tagger as a function of jet $p_{\text{T}}$. The efficiency measurement is shown in data (dots) and in simulated $\text{t}\bar{\text{t}}$ events (red line), together with the total uncertainty (green band). Figures reproduced from Ref. [35]. . . . . 100

6.15 Illustration of boosted event topologies: the distance between the decay products of a boosted boson decreases with increasing transverse momentum of the boosted boson. . . . . 101

6.16 Overview of the large-radius jet reconstruction and calibration procedure. Illustration reproduced from Ref. [51]. . . . . 101

6.17 Illustration of the jet-trimming algorithm for large-radius jets. Figure reproduced from Ref. [70]. . . . . 102

6.18 The fractional jet mass resolution, defined as half the ratio of the $68\,\%$ confidence interval inter-quantile range of the jet mass response distribution and the median jet response, estimated in dependence of the truth jet $p_{\text{T}}$ using simulated hadronic decays of diboson processes. Figure reproduced from Ref. [179]. . . . . 103

6.19 Illustration of the sub-jet reconstruction using either fixed radius (left) or variable radius (right) track jets. Figure reproduced from Ref. [110]. 104

6.20 Distribution of the $E_{\text{T}}^{\text{miss}}$ resolution in dependence of the number of primary vertices $N_{\text{PV}}$ in the event for $E_{\text{T}}^{\text{miss}}$ reconstructed with the LOOSE and TIGHT operating points in $\text{Z} \to \mu\mu$ events. Figure adapted from Ref. [34]. . . . . 106

6.21 Performance of the $E_{\text{T}}^{\text{miss}}$ significance in terms of background rejection versus signal efficiency in simulated $\text{Z} \to \text{ee}$ and $\text{Z} \to \text{ee}\nu\nu$ samples with a Z$to$ee selection. The performance is shown for $E_{\text{T}}^{\text{miss}}$ (orange), event-based $E_{\text{T}}^{\text{miss}}$ significance (pink), and object-based $E_{\text{T}}^{\text{miss}}$ significance (green) as discriminants in events with a $E_{\text{T}}^{\text{miss}} > 100\,\text{GeV}$ preselection. The lower panel shows the ratio of other definitions to the event-based $E_{\text{T}}^{\text{miss}}$ significance. Figure reproduced from Ref. [65]. . . . 108

7.1 Longitudinal view of the barrel and end-cap muon trigger system. Representative tracks of muon trigger candidates for the low-$p_{\text{T}}$ and high-$p_{\text{T}}$ triggers illustrate the coincidence logic of trigger stations used for the trigger decision. Adapted from Ref. [112] . . . . . 116

7.2 Modification of coincidence windows in the $\Delta r$–$\Delta\eta$ plane. The 0-th region-of-interest (ROI) LUTs for the HH CW and LH CW are shown for module 2a before (top row) and after (bottom row) the optimisation of the LH CW. . . . . 119
7.3 Kinematic distributions of *tag* and *probe* muons and invariant mass of the di-muon system after the full event selection. . . . . 121
7.4 L1MU4 trigger efficiency before and after the optimisation of the forward module coincidence windows estimated with the tag-and-probe method based on the J/$\psi$ resonance. . . . . 122
7.5 L1MU4 trigger rate in dependency of the muon track candidate pseudo-rapidity $\eta$ before and after the optimisation of the coincidence windows of the forward TGC modules. In addition, the rate of positive trigger decisions which could be matched with a reconstructed muon satisfying $p_{\mathrm{T}} > 4\,\mathrm{GeV}$ is shown before and after the coincidence window modification. The two insets show the ratio of the L1MU4 trigger rate after and before the coincidence window modification and the ratio of positive trigger decisions matched with reconstructed muons after and before the coincidence window modification, respectively. . . . . 123

8.1 Illustration of the signature indicating dark matter particle production in association with heavy bosons in the transverse plane of the detector. The recoil of the undetected dark matter particles on the heavy boson results in missing transverse momentum. The hadronic decay of the heavy boson results in the formation of hadronic jets. . . . . 127
8.2 Example Feynman graphs for the dominant background processes in searches for dark matter with heavy bosons. . . . . 128
8.3 Illustration of the signal and control region definitions based on the lepton multiplicity. The control regions are enriched in specific background processes which populate the signal region and thereby allow for the estimation of these background contributions in the SR using data.129
8.4 ATLAS data-taking performance during the Run-2 pp data-taking campaign. Figures reproduced from Ref. [36]. . . . . 130
8.5 Combined L1 and HLT efficiency of the $E_{\mathrm{T}}^{\mathrm{miss}}$ triggers with lowest threshold used in each year of data-taking. The $E_{\mathrm{T}}^{\mathrm{miss}}$ trigger efficiency is measured in data using $\mathrm{Z} \to \mu\mu$ events and is shown as a function of the Z boson transverse momentum $p_{\mathrm{T}}^{\mu\mu}$. Figure reproduced from Ref. [75]. . . . . 135

9.1 Dark matter particle ($\chi$) pair production in association with a W or Z boson in the simplified model with a vector or an axial-vector Z′ boson mediator. . . . . 140
9.2 Grid of generated signal model samples in the Z′ vector mediator simplified model for different configurations of $m_{\mathrm{Z}'}$ and $m_{\chi}$. . . . . 141
9.3 DM particle ($\chi$) pair production in association with a Z boson in the $a$-2HDM. In addition to the diagram shown on the right, another graph contributes, which includes the exchange of the pseudo-scalar $A$ instead of $a$. . . . . 143

9.4 Illustrations of the merged and resolved event topologies in the $E_{\mathrm{T}}^{\mathrm{miss}} + V(q\bar{q})$ search. . . . . 146

9.5 Overview of all regions and categories considered in the $E_{\mathrm{T}}^{\mathrm{miss}} + V(q\bar{q})$ search with their relative background composition. The 0 lepton signal region is defined for a selection enriched in signal processes targeting W/ Z mass window and a selection targeting the W/ Z mass side-bands, which are used as a validation region. The control regions are also split by W/ Z mass window and mass side-bands selections. Each region is partitioned in merged and resolved event topology categories, which are defined by the $b$-tag multiplicity. The 0 lepton merged signal region categories with zero or one $b$-tagged jets are further divided in high-purity and low-purity selections, which have different signal efficiencies. . . . . 147

9.6 Distributions of $\min \Delta\varphi(\text{jets}_{1,2,3}, E_{\mathrm{T}}^{\mathrm{miss}})$, $\Delta\varphi(E_{\mathrm{T}}^{\mathrm{miss}}, V)$, and $\Delta\varphi(E_{\mathrm{T}}^{\mathrm{miss}}, E_{\mathrm{T}}^{\mathrm{miss,\,track}})$ after applying the 0 lepton SR merged baseline event selection requirements. The cut value is indicated by a red line and the region of selected events is indicated by the direction of the arrow. The data is shown overlaid on stacked histograms of the simulated background processes, including a MC sample of dijet events for illustration purposes. . . . . 151

9.7 Expected distributions of missing transverse momentum $E_{\mathrm{T}}^{\mathrm{miss}}$ (left) and invariant mass $m_J$ (right), both normalised to the unit area, for two vector-mediator simplified model signals with $m_\chi = 1\,\mathrm{GeV}$ and $m_{\mathrm{Z}'} = 200\,\mathrm{GeV}$ (red), $m_{\mathrm{Z}'} = 600\,\mathrm{GeV}$ (blue) after the full selection in the merged event topology. . . . . 151

9.8 Distributions of the energy correlation ratio $D_2^{(\beta=1)}$ of the most energetic large-radius jet in the event for data, simulated backgrounds and a representative vector mediator simplified model signal with $mZp = 600\,\mathrm{GeV}$ and $m_\chi = 1\,\mathrm{GeV}$. The distributions show events with 0 $b$-tagged jets (left) and 1 $b$-tagged jet (right). . . . . 153

9.9 Selection requirements for the W boson tagger (left) and Z boson tagger (right). The upper panel shows the two-sided requirements on the combined jet mass $m_J$. The lower panel shows the upper cut on the energy correlation ratio $D_2^{(\beta=1)}$. . . . . 153

9.10 Expected distributions of missing transverse momentum $E_{\mathrm{T}}^{\mathrm{miss}}$ (left) and invariant mass $m_{jj}$ (right), both normalised to the unit area, for two vector-mediator simplified model signals with $m_\chi = 1\,\mathrm{GeV}$ and $m_{\mathrm{Z}'} = 200\,\mathrm{GeV}$ (red), $m_{\mathrm{Z}'} = 600\,\mathrm{GeV}$ (blue) after the full selection in the resolved event topology. . . . . 154

9.11 The product of acceptance and efficiency $\mathcal{A} \times \varepsilon$ for the process $\mathrm{pp} \to \mathrm{Z}'V \to \chi\overline{\chi}qq$, defined as the number of signal events satisfying the full set of selection criteria, divided by the total number of generated signal events for the simplified vector-mediator model signals, shown in dependence on the mediator mass $m_{\mathrm{Z}'}$. . . . . 156

9.12 Sketch of the selections used in the multijet background estimate based on a template method. The $E_{\mathrm{T}}^{\mathrm{miss}}$ shape of the multijet background is obtained from a selection enriched in multijet events by inverting the $\min \Delta\varphi(\text{jets}_{1,2,3}, E_{\mathrm{T}}^{\mathrm{miss}})$ requirement. The template is normalised by correcting for the efficiency of the $\min \Delta\varphi(\text{jets}_{1,2,3}, E_{\mathrm{T}}^{\mathrm{miss}})$ cut. The efficiency is determined by a fit of a template and simulated backgrounds to the data in selections enhanced in multijet events. . . . . 160

9.13 The $E_{\mathrm{T}}^{\mathrm{miss}}$ distributions in the 0 lepton VR after the background-only fit ($\mu = 0$) for data (dots) SM background prediction (histograms), shown separately for the merged-topology and resolved-topology event categories with 0 $b$-tags, 1 $b$-tag, and 2 $b$-tags. The expected distribution of a representative vector mediator simplified model with $m_{\chi} = 1\,\mathrm{GeV}$ and $m_{Z'} = 600\,\mathrm{GeV}$ normalised to the theory prediction is overlaid. The total background contribution before the fit to the data is shown as a dotted blue line. The hatched area represents the total background uncertainty. The inset at the bottom of each plot shows the ratio of the data to the total post-fit (dots) and pre-fit (dotted blue line) background expectation. . . . . 168

9.14 The $E_{\mathrm{T}}^{\mathrm{miss,no}\ell}$ distributions in the 1 muon CR (W/ Z mass window) after the background-only fit ($\mu = 0$) for data (dots) SM background prediction (histograms), shown separately for the merged-topology (left) and resolved-topology (right) event categories with 0 $b$-tags (top), 1 $b$-tag (middle), and 2 $b$-tags (bottom). The total background contribution before the fit to the data is shown as a dotted blue line. The hatched area represents the total background uncertainty. The inset at the bottom of each plot shows the ratio of the data to the total post-fit (dots) and pre-fit (dotted blue line) background expectation. . . . . 169

9.15 The $E_{\mathrm{T}}^{\mathrm{miss,no}\ell}$ distributions in the 2 lepton CR (W/ Z mass window) after the background-only fit ($\mu = 0$) for data (dots) SM background prediction (histograms), shown separately for the merged-topology (left) and resolved-topology (right) event categories with 0 $b$-tags (top), 1 $b$-tag (middle), and 2 $b$-tags (bottom). The total background contribution before the fit to the data is shown as a dotted blue line. The hatched area represents the total background uncertainty. The inset at the bottom of each plot shows the ratio of the data to the total post-fit (dots) and pre-fit (dotted blue line) background expectation. . . . . 170

9.16 The $E_{\mathrm{T}}^{\mathrm{miss}}$ distributions in the 0 lepton SR after the background-only fit ($\mu = 0$) for data (dots) SM background prediction (histograms), shown separately for the merged-topology and resolved-topology event categories with 0 $b$-tags, 1 $b$-tag, and 2 $b$-tags. The expected distribution of a representative vector mediator simplified model with $m_{\chi} = 1\,\mathrm{GeV}$ and $m_{\mathrm{Z}'} = 600\,\mathrm{GeV}$ normalised to the theory prediction is overlaid. The total background contribution before the fit to the data is shown as a dotted blue line. The hatched area represents the total background uncertainty. The inset at the bottom of each plot shows the ratio of the data to the total post-fit (dots) and pre-fit (dotted blue line) background expectation. . . . . 172

9.17 Exclusion contours at $95\,\%$ $\mathrm{CL}_s$ for the $V/A$ simplified model at NLO accuracy for vector mediator (top) and axial-vector mediator (bottom) with couplings $g_q = 0.25$, $g_\ell = 0$, and $g_\chi = 1$. The black dashed line shows the median of the expected limit, whereas the solid line shows the observed limit. The dotted magenta curve corresponds to the set of points for which the relic density predicted by the vector mediator simplified model is consistent with the Planck [301] measurements, as computed with MadDM [25]. The region on the right of the curve corresponds to higher predicted relic density than these measurements. 176

9.18 Exclusion contours at $95\,\%$ $\mathrm{CL}_s$ for the $a$-2HDM model in the two-dimensional $m_{\mathrm{H}}$-$m_a$ plane for the fixed choice of parameters $\tan\beta = 1.0$, $m_{\chi} = 10\,\mathrm{GeV}$, and $\sin\theta = 0.35$. . . . . 177

9.19 Observed exclusion limits at $95\,\%$ $\mathrm{CL}_s$ on the signal strength $\mu$ for the $a$-2HDM model as a function of $\sin\theta$, shown for parameters corresponding to a low-mass scenario (top) and a high-mass scenario (bottom). . . . 178

9.20 Exclusion limits at $95\,\%$ $\mathrm{CL}_s$ on the signal strength $\mu$ for the $a$-2HDM model as a function of $m_{\chi}$ for the fixed choices of the parameters $\tan\beta = 1.0$, $m_{\mathrm{H}} = 600\,\mathrm{GeV}$, $m_a = 250\,\mathrm{GeV}$, and $\sin\theta = 0.35$. . . . . 179

10.1 Production of dark matter particles $\chi$ and a Higgs boson h through a new $\mathrm{Z}'$ mediator coupled to the CP-odd Higgs boson A, where the latter decays primarily to $\chi\overline{\chi}$. . . . . 182

10.2 Overview of all regions and $p_{\mathrm{T}}^{V}$ bins considered in the $E_{\mathrm{T}}^{\mathrm{miss}} + \mathrm{h}(\mathrm{b\overline{b}})$ search with their relative background composition, where $p_{\mathrm{T}}^{V}$ denotes $E_{\mathrm{T}}^{\mathrm{miss}}$ in the signal region, $E_{\mathrm{T}}^{\mathrm{miss,no}\mu}$ in the 1 muon control region, and $p_{\mathrm{T}}^{\ell\ell}$ in the 2 lepton control region, respectively. Each region consists of three resolved event-topology $p_{\mathrm{T}}^{V}$ bins and the merged event-topology $p_{\mathrm{T}}^{V}$ bin. . . . . 186

10.3 The efficiency for a large-radius jet from a $\mathrm{h} \to \mathrm{b\overline{b}}$ decay (referred to as Higgs jet) to have its two associated sub-jets with largest transverse momentum matched to truth B-hadrons in dependence of its $p_{\mathrm{T}}$. The error bars include statistical uncertainties only. Figure modified from Ref. [110]. . . . . 188

10.4 Performance of the $E_{\mathrm{T}}^{\mathrm{miss}}$ significance (line with square markers) in terms of the signal efficiency and multijet background rejection in the $E_{\mathrm{T}}^{\mathrm{miss}} + \mathrm{h}(\mathrm{b\bar{b}})$ search, compared to an event-based $E_{\mathrm{T}}^{\mathrm{miss}}$ significance definition $E_{\mathrm{T}}^{\mathrm{miss}}/\sqrt{\sum E_{\mathrm{T}}^{\mathrm{miss}}}$ (dashed line with circular markers), and on $E_{\mathrm{T}}^{\mathrm{miss}}$ itself (densely-dashed line with triangular markers). The signal efficiency is estimated with a Z′-2HDM signal sample with $m_{\mathrm{Z}'} = 400\,\mathrm{GeV}$ and $m_{\mathrm{A}} = 300\,\mathrm{GeV}$, which has a very soft $E_{\mathrm{T}}^{\mathrm{miss}}$ distribution, whereas the background rejection is estimated with a sample of simulated dijet events. The events used for the comparison are selected by the $E_{\mathrm{T}}^{\mathrm{miss}} + \mathrm{h}(\mathrm{b\bar{b}})$ baseline selection requirements, including a requirement on the angular separation between the $E_{\mathrm{T}}^{\mathrm{miss}}$ vector and the three jets with highest $p_{\mathrm{T}}$. . . . . 189
10.5 Product of detector acceptance × selection efficiency in the signal region merged category shown in dependence of $m_{\mathrm{Z}'}$ for a Z′-2HDM signal sample with fixed $m_{\mathrm{A}} = 500\,\mathrm{GeV}$. The performance for VR track jets (filled triangles, solid lines) is compared to that of FR track jets (open triangles, dashed lines). . . . . 193
10.6 Product of detector acceptance × selection efficiency for events with 2 $b$-tagged jets as a function of $m_{\mathrm{Z}'}$ for a Z′-2HDM signal sample with fixed $m_{\mathrm{A}} = 500\,\mathrm{GeV}$. The values obtained for the resolved category are shown in blue with open triangles and a dashed line, the ones for the merged category with filled triangles and a solid line. The combined selection efficiency is shown in black. . . . . 195
10.7 Distributions of the Higgs boson candidate invariant mass $m_{jj}$ for multijet background processes in the multijet-enriched region with 2 $b$-tagged jets, obtained by subtracting all other simulated background processes from the data. The distributions are shown in the bins $150\,\mathrm{GeV} < E_{\mathrm{T}}^{\mathrm{miss}} < 200\,\mathrm{GeV}$ (left), $150\,\mathrm{GeV} < E_{\mathrm{T}}^{\mathrm{miss}} < 200\,\mathrm{GeV}$ (right), $150\,\mathrm{GeV} < E_{\mathrm{T}}^{\mathrm{miss}} < 200\,\mathrm{GeV}$ (bottom). The error bars represent the statistical uncertainty only. . . . . 198
10.8 Sketch of the regions used in the multijet background estimate based on a factorisation method. The multijet-enriched region A is defined by inverting both the $\min \Delta\varphi(\mathrm{jets}_{1,2,3}, E_{\mathrm{T}}^{\mathrm{miss}})$ and $\mathcal{S}$ requirements. The regions B and C are defined by inverting only one of those requirements, whereas both requirements are applied in the signal region D. . . . . 199
10.9 Shape of the object-based $E_{\mathrm{T}}^{\mathrm{miss}}$ significance $\mathcal{S}$ shown for the difference between the data and the other simulated background processes in different selections of $\min \Delta\varphi(\mathrm{jets}_{1,2,3}, E_{\mathrm{T}}^{\mathrm{miss}})$. The selected events have two $b$-tagged jets and satisfy $150\,\mathrm{GeV} < E_{\mathrm{T}}^{\mathrm{miss}} < 200\,\mathrm{GeV}$. . . . . 200
10.10 Two-dimensional distributions of $\mathcal{S}$ and $\min \Delta\varphi(\mathrm{jets}_{1,2,3}, E_{\mathrm{T}}^{\mathrm{miss}})$ for multijet background processes, obtained by subtracting all other simulated background processes from the data. The grey lines indicate the regions used in the multijet estimate. The distributions are shown in the bins $150\,\mathrm{GeV} < E_{\mathrm{T}}^{\mathrm{miss}} < 200\,\mathrm{GeV}$ (left), $150\,\mathrm{GeV} < E_{\mathrm{T}}^{\mathrm{miss}} < 200\,\mathrm{GeV}$ (right), $150\,\mathrm{GeV} < E_{\mathrm{T}}^{\mathrm{miss}} < 200\,\mathrm{GeV}$ (bottom). . . . . 201

10.11 Comparison of the shapes of the Higgs boson candidate invariant mass $m_{jj}$ for the multijet background in the multijet-enriched region and the signal region. The shapes are obtained by subtracting all other simulated background processes from the data. The distributions are shown in the bins $150\,\text{GeV} < E_{\text{T}}^{\text{miss}} < 200\,\text{GeV}$ (left), $150\,\text{GeV} < E_{\text{T}}^{\text{miss}} < 200\,\text{GeV}$ (right), $150\,\text{GeV} < E_{\text{T}}^{\text{miss}} < 200\,\text{GeV}$ (bottom). The error bands represent the statistical uncertainty only. . . . . 202

10.12 $E_{\text{T}}^{\text{miss,no}\mu}$ distributions for the 1 muon CR, positive (top) and negative (bottom) muon charge shown separately. The upper panel shows the comparison of data to the SM background expectation before (dashed lines) and after the background-only fit (solid histograms). The lower panel shows the ratio of the data to SM background expectations after the background-only fit, with the hatched band showing the systematic uncertainty. . . . . 207

10.13 $p_{\text{T}}^{\ell\ell}$ distribution for the 2 lepton CR. The upper panel shows the comparison of data to the SM background expectation before (dashed lines) and after the background-only fit (solid histograms). The lower panel shows the ratio of the data to SM background expectations after the background-only fit, with the hatched band showing the systematic uncertainty. . . . . 208

10.14 Expected median discovery significance $Z^{\text{exp}}$ (top) estimated with the Asimov dataset generated under the assumption of the nominal signal model ($\mu = 1$) and observed discovery significance (bottom) for the Z′-2HDM simplified model signals in dependence of Z′ mediator mass $m_{\text{Z}'}$ and CP-odd Higgs boson mass $m_{\text{A}}$. . . . . 209

10.15 $E_{\text{T}}^{\text{miss}}$ distribution for the SR. The upper panel shows the comparison of data to the SM background expectation before (dashed lines) and after the background-only fit (solid histograms). The expected distribution for a representative Z′-2HDM signal is overlaid (long-dashed line). The lower panel shows the ratio of the data to SM background expectations after the background-only fit, with the hatched band showing the systematic uncertainty. . . . . 210

10.16 Distributions of the Higgs boson candidate invariant mass $m_{jj}$ (resolved) and $m_J$ (merged) in the SR for the four $E_{\text{T}}^{\text{miss}}$ bins. The upper panels show a comparison of data to the SM expectation before (dashed lines) and after the background-only fit (solid histograms). The expected distribution for a representative Z′-2HDM signal is overlaid (long-dashed line) and scaled by factors of 1000 and 100 in the two lowest $E_{\text{T}}^{\text{miss}}$ bins. The lower panels show the ratio of the data to SM background expectations after the background-only fit, with the hatched band indicating the systematic uncertainty. . . . . 211

10.17 Exclusion contours at $95\,\%$ $CL_s$ for the Z′-2HDM simplified model in the $m_{Z'}$-$m_A$ plane for the fixed set of parameters $\tan\beta = 1.0$, $g_{Z'} = 0.8$, and $m_\chi = 100\,\text{GeV}$. The observed limits (solid line) are consistent with the expectation under the SM-only hypothesis (densely dashed line) within uncertainties (filled band). The observed exclusion contour from a previous ATLAS publication at $\sqrt{s} = 13\,\text{TeV}$ (dash-dotted line) [92] is overlaid. . . . . 213

10.18 Expected exclusion limit on the signal strength $\mu$ at $95\,\%$ $CL_s$ in dependence of $m_{Z'}$ for the Z′-2HDM simplified model for the fixed set of parameters $m_A = 500\,\text{GeV}$, $\tan\beta = 1.0$, $g_{Z'} = 0.8$, and $m_\chi = 100\,\text{GeV}$. The expected limit of this search (dashed line) using variable-radius (VR) track jets is compared against that of the search presented in Ref. [92] using fixed-radius (FR) track jets. The latter is scaled to $79.8\,\text{fb}$ and computed by only considering events with two $b$-jets. Other differences between the two searches include the suppression of the multijet background using the object-based $E_T^{miss}$ significance, reduced statistical uncertainties from the MC background simulation, and an improved $b$-tagging calibration for VR track jets. The lower panel shows the ratio of the expected limit obtained with VR track jets and FR track jets. . . . . 214

11.1 Production of dark matter particles $\chi$ and a dark Higgs boson $s$ through $s$-channel exchange of a new Z′ mediator. The dark Higgs boson is decaying to $b$-quarks. . . . . 218

11.2 Workflow for the RECAST reinterpretation of the $E_T^{miss} + h(b\bar{b})$ search. The signal preparation step is performed using centrally provided services for MC event generation, detector simulation, and event reconstruction of the new signal sample. The signal analysis is based on the RECAST framework services by capturing the analysis software and the associated workflow for performing the event selection and the evaluation of experimental systematic uncertainties on the signal estimate. The statistical inference combines the partial likelihood, which is constructed using the preserved data and background estimate, the signal estimate, and the theoretical systematic uncertainties on the signal. The latter are estimated using a simplified implementation of the analysis on particle level neglecting detector effects. . . . . 221

11.3 $E_T^{miss}$ distribution for the SR. The upper panel shows the comparison of data to the SM background expectation before (dashed lines) and after the background-only fit (solid histograms). The expected distribution for a representative 2MDM signal with $m_{Z'} = 1\,\text{TeV}$ and $m_s = 90\,\text{GeV}$ is overlaid (long-dashed line). The signal is scaled to an arbitrary cross-section of $356\,\text{fb}$ for visualisation. The lower panel shows the ratio of data to SM background expectations after the background-only fit, with the hatched band showing the systematic uncertainty. . . . . 222

11.4 Distributions of the Higgs boson candidate invariant mass $m_{jj}$ (resolved), $m_J$ (merged) in the SR for the four $E_{\mathrm{T}}^{\mathrm{miss}}$ bins. The upper panels show a comparison of data to the SM expectation before (dashed lines) and after the background-only fit (solid histograms). The expected distribution for a representative 2MDM signal with $m_{Z'} = 1\,\mathrm{TeV}$ and $m_s = 90\,\mathrm{GeV}$ is overlaid (long-dashed line). The signal is scaled to an arbitrary cross-section of $356\,\mathrm{fb}$ in the resolved category and $178\,\mathrm{fb}$ in the merged category for visualisation. The lower panels show the ratio of data to SM background expectations after the background-only fit, with the hatched band indicating the systematic uncertainty. . . . . 224

11.5 Upper $95\,\%$ $\mathrm{CL}_s$ exclusion limits on the signal strength $\mu$ for the 2MDM simplified model with parameters $m_\chi = 200\,\mathrm{GeV}$, $g_q = 0.25$, and $g_\chi = 1$ for different values of $m_{Z'}$ and $m_s$. The expected exclusion limits are shown at the top, while the observed exclusion limits are shown at the bottom. . . . . 225

11.6 Exclusion contours at $95\,\%$ $\mathrm{CL}_s$ for the 2MDM simplified model in the $m_{Z'}$-$m_s$ plane for the fixed set of parameters $m_\chi = 200\,\mathrm{GeV}$, $g_q = 0.25$, and $g_\chi = 1$. The observed limits (solid line) are consistent with the expectation under the SM-only hypothesis (densely dashed line) mostly within $\pm 2\sigma$ uncertainties (filled bands). . . . . 226

12.1 Illustrations of the merged and intermediate event topologies in the $E_{\mathrm{T}}^{\mathrm{miss}} + s(VV)$ search. . . . . 230

12.2 Overview of all regions and categories considered in the $E_{\mathrm{T}}^{\mathrm{miss}} + s(VV)$ search with their relative background composition. Each region is composed of the merged event topology category and the intermediate event topology category. The merged category is further divided in two $p_{\mathrm{T}}^V$ bins, where $p_{\mathrm{T}}^V$ denotes $E_{\mathrm{T}}^{\mathrm{miss}}$ in the signal region, $E_{\mathrm{T}}^{\mathrm{miss,no}\mu}$ in the 1 muon CR, and $p_{\mathrm{T}}^{\ell\ell}$ in the 2 lepton CR, respectively. . . . . 231

12.3 Flowchart illustrating the TAR jet algorithm. The input objects to the algorithm are shown in blue boxes. Figure adapted from Ref. [109]. . . 232

12.4 Jet mass resolution (top) and $D_2^{(\beta=1)}$ energy correlation ratio resolution (bottom) in simulated events with hadronically decaying W bosons. The resolution of TAR jet observables is compared to that of conventional large-radius jets. Figures adapted from Ref. [109]. . . . . 234

12.5 Dark Higgs boson candidate TAR jet substructure variables $\tau_{42}$ (top) and $\tau_{43}$ (bottom) for two $E_{\mathrm{T}}^{\mathrm{miss}} + s(VV)$ signal processes with $m_{Z'} = 1\,\mathrm{TeV}$ and $m_s = 160\,\mathrm{GeV}$ or $235\,\mathrm{GeV}$ and background processes. The simulated background processes are normalised to the theoretical prediction. The requirements on the SR merged category event selection are applied, except for the requirement on the variable which is shown. The cut value is indicated by a long-dashed line. . . . . 238

12.6 Correlation between the dark Higgs boson candidate mass $m_{VV}$ and the $N$-subjettiness ratio variables $\tau_{42}$ (top) and $\tau_{43}$ (bottom). The distributions are shown separately for events in which not all four partons are contained within the dark Higgs boson candidate TAR jet (left) and events in which all four partons are contained (right). The cut value used in the substructure requirements is indicated by a dashed line. 239

12.7 The product of detector acceptance and selection efficiency ($\mathcal{A} \times \varepsilon$) for the $s \to$ WW (top) and $s \to$ ZZ (bottom) signal processes with the Z′ boson mass $m_{\mathrm{Z}'} = 0.5\,\mathrm{TeV}, 1\,\mathrm{TeV}, 1.7\,\mathrm{TeV}$, shown in dependence on the dark Higgs boson mass $m_s$. The points are connected in order to guide the eye. . . . . 242

12.8 Distributions of the $\min \Delta\varphi(\mathrm{jets}_{1,2,3}, E_{\mathrm{T}}^{\mathrm{miss}})$ (left) and object-based $E_{\mathrm{T}}^{\mathrm{miss}}$ significance (right) variables, which define the multijet-suppression requirements, shown for the observed data (black dots), background processes (stacked histograms) scaled to their theoretical expectation, and two representative signal processes (red and blue dashed lines). The multijet background is estimated with MC simulated events. . . . . 244

12.9 Distributions of the dark Higgs boson candidate invariant mass in the 1 muon CR merged and intermediate categories after the background-only fit to the data. The upper panel shows the comparison of data to the SM background expectation before (dashed lines) and after the background-only fit (solid histograms). The lower panels display the ratio of data to SM expectations after the fit, with the hatched band expressing the systematic uncertainty. No $m_{VV}$ shape information in the CRs is considered in the fit. . . . . 249

12.10 Distributions of the dark Higgs boson candidate invariant mass in the 2 lepton CR merged and intermediate categories after the background-only fit to the data. The upper panel shows the comparison of data to the SM background expectation before (dashed lines) and after the background-only fit (solid histograms). The lower panels display the ratio of data to SM expectations after the fit, with the hatched band expressing the systematic uncertainty. No $m_{VV}$ shape information in the CRs is considered in the fit. . . . . 250

12.11 Expected median discovery significance $Z^{\mathrm{exp}}$ (top) estimated with the Asimov dataset generated under the assumption of the nominal signal model ($\mu = 1$) and observed discovery significance (bottom) for the 2MDM simplified model signals in dependence of the Z′ mediator mass $m_{\mathrm{Z}'}$ and the dark Higgs boson mass $m_s$. . . . . 251

12.12 Data and SM background post-fit yields stacked in each SR and CR category with the maximum likelihood estimators set to the conditional values of the combined signal and control region fit. The hatched uncertainty band includes simulation statistical uncertainties, experimental systematic uncertainties, and $V$ + jets theory modelling systematic uncertainties. The red line in the lower panel shows the ratio of the pre-fit to the post-fit background prediction. . . . . 253

12.13 Distributions of the dark Higgs boson candidate invariant mass in the SR merged and intermediate categories, after the background-only fit to the data. The upper panel shows the comparison of data to the SM background expectation before (dashed lines) and after the background-only fit (solid histograms). The lower panels display the ratio of data to SM expectations after the fit, with the hatched band expressing the systematic uncertainty. A representative 2MDM simplified model signal with $m_{Z'} = 1\,\text{TeV}$, $m_s = 160\,\text{GeV}$, $g_q = 0.25$, $g_\chi = 1$, and $m_\chi = 200\,\text{GeV}$ is overlaid. . . . . 254

12.14 Upper $95\,\%$ $\text{CL}_s$ limits on the signal strength $\mu$ of 2MDM simplified model signals in dependence of the dark Higgs boson mass $m_s$ for the fixed set of parameters $g_q = 0.25$, $g_\chi = 1$, and $m_\chi = 200\,\text{GeV}$ in the scenarios with Z′ boson mediator masses $m_{Z'} = 0.5\,\text{TeV}$ (top), $m_{Z'} = 1.0\,\text{TeV}$ (middle), and $m_{Z'} = 1.7\,\text{TeV}$ (bottom). The observed limits (solid line) are consistent with the expectation under the background-only hypothesis (dashed line) within the uncertainties (filled band), except for a small excess at $m_s = 160\,\text{GeV}$. . . . . 257

12.15 Exclusion contours at $95\,\%$ $\text{CL}_s$ for the 2MDM simplified model in the $m_{Z'}$-$m_s$ plane for the fixed set of parameters $g_q = 0.25$, $g_\chi = 1$, and $m_\chi = 200\,\text{GeV}$. The observed limits are encircled by the solid line, whereas the expected limits are indicated by the dashed line. The expected $\pm 1\sigma$ and $\pm 2\sigma$ uncertainties are shown as filled green and yellow bands. The observed value of the relic density from the Planck [301] measurements is obtained for $m_{Z'} = 850\,\text{GeV}$ (dotted line). The region on the right of the line corresponds to higher predicted relic density than these measurements. . . . . 258

13.1 Regions in the $m_{Z'}$-$m_\chi$ plane in the parameter space of the spin-1 Z′ mediator simplified model excluded at $95\,\%$ $\text{CL}_s$ for the choice of vector (top) and axial-vector (bottom) mediator mediator couplings $g_q = 0.25$, $g_\chi = 1$, $g_\ell = 0$. The dashed curve indicates combinations of mediator mass $m_{Z'}$ and dark matter particle mass $m_\chi$ which are consistent with the Planck [301] dark matter relic density measurements. The dotted line indicates the kinematic threshold where the mediator can decay on-shell into dark matter particles. The shading in the upper left corner indicates regions which are in tension with perturbative unitary considerations. Figures reproduced from Ref. [180]. . . . . 260

13.2 Regions in the $m_{Z'}$-$m_\chi$ plane in the parameter space of the spin-1 Z′ axial-vector mediator simplified model excluded at $95\,\%$ $CL_s$ for the choice of mediator couplings $g_q = 0.25$, $g_\chi = 1$, $g_\ell = 0$. The dashed curve indicates combinations of mediator mass $m_{Z'}$ and dark matter particle mass $m_\chi$ which are consistent with the Planck [301] dark matter relic density measurements. The dotted line indicates the kinematic threshold where the mediator can decay on-shell into dark matter particles. The shaded region in the upper left corner indicates combinations of mediator mass $m_{Z'}$ and dark matter particle mass $m_\chi$ which are in tension with the perturbative unitary considerations. Figure reproduced from Ref. [180]. . . . . 262
13.3 Exclusion contours at $95\,\%$ $CL_s$ for the $a$-2HDM simplified model in the two-dimensional $m_H$-$m_a$ plane for the fixed choice of parameters $\tan\beta = 1.0$, $m_\chi = 10\,\text{GeV}$, and $\sin\theta = 0.35$, due to various $E_T^{miss} + X$ searches and searches for invisible decays of the Higgs boson (H + invisible). The dashed grey regions at the top indicate the region where the width of any of the Higgs bosons exceeds $20\,\%$ of its mass. Figure reproduced from Ref. [40]. . . . . 264
13.4 Observed exclusion limits at $95\,\%$ $CL_s$ on the signal strength $\mu$ for the $a$-2HDM simplified model as a function of $\sin\theta$, shown for parameters corresponding to a low-mass scenario (top) and a high-mass scenario (bottom). Figures reproduced from Ref. [40]. . . . . 265
13.5 Exclusion limits at $95\,\%$ $CL_s$ on the signal strength $\mu$ for the $a$-2HDM simplified model as a function of $m_\chi$ for the fixed choices of the parameters $\tan\beta = 1.0$, $m_H = 600\,\text{GeV}$, $m_a = 250\,\text{GeV}$, and $\sin\theta = 0.35$. The relic density prediction by the $a$-2HDM simplified model is superimposed (long-dashed line). Figure reproduced from Ref. [40]. . . . . 266
13.6 Exclusion limits at $95\,\%$ $CL_s$ on the signal strength $\mu$ for the 2MDM simplified model as a function of $m_s$ for the fixed choices of the parameters $m_{Z'} = 1\,\text{TeV}$, $m_\chi = 200\,\text{GeV}$, $g_q = 0.25$, $g_\chi = 1$, and $\theta = 0.01$. . . . . 267

# List of Tables


3.1 Parameters in the $V/A$ simplified model . . . . . 47
3.2 Parameters in the $a$-2HDM simplified model . . . . . 48
3.3 Parameters in the Z′-2HDM simplified model . . . . . 49
3.4 Parameters in the two mediator dark matter simplified model . . . . . 51

5.1 Essential LHC parameters with their description and values during Run-2 operation [219]. . . . . 67

7.1 Cone size $\Delta R$ used for matching the muon track candidate with a reconstructed muon in the $\eta$–$\phi$, depending on the transverse momentum $p_{\mathrm{T}}$ and pseudorapidity $\eta$ of the reconstructed muon. . . . . 118
7.2 Event selection requirements . . . . . 120
7.3 Selection requirements on tag and probe muons . . . . . 120
7.4 Effect of the coincidence window optimisation in the forward TGC modules on the L1MU4 trigger rate and trigger efficiency $\varepsilon$ for muon triggers with different muon multiplicities. . . . . 122

8.1 List of the simulated background processes in searches for dark matter with heavy vector bosons with the event generators, PDF sets, parton shower models, set of tuned parameters (“tunes”), and the accuracy in QCD of the modelling and the cross-section. . . . . 133
8.2 Common definitions of small-radius jets. . . . . 136
8.3 Common definitions of jets used for boosted heavy boson reconstruction 137
8.4 Common definitions of electron candidates. . . . . 138
8.5 Common definitions of muon candidates. . . . . 138
8.6 Common definition of tau lepton candidates. . . . . 138

9.1 Parameters of the Z′ vector mediator simplified model in the $E_{\mathrm{T}}^{\mathrm{miss}} + V(q\bar{q})$ search. . . . . 142
9.2 Parameters of the $a$-2HDM simplified model in the $E_{\mathrm{T}}^{\mathrm{miss}} + V(q\bar{q})$ search. 143
9.3 List of the signal and background processes with the MC event generators, sets of PDFs and tunes used for their description in the $E_{\mathrm{T}}^{\mathrm{miss}} + V(q\bar{q})$ search. . . . . 145
9.4 Signal region event selection requirements employed in the $E_{\mathrm{T}}^{\mathrm{miss}} + V(q\bar{q})$ search. . . . . 155
9.5 Validation region event selection requirements employed in the $E_{\mathrm{T}}^{\mathrm{miss}} + V(q\bar{q})$ search. . . . . 157
9.6 1 muon control region event selection requirements employed in the $E_{\mathrm{T}}^{\mathrm{miss}} + V(q\bar{q})$ search. . . . . 159

9.7 2 lepton control region event selection requirements employed in the $E_{\mathrm{T}}^{\mathrm{miss}} + V(q\bar{q})$ search. . . . . 160
9.8 Background process normalisation uncertainties and luminosity uncertainty in the profile likelihood fit used to determine the efficiency of the $\min \Delta\varphi(\mathrm{jets}_{1,2,3}, E_{\mathrm{T}}^{\mathrm{miss}})$ requirement. . . . . 161
9.9 Theoretical systematic uncertainties on the normalisation of background processes in the $E_{\mathrm{T}}^{\mathrm{miss}} + V(q\bar{q})$ search. In the description of the jet flavour of $V$ + jets processes, light-flavour jets are abbreviated with $l \in \{\mathrm{u}, \mathrm{d}, \mathrm{s}\}$. . . . . 164
9.10 Relative scale, PDF, and tune uncertainties of dark matter signals in the vector mediator simplified model, which are obtained from studied on generator level. . . . . 166
9.11 Summary of all regions and kinematic distributions considered in the statistical analysis of the $E_{\mathrm{T}}^{\mathrm{miss}} + V(q\bar{q})$ search. . . . . 167
9.12 Expected median discovery significance $Z^{\mathrm{exp}}$ estimated with the Asimov dataset generated under the assumption of the nominal signal model ($\mu = 1$) and observed discovery significance $Z^{\mathrm{obs}}$ for vector mediator simplified model dark matter signals with $m_{\chi} = 1\,\mathrm{GeV}$ and the couplings $g_q = 0.25$, $g_{\chi} = 1$. . . . . 167
9.13 Expected and observed numbers of events in the merged event topology signal region for an integrated luminosity of $36.1\,\mathrm{fb}^{-1}$ and $\sqrt{s} = 13\,\mathrm{TeV}$. The background yields and uncertainties are shown after the profile-likelihood fit to the data. In addition, the expected event yield for a vector mediator model with $m_{\mathrm{Z}'} = 600\,\mathrm{GeV}$ and $m_{\chi} = 1\,\mathrm{GeV}$ is shown. The quoted background uncertainties include both the statistical and systematic contributions. . . . . 171
9.14 Expected and observed numbers of events in the resolved event topology signal region for an integrated luminosity of $36.1\,\mathrm{fb}^{-1}$ and $\sqrt{s} = 13\,\mathrm{TeV}$. The background yields and uncertainties are shown after the profile-likelihood fit to the data. In addition, the expected event yield for a vector mediator model with $m_{\mathrm{Z}'} = 600\,\mathrm{GeV}$ and $m_{\chi} = 1\,\mathrm{GeV}$ is shown. The quoted background uncertainties include both the statistical and systematic contributions. . . . . 173
9.15 Breakdown of expected signal strength uncertainties for three vector mediator simplified model signals each with $m_{\chi} = 1\,\mathrm{GeV}$ and (a) $m_{\mathrm{Z}'} = 200\,\mathrm{GeV}$, (b) $600\,\mathrm{GeV}$, and (c) $2000\,\mathrm{GeV}$. The estimate is based on the Asimov data set generated under the assumption of the nominal signal model. The production cross-section of signal (c) is scaled by a factor of 10. Each systematic uncertainty contribution is provided as the quadratic difference between the total uncertainty and the uncertainty obtained by setting the systematic uncertainty in question to its nominal value and excluding it thereby from the fit. Total denotes the quadrature sum of statistical and total systematic uncertainties. . . . . 174

10.1 Parameters of the Z′-2HDM simplified model in the $E_{\mathrm{T}}^{\mathrm{miss}} + \mathrm{h}(\mathrm{b\bar{b}})$ search.183

10.2 List of the signal and background processes with the MC event generators, sets of PDFs and tunes used for their description in the $E_{\mathrm{T}}^{\mathrm{miss}} + \mathrm{h}(\mathrm{b\bar{b}})$ search. . . . 184
10.3 List of the baseline event selection requirements employed in the $E_{\mathrm{T}}^{\mathrm{miss}} + \mathrm{h}(\mathrm{b\bar{b}})$ search. . . . 191
10.4 Signal region event selection requirements employed in the $E_{\mathrm{T}}^{\mathrm{miss}} + \mathrm{h}(\mathrm{b\bar{b}})$ search. . . . 194
10.5 1 muon control region event selection requirements employed in the $E_{\mathrm{T}}^{\mathrm{miss}} + \mathrm{h}(\mathrm{b\bar{b}})$ search. . . . 196
10.6 2 lepton control region event selection requirements employed in the $E_{\mathrm{T}}^{\mathrm{miss}} + \mathrm{h}(\mathrm{b\bar{b}})$ search. . . . 197
10.7 Event yields of the observed data, the simulated background processes, and their difference in the regions A, B, C, and D. . . . 200
10.8 Theoretical systematic uncertainties on the normalisation of background processes in the $E_{\mathrm{T}}^{\mathrm{miss}} + \mathrm{h}(\mathrm{b\bar{b}})$ search. . . . 205
10.9 Summary of all regions and kinematic distributions considered in the statistical analysis of the $E_{\mathrm{T}}^{\mathrm{miss}} + \mathrm{h}(\mathrm{b\bar{b}})$ search. . . . 206
10.10 Expected and observed numbers of events in the signal region for an integrated luminosity of $79.8\,\mathrm{fb}^{-1}$ and $\sqrt{s} = 13\,\mathrm{GeV}$. The background yields and uncertainties are shown after the profile-likelihood fit to the data. The quoted background uncertainties include both the statistical and the systematic contributions. . . . 208
10.11 Breakdown of expected signal strength uncertainties for three representative Z′-2HDM signal samples (a) $(m_{\mathrm{Z}'}, m_{\mathrm{A}}) = (0.6\,\mathrm{TeV}, 0.3\,\mathrm{TeV})$, (b) $(m_{\mathrm{Z}'}, m_{\mathrm{A}}) = (1.4\,\mathrm{TeV}, 0.6\,\mathrm{TeV})$, and (c) $(m_{\mathrm{Z}'}, m_{\mathrm{A}}) = (2.6\,\mathrm{TeV}, 0.3\,\mathrm{TeV})$. The effect is expressed as the relative uncertainty on the signal strength, assuming total cross-sections of (a) $452\,\mathrm{fb}$, (b) $3.75\,\mathrm{fb}$, and (c) $2.03\,\mathrm{fb}$. Each systematic uncertainty contribution is provided as the quadratic difference between the total uncertainty and the uncertainty obtained by setting the systematic uncertainty in question to its nominal value and excluding it thereby from the fit. Total denotes the quadrature sum of statistical and total systematic uncertainties. . . . 212

11.1 Parameters of the 2MDM simplified model in the searches for dark matter in association with a dark Higgs boson. . . . 219

12.1 List of the signal and background processes with the MC event generators, sets of PDFs and tunes used for their description in the $E_{\mathrm{T}}^{\mathrm{miss}} + s(VV)$ search. . . . 229
12.2 TAR jet definition in the $E_{\mathrm{T}}^{\mathrm{miss}} + s(VV)$ search . . . 233
12.3 List of the baseline selection requirements employed in the $E_{\mathrm{T}}^{\mathrm{miss}} + s(VV)$ search. . . . 236
12.4 List of the SR event selection requirements employed in the $E_{\mathrm{T}}^{\mathrm{miss}} + s(VV)$ search. . . . 241

12.5 Event yields for the simulated multijet background (dijet MC) and their product with the scale factor $SF^{multijet}$ in the SR merged and intermediate categories. The observed data and the corresponding statistical uncertainty are shown in comparison. . . . . 245
12.6 Theoretical systematic uncertainties on the normalisation of background processes in the $E_T^{miss} + s(VV)$ search. . . . . 246
12.7 Summary of all regions and kinematic distributions considered in the statistical analysis of the $E_T^{miss} + s(VV)$ search. . . . . 248
12.8 Expected and observed numbers of events in the merged event topology signal region with an integrated luminosity of $139\,\text{fb}^{-1}$ and $\sqrt{s} = 13\,\text{GeV}$. The background yields and uncertainties are shown after the profile-likelihood fit to the data. The quoted background uncertainties include both the statistical and systematic contributions. . . . . 252
12.9 Breakdown of expected signal strength uncertainties for three representative 2MDM signal samples with $m_{Z'} = 1\,\text{TeV}$ and (a) $m_s = 160\,\text{GeV}$, (b) $m_s = 235\,\text{GeV}$, and (c) $m_s = 310\,\text{GeV}$. The effect is expressed as the relative uncertainty on the signal strength, assuming total cross-sections of (a) $214\,\text{fb}$, (b) $53\,\text{fb}$ fb, and (c) $19\,\text{fb}$. Each systematic uncertainty contribution is provided as the quadratic difference between the total uncertainty and the uncertainty obtained by setting the systematic uncertainty in question to its nominal value and excluding it thereby from the fit. Total denotes the quadrature sum of statistical and total systematic uncertainties. . . . . 255

# Acknowledgements

As every good story comes to an end, so does the scientific narrative of this dissertation. Now it is time to let the protagonist of the story — the elusive dark matter — step back into darkness and leave the stage to all the people who contributed in one way or another to this dissertation. There are many people whom I would like to thank in particular.

First of all, I want to thank Oliver Kortner for supervising my PhD. Already at the time of my master thesis, your enthusiasm and guidance let me grow personally and as a scientist. You taught me to find something that interests me and fully engage in it. I am thankful for your trust and your support in giving me the opportunity of pursuing my research interests. No less, I want to thank Sandra Kortner for all our insightful discussions, always keeping an open door, and supporting my work in every conceivable way. Further, I am thankful for providing many opportunities to visit summer schools, present my research at conferences, and enabling frequent visits to CERN.

Thank you to Peter Fierlinger and Norbert Kaiser for agreeing to be on my dissertation committee as a second examiner and the head of the committee, respectively.

I wish to express my gratitude towards Siegfried Bethke, Hubert Kroha, and the International Max Planck Research School on Elementary Particle Physics under the coordination of Frank Steffen for providing a productive environment for my research at the Max-Planck-Institute for Physics in Munich.

Patrick Rieck's support deserves special mention. Our collaboration was most enjoyable and formative, thanks to your no-nonsense approach to physics analysis. Your supervision provided an ideal transition from an academic apprenticeship in my first days towards learning from your constructive criticism of my later work in your role as a JDM subgroup convener. Furthermore, I thank you for reading and providing comments on selected chapters of this dissertation.

The field of high-energy physics is stimulating not only because of the research itself but also because of getting to collaborate with talented and engaging colleagues. I want to thank Oleg Brandt for his mentoring and thank him and Christopher Lester for the hospitality granted at the Cavendish Laboratory. Equally, I am thankful for the chats about physics and the advice from Shih-Chieh Hsu. Sam Meehan's honest and unbounded enthusiasm about physics and so many other things lifted my spirit more than once and set an example to look up to.

The work presented in this dissertation was conducted in collaboration with many other researchers. I thank Patrick Rieck, Jike Wang, Katharina Behr, Helene Genest, Frank Filthaut, Shih-Chieh Hsu, Stanislava Sevova, and Oleg Brandt for their work as analysis contacts in coordinating the searches for dark matter presented in this

thesis. During my work on these searches, I encountered many persons who taught me about physics analysis and with whom I engaged in joint research. In particular, I enjoyed the collaboration with Junpei Maeda, Xuanhong Lou, Lailin Xu, Kevin Bauer, Krisztian Peters, Koji Terashi, Andrea Matic, Veronica Fabiani, Dilia Portillo, Ruth Pöttgen, Pai-hsien Jennifer Hsu, Lukas Heinrich, Fabrizio Napolitano, Stany Sevova, Danika MacDonell, Cong-qiao Li, Flavia Dias, Jason Veatch, Philipp Mogg, Jeanette Lorenz, Lauren Tompkins, Ning Zhou, Jay Chan, Anindya Ghosh, Jon Burr, Dan Guest, and Spyridon Argyropoulos.

The days at the Max-Planck-Institute were filled with life by Max-Goblirsch-Kolb, Felix Müller, Natascha Savic, Nicolas Köhler, Tom McCarthy, Stefan Maschek, Dominik Duda, Davide Cieri, Nina Wenke, and Michael Holzbock. My wonderful office-mates Katharina Ecker, Verena Walbrecht, Andreas Hönle, and frequent guest Johannes Junggeburth not only endured my moods which directly reflected on the loudness of my keyboard but also provided the best company I could wish for.

My friends Matthias Mader, Andreas Rauscher, Agnes Köhler, Christopher Mittag, Vitaly Wirthl, Christoph Manß, Jan-Thorge Schindler, Daniel Rosenblüh, Wolfgang Neumeyer, Felix Monninger and Sarah Park provided me with welcome distraction and continue to remind me that there is more to life than doing physics.

Lastly, I want to thank my entire family, all aunts, uncles, and cousins who took an interest in what I was doing over the last four years. In particular, my aunt Waltraud, whose literacy knows no bounds, revealed the most beautiful books to me and kindled my interest in science. All this work would not have been possible without the loving and unwavering support of my parents Karin and Richard. I cannot thank you enough for everything you have done for me. You taught me to never stop learning, never give up quickly, and follow my interests.

Finally, I want to thank you, Denise, for your kindness, your patience, and your love. I am glad to have you in my life.

# Colophon

This dissertation was typeset with LaTeX $2_\varepsilon$. It uses the *Clean Thesis* style developed by Ricardo Langner (`http://cleanthesis.der-ric.de/`).

The majority of the figures in this dissertation were created using a number of PYTHON packages, including UPROOT, NUMPY, SCIPY, MATPLOTLIB, ATLAS_MPL_STYLE, and SEABORN. Some figures were created using the ROOT analysis framework.